Mesh Reduction Methods

BEM/MRM XXXI

EDITOR:
C.A. BREBBIA

WIT PRESS

THIRTY-FIRST WORLD CONFERENCE ON BOUNDARY ELEMENTS AND OTHER MESH REDUCTION METHODS

BEM/MRM XXXI

CONFERENCE CHAIRMAN

C.A. BREBBIA
Wessex Institute of Technology, UK

INTERNATIONAL SCIENTIFIC ADVISORY COMMITTEE

J-T. Chen
A.H-D. Cheng
G. De Mey
V.G. DeGiorgi
E. Divo
J. Dominguez
G. Fasshauer
A.N. Galybin
L. Gaul
G.S. Gipson
M.S. Ingber
D.B. Ingham
M. Kanoh
A.J. Kassab
J.T. Katsikadelis
V. Leitao
G-R. Liu
G.D. Manolis
W.J. Mansur
T. Matsumoto
K. Onishi
D. Poljak
V. Popov
H. Power
P. Prochazka
J.J. Rencis
T.J. Rudolphi
B. Sarler
E. Schnack
A.P.S. Selvadurai
L. Škerget
V. Sladek
S. Syngellakis
A. Tadeu
J. Trevelyan
W.S. Venturini
O. von Estorff
L.C. Wrobel
T. Wu
B. Yeigh
S-P. Zhu

Organised by
Wessex Institute of Technology, UK

Sponsored by
International Journal of Engineering Analysis with Boundary Elements (EABE)

WIT Transactions

Transactions Editor

Carlos Brebbia
Wessex Institute of Technology
Ashurst Lodge, Ashurst
Southampton SO40 7AA, UK
Email: carlos@wessex.ac.uk

Editorial Board

Mesh Reduction Methods

BEM/MRM XXXI

Editor

C.A. Brebbia
Wessex Institute of Technology, UK

WIT*PRESS* **Southampton, Boston**

Editor:

C.A. Brebbia
Wessex Institute of Technology, UK

Published by

WIT Press
Ashurst Lodge, Ashurst, Southampton, SO40 7AA, UK
Tel: 44 (0) 238 029 3223; Fax: 44 (0) 238 029 2853
E-Mail: witpress@witpress.com
http://www.witpress.com

For USA, Canada and Mexico

Computational Mechanics Inc
25 Bridge Street, Billerica, MA 01821, USA
Tel: 978 667 5841; Fax: 978 667 7582
E-Mail: infousa@witpress.com
http://www.witpress.com

British Library Cataloguing-in-Publication Data

A Catalogue record for this book is available
from the British Library

ISBN: 978-1-84564-197-9
ISSN: (print) 1746-4064
ISSN: (on-line) 1743-355X

The texts of the papers in this volume were set individually by the authors or under their supervision. Only minor corrections to the text may have been carried out by the publisher.

Printed in Great Britain by Athenaeum Press Ltd

Preface

The success and vitality of Boundary Element research continues to surprise not only all newcomers to the technique but even researchers like myself who have been deeply committed to its development since the very beginning.

The term *Boundary Elements* was coined in 1977 together with the methodology presented in a paper that I wrote with Jose Dominguez and which was published in the *International Journal of Applied Mathematical Modelling*. The paper was the culmination of an effort to link the then recent developments in finite elements with the boundary integral theory. This work set up the basis for the boundary element method as we know it, even providing the notation now widespread in the literature. It also consolidated a series of ideas related to mixed type variational statements, which were essential to pave the way for applications of boundary integral equations beyond the limitations of linearity.

Boundary integral techniques were able to expand their range of applications through their interpretation in terms of BEM. This was the result of cross fertilisation between the Russian school, the mixed principles developed at MIT and the computational advances of the UK Group.

The simplicity and elegance of BEM led to our awareness of the potentialities of the method and the realisation that integral equations were also open to experimentation and approximations.

This was conducive to a new type of development, typical of which was the Dual Reciprocity Method, a totally different conceptual approach. DRM not only applied the novel idea of using localised particular solutions but also allowed for them to be approximated. The fortunate discovery that they worked well with radial basis functions was also of great importance for the development of a whole new generation of meshless methods.

In parallel to the DRM developments, work was proceeding in other ways to transfer internal effects to the boundary using exact solutions, i.e. the Green's functions themselves. The generalisation of that concept led to the development of the Multiple Reciprocity Method. The beauty of this method is that it led not just to meshless domains but that also bypassed the need to have any internal nodes as in the case of DRM. The limitation of requiring analytical expression for the internal terms led however to lack of sustained interest in the MRM, which was seen as less versatile than DRM.

Many other approaches have been put forward following those basic ideas as evidenced by the numerous papers on meshless methods that continue to be published in the *International Journal of Engineering Analysis with Boundary Elements*.

The next stage will be for one or more of the meshless methods to achieve maturity and become a practical tool, in much the same way as classical BEM. The papers published in this book dealing with mesh reduction methods demonstrate their continuous evolution and the possibility of having reliable and robust meshless techniques in engineering practice in the future.

It is always a source of personal pleasure for me to see the way in which the original BEM ideas continue to develop in the hands of new researchers as well as our senior colleagues.

The quality and originality of the papers cited in this book is a demonstration of the continuous evolution of BEM research.

As Editor of this Volume, I am grateful to all contributors for the quality of their papers as well as to those colleagues who helped to review them.

Carlos A. Brebbia
New Forest, 2009

Contents

Section 4: Advanced structural applications

Section 5: Damage mechanics and fracture

Section 6: Dynamics and vibrations

Section 7: Fluid flow

Section 8: Electrical engineering and electromagnetics

Section 1
Advanced formulations

This page intentionally left blank

Multipole expansion BEM for simultaneous Poisson's equations

T. Matsumoto, T. Takahashi & S. Taniguchi
Department of Mechanical Science and Engineering,
Nagoya University, Japan

Abstract

A boundary element method for simultaneous Poisson's equations is presented to solve large scale problems governed by Poisson's equation using multipole expansions of the fundamental solutions. Original Poisson's equation is approximated a set of Poisson's equations and an integral representation for the set of differential equations is derived. The fundamental solutions of the coupled Poisson equations consist of the fundamental solution of Laplace's equation, biharmonic function, and triharmonic function. Multipole expansions of these fundamental solutions are used in the evaluation of the boundary integral equations. The effectiveness of the present formulation is demonstrated through a numerical example.
Keywords: Poisson's equation, fundamental solution, multipole expansion, source distribution.

1 Introduction

Poisson's equation is a good starting point for analyses of potential problems with inhomogeneous material parameters [1]. The integral representation of Poisson's equation has a domain integral term originated from the source term. To avoid the domain discretization, the domain integral can be converted to boundary integrals by means of the dual reciprocity method (DRM) [2] or the multiple reciprocity method (MRM) [3]. In the DRM, the value of the source term at an arbitrary point in the domain is approximated with a linear combination of radial basis functions (RBF) whose collocation points are placed in the domain and on the boundary. In order to convert the domain integral term originated from the source term of Poisson's equation, particular solutions corresponding to the radial basis function are required. Also, the coefficients of the source term approximation have to be deter-

mined in advance by collocation method which requires fully populated matrix to solve and is unstable for large scale problems. On the other hand, MRM requires particular solutions for the sources corresponding to a series of fundamental solutions. By using these particular solutions, the original domain integral term can be converted to a series of boundary integrals and a domain integral. Ochiai proposed a variant of MRM, called triple reciprocity BEM [4, 5], which applies the reciprocity formulation only three times. In this method, instead of using the correct values of the derivatives of the source, they are roughly estimated to be zero. The error of the derivative of the source on the boundary is modified by using the values of the source at collocation points in the domain instead.

For large-scaled problems, the fast multipole methods (FMM) may also be utilized for those governed by Poisson's equation. To circumvent the evaluation of the domain integrals in applying FMM for Poisson's equation, MRM based approach is more straight-forward in applying FMM, because only the multipole expansions of the higher order fundamental solutions found in the boundary integrals are required in the process.

In this study, we consider Poisson's equation and approximate the source term in terms of simultaneous coupled Poisson's equations. Using the fundamental solutions of the simultaneous Poisson's equations, a set of boundary integral equations, equivalent to those proposed by Ochiai, is derived. The fundamental solutions of the coupled Poisson equations consist of the fundamental solution of Laplace's equation, biharmonic function, and triharmonic function. Multipole expansions of them are used in the evaluation of the boundary integral equations. The resulting set of boundary integral equations are evaluated numerically by using the multipole expansions of the fundamental solutions. The effectiveness of the present formulation is demonstrated through a simple numerical example.

2 A boundary only integral formulation for Poisson's equation

Consider a potential problem governed by Poisson's equation

$$\nabla^2 \phi_1(x) + \phi_2(x) = 0, \qquad x \in V \tag{1}$$

with the boundary condition

$$\phi_1(x) = \bar{\phi}_1(x), \quad x \in S_\phi, \tag{2}$$

$$q_1(x) = \frac{\partial \phi_1(x)}{\partial n} = \bar{q}_1(x), \quad x \in S_q, \tag{3}$$

where V is the domain and $S = S_\phi \cup S_q$ is its boundary, $\phi_1(x)$ denotes the potential and $\phi_2(x)$ the source term. Also, $q_1(x) = \partial \phi_1(x)/\partial n$ is the outward normal derivative of $\phi_1(x)$ to the boundary; $\bar{\phi}_1$ and $\bar{q}_1$ are given functions prescribed on the specified boundaries, respectively.

We assume that the source term $\phi_2(x)$ is also assumed to be known both in V and on S.

Now, we assume the source term $\phi_2(x)$ is the solution of the following coupled Poisson equations:

$$\left.\begin{aligned} &\nabla^2\phi_2(x) + \phi_3(x) = 0, \\ &\nabla^2\phi_3(x) + \sum_{k=1}^{M} \alpha^k \delta(x - z^k) = 0, \end{aligned}\right\} \tag{4}$$

where z^k, $k = 1, 2, \ldots, M$ are internal collocation points as shown in Figure 1, and α^k, $k = 1, 2, \ldots, M$ are unknown constants.

The boundary conditions for eqn (4) can be assumed as [4, 5]

$$\phi_2(x) = \bar{\phi}_2(x), \quad x \in S, \tag{5}$$

$$\phi_3(x) = -\nabla^2\phi_2(x) = 0, \quad x \in S. \tag{6}$$

By combining eqns (1) and (4), we have a set of Poisson's equations to be solved, as follows:

$$\left.\begin{aligned} &\nabla^2\phi_1(x) + \phi_2(x) = 0, \\ &\nabla^2\phi_2(x) + \phi_3(x) = 0, \\ &\nabla^2\phi_3(x) + \sum_{k=1}^{M} \alpha^k \delta(x - z^k) = 0 \end{aligned}\right\} \tag{7}$$

with the conditions as a combination of eqns (2), (3), (5) and (6):

$$\left.\begin{aligned} &\phi_1(x) = \bar{\phi}_1(x), \quad x \in S_\phi, \\ &q_1(x) = \frac{\partial\phi_1(x)}{\partial n} = \bar{q}_1(x), \quad x \in S_q, \\ &\phi_2(x) = \bar{\phi}_2(x), \quad x \in S,\ V, \\ &\phi_3(x) = -\nabla^2\phi_2(x) = 0, \quad x \in S. \end{aligned}\right\} \tag{8}$$

The integral representations for the simultaneous Poisson's equations (7) are derived by starting from the following weighted residual form:

$$\int_V \phi^*_{1m}(x,y)(\nabla^2\phi_1(x) + \phi_1(x))\, dV_x + \int_V \phi^*_{2m}(x,y)(\nabla^2\phi_2(x) + \phi_3(x))\, dV_x + \int_V \phi^*_{3m}(x,y) \left(\nabla^2\phi_3(x) + \sum_{k=1}^{M} \alpha^k \delta(x - z^k)\right) dV_x = 0, \tag{9}$$

where $\phi^*_{im}(x,y)$ $(i, m = 1, 2, 3)$ are weighting functions.

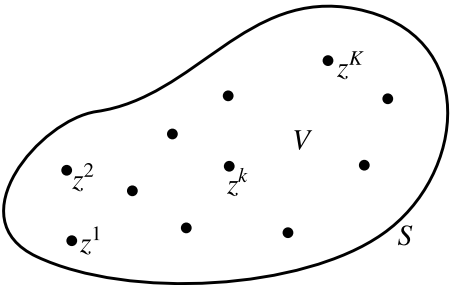

Figure 1: Domain, boundary and internal collocation points.

By integrating eqn (9) by parts repeatedly, we obtain

$$\sum_{i=1}^{3}\left\{\int_S \phi^*_{im}(x,y)q_i(\mathbf{x})\,dS_x - \int_S q^*_{im}(x,y)\phi_i(x)\,dS_x\right\}$$
$$+\int_V \nabla^2\phi^*_{1m}(x,y)\phi_1(x)\,dV_x$$
$$+\int_V \{\nabla^2\phi^*_{2m}(x,y)+\phi^*_{1m}(x,y)\}\phi_2(x)\,dV_x$$
$$+\int_V \{\nabla^2\phi^*_{3m}(x,y)+\phi^*_{2m}(x,y)\}\phi_3(x)\,dV_x + \sum_{k=1}^{M}\alpha^k\phi^*_{3m}(z^k,y) = 0. \quad (10)$$

We now consider particular solutions of the following adjoint form of the original simultaneous Poisson's equations, eqn (4), as the weighting functions $\phi^*_{im}(x,y)$.

$$[L][u^*] + [I]\delta(\mathbf{x}-\mathbf{y}) = \begin{bmatrix}\nabla^2 & 0 & 0\\ 1 & \nabla^2 & 0\\ 0 & 1 & \nabla^2\end{bmatrix}\begin{bmatrix}\phi^*_{11} & \phi^*_{12} & \phi^*_{13}\\ \phi^*_{21} & \phi^*_{22} & \phi^*_{23}\\ \phi^*_{31} & \phi^*_{32} & \phi^*_{33}\end{bmatrix} + [I]\delta(x-y) = 0, \quad (11)$$

where $[\phi^*] = \phi^*_{im}(x,y)C[I]$ denotes the unit matrix and $\delta(x-y)$ is Dirac's delta function.

By applying the property of Dirac's delta function, the second and third terms of eqn (10) becomes

$$\int_V \nabla^2\phi^*_{1m}(x,y)\phi_1(x)\,dV_x + \int_V \{\nabla^2\phi^*_{2m}(x,y)+\phi^*_{1m}(x,y)(x)\}\phi_2(x)\,dV_x$$
$$+\int_V \{\nabla^2\phi^*_{3m}(x,y)+\phi^*_{2m}(x,y)(x)\}\phi_3(x)\,dV_x$$
$$= -\phi_m(y). \quad (12)$$

Substituting eqn (12) into (10), we finally obtain an integral representation of eqn (7), as follows:

$$c(y)\phi_m(y) = \sum_{i=1}^{3} \left\{ \int_S \phi^*_{im}(x,y) q_i(x) dS_x - \int_S q^*_{im}(x,y)\phi_i(x) dS_x \right\} + \sum_{k=1}^{M} \alpha^k \phi^*_{3m}(z^k, y), \tag{13}$$

where $c(y) = 1$ for $y \in V$ and $c(y) = \frac{1}{2}$ for y located on the smooth part of S.

The fundamental solutions ϕ^*_{im} are obtained in the form

$$[\phi^*] = [L]^c \Phi(x,y), \tag{14}$$

where $[L]^c$ is the cofactor of $[L]$, and $\Phi(x,y)$ is the fundamental solution for the determinant operator of $[L]$, i.e.,

$$\det[L]\ \Phi(x,y) + \delta(x-y) = 0. \tag{15}$$

Then, finally, $[\phi^*]$ is obtained as follows:

$$[\phi^*] = \begin{bmatrix} \dfrac{1}{4\pi r} & 0 & 0 \\ \dfrac{-r}{8\pi} & \dfrac{1}{4\pi r} & 0 \\ \dfrac{r^3}{96\pi} & \dfrac{-r}{8\pi} & \dfrac{1}{4\pi r} \end{bmatrix}. \tag{16}$$

where $r = |x - y|$.

3 Discretization of the boundary integral equation

Discretizing eqn (13) by using N constant elements gives

$$\frac{1}{2}\phi_m(y^l) = \sum_{i=1}^{3} \sum_{j=1}^{N} \left\{ \left(\int_{S_j} \phi^*_{im}(x,y^l)\, dS \right) q_i(x^j) - \left(\int_{S_j} q^*_{im}(x,y^l)\, dS \right) \phi_i(x^j) \right\} + \sum_{k=1}^{M} \alpha^k \phi^*_{3m}(z^k, y^l), \tag{17}$$

where x^j and y^l denote the centers of geometry of elements j and l, respectively.

In eqn (17), the unknowns are either of $\phi_i(x^j)$ and $q_i(x^j)$, and α^k, and their total number becomes $3N + M$.

Although from eqn (17), we obtain $3N$ equations, we still need M equations in order to solve for $3N + M$ unknowns. Therefore, we consider additional M

collocation points in the domain and specify the values for the source term $\phi_2(z^k)$, $(k = 1, \ldots, M)$. It is achieved by using the component for $m = 2$ of eqn (17) and substituting z^k, $(k = 1, \ldots, M)$ for y^l as

$$\phi_2(z^l) = \sum_{i=1}^{3}\sum_{j=1}^{N}\left\{\left(\int_{S_j} \phi^*_{i2}(x^j, z^l)\, dS\right) q_i(x^j) - \left(\int_{S_j} q^*_{i2}(x^j, z^l)\, dS\right) \phi_i(x^j)\right\} + \sum_{k=1}^{M} \alpha^k \phi^*_{32}(z^k, z^l). \tag{18}$$

The final linear algebraic equations can be written, by collecting all the unknown quantities on the left-hand side, as

$$[A]\{x\} = \{b\}, \tag{19}$$

where $[A]$ is the coefficient matrix, $\{x\}$ the unknown vector, and $\{b\}$ is the right-hand side vector calculated from known quantities. Equation (19) is solved by using the multipole expansions of the fundamental solutions and an iterative solver. The multipole expansion of the components of $\phi^*_{11}(= \phi^*_{22} = \phi^*_{33})$ is given as follows:

$$\frac{1}{4\pi r} = \frac{1}{4\pi|x-y|} = \frac{1}{4\pi}\sum_{n=0}^{\infty}\sum_{m=-n}^{n} R_{n,m}(\overrightarrow{Ox})\overline{S_{n,m}}(\overrightarrow{Oy}), \quad |\overrightarrow{Ox}| < |\overrightarrow{Oy}|, \tag{20}$$

where $R_{n,m}$ and $S_{n,m}$ are defined as [6]

$$R_{n,m}(\overrightarrow{Ox}) = \frac{1}{(n+m)!} P_n^m(\cos\theta) e^{im\phi} r^n, \tag{21}$$

$$S_{n,m}(\overrightarrow{Ox}) = (n-m)! P_n^m(\cos\theta) e^{im\phi} \frac{1}{r^{n+1}}, \tag{22}$$

with the polar coordinates (r, θ, ϕ) of the point x. P_n^m is the associated Legendre functions. ϕ^*_{21}, ϕ^*_{32} and ϕ^*_{31} are also given as

$$\phi^*_{21} = \phi^*_{32} = -\frac{r}{8\pi} = -\frac{1}{8\pi}\sum_{n=0}^{\infty}\sum_{m=-n}^{n}\left\{\frac{|\overrightarrow{Ox}|^2 R_{n,m}(\overrightarrow{Ox})\overline{S_{n,m}}(\overrightarrow{Oy})}{2n+3}\,\frac{R_{n,m}(\overrightarrow{Ox})|\overrightarrow{Oy}|^2\overline{S_{n,m}}(\overrightarrow{Oy})}{2n-1}\right\} \tag{23}$$

$$\phi^*_{31} = \frac{r^3}{96\pi} = \frac{1}{96\pi}\sum_{n=0}^{\infty}\sum_{m=-n}^{n}\left\{\frac{3|\overrightarrow{Ox}|^4 R_{n,m}(\overrightarrow{Ox})\overline{S_{n,m}}(\overrightarrow{Oy})}{(2n+3)(2n+5)} - \frac{6|\overrightarrow{Ox}|^2 R_{n,m}(\overrightarrow{Ox})|\overrightarrow{Oy}|^2\overline{S_{n,m}}(\overrightarrow{Oy})}{(2n-1)(2n+3)} + \frac{3R_{n,m}(\overrightarrow{Ox})|\overrightarrow{Oy}|^4\overline{S_{n,m}}(\overrightarrow{Oy})}{(2n-3)(2n-1)}\right\}. \tag{24}$$

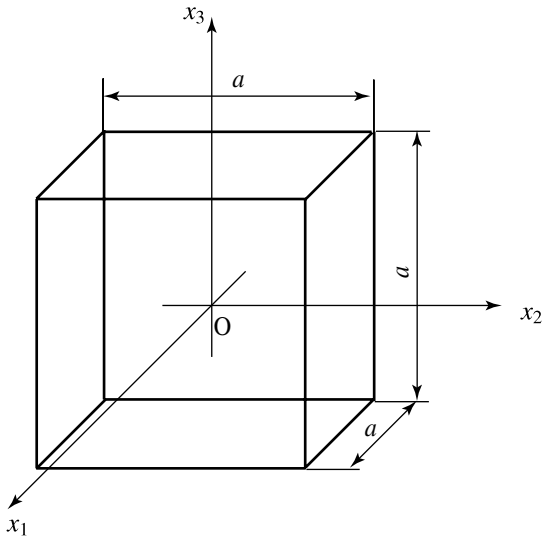

Figure 2: A cube model.

4 Numerical example

Consider a cubic region having an edge of $a = 10$ as shown in Figure 2. All sides of the cube are divided uniformly into 3072 triangular constant elements, and 45 internal collocation points are placed as shown in Figure 3. The boundary condition for $\phi_1(x)$ and the known distribution of $\phi_2(x)$ are given by

$$\phi_1(x) = \begin{cases} 0 & \text{at } x_3 = -5 \\ 100 & \text{at } x_3 = 5 \end{cases}, \tag{25}$$

$$q_1(x) = 0 \quad \text{at } x_1, x_2 = \pm 5, \tag{26}$$

$$\phi_2(x) = 10 \sin\Big(\frac{\pi}{5} x_3 + \pi\Big). \tag{27}$$

The infinite series of the multipole expansions of the fundamental solutions are truncated at 7th terms and GMRES is used as the iterative solver with the convergence criterion $\varepsilon = 10^{-5}$.

Figure 4 shows the results for $\phi_1(x_3)$ at the internal collocation points. The results obtained by the present approach show good agreements with the exact solutions.

5 Concluding remarks

A boundary element method for Poisson's equation has been presented. The source term is approximated with simultaneous coupled Poisson's equations. The funda-

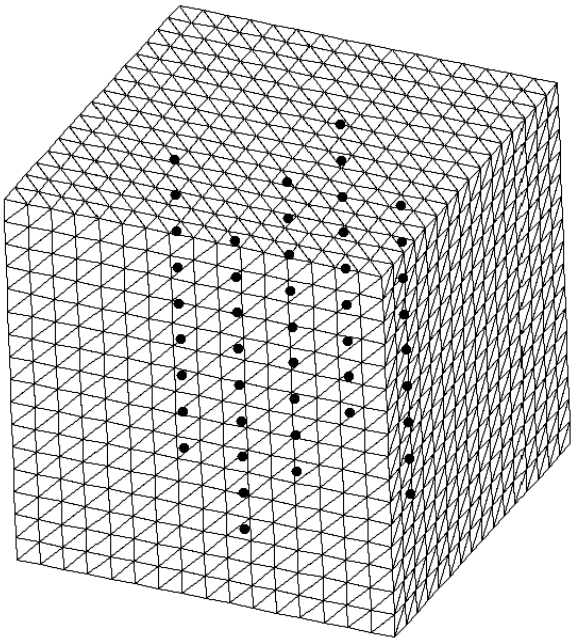

Figure 3: Boundary elements and internal collocation points.

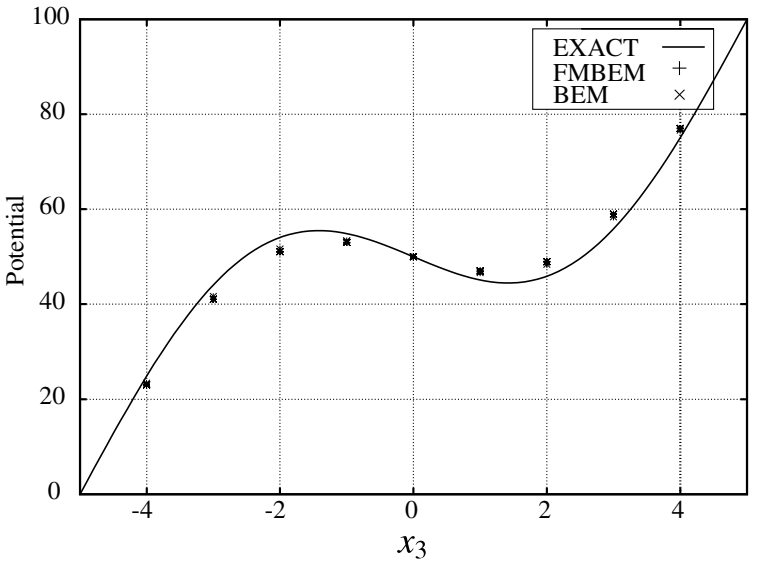

Figure 4: Result for ϕ_1 at internal points.

mental solutions of the coupled Poisson's equations have been derived and the corresponding boundary integral equation has been presented. The fundamental solutions of the coupled Poisson equations consist of the fundamental solution of Laplace's equation, biharmonic function, and triharmonic function. Multipole expansions of these fundamental solutions have been used in the evaluation of the boundary integral equations. The numerical test example has demonstrated the effectiveness of the present approach.

References

[1] Matsumoto, T., Guzik, A. & Tanaka, M., A boundary element method for analysis of thermoelastic deformations in materials with temperature dependent properties *International Journal for Numerical Methods in Engineering*, **64(11)**, pp. 1432–1458, 2005.

[2] Partridge, P.W., Brebbia C.A. & Wrobel, L.C., *The Dual Reciprocity Boundary Element Method*, Computational Mechanics Publications, Southampton, 1992.

[3] Nowak, A.J., *The Multiple Reciprocity Boundary Element Method*, Neves, A.C. (Ed.), Computational Mechanics Publications, Southampton, 1994 .

[4] Ochiai, Y., Three-dimensional steady thermal stress analysis by triple-reciprocity boundary element method, *International Journal for Numerical Methods in Engineering*, **63(12)**, pp. 1741–1756, 2005.

[5] Ochiai, Y., Sladek, V. & Sladek, J., Transient heat conduction analysis by triple-reciprocity boundary element method, *Engineering Analysis with Boundary Elements*, **30(3)**, pp. 194–204, 2006.

[6] Yoshida, K., Applications of Fast Multipole Method to Boundary Integral Equation Method, PhD Thesis, Kyoto Univ., Japan, 2001.

This page intentionally left blank

Numerical Green's function for a two-dimensional diffusion equation

C. A. B. Vasconcellos[1], M. A. C. Ferro[1], W. J. Mansur[2], F. S. Loureiro[2] & J. P. L. Santos[2]
[1]*Department of Fortification and Construction Engineering, Military Institute of Engineering, Brazil*
[2]*Department of Civil Engineering, COPPE/Federal University of Rio de Janeiro, Brazil*

Abstract

This paper presents a novel form to calculate Green's function by using a numerical method. In this paper, Green's function is calculated for the two-dimensional diffusion equation. The numerical Green's function is defined as Green's matrix that represents the domain of the problem to be solved in terms of the physical properties and geometrical characteristic. Green's matrix is the basis of the numerical method called 'Explicit Green's Approach' (ExGA) that allows explicit time marching with a time step larger than the one required by other methods found in the literature, without losing precision. The method uses Green's matrix which is determined numerically by the Finite Element Method (FEM). The paper presents one application in heat conduction and another in groundwater flow, demonstrating that the results are quite accurate when compared to analytical solutions and to other numerical solutions.

Keywords: Green's function, Green's matrix, ExGA, time integration, diffusion equation.

1 Introduction

Green's functions are very powerful tools for obtaining solutions to diffusion equation. They can also be applied to find solution of other phenomena which are described by the same type of equation, i.e., those that involve solution of diffusion-type partial differential equations. A Green's function (GF) is a basic solution of a specific differential equation with homogeneous boundary

conditions; for transient heat conduction, a GF describes the temperature caused by an instantaneous, local energy pulse. In addition to originating efficient numerical solution procedures, GF based methods also provide a better understanding of the nature of diffusion processes for heat conduction.

Besides, the application of GFs in diffusion equation has several advantages. First, it is a powerful and flexible method, since the derived GFs for a given geometry may be used in conjunction with a variety of initial and boundary conditions; second, a systematic procedure is available for obtaining GFs, i.e., once these functions are obtained and tabulated, they may be used without any effort spent on the details of their derivation; third, 1-D GFs may be used as building blocks to obtain 2- and 3-D solutions to suitable problems. The specifics of the multiplication process to obtain 2- and 3-D solutions are presented by Özişik [1].

Finding GFs corresponding to certain physical phenomena, possibly incorporated with suitably prescribed boundary data, is one of the fundamental subjects in mathematical physics. The knowledge of GFs can serve as a basic ingredient to construct the fields via superposition under distributed sources and general boundary data.

GFs have been used in the solution of equations of transient heat conduction for many decades, a classic text on the subject is the book by Carslaw and Jaeger [2], in which an introduction to the use of GFs based methods for heat conduction problems is presented. In that study they obtained the GFs through Laplace transforms. Other important reference concerning GFs is the book of Özişik [1] where the use and advantages of GFs based methods are described.

A short review about the Green's function can be found in Mansur *et al.* [3]. Moreover, in this article it is presented the ExGA method for linear transient heat conduction. Before that, this method had been presented to wave propagation equation by Mansur *et al.* [4]. Recently, Loureiro *et al.* [5] presented a hybrid time/Laplace integration method based on numerical Green's functions in conduction heat transfer, that utilizes the Stehfest and the Zakian Laplace inversion schemes to compute numerically Green's functions.

The framework proposed in this article includes a novel calculating form to GF using a numerical method. The numerical GF is defined as Green's matrix, that is the basis of numerical method called 'Explicit Green's Approach' (ExGA) that allows explicit time marching with a time step larger than the one required by other methods found in the literature, without losing precision. The method uses the Green's matrix that is determined numerically by the Finite Element Method.

The paper presents one application in heat conduction and another in groundwater flow, where it is shown that the results are quite accurate when compared to analytical solutions and to other numerical solutions

In the next section, a review and the mathematical background of the GF are shown. In section 3 Green's matrix and the ExGA method are presented. In section 4, two examples are discussed. Finally, in the last section, some conclusions about this work are presented.

2 Analytical Green's function

This section presents a discussion about the physical significance of the GF and a general expression for the solution of the diffusion equation with energy generation, non-homogeneous boundary conditions, and a given initial condition, in terms of the GF.

In this paper, we consider the following two-dimensional non-homogeneous initial boundary-value problem of heat conduction in homogeneous and isotropic medium:

$$\nabla^2 T(x,y,t) + \frac{1}{k} g(x,y,t) = \frac{1}{\alpha}\frac{\partial T(x,y,t)}{\partial t}, \text{ in } \Omega, \; t > 0, \tag{1}$$

$$k_i \frac{\partial T}{\partial n_i} + h_i T = h_i T_{\infty i} \equiv f_i(x,y,t), \quad \text{on } \Gamma, \; t > 0, \tag{2}$$

$$T(x,y,t) = T_0(x,y), \text{ in } \Omega, \; t = 0, \tag{3}$$

where ∇^2 is the two-dimensional Laplace operator, $\frac{\partial}{\partial n_i}$ denotes differentiation along the outward-draw normal to the boundary Γ_i, i = 1, 2,..., N; N being the number of continuous boundaries in the domain. For generality it is assumed that the generation term $g(x,y,t)$ and the boundary-condition function $f_i(x,y,t)$ vary with both position and time; and α (thermal diffusivity), T_∞ (external ambient temperature), k_i (thermal conductivity) and h_i (heat transfer coefficient) are treated as constants.

According to Özişik [1], the GF concerning (1)-(3) can be determined by considering the following auxiliary problem for the same domain Ω:

$$\nabla^2 G(x,y,t \,|\, x',y',\tau) + \frac{1}{k}\delta(x-x')\delta(y-y')\delta(t-\tau) = \frac{1}{\alpha}\frac{\partial G}{\partial t}, \; t > \tau, \tag{4}$$

$$k_i \frac{\partial G}{\partial n_i} + h_i G = 0, \quad t > 0, \tag{5}$$

Notice that the GF obeys the causality requirement which states that the GF is zero for $t < \tau$ [6]. Furthermore, the source term in (4) is a unit impulsive source for the two-dimensional problem considered here. The delta function $\delta(x-x')\delta(y-y')$ represents a line heat source located at (x',y'), while the delta function $\delta(t-\tau)$ indicates that it is an instantaneous heat source releasing its energy spontaneously at time $t = \tau$.

GF $G(x,y,t \,|\, x',y',\tau)$ for the two-dimensional represents the temperature at point (x,y) in the domain Ω and at time t due to an instantaneous point source of

unit strength, located at point (x',y'), releasing its energy spontaneously at time $t = \tau$.

The auxiliary problem satisfied by the GF is valid over the same domain Ω as the original physical problem presented by (1), but the boundary conditions given by (5) is the homogeneous version of the boundary conditions given by (2) and the initial condition is zero.

On the basis of this definition, the physical significance of GF may be interpreted as:

$$G(x, y, t \mid x', y', \tau) \equiv G(\text{effect} \mid \text{impulse}). \tag{6}$$

3 Numerical Green's function

The present section describes the Explicit Green's Approach for integrating the diffusion equation. The algorithm is based on the calculation of the GF in nodal coordinates by the finite element method. The spatial discretization, using the finite element method (FEM), of the two-dimensional diffusion equation can be represented in matrix form as (Hughes [7]):

$$[C]\{\dot{T}(t)\} + [K]\{T(t)\} = \{F(t)\}, \tag{7}$$

with the initial condition,

$$\{T(0)\} = \{T\}^0, \tag{8}$$

where [C] is the capacitance matrix, [K] is the thermal conductance matrix, and {F} is a vector of equivalent nodal heat loads [3].

Applying the Laplace transform to (7) (Boyce and DiPrima [8]), and following the procedure presented by Mansur *et al.* [3], the final expression of the vector temperature in terms of Green's matrix is:

$$\{T(t)\} = [G(t)][C]\{T(0)\} + \int_0^t [G(t-\tau)]\{F(\tau)\}d\tau. \tag{9}$$

GF is usually called impulsive response of the system, as it is explained in Özişik [9]. It can be obtained numerically from (7), considering homogeneous boundary conditions and an impulsive heat source applied at a source point, which coincides with a node of the space mesh. Then, Green's matrix can be obtained by the solution of the following system of ordinary differential equations in the time:

$$[C][\dot{G}(t)] + [K][G(t)] = [I]\delta(t), \tag{10}$$

with the initial condition,

$$[G(0)] = 0, \tag{11}$$

where [I] represents the identity matrix and δ(t) is the Dirac delta function.

The problem described by (10) is equivalent to the homogeneous initial value problem with application of a certain initial condition (see Özişik [9]). In the present work, it was verified that the correct equivalence is given by the problem presented below:

$$[C][G(t)] + [K][G(t)] = 0, \tag{12}$$

with the initial condition,

$$[G(0)] = [C]^{-1}. \tag{13}$$

Here Green's matrix is computed implicitly through the range [0,Δt] with the Crank–Nicolson scheme. It is worth to point out that the new method becomes more stable and accurate when a sub-step procedure is adopted to obtain the Green's matrix. If the capacitance matrix is lumped (diagonal), computing its inverse is fairly cheap.

Assuming that the time step is Δt the temperature solution vector at any time can be evaluated recursively as:

$$\{T(t)\} = [G]^{\Delta t}[C]\{T\}^t + \int_0^{\Delta t} [G(\Delta t - \tau)]\{F(t+\tau)\}d\tau. \tag{14}$$

Observe that the convolution integral of the above equation can be evaluated by any integral quadrature formulae. In the present work, the convolution integral is calculated by Newton–Cotes approximations with interpolation polynomials of order one (trapezoidal rule).

4 Numerical examples

In this section, two examples are presented to illustrate the methodology employed in this work. The objectives of the examples are to simulate two-dimensional diffusion problems with applications in heat conduction and groundwater flow. In the following analyses, the relation $(\Delta t)_{FEM} = (\Delta t)_{ExGA} / ss$ is adopted, so that *ss* stands for the number of sub-steps employed to compute the Green's matrix.

Example 1

In the first example a thin rectangular plate of sides a = 10.0 m and b = 8.0 m was considered. The adopted physical coefficients were α = 1.0 m^2/s, k = 1.0 W/^{o}C.m. The Green's matrix was determined by the FEM using 80 and

320 square elements for the spatial discretization and the finite difference method with Crank–Nicolson scheme for time integration. The ExGA method was compared to the FEM with the same spatial discretization and with the same implicit scheme in the time discretization used in the calculus of the Green's matrix, i.e., FEM-CN.

The initial condition is T(x,y,0) = 0.0 ºC over the entire domain. The boundaries condition are: q(x,0,t) = 0.0 W/m, q(0,y,t) = 10.0 W/m, T(x,b,t) = 300.0ºC and T(a,y,t) = 0.0ºC, as shown in fig. 1 below.

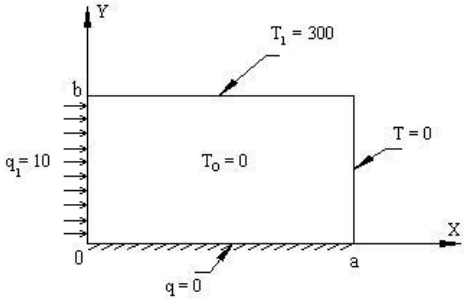

Figure 1: Domain, initial condition and boundaries conditions for example 1.

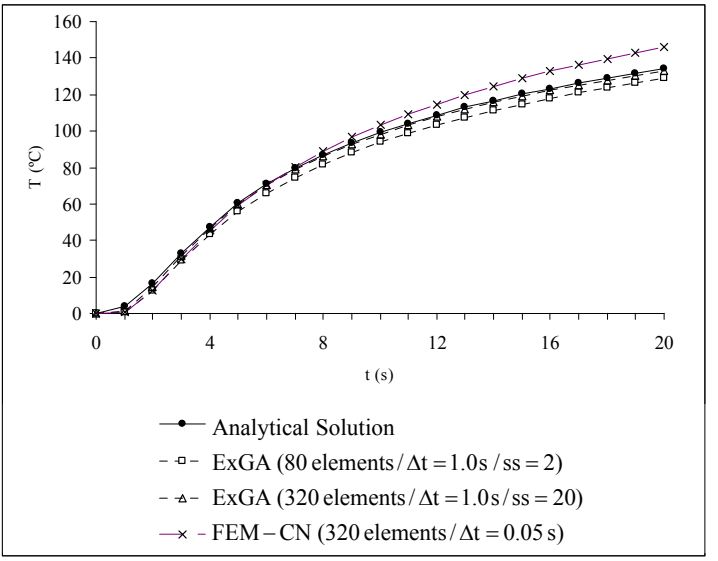

Figure 2: Temperature at the central point of domain of example 1.

Note that the boundary conditions are different on each side of the domain, which makes convergence more difficult. However, the ExGA method converges to the analytical solution when the mesh is refined from 80 to 320 elements. The

time step used by ExGA method was $\Delta t = 1.0$ s with 2 and 20 sub-steps to calculate Green's matrix, while $\Delta t = 0.05$ s was used by FEM-CN. The results are shown in fig. 2, where the ExGA method is compared with the analytical solution presented by Beck *et al* [10].

Example 2 – Theis problem

Consider a transient well drawdown problem. The well is discharging at a constant rate Q from an extensive confined aquifer where the potentiometric surface is initially horizontal, its hydraulic head being equal to h_0. This problem was solved analytically by Theis in 1935 [11] and the drawdown at a radius r from the well is shown in the classical book by Wang and Anderson [12].

The horizontal confined aquifer of this example, whose area is 2000 x 2000 m², has the following physical properties: T = 300 m²/day (transmissivity) and S = 0.002 (storage coefficient). The well is discharging at a constant flow equal to 2000 m³/day and their area of influence is marked in a tone of gray in fig.3. The initial condition of the problem is h_0 (x,y,0) = 10.0 m, and the boundaries conditions are zero flow on all sides of the aquifer.

Wang and Anderson [12] presented numerical solutions for this example using FDM and FEM methods, with the same spatial discretization ($\Delta x = \Delta y =$ 100.0 m) and the Crank–Nicolson scheme to carry out time marching with time step equal to $\Delta t = 0.01$ day.

In order to maintain the same conditions for comparison, the same mesh discretization was used for the ExGA method. Two simulations were carried out. In the first simulation we used the time step $\Delta t = 5.0$ days and 10 sub-steps in the calculation of the Green's matrix. These results are compared with the analytical Theis solution as depicted in fig. 4 for points located 100 m from the well.

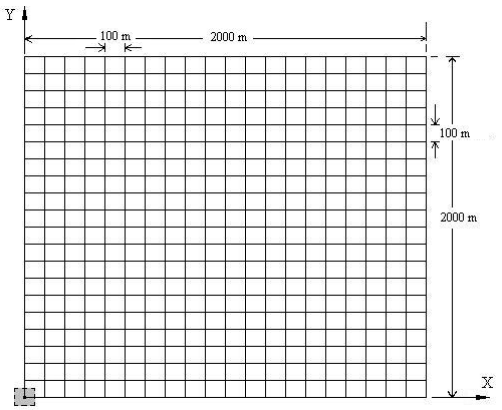

Figure 3: Confined aquifer – domain and spatial discretization.

In the second simulation, the final time of simulation is set to be equal to t = 13.12 days. Time steps $\Delta t = 0.01$ days were used in the FDM-CN and FEM-CN

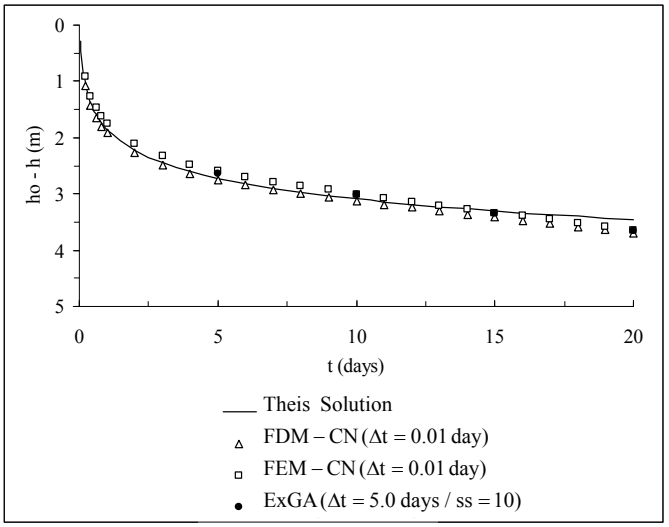

Figure 4: The time-drawdown curve to 100 m from the well.

Table 1: Results for r = 100 m and t = 13.12 days.

Method	Δt (days)	h_0 - h (m)	Relative errors (%)
FDM-CN	0.01	3.2582	0.80
FEM-CN	0.01	3.2170	0.47
ExGA	13.12	3.2798	1.47
ExGA	1.312	3.2169	0.47

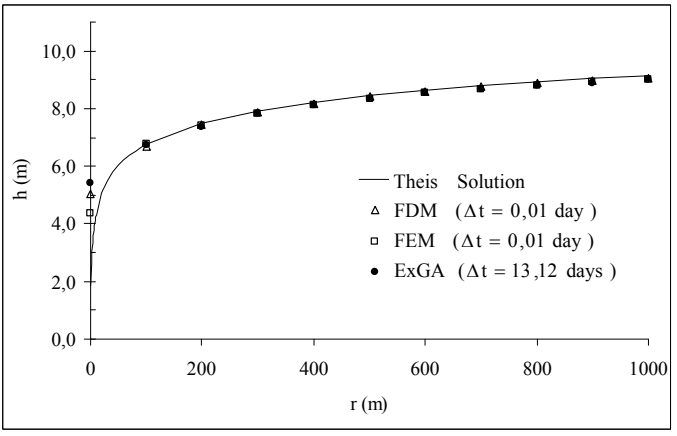

Figure 5: Hydraulic head versus distance of the well for t = 13.12 days.

methods, while time steps equal to $\Delta t = 13.12$ days (with 20 sub-steps) and $\Delta t = 1.312$ days (with 10 sub-steps) were used in the ExGA method.

Table 1 presents the results for the distance r = 100 m from the well, and their relative errors, considering the Theis Solution as reference, which in this case is equal to 3.2322 m. Fig. 5 shows, for t = 13.12 days, the cone of depression formed by the lowering of water level near the well due to the constant flow pump.

5 Conclusions

The results of the examples display the expected behavior of a robust numerical method. In all the studied cases, the ExGA method provided accurate results and converged to the correct answer with refinements that do not demand great computational efforts.

This work presented a new approach for the solution of diffusion equation with application in heat conduction and groundwater flow.

Note that the inverse of the capacitance matrix is an equivalent initial condition to the unitary pulse given by the Dirac delta function. If this were not possible, less accurate numerical Green's function would be obtained, and the ExGA method would not be competitive with the classic ones.

In the ExGA method, the temperature field is calculated explicitly on time through the Green's matrix which is determined by FEM using an implicit algorithm. The use of this implicit algorithm with sub-steps to compute Green's matrix increases the computational cost; however, this apparent disadvantage becomes a positive aspect since the unconditional stability property inherent to implicit methods, such as the Crank–Nicolson scheme, is transmitted through the Green's matrix to the ExGA method.

Thus, with sub-steps not too small, one obtains an explicit algorithm which for any practical purpose can be considered unconditionally stable. In the example 1, a time step 20 times bigger than that of the FEM was considered. Already in example 2 it becomes 1000 times bigger than these. In fact using sub-steps allow the time-step 'length' to be as large as one wishes, the only limitation being a good representation of the time response picture.

Finally, the present paper has presented that the ExGA method can be very suitable to multiple cases where only the load conditions (boundary or source) change while domain and physical properties remain unchanged, as in this case is possible to use the same Green's matrix for all analyses.

References

[1] Özişik, M. N. *Heat Conduction*. Wiley, New York, 1980.
[2] Carslaw, H.S. and Jaeger, J.C. *Conduction of Heat in Solids*, 2nd edition, Oxford University Press, 1959.
[3] Mansur, W. J., Vasconcellos, C.A.B., Zambrozuski, N.J.M. & Rotunno Filho, O.C., Numerical solution for the linear transient heat conduction

equation using an explicit Green's Approach. *International Journal of Heat and Mass Transfer*, 52, pp. 694–701, 2009.

[4] Mansur, W. J., Loureiro, F. S., Soares Jr. D. & Dors, C. Explicit time-domain approaches based on numerical Green's functions computed by finite differences - The ExGA family. *Journal of Computational Physics*, 227(1), pp. 851–870, 2007.

[5] Loureiro, F.S., Mansur, W. J. & Vasconcellos, C.A.B, A hybrid time/Laplace integration method based on numerical Green´s functions in conduction heat transfer. *Computational Methods in Applied Mechanical and Engineering*, accepted in 20 March 2009.

[6] Morse, P. M. & Feshbach, H. *Methods of Theoretical Physics*, volumes I and II. McGraw-Hill, New York, 1st edition, 1953.

[7] Hughes, T.J.R. *The Finite Element Method, Linear Static and Dynamic Finite Element Analysis*. Prentice-Hall, Englewood Cliffs, New Jersey, 1987.

[8] Boyce, W.E. & DiPrima, R.C. *Elementary Differential Equation and Boundary Value Problems*. John Willey and Sons, Inc., 8th edition, 2005.

[9] Özişik, M. N. *Heat Conduction*. John Wiley & Sons, Inc., New York, 2nd edition, 1993.

[10] Beck, J.V., Cole, K.D., Haji-Sheikh, A. & Litkouhi, B. *Heat conduction using Green's function*. Hemisphere Press. Washington, DC, 1992.

[11] Freeze, R.A. & Cherry, J.A., *Groundwater*, Ed. Prentice-Hall, Inc., New Jersey, USA, 1979.

[12] Wang, H.F. & Anderson, M.P., *Introduction to Groundwater Modeling: Finite Difference and Finite Element Methods*. Academic Press, Inc. San Diego, 1982.

Equivalence between the Trefftz method and the method of fundamental solutions for Green's function of concentric spheres using the addition theorem and image concept

J. T. Chen[1,2], H. C. Shieh[1], J. J. Tsai[1] & J. W. Lee[1]
[1]*Department of Harbor and River Engineering, National Taiwan Ocean University, Taiwan*
[2]*Department of Mechanical and Mechatronic Engineering, National Taiwan Ocean University, Taiwan*

Abstract

Following the success of the mathematical equivalence between the Trefftz method and the method of fundamental solutions for the annular Green's function, we extend to solve the Green's function of 3-D problems in this paper. The Green's function of the concentric sphere is first derived by using the image method which can be seen as a special case of method of fundamental solutions. Fixed-fixed boundary conditions are considered. Also, the Trefftz method is employed to derive the analytical solution by using the T-complete sets. By employing the addition theorem, both solutions are found to be mathematically equivalent when the number of Trefftz bases and the number of image points are both infinite. In the successive image process, the final two images freeze at the origin and infinity, where their singularity strengths can be analytically and numerically determined in a consistent manner. The agreement among the three results, including two analytical solutions by using the Trefftz method and the image method, and one numerical solution by using the conventional MFS is observed.

Keywords: Green's function, method of fundamental solutions, image method, Trefftz method.

1 Introduction

In 1926, Trefftz presented the Trefftz method for solving boundary value problems by superimposing the functions which satisfy the governing equation [1]. The unknown coefficients are determined by matching the boundary condition. In the potential theory, it is well known that the method of fundamental solutions (MFS) can solve potential problems when a fundamental solution is known. This method was proposed by Kupradze [2] in Russia. The MFS can be viewed as an indirect boundary element method containing concentrated sources instead of boundary distributions. The initial idea is to approximate the solution through a linear combination of fundamental solutions where sources are located outside the domain of the problem. Moreover, it has certain advantages over BEM, e.g., no singularity and no boundary integrals are required. Bogomolny [3] studied the stability and error bound of the MFS. Li et al. [4] used the effective condition number to study the ill-poseness of collocation approaches, the MFS and the Trefftz method. They found that the condition number of the MFS is much worst than that of the Trefftz method. Although the Trefftz method and the MFS individually have a long history, the link between the two methods was not discussed in the literature until Chen et al.'s papers [5, 6]. Researchers have paid attention to construct the mathematical relationship between the Trefftz method and MFS since 2006. For example, Schabck [7] found that the MFS with singularity at infinity behaves like the Trefftz base of harmonic polynomials. Chen et al. proved the equivalence between the Trefftz method and the MFS for Laplace and biharmonic problems containing a circular domain [5]. The key point is the use of the degenerate kernel or so-called the addition theorem. They only proved the equivalence by demonstrating a simple circle with angular distribution of singularity to link the two methods. Following the success of deriving the annular Green's function [6], we plan to derive the Green's function of a concentric sphere. Here, we also distribute singularities along the radial direction by using the method of image. Image solutions and Trefftz results for the annular Green's function were obtained [6]. Since a two-dimensional problem can be solved easily by using the complex variable, the image method can be seen as an alternative way to obtain the solution. However, the extension to 3-D problem is limited for the theory of complex variable. The image method can deal with the 3-D problems without any difficulty.

In this paper, we focus on proving the mathematical equivalence on the Green's functions for the Laplace problem of a concentric sphere derived by using the Trefftz method and the image method. Both surfaces of inner and outer boundaries are specified by the Dirichlet boundary conditions. By employing the image method and the addition theorem, the mathematical equivalence of the two solutions derived by using the Trefftz method and the image method will be proved when the number of successive image points and the number of the Trefftz bases are both infinite. The image method can be seen as a special case of the conventional MFS, since its image singularities locate outside the domain. The solution by using the image method for constructing the 2-D Green's

function also indicates that a free constant is required for the completeness of the solution which is always neglected in the conventional MFS. In the 3-D case, the free constant becomes zero as the number of successive image points become infinity.

2 Construction of the Green's function for the domain bounded by concentric spheres using the image method and the conventional MFS

2.1 The image solution

For the problem of concentric sphere as shown in Fig. 1, the Green's function satisfies

$$\nabla^2 G(x,s) = \delta(x-s)\,,\ x \in D\,, \tag{1}$$

where D is the domain of interest and δ denotes the Dirac-delta function for the source at s. For simplicity, the Green's function is considered to be subject to the Dirichlet boundary condition,

$$G(x,s) = 0\,,\ x \in B_1 \cup B_2\,, \tag{2}$$

where B_1 and B_2 are the inner and outer boundaries of the sphere, respectively.

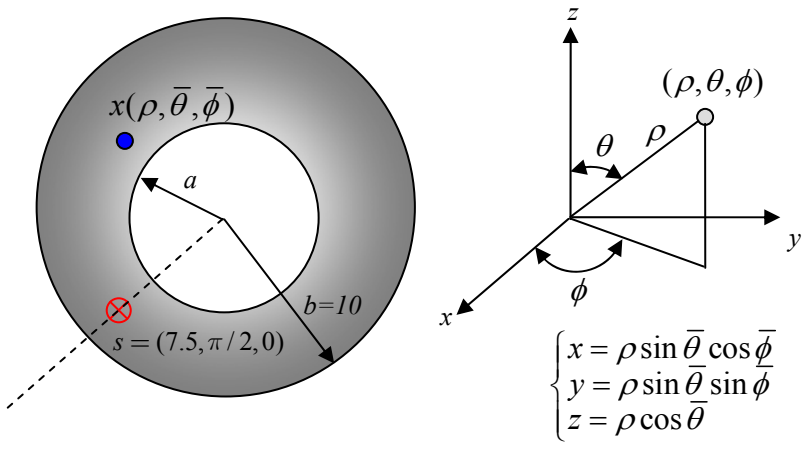

Figure 1: Sketch of an annular sphere subject to a concentrated load.

We consider the fundamental solution $U(s,x)$ for a source singularity which satisfies

$$\nabla^2 U(x,s) = \delta(x-s)\,. \tag{3}$$

Then, we obtain the fundamental solution as follows:

$$U(x,s) = \frac{-1}{4\pi r}\,, \tag{4}$$

where r is the distance between s and x ($r \equiv |x-s|$). Based on the separable property of the addition theorem or degenerate kernel, the fundamental solution $U(x,s)$ can be expanded into series form in the spherical coordinates:

$$U(x,s)=\begin{cases}\dfrac{-1}{4\pi R_s} \\ -\displaystyle\sum_{n=1}^{\infty}\sum_{m=0}^{n}\frac{\varepsilon_m}{4\pi}\frac{(n-m)!}{(n+m)!}\cos\left(m(\bar{\phi}-\phi)\right)P_n^m(\cos\bar{\theta})P_n^m(\cos\theta)\frac{\rho^n}{R_s^{n+1}}, & R_s \geq \rho, \\ \dfrac{-1}{4\pi\rho} \\ -\displaystyle\sum_{n=1}^{\infty}\sum_{m=0}^{n}\frac{\varepsilon_m}{4\pi}\frac{(n-m)!}{(n+m)!}\cos\left(m(\bar{\phi}-\phi)\right)P_n^m(\cos\bar{\theta})P_n^m(\cos\theta)\frac{R_s^n}{\rho^{n+1}}, & R_s < \rho,\end{cases} \tag{5}$$

where $x=(\rho,\bar{\theta},\bar{\phi})$, $s=(R_s,\theta,\phi)$, $P_n^m(\bullet)$ is the associated Legendre polynomial, the superscripts of *i* and *e* denote the interior and exterior regions, respectively, and ε_m is the Neumann factor which defined by,

$$\varepsilon_m=\begin{cases}1, & m=0, \\ 2, & m=1,2,\cdots\infty.\end{cases} \tag{6}$$

As mentioned in [8], the interior and exterior Green's functions can satisfy the homogeneous Dirichlet boundary conditions if the image source is correctly selected. The closed-form Green's functions for both interior and exterior problems are written to be the same form

$$G(x,s;s')=\frac{1}{4\pi}\left(\frac{-1}{|x-s|}+\frac{R_s}{a}\frac{1}{|x-s'|}\right),\ x\in D, \tag{7}$$

where *a* is the radius of the sphere, $s=(R_s,\pi/2,0)$, and s' is the image source and its position is at $(a^2/R_s,\ \pi/2,\ 0)$ as shown in Fig. 2. It is interesting that the formulae for the location of image are the same as the 2-D case [6]. However, the magnitude of strength (R_s/a) is different from the 2-D case [6].

In order to match the inner and outer homogenous Dirichlet boundary conditions, the image relation between the source point and successive image points yields

$$\begin{aligned}
&R_1=\frac{b^2}{R_s},\quad R_5=\frac{b^2}{R_s}\frac{b^2}{a^2}\text{.....},\ R_{4i-3}=\frac{b^2}{R_s}(\frac{b^2}{a^2})^{i-1}, \\
&R_2=\frac{a^2}{R_s},\quad R_6=\frac{a^2}{R_s}\frac{a^2}{b^2}\text{.....},\ R_{4i-2}=\frac{a^2}{R_s}(\frac{a^2}{b^2})^{i-1}, \\
&R_3=\frac{b^2R_s}{a^2},\ R_7=\frac{b^2R_s}{a^2}\frac{b^2}{a^2}\text{...},\ R_{4i-1}=\frac{b^2R_s}{a^2}(\frac{b^2}{a^2})^{i-1}, \\
&R_4=\frac{a^2R_s}{b^2},\ R_8=\frac{a^2R_s}{b^2}\frac{a^2}{b^2}\text{...},\ R_{4i}=\frac{a^2R_s}{b^2}(\frac{a^2}{b^2})^{i-1}.
\end{aligned} \tag{8}$$

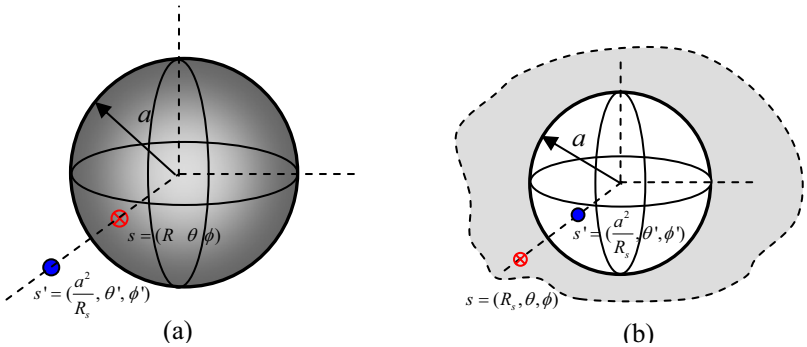

Figure 2: Sketch of position of image point (a) interior case and (b) exterior case.

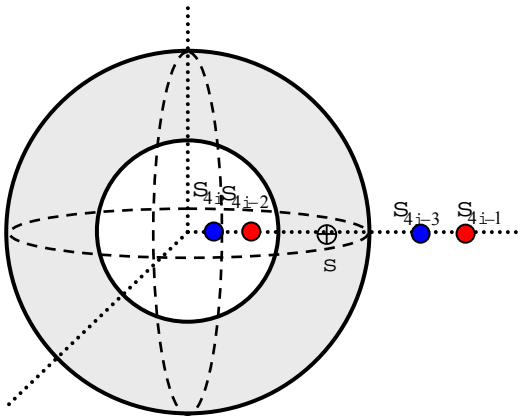

Figure 3: Successive images for an annular problem.

The successive image points for the concentric sphere are shown in Fig. 3. After successive image process, the main part of Green's function is expressed by

$$G_m(x,s) = \frac{1}{4\pi}\left\{\frac{-1}{|x-s|} + \lim_{N\to\infty}\sum_{i=1}^{N}\left[\frac{w_{4i-3}}{|x-s_{4i-3}|} + \frac{w_{4i-2}}{|x-s_{4i-2}|} - \frac{w_{4i-1}}{|x-s_{4i-1}|} - \frac{w_{4i}}{|x-s_{4i}|}\right]\right\}, \tag{9}$$

where w is the weighting of image point which is determined by [8]

$$\begin{aligned}
&w_1 = \frac{R_1}{b} = \frac{b}{R_s},\ w_5 = \frac{aR_5}{b^2} = \frac{b}{R_s}(\frac{b}{a}), \quad w_9 = \frac{a^2R_9}{b^3} = \frac{b}{R_s}(\frac{b}{a})^2 \cdots\cdots, w_{4i-3} = \frac{b}{R_s}(\frac{b}{a})^{i-1},\\
&w_2 = \frac{a}{R_s}, \qquad w_6 = \frac{a^2}{bR_s} = \frac{a}{R_s}(\frac{a}{b}), \quad w_{10} = \frac{a^3}{b^2R_s} = \frac{a}{R}(\frac{a}{b})^2 \cdots\cdots, w_{4i-2} = \frac{a}{R_s}(\frac{a}{b})^{i-1},\\
&w_3 = \frac{aR_3}{bR_s} = \frac{b}{a},\ w_7 = \frac{a^2R_7}{b^2R_s} = \frac{b}{a}(\frac{b}{a}), \quad w_{11} = \frac{a^3R_{11}}{b^3R_s} = \frac{b}{a}(\frac{b}{a})^2 \cdots, \quad w_{4i-1} = \frac{b}{a}(\frac{b}{a})^{i-1},\\
&w_4 = \frac{a}{b}, \qquad w_8 = \frac{a^2}{b^2} = \frac{a}{b}(\frac{a}{b}), \qquad w_{12} = \frac{a^3}{b^3} = \frac{a}{b}(\frac{a}{b})^2 \cdots\cdots\cdots, w_{4i} = \frac{a}{b}(\frac{a}{b})^{i-1}.
\end{aligned} \tag{10}$$

2.1.1 Satisfaction of the boundary condition by using interpolation functions

We set $G_m(x,s)$ to be the main part of the Green's function in Eq.(9). Unfortunately, $G_m(x,s)$ in Eq.(9) can not simultaneously satisfy both the inner and outer boundary conditions of $G_m(x_a,s)=G_m(x_b,s)=0$, where $x_a=(a,\bar{\theta},\bar{\phi})$, $x_b=(b,\bar{\theta},\bar{\phi})$, $0\le\bar{\theta}\le\pi$, $0\le\bar{\phi}\le 2\pi$. In order to satisfy both the inner and outer boundary conditions, an alternative method is introduced such that we have

$$G(x,s)=G_m(x,s)-\left(\frac{b(\rho-a)}{\rho(b-a)}\right)G_m(x_b,s)-\left(\frac{a(b-\rho)}{\rho(b-a)}\right)G_m(x_a,s),\ a\le\rho\le b, \tag{11}$$

where $\left(b(\rho-a)/\rho(b-a)\right)$ and $\left(a(b-\rho)/\rho(b-a)\right)$ are the interpolation functions, $G_m(x_b,s)=-(\frac{a}{b})^N\frac{1}{b}$ and $G_m(x_a,s)=\frac{-1}{R_s}(\frac{a}{b})^N$. Therefore, Eq.(11) can be simplified to

$$G(x,s)=\frac{1}{4\pi}\left\{\frac{-1}{|x-s|}+\lim_{N\to\infty}\sum_{i=1}^{N}\left[\frac{w_{4i-3}}{|x-s_{4i-3}|}+\frac{w_{4i-2}}{|x-s_{4i-2}|}-\frac{w_{4i-1}}{|x-s_{4i-1}|}-\frac{w_{4i}}{|x-s_{4i}|}\right]+C+D\frac{1}{\rho}\right\} \tag{12}$$

where $C=(\frac{a}{b})^N\left[\frac{a-R_s}{R_s(a-b)}\right]$ and $D=(\frac{a}{b})^N\left[\frac{a(R_s-b)}{R_s(a-b)}\right]$. Equation (12) indicates that not only image singularities at s_{4i-3}, s_{4i-2}, s_{4i-1} and s_{4i}, but also one singularity at the origin and one rigid body term for one singularity at infinity are required. The Green's function in Eq.(12) satisfies the governing equation and boundary conditions at the same time. It is found that a conventional MFS always loses a free constant and completeness may be questionable.

2.1.2 Satisfaction of boundary conditions to determine two singularity strengths at the origin and infinity

After successive image process, the final two image locations freeze at the origin and infinity. There are two strengths of singularities to be determined. Therefore, the Green's function is rewritten as

$$G(x,s)=\frac{1}{4\pi}\left\{\frac{-1}{|x-s|}+\lim_{N\to\infty}\sum_{i=1}^{N}\left[\frac{w_{4i-3}}{|x-s_{4i-3}|}+\frac{w_{4i-2}}{|x-s_{4i-2}|}-\frac{w_{4i-1}}{|x-s_{4i-1}|}-\frac{w_{4i}}{|x-s_{4i}|}\right]+c(N)+\frac{d(N)}{\rho}\right\}, \tag{13}$$

where the final two images locate at the center of sphere and infinity with strength of $c(N)$ and $d(N)$, respectively, which can be analytically and numerically determined by matching the inner and outer boundary conditions.

After matching the inner and outer boundary conditions, the unknown coefficients $c(N)$ and $d(N)$ are determined by using the numerical method and analytical approach are shown in Fig 4. Agreement is made.

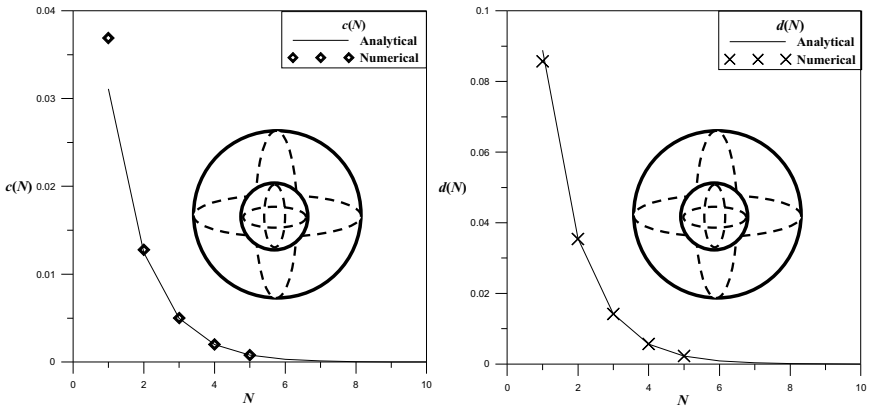

Figure 4: Coefficients of $c(N)$ and $d(N)$ versus N for the fixed-fixed case.

2.2 The conventional MFS [2]

In the method of fundamental solutions, the Green's function $G(x,s)$ is superimposed by using the fundamental solutions $U(x,s)$, as follows:

$$G(x,s) = \frac{-1}{4\pi r} + \sum_{j=1}^{N_M} \alpha_j U(x,s_j), \quad x \in D, \tag{14}$$

where the N_M is the number of source points which are distributed outside the domain, α_j is the j^{th} unknown coefficient. By similarly matching the boundary conditions in Eq.(2), the unknown coefficient α_j can be determined. Then, we have a numerical solution. By comparing Eq.(13) with Eq.(14), the image method of Eq.(13) can be seen as a special MFS of Eq.(14) with optimal locations and specified strengths for the singularities except the two strengths at two frozen points.

3 Derivation of the Green's function for the domain bounded by concentric spheres by using the Trefftz method

The problem of a concentric sphere in Fig. 5 can be decomposed into two parts. One is an infinite space with a concentrated source (fundamental solution) in Fig. 5(a) and the other is subject to specified boundary conditions as shown in Fig. 5(b). The first-part solution can be obtained from the fundamental solution. Here, the second part is solved by using the Trefftz method. The solution can be superposed by using the Trefftz bases as shown below:

$$G_T(x,s) = \sum_{j=1}^{N_T} p_j \Phi_j, \tag{15}$$

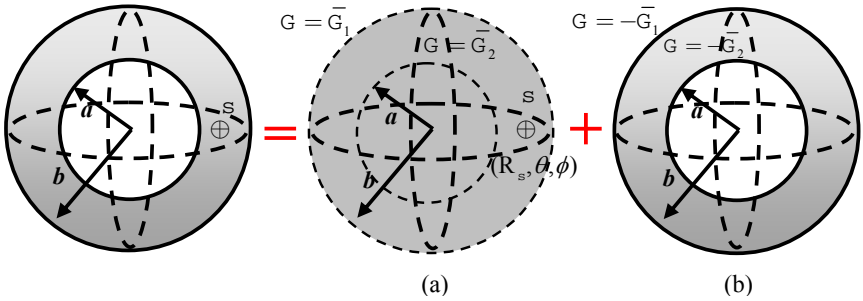

Figure 5: Sketch of the superposition approach. (a) An infinite space with a concentrated source. (b) A concentric sphere subject to the Dirichlet boundary condition.

where p_j is the weighting, Φ_j is the j^{th} T-complete function and N_T is the number of T-complete functions.

Here, the T-complete functions are given as 1, $\rho^n P_n^m(\cos\bar{\theta})\cos(m\bar{\phi})$ and $\rho^n P_n^m(\cos\bar{\theta})\sin(m\bar{\phi})$ for the interior case and $1/\rho$, $\rho^{-(n+1)} P_n^m(\cos\bar{\theta})\cos(m\bar{\phi})$ and $\rho^{-(n+1)} P_n^m(\cos\bar{\theta})\sin(m\bar{\phi})$ for the exterior case. The second-part solution can be represented by

$$\begin{aligned} G_T(x,s) = A_{00} + \frac{B_{00}}{\rho} + \sum_{n=1}^{\infty}\sum_{m=0}^{n}[&A_{nm}\rho^n P_n^m(\cos\bar{\theta})\cos(m\bar{\phi}) + B_{nm}\rho^{-(n+1)} P_n^m(\cos\bar{\theta})\cos(m\bar{\phi}) \\ &+ C_{nm}\rho^n P_n^m(\cos\bar{\theta})\sin(m\bar{\phi}) + D_{nm}\rho^{-(n+1)} P_n^m(\cos\bar{\theta})\sin(m\bar{\phi})], \end{aligned} \tag{16}$$

where A_{00}, B_{00}, A_{nm}, B_{nm}, C_{nm} and D_{nm} are unknown coefficients. By matching the boundary conditions, the unknown coefficients can be determined. Then, the series-form Green's function is obtained by superimposing the solutions of $U(x,s)$ and $G_T(x,s)$ as shown below:

$$\begin{aligned} G(x,s) = \frac{-1}{4\pi|x-s|} + A_{00} + \frac{B_{00}}{\rho} \\ + \sum_{n=1}^{\infty}\sum_{m=0}^{n}[&A_{nm}\rho^n P_n^m(\cos\bar{\theta})\cos(m\bar{\phi}) + B_{nm}\rho^{-(n+1)} P_n^m(\cos\bar{\theta})\cos(m\bar{\phi}) \\ &+ C_{nm}\rho^n P_n^m(\cos\bar{\theta})\sin(m\bar{\phi}) + D_{nm}\rho^{-(n+1)} P_n^m(\cos\bar{\theta})\sin(m\bar{\phi})], \end{aligned} \tag{17}$$

where the unknown coefficients are obtained as shown below:

$$\begin{Bmatrix} A_{00} \\ B_{00} \end{Bmatrix} = \begin{Bmatrix} \dfrac{R_s - a}{4\pi R_s (b-a)} \\ \dfrac{a(b-R_\xi)}{4\pi R_s (b-a)} \end{Bmatrix}, \tag{18}$$

$$\begin{Bmatrix} A_{nm} \\ B_{nm} \end{Bmatrix} = \begin{Bmatrix} \dfrac{\varepsilon_m}{4\pi}\dfrac{(n-m)!}{(n+m)!}\left[\dfrac{R_s^{2n+1}-a^{2n+1}}{R_s^{n+1}\left(b^{2n+1}-a^{2n+1}\right)}\right]P_n^m(\cos\theta)\cos(m\phi) \\ \dfrac{\varepsilon_m}{4\pi}\dfrac{(n-m)!}{(n+m)!}\left[\dfrac{a^{2n+1}\left(b^{2n+1}-R_s^{2n+1}\right)}{R_s^{n+1}\left(b^{2n+1}-a^{2n+1}\right)}\right]P_n^m(\cos\theta)\cos(m\phi) \end{Bmatrix}, \tag{19}$$

$$\begin{Bmatrix} C_{nm} \\ D_{nm} \end{Bmatrix} = \begin{Bmatrix} \dfrac{\varepsilon_m}{4\pi}\dfrac{(n-m)!}{(n+m)!}\left[\dfrac{R_s^{2n+1}-a^{2n+1}}{R_s^{n+1}\left(b^{2n+1}-a^{2n+1}\right)}\right]P_n^m(\cos\theta)\sin(m\phi) \\ \dfrac{\varepsilon_m}{4\pi}\dfrac{(n-m)!}{(n+m)!}\left[\dfrac{a^{2n+1}\left(b^{2n+1}-R_s^{2n+1}\right)}{R_s^{n+1}\left(b^{2n+1}-a^{2n+1}\right)}\right]P_n^m(\cos\theta)\sin(m\phi) \end{Bmatrix}, \tag{20}$$

It is interesting to find that Eq.(18) can be included into Eq.(19) since we introduce the Neumann factor and set *n=m=0.* We will prove the equivalence of solutions derived by using the Trefftz method and the image method (special MFS) in the next section.

4 Mathematical equivalence for the solutions derived by the MFS and Trefftz method

4.1 Method of fundamental solutions (image method)

The image method can be seen as a special case of the MFS, since its singularities are located outside the domain. The Green's function of Eq.(13) can be expanded into a series form by separating the field point *x* and source point *s* for the fundamental solution in the spherical coordinates of Eq.(5) as shown below:

$$\begin{aligned} G(x,s) = {} & \frac{1}{4\pi}\left[\frac{-1}{|x-s|}+\frac{R_s-a}{R_s(b-a)}+\frac{a(b-R_s)}{R_s\rho(b-a)}\right] \\ & +\sum_{i=1}^{\infty}\sum_{n=1}^{\infty}\sum_{m=0}^{n}\frac{\varepsilon_m}{4\pi}\frac{(n-m)!}{(n+m)!}\left[w_{4i-3}\left(\frac{\rho^n}{R_{4i-3}^{n+1}}\right)+w_{4i-2}\left(\frac{R_{4i-2}^n}{\rho^{n+1}}\right)\right. \\ & \left.-w_{4i-1}\left(\frac{\rho^n}{R_{4i-1}^{n+1}}\right)-w_{4i}\left(\frac{R_{4i}^n}{\rho^{n+1}}\right)\right]\cos[m(\bar{\phi}-\phi)]P_n^m(\cos\bar{\theta})P_n^m(\cos\theta). \end{aligned} \tag{21}$$

By using Eqs. (8) and (10), the series containing four geometry series with the same ratio of $(a/b)^{2n+1}$ which is smaller than one in Eq.(13) can be rearranged into

$$\begin{aligned} G(x,s) = {} & \frac{1}{4\pi}\left[\frac{-1}{|x-s|}+\frac{R_s-a}{R_s(b-a)}+\frac{a(b-R_s)}{R_s\rho(b-a)}\right] \\ & +\sum_{n=1}^{\infty}\sum_{m=0}^{n}\frac{\varepsilon_m}{4\pi}\frac{(n-m)!}{(n+m)!}\left[\frac{R_s^{2n+1}\rho^{2n+1}-a^{2n+1}\rho^{2n+1}+a^{2n+1}b^{2n+1}-a^{2n+1}R_s^{2n+1}}{R_s^{n+1}\rho^{n+1}(b^{2n+1}-a^{2n+1})}\right] \\ & \cos[m(\bar{\phi}-\phi)]P_n^m(\cos\bar{\theta})P_n^m(\cos\theta), \end{aligned} \tag{22}$$

after expanding all the image singularities of $-1/r$ functions. It is interesting to find that the optimal location may not be the expansion type of Fig. 6(a) or angular distribution of Fig. 6(b) but a lump singularity in one radial direction shown in Fig. 6(c) as mentioned by Antunes [9]. In this paper, our image location in the MFS only distribute along the radial direction which agrees with the optimal location in [9]. This finding agrees with the experience in the annular case [6] and the present case of a concentric sphere.

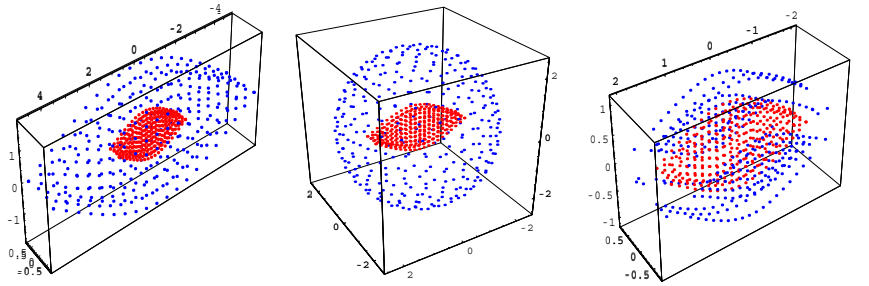

(a) Expansion (b) Sphere (c) Lump (Optimal case)

Figure 6: Optimal locations of source distribution for the MFS [9].

4.2 Trefftz method

Substitution of Eqs.(18)-(20) into Eq.(17) yields

$$G(x,s)=\frac{1}{4\pi}\left[\frac{-1}{|x-s|}+\frac{R_s-a}{R_s(b-a)}+\frac{a(b-R_s)}{R_s\rho(b-a)}\right] +\sum_{n=1}^{\infty}\sum_{m=0}^{n}\frac{\varepsilon_m}{4\pi}\frac{(n-m)!}{(n+m)!}\left[\frac{R_s^{2n+1}\rho^{2n+1}-a^{2n+1}\rho^{n+1}+a^{2n+1}b^{2n+1}-a^{2n+1}R_s^{2n+1}}{R_s^{n+1}\rho^{n+1}(b^{2n+1}-a^{2n+1})}\right] \cos[m(\bar{\phi}-\phi)]P_n^m(\cos\bar{\theta})P_n^m(\cos\theta). \quad (23)$$

After comparing Eq.(22) with Eq.(23), it is found that the two solutions, Eqs. (13) and (17) are proved to be mathematically equivalent by using the addition theorem when the number of images and the number of Trefftz bases are both infinite. To verify the Trefftz and image solutions, the conventional MFS is utilized for comparison. The distribution of collocation nodes and images (sources of MFS) is shown in Fig. 7. Contour plots by using the three approaches are shown in Fig. 8. Good agreement is observed.

5 Concluding remarks

In this paper, not only the image method (a special MFS) but also the Trefftz method was employed to solve the Green's function of 3-D Laplace problems bounded by concentric sphere. The two solutions using the Trefftz method and MFS for the case were proved to be mathematically equivalent by using the

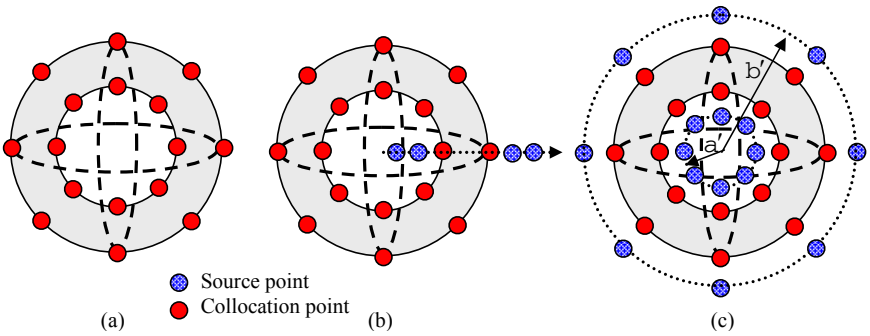

Figure 7: Sketches of (a) Trefftz method, (b) image method (special MFS, radial distribution of singularities) and (c) conventional MFS (angular distribution of singularities).

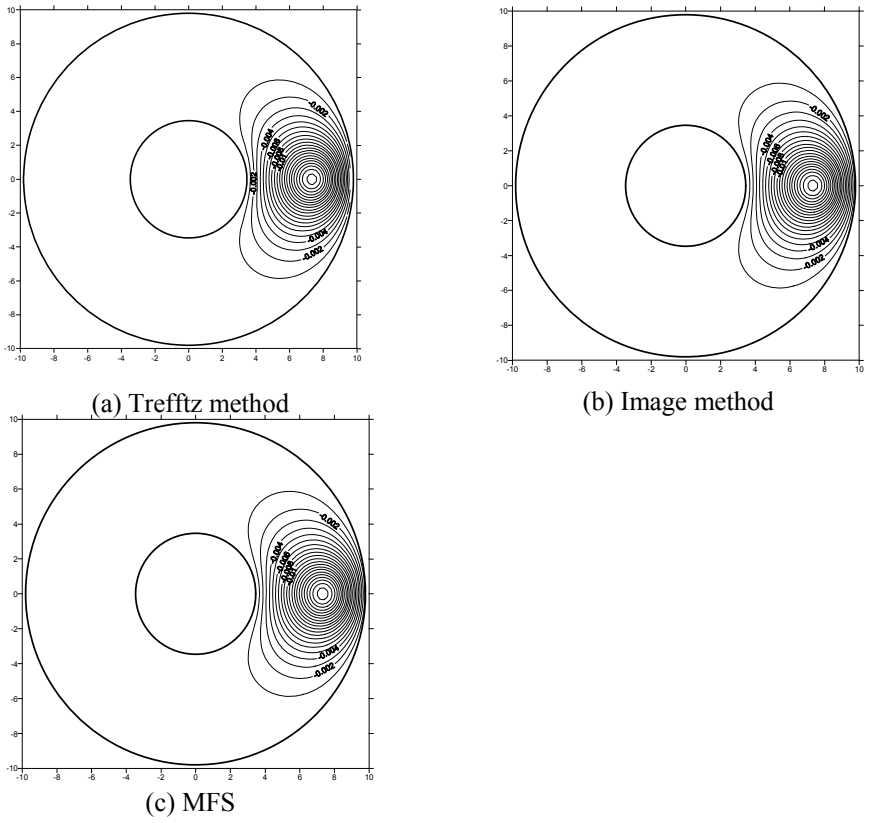

Figure 8: Contour plots by using three approaches, (a) Trefftz method, (b) image method and (c) MFS (z=2 plane).

addition theorem or so-called degenerate kernel. Also, the solution of image method shows the existence of the free constant which is always overlooked in the conventional MFS although it becomes zero as the number of images approaches infinity. Finally, we also found the final two frozen image points at the origin and infinity where their strengths can be determined numerically and analytically in a consistent manner. Contour plots by using the three approaches, Trefftz method, image method and conventional MFS, agree well.

References

[1] Kita E. Kamiya N. Trefftz method: an overview. Adv Engng Softw 1995;24:3-12.
[2] Kupradze VD. A method for the approximate solution of limiting problems in mathematical physics. Computat Math Math Phys 1964;4:199-205.
[3] Bogomolny A. Fundamental solutions method for elliptic boundary value problems. SIAM J Numer Anal 1985;22(4):644-669.
[4] Li ZC. Lu TT. Hu HY. Cheng AHD. Trefftz and collocation methods. Boston-Southampton: WIT Press; 2007.
[5] Chen JT. Wu CS. Lee YT. Chen KH. On the equivalence of the Trefftz method and method of fundamental solutions for Laplace and biharmonic equations. Computers and Mathematics with Applications 2007;53:851–879.
[6] Chen JT. Lee YT. Yu SR. Shieh SC. 2009, Equivalence between Trefftz method and method of fundamental solution for the annular Green's function using the addition theorem and image concept, Engineering Analysis with Boundary Elements, Vol.33, pp.678-688.
[7] Schaback R. Adaptive numerical solution of MFS systems. A plenary talk at the first Inter Workshop on the Method of Fundamental Solution, Ayia Napa, Cyprus, June 11-13; 2007.
[8] Chen JT. Wu CS. Alternative derivations for the Poisson integral formula. Int. J Math Educ. Sci. Technol 2006;37:165-185.
[9] Antunes PRS. The Method of Fundamental Solutions applied to the eigenproblems in partial differential equations, Ph.D. Dissertation, IST, Portugal, 2008.

On stress reconstruction in composite domains from discrete data on principal directions

A. N. Galybin
Wessex Institute of Technology, Southampton, UK

Abstract

The problem considered in this paper deals with reconstruction of plane stress tensors in domains with multiple interfaces representing the boundaries of subdomains. No boundary stresses or displacements are imposed; instead the discrete data on stress orientations are used for problem setting. Continuity of the stress vector across the interfaces is also accepted. Solutions in every subdomain are sought by assuming linear approximations for the complex potentials with unknown coefficients. These are found by solving a minimisation problem. An application to the geophysical problem of stress identification in tectonic plates is considered to illustrate effectiveness of the proposed numerical approach.

Keywords: stress orientations, 2D stress tensor, complex potentials, plate tectonics.

1 Introduction

The problem of stress reconstruction from discrete data on stress orientation has been addressed in [1, 2] for a single domain and in [3–4] for two subdomains. In all these cases the domains have been associated with either tectonic plates or with certain regions of the earth's crust and real data on stress orientations supplied by the World Stress Map Project [5] have been used. The present study is aimed at the further development of the previously reported method for the case when the entire domain consists of several plane elastic subdomains whose deformation properties may be, in general, different.

This study is also aimed at the development of algorithms capable of dealing with the data widely used in geodynamics, namely, experimentally obtained stress orientations around the globe and geographical coordinates of the tectonic plate margins [6].

WIT Transactions on Modelling and Simulation, Vol 49, © 2009 WIT Press
www.witpress.com, ISSN 1743-355X (on-line)
doi:10.2495/BE090041

The paper is structured as follows. Typical data accepted in this study are described in section 2 where also the outcomes of the developed algorithms are presented. Section 3 presents mathematical formulation of the problem and its numerical implementation is described in section 4. Results of computations for a particular plane domain are discussed in section 5.

2 Data

Data on stress orientations have been extracted from the WSM database which current 2008 release contains 21,750 stress data records, [5]. Only data of A-B quality [7] are used further on, this assumes stress orientations are recorded with the following errors: ±10°–15° (A-quality) and within ±15°–20° (B-quality).

Data on plate boundaries [6] contains 52 entries. Each plate is presented by an ordered set of boundary points (in geographical coordinates) that constitutes a closed curve traversed in the counterclockwise direction. The last point coincides with the first point.

A fragment of the earth's crust with the data is shown in Fig 1. The domain consists of 16 subdomains (presenting tectonic plates); short segments show 53 orientations of major compressive principal stresses. It is evident that the data are highly irregular and not all subdomains contain data points.

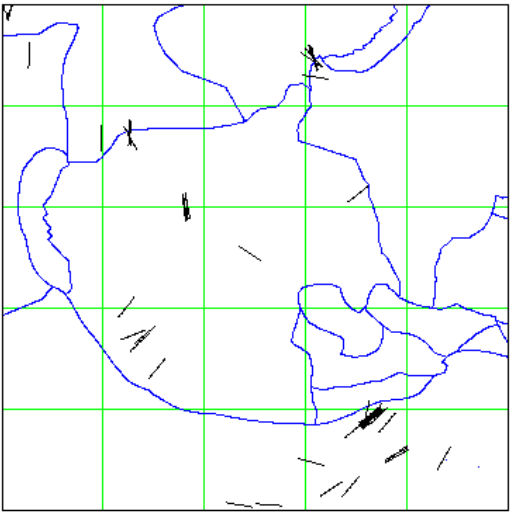

Figure 1: Domain consisting of 16 subdomains, 35 interfaces, 53 data on stress orientations.

Several special procedures have been designed to deal with the boundary data with the aim of identification of the interfaces between the subdomains and placing equidistant collocation points on the interfaces. The number of interfaces depends on a particular subdomain pattern and cannot be calculated in a simple

way as it can be done for regular grids. For instance, 35 interfaces have been identified for the example presented in Fig 1. They represent common boundaries between adjacent subdomains and therefore there is one-to one correspondence between an interface number and a pair of subdomain numbers.

Linear interpolation has been applied through the discrete points representing an interface; therefore a set of nodes has been introduced for each interface that is further used for forming the entire set of collocation points. The number of nodes in every set is different, it is defined by the length, L_j, of the j-th interface (j=1…N_{int}) and the step, Δ, specified as a global input parameter; therefore the number of nodes on the j-th interface is defined as $Nnode_j=floor(L_j/\Delta)$.

After initial treatment of data the following output is obtained:

a. The table of correspondence between interfaces and subdomains; it is a two row array with N_{int} columns, its first column shows the interface number and its second column contains the numbers of two adjacent subdomains whose boundaries form the interface shown in the first column;

b. complex coordinates of the nodes on all interfaces $\zeta_k,\ k=1\ldots\sum_{j=1}^{N\text{int}} Nnode_j$

c. principal directions, angles θ_m, at points z_m, m=1…N_{data}; and

d. complex coordinates of the data points z_m, m=1…N_{data} sorted with respect to subdomains.

A special procedure for the identification of the subdomain to which a particular datum belongs to has been designed for data sorting. This procedure is further used for mapping of the calculated stress field.

3 Formulation of the problem

A plane elastic domain Ω composed by the union of plane subdomains Ω_i (i=1…N) having, in general, different elastic moduli is considered (elastic moduli are not specified because no conditions regarding discontinuity of displacements across the interfaces are assumed in formulation). Principal directions are given at some points, belonging to some subdomains (not necessarily all subdomains are populated with data); the discrete set of given principal directions as assumed to be finite and contain N_{data} points. It is accepted that the stress vector is continuous across the interfaces Γ_j between all adjacent subdomains (j=1…N_{int}). Given these conditions it is required to *determine all possible stress states satisfying the given data on principal directions*.

It should be noted that the problem formulated above is not a classical boundary value problem of plane elasticity. In contrast to classical formulations, the number of boundary conditions (two for each interface, presenting continuity of the stress vector) is insufficient, and therefore the solution is not unique and may contain arbitrary functions. In order to overcome such high indeterminedness one should seek possible solutions in a certain class of functions. A simple set of basis functions, namely piecewise linear holomorphic functions, is used further in numerical implementation. However this does not make the problem to be fully well posed, there still may be a finite number of

free parameters included in the solution. This is evident from the fact that no stress magnitudes are involved in the formulation, therefore at least two parameters remains undetermined in the total solution. They are (*i*) a multiplicative constant at the stress deviator; and (*ii*) an additive constant to the mean hydrostatic stress. These can be selected randomly and affect neither principal directions nor equilibrium equations. It has been shown [8] that up to 5 free parameters can be included in the total solution for a simply connected elastic isotropic domain when it is being built from the know stress trajectory pattern. For a composite domain considered here no theoretical results regarding the number of free parameters are available. Therefore, the presence of free parameters will further be verified by assessing the rank of the matrix of the corresponding linear system of equations.

General solution for the stress tensor for a plane elastic domain subjected to boundary forces only has the form [9]

$$\begin{aligned} P(z,\bar{z}) &\equiv \frac{\sigma_{11}+\sigma_{22}}{2} = \Phi(z)+\overline{\Phi(z)} \\ D(z,\bar{z}) &\equiv \frac{\sigma_{22}-\sigma_{11}}{2}+i\sigma_{12} = \bar{z}\Phi'(z)+\Psi(z) \end{aligned} \tag{1}$$

Here $\Phi(z)$ and $\Psi(z)$ are complex potentials (holomorphic functions) to be determined from boundary conditions; harmonic function P and complex-valued function D represent mean hydrostatic stress and stress deviator respectively, they are functions of stress components σ_{ij}; $z.=x_1+ix_2$ is a complex coordinate, over-bar stands for complex conjugation.

The complex conjugated stress vector $N(\zeta)–iT(\zeta)$ (where $N(\zeta)$ and $T(\zeta)$ are normal and shear components respectively) on an arbitrary interface Γ_j is determined as follows [9]

$$N(\zeta)-iT(\zeta) = P(\zeta)+\frac{d\zeta}{d\bar{\zeta}}D(\zeta), \quad \zeta\in\Gamma_j, \quad j=1\ldots N_{\text{int}} \tag{2}$$

where $P(\zeta)$ and $D(\zeta)$ are the boundary values of the stress function obtained by limiting transition of the field variable, z, to a boundary point, ζ. These values can suffer jumps when the point crosses interfaces, however, the stress vector is assumed to be continuous across every interface, which leads to the following boundary condition in terms of complex potentials

$$2\,\mathrm{Re}\langle\Phi(\zeta)\rangle+\zeta\frac{d\zeta}{d\bar{\zeta}}\langle\Phi'(\zeta)\rangle+\frac{d\zeta}{d\bar{\zeta}}\langle\Psi(\zeta)\rangle=0, \quad \zeta\in\Gamma_j, \quad j=1\ldots N_{\text{int}} \tag{3}$$

where <…> denoted the jump of the quantity across the j-th interface.

The second set of conditions expresses the fact that the maximum shear stress, $\tau_{max}=|D|$, is a real valued function, that allows one to write

$$\mathrm{Im}\left[e^{2i\theta_m}\left(\bar{z}_m\Phi'(z_m)+\Psi(z_m)\right)\right]=0, \quad z_m\in\Omega, \quad m=1\ldots N_{data} \tag{4}$$

It is taken into account here that $\arg(D)=\pi-2\theta$, where θ is principal direction (the angle between the major principal stress and the real axis) at an arbitrary point.

4 Numerical approach

Complex potential are further sought as piecewise holomorphic linear functions

$$\Psi(z)=\sum_{i=1}^{N} H_i(z), \quad \Phi(z)=\sum_{i=1}^{N} H_{N+i}(z) \tag{5}$$

where $H_i(z)$ are linear in Ω_i and vanish outside

$$H_i(z)=\begin{cases} c_0^{(i)}+c_1^{(i)}z & z\in\Omega_i \\ 0 & z\notin\Omega_i \end{cases}, \quad H_{N+i}(z)=\begin{cases} \frac{1}{2}a^{(i)}+c_2^{(i)}z & z\in\Omega_i \\ 0 & z\notin\Omega_i \end{cases}, \quad i=1\ldots N \tag{6}$$

Here $c_l^{(i)}$, $l=0,1,2$ are complex constants while $a^{(i)}$ are real.

It follows from (1), (5),(6) that the stress functions assume the form

$$\begin{aligned} D(z,\bar{z})&=\sum_{i=1}^{N} D^{(i)}(z,\bar{z}), \quad D^{(i)}(z,\bar{z})=\begin{cases} c_0^{(i)}+c_1^{(i)}z+c_2^{(i)}\bar{z} & z\in\Omega_i \\ 0 & z\notin\Omega_i \end{cases} \\ P(z,\bar{z})&=\sum_{i=1}^{N} P^{(i)}(z,\bar{z}), \quad P^{(i)}(z,\bar{z})=\begin{cases} a^{(i)}+c_2^{(i)}z+\bar{c}_2^{(i)}\bar{z} & z\in\Omega_i \\ 0 & z\notin\Omega_i \end{cases} \end{aligned} \tag{7}$$

Although expressions (7) are simple they are general enough to address the presence of the singular (isotropic) points of two types known from photoelasticity [10]. The type of isotropic points is distinguished in accordance with the asymptotics near the roots of the stress deviator function [11].

There are seven unknown real coefficients for every subdomain, which are further considered as the coefficients in an ordered row as follows

$$\mathbf{C}^{(i)}=\left(a^{(i)},\mathrm{Re}\,c_0^{(i)},\mathrm{Im}\,c_0^{(i)},\mathrm{Re}\,c_1^{(i)},\mathrm{Im}\,c_1^{(i)},\mathrm{Re}\,c_2^{(i)},\mathrm{Im}\,c_2^{(i)}\right), \quad i=1\ldots N \tag{8}$$

These form the vector of unknowns $\mathbf{C}$ as a transpose of the augment of rows $\mathbf{C}^{(i)}$

$$\mathbf{C}^T=\left(\mathbf{C}^{(1)},\mathbf{C}^{(2)},\ldots,\mathbf{C}^{(N)}\right) \tag{9}$$

The first set of equations is obtained by satisfying the continuity condition (3) at collocation points, ζ_k as follows

$$\mathbf{M_{Con}}=\left(\mathbf{U}^{(1)},\mathbf{U}^{(1)},\ldots\mathbf{U}^{(N_{\mathrm{int}})},\mathbf{E}\right)^T, \quad \mathbf{U}^{(n)}=\begin{pmatrix} 0,\ldots,\mathrm{Re}\,\mathbf{V}^{(k)},0\ldots,\mathrm{Re}\,\mathbf{V}^{(j)},\ldots,0 \\ 0,\ldots,\mathrm{Im}\,\mathbf{V}^{(k)},0\ldots,\mathrm{Im}\,\mathbf{V}^{(j)},\ldots,0 \end{pmatrix}^T \tag{10}$$

where n is the number of the interface between the k-th and j-th subdomains, calculated in accordance with the correspondence table mentioned in section 2; and the vectors $\mathbf{V}^{(k)}$ and $\mathbf{E}$ are defined as follows

$$\begin{aligned} \mathbf{V}^{(k)}&=\left(1,\frac{d\zeta_k}{d\bar{\zeta}_k},i\frac{d\zeta_k}{d\bar{\zeta}_k},\zeta_k\frac{d\zeta_k}{d\bar{\zeta}_k},i\zeta_k\frac{d\zeta_k}{d\bar{\zeta}_k},2\,\mathrm{Re}\,\zeta_k+\frac{d\zeta_k}{d\bar{\zeta}_k},-2\,\mathrm{Im}\,\zeta_k+i\bar{\zeta}_k\frac{d\zeta_k}{d\bar{\zeta}_k}\right) \\ \mathbf{E}&=(1,0,0,0,0,0,0,1,0,\ldots,1,0,0,0,0,0,0,0)^T \end{aligned} \tag{11}$$

The vector **E** has been introduced to add an extra equation expressing the fact that the coefficients $a^{(i)}$, $i=1\ldots N$ are not independent, which is a consequence of the field data type that does not include magnitudes of stresses in formulation.

The right-hand side corresponding the first set of equation has the form

$$\mathbf{R_{Con}} = (0,0,\ldots,0,\lambda)^T \tag{12}$$

where the coefficient λ can be chosen arbitrary, in particular, set to zero.

The second set of equations addresses the field data and employs conditions (4), which lead to the following matrix

$$\mathbf{M_{data}} = \left(\mathbf{W}^{(1)}, \mathbf{W}^{(2)}, \ldots \mathbf{W}^{(N_{data})}, \mathbf{J}\right)^T, \quad \mathbf{W}^{(m)} = \left(0,\ldots, \operatorname{Im}\mathbf{V}^{(m)},\ldots,0\right)^T \tag{13}$$

where the vectors $\mathbf{V}^{(m)}$ and **J** are as follows

$$\begin{aligned} \mathbf{V}^{(m)} &= \left(0, -e^{2i\theta_m},\ ie^{2i\theta_m},\ z_m e^{2i\theta_m},\ i\,z_m\, e^{2i\theta_m},\ \bar{z}_m\, e^{2i\theta_m},\ i\,\bar{z}_m\, e^{2i\theta_m}\right) \\ \mathbf{J} &= (0,1,1,1,1,1,1,0,1\ldots,0,1,1,1,1,1,1)^T \end{aligned} \tag{14}$$

The latter vector has been introduced into the system in order to make it inhomogeneous and acknowledge the fact that only the normalised maximum shear stress can be determined, i.e. one multiplicative arbitrary positive constant remains unknown.

The total system is obtained by the union of (10)–(14) as follows

$$\mathbf{MC} = \mathbf{b}, \quad \mathbf{M} = \begin{pmatrix} \mathbf{M_{Con}} \\ \mathbf{M_{data}} \end{pmatrix}, \quad \mathbf{b} = \begin{pmatrix} \mathbf{R_{Con}} \\ \mathbf{R_{data}} \end{pmatrix} \tag{15}$$

The system is overdetermined it has $2N_{\text{int}} + N_{\text{data}} + 2$ equations and $7N$ unknowns. Therefore its approximate solution is found by the least squares method (consistency is cheeked by calculating the rank of the matrix).

As soon as the coefficients c_k are found the solutions for each subdomains are determined by the stress functions in (7).

5 Model example

This section presents an example of stress field reconstruction in a plane quadratic domain consisting of 9 subdomains as shown in Fig 2. The number of interfaces identified for this configuration is 18. The length of interfaces varies between 0.1 and 1.32 with the average value of 0.54 making the total length of all interfaces of 9.77. The number of collocation points introduced on the interfaces is 105, they are shown in Fig. 2 by circles. The number of data on principal stresses is 116, the data has been taken from the WSMP [5] from the geographical domain between longitudes -95^o to -35^o and latitudes -20^o to 30^o; the only quality A-B has been selected. Two subdomains contain no data, and 4 subdomains have 1-2 data. The SLAE has 329 equations imposed on 63 unknowns.

The results of calculations of the stress field are presented in Figs. 3–5. Fig. 3 shown the map of normalised maximum shear stress, i.e. the function $F(z)$ in the expression $\tau_{\max}(z)=\mu F(z)$, where $\mu > 0$ is an arbitrary positive constant. This

function reaches minimum at z^*=-0.303-0.648i inside the white area, and this minimum is associated with the isotropic point where $F(z^*)=0$. Fig. 4 presents the map of the mean hydrostatic stress in the scaled form, i.e. the function $H(z)$ in expression $P(z)=\mu H(z)+\nu$, where $\nu>0$ is an arbitrary constant. The field of stress trajectories is shown in Fig. 5, from which the presence of the isotropic point is evident.

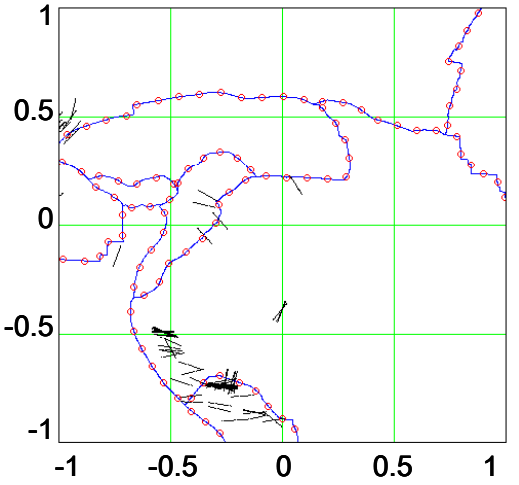

Figure 2: Computational domain and data; the boundaries of subdomains are shown by solid lines; circles show collocation points on the interfaces; short segments represent data on principal stress orientations.

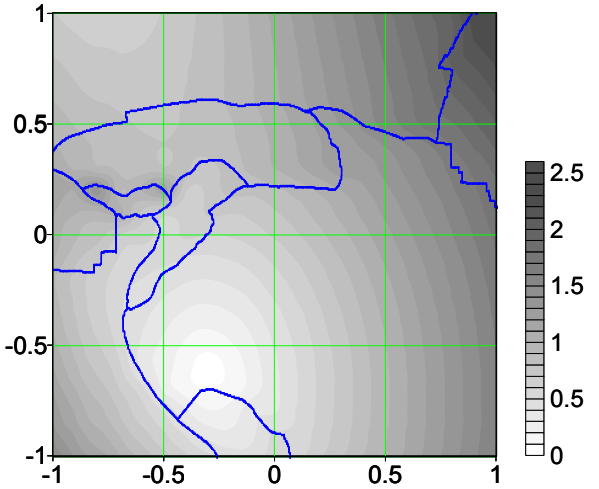

Figure 3: The map of maximum shear stress.

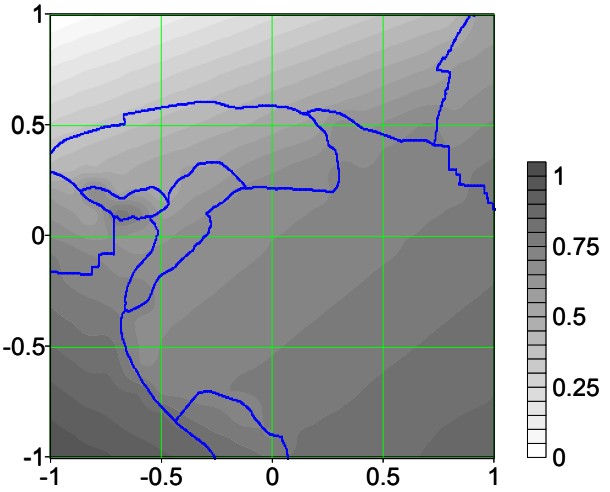

Figure 4: The map of mean hydrostatic stress.

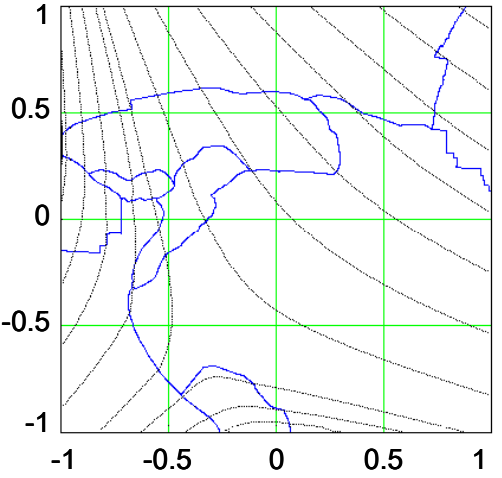

Figure 5: Stress trajectory field.

Although the fields of $\tau_{max}(z)$ and $P(z)$ are discontinuous on the interfaces this is not clearly seen in Figs 3–4 because of interpolation used for plotting these maps. Stress trajectories also look smooth in the figure, however, the tangents to them presenting. the stress orientations suffer certain jump at the interfaces; at some collocation points the jump is up to 10^o.

6 Conclusion

A numerical approach for the reconstruction of plane stress tensors in a composite domain with multiple interfaces is suggested in this paper. It provides

essential tool for stress states identification by discrete data on principal directions and assumes neither boundary stresses nor displacements. The example considered in section 5 demonstrates that the proposed approach is capable for dealing with for geophysical applications with real data and complex geometries.

Acknowledgement

The author acknowledges the financial support of this study by EPSRC through the Research Grant EP/E032494/1.

References

[1] Galybin, A.N. and Sh.A. Mukhamediev, 2004. Determination of elastic stresses from discrete data on stress orientations, *Int J Solids and Structures*, 41 (18-19), 5125-5142.
[2] Mukhamediev Sh.A., A.N. Galybin and B.H.G. Brady, 2006. Determination of stress fields in elastic lithosphere by methods based on stress orientations, *Int J Rock Mech Min Sci*, 43 (1), 66-88.
[3] Mukhamediev, Sh.A. and A..N. Galybin, 2006. Where and how did the ruptures of December 26,2004 and March 28, 2005 earthquakes near Sumatra originate? *Doklady Earth Sciences*. 406 (1), 52-55.
[4] Galybin, A. N., 2006. Stress fields in joined elastic regions: Modelling based on discrete stress orientations. In Situ Rock Stress – Lu, Li, Kjerholt & Dahle (eds), Taylor & Francis/Balkema, Leiden, 193-199.
[5] Heidbach, O., Tingay, M., Barth, A., Reinecker, J., Kurfeß, D. and B. Müller, 2008. The 2008 release of the World Stress Map (available online at www.world-stress-map.org)
[6] Bird, P., 2003. An updated digital model for plate boundaries. *Geochem. Geophys. Geosyst.*, 4(3): 1027, doi:10.1029/2001GC000252.
[7] Zoback, M. L. and M. D. Zoback, 1989. Tectonic stress field of the conterminous United States, *Mem. Geol. Soc. Am*. 172: 523-539
[8] Mukhamediev Sh. A. and A. N. Galybin, 2007. Determination of Stresses from the Stress Trajectory Pattern in a Plane Elastic Domain; *Mathematics and Mechanics of Solids*; 12; 75.
[9] Muskhelishvili N.I., *Some basic problems of the mathematical theory of elasticity,* P. Noordhoff Ltd.: Groningen-Holland, 1953.
[10] Kuske A. and Robertson G., *Photoelastic stress analysis*, John Wiley & Sons Ltd.: Bristol, 1974.
[11] Karakin, A.V., Mukhamediev, Sh. A., 1994. Singularities in nonuniform field of trajectories of the principal tectonic stresses. *Izvestiya, Physics of the Solid Earth* 29, 956-965.

This page intentionally left blank

The boundary element method for the determination of nonlinear boundary conditions in heat conduction

D. Lesnic[1], T. T. M. Onyango[1] & D. B. Ingham[2]
[1] *Department of Applied Mathematics, University of Leeds,UK*
[2] *Centre for Computational Fluid Dynamics, University of Leeds, UK*

Abstract

Physical problems involving heat exchange between the ends of a rod and the surrounding environment can be formulated as a set of equations representing the heat equation and boundary conditions relating the heat fluxes to the difference between the boundary temperatures and the temperature of the surrounding fluid through a function f which represents the heat transfer coefficient. When the heat transfer is purely convective, or solely radiative, then one assumes that f is a linear functional (Newton's law of cooling), or obeys a fourth-order power law (Stefan's law), respectively. However, there are many practical heat transfer situations in which either the governing equation does not take a simple form or the actual method of heat transfer is unknown. In such cases the heat transfer coefficient depends on the boundary temperature and the dependence has a complicated or unknown structure. Processes, such as fast cooling of hot steel or glass in fluids or gases, involve limited opportunities to accurately measure the temperatures and heat fluxes at the surface and in such a case one has to set up an inverse problem that would allows us to reconstruct the exact form of the function f. In this study, we investigate a one-dimensional inverse heat conduction problem with unknown nonlinear boundary conditions. We develop the boundary element method to construct and solve numerically the missing terms involving the boundary temperature, the heat flux and the boundary condition law function f which is approximated as a piecewise constant function of temperature. Since the inverse problem under investigation is ill-posed, in order to stabilise the solution we employ the Tikhonov regularization method. Numerical results are presented and discussed.
Keywords: boundary element method, nonlinear boundary conditions, inverse heat conduction problem, Tikhonov's regularization.

WIT Transactions on Modelling and Simulation, Vol 49,
www.witpress.com, ISSN 1743-355X (on-line)
doi:10.2495/BE090051

1 Introduction

An interesting, mathematically challenging and well-investigated problem is the identification of coefficients that appear in partial differential equations, e.g. [1,2]. In contrast, the identification of the nonlinear boundary conditions is less well-developed. In one-dimensional transient heat conduction these boundary conditions relate the heat flux at the ends of a rod to the boundary temperature through some unknown function f. For example, if the heat exchange between the ends of the rod and its environmental surroundings is solely by convection, then one commonly assumes that f is a linear function of the difference in temperature between the ends of the rod and that of the surrounding fluid with the slope given by the heat transfer coefficient (Newton's law of cooling). Identification of a time, space or both space-time dependent heat transfer coefficient in this case has been investigated in, for example [3–5]. For the case of purely radiative transfer of energy, a fourth-power law of the temperature for the function f is usually employed, (Stefan's law), [6].

However, there are many practical heat transfer situations at high temperatures, or in hostile environments, e.g. combustion chambers, cooling steel processes, gas turbines, etc. in which either the actual method of heat transfer is not known, or it cannot be assumed that the governing boundary laws have such a simple form. For example, in the cooling of hot steel or glass in fluids or gases, the heat transfer coefficient depends on the boundary temperature and this dependence has a complicated and unknown structure, [7,8]. From a technical point of view, fast cooling and processes with limited opportunities to accurately measure surface temperatures and/or heat fluxes are of much interest. In such situations one can set up an inverse experiment that would allow the reconstruction (recovery) of the exact form of the function f. It is well-known that the identification of nonlinear boundary conditions is an ill-posed problem, [9]. It has been shown elsewhere, [10], that by monitoring (recording, measuring) the transient temperature at one end of the rod then one can recover uniquely the unknown function f. However, even if a solution exists and is unique, it will not depend continuously on the input data. Therefore, in order to stabilize the solution one can employ the Tikhonov regularization method, [11], or adopt an engineering approach in which the unknown function f is approximated by a polynomial function with unknown coefficients to be determined.

In this paper we investigate the application of the boundary element method (BEM) for solving numerically the inverse problem of boundary condition law identification in heat conduction.

2 Mathematical formulation of the inverse problem

We consider the initial boundary value problem

$$\frac{\partial T}{\partial t}(x,t) = \frac{\partial^2 T}{\partial x^2}(x,t), \quad (x,t) \in (0,1) \times (0,t_f], \tag{2.1}$$

$$T(x,0) = g(x) \quad x \in [0,1], \tag{2.2}$$

$$\frac{\partial T}{\partial n}(0,t) = -\frac{\partial T}{\partial x}(0,t) = f(T(0,t)), \quad t \in [0,t_f], \tag{2.3}$$

$$\frac{\partial T}{\partial n}(1,t) = \frac{\partial T}{\partial x}(1,t) = f(T(1,t)), \quad t \in [0,t_f], \tag{2.4}$$

$$T(0,t) = h(t), \qquad t \in [0,t_f], \tag{2.5}$$

where T represents the unknown temperature of the one-dimensional rod (0,1), the function f represents the unknown law for the boundary conditions, $t_f > 0$ is an arbitrary final time of interest, n is the outward unit normal, i.e. $n(0) = -1$, $n(1) = 1$, g is the given initial temperature, h is the given additional measured boundary temperature, and, for simplicity, we have assumed that there are no heat sources. The thermal diffusivity has been taken equal to unity for simplicity. For certain conditions on f, the direct problem (2.1)–(2.4) is well-posed, [12]. Moreover, the Fréchet differentiability of the solution T of the direct problem (2.1)–(2.4) with respect to f has been established in [13]. The compatibility conditions associated with (2.2)–(2.5) require that $-g'(0) = f(g(0))$, $g'(1) = f(g(1))$ and $g(0) = h(0)$. For the inverse problem (2.1)−(2.5) we assume that:

(i) $g \in C^{2+1/2}([0,1])$,

(ii) $h \in C^{1+1/2}([0,t_f])$ is strictly monotone and $h(0) = g(0)$,

(iii) $T(1,t;f) \in [h(0),h(t)]$ for all $t \in [0,t_f]$,

where $T(x,t;f)$ is the solution of the direct mixed problem (2.1), (2.2), (2.4) and (2.5) when f is known. Solvability results for this latter direct problem are given in [14].

It is worth noting that for condition (iii), one cannot guarantee that the range of temperatures on the boundary $x = 1$ is contained in the range of temperature measured data (2.5) by giving conditions on the data g and h alone, since condition (iii) depends on the unknown function f. However, from the maximum principle for the heat equation, [15], there are easily obtainable conditions under which condition (iii) can be made to hold. For example, if it is known *a priori* that $f \leq 0$, and if $g(0) = g(1)$, then it is easy to give conditions under which h will be a decreasing function and

$$h(t) = T(0,t) \leq T(1,t) \leq T(1,0) = g(1) = g(0) = h(0), \quad t \in [0,t_f]. \tag{2.6}$$

Under the assumptions (i)–(iii), there is a unique local solution (T,f) of the inverse problem (2.1)–(2.5), [10].

Several factors may allow us to extend this theorem to global solvability. For example, if the admissible (allowable) class of functions f is restricted to uniformly Lipschitz functions C^{0+1}, this will be the case, [10]. Other solvability results are given in [16].

At this stage, it is probably difficult to say definitely how ill-posed (unstable) is the inverse problem (2.1)–(2.5), but it may be worth mentioning, [11], that part

of the ill-posedness comes from the fact that calculating the normal derivative $\frac{\partial T}{\partial n}$ from the boundary Dirichlet noisy data is a typical linear ill-posed problem, [17, 18].

3 The boundary element method (BEM)

Using the BEM, and applying the initial and boundary conditions (2.2)–(2.4), we obtain the integral representation, e.g. [19],

$$\eta(x)T(x,t) = \int_0^t \left[G(x,t;\xi,\tau) f(T(\xi,\tau)) - T(\xi,\tau) \frac{\partial G}{\partial n(\xi)}(x,t;\xi,\tau) \right]_{\xi\in\{0,1\}} \mathrm{d}\tau + \int_0^1 g(y) G(x,t;y,0) \mathrm{d}y, \quad (x,t) \in [0,1] \times (0,t_f], \tag{3.1}$$

where $\eta(0) = \eta(1) = 0.5$, $\eta(x) = 1$ for $x \in (0,1)$ and

$$G(x,t;\xi,\tau) = \frac{H(t-\tau)}{2\sqrt{\pi(t-\tau)}} \exp\left[-\frac{(x-\xi)^2}{4(t-\tau)} \right], \tag{3.2}$$

where H is the Heaviside function.

Applying (3.1) at the boundaries $x = 0$ and $x = 1$ and using (2.2)–(2.5) we obtain two nonlinear boundary integral equations in the unknowns f and $T(1,t)$, namely

$$\frac{1}{2}h(t) = \int_0^t \left[G(0,t;0,\tau) f(h(\tau)) + G(0,t;1,\tau) f(T(1,\tau)) - h(\tau) \frac{\partial G}{\partial n(0)}(0,t;0,\tau) - T(1,\tau) \frac{\partial G}{\partial n(1)}(0,t;1,\tau) \right] \mathrm{d}\tau + \int_0^1 g(y) G(0,t;y,0) \mathrm{d}y, \quad t \in (0,t_f], \tag{3.3}$$

$$\frac{1}{2}T(1,t) = \int_0^t \left[G(1,t;0,\tau) f(h(\tau)) + G(1,t;1,\tau) f(T(1,\tau)) - h(\tau) \frac{\partial G}{\partial n(0)}(1,t;0,\tau) - T(1,\tau) \frac{\partial G}{\partial n(1)}(1,t;1,\tau) \right] \mathrm{d}\tau + \int_0^1 g(y) G(1,t;y,0) \mathrm{d}y, \quad t \in (0,t_f]. \tag{3.4}$$

where

$$\frac{\partial G}{\partial n(\xi)}(x,t;\xi,\tau) = \frac{(x-\xi) n(\xi) H(t-\tau)}{4\sqrt{\pi(t-\tau)^3}} \exp\left[-\frac{(x-\xi)^2}{4(t-\tau)} \right]. \tag{3.5}$$

We discretise the time interval $(0, t_f]$ into a series of N boundary elements, namely

$$(0, t_f] = \bigcup_{j=1}^{N} (t_{j-1}, t_j],$$

and assume that the boundary temperature is constant over each boundary element $(t_{j-1}, t_j]$ and takes its value at the mid point $\tilde{t}_j = (t_{j-1} + t_j)/2$, i.e.

$$T(0,t) = h(\tilde{t}_j) = h_j, \quad T(1,t) = T(1,\tilde{t}_j) = T_{1j}, \quad t \in (t_{j-1}, t_j]. \tag{3.6}$$

We also discretise the space interval $[0, 1]$ into a series of N_0 cells, namely

$$[0, 1] = \bigcup_{k=1}^{N_0} [x_{k-1}, x_k],$$

and assume that the initial temperature is constant over each space cell $[x_{k-1}, x_k]$ and takes its value at the mid point $\tilde{x}_k = (x_{k-1} + k_k)/2$, i.e.

$$T(x,0) = g(\tilde{x}_k) = g_k, \quad \text{for} \quad x \in (x_{k-1}, x_k]. \tag{3.7}$$

On discretizing the boundary integral equations (3.3) and (3.4), and using the piecewise constant boundary element approximations (3.6) and (3.7), all the BEM integrals that result can be evaluated analytically, [20], and the inverse problem (2.1)–(2.5) recasts as a nonlinear system of $2N$ equations which, in a generic matrix form, can be written as

$$A_f(\mathbf{T}_1) = \mathbf{b}, \tag{3.8}$$

where $\mathbf{T}_1 = (T_{1j})_{j=\overline{1,N}}$, $\mathbf{b}$ contains expressions of the known data g and h, and A_f is a nonlinear operator associated to the unknown function f.

4 Numerical procedure for the inverse problem

In a previous work, [21], we found the pair solution (f, T) by assuming that f belongs to the global class of polynomial functions with unknown coefficients. In this paper we extend the analysis by assuming that f belongs to a class of piecewise constant functions.

Assuming that the boundary temperature measurement (2.5) is strictly increasing, see condition (ii) of Section 2, we denote by

$$q_k := h(0) + \frac{k(h(t_f) - h(0))}{K}, \qquad k = \overline{0, K}$$

a uniform discretization in K equal sub-intervals of the interval $[h(0), h(t_f)]$.

Next we seek a piecewise function $f : [q_0, q_K] \to \mathbb{R}$ defined by

$$f(T) = \begin{cases} a_1, & T \in [q_0, q_1), \\ a_2, & T \in [q_1, q_2), \\ \vdots & \\ a_K, & T \in [q_{K-1}, q_K], \end{cases} \tag{4.1}$$

where the coefficients $\mathbf{a} = (a_k)_{k=\overline{1,K}}$ are unknown and yet to be determined by imposing (4.3) in a nonlinear least-squares sense. From (4.1) and the assumption that the condition (iii) of Section 2 is satisfied we have

$$f(h(\widetilde{t_l})) = a_{\varphi(l)},\ f(T(1, \tilde{t_l})) = a_{\psi(l)}, \quad l = \overline{1, N}, \tag{4.2}$$

where for each $l \in \{1, \ldots, N\}$, $\varphi(l)$ is the unique number in the set $\{1, \ldots, K\}$ such that $h(\tilde{t_l}) \in \left[q_{\varphi(l)-1}, q_{\varphi(l)}\right)$, and $\psi(l)$ is the unique number in the set $\{1, \ldots, K\}$ such that $T(1, \tilde{t_l}) \in \left[q_{\psi(l)-1}, q_{\psi(l)}\right)$. Based on (4.2), the system of nonlinear equations (3.8) is solved using the minimization of the Tikhonov regularization functional $S : \mathbb{R}^K \times \mathbb{R}^N \to \mathbb{R}_+$ defined by

$$S(\mathbf{a}, \mathbf{T_1}) = ||A_f(\mathbf{T}_1) - \mathbf{b}||^2 + \kappa ||a||^2, \tag{4.3}$$

where $\kappa \geq 0$ is the regularization parameter to be prescribed.

In (4.3) we have included the regularization term in order to stabilize the solution of the inverse and ill-posed problem under investigation with respect to noisy errors in the input measurements (2.5), namely

$$h^{\epsilon}(t) = h(t) + \epsilon, \tag{4.4}$$

where ϵ are Gaussian random variables with mean zero and deviation $\sigma = \rho \times \max\{|h(t)|,\ t \in [0, t_f]\}$ generated using the NAG routine G05DDF, and 100ρ represents the percentage of noise. The minimization of the functional (4.3) is performed using the NAG routine E04FCF. This routine is minimizing iteratively an arbitrary sum of squares with no constraints on the variables and no gradient needed to be supplied by the user.

5 Numerical results and discussion

In this section we illustrate and discuss numerical results for two benchmark test examples consisting of retrieving the pair solution (f, T) satisfying (2.1)–(2.5), when f has the piecewise constant parametrization (4.1). Higher-order (e.g linear, quadratic) piecewise constant polynomial approximations are deferred to a future work.

The BEM described in Section 3 is applied with $(N, N_0) = (40, 40)$ to generate the forward nonlinear operator $A_f(T_1)$. The parametrization (4.1) is sought with a typical value of $K = 10$ large enough to capture all the significant features of the examples below.

The initial guess for minimizing the functional (4.3) was taken $(a^0, T_1^0) = (3, 3)$ for Example 1 and $(a^0, T_1^0) = (3, 50)$ for Example 2. In both examples, the analytical temperature function to be retrieved was taken to be

$$T(x,t) = x^2 - x + 1 + 2t, \quad (x,t) \in [0,1] \times [0,t_f]. \tag{5.1}$$

Equation (5.1) then generates the initial condition (2.2) and the measurement boundary condition (2.5) be given by

$$T(x,0) = g(x) = x^2 - x + 1, \quad x \in [0,1], \tag{5.2}$$

and

$$T(0,t) = h(t) = 1 + 2t, \qquad t \in [0,1]. \tag{5.3}$$

Remark that for the example (5.1) conditions (i)−(iii) of Section 2 are satisfied such that the local solvability of the inverse problem (2.1)−(2.5) is ensured.

5.1 Example 1

In this simple example, we solve for T and f the inverse problem in the domain $(0,1) \times (0, t_f = 1]$ given by the heat equation (2.1) subject to the initial condition (5.2), the boundary conditions (2.3) and (2.4), and the additional measurement (5.3). The analytical solution to be retrieved is given by equation (5.1) for the temperature $T(x,t)$ and $f(T) \equiv 1$, i.e. the constant vector $\mathbf{a} \equiv \mathbf{1}$.

Figures 1(b) and (c) show the numerical results for $\mathbf{T_1}$ and $\mathbf{a}$, respectively, when the input measured data (5.3) is contaminated by various amounts of additive noise $\rho\%$, as in (4.4), see Figure 1(a). Whilst from Figure 1(b) it can be seen that the analytical value of $T(1,t) = 1 + 2t$ is excellently retrieved almost independent of ρ, from Figure 1(c) it can be seen that the numerically obtained solution for $\mathbf{a}$ is proportionally accurate with the amount of noise ρ introduced in the input data. This indicates that we have obtained a stable solution. We also report that no regularization, i.e. $\kappa = 0$ in (4.3), was found necessary for this simple example.

5.2 Example 2

It is well-known that, in general, the heat flux on a surface is the sum of two terms corresponding to convection and surface radiation, [6]. We therefore examine an interesting and important example of a nonlinear inverse heat conduction problem in which the relation between the heat flux and temperature at the boundaries, from a physical point of view, is a fourth power in the temperature and this represents radiative boundary conditions, i.e. we seek to retrieve $f(T) = T^4$. In this case, the boundary conditions (2.3) and (2.4) are slightly modified as

$$\frac{\partial T}{\partial n}(x,t) = f\left(T(x,t)\right) + 1 - (1+2t)^4, \quad (x,t) \in \{0,1\} \times (0,t_f], \tag{5.4}$$

such that the temperature (5.1) and the nonlinear boundary law $f(T) = T^4$ represent the analytical solution of the inverse problem (2.1), (5.2)–(5.4).

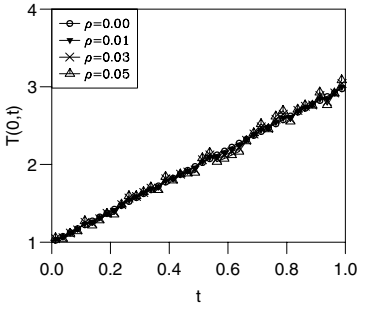

(a)

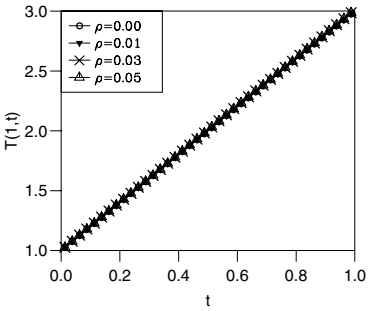

(b)

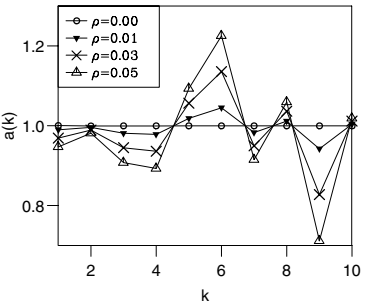

(c)

Figure 1: (a) The analytical boundary temperature $T(0,t)$, (b) the numerical boundary temperature $T(1,t)$, as functions of time t, and (c) the numerical vector $\mathbf{a} = (a_k)_{k=\overline{1,10}}$, when the amount of noise in (4.4) is: ($\circ$) $\rho = 0$, ($\blacktriangledown$) $\rho = 0.01$,($\times$) $\rho = 0.03$,($\triangle$) $\rho = 0.05$. No regularization parameter, $\kappa = 0$.

Figures 2(a) and (b) show the results for the boundary temperature $T(1,t)$ and the function $f(T)$, respectively, when various amounts of noise $\rho \in \{0,1,3,5\}\%$ are included in the measured data (5.3), as shown in Figure 1(a). No regularization has been added in the functional (4.3). From Figure 2 it can be seen that as the amount of noise ρ decreases the numerical solution approaches the exact solution. The numerical results can be further improved by employing some regularization, say $\kappa = 10^{-3}$, in (4.3), as shown in Figure 3.

6 Conclusions

In this paper, we have investigated an inverse heat conduction problem with unknown nonlinear boundary conditions. We have used the BEM in conjunction with the Tikhonov regularization procedure to construct and solve numerically the

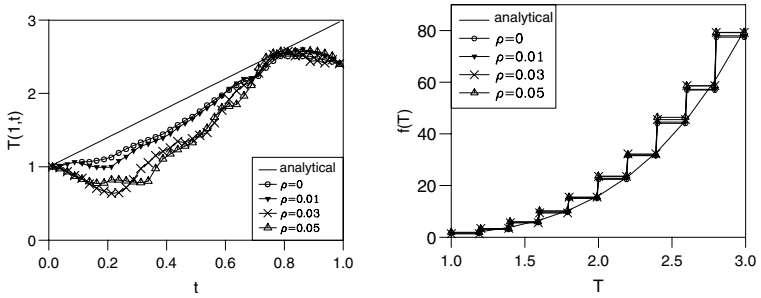

(a) (b)

Figure 2: The analytical and numerical approximations of (a) the boundary temperature $T(1,t)$ and (b) the function $f(T)$, when $\rho \in \{0,1,3,5\}\%$ and $\kappa = 0$.

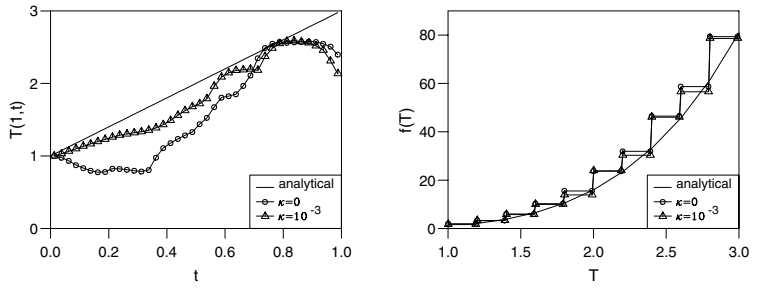

(a) (b)

Figure 3: The analytical and numerical approximations of (a) the boundary temperature $T(1,t)$ and (b) the function $f(T)$, when $\rho = 5\%$, $\kappa = 0$ and 10^{-3}.

missing terms involving the boundary temperature, the heat flux, and a piecewise constant approximation of the function relating the boundary temperature and heat flux in one-dimensional transient heat conduction. The numerical results obtained showed that a stable and accurate solution was obtained. Future work will concern extensions to higher dimensions.

References

[1] N.V. Muzylev, Uniqueness theorems for some converse problems of heat conduction, *U.S.S.R. Comput. Maths. Math. Phys.*, **20**, 120-134, (1980).

[2] M. Pilant and W. Rundell, Undetermined coefficient problems for nonlinear elliptic and parabolic equations, *Int. Ser. Numer. Math.*, **77**, 139-154, (1986).

[3] S. Chantasiriwan, Inverse heat conduction problem of determining time-dependent heat transfer coefficients, *Int.J. Heat Mass Transfer*, **42**, 4275-4285, (1999).
[4] E. Divo, A.J. Kassab, J.S. Kapat and M.-K Chyu, Retrieval of multidimensional heat transfer coefficient distributions using an inverse BEM-based regularized algorithm: numerical and experimental results, *Eng. Anal. Boundary Elements*, **29**, 150-160, (2005).
[5] C.-H. Huang, D.-M. Wang and H.-M. Chen, Prediction of local thermal contact conductance in plate finned-tube heat exchangers, *Inverse Problems in Engineering*, **7**, 119-141, (1999).
[6] H.S. Carslaw and J.C. Jaeger, *Conduction of Heat in Solids*, 2nd edition, Clarendon Press, Oxford (1959).
[7] A. Rösch, A Gauss-Newton method for the identification of non-linear heat transfer laws, *Int. Ser. Numer. Math.*, **139**, 217–230, (2002).
[8] D.H. Wolf, F.P. Incropera and R. Viskanta, Jet impingement boiling, *Adv. Heat Transfer*, **23**, 1–132, (1993).
[9] A. Rösch, Identification of nonlinear heat transfer laws by optimal control, *Numer. Funct. Anal. Optimiz.*, **15**, 417–434, (1994).
[10] M. Pilant and W. Rundell, An iteration method for the determination of an unknown boundary condition in a parabolic initial-boundary value problem, *Proc. Edinburgh Math. Soc.*, **32**, 59–71, (1989).
[11] T. Kaiser and F. Tröltzsch, An inverse problem arising in the steel cooling process, *Wissenschaftliche Zeitung TU Karl-Marx-Stadt*, **29**, 212–218, (1987).
[12] A. Rösch, Identification of nonlinear heat transfer laws by means of boundary data, In *Progress in Industry*, Wiley, Teubner, 405–412, (1996).
[13] A. Rösch, Fréchet differentiability of differential of the solution of the heat equation with respect to a nonlinear boundary condition, *Z. Anal. Anw.* **15**, 603–618, (1996).
[14] A. Friedman, *Partial Differential Equations of Parabolic Type,* Prentice Hall, Englewood Cliffs, N.J. (1964).
[15] M.H. Protter and H.F. Weinberger, *Maximum Principles in Differential Equations*, Prentice-Hall, Englewood Cliffs, N.J. (1967).
[16] A. Shidfar and H. R. Nikoofar, An inverse problem for a linear diffusion equation with non-linear boundary conditions, *Appl. Math. Lett.*, **2**, 385–388, (1989).
[17] W. Gerlach and L. von Worfersolorf, On approximate computation of the values of the normal derivative of solutions to linear partial differential equations of second order with applications to Abel's integral equation, *ZAMM*, **66**, 31–36, (1986).
[18] R. Bialecki, E. Divo and A.J. Kassab, Reconstruction of time-dependent boundary heat flux by a BEM based inverse algorithm, *Eng. Anal. Boundary Elements*, **30**, 767–773, (2006).
[19] C.A. Brebbia, J.C.F. Telles and L.C. Wrobel, *Boundary Element Techniques*, Springer-Verlag, Berlin (1984).

[20] T.T.M Onyango, D.B. Ingham and D. Lesnic, Restoring boundary conditions in heat conduction, *J. Eng. Math.*, **62**, 85–101, (2008).
[21] T.T.M. Onyango, D.B. Ingham and D. Lesnic, Reconstruction of boundary condition laws in heat conduction using the boundary element method, *Comput. Math. Appl.,* **57**, 157–168, (2009).

This page intentionally left blank

FEM type method for reconstruction of plane stress tensors from limited data on principal directions

J. Irša & A. N. Galybin
Wessex Institute of Technology, Southampton, UK

Abstract

This paper presents a method for reconstruction of maximum shear stress and stress trajectories from discrete data on principal directions. The domain is divided into smaller subdomains where stress potentials are assumed to be linear holomorphic functions. The functions obey continuity along element interfaces, which is used to form the first group of equations. The known data on principal directions are used in the second group of equations. Therefore, no stress magnitudes are involved in formulations, which eventually leads to a homogeneous system of linear algebraic equations. In order to make the system inhomogeneous an extra equation is added. It represents mean value of maximum shear stress over the domain. The reconstructed maximum shear stress, therefore, includes an arbitrary positive multiplicative parameter.

Keywords: photoelasticity, stress trajectories, holomorphic function.

1 Introduction

Numerical method presented in this paper aims to reconstruct maximum shear stresses from discrete data on principal directions. Several examples from photoelasticity [1, 2] are considered to verify effectiveness of the method.

In the past photoelasticity was widely used in mechanics of solids [1, 2]. It is an optical method to determine stresses in plane models on the basis of birefringence, the property, observed in certain transparent material. The optical properties of such materials are modified with intensity of loading. The normal incidence of light is resolved into two components, each one coinciding with a principal plane of stress. Placing photoelastic sample between polarizers whose axes are perpendicular, one can observe black fringes in the sample, these are referred to as isoclinics. Orientations of the two principal stresses are obtained by

WIT Transactions on Modelling and Simulation, Vol 49, © 2009 WIT Press
www.witpress.com, ISSN 1743-355X (on-line)
doi:10.2495/BE090061

rotating the polarizers from 0^o to 90^o, and drawing the isoclinics. The stress trajectory presents a curve the tangents to which coincide with the principal direction of one of the principal stresses, therefore the pattern of stress trajectories is further drawn by using the obtained set of discrete stress orientations.

The procedures for obtaining stress trajectories and determination of stresses from the photoelastic data, so called process of stress separation, are detailed in textbooks [1, 2]. They are based on relatively dense set of uniformly distributed data, which allows one to determine the stress field with high accuracy and even to consider this field as a continuous one.

In geophysics, the data on stress orientations in the earth's crust can be obtained by different experimental methods (see the WSM project for detail [3]). However these data are significantly inhomogeneous and irregular. Moreover, the data are mostly related to the tectonic plate margins and large regions of the crust are not populated with the data at all. This structure of the data makes it impossible to directly transfer the methods used in photoelasticity to the problem of stress identification in the lithosphere. Therefore special approaches have recently been developed in [4–6]. These approaches make use of mathematical theory of plane elasticity [7], where the mean stress and deviatoric stress functions are described by means of two holomorphic functions, complex potentials. A method for reconstructing maximum shear stress field from discrete data on stress trajectories, using approximation of holomorphic functions across whole domain has firstly been applied in [4]. In this paper an example from photoelasticity for a beam under three point bending test is presented to verify the effectiveness of the proposed approach. It is further applied for geophysical data to study stresses in the Australian continent [4, 5]. In these papers single plane domains have been considered. The method has also been applied for a pair of adjacent elastic regions to study elastic stress field of Antarctica plate, where the most data are known on the continent boundaries [6]. Apart from data on stress orientations, the continuity of the stress vector across the margins of the plate has been used in this paper as an additional conditions imposed on the sought solutions.

The present paper presents a method where the domain is divided into smaller subdomains and approximation is performed within each subdomain with implied continuity of approximating functions across the subdomain boundaries. Similar method has recently been developed for harmonic problem of heat flux reconstruction from temperature data [8].

The method is further verified with synthetic data, as well as with experimental data extracted from photoelasticity experiments.

2 The method

2.1 Equation of plane elasticity

In 2D stress field, the plane symmetric stress tensor is given by its components σ_{11}, σ_{12}, σ_{22}. The stress tensor can be described by means of the following stress functions [7]:

$$P(z,\bar{z}) = \frac{1}{2}(\sigma_{11} + \sigma_{22}), \quad D(z,\bar{z}) = \frac{1}{2}(\sigma_{22} - \sigma_{11}) + i\sigma_{12} \tag{1}$$

Functions P and D represent the mean stress and the stress deviatoric respectively. The mean stress function is a real-valued function and the deviatoric stress is a complex valued function of complex conjugated variables $z = x + iy,\ \bar{z} = x - iy$. The functions P and D satisfy equations of equilibrium that can be expressed in the following complex form:

$$\frac{\partial P}{\partial z} = \frac{\partial D}{\partial \bar{z}} \tag{2}$$

The deviatoric stress function D can be written in the form:

$$D(z,\bar{z}) = \tau_{\max}(z,\bar{z}) e^{i\alpha(z,\bar{z})} \tag{3}$$

Here the modulus of function D presents the maximum in-plane shear stress $\tau_{\max} = |D|$ and $\alpha = \arg(D)$ can be expressed as follows:

$$\alpha = \pi - 2\varphi \tag{4}$$

where φ is the principal direction.

For homogenous isotropic elastic medium following equation is satisfied:

$$\Delta P = 0 \tag{5}$$

The stress functions P and D according to the Kolosov–Muskhelishvili formulae [7] can be expressed in terms the form:

$$P(z,\bar{z}) = \Phi(z) + \overline{\Phi(z)}, \quad D(z,\bar{z}) = \bar{z}\Phi'(z) + \Psi(z) \tag{6}$$

where the complex potentials $\Phi(z)$ and $\Psi(z)$ are holomorphic functions.

2.2 Problem description

Let Ω be a simply connected elastic domain. It is assumed that principal directions φ_j are known as a discrete set of points z_j (j=1…N), located within the domain. The task is to reconstruct the stress field from principal directions, in particular, the stress deviator, presented by the function D.

The data on principal directions have no restrictions on the type of distribution. In examples considered in section 3 synthetic data are uniformly distributed while photoelastic data are not uniform.

It has been shown in [4] that the reconstruction of stress trajectories is unique, while the solution of $\tau_{\max}$ contains one multiplicative positive constant, and therefore the solution for P contains an extra additive real parameter caused by integration of (3). We further concentrate on the reconstruction of the stress deviator only and therefore do not pay much attention to the additive free parameter.

The domain is divided into n smaller subdomains of an arbitrary shape. In every subdomain, the holomorphic functions entering in the second equation (6) are approximated by linear holomorphic functions are specified as follows:

$$\begin{aligned} \Phi'^{(m)}(z) &= a_0^{(m)} + a_1^{(m)} z \\ \Psi^{(m)}(z) &= a_2^{(m)} + a_3^{(m)} z \end{aligned}, \quad m = 1 \ldots n \tag{7}$$

a, b, c and *d* are unknown complex constants, therefore 8 unknown real constants can be associated with every single subdomain. Principal directions are associated with the stress deviators in subdomains, i.e. the arguments of the functions $D^{(m)}(z,\bar{z}) = \bar{z}\Phi'^{(m)}(z) + \Psi^{(m)}(z)$, therefore the arguments of complex potentials cannot be specified separately.

2.2.1 Discretization

The discretization of the domain and introduction of collocation points on its interfaces are performed with respect to the examples considered in section 3. Rectangular elements are used for the rectangular domain and polar elements are used for circular ring domain (Figure 1).

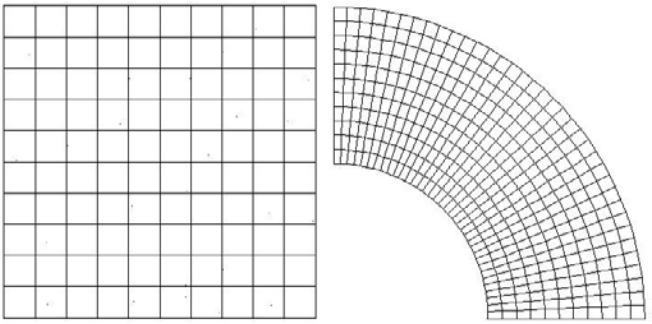

Figure 1: Rectangular element type (left) and polar element type (right).

2.2.2 Equations of continuity, condition equations and non-homogenous equation

In is assumed that stresses are continuous in Ω. Thus, the approximating holomorphic functions, representing $\Phi'(z)$ and $\Psi(z)$ obey continuity across interfaces at collocation points. For the *k-th* collocation point, lying on the interface between the elements numbered *m* and *m+1*, the equations of continuity for $\Phi'(z)$ and $\Psi(z)$ are as follows:

$$\begin{aligned} \Phi'^{(m)}(z_k) - \Phi'^{(m+1)}(z_k) &= 0 \\ \Psi^{(m)}(z_k) - \Psi^{(m+1)}(z_k) &= 0 \end{aligned}, \quad m = 1\ldots n; \quad k = 1\ldots N_{CP} \tag{8}$$

As mentioned above these two equations do not include information about the principal directions and therefore the following expression for the stress deviators is used to impose data:

$$D^{(m)}(z,\bar{z}) = (a_0\bar{z} + a_1 z)\bar{z} + a_2 + a_3 z \tag{9}$$

The maximum shear stress is a real valued function; therefore the following equations are valid in every subdomain:

$$\mathrm{Im}\left[\left(a_0^{(m)}\bar{z}_j + a_1^{(m)} z_j \bar{z}_j + a_2^{(m)} + a_3^{(m)} z_j\right) e^{-i\alpha_j}\right] = 0\,, \quad j = 1\ldots N \tag{10}$$

This equation is satisfied for every known location z_j.

A non-homogenous equation has to be added to the system to address the fact that the field of τ_{max} has one multiplicative arbitrary parameter. It is further assumed that the average value of τ_{max} over the whole region as unity, which leads to the following equation:

$$\sum_{m=1}^{N_{elem}}\left[\left(a_0^{(m)}\bar{z}_j + a_1^{(m)} z_j \bar{z}_j + a_2^{(m)} + a_3^{(m)} z_j\right) e^{-i\alpha_j}\right] = N_{elem} \tag{11}$$

The total system consists of equations given by (8), (10) and (11).

By extracting the real and imaginary parts of equations (8), (10) and (11) the real system of linear algebraic equations (SLAE) can be obtained and rewritten in a matrix form:

$$\mathbf{Ax} = \mathbf{b} \tag{12}$$

where $\mathbf{A} \in R^{mxn}$, $\mathbf{b} \in R^m$ and $m>n$. $\boldsymbol{x}$ is the vector of the unknown real coefficients, of the length n. The vector $\boldsymbol{x}$ is composed of real and imaginary parts of unknown complex coefficients. Vector $\boldsymbol{b}$ is known exactly, while, $\boldsymbol{A}$ the matrix of the SLAE depends on data quality, type and size of element. The matrix A is not a square matrix, the system is over-determined and therefore the left-hand side $\boldsymbol{Ax}$ does not exactly equal to $\boldsymbol{b}$ and thus the system is inconsistent. However an approximate solution, $\mathbf{x}^*$, can be found by the least squares method [9] that minimises the residual to bring the error below the given level:

$$\left\|\mathbf{Ax}^* - \mathbf{b}\right\|_2 \le \varepsilon \tag{13}$$

where $\|...\|_2$ stands for the L_2 norm.

If the system is well-posed and not large, then the inversion of the matrix does not meet difficulties and the approximate solution takes the form:

$$\mathbf{x}^* = (\mathbf{A}^T\mathbf{A})^{-1}\mathbf{A}^T\mathbf{b} \tag{14}$$

The condition number (*CN*) is used in the numerical examples to control well-posedness of the SLAE.

3 Results

The method was first tested for a simple synthetic example in order to verify the accuracy. Other tests include data compiled from photoelastic experiments for rectangular and polar domains.

3.1 Results for synthetic example

Let potentials Φ' and Ψ be known in Ω. Given these, one can calculate the stress deviator and obtain maximum shear stress and stress trajectories. Synthetic data extracted from the given potentials are referred to as the ideal data.

The potentials are chosen as low degree polynomials:

$$\begin{aligned}\Phi'(z) &= 0.2 + (0.2 + i\,0.4)z \\ \Psi(z) &= -0.1 + i\,0.5 + (-0.4 + i\,0.1)z + (-0.4 + i\,0.7)z^2\end{aligned} \tag{15}$$

Computational domain is the square $-1 < x < 1$ and $-1 < y < 1$. One singular point is found inside of this area, which refers zero maximum shear stress.

Within this area 36 uniformly distributed data on principal directions and 64 rectangular elements with 2 collocation points in every interface have been used (Figure 2). The system consisting of 933 equations and 512 unknowns produced CN=422 and residual equal to 5.7.

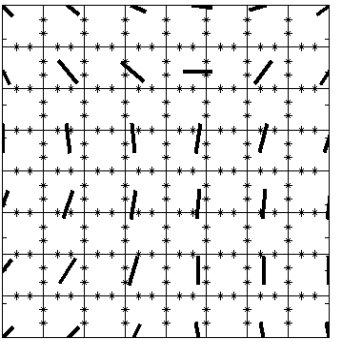

Figure 2: Computational domain showing subdomains, data on principal directions and collocation points.

The results of reconstruction are compared with the characteristics of the ideal stress field given by (15); Figure 3 presents contour map of the reconstructed and ideal maximum shear stress stresses; Figure 4 shows the profiles of maximum shear stresses over several cross sections. Ideal and reconstructed stress trajectory fields are plotted in Figure 5, which illustrates to illustrate that the singular point has been identified with high accuracy.

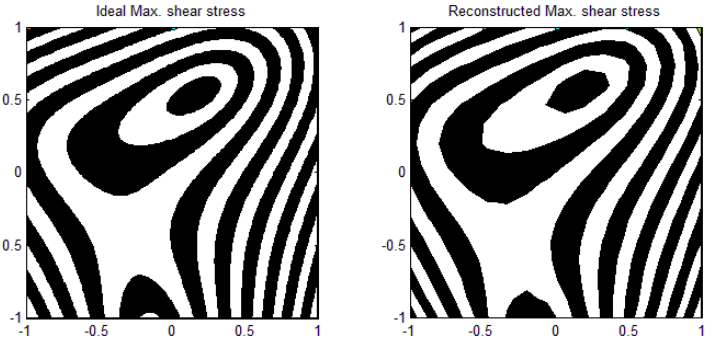

Figure 3: Ideal (left) and reconstructed (right) maximum shear stress

3.2 Results for gas turbine blade under thermal shock

A photoelastic experiment on stress determination in a gas turbine blade caused by of thermal shock [2] is used to collect 300 data subjected to errors, Figure 6.

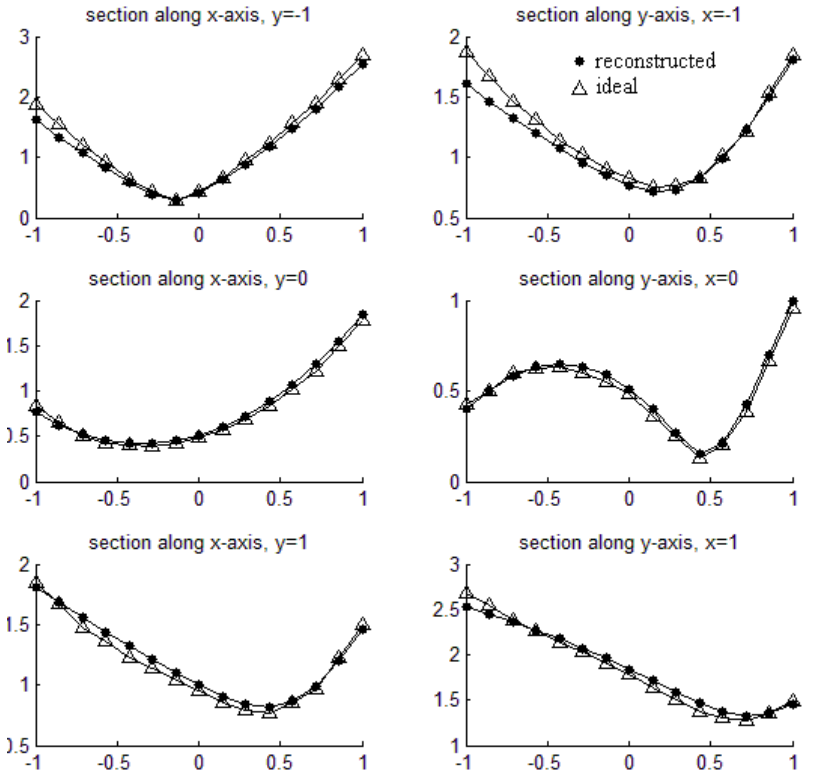

Figure 4: Profiles of reconstructed (dots) and ideal (triangles) maximum shear stress.

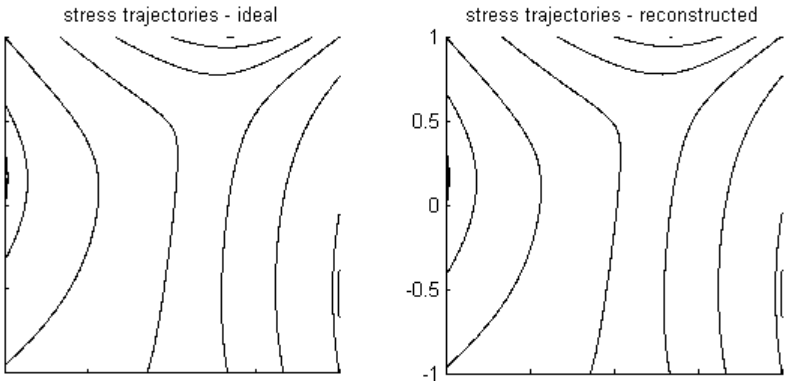

Figure 5: Stress trajectories, ideal (left) and reconstructed (right).

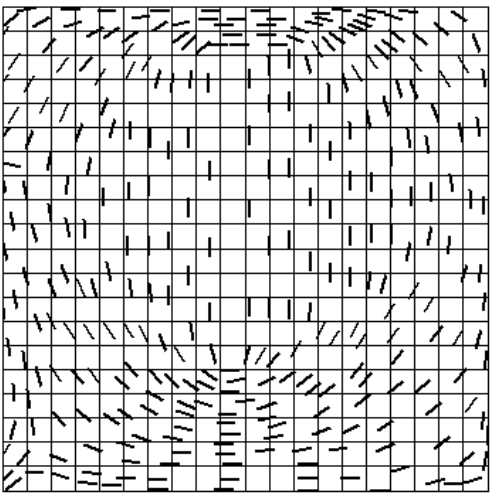

Figure 6: Manually picked data and discretization.

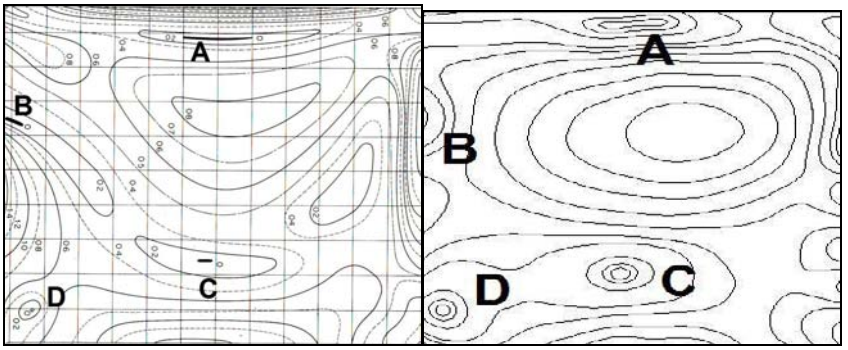

Figure 7: Experimental result for isochromatics [2] (left) and reconstructed isochromatics (right).

The errors are due to approximation used in [2] for plotting of stress trajectories and to manual pick up. The data have been picked from stress trajectories image, using MATLAB software.

Computational domain consists of 400 elements with two collocation points on each interface, Figure 6. The SLAE consisted of 6381 equations and 3200 unknowns. The condition number of this system was 10^4 and the residual was 288.

Isochromatics obtained from photoelasticity and the reconstructed isochromatics are shown in Figure 7 where A,B,C,D are singular (isotropic) points. Experimental and reconstructed stress trajectories are shown in Figure 8. It is remarkable that in this example three singular points (A, C, D) are inside the domain and one B is on its boundary. All of them have been recovered from principal directions data.

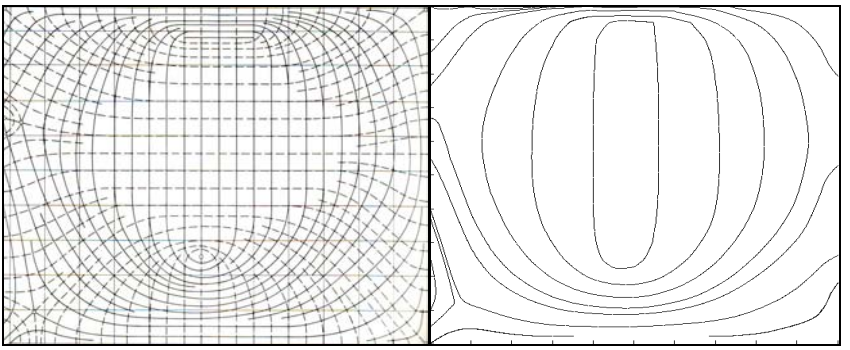

Figure 8: Stress trajectories from experiment [2] (left) and reconstructed stress trajectories (right).

3.3 Results for Bakelite ring under concentrated diametral loads

The data from a photoelastic experiment for a ring subjected to the action of two concentrated forces have been used. In this example almost all boundary is free of stresses except of two small loading areas. The stress trajectories image was used to obtain 300 data on principal direction, Figure 9. The stress pattern for compressed circular ring is shown in Figure 10 (left).

Computational domain has been discretized into 320 polar elements, with following distribution: 8 elements placed along radius and 40 elements placed along the circumference with 2 collocation points on each interface. The discretization is shown in Figure 9 (right). The system consisted of 5007 equations and 2560 unknowns. Condition number is 2465 and residual is 176.

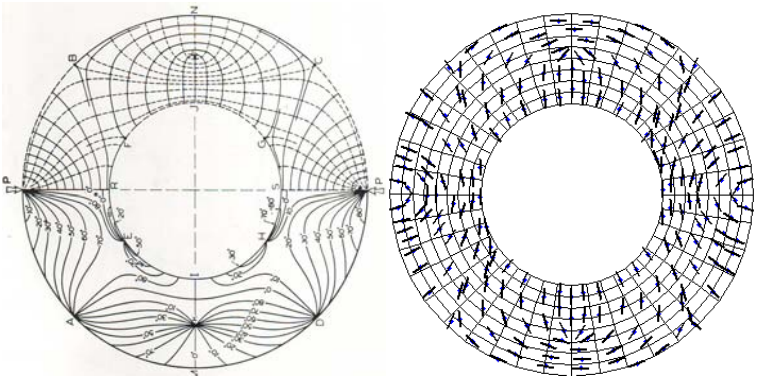

Figure 9: Stress trajectories and isoclinics from [1] (left) and discretization (right).

Reconstructed maximum shear stress is shown in Figure 10 (right). Comparison between photoelasticity isoclinics and reconstructed ones is shown in Figure 11.

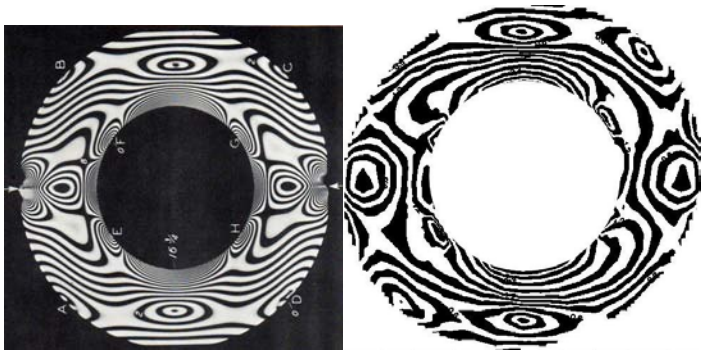

Figure 10: Fringe pattern from [1] (left) and reconstructed fringe pattern (right).

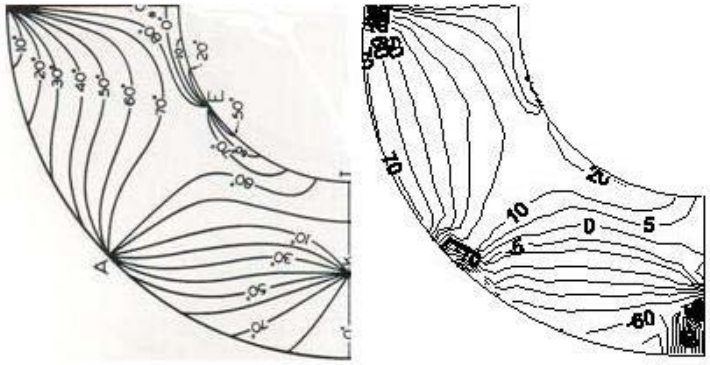

Figure 11: Comparison of isoclinics, photoelasticity (left) and reconstruction (right).

4 Conclusions

An approach capable to reconstruct maximum shear stress field from discrete data of principal directions have been proposed. Although the approach is somewhat similar to FEM it does not require consideration of plane elastic boundary value problems and uses approximation of holomorphic functions in subdomains.

The effectiveness of the proposed approach has been confirmed by satisfactory results of reconstruction as synthetic as well as real photoelastic data including identification of internal and boundary singular points.

Acknowledgement

The authors are grateful to EPSRC for the financial support of this work through the Research Grant EP/E032494/1.

References

[1] Frocht M.M., *Photoelasticity, vol.1.*, John Wiley & Sons Inc.: London, 1962.
[2] Kuske A. and Robertson G., *Photoelastic stress analysis*, John Wiley & Sons Ltd.: Bristol, 1974.
[3] Heidbach O., Tingay M., Barth A., Reinecker J., Kurfess D. and Műller B., *The 2008 release of the World Stress Map* (available online at www.world-stress-map.org).
[4] Galybin A.N. and Mukhamediev Sh.A., *Determination of elastic stresses from discrete data on stress orientations,* IJSS, 41 (18-19), 5125-5142, 2004.
[5] Mukhamediev Sh.A., Galybin A.N. and Brady B.H.G., *Determination of stress fields in the elastic lithosphere by methods based on stress orientations*, IJRMMS, 43 (1), 66-88, 2006.
[6] Galybin A.N., *Stress fields in joined elastic regions: Modelling based on discrete stress orientations*. Int. symposium on In-situ Rock Stress, Trondheim-Norway, 2006.
[7] Muskhelishvili N.I., *Some basic problems of the mathematical theory of elasticity,* P. Noordhoff Ltd.: Groningen-Holland, 1953.
[8] Irsa J., Galybin A.N., Heat flux reconstruction in grinding process from temperature data, *Proc. of the 14th Int. Conf. On Computational Methods and Experimental Measurements*, eds. C.A. Brebbia & G.M. Carlomagno, WIT Press: Southampton, 2009, In print.
[9] Golub G.H. and Van Loan C.F., *Matrix computations*, The Johns Hopkins Press Ltd.: London, 1996.

This page intentionally left blank

Section 2
Advanced meshless and mesh reduction methods

This page intentionally left blank

Meshless implementations of local integral equations

V. Sladek[1], J. Sladek[1] & Ch. Zhang[2]
[1]*Institute of Construction and Architecture, Slovak Academy of Sciences, Slovakia*
[2]*Department of Civil Engineering, University of Siegen, Germany*

Abstract

The paper deals with the development of the meshless computational techniques based on the Local Integral Equations and analytical integrations. The development is illustrated on 2-d potential problems in functionally graded media. The MLS-approximation is used for simulation of spatial variations of the potential field. Efficient differentiation is proposed for calculation of derivatives of shape functions. The accuracy and efficiency are studied on simple example providing the exact solution for the benchmark solution.

Keywords: MLS-approximation, local integral equations, differentiation of shape functions, accuracy, efficiency.

1 Introduction

The advantages of mesh-free formulations in comparison with the mesh-based ones have been appreciated extensively in solution of problems for separable media. In two last decades, many mesh-free formulations are becoming popular also in numerical analyses for solids because of their high adaptivity and a low cost preparation of input data. A variety of meshless approximations have been implemented in discretizations of various formulations for numerical solution of boundary value problems. The application of the weak formulation on local sub-domains enables development of truly mesh-free formulations in contrast to the weak formulations considered in the global sense, where the background mesh is still required. Nevertheless, there is a criticism as regards the time requirements for evaluation of the shape functions in various meshless approximations. This is so owing to rather complicated form of the shape functions, hence certain algorithm is to be repeated for evaluation of them at each integration point.

WIT Transactions on Modelling and Simulation, Vol 49, © 2009 WIT Press
www.witpress.com, ISSN 1743-355X (on-line)
doi:10.2495/BE090071

In this paper, we shall consider Moving Least Squares (MLS) approximations [1] in potential problems. Then, the physical field values are expressed in terms of certain nodal unknowns which are different from the nodal values of the approximated field, in general. The nodes playing the role in approximation of the potential field at certain point $\mathbf{x}$ are selected by weight functions associated to nodes. For each integration point $\mathbf{x}$, it is necessary to find if the weight function is different from zero at $\mathbf{x}$. Certain time savings can be achieved by using MLS-CAN formulation [2], where the Central Approximation Node is taken as the nearest node to the point $\mathbf{x}$ and the nodes influencing the approximation at the CAN are employed as the nodes contributing to the approximation at the point $\mathbf{x}$ too. Recall that the nodes associated with each CAN are specified in advance and saved in memory.

In this paper, we develop a weak formulation for solution of potential problems based on the local integral equations and several kinds of approximations for derivatives of the potential field represented by the MLS-approximation. Performing the integrations analytically, the amount of evaluations of the shape functions is drastically reduced, since these are constrained to nodal points alone. Thus, the computational effort resembles that in the finite difference method. The relationship with the strong formulation based on the collocation of the partial differential equation at nodal points is discussed too. Consideration of the material non-homogeneity does not give rice to any complication as compared with the homogeneous case. The accuracy and computational efficiency is studied in numerical experiments.

2 Local integral equation formulation for solution of b.v.p.

The potential problem (e.g. stationary heat conduction) in anisotropic and continuously non-homogeneous media is governed by the following partial differential equation with variable coefficients [3]

$$\left(\lambda_{ik}(\mathbf{x})u_{,k}(\mathbf{x})\right)_{,i} = -Q(\mathbf{x}), \quad \text{in} \quad \Omega \tag{1}$$

where $u(\mathbf{x})$ is the unknown potential field, $Q(\mathbf{x})$ is the known body source density, and $\lambda_{ik}(\mathbf{x})$ describe the spatial variation of the material coefficients related to the flux vector $q_i(\mathbf{x})$ as

$$q_i(\mathbf{x}) = -\lambda_{ik}(\mathbf{x})u_{,k}(\mathbf{x}) \tag{2}$$

Physically, Eq. (2) is known as the Fourier law for heat conduction or also as the first Fick's law in diffusion problems.

The prescribed boundary conditions (b.c.) can be classified as

(i) Dirichlet b.c.: $u(\mathbf{x}) = \overline{u}(\mathbf{x})$ at $\mathbf{x} \in \partial\Omega_D$

(ii) Neumann b.c.: $n_i(\mathbf{x})q_i(\mathbf{x}) = \overline{q}(\mathbf{x})$ at $\mathbf{x} \in \partial\Omega_N$

(iii) Robin b.c.: $\alpha u(\mathbf{x}) + \beta n_i(\mathbf{x}) q_i(\mathbf{x}) = 0$ at $\mathbf{x} \in \partial\Omega_R$, ($\alpha, \beta \in R$)

where $\partial\Omega = \partial\Omega_D \cup \partial\Omega_N \cup \partial\Omega_R$, $n_i(\mathbf{x})$ is the unit outward normal vector to the boundary, and an over bar denotes the prescribed quantities.

Recall that Eq. (1) is the differential form (strong form) of the of the energy balance and can be deduced from its integral form

$$\int_{\partial\Omega^C} n_i(\mathbf{x}) q_i(\mathbf{x}) d\Gamma(\mathbf{x}) = \int_{\Omega^C} Q(\mathbf{x}) d\Omega(\mathbf{x}) , \tag{3}$$

holding for all arbitrary but small material domains $\Omega^C \subset \Omega$. In view of Eq. (2), we can rewrite Eq. (3) as

$$\int_{\partial\Omega^C} n_i(\mathbf{x}) \lambda_{ik}(\mathbf{x}) u_{,k}(\mathbf{x}) d\Gamma(\mathbf{x}) = - \int_{\Omega^C} Q(\mathbf{x}) d\Omega(\mathbf{x}) , \tag{4}$$

which is the local weak form of the governing equations. Note that Eq. (4) is a physically admissible constraint that can be used as a coupling equation in the computation of unknown degrees of freedom of the discretized problem. Recall that the local integral equations (4) are non-singular, since there are no singular fundamental solutions involved in contrast to the singular integral equations employed in the boundary integral equation method. Moreover, the integration of unknown (approximated) field variables is constraint to the boundary of local sub-domains even in the case of non-homogeneous media. This can be effectively utilized by decreasing the amount of integration points as compared with the formulations involving domain integrals. As regards the computational time, it is independent on the fact if the medium is homogeneous or non-homogeneous.

3 Moving Least Squares approximation (MLS)

3.1 Standard MLS approximation

The primary field variable (potential field) is assumed to be approximated at a vicinity of the point $\mathbf{x}$ as

$$u(\mathbf{x}) \approx \sum_{\mu=1}^{m} p_\mu(\mathbf{x}) c_\mu(\mathbf{x}) , \tag{5}$$

where $\{p_1(\mathbf{x}), \ldots, p_m(\mathbf{x})\}$ is a complete monomial basis and $c_\mu(\mathbf{x})$ are expansion coefficients which can be obtained by minimizing a weighted functional

$$J(\mathbf{x}) = \sum_{a=1}^{N_L} w^a(\mathbf{x}) \Big[p_\mu(\mathbf{x}^a) c_\mu(\mathbf{x}) - \hat{u}^a \Big] \Big[p_\mu(\mathbf{x}^a) c_\mu(\mathbf{x}) - \hat{u}^a \Big] . \tag{6}$$

Hence, one can get the expansion coefficients and the approximation (5) becomes

$$u(\mathbf{x}) \approx \sum_{a=1}^{N_t} \phi^a(\mathbf{x})\hat{u}^a, \qquad \phi^a(\mathbf{x}) = \sum_{\alpha,\gamma=1}^{m} p_\alpha(\mathbf{x})\mathrm{A}^{-1}_{\alpha\gamma}(\mathbf{x})\mathrm{B}^a_\gamma(\mathbf{x}), \tag{7}$$

where

$$\mathrm{A}_{\alpha\beta}(\mathbf{x}) = \sum_{a=1}^{N_t} w^a(\mathbf{x}) p_\alpha(\mathbf{x}^a) p_\beta(\mathbf{x}^a), \qquad \mathrm{B}^a_\alpha(\mathbf{x}) = w^a(\mathbf{x}) p_\alpha(\mathbf{x}^a). \tag{8}$$

The weight function for each node $\mathbf{x}^a$ is chosen as a function with a compact support given by the radius r^a. In this paper, we shall consider Gaussian weight functions:

$$w^a(\mathbf{x}) = \begin{cases} \left[e^{-(d^a/c^a)^2} - e^{-(r^a/c^a)^2} \right] \Big/ \left[1 - e^{-(r^a/c^a)^2} \right], & \text{for } 0 \le d^a \le r^a \\ 0, & \text{for } d^a \ge r^a \end{cases}$$

N_t is the total number of nodes, but the actual number of nodes contributing to the approximation (7) is less than N_t, since $\phi^a(\mathbf{x}) = 0$, if $w^a(\mathbf{x}) = 0$. Nevertheless, all the N_t nodes are involved into the evaluation algorithm for the shape functions. Recall that the shape functions do not satisfy the Kronecker delta property $\phi^a(\mathbf{x}^b) \neq \delta_{ab}$, in general, and the expansion coefficients $\hat{u}^a$ are fictitious nodal values. These nodal unknowns are discrete degrees of freedom in the discretized formulation.

3.2 MLS-CAN concept

Besides the standard MLS-approximation, we shall consider also the Central Approximation Node (CAN) concept. Let $\mathbf{x}^q$ be the CAN for the approximation at a point $\mathbf{x}$. Then, the amount of nodes involved into the approximation at $\mathbf{x}$ is reduced a-priori from N_t to N^q, where N^q is the number of nodes supporting the approximation at the CAN $\mathbf{x}^q$, i.e. the amount of nodes in the set $\mathcal{M}^q = \left\{ \forall \mathbf{x}^a;\ w^a(\mathbf{x}^q) > 0 \right\}_{a=1}^{N_t}$. Then, instead of the approximation given by Eq. (7), we shall use

$$u(\mathbf{x}) = \sum_{\alpha=1}^{N^q} \hat{u}^{n(q,\alpha)} \phi^{n(q,\alpha)}(\mathbf{x}), \tag{9}$$

where $n(q,\alpha)$ is the global number of the α-th local node from $\mathcal{M}^q$. In this paper, we shall specify the CAN $\mathbf{x}^q$ as the nearest node to the approximation point $\mathbf{x}$.

3.3 Approximation of potential field derivatives

The gradients of the potential field can be approximated as gradients of the approximated potential by

$$u_{,j}(\mathbf{x}) \approx \sum_{a=1}^{N_t} \phi_{,j}^{a}(\mathbf{x})\hat{u}^{a}, \qquad u_{,j}(\mathbf{x}) \approx \sum_{\alpha=1}^{N^q} \hat{u}^{n(q,\alpha)}\phi_{,j}^{n(q,\alpha)}(\mathbf{x}) \ . \tag{10}$$

Note that calculation of gradients of the shape functions is rather complex procedure according to the formula

$$\phi_{,j}^{a}(\mathbf{x}) = \sum_{\alpha,\gamma=1}^{m} p_{\alpha,j}(\mathbf{x})\mathrm{A}_{\alpha\gamma}^{-1}(\mathbf{x})\mathrm{B}_{\gamma}^{a}(\mathbf{x}) + \\ + \sum_{\alpha,\gamma=1}^{m} p_{\alpha}(\mathbf{x})\left[\mathrm{A}_{\alpha\gamma}^{-1}(\mathbf{x})\mathrm{B}_{\gamma,j}^{a}(\mathbf{x}) - \sum_{\beta,\mu=1}^{m} \mathrm{A}_{\alpha\beta}^{-1}(\mathbf{x})\mathrm{A}_{\beta\mu,j}(\mathbf{x})\mathrm{A}_{\mu\gamma}^{-1}(\mathbf{x})\mathrm{B}_{\gamma}^{a}(\mathbf{x})\right]. \tag{11}$$

The higher order derivatives can be obtained in a similar way

$$u_{,j\ldots k}(\mathbf{x}) = \sum_{\alpha=1}^{N^q} \hat{u}^{n(q,\alpha)}\phi_{,j\ldots k}^{n(q,\alpha)}(\mathbf{x}) \tag{12}$$

with increasing complexity of the evaluation. For instance, the second order derivatives are required in meshless implementation of the strong formulation given by the governing PDE (1). According to experience we know that the accuracy of higher order derivatives fails.

Beside the *standard differentiation* (referred as *sdif*), we can express the higher order derivatives of the potential field in terms of the first order derivatives of the shape functions $F_k^{ca} = \phi_{,k}^{(c,a)}(\mathbf{x}^c)$ and the nodal values $\hat{u}^{n(c,\alpha)}$ using the recurrent formula

$$u_{,ij\ldots k}^{(\alpha)}(\mathbf{x}^c) = \sum_{a=1}^{N^c} u_{,ij\ldots}^{(\alpha-1)}(\mathbf{x}^{n(c,a)})\phi_{,k}^{(c,a)}(\mathbf{x}^c) \tag{13}$$

where the superscript (α) shows the order of the derivative. Thus,

$$u_{,ij}(\mathbf{x}^c) = \sum_{a=1}^{N^c} F_j^{ca} \sum_{\substack{b=1 \\ v=n(c,a)}}^{N^v} F_i^{vb}\hat{u}^{n(v,b)} \ , \tag{14}$$

$$u_{,ijk}(\mathbf{x}^c) = \sum_{a=1}^{N^c} F_k^{ca} \sum_{\substack{b=1 \\ v=n(c,a)}}^{N^v} F_j^{vb} \sum_{\substack{d=1 \\ w=n(v,b)}}^{N^w} F_i^{wd} \hat{u}^{n(w,d)} \text{ , etc.} \tag{15}$$

Note that Eqs. (14) and (15) can be rewritten as

$$u_{,ij}(\mathbf{x}^c) = \sum_{a=1}^{M^c} F_{ij}^{ca} \hat{u}^{m(c,a)} , \tag{16}$$

$$u_{,ijk}(\mathbf{x}^c) = \sum_{a=1}^{N^c} F_k^{ca} \sum_{\substack{b=1 \\ v=n(c,a)}}^{M^v} F_{ij}^{vb} \hat{u}^{m(v,b)} = \sum_{a=1}^{K^c} F_{ijk}^{ca} \hat{u}^{k(c,a)} , \tag{17}$$

where the global numbers $m(c,a)$ as well as M^c and F_{ij}^{ca} can be obtained from comparison of Eqs. (16) and (14). Similarly from (17) and (15), one can find $k(c,a)$, K^c and F_{ijk}^{ca}. These approaches will be referred as *modified differentiation* (*mdif*).

4 Discretization of governing equations and boundary conditions

4.1 Strong formulation

Collocating the prescribed boundary conditions at boundary nodes and the governing equations

$$\lambda_{ik}(\mathbf{x}^c) u_{,ki}(\mathbf{x}^c) + \lambda_{ik,i}(\mathbf{x}^c) u_{,k}(\mathbf{x}^c) = -Q(\mathbf{x}^c) , \tag{18}$$

at interior nodal points $\mathbf{x}^c$ with substituting the approximations for the potential field and their gradients discussed in Sect. 3, we obtain the system of algebraic equations for the nodal unknowns. The numerical results achieved by this approach will be referred as CPDE (Collocation of PDE).

4.2 Weak formulation

Strictly speaking we present a mixed formulation, since the boundary conditions are considered in strong form. Surrounding each interior node $\mathbf{x}^c$ with a sub-domain Ω^c and substituting an approximation for gradients of potential field at each integration point, one can complete the system of algebraic equations for computation of nodal unknowns $\hat{u}^a$ by equations

$$\sum_{a=1}^{N_t} \hat{u}^a \int_{\partial\Omega^c} n_i(\mathbf{x}) \lambda_{ik}(\mathbf{x}) \phi_{,k}^a(\mathbf{x}) d\Gamma(\mathbf{x}) = -\int_{\Omega^c} Q(\mathbf{x}) d\Omega(\mathbf{x}) . \tag{19}$$

In Eq. (19), we have used the standard MLS approximation, but the MLS-CAN approximation is applicable too. In general, the integrations are to be performed numerically with evaluating the gradients of the shape functions at each integration point.

In order to reduce the amount of points at which the shape function gradients are to be evaluated, we try to accomplish the integration in a closed form. For this purpose, we shall assume the circular sub-domains centred at nodes $\mathbf{x}^c$. Furthermore, the radius of the circle r_o is taken sufficiently small, in order to justify the Taylor series expansion of the material coefficients as well as gradients of the shape functions within the sub-domain. If the material coefficients are prescribed by analytical functions, there is no basic problem to calculate their derivatives at nodal points. Expecting failure of accuracy of higher order derivatives of the shape functions, the size of the radius of sub-domains should guarantee fast convergence of the Taylor series expansion. For the sake of simplicity, we shall consider isotropic medium $\lambda_{ij} = \delta_{ij}\lambda$. Assuming the Taylor series expansions up to 6th and 4th orders for $\lambda(\mathbf{x})$ and $\phi_{,i}(\mathbf{x})$, respectively, and neglecting the terms $O(r_o^8)$, one obtains

$$\frac{1}{\pi r_o^2}\int_{\partial\Omega^c} n_i(\mathbf{x})\lambda(\mathbf{x})u_{,i}(\mathbf{x})d\Gamma = \left(\lambda^c_{,i} + \frac{r_o^2}{8}\lambda^c_{,imm} + \frac{r_o^4}{24}\frac{1}{8}\lambda^c_{,immss}\right)u_{,i}(\mathbf{x}^c) +$$

$$+\left[\lambda^c\delta_{ip} + \frac{r_o^2}{8}\left(2\lambda^c_{,ip} + \lambda^c_{,jj}\delta_{ip}\right) + \frac{r_o^4}{24}\left(\frac{1}{2}\lambda^c_{,ipjj} + \frac{\delta_{ip}}{8}\lambda^c_{,ssjj}\right) + \right.$$

$$\left. + \frac{r_o^6}{256}\left(\frac{1}{6}\lambda^c_{,ipjjss} + \frac{\delta_{ip}}{36}\lambda^c_{,ssjjll}\right)\right]u_{,ip}(\mathbf{x}^c) + \left[\frac{r_o^2}{8}3\lambda^c_{,i}\delta_{ps} + \frac{r_o^4}{24}\left(\frac{3}{4}\lambda^c_{,ijj}\delta_{ps} + \frac{1}{2}\lambda^c_{,ips}\right) + \right.$$

$$\left. + \frac{r_o^6}{256}\left(\frac{1}{4}\lambda^c_{,ijjll}\delta_{ps} + \frac{1}{3}\lambda^c_{,ispjj}\right)\right]u_{,ips}(\mathbf{x}^c) + \left[\frac{r_o^2}{8}\lambda^c\delta_{ip}\delta_{kf} + \frac{r_o^4}{24}\left(\lambda^c_{,ip}\delta_{kf} + \frac{1}{4}\lambda^c_{,jj}\delta_{ip}\delta_{kf}\right) + \right.$$

$$\left. + \frac{r_o^6}{6\times 24\times 192}\left(72\lambda^c_{,ipjj}\delta_{kf} + 24\lambda^c_{,ipkf} + 9\lambda^c_{,jjll}\delta_{ip}\delta_{kf}\right)\right]u_{,ipkf}(\mathbf{x}^c) =$$

$$= -\frac{1}{\pi r_o^2}\int_{\Omega^c} Q(\mathbf{x})d\Omega(\mathbf{x}) \tag{20}$$

In the derivation of this equation, we have utilized the following integrals

$$\frac{1}{r_o}\int_{\partial\Omega^c} n_i n_j d\Gamma = \int_0^{2\pi} n_i n_j d\omega = \pi\delta_{ij},$$

$$\int_0^{2\pi} n_i n_j n_m n_p d\omega = \frac{\pi}{4}\left(\delta_{ij}\delta_{mp} + \delta_{im}\delta_{jp} + \delta_{ip}\delta_{jm}\right) \equiv Y_{ijmp},$$

$$\int_0^{2\pi} n_i n_j n_m n_p n_t n_s d\omega = \frac{\pi}{24}\left(\delta_{ij}Y_{mpts} + \delta_{im}Y_{jpts} + \delta_{ip}Y_{jmts} + \delta_{it}Y_{jmps} + \delta_{is}Y_{jmpt}\right) \equiv$$

$$\equiv Y_{ijmpts}$$

$$\int_0^{2\pi} n_i n_j n_m n_p n_t n_s n_r n_l d\omega = \frac{\pi}{192}\left(\delta_{ij}Y_{mptsrl} + \delta_{im}Y_{jptsrl} + \delta_{ip}Y_{jmtsrl} + \delta_{it}Y_{jmpsrl} + \right.$$

$$\left. + \delta_{is}Y_{jmptrl} + \delta_{ir}Y_{jmptsl} + \delta_{il}Y_{jmptsr}\right)$$

and the integrals of the product of odd number of normal vectors are vanishing.

Note that in the discretized form, the weak formulation given by Eq. (20) converges to the strong formulation (18) in the limit $r_o \to 0$. Moreover, the strong formulation corresponds to the lowest expansion terms in the weak formulation when the material coefficients and the shape functions gradients are expanded into Taylor series. Hence, one can expect better accuracy by the weak formulation than by the CPDE approach especially for problems in considerably graded materials.

5 Numerical experiments

Let us consider the square domain $L \times L$ with prescribed temperatures on the bottom and top of domain as u_o and u_L, respectively, and thermally insulated lateral sides. The material medium is assumed to be isotropic with exponentially graded heat conduction coefficient as $\lambda(\mathbf{x}) = \lambda_o \exp(n\delta x_2 / L)$ with $n = 2$ and $\delta = 1$. The benchmark solution is given by the exact solution of this 1-d problem

$$u(x_2) = u_o + \frac{u_L - u_o}{e^{-n\delta} - 1}\left(e^{-n\delta x_2 / L} - 1\right).$$

Before investigating the accuracy and efficiency of various meshless implementations of LIE and/or PDE, we discuss shortly the accuracy of approximations for derivatives of the potential field.

It can be seen from Fig. 1 that the approximation of the first order derivative is acceptable within the whole domain, while the accuracy for the second derivatives fails near the boundary. This can be explained by non-symmetric distribution of nodes w.r.t. the evaluation point in boundary layers. The *sdif* approach fails completely even in the case of the third derivative, while the *mdif* approach works well at points far from the boundary.

Fig. 2(a) shows the accuracy of numerical results achieved by analytical integrations and using the *sdif* approach for approximation of shape function derivatives with the highest order either two (*sfdo*=2) or three (*sfdo*=3). The h parameter is the distance of two nearest nodes in uniform meshes, and the

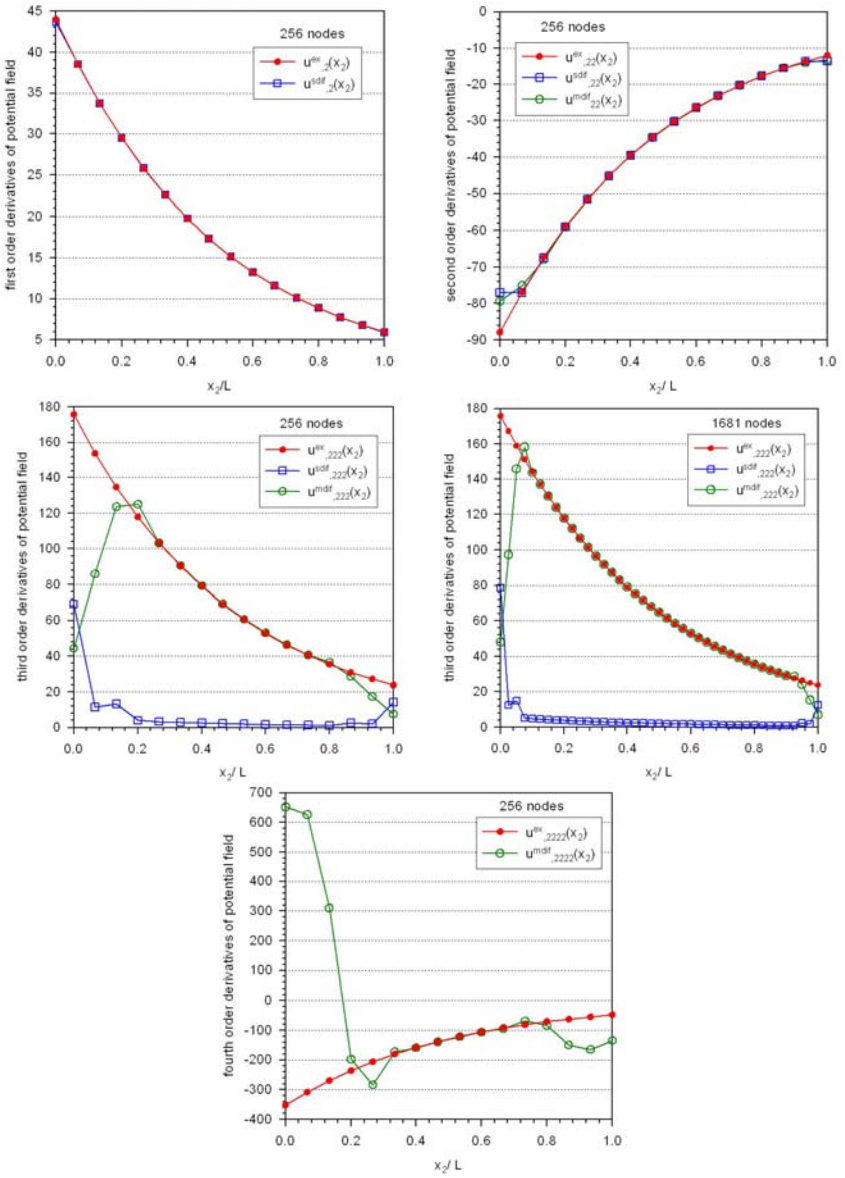

Figure 1: Comparison of approximated derivatives of potential with exact values.

radius of circular sub-domains was taken either independent on h (rsd=0.01) or variable (rsd=0.01$*h$). One can see the negative influence of the third order derivative on accuracy. In the case of variable rsd, this influence is depressed because of minimization of the third order contribution with decreasing rsd as h is decreasing.

In the case of LIE combined with the analytical integration, we have used various programming techniques for calculation of derivatives of shape functions within *mdif* approach. Although there was no influence on the accuracy, there was on the efficiency visible through the CPU times. When $rsd = 0.01 * h$, the accuracy is independent on the choice of the highest order of the shape function derivatives owing to vanishing contribution of higher order terms with decreasing the radius of sub-domain. On the other hand, the influence of the *sfdo* is visible when $rsd = 0.01$. The best accuracy as well as the convergence rate is achieved for $sfdo = 3$. The less accurate results correspond to $sfdo = 4$ because of worse approximations of the 4th order derivatives of shape functions.

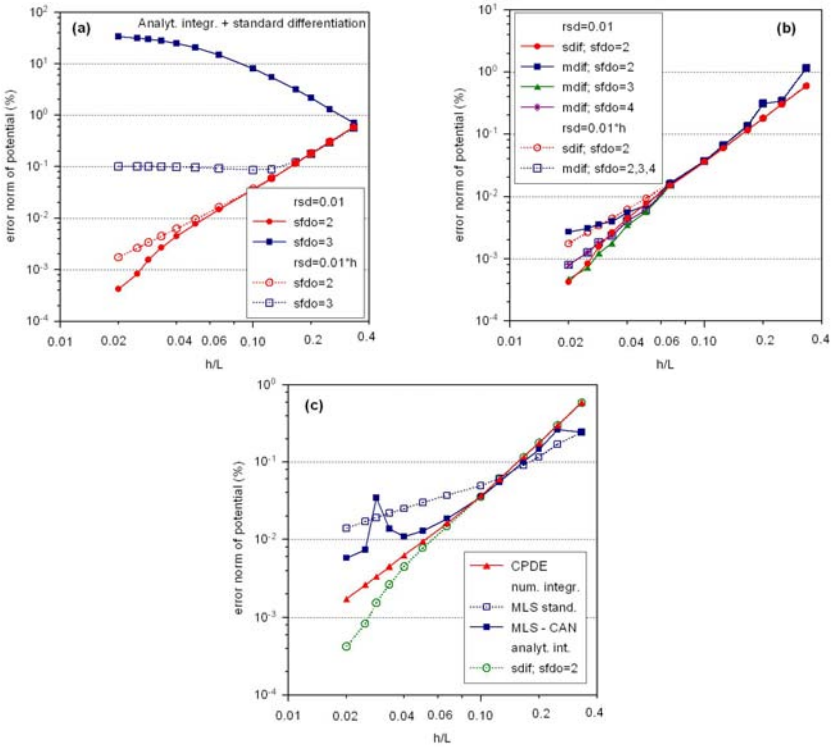

Figure 2: Convergence study for various techniques: (a) analyt. integration with *sdif*; (b) analyt. integration with either *sdif* or *mdif*; (c) CPDE, LIE+numer. integration, LIE+analyt. integr.

Finally, from Fig. 2(c), one can see that the LIE approach combined with numerical integration yield the worst accuracy as well as the convergence rate in comparison with the CPDE and the LIE+analytical integration approaches. As regards the LIE+analytical integration approaches, the best accuracy is achieved by the $sdif + (sfdo = 2)$ technique and comparable results are obtained by the $mdif + (sfdo = 3)$ technique.

The efficiency of various meshless computational techniques will be assessed by studying the CPU-times needed for creation of the system matrix (t_m) and for complete solution (t_f), where $t_f = t_m + t_s$ and t_s is time needed for solution of the system of algebraic equations. Fig. 3(a) is a confirmation of the expectation that the LIE approach with numerical integration is less effective than CPDE in creation of the system matrix. It can be seen that for nodal point distributions with low density t_m is a substantial part of t_f, while for high densities t_m is a negligible part of t_f for CPDE in contrast to the LIE+num. integr. approach.

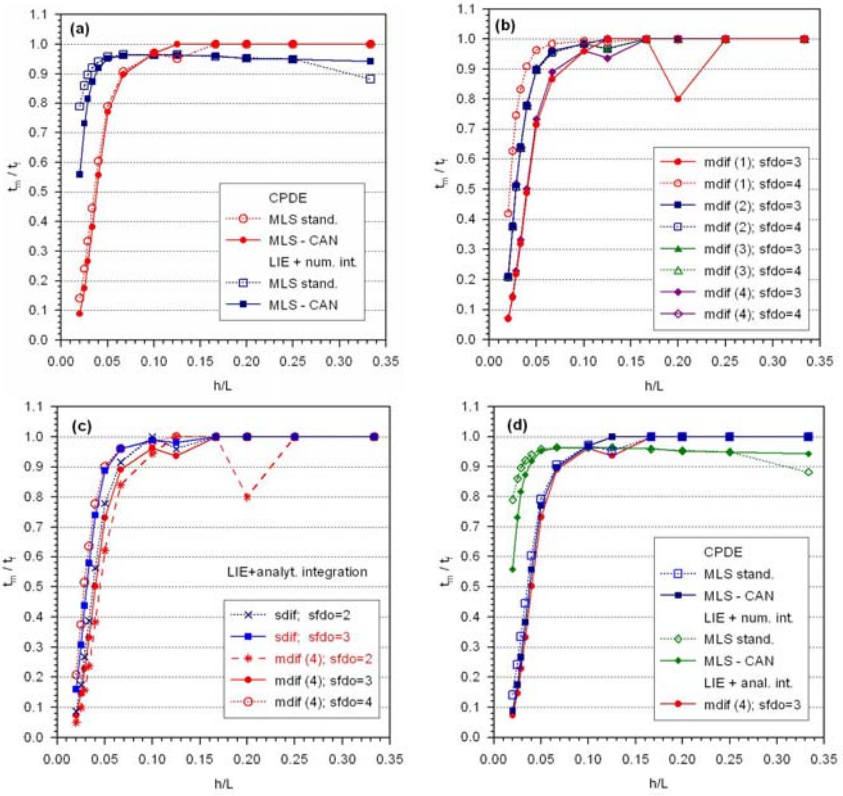

Figure 3: Variations of the time ratio t_m / t_f with h parameter for various meshless computational techniques.

Fig. 3(b) shows the dependence of the time ratio t_m / t_f on h parameter for LIE+analyt. integr. combined with four programming variants for modified calculation of shape function derivatives. Recall that all the variants $mdif(\alpha)$ with the same $sfdo$ yield the same accuracy. The cases with $sfdo = 2$ are not presented because of lower accuracy. It can be seen that the

most effective variants are $mdif\,(1)+(sfdo=3)$ and $mdif\,(4)+(sfdo=3)$. In Fig. 3(c), we compare the efficiency of various approaches based on LIE+analytical integration. We presented also the results for $sdif+(sfdo=3)$ and $mdif\,(4)+(sfdo=2)$ despite bad accuracy by these approaches. The approaches $sdif+(sfdo=2)$ and $mdif\,(4)+(sfdo=3)$ exhibit almost the same efficiency as well as the accuracy. Fig. 3(d) shows a comparison of efficiencies achieved by various meshless computational techniques.

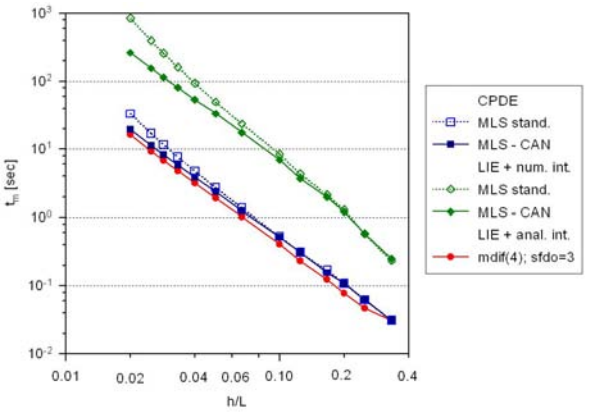

Figure 4: Dependence of t_m on the h parameter.

Finally, Fig. 4 shows the dependence of time needed for creation of the system matrix by various meshless computational techniques.

6 Conclusions

There was developed a meshless technique based on the LIE and analytical integration with effective computation of derivatives of shape functions. The efficiency in creation of the system matrix of discretized equations is comparable with the strong formulation based on the collocation of PDE at nodal points but the accuracy as well as the convergence rate is better in the proposed technique.

References

[1] Lancaster, P., Salkauskas, K., Surfaces generated by moving least square methods. *Math. Comput*., **37**, pp. 141-158, 1981.
[2] Sladek, V., Sladek, J., Zhang, Ch., Computation of stresses in non-homogeneous elastic solids by local integral equation method: a comparative study. *Computational Mechanics*, **41**, pp. 827-845, 2008.
[3] Wrobel, L.C., *The Boundary Element Method, Vol. 1: Applications in Thermo-Fluids and Acoustics*, John Wiley & Sons, Ltd., New York, 2002.

Local and virtual RBF meshless method for high-speed flows

S. Gerace[1], K. Erhart[1], E. Divo[2] & A. Kassab[2]
[1] *Convergent Modeling, Inc., USA*
[2] *Department of Mechanical, Materials, and Aerospace Engineering, University of Central Florida, USA*

Abstract

Existing Computational Fluid Dynamic solutions suffer from several major limitations that prevent widespread use within the scope of many complex aerospace flow situations. These limitations include requiring significant model setup time, requiring skilled labor to generate the underlying computational grid, and requiring extensive computational resources to construct large-scale models using conventional techniques. In response to these issues, this work has developed a solution utilizing a novel Meshless method that eliminates the need for structured meshes, and thus, the need for complicated meshing procedures that demand both time and labor to complete. The presented Meshless method, which is based upon two collocation techniques, Local Radial Basis Function (LRBF) collocation and Virtual Radial Basis Function (VRBF) collocation, has shown promising results within the areas of heat transfer and elasticity, as well as incompressible and compressible fluid flow. Incorporation of an automated refinement process based on boundary and interior values provides the method with a high level of robustness with respect to initial point distribution. Additionally, the inclusion of shadow nodes in near-boundary regions allows the method to accurately capture the high gradients present in typical high-speed boundary layers. Several examples are presented within the area of high-speed flow in an attempt to highlight the ease of use, as well as the accuracy of the described techniques.
Keywords: meshless methods, radial basis functions, generalized finite differencing, CFD, Navier-Stokes.

WIT Transactions on Modelling and Simulation, Vol 49, © 2009 WIT Press
www.witpress.com, ISSN 1743-355X (on-line)
doi:10.2495/BE090081

1 Introduction

As compared to traditional, mesh-based solution techniques, the so-called Meshless, or mesh-reduction methods promise to eliminate the tedious mesh-generation process by improving the robustness of the algorithm with respect to the underlying point distribution. This mesh-generation process is currently a major requirement of time and effort when attempting to solve problems involving complex geometries where automatic Finite Element or Finite Volume meshes provide unacceptable solution quality.

Through presentation of both the underlying theory and basic algorithm structure, we attempt to illustrate the advantages of the presented Meshless method over more conventional techniques. Throughout the development of these techniques, focus was placed on accuracy as well as automation, allowing for a highly user friendly CFD solution. Several test cases with comparisons to experimental data, as well as to existing commercially available CFD technology are presented as evidence supporting the adoption of this method as a viable alternative to more conventional CFD approaches.

2 Meshless collocation techniques

Conventional numerical methods commonly used in most engineering applications (Finite Element, Finite Volume, and to some degree, Boundary Element methods) all introduce the idea of a defined connectivity between nodes or volumes. This connectivity is what allows the various techniques to determine the influence of any node to its neighbors. While it is true that for simple models, development of this connectivity can be largely automated, as the complexity and size of the problem increases, it becomes exceedingly difficult to automate this procedure. With Meshless methods, on the other hand, the underlying goal is to eliminate this need for a defined connectivity mesh. Instead, the influence of one node on its neighbors is defined by an interpolation technique that can be used regardless of model geometry or nodal spacing.

Although many interpolation techniques exist that may be used to arrive at a Meshless formulation, this paper will present the two specific techniques that have shown promising results within the area of high-speed flow.

2.1 Localized radial basis function collocation

Localized Radial Basis Function collocation begins with the principle that any arbitrary domain, Ω, can be interpolated over by collocating about a number of points using some basis function, χ. This method (and in fact, both Meshless collocation techniques implemented in this paper) divides the overall region into smaller sub-domains, called topologies, which allow for a more efficient and accurate solution method when compared to global interpolation techniques. As a simple example, the process of breaking down a two-dimensional region into representative topologies is demonstrated in Figure 1(a).

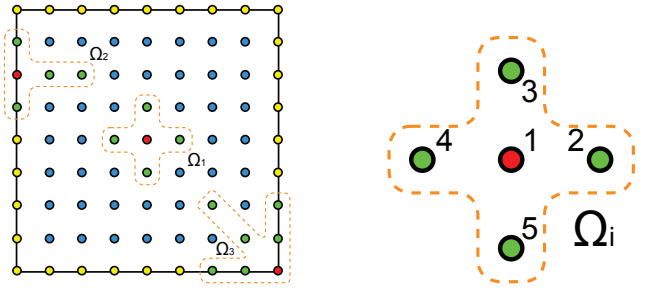

(a) Representative 2D Domain (b) Representative 2D Topology

Figure 1: Localized topology representation.

The region shown is a two-dimensional representation, however, in general, the nodes can describe an n-dimensional field (where n is generally 2 or 3). The represented field, ϕ, can be shown to be globally interpolated [1] by multiplying the basis functions by a set of expansion coefficients as

$$\phi(x) = \sum_{j=1}^{N} \alpha_j \chi_j(x) + \sum_{k=1}^{NP} \alpha_{(k+N)} P_k(x) \tag{1}$$

where N is the total number of points in the domain, α_j are the expansion coefficients for ϕ, and $\chi_j(x)$ are a-priori defined expansion functions. Additionally, a similar expansion is performed over NP polynomial functions (or any additional expansion function), $P_k(x)$, which must be added to the overall expansion to guarantee that constant and linear fields can be retrieved exactly [2]. However, this formulation assumes a global collocation, which, as already stated, is not ideal. Thus, the concept of local topologies can be used to reformulate Eq. (1) such that instead of summing over the entire domain, the basis function is now applied to the local topologies, Ω_i. Therefore, the locally interpolated field may be expressed as

$$\phi(x) = \sum_{j=1}^{NF} \alpha_j \chi_j(x) + \sum_{k=1}^{NP} \alpha_{(k+NF)} P_k(x) \tag{2}$$

where instead of summing over the entire region, Eq. (2) is instead summed over the number of points in a given topology, expressed as NF. For example, looking at the two-dimensional representative topology shown in Figure 1(b), NF is equal to 5, as there are 5 nodes included in the topology for the data center (Node 1).

A critical component to this type of Meshless collocation technique is determining a suitable basis function, χ, that will accurately interpolate between data points. Much research has gone into analyzing the behavior of the most common basis functions for this type of technique [2, 3], and the most accurate and stable was determined to be the family of so-called Inverse Hardy Multiquadrics [4] (an

Inverse Multiquadric function where $n = 1$) which follows the form

$$\chi(x_i) = \frac{1}{\sqrt{r_j\left(x_i\right)^2 - c^2}} \tag{3}$$

where x is the position vector at a given location i, r_j is the Euclidean distance from point i to point j, and c is a free constant commonly referred to as the basis shape parameter. Optimizing this shape parameter is critical to obtaining accurate results and fortunately our research group has developed a very novel method of arriving at an optimal value on a topology by topology basis by means of Singular Value Decomposition [2,5]. Thus, this expansion function $\phi\left(x\right)$ is used to locally interpolate the field about a surrounding node, providing the "connectivity" (more appropriately referred to as influence) required to evaluate the necessary derivatives of the field.

Having defined the interpolation method used in this collocation technique, the next step is to construct the weights associated with the derivative operators. To accomplish this, Eq. (2) may be applied to all nodes within a topology, which results in a field interpolation within each local topology region; however, it may also be differentiated, thus providing a means of evaluating derivative values. Thus, to represent a particular derivative of the field ϕ,

$$\partial\phi\left(x\right) = \sum_{j=1}^{NF} \alpha_j \partial\chi_j\left(x\right) + \sum_{k=1}^{NP} \alpha_{(k+NF)} \partial P_k\left(x\right) \tag{4}$$

where ∂ may represent any differential operator. For example, the Laplacian operator would be evaluated as

$$\nabla^2\phi\left(x\right) = \sum_{j=1}^{NF} \alpha_j \nabla^2\chi_j\left(x\right) + \sum_{k=1}^{NP} \alpha_{(k+NF)} \nabla^2 P_k\left(x\right) \tag{5}$$

Although the Localized RBF collocation process provides adequate numerical results in most cases, it suffers from several key issues which prevent it from being used in all cases:

1. Since the basis functions were chosen to be radially symmetric, optimal results are only obtained for radially symmetric derivative operators. One-sided operators (such as upwinded derivatives) are not represented well by the radial nature of the interpolator.
2. In areas consisting of locally structured nodes, it can be shown that the weights obtained through this process are identical to those obtained through traditional finite differencing; we would like to take advantage of this case without having to compute unnecessary quantities.
3. Areas of very high gradients (shocks, boundary layers, etc.) may cause oscillations in the RBF interpolator, resulting in poor numerical stability.

In response to these issues, a second collocation technique is utilized and is applied at areas with local structure, and for those derivative operators that are

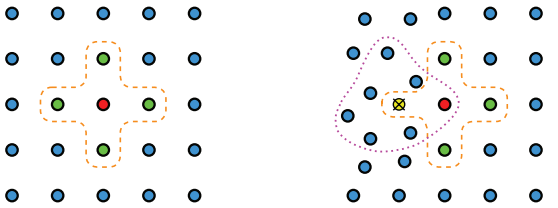

(a) Structured Topology (b) Unstructured Topology

Figure 2: Structured and unstructured meshless topologies.

not symmetric. Additionally, if an RBF interpolation value is deemed oscillatory in nature (by looking at the local field values), it is (temporarily) replaced with the second type of collocation technique to assist in numerical stability.

2.2 Virtual radial basis function collocation

Conventional Finite Difference collocation techniques involve truncating the Taylor series expansion to approximate a given derivative at a specific location within a field. The Finite Difference formulations can therefore be directly applied to any regular point distribution when the surrounding nodes are properly located within the bounds of the approximation. However, this technique has a limitation in that it requires a regular, defined distribution of nodes, something that is not possible for an unstructured, Meshless domain. By utilizing some of the concepts of Localized Radial Basis collocation, the standard Finite Difference formulation may be extended to non-regular nodal distributions and be made into a Meshless technique.

Virtual Radial Basis Function (VRBF) collocation departs from the standard Finite Difference formulations for the required derivatives, including all necessary upwinding states. In the case of locally structured regions, such as depicted in Figure 2(a), the Finite Difference formulations may be directly applied. Although this is a Meshless technique, we still attempt to create as much structured region as possible (by utilizing an octree point distribution method) to provide the maximum accuracy and performance of the algorithm; as such, a large portion of the domain is usually structured. For those regions that are not completely structured, such as depicted in Figure 2(b), additional, virtual nodes are placed in the necessary locations (in this case, in the negative x direction, indicated by the yellow $\otimes$) in order to facilitate use of the Finite Difference equations. However, since this is a virtual node that does not actually exist (and thus, no governing equations are solved), we require a means of evaluating the field at the virtual node location. To accomplish this, a topology is constructed around about this node (purple dotted region), and LRBF is used to interpolate to the virtual location. Thus, despite there being no node at a necessary Finite Difference point, we may still apply these equations due to the interpolation capabilities of the Localized Radial Basis Function collocation method.

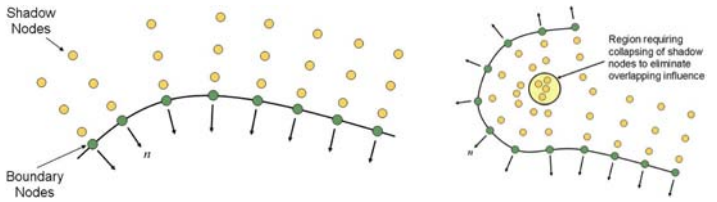

(a) Convex Boundary Layer (b) Concave Boundary Layer

Figure 3: Illustration of shadow nodes.

3 Model construction and refinement

One of the critical advantages of Meshless methods is allowing for the capability of completely automated point and topology generation in arbitrarily complex three dimensional models. Therefore, we have spent considerable efforts toward the development of techniques for automated nodal distributions as well as solution-based adaptive refinement of these discretizations.

Our models are first constructed from a triangulated surface which defines the boundary of the problem. Triangulated, or tessellated, volumes were chosen for several reasons. First, because the tessellated volume is a very common entity in computer geometry and graphics, extensive literature exists describing how best to control refinement on the surface. Second, because the triangulated surfaces are relatively simple compared to other analytical surfaces, calculations required for surface integrations, volume calculations (volume, centroid, containment tests), and other necessary components, are relatively straightforward to implement and fast in calculation. Third, even though solutions may be obtained using Meshless methods without a defined boundary connectivity, in order to post process terms such as surface forces, stresses, moments, and other area based values, each boundary node must have a defined area and normal direction. By using a triangulated surface representation, the boundary nodes inherit their parent facet's area and normal properties, facilitating easy translation from the Meshless solution domain into the geometric domain of the problem.

Once the boundary has been discretized to a sufficient level, the next step in the point distribution process is to create the so-called "shadow" nodes, which serve to function as a boundary layer distribution in the problem solution. The process of adding shadow nodes is shown for a simple two dimensional boundary in Figure 3(a).

It is important to realize that this process of adding shadow nodes can potentially introduce problems in highly convex or concave boundary situations (an issue which is compounded in three dimensions). For the case of convex boundaries (like that shown in Figure 3(a)) any gaps may still be filled with interior nodes once the octree distribution is applied. The rules governing interior node placement do not preclude nodes from entering gaps in the boundary layer. For the case of highly concave boundaries (like that shown in Figure 3(b)) a technique of collapsing

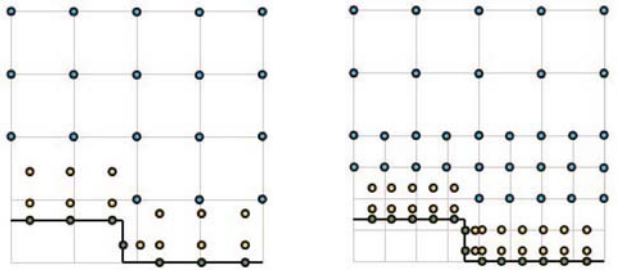

(a) Before Boundary Refinement (b) After Boundary Refinement

Figure 4: Sample boundary interior refinement.

shadow nodes which are very close to one another is necessary in order to eliminate instability in the underlying Meshless interpolations.

The collapsing process entails producing an interpolation sphere about all of the shadow nodes affected, and "lumping" their combined values into a single common location. This lumping process is achieved by the Radial Basis Function interpolation that is used throughout the Meshless process. Although each node will still act as a single entity and the solution is still solved at each node independently, to all the other nodes (ones that are not part of the sphere) the cluster appears as a single node.

The final development in the point distribution process is to construct the recursive octree structure used throughout the bulk of the domain interior. An octree structure is used for several reasons, the most important being its ability to refine itself in a very straightforward and automated fashion. It is important to realize that the refinement of the interior, shadow, and boundary nodes is inherently a disconnected process, so compatibility conditions must be included in order properly marry the refinements. We have implemented a process where, as one local region is refined, all other regions which exist in this nearby area will be refined as well. Take, for example, the situation shown in Figure 4. In Figure 4(a), we see an initial discretization for part of a two dimensional boundary. After some number of iterations, it is determined that the current discretization at the boundary layer (yellow shadow nodes) is not sufficient to accurately capture the high gradients that were detected. Rather than simply refine only the boundary nodes (green nodes) and their associated shadow nodes, the interior octree distribution (blue nodes) knows to refine to an appropriate level to match the nearby boundary discretization, as shown in Figure 4(b).

It is important to note that this refinement can begin anywhere within the region (boundary, shadow or interior nodes) and will propagate to all nearby regions. So, for example, a wake zone occurring completely within the interior may still be refined, even though it is not close to any boundary zones.

4 Governing equations

The current Meshless formulation begins with the three-dimensional Navier-Stokes equations in conservative variable form, given in vector form as

$$\frac{\partial Q}{\partial t} + \frac{\partial E}{\partial x} + \frac{\partial F}{\partial y} + \frac{\partial G}{\partial z} = \frac{\partial E_v}{\partial x} + \frac{\partial F_v}{\partial x} + \frac{\partial G_v}{\partial x} \tag{6}$$

where

$$= \begin{bmatrix} \\ \\ \\ t \end{bmatrix} \quad = \begin{bmatrix} {}^2 + \\ \\ \\ (\quad t + \ ) \end{bmatrix} \quad = \begin{bmatrix} {}^2 + \\ \\ \\ (\quad t + \ ) \end{bmatrix} \quad = \begin{bmatrix} \\ \\ {}^2 + \\ (\quad t + \ ) \end{bmatrix}$$

$$v = \begin{bmatrix} 0 \\ xx \\ xy \\ xz \\ {}' \\ v \end{bmatrix} \quad v = \begin{bmatrix} 0 \\ yx \\ yy \\ yz \\ {}' \\ v \end{bmatrix} \quad v = \begin{bmatrix} 0 \\ zx \\ zy \\ zz \\ {}' \\ v \end{bmatrix}$$

and $E_v^{'} = u\tau_{xx} + v\tau_{xy} + w\tau_{xz} - q_x$, $F_v^{'} = u\tau_{yx} + v\tau_{yy} + w\tau_{yz} - q_y$, and $G_v^{'} = u\tau_{zx} + v\tau_{zy} + w\tau_{zz} - q_z$. Note that Eq. (6) represents the full Navier-Stokes equations, where E, F, and G represent the convective terms of the governing equations and E_v, F_v, and G_v represent the viscous terms. Additionally, the shear stress component τ_{ij} may be expressed in vector form as

$$\tau_{ij} = \mu \left(\frac{\partial u_i}{\partial x_j} + \frac{\partial u_j}{\partial x_i} \right) - \delta_{ij} \frac{2}{3} \mu \frac{\partial u_k}{\partial x_k} \tag{7}$$

where δ_{ij} is the Kronecker Delta. Also, in order to arrive at a complete set of equations the ideal gas equation of state $p = \rho RT$ must be imposed.

In order to solve this set of equations our solution approach utilizes a fully explicit time-marching scheme to reach steady-state solutions. It is worth noting that this approach is completely applicable to unsteady flows as long as a suitable initial condition is provided. However, since our current efforts are focused on reaching steady-state solutions in an efficient manner, a local time-stepping procedure has been implemented to expedite convergence. Local time stepping is well described in many resources (such as Hoffman [6]) and is based on maintaining the local CFL number below the stability threshold. The standard explicit time marching scheme allows all unknown field derivatives to be evaluated at the previous time step, thereby creating a very simple update or advancement equation. The required field derivatives however, must be captured in an accurate fashion in order to produce a reliable CFD approach. It is well known that standard central type differencing produces accurate and stable results for the diffusion/stress terms as these terms generally promote changes nearly uniformly in all directions. The

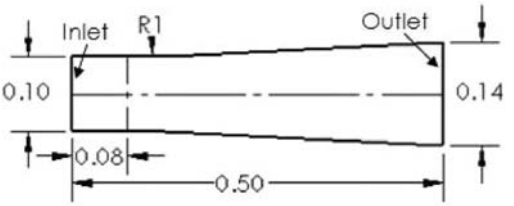

Figure 5: Smooth expanding nozzle geometry (all units in meters).

convective terms however, carry much of the flow information with them so that symmetry in the derivatives is typically never seen. It is this lack of symmetry that produces the need to upwind the convective derivatives in order to ensure the proper direction of travel of the flow field information. The importance of the upwinding procedure is widely known and our Meshless method approach has been found to have similar behavior to that of Finite Differencing in terms of the effects of improper upwinding. For this reason we have implemented a form of the Advection Upstream Splitting Method (AUSM) proposed by Liou and Steffen [7], which seeks to combine the accuracy of the Roe splitting method with the speed of more simplified splitting methods such as the Van Leer Splitting scheme.

5 Results

To illustrate the concepts and developments presented in this paper, two test cases will be presented. These test cases were designed to either highlight a particular developmental effort, or to illustrate the overall effectiveness and applicability of our Meshless CFD techniques.

5.1 Supersonic smooth expanding nozzle

The first quantitative test case will deal with analyzing viscous flow through a simple smooth expanding nozzle. A two-dimensional depiction of the problem geometry is given in Figure 5, with an understanding that this problem was constant in the z direction, having a domain thickness of 0.05m.

To generate a supersonic flow field, an inlet Mach number of $M = 2$ and a stagnation pressure and temperature of $P_0 = 100000$Pa and $T_0 = 300$K, respectively, were imposed. Additionally, all non-inlet and outlet walls were assumed to be friction free (slip walls).

This case, due to the steepness of the transition within the nozzle, exhibits a series of interacting compression waves within the nozzle. Although this indicates a poor nozzle design, it serves as an interesting test problem due to the multiple shock interactions which take place within the computational domain. For this particular problem, the Meshless solution began with an initial discretization of approximately 45,000 nodes and was allowed 3 levels of refinement at intervals of 4000 iterations, resulting in a final grid consisting of approximately 160,000

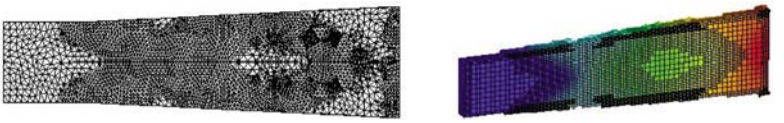

(a) Surface Distribution (b) Octree Distribution

Figure 6: Point distributions for supersonic smooth expanding nozzle.

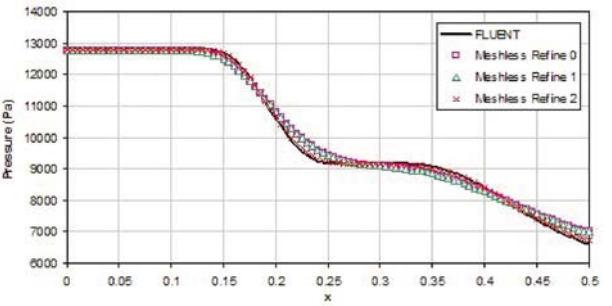

Figure 7: Midline pressure comparison.

nodes. Additionally, the results from this case were compared against a two dimensional solution generated by the commercial CFD package FLUENT, whose computational grid consisted of approximately 70,000 cells (which, in equivalent 3D, would correspond to more than 500,000 cells).

To illustrate the refinement process, Figure 6(a) shows the final surface distribution generated and Figure 6(b) shows a slice exposing the final octree distribution. Note that these point distributions were the result of 3 levels of refinement on both Mach and pressure gradients on the boundary and interior.

For a quantitative comparison, the pressure levels along a mid line ($y = 0$, $z = 0.025$) were compared to those obtained via FLUENT and shown in Figure 7, with several Meshless solutions shown, representing the different stages of adaptive refinement. By examining the Meshless results as more points are added, we see that the solution quality is improving as the point distribution is adaptively refined.

Thus, there is excellent agreement between the solutions obtained using FLUENT and the final refined point distribution solved using the proposed Meshless method technique. Additionally, this problem illustrates a major advantage of the proposed technique over other methods in that an initially poor discretization does not prevent the user from obtaining a good final solution. Furthermore, the user need not be aware of any characteristic flow phenomenon prior to obtaining results as the proposed technique is capable of capturing enough of the underlying flow characteristics to allow for proper localized refinement.

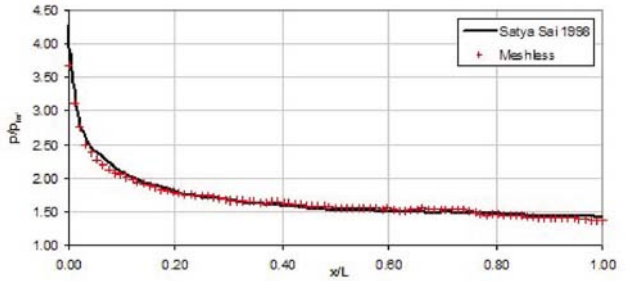

(a) Pressure distribution along plate.

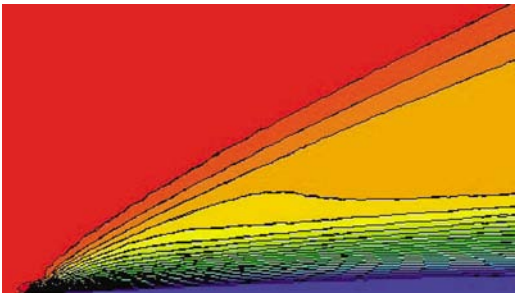

(b) Mach contours.

Figure 8: Supersonic flat plate results.

5.2 Supersonic flat plate

In the second test case, a flat plate of unit length was modeled, with the inlet at a distance of 0.2 units from the front of the leading edge and the vertical boundary at a distance of 0.8 units from the flat plate. The plate was therefore assumed to be infinite in length, as the outlet immediately followed the unit length plate. The inlet conditions imposed include a Reynolds number of $Re_\infty = 1000$, and a Mach number of $M_\infty = 3.0$. Once again an initial distribution was created and the solution was allowed to refine 3 levels, resulting in a final point distribution consisting of approximately 200,000 nodes. As a comparison, Marshall [8] solved a similar problem with a finite plate whereby the results were verified against those obtained by Satya Sai et al., which detail an infinite plate. As such, the normalized pressure distribution along the length of the flat plate is directly compared to the Satya Sai et al. results quoted by Marshall, and can be seen in Figure 8(a).

Analyzing Figure 8(a), there appears a very good correlation between the results obtained by Satya Sai et al. and the proposed Meshless methods, even in the high pressure region at the onset of the flat plate. To further illustrate the obtained solution, Figure 8b shows the obtained Mach contours near the onset of the flat plate. This figure illustrates that the shock wave is being accurately captured, as well as the resulting boundary layer downstream from the beginning of the flat plate.

6 Conclusions

In conclusion, we have presented a localized Meshless method for the solution of compressible, viscous flows utilizing an innovative blend of Localized and Virtual Radial Basis Function collocation techniques. Through implementation of an adaptive point distribution method which is capable of both boundary and interior refinement, we were able to demonstrate promising results for two high-speed flow test cases. In the process, we have illustrated one of the key advantages of this technique over more traditional methods; because of the robustness of the algorithm, even a very rough initial point distribution is capable of arriving at some fundamentally correct solution. Thus, by coupling with an automatic refinement procedure, the operator truly need not have any prior inclination about the underlying flow characteristics in order to arrive at accurate results. Any flow characteristics (such as boundary layers, shocks, etc.) that were not accurately captured in the original point distribution will be automatically detected, properly refined, and captured.

Acknowledgements

Convergent Modeling, Inc. would like to acknowledge the funding received in support of this project from the Naval Air Systems Command under the STTR topic N08-T008.

References

[1] Gerace, S., *A Meshless Method Approach for Solving Coupled Thermoelasticity Problems*. Honors in the Major Thesis, University of Central Florida, 2006.
[2] Kassab, A. & Divo, E., An efficient localized radial basis function meshless method for fluid flow and conjugate heat transfer. *ASME Journal of Heat Transfer*, **129**, pp. 179–183, 2007.
[3] Divo, E. & Kassab, A., A meshless method for conjugate heat transfer. *Engineering Analysis*, **29**, pp. 136–149, 2005.
[4] Hardy, R.L., Multiquadric equations of topography and other irregular surfaces. *Journal of Geophysical Research*, **76**, pp. 1905–1915, 1971.
[5] Gerace, S., *An Interactive Framework for Meshless Methods Analysis In Computational Mechanics And Thermofluids*. Master's thesis, University of Central Florida, 2007.
[6] Hoffmann, K.A. & Chiang, S.T., *Computational Fluid Dynamics*, volume 2. Engineering Education System, 4th edition, 2004.
[7] Liou, M.S. & Steffen, C.J., A new flux splitting scheme. *Journal of Computational Physics*, **107**, pp. 23–39, 1993.
[8] Marshall, D.D., *Extending the Functionalities of Cartesian Grid Solvers: Viscous Effects Modeling and MPI Parallelization*. Ph.D. thesis, Georgia Institute of Technology, 2002.

The radial basis integral equation method for convection-diffusion problems

T. T. Bui & V. Popov
Wessex Institute of Technology, Environmental and Fluid Mechanics, Southampton, UK

Abstract

The Boundary Element Dual Reciprocity Method has been implemented as a meshless approach. The method uses circular sub-domains with overlapping distributed inside the original domain of the problem. Since the source point is always in the centre of the circular sub-domain singular integrals are avoided regardless of the order of the derivative of the original integral equation. Three equations for two-dimensional (2D) potential problems are required at each node. The first equation is the usual BEM integral equation arising from the application of the Green's identities and the remaining equations are the derivatives of the first equation in respect to space coordinates. In the current approach Radial Basis Function interpolation is applied to obtain the values of the field variables and partial derivatives at the boundary of the circular sub-domains. Dual reciprocity method (DRM) has been applied to convert the domain integrals into boundary integrals. The method has been tested on a convection-diffusion problem. The results obtained using the current approach are compared to previously reported results obtained using the Finite Element Method (FEM), and the DRM multi-domain approach (DRM-MD) showing similar level of accuracy.

Keywords: meshless method, integral equations, circular sub-domains, radial basis functions.

1 Introduction

The local boundary integral equation (LBIE) was proposed by Zhu et al. [1, 2]. In the LBIE the domain is sub-divided in a large number of sub-domains in a shape of a circle, with the source point in the centre of the circle. The most often

WIT Transactions on Modelling and Simulation, Vol 49, © 2009 WIT Press
www.witpress.com, ISSN 1743-355X (on-line)
doi:10.2495/BE090091

used interpolation for field variables were the moving least-squares, though Sellountos and Sequeira [3] used augmented thin plate spline (ATPS) Radial Basis Functions (RBFs) for interpolation of the field variable and gradients over the circular boundaries. The concept of "companion solution" is introduced in order to eliminate the single layer integral from the local boundary integral equation. In this way the potential field is the only unknown in the equations. For source points that are located on the (global) boundary of the given problem integration over the boundary has to be performed.

The present formulation similarly to the LBIE is implemented over circular sub-domains where the source points are placed in the centres of the circles. The work follows the idea of Bui and Popov [4] who proposed using three equations at each source point for 2D problems solved using BEM with overlapping sub-domains. One equation is the original integral equation usually used in the direct formulation BEM, while the other two equations are the derivatives in respect to spatial coordinates of the original equation at the source point. In this work the augmented thin plate spline (ATPS) radial basis functions (RBFs) were used for interpolation of the field variable and gradients over the circular boundaries. This RBF was selected in order to use the same interpolation function for representing the field variables for the approximation in the DRM part of the formulation. Further in this paper it will be referred to the current meshless approach as the radial basis integral equation method (RBIEM).

The LBIE uses the concept of "companion solution" in order to avoid solution for the gradients/normal derivatives inside the problem domain, while the RBIEM solves for the potential and partial derivatives at each node. This enables the RBIEM to be a truly meshless approach since the values of the normal derivatives are obtained everywhere including the source points located on the global boundary of the problem domain. The boundary conditions in the RBIEM are imposed directly at the source points on the global boundary. In the RBIEM there is no need for integration over any part of the global boundary of the problem domain.

The RBIEM always produces a closed system of equations, unlike the DRM-MD and the Boundary-Domain Integral Method (BDIM) which produce over-determined systems of equations.

The RBIEM is especially effective in applications where the partial derivatives in respect to coordinates are required, e.g., the convection-diffusion equation, the Navier-Stokes equation.

Further in the paper the "global boundary" will mean the boundary of the given problem and the "local (circular) boundary" will mean the boundary of the circular sub-domains.

2 The boundary element dual reciprocity method

Let us consider the following equation:

$$\nabla u^2(r) = b\left(r, u(r), \frac{\partial u(r)}{\partial x_i}, \frac{\partial u(r)}{\partial t}\right) \tag{1}$$

where $u(r)$ is a potential field, r is a position vector, x_i is component of r, and t is time. Given a point r *inside a* domain Ω, by applying the Green integral formula equation (1) can be transformed into the following integral form:

$$u(r) + \int_{\Gamma} q^*(r,\xi)u(\xi)d\Gamma_\xi - \int_{\Gamma} u^*(r,\xi)q(\xi)d\Gamma_\xi = \int_{\Omega} u^*(r,\xi)b(\xi)d\Omega_\xi. \tag{2}$$

where $u^*(r,\xi)$ is the fundamental solution of the Laplace problem, $q(\xi) = \partial u(\xi)/\partial n$ and $q^*(r,\xi) = \partial u^*(r,\xi)/\partial n$.

The DRM approximation [5] is introduced to transform the domain integral in (2) in terms of equivalent boundary integrals. The implementation of the DRM with multidomain technique is explained by Natalini and Popov [6]. After application of the DRM, the following integral representation formula is obtained:

$$u(r) + \int_{\Gamma} q^*(r,\xi)u(\xi)d\Gamma_\xi - \int_{\Gamma} u^*(r,\xi)q(\xi)d\Gamma_\xi = \sum_{k=1}^{J_{bn}+J_{in}} \left\{ \alpha_k \left(\hat{u}(r,\eta_k) + \int_{\Gamma} q^*(r,\xi)\hat{u}(\xi,\eta_k)d\Gamma_\xi - \int_{\Gamma} u^*(r,\xi)\hat{q}(\xi,\eta_k)d\Gamma_\xi \right) \right\} \tag{3}$$

where J_{bn} and J_{in} are the number of boundary nodes and internal nodes on the domain, respectively.

3 The radial basis integral equation method

The proposed formulation solves in each interior node three integral equations in order to obtain the potential u, and the partial derivatives $\partial u/\partial x_j$. Equation (3) is used to find the potential while the equations for derivatives $\partial u/\partial x_j$ are obtained by differentiating (3) in respect to x_j, where x_j are components of r. The derivatives of (3) are given below:

$$\frac{\partial u(r)}{\partial x_j} = -\int_{\Gamma_i} \frac{\partial q^*(r,\xi)}{\partial x_j} u(\xi)d\Gamma_\xi + \int_{\Gamma_i} \frac{\partial u^*(r,\xi)}{\partial x_j} q(\xi)d\Gamma_\xi + \tag{4}$$

$$\sum_{k=1}^{J_{bn}+J_{in}} \left\{ \alpha_k \left(\frac{\partial \hat{u}(r,\eta_k)}{\partial x_j} + \int_{\Gamma_i} \frac{\partial q^*(r,\xi)}{\partial x_j} \hat{u}(\xi,\eta_k)d\Gamma_\xi - \int_{\Gamma_i} \frac{\partial u^*(r,\xi)}{\partial x_j} \hat{q}(\xi,\eta_k)d\Gamma_\xi \right) \right\}$$

The normal derivative q in (4) can be written as:

$$q = \frac{\partial u}{\partial n} = \nabla u \cdot \vec{n} = \sum_k \frac{\partial u}{\partial x_k} n_k \tag{5}$$

where n_k are components of the unit normal vector.

4 Interpolation for the unknown values at the circular boundary of the sub-domain

In order to perform the integration over the local boundaries of the circular sub-domains, values of the potentials and partial derivatives must be known on the circles. Eight fictitious nodes were introduced on the circular boundaries in order

to define four quadratic elements used in the integration over the circles. The values of the field variables at the eight nodes were determined through interpolation using the values of field variables at neighbouring nodes. The final system of equations solves for potentials and derivatives only at source points at centres of circular sub-domains, and not at the fictitious nodes on the circular boundaries. Only nodes at centres of sub-domains are used in the interpolation for obtaining the values of field variables at fictitious nodes on the circular boundaries. The unknown potential at one of the eight nodes, denoted by ω is approximated by n neighboring nodes x_i by the following formula:

$$u(\omega) = \sum_{i=1}^{n} f(\omega, x_i) \cdot a_i \tag{6}$$

Here f is the Augmented Thin Plate Spline Radial Basis function and a_i are the unknown coefficients.

The partial derivatives at ω are interpolated in a similar way:

$$\frac{\partial u(\omega)}{\partial x_l} = F(\omega, x_i) F_0^{-1} q_{0l} \tag{7}$$

where $F_0 = f_{ji} = f(x_j, x_i)$, $q_{0l} = [q_l(x_1), q_l(x_2), \ldots, q_l(x_n)]^T$ and $q_l = \partial u / \partial x_l$.

5 Solution on the boundary of the domain

Unlike the LBIE, the RBIEM does not require integration over any part of the global boundary. When the source point is on the global boundary, the part of the local boundary Γ_i of the sub-domain Ω_i containing the source point would partially be located outside the problem domain Ω, see Figure 1. For the nodes on Γ_i which are outside Ω and Γ, extrapolation for the potential and the partial derivatives is required, as can be seen in Figure 1, in order to be able to solve (3) and (4) at x_ξ. The values extrapolated at ω for parts of circles outside the problem domain are required in the solution procedure, but do not have a physical meaning. However, these values are not presented in the final solution and therefore do not affect the validity of the approach.

The boundary conditions (BC) are imposed at the nodes, e.g. x_ξ, located at the boundary Γ. Therefore, it is necessary to place some of the nodes on Γ in order to define the geometry of the problem and to be able to impose the BCs. If Dirichlet BCs are imposed on the part of the boundary where x_ξ is located, the following equation would be applied at x_ξ

$$u(x_\xi) = U_0 \tag{8}$$

which would reduce the number of equations at x_ξ to two. If Neuman BCs are given on the part of the boundary where x_ξ is located, one of the partial derivatives would be eliminated by using (5) and only two equations would remain at x_ξ.

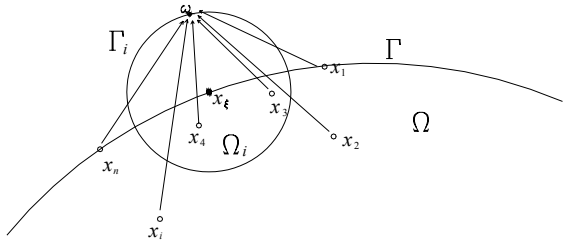

Figure 1: Extrapolation of field variables at a point on Γ_i of sub-domain Ω_i located outside the problem domain Ω.

6 Solution procedures

The RBIEM generates one circular sub-domain for each of the nodes located inside the domain Ω or on the boundary Γ. In Figure 2 several such sub-domains are shown. The eight nodes on the boundary of the circles are introduced as nodes where the potential and derivatives are evaluated using interpolation (6). The values at the eight nodes are than used to calculate the integrals in (3) and (4) at node *i*.

Since the current formulation employs the DRM approach, an approximation procedure is used to represent the non-homogeneous term in (1) as is shown in (4). The DRM approximation employs a number of nodes located around node *i*. It is possible to use different set of nodes for the approximation of the field variables on the boundary of the sub-domain to the ones used for the DRM approximation. In this case, for each sub-domain, the same set of nodes was used for interpolation of the field variables over the circular local boundaries; this means the same set was used for each of the eight nodes on the circle, and for the DRM approximation. This significantly simplifies the search for the neighbouring nodes and saves CPU time.

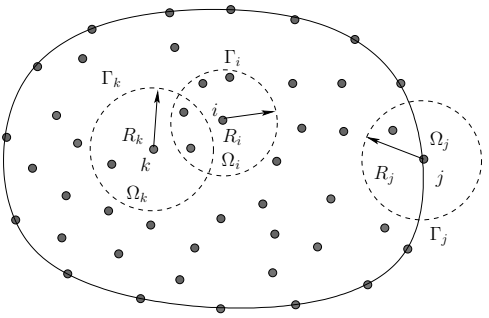

Figure 2: Distribution of some of the circular sub-domains in the problem domain.

7 Numerical examples - convection-diffusion equation

The numerical example used to test the developed approach is a Convection-Diffusion equation with variable velocity field and reaction term [7]:

$$D\frac{d^2u}{dx^2} - V_x\frac{du}{dx} - ku = 0 \tag{9}$$

A rectangular domain with length L and width W is considered. The following BCs were applied:

$$u(0,y) = U_0;\ u(L,y) = U_1;\quad \frac{\partial u}{\partial y}|_{y=W/2} = \frac{\partial u}{\partial y}|_{y=-W/2} = 0 \tag{10}$$

The velocity field is defined as:

$$V_x = \ln\frac{U_1}{U_0} + k\left(x - \frac{1}{2}\right). \tag{11}$$

The analytical solution of the above problem for L = 1m and D =1 m^2s^{-1} is given by:

$$u(x) = U_0 \exp\left\{\frac{k}{2}x^2 + \left(\ln\frac{U_1}{U_0} - \frac{k}{2}\right)x\right\} \tag{12}$$

Two values for k in (11) are used; k = 10 and k = 40. The maximum Peclet number for the examples is Pe_{max} = 8.4, for k = 10, and Pe_{max} = 23.4 for k = 40.

The accuracy of the RBIEM is studied by comparing the numerical results with the analytical solution (12) and with the numerical results obtained from the DRM-MD [7] and the FEM.

In the following examples the distribution of the nodes in the domain was the same irrespective of the approach applied. The distribution of the 185 nodes used and the boundaries of the sub-domains used in the RBIEM are shown in Figure 3. The nodes are located at the centres of circles. In the examples 15 neighbouring nodes are used in the DRM approximation and to approximate the value of nodes on the local circular boundaries.

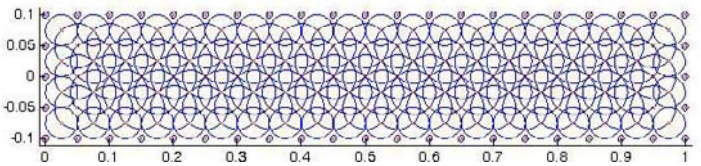

Figure 3: Distribution of the 185 nodes and the size of the circular sub-domains used.

In Table 1 the value of potentials for the case of k = 40 obtained by using the RBIEM are compared with the analytical results and the results obtained using the DRM-MD [7], and the FEM. It can be seen that the RBIEM produces more accurate results than the other two approaches. The only part where RBIEM did not perform better was the first part of the domain, x = 0.02, which is close to the

boundary. It could be the influence of the boundary conditions or the very high gradients in this part of the domain. However, even in this part the error for RBIEM is less than 5.5% and it is the only approach of the presented ones that did not have error higher than 10% within the domain.

Table 1: Potential values at internal points obtained using the RBIEM and compared with the analytical solution, DRM-MD [7], and Galerkin FEM for a mesh with 185 nodes (case k=40).

x	Analytical solution	RBIEM	DRM-MD	FEM (Galerkin)
0.00	300.00000	300.00000	300.00000	300.00000
0.02	189.38055	179.04666	186.34900	187.68159
0.04	121.47817	118.35698	117.97600	119.41530
0.07	64.30894	63.18108	60.98710	61.66200
0.10	35.29222	35.16106	32.87830	33.14000
0.14	16.77039	17.05505	15.19730	15.10380
0.19	7.23952	7.47060	6.38346	6.12290
0.25	3.01465	3.14630	2.60870	2.36960
0.32	1.30135	1.34937	1.12280	0.96120
0.40	0.63337	0.66253	0.55476	0.45580
0.56	0.32339	0.34728	0.29582	0.25190
0.75	0.55040	0.59498	0.52845	0.48900
0.85	1.30052	1.32975	1.29153	1.21380
0.93	3.45102	3.28041	3.46916	3.33370
1.00	10.00000	10.00000	10.00000	10.00000

The results for the derivative of the potential at internal points for the case k=40 obtained by using the RBIEM and DRM-MD are shown in Table 2. It can be seen that RBIEM follows accurately the analytical solution and shows higher errors only at the boundary x=0, where the values are the highest.

7.1 The convergence of the meshless method

To test the convergence different number of nodes were used for the same problem given above. Five different distributions of nodes were used with 95 nodes, 185 nodes, 689 nodes, 1513 nodes and 2657 nodes distributed inside the domain and on the boundary.

The convergence of the proposed method is tested by examining the maximum error and average error of the numerical results compared with the analytical results. The maximum error is defined as

Table 2: Results for the derivative of the potential at internal points obtained using the RBIEM and compared with the analytical solution and DRM-MD for $k = 40$ and mesh with 185 nodes.

x	Analytical	RBIEM	DRM-MD -NOSD
0.00	-7020.35921	-6177.92330	-7161.47021
0.10	-684.71146	-643.60917	-639.22498
0.25	-40.39990	-38.82190	-33.38770
0.40	-4.68772	-4.52786	-3.80930
0.56	-0.32378	-0.19140	-0.23255
0.63	0.59819	0.77870	0.61766
0.75	3.63196	4.08681	3.62576
0.80	6.92022	7.63943	6.89101
0.85	13.78396	14.96371	13.81320
0.93	47.61990	50.71610	46.83430
0.97	95.28866	99.77956	93.10570
1.00	165.98803	165.13214	159.87601

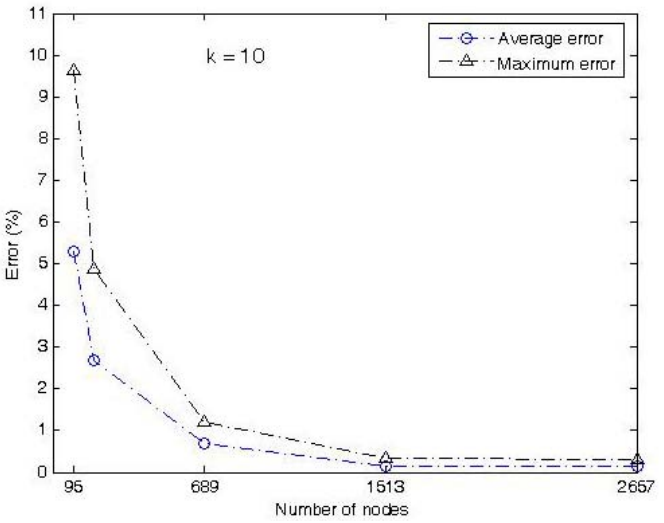

Figure 4: The convergence of the RBIEM (case k=10).

$$e_{\max} = \frac{\max\left|u_i^n - u_i\right|}{u_i} 100\% \tag{13}$$

The average error is defined as

$$e_{average} = \frac{1}{N}\sum_{i=1}^{N}\frac{\left|u_i^n - u_i\right|}{u_i} 100\% \tag{14}$$

where N is number of nodes, u_i^n is the potential at node i obtained by numerical method and u_i is the analytical solution for potential at node i.

In the tests of convergence the values for $k = 10$ was considered. Figure 4 shows the convergence of the proposed method. It is clear from the figure that the maximum error reduces from 9.6% when 95 nodes are used to 0.32% for the case when 2657 nodes are used. The average error also reduces from 5.27% for the case with 95 nodes to 0.13% for the case with 2657 nodes. It is seen that both maximum error and average error decrease continuously as the number of nodes increase from 95 nodes to 2657 nodes.

8 Conclusions

A meshless method based on the BEM and combined with the sub-domain approach has been proposed for solving the convection-diffusion equation. The approach uses circular sub-domains and places source points in the centres of the sub-domains. Three equations in 2D are solved at each node, where one equation is used for solving the potential and the remaining equations are used for solving the partial derivatives. Radial basis function interpolation is applied in order to obtain the values of the field variable and normal derivatives on the boundary of the circular sub-domains. DRM has been applied to convert the domain integrals into integrals over the boundary of the sub-domains. The current approach does not require any integration over the boundary of the computational domain and the application of the boundary conditions is straightforward. The only evaluation of the integrals is performed over the circular boundaries of the sub-domains. The accuracy of the method has been compared with the accuracy of the DRM-MD with overlapping sub-domains. In all cases the current approach has shown comparable to higher accuracy than the formulations which used a mesh, in this case DRM-MD and the FEM. The method shows good convergence for the tested convection-diffusion problem. Though the method has been applied to 2D problems, extension of the approach to 3D problems is straightforward.

References

[1] Zhu T, Zhang J-D, Atluri S.N. A local boundary integral equation (LBIE) method in computational mechanics, and a meshless discretization approach. *Computational Mechanics* 1988; 21: 223-235.

[2] Zhu T, Zhang J-D, Atluri S.N. A meshless local boundary integral equation (LBIE) method for solving nonlinear problems. *Computational Mechanics* 1998; 22: 174-186.

[3] Sellountos EJ, Sequeira A. An advanced meshless LBIE/RBF method for solving two-dimensional incompressible fluid flows. *Computational Mechanics* 2008; 44: 617–631.

[4] Bui TT, Popov V. Domain decomposition boundary element method with overlapping sub-domains. *Engineering Analysis with Boundary Elements*, 2009; 33; 456-466.

[5] Nardini D, Brebbia C.A. A new approach to free vibration analysis using boundary elements. *Applied Mathematical Modelling* 1983; 7: 157-162.
[6] Natalini B, Popov V. On the optimal implementation of the dual reciprocity method – multi domain approach for 3D problems. *Engineering Analysis with Boundary Elements* 2007; 31: 275-287.
[7] Popov V, Power H. The DRM-MD integral equation method: an efficient approach for the numerical solution of domain dominant problems. *International Journal for Numerical Methods in Engineering* 1999; 44: 327-353.

A method of fundamental solution without fictitious boundary

W. Chen & F. Z. Wang
Center for Numerical Simulation Software in Engineering and Sciences, Department of Engineering Mechanics, Hohai University, China

Abstract

This paper proposes a novel meshless boundary method called the singular boundary method (SBM). This method is mathematically simple, easy-to-program, and truly meshless. Like the method of fundamental solution (MFS), the SBM employs the singular fundamental solution of the governing equation of interest as the interpolation basis function. However, unlike the MFS, the source and collocation points of the SBM coincide on the physical boundary without the requirement of fictitious boundary. In order to avoid the singularity at origin, this method proposes an inverse interpolation technique to evaluate the singular diagonal elements of the interpolation matrix. This study tests the SBM successfully to three benchmark problems, which shows that the method has rapid convergent rate and is numerically stable.
Keywords: singular boundary method, singular fundamental solution, inverse interpolation technique, singularity at origin.

1 Introduction

Meshless methods and their applications have attracted huge attention in recent decades, since methods of this type avoid the perplexing mesh-generation in the traditional mesh-based methods such as the finite element method and the finite difference method. In comparison with the boundary element method, a variety of boundary-type meshless methods have been developed. For instance, the method of fundamental solutions (MFS) [1–4], boundary knot method [5], boundary collocation method [6], boundary node method [7, 8], regularized meshless method (RMM) [9, 10], and modified method of fundamental solution [11] etc.

Since the boundary node method still requires meshes in its numerical integration, it is not a truly meshless scheme like those moving least square based meshless finite element method [12].

WIT Transactions on Modelling and Simulation, Vol 49, © 2009 WIT Press
www.witpress.com, ISSN 1743-355X (on-line)
doi:10.2495/BE090101

The MFS is an attractive method with merits being integration-free, truly meshless, super-convergent, and easy-to-use. On the downside, the MFS requires fictitious boundaries outside the physical domain to avoid the singularity at origin because of its use of singular fundamental solution of the governing equation. In practical applications, this artificial boundary is somewhat arbitrary and not easy to determine optimally and makes the MFS unstable in the solution of complex-shaped boundary problems.

As an alternative method, the BKM [5] has been introduced to use the non-singular kernel functions such as general solutions or T-complete functions [13] which also satisfy the governing equation. The collocation and source points are coincident and are placed on the physical boundary of the problem in the BKM. However, the nonsingular kernel functions are not available in some important cases such as Laplace equation.

The RMM has recently been introduced by Young *et al*. [9]. This method has advantages over the above-mentioned meshless boundary methods in that it applies the desingularization of subtracting and adding-back technique to regularize the singularity and hypersingularity of its interpolation basis function, namely, double-layer potential. With the increasing of the boundary knot number, the condition number of this method remains small and almost not changed. However, our numerical experiments find that the solution accuracy and the convergence rate of the RMM are not very accurate. In addition, the method requires the equally spaced points to guarantee the solution accuracy and stability, which seriously restricts its applicability to the real-world problems. Based on an idea similar to the RMM, Božidar Šarler [11] proposes the modified method of fundamental solution (MMFS), which has better accuracy than the RMM, but the MMFS method requires numerical integration.

In this study, we propose a novel meshless boundary method called the singular boundary method (SBM) [14]. This method is mathematically simple, accurate, easy-to-program, and truly meshless. Similar to the MMFS, the SBM also directly uses the singular fundamental solution of governing equation of interest as the interpolation basis function. Dissimilar to the MMFS and all other boundary-type meshless methods, the SBM uses an inverse interpolation technique to evaluate the diagonal elements of the interpolation matrix to circumvent the singularity at origin of fundamental solutions. In the rest part of this paper, numerical experiments of this method are presented to demonstrate its convergence, accuracy and stability.

2 Formulation of singular boundary method

Without loss of generality, we consider the Laplace equation boundary value problems as described below

$$\Delta u(x) = 0 \quad \text{in } \Omega \tag{1}$$

$$u(x) = \bar{u}(x) \quad \text{on } \Gamma_1 \tag{2}$$

$$m(x) = \bar{m}(x) \quad \text{on } \Gamma_2 \tag{3}$$

where $u(x)$ and $m(x) = \frac{\partial u(x)}{\partial n}$ are the potential and its normal derivative (flux), respectively, n denotes the unit outward normal, Ω is the physical solution domain in $\mathcal{R}^d$, where d denotes the dimensionality of the space, and $\partial\Omega = \Gamma_1 \cup \Gamma_2$ represents its boundary. For the two dimensional Laplace equation, the fundamental solution is given by

$$u_L^* = \frac{1}{2\pi} \ln \|x_i - x_j\|. \tag{4}$$

The approximate representation of the MFS solution for this problem is written as [3, 15–17]

$$u(x_i) = \sum_{j=1}^{N} \nu_j \ln \|x_i - x_j\| \tag{5}$$

where N represents the total number of boundary collocation points, ν_j are the unknown coefficients. Obviously, the superposition of the collocation points x_i and source points x_j will lead to the well-known singularity at origin, namely, $\ln \|x_i - x_j\| = \ln 0$ for $i = j$. In order to circumvent this troublesome problem, the MFS places the source nodes on the fictitious boundary outside the physical domain. However, despite of great effort of 40 years, the placement of fictitious boundary in the MFS remains a perplexing problem for complex-shaped boundary problems.

Like the MFS, the SBM also uses the fundamental solution as the kernel function of approximation. Unlike the MFS, the collocation and source points of the SBM are coincident and are placed on the physical boundary without the need of fictitious boundary. The interpolation formula of the SBM is given by

$$u(x_i) = \sum_{j=1, j\neq i}^{N} \alpha_j \ln \|x_i - x_j\| + \alpha_i q_{ii} \tag{6}$$

where α_j are the unknown coefficients, q_{ii} are defined as the origin intensity factor. Eqn (6) of the SBM differs from eqn (5) of the MFS in that the fundamental solution at origin is replaced by q_{ii} when the collocation point x_i and source point x_j coincide $(i = j)$.

The MMFS [4] also uses the fundamental solution as the interpolation basis function while placing the source and collocation nodes at the same physical domain. The essential difference between the SBM and MMFS is how to evaluate the origin intensity factor q_{ii}. The latter uses the numerical integration approach, while the SBM develops an inverse interpolation technique as detailed below to calculate q_{ii}.

The matrix form of equation (6) can be written as

$$\{q_{ij}\}\{\alpha_j\} = \{u(x_i)\} \tag{7}$$

where $q_{ij} = \ln \|x_i - x_j\|$. We can see that q_{ii} are actually the diagonal elements of matrix $Q = \{q_{ij}\}$. By collocating N source points on physical boundary to satisfy

the Dirichlet boundary condition eqn (2) and the Neumann boundary condition eqn (3), we obtain the following discretization algebraic equations

$$\sum_{j=1}^{N_1} \alpha_j \ln \|x_i - x_j\| = \bar{u}(x_i), \quad x_i \in \Gamma_1, \tag{8}$$

$$\sum_{j=N_1+1}^{N} \alpha_j \frac{\partial \ln \|x_i - x_j\|}{\partial n} = \bar{m}(x_i), \quad x_i \in \Gamma_2, \tag{9}$$

where N_1 denotes the number of source points placed on the Dirichlet boundary. Obviously, we can not simply use the fundamental solutions to compute q_{ii}. Instead we propose an inverse interpolation technique (IIT) to evaluate the diagonal elements q_{ii} of interpolation matrix Q in the SBM.

For the boundary value problem eqns (1)–(3), we locate source points x_j on the physical boundary and place computational collocation points x_k inside physical domain. And then, we use a simple particular solution as the sample solution of Laplace equation (1), for example, $u = x + y$. Using the interpolation formula eqn (6), we can get

$$\{b_{jk}\}\{s_j\} = \{x_k + y_k\}, \tag{10}$$

where $b_{jk} = \ln \|x_k - x_j\|$. Thus, the influence coefficients s_j can be evaluated.

Replacing the computational collocation points x_k with the boundary source points x_j, we have

$$\{q_{jk}\}\{s_j\} = \{x_j + y_j\}, \tag{11}$$

where the off-diagonal elements of interpolation matrix $Q = \{q_{jk}\}$ can be computed by $q_{jk} = \ln \|x_k - x_j\|$. It is noted that the influence coefficients of the eqn (10) are the same as in eqn (11). Therefore, eqn (11) can be solved to calculate the unknown diagonal elements q_{ii} of the matrix Q.

With the previously-calculated origin intensity factor, the SBM can be used to compute arbitrary Laplace problems with the same geometry by using interpolation formula eqn (6). Here we summarize the SBM solution procedure by the following two steps:

Step 1. First, we place source points x_j on the physical boundary and select computational collocation points x_k inside physical domain. And then we choose a simple sample solution of the governing equation of interest and us the SBM interpolation formula to get its physical solutions at these interior nodes. Since the sample solution is known, we can calculate the influence coefficients s_j of the boundary source points x_j. Finally, replacing the computational collocation points x_k by the boundary source points x_j, we can calculate the origin intensity factor q_{ii}.

Step 2. Using the origin intensity factor evaluated from Step 1 and the interpolation formula (6), we can solve arbitrary problems with the same geometry and governing equation.

As discussed in the following section 3, the diagonal elements of Laplace equation with circular physical domain do not need to use the inverse interpolation technique to evaluate numerically. They are simply a summation of the corresponding off-diagonal elements, that is,

$$Q(i,i) = \sum_{i \neq j, j=1}^{N} q(i,j). \tag{12}$$

However, this is an very exceptional case. To our numerical experiments, the inverse interpolation technique has to be used to determine the diagonal elements in all other geometric domains, irrespective of domain regularity and nodes placement.

3 Numerical results and discussions

In this section, based on the above-mentioned numerical formulation, we examine three benchmark examples. The relative average error(root mean square relative error: RMSRE) is defined as follows [18]:

$$\mathrm{RMSRE} = \sqrt{\frac{1}{K}\sum_{j=1}^{K} \mathrm{Rerr}^2}, \tag{13}$$

where $\mathrm{Rerr} = \left|\frac{u(x_j)-\tilde{u}(x_j)}{u(x_j)}\right|$ for $|u(x_j)| \geq 10^{-3}$ and $\mathrm{Rerr} = |u(x_j) - \tilde{u}(x_j)|$, for $|u(x_j)| < 10^{-3}$, respectively, j is the index of inner point of interest, $u(x_j)$ and $\overline{u}(x_j)$ denote the analytical and numerical solutions at the j-th inner point, respectively, and K represents the total number of test points of interest.

Unless otherwise stated, the diagonal elements of interpolation matrices in the following three cases are all numerically evaluated by using the inverse interpolation technique. For Laplace governing equation, we use $u = x + y$ as the known sample solution; for Helmholtz equation

$$\Delta u(x) + \lambda^2 u(x) = 0,$$

$u = \sin(x)\cos(y)$ is chosen as the known sample solution, where λ represents the wave number.

3.1 Case 1: Circular domain case

For convenience, the boundary points are distributed uniformly on a unit circle. The exact solution of this case is $u = x^2 - y^2$. To examine the resulting solution accuracy, the number of testing points scattered over the region of interest is chosen to be 620.

Here, the diagonal elements of the SBM interpolation matrix are evaluated by two different approaches: (1) eqn (13), a summation of the corresponding off-diagonal elements and (2) the inverse interpolation technique introduced in Section 2.

The relative average error versus boundary point numbers for this problem is illustrated in fig. 1. It is noted that the SBM error curves using the approach of a summation of the corresponding off-diagonal elements (called the summation approach in fig. 1) and the inverse interpolation technique for the diagonal elements are very close. To our experimental experiences, it is stressed that a summation of the corresponding off-diagonal elements to evaluate diagonal elements only works for the circular domain Laplace problems. On the other hand, it is observed that error curves of both the SBM and the RMM are decreasing with increasing boundary points, while the SBM converges faster than the RMM. When the boundary point number $K = 100$, the SBM solution accuracy is of order 10^{-5}, which is three orders of magnitude less than the RMM one 10^{-2}.

Figures 2 and 3 show the condition numbers of the RMM and the SBM against the boundary point numbers, respectively. We can see that the RMM condition number is relatively smaller than the SBM ones, which may be an attractive advantage in solving large-scale problems.

3.2 Case 2: Multiply connected domain case

Here we consider a multiply connected domain case. The geometric configuration is depicted in fig. 4, and the exact solution is $u = x^2 - y^2 + xy$. The number of testing points scattered across the connected domain is 651.

Figure 5 shows the convergence rate of relative average error versus boundary point numbers, which indicates that the SBM has a faster convergence rate than the RMM. We also observe that SBM convergence curves oscillates, while the RMM has a stable convergence. The reason for the SBM oscillatory convergence curve may be due to the severely ill-conditioned interpolation matrix. On the other hand, the solution accuracy of the SBM solution appears higher than that of the RMM.

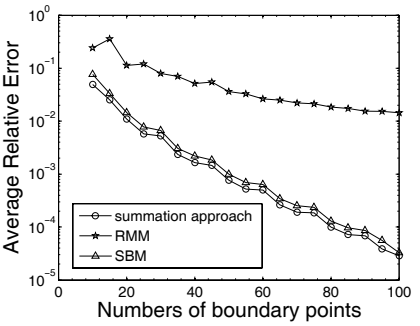

Figure 1: Relative average error curves for Case 1.

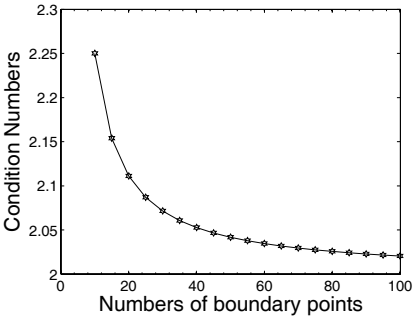

Figure 2: Condition number curve for Case 1 by using RMM.

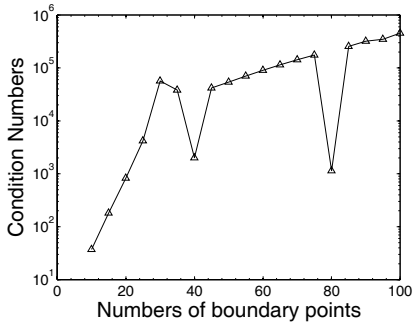

Figure 3: Condition number curve for Case 1 by using SBM.

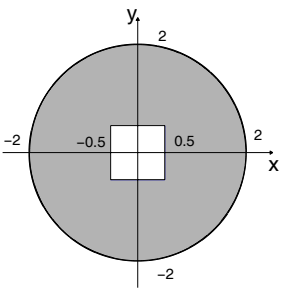

Figure 4: Configuration of 2D multiply connected domain.

For example, the SBM relative average error is $\mathrm{RMSRE} = 3.734 \times 10^{-4}$ with boundary point number $K = 200$, in contrast to $\mathrm{RMSRE} = 1.069 \times 10^{-1}$ for the RMM.

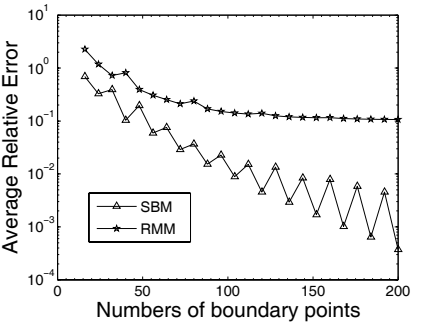

Figure 5: Relative average error curves for Case 3.

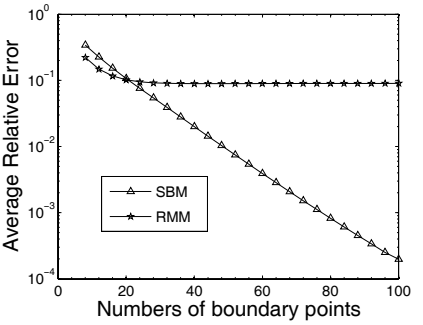

Figure 6: Relative average error curves for Case 4.

3.3 Case 3: Helmholtz equation case

Besides the previous Laplace equation cases, we also examine Helmholtz problems with wave number $k = \sqrt{2}$ and its exact solution is $u = \sin(x + 0.5)\cos(y)$. The boundary points are distributed uniformly on a unit square domain. We choose 1369 test points scattered across the physical domain.

Figures 6 and 7 show the relative average errors and the condition numbers versus boundary point numbers of the SBM and the RMM, respectively. Unlike the previous two Laplacian cases, we can see that the RMM accuracy is better than the SBM one when the boundary point number $K \leq 20$. But with the increasing number of boundary points, the relative average error of the SBM improves faster and exhibits a rapid convergence rate, while the relative average error of the RMM remains $\mathrm{RMSRE} = 1.0 \times 10^{-1}$.

Figure 7 shows that the condition numbers of the RMM are relatively lower than those of the SBM. For both methods, the condition numbers are no more than 10^2.

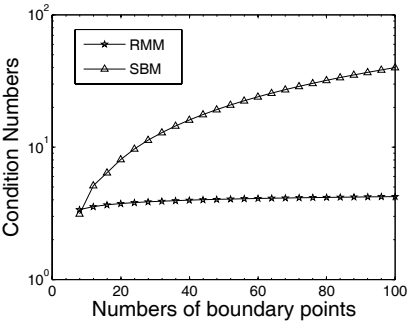

Figure 7: Condition number curves for Case 4.

4 Conclusions

This paper introduces a novel meshless singular boundary method. Like the MFS, the RMM and the MMFS, the SBM uses the fundamental solution as the interpolation basis function. Unlike the MFS, the source and collocation points coincide in the present method and the fictitious boundary in the MFS is no longer required. Also, unlike the RMM and the MMFS, the SBM uses a new inverse interpolation technique to remedy the singularity at origin of the fundamental solutions. Numerical solutions of the SBM agree well with the analytical solutions. From the foregoing figures of relative average error versus the increasing number of boundary points, we can see that numerical results of both the SBM and the RMM exhibit stable convergence trend in all tested cases, while the SBM converges faster than the RMM. However, it is also observed that the RMM condition number is in general much smaller than the SBM one in all tested cases.

Mathematical analysis of the SBM is now still under study and will be reported in a subsequent paper.

Acknowledgement

The work described in this paper was supported by a research project funded by the National Natural Science Foundation of China (Project No. 10672051).

References

[1] Bogomolny, A., Fundamental solutions method for elliptic boundary value problems. *SIAM Journal on Numerical Analysis,* **22**, pp. 644–69, 1985.

[2] Fairweather, G. & Karageorghis, A., The method of fundamental solutions for elliptic boundary value problems, *Advances in Computational Mathematics,* **9**, pp. 69–95, 1998.

[3] Golberg, M.A. & Chen, C.S., *The method of fundamental solutions for potential, Helmholtz and diffusion problems,* In: Golberg MA, editor. Boundary integral methodsłnumerical and mathematical aspects. Southampton: Computational Mechanics Publications; pp. 103–76, 1998.
[4] Chen, C.S., Hokwon A. Cho. & Golberg, M.A., Some comments on the ill-conditioning of the method of fundamental solutions, *Engineering Analysis with Boundary Elements,* **30**, pp. 405–410, 2006.
[5] Chen, W. & Hon, Y.C., Numerical investigation on convergence of boundary knot method in the analysis of homogeneous Helmholtz, modified Helmholtz and convection-diffusion problems, *Computer Methods in Applied Mechanics and Engineering,* **192**, pp. 1859–1875, 2003.
[6] Chen, J.T., Chen, I.L., Chen, K.H. & Y.T. Yeh. A meshless method for free vibration of arbitrarily shaped plates with clamped boundaries using radial basis function, *Engineering Analysis with Boundary Elements,* **28**, pp. 535–545, 2004.
[7] Mukherjee, Y.X. & Mukherjee, S., The boundary node method for potential problems, *International Journal for Numerical Methods in Engineering,* **40**, pp. 797–815, 1997.
[8] Zhang, J.M., Yao, Z.H. & Li, H., A hybrid boundary node method, *International Journal for Numerical Methods in Engineering,* 2002;**53**:751–763.
[9] Young, D.L., Chen, K.H. & Lee, C.W., Novel meshless method for solving the potential problems with arbitrary domains, *Journal of Computational Physics,* **209**, pp. 290–321, 2005.
[10] Young, D.L., Chen, K.H., Chen, J.T. & Kao, J.H., A Modified Method of Fundamental Solutions with Source on the Boundary for Solving Laplace Equations with Circular and Arbitrary Domains, *CMES: Computer Modeling in Engineering and Science,* **19(3)**, pp. 197–221, 2007.
[11] Božidar, Š. A modified method of fundamental solutions for potential problem, In: Chen, C.S., Karageorghis, A. & Smyrlis, Y.S., editor. *The Method of Fundamental Solutions – A Meshless Method*, Dynamic Publishers, pp. 299–321, 2008.
[12] Atluri, S.N. & Zhu, T., New concepts in meshless methods, *International Journal for Numerical Methods in Engineering,* **47**, pp. 537–556, 2000.
[13] Kita, E., Kamiya, N. & Ikeda, Y., An application of Trefftz method to the sensitivity analysis of two-dimensional potential problem. *International Journal for Numerical Methods in Engineering,* **38**, pp. 2209-2224, 1995.
[14] Chen, W., Singular boundary method: A novel, simple, meshfree, boundary collocation numerical method. *Acta Mechanica Solida Sinica*, (in Chinese)(acceptted).
[15] Barnett, A.H. & Betcke, T., Stability and convergence of the method of fundamental solutions for Helmholtz problems on analytic domains. *Journal of Computational Physics,* **227**, pp. 7003–7026, 2008.
[16] Wei, T., Hon, Y.C. & Ling, L., Method of fundamental solutions with regularization techniques for Cauchy problems of elliptic operators, *Engineering Analysis with Boundary Elements,* **31**, pp. 373–385, 2007.

[17] Johansson, B.T. & Lesnic, D., A method of fundamental solutions for transient heat conduction, *Engineering Analysis with Boundary Elements,* **32**, pp. 697–703, 2008.
[18] Wang, F.Z., Chen, W. & Jiang, X.R., Investigation of regularized techniques for boundary knot method, *Communications in Numerical Methods in Engineering,* (acceptted).

This page intentionally left blank

Extending the local radial basis function collocation methods for solving semi-linear partial differential equations

G. Gutierrez[1], O. R. Baquero[1], J. M. Valencia[1] & W. F. Florez[2]
[1] *Universidad Popular del Cesar, Valledupar, Colombia*
[2] *Universidad Pontificia Bolivariana, Medellín, Colombia*

Abstract

This work addresses local radial basis function (RBF) collocation methods for solving a major class of non-linear boundary value problems, i.e., $Lu = f(x, u)$ being f a non-linear function of u. This class of problems has been largely analyzed in the BEM community.

To our knowledge, few works are reported where the local RBF collocation methods (LRBFCM) based on the generalized Hermite RBF interpolation (double collocation) have been extended successfully to solve semi-linear problems even when extending to more complex nonlinear cases are not reported yet. The studied schemes are based on a strong-form approach of the PDE and an overlapping multi-domain procedure combining with standard iterative schemes. At each sub-domain, a locally meshless approximation solution by a standard or Hermite RBF expansion can be constructed. We studied also the performance respect to the shape parameter of RBF. It is confirmed that the local RBF double collocation can improve greatly the accuracy order. Some *2D* benchmark problems with mixed boundary conditions showing the accuracy, convergence property and implementation issues of LRBFCM are presented.
Keywords: RBF interpolation, double collocation, Domain decomposition methods, semi-linear equation, fully Newton method, Picard iteration.

1 Introduction

The PDE $Lu = f(x, u)$ where x represents the vector of position, u being the field variable and f the only nonlinearity arising from the source term, is encoun-

WIT Transactions on Modelling and Simulation, Vol 49, © 2009 WIT Press
www.witpress.com, ISSN 1743-355X (on-line)
doi:10.2495/BE090111

tered in heat conduction, chemical rate models, gas dynamics, among other practical applications [1–5]. Its numerical solution in steady-state or unsteady-state with advantaged boundary element methods (BEM) is well established. In the context of dual-reciprocity boundary element method (DRM) [3], it is introduced in turn the normal gradient information at the boundary to improve the needed RBF interpolations (Hermite type) providing more accuracy for permitting additional degree of freedom (DOF) for the same number of interior knots. Extending from this approach in the method of fundamental solution (MFS) is carried out elsewhere [5], improvements of accuracy were also observed when solving aforementioned equations. In unsteady-state solution cases, an efficient formulation that combining DRM and Laplace transforms (LTDRM) can be performed [2]. There a clear advantage of the LTDRM over time-stepping methods was demonstrated through the numerical results, especially if the solution at a particular time is sought. It has been shown that the success relies mainly on the linearization of the nonlinear source term by a first-order Taylor series expansion over u, namely a second-order Picard iteration.

Meshless methods have been proposed and achieved remarkable progress over the past years [6, 7]. They were born with the objective of eliminating part of the inherent difficulties that rely on complex, connected meshes or elements. According to the formulation procedures, they can be mainly classify in global and local weak-forms and global and local strong-forms [8]. For instance, the global element-free Galerkin (EFG) method and the very popular meshless local Petrov-Galerkin (MLPG) method are including under the first group which were developed in 1994 and 1998, respectively [8]. These two methods are widely employed in different complex areas of applications.

On another group of meshless methods, there exists RBF-based methods that have enjoyed tremendous research for solving PDEs. Kansa [9] was the first to use directly globally-supported RBF interpolant, particularly multiquadrics like basis functions, in a point collocation technique to approximate the strong-form of PDEs. Following this idea, Fasshauer [10] suggests to change to generalized Hermite-RBF interpolation. These two techniques are known as unsymmetric and symmetric methods, respectively. The last turns out a collocation matrix that is dense, symmetric and non-singular, whereas Kansa's collocation matrix is dense, non-symmetric and the non-singularity is not guaranteed [11]. This group of meshless methods possesses the following advantages: straight forward process for obtaining discrete equations by directly use the PDE (strong-form), simple implementation, computationally efficient (no numerical integration is required) and truly meshless (by using mainly a meshless interpolation/approximation function). It should be to point out that in [11], the author finds well-suited to solve variable coefficient elliptic and time-dependent PDEs through unsymmetric method. But applying Fasshauer's method to solve a variable coefficient problem finds it very cumbersome. Moreover, he says to be not clear to deal with nonlinear problems using the symmetric method. For a treatment of time-dependent PDEs and one unsteady non-linear heat conduction equation based on the symmetric method together with an implicit time-stepping algorithm looks at [12, 13].

In addition, it has been shown that global RBF collocation methods using some infinitely smooth RBFs are highly accurate and converge exponentially [14]. Even shortcomings are also known as the trade-off principle between the accuracy gained by increasing the c-shape parameter of RBF or the system size and the stability lost due to large matrix condition number created [14], and poor performance accounts for derivative boundary condition [15–17] and non-smooth boundary conditions [18]. To circumvent the ill-conditioning problem and to improve the solution accuracy, several techniques have been explored as matrix preconditioner, multizone methods, variable RBF shape parameter and overlapping and nonoverlapping domain decomposition methods (DDM) [19–22].

A very promising based-LRBFCM have been proposed in [23–27]. They can be seen like a novel implementation of overlapping sub-domain RBF collocation DDM in the limiting case of a very large number of sub-domains. Standard DDM deal with an iterative procedure due to transmission of information for yielding the numerical solution; herein the multi-domain formulation generates a discretized equation for each sub-domain (based on a localized RBF interpolation function) and together with a point collocation technique then arises a global, sparse and well-conditioned collocation matrix as result from an easy assembling process. The major difference between the local RBF methods and the previously presented global ones is the set of unknowns obtained from steady-state governing equations; for the former the unknowns represent the discrete values of the field variable (by defining approximations in term of shape functions) whereas for the latter the unknowns represent the coefficients of a linear combination of basis functions. This is a key step that makes local methods much more flexibility than global ones [25, 26]. For instance, LRBFCM have been more effective than global RBF collocation approaches when solving 2D convection-diffusion problems with moderate-to-high Peclet number [28, 29]. Various strategies have been proposed for determining the number of sub-domain nodes, mostly based on counting the number of them into a specified regular-shaped form of the sub-domains, i.e., circle, rectangles, etc.; or the number of nodes n is fixed and selecting them according to certain criterion, i.e., nearest searching, four quadrant, among other more elaborates [8, 26, 30, 31]. This mild connectivity can be accomplished in a preprocessing stage in the cases that collocation points does not alter its distribution. From here on we will call computational molecules with their star points instead of the so-called sub-domains.

A recent approach was proposed in [32], it aimed to exploit the combination between LRBFCM and the classical control volume (CV) method. There a boundary value problem is solved for every cell and then constructing the cell shape functions from which the evaluation of the flux across the cell faces is obtained. By this way, they were able to improve the performance of the CV method. So far we believe that this approach has been applied successfully to 3D linear convention-diffusion problems for predicting high Péclec number models.

LRBFCM are essentially one truly meshless version that can be applied to large problems reasonably inexpensive and without numerical conditioning issues like 3D problems and Navier-Stokes equations in fluid dynamics, see very recent

papers in [29, 33, 34]. The major goal of this paper is to present new numerical results of LRBFCM for semi-linear problems with further findings compared to few prior implementations [26, 35].

2 PDE model

We consider a PDE model in which the nonlinearities arises from source terms. For simplicity, it has been considered of the form

$$Lu = \Delta u = f(x, u), \quad \text{in } \Omega \tag{1}$$

the boundary conditions are assumed to be of the form

$$u = \overline{u}, \quad \text{on } \Gamma_1 \tag{2}$$

$$q = \frac{\partial u}{\partial \boldsymbol{n}} = \overline{q}, \quad \text{on } \Gamma_2 \tag{3}$$

where u is the unknown field variable, Δ is the Laplacian operator, q is the flux, $\boldsymbol{n}$ being the unit outward normal, $\overline{u}$ and $\overline{q}$ are given functions and $\Gamma = \Gamma_1 \cup \Gamma_2$ is the boundary of the whole problem domain Ω. A fully Newton scheme can be applied straightforward due to the use of the RBF shape functions and discrete values of the field variable.

An alternative numerical treatment is as follow. Let us linearize the nonlinear source term by a first-order Taylor series expansion as

$$f(x, u) =: f_1(x, \widetilde{u}) + f_2(x, \widetilde{u})u \tag{4}$$

where

$$f_1(x, \widetilde{u}) = f(x, \widetilde{u}) - \widetilde{u} \left.\frac{\partial f}{\partial u}\right|_{\widetilde{u}}, \qquad f_2(x, \widetilde{u}) = \left.\frac{\partial f}{\partial u}\right|_{\widetilde{u}} \tag{5}$$

and thus eqn. (1) can be rewritten for a suitable iterative scheme of which arises the Picard iterations

$$L^{\widetilde{u}}u = \Delta u - f_2(x, \widetilde{u})u = f_1(x, \widetilde{u}), \quad \text{in } \Omega \tag{6}$$

where $\widetilde{u}$ is the previously iterated solution and f to be a differentiable function. Note that the discretization of eqn. (6) and its corresponding global system of equations need to be recalculated at each iteration because of new linearized variable coefficient operator depends on the solution iterates.

3 Meshless shape functions and implementations

Let us assume that at each collocation point (node) $x_j \in \theta_h = \{x_j\}_{j=1}^{N}$ is selected (in some way) a subset $S_j \subset \theta_h$, named the computational molecule of x_j such that S_j is the set of surrounding points (centers) of x_j (the star point) which

includes $n << N$ distinct grid-points of which $m \leq n$ could be used in a double collocation way. It assumes that $x_j \in S_j$, and it is the first element. At every molecule S_j, a locally meshless approximate solution $\hat{u}_j$ is sought by a generalized Hermite *RBF interpolation* function augmented with a constant polynomial term [11]:

$$\hat{u}_j(x) = \sum_{i=1}^{n} \lambda_i \phi\left(\|x - \xi_i\|\right) + \sum_{k=1}^{m} \alpha_k \gamma^{\boldsymbol{\xi}} \phi\left(\|x - \xi_k\|\right) + \chi \tag{7}$$

which interpolates both functional values $u(x)$ on all points and derivative information $\gamma u(x)$ at the double collocation points. Note that this interpolant guarantees reproduction of constant functions. If $m = 0$ (the simplest RBF interpolant), it interpolates functional values only, and if $m \neq 0$ then a RBF double collocation is possible to exploit, i.e., in these locations two interpolation conditions are simultaneously satisfied. The latter can be a way to increase the accuracy, without increasing the size of the molecule, whether there is information about the derivatives of the unknown function at some data points. The coefficients of the basis functions have to be determined.

By evaluating the different interpolation conditions into eqn. (7) at the corresponding supporting points n of the molecule for leading to $n + m + 1$ linear equations, that is, n equations by function values, m equations by derivative values and add one standard homogeneous constraint by the polynomial term. The block matrix form of these equations is:

$$\underbrace{\begin{vmatrix} \boldsymbol{\phi}\left(\|x - \xi\|\right) & \gamma^{\xi}\boldsymbol{\phi}\left(\|x - \xi\|\right) & \boldsymbol{e} \\ \gamma\boldsymbol{\phi}\left(\|x - \xi\|\right) & \gamma\gamma^{\xi}\boldsymbol{\phi}\left(\|x - \xi\|\right) & \gamma\boldsymbol{e} \\ \boldsymbol{e}^T & \gamma\boldsymbol{e}^T & 0 \end{vmatrix}}_{A} \begin{vmatrix} \boldsymbol{\lambda} \\ \boldsymbol{\alpha} \\ \chi \end{vmatrix} = \begin{vmatrix} \boldsymbol{u} \\ \boldsymbol{\gamma u} \\ 0 \end{vmatrix} \tag{8}$$

where $\boldsymbol{e}_i = 1$ and the local interpolation matrix A is symmetric, small and nonsingular [26]. As always, the centers ξ and nodes x physically coincide. Also, $\gamma\phi$ is equal to $\gamma^{\xi}\phi$ up to a possible difference in sign [12]. It is worth noting that the interpolation matrix A is a constant matrix for a given star point x_j. As such, it shall change only if the distribution of collocation points or the derivative functional are changed.

Combining eqn. (7) along with the linear system eqn. (8), it leads to that the approximation function can be expressed in term of a linear combination of *meshless shape functions* (called cardinal basis functions in interpolation terminology) with discrete values of the field variable and their derivatives as the coefficients [26]:

$$\hat{u}_j(x) = \sum_{i=1}^{n} u_i \Phi_i(x) + \sum_{k=1}^{m} \gamma u_k \tilde{\Phi}_k(x) \tag{9}$$

like shape functions possess the Kronecker delta property [26] then it is easy to implement the essential (Dirichlet) boundary conditions, e.g., not molecules are

sought at star points belonging to not-derivative boundary. For a linear differential operator $\mathcal{L}$ with variable coefficients, it can be easily discretized by applying to shape functions, i.e.

$$\mathcal{L}\hat{u}_j(x) = \sum_{i=1}^{n} u_i \mathcal{L}\Phi_i(x) + \sum_{k=1}^{m} \gamma u_k \mathcal{L}\tilde{\Phi}_k(x) \tag{10}$$

The derivative functional $\gamma u(x)$ in eqn. (9) can be assumed in several ways for the construction of approximations. Further details on constructing shape functions look at the reference [28]. Herein three options have been proposed

1. When $m = 0$, i.e., it is not assumed a derivative functional as known, so there is not a special treatment for the derivative boundary conditions. This is the simplest formulation that we refer as the local RBF single collocation approach [24].
2. When $m \neq 0$ for molecules that intersect the global derivative boundary since the derivative functional is assumed to come from $\gamma u(x) = \frac{\partial u}{\partial \boldsymbol{n}} = q$. In these m intersecting points within a molecule, their normal derivatives q are included as additional unknowns. At derivative star points, the PDE and the normal derivative boundary condition are satisfied simultaneously with the advantage does not need more meshing work outside the domain; it increases the number of collocation equations needed to close the system. This formulation gives rise to the local RBF double boundary collocation approach [8].
3. When $m \neq 0$ in all molecules since the derivative information is assumed to come from the source term, i.e., $\gamma u(x) = \mathcal{L}u(x) = \mathfrak{f}(x)$. This formulation gives rise to the local RBF PDE collocation approach [26]. In our tests, $m < n$ in interior molecules and $m \leq n$ in molecules with the star point along of the derivative boundary were assumed, reported also in [28]. The former condition rejects explicitly the derivative information at the star point [26].

Applications of whichever above approaches for constructing the approximation functions and the simple point collocation technique, using eqns (1), (2) and (3), lead to a set of nonlinear algebraic equations which can express in the standard valued-vector residual form:

$$\boldsymbol{\varphi}(\boldsymbol{U}) = \boldsymbol{0} \tag{11}$$

where $\boldsymbol{U}$ is the vector of nodal unknowns at all collocation points.

Alternatively, we use eqns (6), (2) and (3) to lead a set of linear algebraic equations at each iteration which can express in the standard matrix-vector notation:

$$\boldsymbol{K}\boldsymbol{U}^{(k)} = \boldsymbol{F} \tag{12}$$

where $\boldsymbol{K}$ is the collocation matrix, $\boldsymbol{U}^{(k)}$ is the vector of unknowns in the kth Picard iteration and the vector $\boldsymbol{F}$ collects the source terms in both the interior and on the boundary. Notice that at each iteration, $\boldsymbol{K}$ and $\boldsymbol{F}$ must be updated. The iteration process is continued until the convergence criteria are satisfied. It is worth noting that the unknown vector $\boldsymbol{U}$ is given term of $(\boldsymbol{u}, \boldsymbol{q})^T$ into eqns (11) and (12) when using the above second option.

4 Numerical evaluations

For eqn. (11) we use a Newton method with line-search, without attempting to optimize, and the Jacobian matrix required by the general-purpose solver is supplied analytically. For deciding the convergence of the solutions by Newton method, tolerances $TolFun = 10^{-7}$ for residual function and $TolX = 10^{-8}$ for incremental correction of the solution vector have been used. For eqn. (12) we use a direct solver in order to invert the linear system and $\left\|U^k - U^{k-1}\right\| / \left\|U^k\right\| < 10^{-4}$ for convergence criterion. In both cases a data structure based on a sparse storage format is used which stores a list of coordinates of non-zero elements. To deal with eqn. (8), it is used an appropriate direct solver in order to invert the small symmetric matrix A. Also the most popular RBF is used, namely $\phi(r) = \sqrt{r^2 + c^2}$ (MQ-multiquadric) along with a constant shape parameter c^2 given by end-user. In our computations, uniformly distributed collocation points and five $n = 5$ and nine nodes $n = 9$ in the molecules have been used. The relative total error norm at the end iteration is taken to measure the accuracy of the numerical results.

For the sake of clarity, we point out the three RBF local methods and their legends that we will use throughout the section. The local single collocation method to be refereed as *meth1*, the local RBF PDE collocation approach to be refereed as *meth2* and the local RBF double boundary collocation method to be refereed as *meth3*. It is worth noting that *meth2* is well suited when the problem has mixed boundary conditions. The other approaches can be well applied to problems with only Dirichlet and also mixed boundary conditions.

4.1 Analytic case

We consider a smooth solution problem in a square domain 1×1 given

$$\begin{aligned} \Delta u &= \exp(-2x)u^3 \quad \text{in } \Omega \\ u &= g \quad \text{on } \Gamma_1 = \{(x,y) \mid y = 0,\ 1,\ 0 \le x \le 1\} \\ \frac{\partial u}{\partial x} &= h \quad \text{on } \Gamma_2 = \{(x,y) \mid x = 0,\ 1,\ 0 < y < 1\} \end{aligned} \tag{13}$$

Exact solution of this problem is

$$u(x,y) = \exp x \tanh \frac{y}{\sqrt{2}} \tag{14}$$

where g and h functions are obtained from the exact solution.

The computations are performed on two uniform point distributions 21×21 ($N = 441$) and 41×41 ($N = 1681$) and different shape parameters ($0.05 < c < 1$). The solution is approximated using meth1 with $n = 5$, meth2 with $n = 9$ and meth3 with $n = 9$. Figure 1 shows the discretization of the domain and the choice of different molecule sizes used in meth1 and meth2.

Figure 2 displays the error norm of the local RBF collocation methods combining with Picard iterations for different c's and two point distributions. In general,

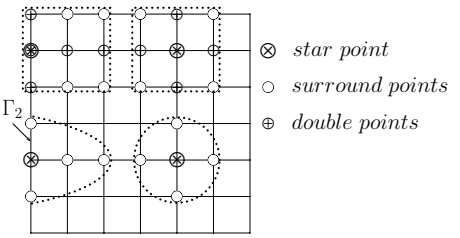

Figure 1: Computational molecules including five and nine supporting points assumed on derivative boundary and internal star points.

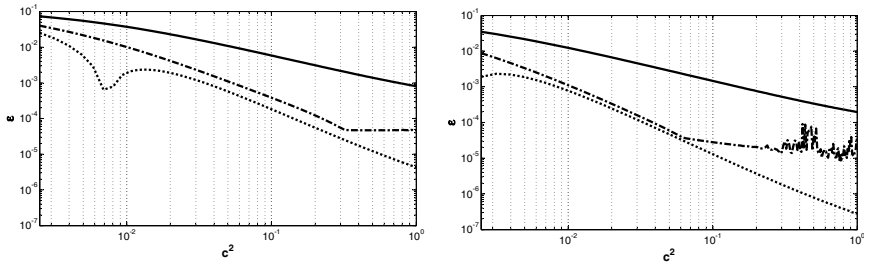

Figure 2: Convergence of the relative error with c^2. Solid line: meth1, dotted line: meth2 and dash-dot line: meth3. On the left uses 21×21 and on the right uses 41×41.

one can see that the error decreases as c increases. Also the error looks to be decreasing as point density increases. Furthermore, we can see also that the accuracy greatly improved using both Hermite collocation approaches (double collocation near and at the derivative boundary and throughout domain), i.e., meth3 and meth2. Accordingly they have the line slope values larger than meth1, i.e., recovering a higher order of accuracy. We observe that beyond to a certain shape parameter presents unavoidable instabilities in the local and/or global systems. To this respect, we felt that *meth1* with a five molecule size is more attractive compared with meth2 and meth3 because less sensitive to c and very much stable and fast computationally. In the present study, at meth1 passing from five to nine molecule size, the computational effort increases more than two times and the error norm does not decrease generally in accordingly (see also [33, 34]). Comparing the meth1 with five molecule size and meth2 with nine molecule size, the former is faster than the latter about 10 times because a less elaborate assembling matrix and less terms in the approximations. Though the latter can be more accurate than the former over 100 times into a wide range of c's. After many tests, on the full range of shape parameter tested, always converged solutions were achieved.

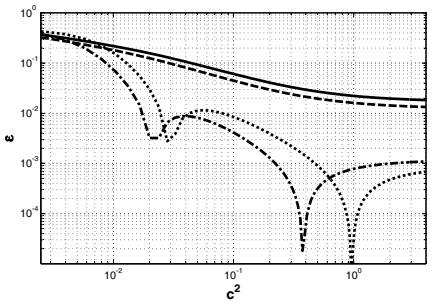

Figure 3: Convergence of the relative error with c^2. Solid line: meth1 and 11×11, dashed line: meth1 and 13×13, dotted line: meth2 and 11×11 and dash-dot line: meth2 and 13×13.

4.2 Kinetic rate problem in a square

Simplified kinetic rate problem in steady-state can be analyzed by means the forced diffusion equation

$$\Delta u = \Psi^2 u^\eta \tag{15}$$

which governs kinetic and diffusional phenomena in a homogeneous medium where Ψ and η are known parameters. Our computations are compared with an exact solution from [4] which is given for $u = 0.4352$ at point $(0, 0)$. There the problem domain is the unit square centered at $(0, 0)$, only Dirichlet boundary condition $u = 1$ is prescribed on whole domain, using $\Psi = 5$ and $\eta = 2$. The computations are performed on two uniform point distributions 11×11 ($N = 121$) and 13×13 ($N = 169$) and different parameters ($0.05 < c < 2$). The other parameters are similar to previous problem.

Figure 3 shows the accuracy of the solution as a function of MQ shape parameter, different point distributions and two local RBF methods combining with Newton method. One can observe also that both methods can achieve an accuracy improvement with higher values of c and denser collocation points. It can be seen that solution error at meth1 decreases very smooth as c increases until to be nearly constant. On the other hand, meth2 (double collocation) is more sensitive to c owing to the error decreases as c increases but now one observes a certain recovery of spectral convergence for a range of c's. Always converged solutions were found with less than five iterations. With this problem, we confirm the applicability of local RBF collocation methods to deal with the simplest nonlinear problems.

5 Conclusions

Here we show that meshless local RBF collocation methods (LRBFCM) are well suited to solve the simplest nonlinear boundary value problems. Particularly we were able to incorporate standard iterative procedures based on fully Newton and

second order Picard methods in all local methods. Though the performance of both procedures was not compared in this work. However, the combination with Newton method can require optimization for reducing the computational cost. In addition, the molecule size can also affect adversely the efficiency due to higher sizes require many computations, e.i., roughly $O(Nn^3)$, see [29]. New details about the performance of the schemes varying the constant shape parameter are shown as such can affect strongly the convergence order and accuracy itself even though it seems dependent on the problems. Furthermore, in the full range of shape parameter tested, always converged solutions were found with few iterations. We are to sure that local RBF methods are quite stables and efficients compared to the counterpart global ones. By the simplicity of these methods, we hope that they can follow up being applied to a wide variety of important applications in the near future.

Acknowledgement

Special thanks are due to COLCIENCIAS, UPB and UNICESAR for providing financial supports.

References

[1] Ames, W., *Numerical methods for partial differential equations*. Academic press, inc., 3rd edition, 1992.
[2] Zhu, S. & Satravaha, P., An efficient computational method for modelling transcient heat conduction with nonlinear source terms. *Appl Math Modelling*, **20**, pp. 513–522, 1996.
[3] Ramachandran, P.A. & Karur, S.R., Multidimensional interpolation using osculatory radial basis functions. *Computers Math Applic*, **35 (11)**, pp. 63–73, 1998.
[4] Balakrishnan, K. & Ramachandran, P.A., A particular solution Trefftz method for non-linear poisson problems in heat and mass transfer. *J Comput Phys*, **150(1)**, pp. 239 – 267, 1999.
[5] Balakrishnan, K. & Ramachandran, P.A., Osculatory interpolation in the method of fundamental solution for nonlinear poisson problems. *J Comput Phys*, **172 (1)**, pp. 1–18, 2001.
[6] Belytschko, T., Krongauz, Y., Organ, D., Fleming, M. & Krysl, P., Meshless methods: An overview and recent developments. *Comput Methods Appl Mech Engrg*, **139**, pp. 3–47, 1996.
[7] Nguyen, V., Rabczuk, T., Bordas, S. & Duflot, M., Meshless methods: A review and computer implementation aspects. *Mathematics and Computer in Simulation*, **79**, pp. 763–813, 2008.
[8] Liu, G. & Gu, Y., *An introduction to meshfree methods and their programming*. Springer, 2005.
[9] Kansa, E.J., Multiquadrics– A scattered data approximation scheme with

applications to computational fluid-dynamics– II: Solution to parabolic, hyperbolic and elliptic partial differential equations. *Computers Math Applic*, **19**, pp. 147–161, 1990.

[10] Fasshauer, G., Solving partial differential equations by collocation with radial basis functions. *In: Surface Fitting and Multiresolution Methods*, eds. A.L. Méhauté, C. Rabut & L.L. Schumaker, Vanderbilt University Press, pp. 131–138, 1997.

[11] Fasshauer, G., *Meshfree approximation methods with Matlab*, volume 6 of *Interdisciplinary Mathematical Sciences*. World Scientific, 2007.

[12] La Rocca, A., Hernandez, A. & Power, H., Radial basis function Hermite collocation approach for the solution of time dependent convection–diffusion problems. *Eng Anal Bound Elements*, **29**, pp. 359–370, 2005.

[13] La Rocca, A., Power, H., La Rocca, V. & Morale, M., A meshless approach based upon radial basis function hermite collocation method for predicting the cooling and the freezing times of foods. *CMC*, **2 (4)**, pp. 239–250, 2005.

[14] Cheng, A.H.D., Golberg, M.A., Kansa, E.J. & Zammito, G., Exponential convergence and h-c multiquadric collocation method for partial differential equations. *Numer Meth Part Differ Equat*, **19 (5)**, pp. 571–594, 2003.

[15] Zuppa, C. & Cardona, A., A collocation meshless method based on local optimal point interpolation. *Int J Numer Meth Engng*, **57**, pp. 509–536, 2003.

[16] Kee, B.B.T., Liu, G. & Lu, C., A regularized least-squares radial point collocation method (RLS-RPCM) for adaptive analysis. *Comp mech*, **40**, pp. 837–853, 2007.

[17] Gutierrez, G. & Florez, W., Issues of the local radial basis collocation method implementation for solving second order partial differential equation. *Mec Comput*, **XXVII**, pp. 2241–2252, 2008.

[18] Bernal, F., Gutierrez, G. & Kindelan, M., Use of singularity capturing functions in the solution of problems with discontinuous boundary conditions. *Eng Anal Bound Elements*, **33(2)**, pp. 200–208, 2009.

[19] Kansa, E.J. & Hon, Y.C., Circumventing the ill-conditioning problem with multiquadric radial basis functions: Applications to elliptic partial differential equations. *Computers Math Applic*, **39**, pp. 123–137, 2000.

[20] Ling, L. & Kansa, E., Preconditioning for radial basis functions with domain decomposition methods. *Mathematical and Computer Modelling*, **40 (13)**, pp. 1413–1427, 2004.

[21] Wertz, J., Kansa, E.J. & Ling, L., The role of the multiquadric shape parameters in solving elliptic partial differential equations. *Computers Math Applic*, **51 (8)**, pp. 1335–1348, 2006.

[22] Rosales, A.H. & Power, H., Non-overlapping domain decomposition algorithm for the hermite radial basis function meshless collocation approach: applications to convection diffusion problems. *Journal of Algorithms & Computational Technology*, **1 (1)**, pp. 127–159, 2007.

[23] Tolstykh, A. & Shirobokov, D., On using radial basis functions in a finite difference mode with applications to elasticity problems. *Comp mech*, **33**, pp. 68–79, 2003.

[24] Lee, C., Liu, X. & Fan, S., Local multiquadric approximation for solving boundary value problems. *Comp mech*, **30**, pp. 396–409, 2003.
[25] Shu, C., Ding, H. & Yeo, K., Local radial basis function–based differential quadrature method and its application to solve two-dimensional incompressible Navier–Stokes equations. *Comput Methods Appl Mech Engrg*, **192**, pp. 941–954, 2003.
[26] Wright, G. & Fornberg, B., Scattered node compact finite difference–type formulas generated from radial basis functions. *J Comput Phys*, **212**, pp. 99–123, 2006.
[27] Šarler, B. & Vertnik, R., Meshfree explicit local radial basis function collocation method for diffusion problems. *Computers Math Applic*, **51 (8)**, pp. 1269–1282, 2006.
[28] Gutierrez, G. & Florez, W., Comparison between global, classical domain decomposition and local, single and double collocation methods based on RBF interpolation for solving convection-diffusion equation. *Int J Mod Phys C*, **19(11)**, pp. 1737–1751, 2008.
[29] Stevens, D., Power, H. & Morvan, H., An order–N complexity meshless algorithm for transport-type PDEs, based on local Hermitian interpolation. *Eng Anal Bound Elements*, **33(4)**, pp. 425–411, 2009.
[30] Liszka, T., Duarte, C. & Tworzydlo, W., hp–meshless cloud method. *Comput Methods Appl Mech Engrg*, **139**, pp. 263–268, 1996.
[31] Ipinza, N., Perazzo, F., Aranda, J. & Pérez, L., Generación de sub–dominios locales de interpolación en un método sin malla. *Ingeniare Revista chilena de ingeniería*, **15 (2)**, pp. 204–215, 2007.
[32] Orsini, P., Power, H. & Morvan, H., Improving volumen element methods by meshless radial basis function techniques. *CMES*, **23(2)**, pp. 187–208, 2008.
[33] Shan, Y., Shu, C. & Lu, Z., Application of local MQ–DQ method to solve 3D incompressible viscous flows with curved boundary. *CMES*, **25 (2)**, pp. 99–113, 2008.
[34] Sanyasiraju, Y. & Chandhini, G., Local radial basis function based gridfree scheme for unsteady incompressible viscous flows. *J Comput Phys*, **227(20)**, pp. 8922 – 8948, 2008.
[35] Liu, X., Liu, G., Tai, K. & Lam, K., Radial point interpolation collocation method (RPICM) for the solution of nonlinear poisson problems. *Comp mech*, **36**, pp. 298–306, 2005.

Three-dimensional unsteady heat conduction analysis by the triple-reciprocity boundary element method

Y. Ochiai & Y. Kitayama
Department of Mechanical Engineering, Kinki University, Japan

Abstract

The conventional boundary element method (BEM) requires a domain integral in heat conduction analysis with heat generation or an initial temperature distribution. In this paper it is shown that the three-dimensional heat conduction problem can be solved effectively using the triple-reciprocity boundary element method without internal cells. In this method, the distributions of heat generation and initial temperature are interpolated using integral equations and time-dependent fundamental solutions are used. A new computer program was developed and applied to solving several problems.

Keywords: boundary element method, heat conduction, meshless method.

1 Introduction

The unsteady heat conduction problem without arbitrary heat generation and a nonuniform initial temperature distribution can be easily solved, without using internal cells, by the conventional boundary element method (BEM). For special cases, unsteady heat conduction problems with constant heat generation and uniform initial temperature distribution can solved by the standard BEM without the need for internal cells. When an analysis of heat conduction under arbitrary heat generation or a non-uniform initial temperature distribution within the domain is carried out by the BEM, a domain integral is generally necessary [1, 2]. However, by including the domain integral, the merit of BEM, that the preparation of data is simple, is lost. Thus, several other methods have been considered. Nowak and Neves proposed a multiple-reciprocity method [3]. Tanaka et al. have proposed a dual-reciprocity BEM for transient heat conduction problems, and V. Sladek and J. Sladek proposed a local boundary

WIT Transactions on Modelling and Simulation, Vol 49, © 2009 WIT Press
www.witpress.com, ISSN 1743-355X (on-line)
doi:10.2495/BE090121

integral equation for unsteady heat conduction problems. However, these methods do not employ a time-dependent fundamental solution, which gives an accurate result.

Ochiai proposed the triple-reciprocity BEM or improved multi-reciprocity BEM for steady heat conduction, steady thermal stress and elastoplastic problems [4–6]. The triple-reciprocity BEM for two-dimensional heat conduction and thermal stress analysis for an unsteady state has also been proposed [7, 8]. In this paper the triple-reciprocity BEM is used for three-dimensional unsteady heat conduction problems. In this method, heat generation and the initial temperature distributions are interpolated using the boundary integral equations. The triple-reciprocity method, which does not require internal cells, uses a time-dependent solution.

2 Theory

2.1 Unsteady heat conduction

In unsteady heat conduction problems with heat generation $W_1^S(q,t)$, a temperature T is obtained by solving

$$\nabla^2 T + \frac{W_1^S}{\lambda} = \kappa^{-1}\frac{\partial T}{\partial t}, \tag{1}$$

where κ, λ and t are the thermal diffusivity, heat conductivity and time, respectively. Denoting an arbitrary time and the initial temperature by τ and $T^{0S}(q,0)$, respectively, the boundary integral equation for the temperature in the case of unsteady heat conduction problems is expressed by [1, 2]

$$cT(P,t) = -\kappa\int_0^t\int_\Gamma [T(Q,\tau)\frac{\partial T_1^*(P,Q,t,\tau)}{\partial n} - \frac{\partial T(Q,\tau)}{\partial n}T_1^*(P,Q,t,\tau)]d\Gamma d\tau$$
$$+\kappa\int_0^t \int_\Omega T_1^*(P,q,t,\tau)\frac{W_1^S(q,\tau)}{\lambda}d\Omega d\tau + \int_\Omega T_1^*(P,q,t,0)T_1^{0S}(q,0)d\Omega, \tag{2}$$

where c=0.5 on the smooth boundary and c=1 in the domain. Γ and Ω represent the boundary and the domain, respectively, p and q are respectively an observation point and a loading point, and r is the distance between p and q. The notations p and q are written as P and Q on the boundary, respectively. In the case of three-dimensional problems, the time-dependent fundamental solution $T_1^*(p,q,t,\tau)$ in Eq. (2) for the unsteady temperature analysis problem and its normal derivative are given by [1, 2]

$$T_1^*(p,q,t,\tau) = \frac{1}{[4\pi\kappa(t-\tau)]^{3/2}}\exp[-a] \tag{3}$$

$$\frac{\partial T_1^*(p,q,t,\tau)}{\partial n} = \frac{-2r}{\pi^{3/2}[4\kappa(t-\tau)]^{5/2}}\frac{\partial r}{\partial n}\exp(-a) \tag{4}$$

where

$$a = \frac{r^2}{4\kappa(t-\tau)} \tag{5}$$

As shown in Eq. (2), when there is an arbitrary initial temperature or heat generation distribution, a domain integral becomes necessary.

2.2 Interpolation

An interpolation method for a distribution of heat generation $W_1^S(q,\tau)$ is shown using the boundary integral equations to avoid the use of internal cells. The polyharmonic function $T_1^{[f]}(p,q)$ for the steady state is given by

$$T^{[f]}(P,Q) = \frac{r^{2f-3}}{4\pi(2f-2)!}. \tag{6}$$

In reference [15], the polyharmonic function of body distribution is used. However, the corresponding functions for the unsteady three-dimensional case are very difficult to obtain. In this paper, the polyharmonic functions of the surface distribution are used. Figure 1 shows the shape of polyharmonic functions; the biharmonic function $T^{[2]}$ is not smooth at $r=0$. In the three-dimensional case, smooth interpolation cannot be achieved using only the biharmonic function $T^{[2]}$. To achieve smooth interpolation, the polyharmonic function with surface distribution $T^{[2]A}$ is introduced. A polyharmonic function with surface distribution $T^{[f]A}$, as shown in Fig. 2, is defined as [14]

$$T^{[f]A} = \int_0^{2\pi}\left(\int_0^{\pi} T^{[f]} A^2 \sin\theta\, d\theta\right) d\phi. \tag{7}$$

$T^{[f]A}$ can be easily obtained using the relationships $r^2 = R^2 + A^2 - 2AR\cos\theta$ and $dr = AR\sin\theta d\theta$, as shown in Fig. 2. This function is written using r instead of R, similarly to Eqs. (3) and (6), although the function in Eq. (7) is a function of R. The newly defined function $T^{[f]A}$ can be explicitly written as

$$T^{[f]A} = \frac{A\{(r+A)^{2f-1} - (r-A)^{2f-1}\}}{2(2f-1)!r} \qquad r > A \tag{8}$$

$$T^{[f]A} = \frac{A\{(A+r)^{2f-1} - (A-r)^{2f-1}\}}{2(2f-1)!r} \qquad r \le A. \tag{9}$$

The following equations can be used for the three-dimensional interpolation [9]:

$$\nabla^2 W_1^S(q,\tau) = -W_2^S(q,\tau) \tag{10}$$

$$\nabla^2 W_2^S(q,\tau) = -\sum_{m=1}^{M} W_3^{PA}(q_m,\tau)\delta(q-q_m) \tag{11}$$

M is the number of internal points for interpolation. Assuming the spatial distribution of $W_2^s(q,\tau)$ to be governed by Eq. (11) with point sources, it is known that $W_2^s(q,\tau)$ will be divergent at these source points as the particular

solution $\sum_{m=1}^{M} T^{[1]}(p,q_m)W_3^{PA}(q_m,\tau)$. Nevertheless, we can evaluate $W_2^S(q,\tau)$ on the boundary. The term W_2^S of Eq. (10) corresponds to the sum of the curvatures $\partial^2 W_1^S/\partial x^2$, $\partial^2 W_1^S/\partial y^2$ and $\partial^2 W_1^S/\partial z^2$. The term W_3^{PA} is the unknown strength of a Dirac function. From Eqs. (10) and (11), the following equation can be obtained.

$$\nabla^4 W_1^S(q,\tau) = \sum_{m=1}^{M} W_3^{PA}(q_m,\tau)\delta(q-q_m) \tag{12}$$

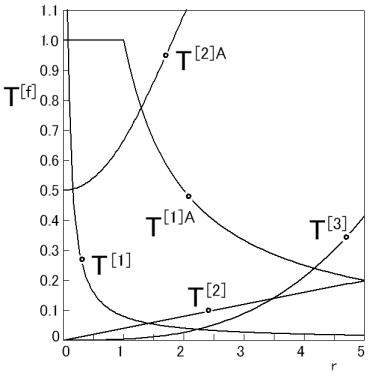

Figure 1: Polyharmonic functions.

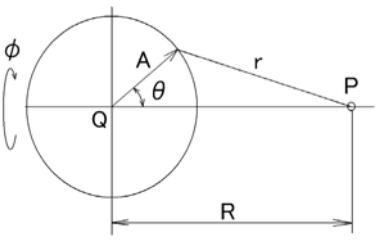

Figure 2: Notation for polyharmonic function with surface distribution.

This equation corresponds to equation for the deformation of an idealized thin plate with M point loads. The deformation $W_1^S(q,\tau)$ is given, but the force of the point load $W_3^{PA}(q,\tau)$ is unknown. $W_3^{PA}(q,\tau)$ is obtained inversely from the deformation $W_1^S(q,\tau)$ of the fictitious thin plate. W_2^S corresponds to the moment of the thin plate. The moment W_2^S on the boundary is assumed to be 0, which is the same as that in a natural spline. This indicates that the thin plate is simply supported. Moreover, the distribution of the initial temperature can be interpolated as follows.

$$\nabla^2 T_1^{0S}(q,0) = -T_2^{0S}(q,0) \tag{13}$$

$$\nabla^2 T_2^{0S}(q,0) = -\sum_{m=1}^{M} T_3^{0PA}(q_m,0)\delta(q-q_m) \tag{14}$$

On the other hand, the polyharmonic function $T_f^*(p,q,t,\tau)$ in the unsteady heat conduction problem and $T_{fA}^*(p,q,t,\tau)$ are defined by

$$\nabla^2 T_{f+1}^*(p,q,t,\tau) = T_f^*(p,q,t,\tau) \tag{15}$$

$$T_f^{*A}(p,q,t,\tau)=\int_0^{2\pi}[\int_0^{\pi}T_f^*(p,q,t,\tau)A^2\sin\theta\,d\theta]d\phi \tag{16}$$

Using Green's theorem twice, and Eqs. (10)-(16), Eq. (2) becomes

$$\begin{aligned}cT(P,t)=&-\kappa\int_0^t\int_\Gamma[T(Q,\tau)\frac{\partial T_1^*(P,Q,t,\tau)}{\partial n}-\frac{\partial T(Q,\tau)}{\partial n}T_1^*(P,Q,t,\tau)]d\Gamma d\tau\\&+\frac{\kappa}{\lambda}\sum_{f=1}^{2}(-1)^f\int_0^t\int_\Gamma[T_{f+1}^*(P,Q,t,\tau)\frac{\partial W_f^S(Q,\tau)}{\partial n}\\&-\frac{\partial T_{f+1}^*(P,Q,t,\tau)}{\partial n}W_f^S(Q,\tau)]d\Gamma d\tau+\frac{\kappa}{\lambda}\sum_{m=1}^{M}\int_0^t W_{3(m)}^P(q,\tau)T_3^{*A}(P,q,t,\tau)d\tau\\&+\sum_{f=1}^{2}(-1)^f\int_\Gamma[T_{f+1}^*(P,Q,t,0)\frac{\partial T_f^{0S}(Q,0)}{\partial n}-\frac{\partial T_{f+1}^*(P,Q,t,0)}{\partial n}T_f^{0S}(Q,0)]d\Gamma\\&+\sum_{m=1}^{M}T_3^{0PA}(q_m,0)T_3^{*A}(P,q_m,t,0)\,.\end{aligned} \tag{17}$$

Using Green's second identity and Eqs. (10) and (11), we obtain for W_1^S and W_2^S [7–9]

$$\begin{aligned}cW_1^S(P,\tau)=&\sum_{f=1}^{2}(-1)^f\int_\Gamma\{T^{[f]}(P,Q)\frac{\partial W_f^S(Q,\tau)}{\partial n}\\&-\frac{\partial T^{[f]}(P,Q)}{\partial n}W_f^S(Q,\tau)\}d\Gamma-\sum_{m=1}^{M}T^{[2]A}(P,q)W_3^{PA}(q_m,\tau)\end{aligned} \tag{18}$$

$$\begin{aligned}cW_2^S(P,\tau)=&\int_\Gamma\{T^{[1]}(P,Q)\frac{\partial W_2^S(Q,\tau)}{\partial n}\\&-\frac{\partial T^{[1]}(P,Q)}{\partial n}W_2^S(Q,\tau)\}d\Gamma+\sum_{m=1}^{M}T^{[1]A}(P,q_m)W_3^{PA}(q_m,\tau)\end{aligned} \tag{19}$$

2.3 Unsteady polyharmonic function

The three-dimensional unsteady polyharmonic function $T_f^*(P,q,t,\tau)$ in Eq. (17) is determined as

$$T_{f+1}^*(p,q,t,\tau)=\int\frac{1}{r^2}\int r^2T_f^*(p,q,t,\tau)drdr \tag{20}$$

The polyharmonic function $T_f^*(P,q,t,\tau)$ in the unsteady state and its normal derivative are explicitly given by

$$T_2^*(q,p,t,\tau)=\frac{1}{2\pi^{3/2}r}\{-\gamma(1.5,a)+a^{1/2}[1-\exp(-a)]\}=\frac{-1}{2\pi^{3/2}r}\gamma(0.5,a) \tag{21}$$

$$\frac{\partial T_2^*(q,p,t,\tau)}{\partial n}=\frac{1}{2\pi^{3/2}r^2}\gamma(1.5,a)\frac{\partial r}{\partial n} \tag{22}$$

$$T_3^* = \frac{r}{12\pi^{3/2}}\{-3\gamma(1.5,a) + 6a^{-1/2}\gamma(2,a) - 3a^{-1}\gamma(2.5,a) + a^{1/2} + 3\gamma(1.5,a)\frac{1}{a} - 3a^{-1/2}[1-\exp(-a)]\}$$

$$= \frac{r}{4\pi^{3/2}}\{-\gamma(0.5,a) + 2\gamma(1.5,a)\frac{1}{a} - 2a^{-1/2}[1-\exp(-a)]\} \quad (23)$$

$$\frac{\partial T_3^*}{\partial n} = \frac{1}{4\pi^{3/2}}[\gamma(0.5,a) - \frac{1}{a}\gamma(1.5,a)]\frac{\partial r}{\partial n} \ , \quad (24)$$

where $\gamma(,)$ is an incomplete gamma function of the first kind and $r_{,i} = \partial r / \partial x_i$. Using Eqs. (7) and (17), the polyharmonic function with a surface distribution is obtained as follows:

$$T_3^{*A} = \frac{2A(kt)^{3/2}}{3\pi^{1/2}r}\{-2{u_2}^{3/2}\gamma(1.5,u_2) + 2{u_1}^{3/2}\gamma(1.5,u_1) + 2\gamma(3,u_2) - 2\gamma(3,u_1) + 6u_2\gamma(2,u_2) - 6u_1\gamma(2,u_1) - 6{u_2}^{1/2}\gamma(2.5,u_2) + 6{u_1}^{1/2}\gamma(2.5,u_1) + \frac{1}{2}{u_2}^2 - \frac{1}{2}{u_1}^2 + 6{u_2}^{1/2}\gamma(1.5,u_2) - 6{u_1}^{1/2}\gamma(1.5,u_1) - 6\gamma(2,u_2) + 6\gamma(2,u_1) - 3u_2 + 3u_1 - 3\exp(-u_2) + 3\exp(-u_1)\} \ , \quad (25)$$

where

$$u_1 = \frac{(r-A)^2}{4\kappa(t-\tau)} \quad , \quad u_2 = \frac{(r+A)^2}{4\kappa(t-\tau)} \quad (26)$$

Numerical solutions are obtained using the interpolation functions for time and space. If a constant time interpolation and time step ($t_k - t_{k-1}$) are used, the time integral can be treated analytically. The time integrals for $T_f^*(P,q,t,\tau)$ and $\partial T_f^* / \partial n$ from t_f to t_F are given as follows:

$$\int_{t_f}^{t_F} T_1^*(p,q,t,\tau)d\tau = \frac{1}{4\kappa\pi^{3/2}r}\Gamma(0.5,a_f) \quad (27)$$

$$\int_{t_f}^{t_F} \frac{\partial T_1^*(p,q,t,\tau)}{\partial n}d\tau = \frac{1}{2\kappa\pi^{3/2}r^2}\frac{\partial r}{\partial n}\Gamma(1.5,a_f) \quad (28)$$

$$\int_{t_f}^{t_F} T_2^*(p,q,t,\tau)d\tau = \frac{r}{8\kappa\pi^{3/2}}[\gamma(1.5,a_f)\ \frac{-1}{a_f} - \Gamma(0.5,a_f) + \frac{2}{{a_f}^{1/2}} - \Gamma(-0.5,a_f)]$$

$$= \frac{r}{8\kappa\pi^{3/2}}[\gamma(0.5,a_f)\ \frac{1}{a_f} - \Gamma(-0.5,a_f)] \quad (29)$$

$$\int_{t_f}^{t_F} \frac{\partial T_2^*(p,q,t,\tau)}{\partial n}d\tau = \frac{1}{8\kappa\pi^{3/2}}\frac{\partial r}{\partial n}[\gamma(1.5,a_f)\frac{1}{a_f} + \Gamma(0.5,a_f)] \quad (30)$$

$$\int_{t_f}^{t_F} T_3^*(p,q,t,\tau)d\tau = \frac{r^3}{96\kappa\pi^{3/2}}[-6\gamma\,(1.5,a_f)\frac{1}{a_f} - \Gamma(0.5,a_f) + 8\gamma\,(2,a_f)\frac{1}{a_f^{3/2}}$$

$$-3\gamma(2.5,a_f)\frac{1}{a_f^{2}} + \frac{4}{a_f^{1/2}} + 3\gamma(1.5,a_f)\frac{1}{a_f^{2}} + 3\Gamma(-0.5,a_f)$$

$$-\frac{4}{a_f^{3/2}} + 6\Gamma(-1.5,a_f)] \tag{31}$$

$$\int_{t_f}^{t_F} \frac{\partial T_3^*(p,q,t,\tau)}{\partial n}d\tau = \frac{r^2}{96\kappa\pi^{3/2}}\frac{\partial r}{\partial n}[-6\gamma\,(1.5,a_f)\frac{1}{a_f} - 3\Gamma(0.5,a_f)$$

$$+3\gamma\,(2.5,a_f)\frac{1}{a_f^{2}} + \frac{8}{a_f^{1/2}} - \gamma(1.5,a_f)\frac{3}{a_f^{2}} - 3\Gamma(-0.5,a_f)] \tag{32}$$

where

$$a_f = \frac{r^2}{4\kappa(t_F - t_f)} \tag{33}$$

$\Gamma(,)$ is an incomplete gamma function of the second kind. The time integral of Eq. (25) can be obtained as follows:

$$\int_{t_f}^{t_F} T_3^{*A}(p,q,t,\tau)d\tau = \frac{A}{48\pi^{1/2}r}\frac{(r-A)^5}{\kappa}\{2\gamma\left(1.5,a_{1f}\right)\frac{1}{a_f} + \frac{1}{5}\Gamma(0.5,a_{1f})$$

$$-\frac{4}{5}\gamma\left(3,a_{1f}\right)\frac{1}{a_{1f}^{5/2}} - 4\gamma\left(2,a_{1f}\right)\frac{1}{a_{1f}^{3/2}} + 3\gamma\left(2.5,a_{1f}\right)\frac{1}{a_{1f}^{2}} - \frac{1}{a_{1f}^{1/2}}$$

$$-3\gamma\left(1.5,a_{1f}\right)\frac{1}{a_{1f}^{2}} - \frac{3}{5}\Gamma\left(-0.5,a_{1f}\right)$$

$$+\frac{12}{5}\gamma\left(2,a_{1f}\right)\frac{1}{a_{1f}^{5/2}} + \frac{2}{a_{1f}^{3/2}} + 3\Gamma(-2.5,a_{1f})\}, \tag{34}$$

where

$$a_{1f} = \frac{(r-A)^2}{4\kappa(t_F - t_f)}\ . \tag{35}$$

For the sake of conciseness, the terms involving u_2 in Eq. (34) are omitted.

If there are no arbitrary heat generation or initial temperature distributions, internal points are not necessary. Also, for the special case of the formulation of an unsteady state from a steady state, internal points are not necessary. If the heat generation and initial temperature distributions are governed by Laplace equation instead of Eqs. (10)-(14), Eq. (17) becomes

$$cT(P,t) = -\kappa\int_0^t\int_\Gamma [T(Q,\tau)\frac{\partial T_1^*(P,Q,t,\tau)}{\partial n} - \frac{\partial T(Q,\tau)}{\partial n}T_1^*(P,Q,t,\tau)]d\Gamma d\tau$$

$$+\frac{\kappa}{\lambda}\int_0^t \int_\Gamma [T_2^*(P,Q,t,\tau)\frac{\partial W_1^S(Q,\tau)}{\partial n} - \frac{\partial T_2^*(P,Q,t,\tau)}{\partial n}W_1^S(Q,\tau)]d\Gamma d\tau$$

$$+\int_{\Gamma}[T_2^*(P,Q,t,0)\frac{\partial T_1^{0S}(Q,0)}{\partial n}-\frac{\partial T_2^*(P,Q,t,0)}{\partial n}T_1^{0S}(Q,0)]d\Gamma\,. \tag{36}$$

3 Numerical examples

To verify the efficiency of this method, an unsteady temperature distribution in a sphere is obtained. The initial temperature of the sphere is $T_0=10°C$, and the temperature on the surface suddenly becomes 0° at time $t=0$. It is assumed that the thermal diffusivity is $\kappa=16$ mm^{2}s^{-1} and the radius of the sphere is $b=10$ mm. Figure 3 shows the boundary elements. In this example, Eq. (36) is used; therefore, internal points are not necessary. Figure 4 shows the temperature change. The solid lines in Fig.4 show the exact solutions, which are given by

$$T(r,t)=\frac{2bT_0}{\pi r}\sum_{n=1}^{\infty}\frac{(-1)^{n+1}}{n}\sin\frac{n\pi r}{b}\exp(-\frac{\kappa n^2\pi^2 t}{b^2})\,. \tag{37}$$

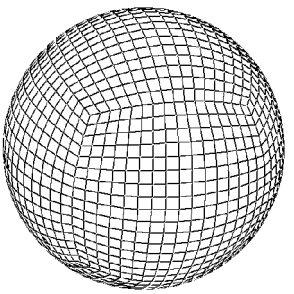

Figure 3: Boundary elements of spherical region.

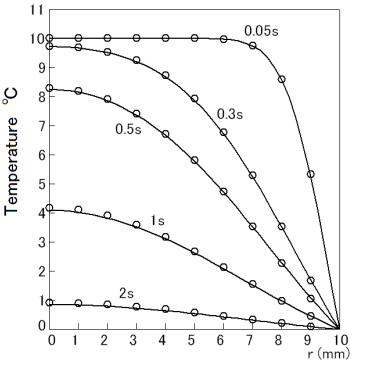

Figure 4: Temperature distributions in sphere.

The next numerical example is a cubic region with length $L=10$ mm with heat generation. Using internal points as shown in Fig. 5, it is assumed that the thermal diffusivity κ is 16 mm^{2}s^{-1}. The number of boundary elements and internal points are 600 and $M=729$, respectively. The surface temperature is 0℃ and the initial temperature is 0℃. Step heating is assumed. The heat generation is given by

$$W(x,y,z)=W_0\sin\frac{\pi x}{L}\sin\frac{\pi y}{L}\sin\frac{\pi z}{L}\quad(t\geq 0)\,. \tag{38}$$

Using a Laplace transformation and a finite sine transformation, an exact solution is obtained as follows:

$$T(x,y,z,t)=\frac{\kappa W_0}{\lambda E}\sin\frac{\pi x}{L}\sin\frac{\pi y}{L}\sin\frac{\pi z}{L}[1-\exp(-Et)] \tag{39}$$

$$E = \frac{3\kappa\pi^2}{L^2}. \tag{40}$$

$W_0/\lambda = 10\,K/mm^2$ is assumed. Figure 6 shows the comparison between this method and exact solution given by Eq. (39) at t =0.05, 0.1, 0.2, 0.4 and 1 s.

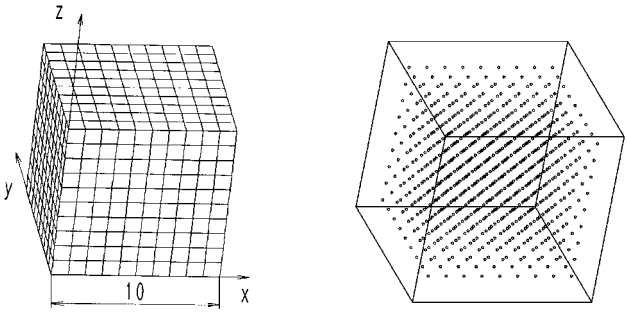

(a) Boundary elements (b) Internal points

Figure 5: Cubic region.

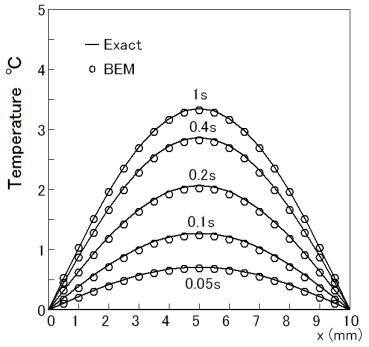

Figure 6: Temperature distributions in cube $(y = z = 5)$.

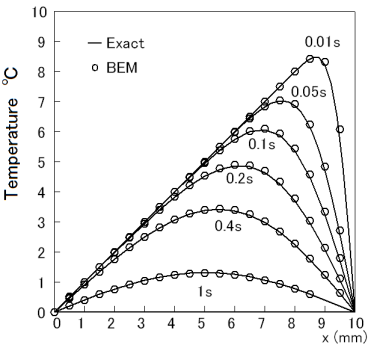

Figure 7: Temperature distributions in cube $(y = z = 5)$.

For the special case of the formulation of an unsteady state from a steady state, internal points are not necessary. Temperature of cubic region is obtained using boundary elements as shown in Fig. 5. In this calculation, internal points are not necessary. The thermal diffusivity κ is 16 mm^2s^{-1}. The temperatures at x=0 and x=10 are 0℃ and $T_0 = 10$ ℃, respectively. The other surfaces are adiabatic. Initial temperature is given by

$$T(x,0) = \frac{T_0 x}{L}. \tag{41}$$

The temperature at x=10 suddenly becomes $T_0 = 0\ ℃$ at time $t = 0\ s$. The unsteady temperature distribution is obtained by Eq. (36). Using a Laplace transformation and a finite sine transformation, the exact solution is obtained as follows:

$$T(x,t) = \frac{-2T_0}{\pi}\sum_{n=1}^{\infty}\frac{\cos(\pi n)}{n}\sin\frac{\pi n x}{L}\exp(-\frac{\kappa n^2\pi^2 t}{L^2}). \tag{42}$$

Figure 7 shows the comparison between this method and the exact solution given by Eq. (42) at t =0.01, 0.05, 0.1,0.2, 0.4 and 1 s.

4 Conclusion

It has been shown that it is possible to express the distributions of heat generation and initial temperature for the three-dimensional case using only the fundamental solution of lower order by the triple-reciprocity boundary element method. It has also been shown that highly accurate unsteady heat conduction analysis using the boundary integral is only possible using the polyharmonic function and the surface-distributed polyharmonic function, even in the case of arbitrary distributions of heat generation and initial temperature. Therefore, by adding only the data of the values at internal points and on the boundary for the distributions of heat generation and initial temperature, the analysis of three-dimensional heat conduction for the unsteady state with heat generation and initial temperature distributions has become possible. A reduction of the dimensionality of the problem has been effectively achieved.

References

[1] C. A. Brebbia, J. C. F. Telles and L. C. Wrobel, Boundary Element Techniques－Theory and Applications in Engineering, pp. 47-107, Berlin, Springer-Verlag, 1984.
[2] L. C. Wrobel, The Boundary Element Method, Volume 1, John Wiley & Sons, West Sussex, pp.97-117 (2002).
[3] Nowak, A. J., and Neves, A. C., The Multiple Reciprocity Boundary Element Method, Computational Mechanics Publication, Southampton, Boston, (1994).
[4] Ochiai, Y. and Sekiya, T., Steady Heat Conduction Analysis by Improved Multiple-Reciprocity Boundary Element Method, Engineering Analysis with Boundary Elements, Vol. 18, pp. 111-117, (1996).
[5] Ochiai, Y. and Kobayashi, T., Initial Strain Formulation without Internal Cells for Elastoplastic Analysis by Triple-Reciprocity BEM, International Journal for Numerical Methods in Engineering, Vol. 50, pp. 1877-1892, (2001).
[6] Y. Ochiai, Two-Dimensional Unsteady Heat Conduction Analysis with Heat Generation by Triple-Reciprocity BEM, International Journal of Numerical Methods in Engineering, Vol. 51, No. 2, pp. 143-157(2001).

[7] Y. Ochiai, V. Sladek and J. Sladek, Transient Heat Conduction Analysis by Triple-Reciprocity Boundary Element Method, Engineering Analysis with Boundary Elements, Vol. 30, pp. 194-204 (2006).
[8] Ochiai, Y., Two-Dimensional Unsteady Thermal Stress Analysis by Triple-Reciprocity Boundary Element Method, Journal of Thermal Stresses, Vol. 24, No. 3, pp. 233-253, (2001).
[9] Y. Ochiai and V. Sladek, Numerical Treatment of Domain Integrals without Internal Cells in Three-Dimensional BIEM Formulations, CMES (Computer Modeling in Engineering & Sciences), Vol. 6, No. 6, pp. 525-536, 2004.

This page intentionally left blank

Radial basis integral equation method for Navier-Stokes equations

T. T. Bui & V. Popov
Wessex Institute of Technology, Environmental and Fluid Mechanics, Southampton, UK

Abstract

A meshless BEM approach has been developed, which has been applied for solution of the Navier-Stokes equations. The approach subdivides the original problem domain in a number of circular sub-domains around nodes used to represent the solution of the problem. Dual reciprocity method has been used to convert the domain integrals into integrals over the boundary of the sub-domains. Six equations are solved in 2D to obtain the solution of the Navier-Stokes equations, of which two are for solving the velocity components, one for pressure and the remaining equations are for solving for stresses. The developed formulation has been tested on the lid-driven cavity problem and the results have been compared to the results of Ghia *et al.*, showing good agreement.
Keywords: Meshless method, integral equations, circular sub-domains, radial basis functions, Navier-Stokes equations.

1 Introduction

Meshless approaches based on the integral equations are receiving increased attention due to their accuracy associated with the integral equations methods, of which the most widely used so far has been the BEM, and the flexibility they offer as the meshing requirements are either eliminated or largely reduced.

The Local Boundary Integral Equation (LBIE) method [2,3] uses domain decomposition into a large number of circular sub-domains, with the source point in the centre of the circle. The LBIE uses the concept of "companion solution" in order to eliminate the single layer integral from the local boundary integral equation, leaving the potential field as the only unknown in the equations. For source points that are located on the boundary of the given problem part of the local circular bound-


WIT Transactions on Modelling and Simulation, Vol 49, © 2009 WIT Press
www.witpress.com, ISSN 1743-355X (on-line)
doi:10.2495/BE090131

ary is replaced by the part of the global boundary and the integrals are evaluated over this part of the global boundary and remaining part of the circle.

Recently [4] LBIE has been employed for solution of the Navier-Stokes equations by using the velocity-vorticity formulation in combination with the radial basis functions (RBFs) used for interpolation of the field variables over the circular boundaries of the sub-domains.

Though the present formulation may seem similar to the LBIE in certain aspects, overall it is a fundamentally different approach. Similarly to the LBIE it is implemented over circular sub-domains where the source points are placed in the centres of the circles and uses RBFs for interpolation of the field variables over the circular boundary. However, the present approach is implemented using the velocity-pressure formulation, it does not use the companion solution concept and does not need any integration over the boundary. More on the current formulation can be found in Bui and Popov [5].

2 Velocity-pressure formulation

For the incompressible flow, the equation of continuity is

$$\nabla \cdot \boldsymbol{u} = 0 \tag{1}$$

The conservation of momentum for an incompressible fluid is expressed as:

$$\rho \frac{\partial u_i}{\partial t} + \rho u_j \frac{\partial u_i}{\partial x_j} = \frac{\partial \sigma_{ij}}{\partial x_j} + \rho F_i \tag{2}$$

where u_i is the component of the velocity vector along the i direction, ρ is the density and F_i is the net body force along the i direction; σ_{ij} is stress tensor corresponding to the flow $\boldsymbol{u}, p$. For Newtonian fluid

$$\sigma_{ij} = -p\delta_{ij} + \mu \left(\frac{\partial u_i}{\partial x_j} + \frac{\partial u_j}{\partial x_i} \right) \tag{3}$$

where p is the fluid pressure, δ_{ij} is the Kronecker delta and μ is the viscosity coefficient.

The integral representation for Navier-Stokes equations for a given point x *inside the domain* Ω bounded by boundary S is given by Ladyzhenskaya (1963) [6] as:

$$u_i(x) = \int_S t^*_{ki}(x,y) u_i(y) dS_y - \int_S u^*_{ki}(x,y) t_i(y) dS_y + \int_\Omega u^*_{ki}(x,y) g_i(y) d\Omega \tag{4}$$

where $g_i = \rho u_j u_{i,j}$ are convective terms; $t_i = \sigma_{ij} n_j$ are the traction components, n_j is the outward normal vector; u^k_i is the velocity field fundamental solution of

the Stokes equations. In two dimensions, u^*_{ki} is given as [6]

$$u^*_{ki}(x,y) = -\frac{1}{4\pi\mu}\left[\ln\left(\frac{1}{r}\right)\delta_{ik} + \frac{(x_i - y_i)(x_k - y_k)}{r^2}\right] \tag{5}$$

with a corresponding pressure q^k which is given by

$$q^k(x,y) = -\frac{1}{2\pi}\frac{(x_k - y_k)}{r^2} \tag{6}$$

where $r = |x - y|$. The fundamental traction $t^*_{ki}(x,y)$ is defined as

$$\begin{aligned} t^*_{ki}(x,y) &= \sigma'_{ij}(\boldsymbol{u}^k(x,y), q^k(x,y))n_j(y) \\ t^*_{ki}(x,y) &= -\frac{1}{\pi r}\frac{(x_i - y_i)(x_k - y_k)(x_j - y_j)}{r^3}n_j \end{aligned} \tag{7}$$

The DRM approximation was introduced to express the domain integral in (4) in terms of equivalent boundary integrals. The convective term is expanded in the form

$$g_i(x) = \sum_{m=1}^{N+A} f^m(x)\alpha^m_l\delta_{il}. \tag{8}$$

The coefficient α^m_l is unknown which can be determined by applying (8) on N collocation nodes y^m, $(m = 1, \ldots, N)$. The collocation nodes are the nodes on the boundary S and the nodes inside the domain Ω.

With the approximation (8), the domain integral in (4) becomes

$$\int_\Omega u^*_{ki}(x,y)g_i(y)d\Omega = \sum_{m=1}^{N+A}\alpha^m_l\int_\Omega u^*_{ki}(x,y)f^m(x)\delta_{il}d\Omega \tag{9}$$

The new auxiliary velocity field $(\hat{u}^{lm}_i(x), \hat{p}^{lm}(x))$ is defined by the following equations

$$\mu\frac{\partial^2\hat{u}^{lm}_i(x)}{\partial x_j\partial x_j} - \frac{\partial\hat{p}^{lm}(x)}{\partial x_i} = f^m(x)\delta_{il} \tag{10}$$

$$\frac{\partial\hat{u}^{lm}_i}{\partial x_i} = 0 \tag{11}$$

Applying the Green's identity to the new flow field $(\hat{u}^{lm}_i(x), \hat{p}^{lm}(x))$ yields

$$\begin{aligned} \hat{u}^{lm}_i(x) = &\int_S t^*_{ki}(x,y)\hat{u}^{lm}_i(y)dS_y \\ &- \int_S u^*_{ki}(x,y)\hat{t}^{lm}_i(y)dS_y + \int_\Omega u^*_{ki}(x,y)f^m(y)\delta_{il}d\Omega \end{aligned} \tag{12}$$

where the traction $\hat{t}^{lm}_i$ is defined as

$$\hat{t}^{lm}_i(y) = \sigma_{ij}(\hat{u}^{lm}_i(y), \hat{p}^{lm}(y))n_j(y) \tag{13}$$

Rearranging the terms in (12) we have the transformation from the domain integral to the boundary integral

$$\int_\Omega u^*_{ki}(x,y)f^m(y)\delta_{il}d\Omega = -\int_S t^*_{ki}(x,y)\hat{u}^{lm}_i(y)dS_y + \int_S u^*_{ki}(x,y)\hat{t}^{lm}_i(y)dS_y + \hat{u}^{lm}_i(x) \tag{14}$$

Substitution of (14) and (9) into (4) leads to integral representation formula in which only boundary integrals are present

$$u_i(x) - \int_S t^*_{ki}(x,y)u_i(y)dS_y + \int_S u^*_{ki}(x,y)t_i(y)dS_y = \sum_{m=1}^{N+A}\alpha^m_l\left\{-\int_S t^*_{ki}(x,y)\hat{u}^{lm}_i(y)dS_y + \int_S u^*_{ki}(x,y)\hat{t}^{lm}_i(y)dS_y + \hat{u}^{lm}_i(x)\right\} \tag{15}$$

3 Implementation of the meshless method

The proposed method will solve at each interior node six integral equations in order to obtain the velocities u_1, u_2, stresses σ_{11}, σ_{12}, σ_{22} and pressure p. The integral equation for velocity components is given by (15). Equations for stresses and pressure will be described as follows.

3.1 Integral equation for stresses

Stresses are obtained from

$$\sigma_{kh} = -p\delta_{kh} + \mu\left(\frac{\partial u_k}{\partial x_h} + \frac{\partial u_h}{\partial x_k}\right) \tag{16}$$

The value of derivatives $\partial u_k/\partial x_h$ are obtained by differentiating (15) in respect to x_h, where x_h is the component of x.

$$\frac{\partial u_k(x)}{\partial x_h} = \int_S \frac{\partial t^*_{ki}(x,y)}{\partial x_h}u_i(y)dS_y - \int_S \frac{\partial u^*_{ki}(x,y)}{\partial x_h}\sigma_{ij}(y)n_j(y)dS_y + \sum_{m=1}^{N_r+A}\alpha^m_l\left\{-\int_S \frac{\partial t^*_{ki}(x,y)}{\partial x_h}\hat{u}^{lm}_i(y)dS_y + \int_S \frac{\partial u^*_{ki}(x,y)}{\partial x_h}\hat{t}^{lm}_i(y)dS_y + \frac{\partial \hat{u}^{lm}_k(x)}{\partial x_h}\right\} \tag{17}$$

Substituting (17) into (16) yields equation for $\sigma_{kh}(x)$

$$\begin{aligned}\frac{\sigma_{kh}}{\mu} =& -\frac{p}{\mu}\delta_{kh} + \int_S \left[\frac{\partial t^*_{ki}(x,y)}{\partial x_h} + \frac{\partial t^*_{hi}(x,y)}{\partial x_k}\right] u_i(y)dS_y \\ &- \int_S \left[\frac{\partial u^*_{ki}(x,y)}{\partial x_h} + \frac{\partial u^*_{hi}(x,y)}{\partial x_k}\right] \sigma_{ij}(y)n_j(y)dS_y \\ &+ \sum_{m=1}^{N_r+A} \alpha_l^m \left\{ -\int_S \left[\frac{\partial t^*_{ki}(x,y)}{\partial x_h} + \frac{\partial t^*_{hi}(x,y)}{\partial x_k}\right] \hat{u}_i^{lm}(y)dS_y \right. \\ &\left. + \int_S \left[\frac{\partial u^*_{ki}(x,y)}{\partial x_h} + \frac{\partial u^*_{hi}(x,y)}{\partial x_k}\right] \hat{t}_i^{lm}(y)dS_y + \left[\frac{\partial \hat{u}_k^{lm}(x)}{\partial x_h} + \frac{\partial \hat{u}_h^{lm}(x)}{\partial x_k}\right]\right\}\end{aligned} \tag{18}$$

3.2 Integral equation for pressure

The pressure corresponding to the velocity field for the Newtonian fluid can be obtained in the integral form as (for more details, see Ladyzhenskaya [6])

$$\begin{aligned}p(x) =& -\int_S q^k(x,y)t_j(y)dS_y - 2\mu \int_S \frac{\partial q^k(x,y)}{\partial x_j} u_k(y)n_j(y)dS_y \\ &+ \int_\Omega q^k(x,y)g_k(y)dy\end{aligned} \tag{19}$$

With the approximation (8), the domain integral in (19) becomes

$$\int_\Omega q^k(x,y)g_k(y)d\Omega = \sum_{m=1}^{N+A} \alpha_l^m \int_\Omega q^k(x,y)f^m(x)\delta_{kl}d\Omega \tag{20}$$

Applying the Green's identity to the new flow field $(\hat{u}_i^{lm}(x), \hat{p}^{lm}(x))$ produces

$$\begin{aligned}\hat{p}^{lm}(x) =& -\int_S q^k(x,y)\hat{t}_k^{lm}(y)dS_y - 2\mu \int_S \frac{\partial q^k(x,y)}{\partial x_j} \hat{u}_k^{lm}(y)n_j(y)dS_y \\ &+ \int_\Omega q^k(x,y)f^m(y)\delta_{kl}dy\end{aligned} \tag{21}$$

Substitution of (21) and (20) into (19) leads to

$$\begin{aligned}p(x) =& -\int_S q^k(x,y)t_k(y)dS_y - 2\mu \int_S \frac{\partial q^k(x,y)}{\partial x_j} u_k(y)n_j(y)dS_y \\ &+ \sum_{m=1}^{N+A} \alpha_l^m \left(\hat{p}^{lm}(x) + \int_S q^k(x,y)\hat{t}_k^{lm}(y)dS_y + 2\mu \int_S \frac{\partial q^k(x,y)}{\partial x_j} \hat{u}_k^{lm}(y)n_j(y)dS_y\right)\end{aligned} \tag{22}$$

4 Interpolation for the unknown fields

In order to perform the integration over the local boundaries of the circular sub-domains, values of the velocities and stresses must be known on the circles. The unknown velocity at any node on the local boundary is approximated by N neighboring nodes by the following formula:

$$u(x) = \sum_{i=1}^{N} f(x, x_i).a_i \tag{23}$$

Equation (23) is applied on all N neighboring nodes x_j, $j = 1, \ldots, N$ and the following system of equations is formed

$$u(x_j) = \sum_{i=1}^{N} f(x_j, x_i).a_i \tag{24}$$

Equation (24) can be written in the matrix form as

$$\mathbf{u_0} = \mathbf{F_0 a} \tag{25}$$

where $\mathbf{u_0} = [u(x_1), u(x_2), \ldots, u(x_N)]^T$; $\mathbf{F_0} = [f_{ji}] = [f(x_j, x_i)]$, $j = 1, 2, \ldots, N; i = 1, 2, \ldots, N$. The unknown coefficients $\mathbf{a}$ are determined by $\mathbf{a} = \mathbf{F_0^{-1} u_0}$. Hence, the potential at point x can be written as

$$u(x) = F(x)\mathbf{F_0^{-1} u_0} \tag{26}$$

where $F(x) = [f(x, x_1), f(x, x_2), \ldots, f(x, x_N)]$.

In the similar way, the stresses are approximated by the following formula

$$\sigma_{ij}(x) = F(x)\mathbf{F_0^{-1}}\sigma_{\mathbf{ij}}^{\mathbf{0}} \tag{27}$$

where $\sigma_{\mathbf{ij}}^{\mathbf{0}} = [\sigma_{ij}(x_1), \sigma_{ij}(x_2), \ldots, \sigma_{ij}(x_N)]^T$.

5 Solution procedures

The RBIEM generates one circular sub-domain around each of the nodes located inside the domain or on the boundary (see [7]). The eight nodes on the boundary of the sub-domains are introduced as nodes where the velocities and stresses are evaluated using interpolation by employing the surrounding nodes located at centers of surrounding sub-domains. For each sub-domain, the same set of nodes was used for interpolation of the field variables over the circular local boundaries; this means the same set was used for each of the eight nodes on the circle, and for the DRM approximation. This significantly simplifies the search for the neighbouring nodes and saves CPU time. The set of nodes was found by prescribing the required number of nodes in the interpolation/approximation and then the code defined the set by selecting the required number of the nearest nodes to node i.

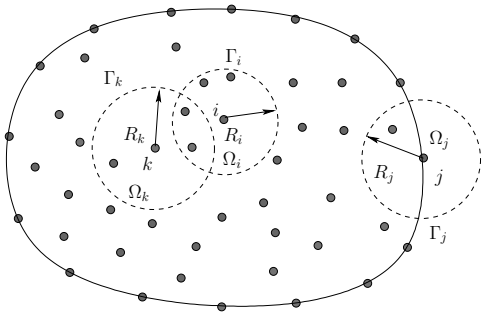

Figure 1: The circular sub-domains distributed in the problem domain.

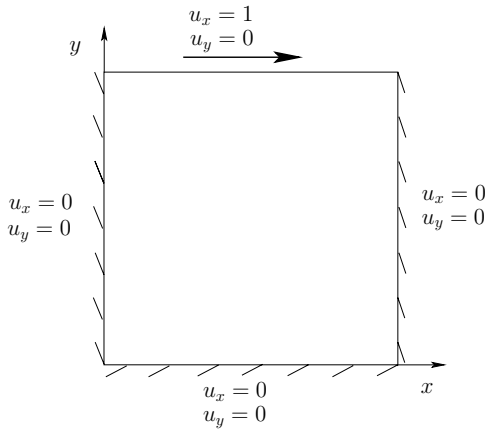

Figure 2: Lid-driven cavity configuration with boundary conditions.

6 Numerical examples

The laminar incompressible flow in a square cavity whose upper boundary is moving at a constant velocity (see Figure 2) is considered for benchmarking the numerical approach. The velocity is given as zero on all the walls except at the top, where the horizontal velocity equals to unity. The problem is solved by the proposed method for two different Reynolds number $Re = 100$, $Re = 400$. The results obtained by the proposed method are compared with the benchmark values obtained by Ghia et al. [1], using a finite difference multigrid numerical scheme with very fine mesh. For the both cases, the radius of the sub-domain for boundary nodes is set as small as 5.10-3 to reduce the error due to the extrapolation by reducing the distance between the nodes on the external part of the local circular boundary. The radius of the sub-domain for internal nodes is the distance to the nearest node. All simulations are done on a PC Pentium IV 3.0 Ghz, 1.0 Gb of RAM. The resulting sparse matrix produced by the method is solved by SPARSKIT solver.

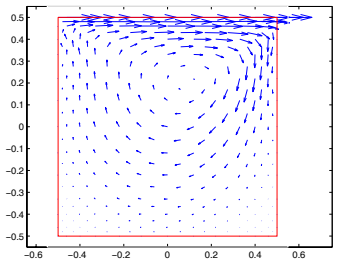

Figure 3: Velocity field at $Re = 100$ obtained with 313 nodes in the domain.

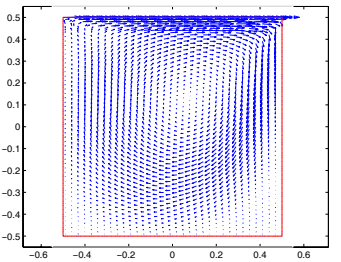

Figure 4: Velocity field at $Re = 400$ obtained with 5951 nodes in the domain.

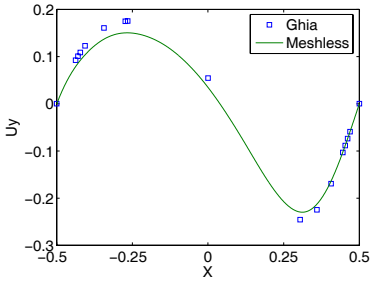

Figure 5: Horizontal fluid velocity distribution at the vertical center line, at $Re = 100$ with 313 nodes in the domain.

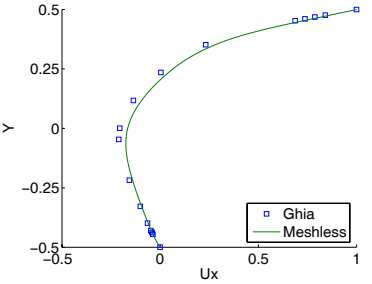

Figure 6: Vertical fluid velocity distribution at the horizontal center line, at $Re = 100$ with 313 nodes in the domain.

The domain for the case $Re = 100$ has 313 nodes. Velocities of the flow for the case $Re = 100$ are depicted in figure 3. Figures 5 and 6 show horizontal fluid velocity distribution at the vertical center line and vertical fluid velocity distribution at the horizontal center line, respectively. They are in good agreement with the results obtained by Ghia et al. [1].

As pointed out by Power and Mingo [8], at the flow regions near the corners, the flow has singularities associated with infinite values of the velocity and surface traction. One way to circumvent these problems is to use a high density of boundary elements in the vicinity of the singular points. In the case $Re = 400$ there are 5951 nodes in the domain. Figure 4 shows the obtained velocity filed which is in good agreement with previous method. Figures 7 and 8 show a comparison between velocities obtained by proposed approach and those reported by Ghia et al. [1] on the horizontal and vertical center-line fluid. Good agreement of the results has been archived.

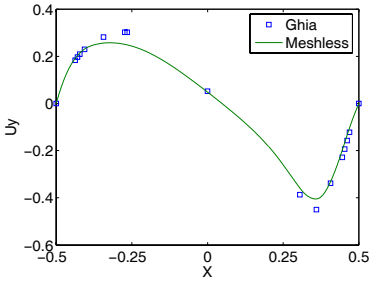

Figure 7: Horizontal fluid velocity distribution at the vertical center line, at $Re = 400$ with 5951 nodes in the domain.

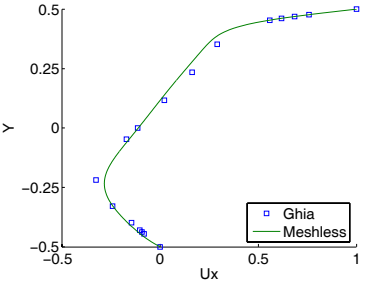

Figure 8: Vertical fluid velocity distribution at the horizontal center line, at $Re = 400$ with 5951 nodes in the domain.

7 Conclusions

A meshless method based on the integral equations and combined with the sub-domain approach is applied to the Navier-Stokes equation. Six equations in 2D are solved at each node, where two equations are for velocities, one equation is for pressure and the remaining equations are used for solving stresses. Radial basis function interpolation is applied in order to obtain the values of the field variable and normal derivatives on the boundary of the circular sub-domains. The inversion of the matrix is calculated only once for every nodal point. Every nodal point is connected with few surrounding nodal points, leading to a banded system. The DRM has been applied to convert the domain integrals into integrals over the boundary of the sub-domains. The numerical results produced by meshless method for two cases $Re = 100$ and $Re = 400$ are in good agreement with the results obtained by Ghia *et al.* showing that proposed method can be used for solving the Navier-Stokes equations.

References

[1] Ghia, U., Ghia, K. & Shin, C., High-re solutions for incompressible flow using the Navier-Stokes equations and a multigrid method. *Journal of Computational Physics*, **48**, pp. 387–411, 1982.

[2] Zhu, T., Zhang, J. & N.Atluri, S., A local boundary integral equation (LBIE) method in computational mechanics, and a meshless discretization approach. *Computational Mechanics*, **21**, pp. 223–235, 1988.

[3] Zhu, T., Zhang, J. & N.Atluri, S., A meshless local boundary integral equation (LBIE) method for solving nonlinear problems. *Computational Mechanics*, **22**, pp. 174–186, 1998.

[4] Sellountos, E.J. & Sequeira, A., An advanced meshless LBIE/RBF method for solving two-dimensional incompressible fluid flows. *Computational Mechanics*, **44**, pp. 617–631, 2008.
[5] Bui, T.T. & Popov, V., *The Radial Basis Integral Equation Method for Convection-Diffusion Problems*. Ashurst Lodge, Southampton, UK, 2009.
[6] Ladyzhenskaya, O.A., *The Mathematical Theory of Viscous Incompressible Flow*. Gordon and Breach, New York, 1963.
[7] Popov, V. & Bui, T.T., A meshless solution to convection-diffusion problems. *Submited to Engineering Analysis with Boundary Elements*, 2009.
[8] Power, H. & Mingo, R., The DRM subdomain decomposition approach to solve the two-dimensional Navier-Stokes system of equations. *Engineering Analysis with Boundary Elements*, **24(1)**, pp. 107–119, 2000.

Efficient Boundary Element Method for a focused domain

S. Takiguchi, K. Amaya & Y. Onishi
Department of Mechanical and Environmental Informatics, Tokyo Institute of Technology, Japan

Abstract

An efficient Boundary Element Method for focused domain is developed. In this method, whole boundaries are divided into near boundaries which are near to the focused domain and far boundaries which are sufficiently far from it. We set up boundary integral equations and express these integrals which contain unknown quantities on the far boundaries as low order multipole moments, approximately. Thus the number of unknowns and boundary integral equations set up are decreased drastically by this method, and enables us to compute them efficiently. When unknown quantities are required only in a specific domain, especially on large-scale boundary value problems, this method enables us to compute them efficiently. The capability of this method is verified with some numerical experiments.
Keywords: Boundary Element Method, 2D potential problem, focused domain, multipole expansion, generalized inverse matrix.

1 Introduction

The Boundary Element Method (BEM) is one of the major numerical solutions for boundary value problems and the Fast Multipole Boundary Element Method (FMBEM), is in widespread use as an efficient solution for large-scale boundary value problems.

The BEM is generally used to obtain all unknown quantities with uniform accuracy in a whole analytical domain. However, in reality, there are not a few cases where the unknown quantities are required only in a specific domain, that is, the focused domain for practical purpose. For example, we can point to corrosion or anticorrosion analysis for the evaluation of anti-corrosion effect on specific parts of structures such as boats and ships, and elastic analysis for the evaluation of

WIT Transactions on Modelling and Simulation, Vol 49, © 2009 WIT Press
www.witpress.com, ISSN 1743-355X (on-line)
doi:10.2495/BE090141

strength on stress concentration zones. In such cases, it is advantageous to compute more efficiently unknown quantities only in focused domain with the same accuracy as the conventional BEM[1].

Based on the above-mentioned background, we developed a new efficient boundary element method for a focused domain.

In this method, a whole boundary is divided into near boundaries which are near to a focused domain and far boundaries which are sufficiently far from it (Fig. 1). Then, we set up boundary integral equations (BIEs) whose collocation points are on all the elements of the near boundaries and express these integrals which contain unknown quantities on far boundaries as low order multipole moments by using a multipole expansion of the fundamental solution. Moreover, we also set up boundary integral equations whose weighting functions are harmonic functions by the number of those multipole moments. The boundary integrals which contain unknown quantities on the far boundaries are expressed approximately as the multipole moments by using a generalized inverse matrix. Thus the number of unknowns and boundary integral equations set up are decreased drastically by this method, and enables us to compute them efficiently (Fig. 2).

This paper presents the efficient boundary element method for the focused domain, that is the "Focused Domain Efficient Boundary Element Method (FD–EBEM)". The capability of this method extended to 2D potential problems is verified with some numerical experiment.

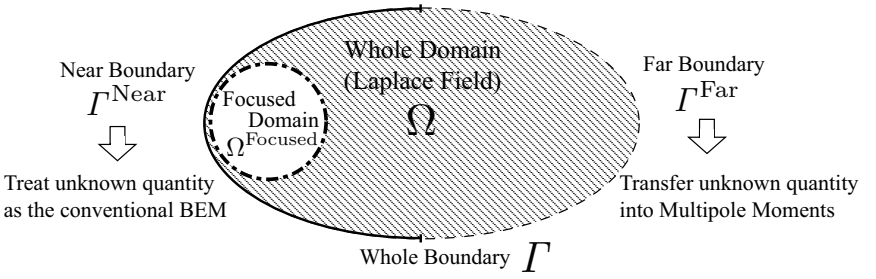

Figure 1: Division of boundary into near and far boundaries.

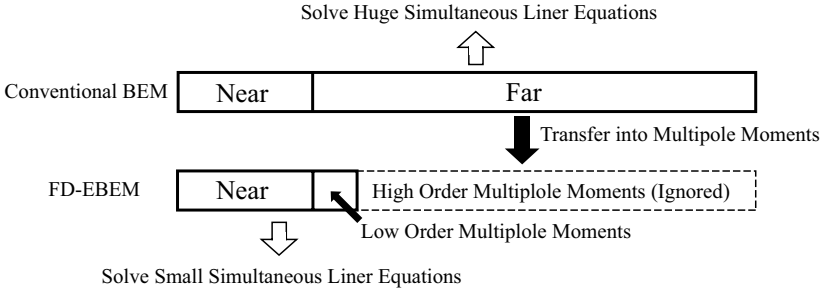

Figure 2: Reduction of the number of unknown quantities.

2 BIE formulation and the conventional BEM approach

The BIE formulation and its discretization using the conventional BEM for 2D potential problems are summarized in this section. They are fundamental to FD–EBEM.

2.1 Setup of boundary value problem

For simplicity, consider the following Laplace equation governing a potential problem in a 2D domain Ω (Fig. 3):

$$\nabla^2 u(z) = 0 \qquad (\forall z \in \Omega) \tag{1}$$

under the boundary condition $u(z_0) = u' \ (z_0 \in \Gamma)$. $u(z)$ is potential field in domain Ω, Γ is the boundary of the Ω, and *the symbol prime*($'$) quantities indicate given values on the boundary.

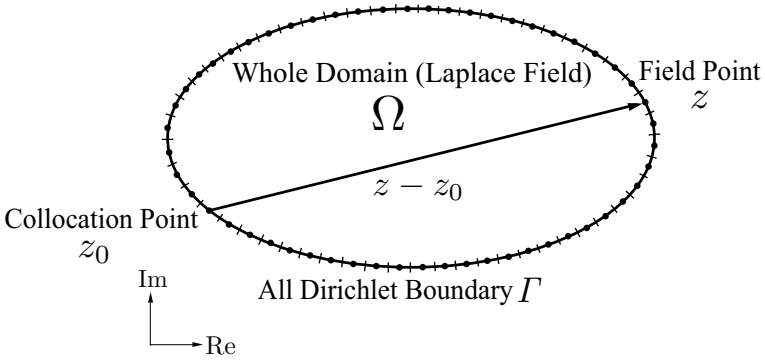

Figure 3: Domain Ω and boundary Γ (discretized).

2.2 BIE of potential problems

The BIE for this boundary value problem can be expressed as the following formula:

$$c(z)u(z) = \mathrm{Re}\left[\int_\Gamma u^*(z_0, z)q(z)|\mathrm{d}z| - \int_\Gamma q^*(z_0, z)u(z)|\mathrm{d}z|\right], \tag{2}$$

where q the flux $q(z) = \partial u(z)/\partial n(z)$, $n(z)$ outward normal, z_0 the collocation point, z field point and $c(z_0)$ coefficients that are equal to $1/2$ if $z_0 \in \Gamma$ and Γ is smooth around z_0, or 1 if $z_0 \in \Omega$; $u^*(z_0, z)$ and $q^*(z_0, z)$ are the fundamental solution given by:

$$u^*(z_0, z) = -\frac{1}{2\pi}\ln(z - z_0), \qquad q^*(z, z_0) = -\frac{n(z)}{2\pi(z - z_0)}. \tag{3}$$

2.3 Discretization

In this subsection, discretization with constant boundary elements is explained for simplicity. The boundary Γ is divided into N line elements Γ_k $(k = 1, 2, \cdots, N)$ and one node z_0^j is placed on each element. We obtain the following discretized equation of BIE (2) in matrix form:

$$\boldsymbol{G}_\Gamma \boldsymbol{q}_\Gamma = \boldsymbol{H}_\Gamma \boldsymbol{u}'_\Gamma, \tag{4}$$

where

$$\boldsymbol{H}_\Gamma = \begin{bmatrix} h_{11} & \cdots & h_{1N} \\ \vdots & \ddots & \vdots \\ h_{N1} & \cdots & h_{NN} \end{bmatrix}, \qquad \boldsymbol{G}_\Gamma = \begin{bmatrix} g_{11} & \cdots & g_{1N} \\ \vdots & \ddots & \vdots \\ g_{N1} & \cdots & g_{NN} \end{bmatrix},$$

$$h_{jk} = \frac{\delta_{jk}}{2} + \int_{\Gamma_k} q^*(z_0^j, z)|\mathrm{d}z|, \qquad g_{jk} = \int_{\Gamma_k} u^*(z_0^j, z)|\mathrm{d}z|, \tag{5}$$

$$\boldsymbol{u}'_\Gamma = \begin{Bmatrix} u'_1 \\ \vdots \\ u'_N \end{Bmatrix}, \qquad \boldsymbol{q}_\Gamma = \begin{Bmatrix} q_1 \\ \vdots \\ q_N \end{Bmatrix}, \tag{6}$$

u_k and q_k $(k = 1, 2, \ldots, N)$ are nodal values of u and q on the element Γ_k, respectively. Obviously, the construction of matrix $\boldsymbol{H}_\Gamma$ and $\boldsymbol{G}_\Gamma$ requires $O(N^2)$ operations using the two expressions in Eq. (5) and the size of the required memory for storing them is also $O(N^2)$ since they are in general non-symmetric and dense matrices. The solution of system in Eq. (4) using direct solvers such as Gauss elimination is even worse, requiring $O(N^3)$ operations because of this general matrix. That is why the conventional BEM is not so efficient for large-scale problems, despite its robustness in the meshing stage as compared with other domain based methods [2].

3 FD–EBEM formulation for 2D potential problems

As stated in the previous section, the conventional BEM is not so efficient for large-scale problems because of requiring vast operations and memory. FMBEM was developed for getting over this weak point of the conventional BEM. But, it is hard to say that FMBEM is always efficient, especially, in the case where the unknown quantities are required only in a specific domain, because, FMBEM is the method for obtaining all unknown quantities with uniform accuracy in a whole analytical domain. In such cases, FD–EBEM enables us to compute efficiently the unknown quantities only in a specific domain. In this section, we explain the formulation of FD–EBEM for 2D potential problems.

3.1 Setup of boundary value problem

For simplicity, consider the same Laplace equation (1) governing potential problem in a 2D domain Ω (Fig. 4) under the boundary condition $u(z_0) = u' \ (z_0 \in \Gamma)$ as given in the previous section. We also assume that a specific domain is focused domain $\Omega^{\mathrm{Focused}}$ in the whole domain Ω and potential $u(z_0)$, $z_0 \in \Omega^{\mathrm{Focused}}$ is a requisite unknown quantity. Far boundary Γ^{Far} is sufficiently far from the focused domain $\Omega^{\mathrm{Focused}}$. Far boundary Γ^{far} and the center of multipolar moments z_c are determined so that $\forall z \in \Gamma^{\mathrm{Far}} (\subseteq \Gamma)$ satisfy the following formula for $\forall z_0 \in \Omega^{\mathrm{Focused}}$:

$$|z - z_c| \ll |z_0 - z_c|, \tag{7}$$

Additionally, the boundary near the focused domain $\Omega^{\mathrm{Focused}}$ is denoted near boundary $\Gamma^{\mathrm{Near}} \left(= \Gamma \cap \overline{\Gamma^{\mathrm{Far}}}\right)$, and $\exists z_0 \in \Gamma^{\mathrm{Near}}$ satisfies Eq. (7) for $\forall z \in \Gamma^{\mathrm{Far}} (\subseteq \Gamma)$.

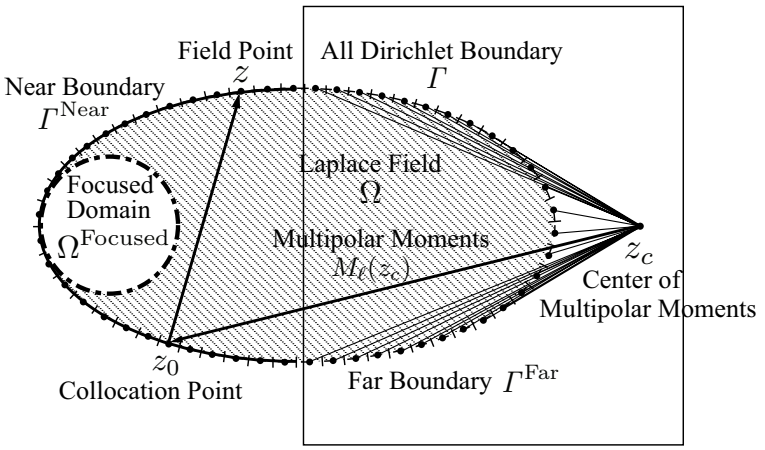

Figure 4: Focused domain and classification of boundary.

3.2 Division of boundary integral into near and far boundary

Now, we deal with the boundary value problem where the potential u on the whole boundary Γ is given. Thus, the boundary integral contains unknown quantity in the first right-hand term of Eq. (2), where $z_0 \in \Gamma$. In this method, the first right-hand

term of Eq. (2) is devided into the near boundary Γ^{Near} and the far boundary Γ^{Far} part as follows:

$$c(z_0)u(z_0) = \mathrm{Re}\left[\int_{\Gamma^{\mathrm{Near}}} u^*(z_0,z)\cdot q(z)|\mathrm{d}z| + \int_{\Gamma^{\mathrm{Far}}} u^*(z_0,z)\cdot q(z)|\mathrm{d}z| - \int_{\Gamma} q^*(z_0,z)\cdot u(z)|\mathrm{d}z|\right]. \quad (8)$$

3.3 Multipole expansion of boundary integral on far boundary

The displacement component of the fundamental solution in complex notation $u^*(z_0,z)$ can be transformed as the following formula:

$$u^*(z_0,z) = -\frac{1}{2\pi}\left\{\log|z_0-z_c| + \log\left(1-\frac{z-z_c}{z_0-z_c}\right)\right\} \quad (9)$$

In the case where z_0, z and z_c satisfy Eq. (7), we can apply the following Taylor series expansion:

$$\log(1-\xi) \approx \sum_{\ell=1}^{L}\frac{\xi^\ell}{\ell} \qquad |\xi|<1, \quad (10)$$

and we obtain

$$u^*(z_0,z) \approx -\frac{1}{2\pi}\left\{\log|z_0-z_c| - \sum_{\ell=1}^{L}\frac{1}{(z_0-z_c)^\ell}\cdot\frac{(z-z_c)^\ell}{\ell}\right\} \quad (11)$$

Therefore, the second right-hand term of Eq. (8) is described by Eq. (11) as follows.

$$\int_{\Gamma^{\mathrm{Far}}} u^*(z_0,z)\cdot q(z)|\mathrm{d}z| \approx \frac{1}{2\pi}\sum_{\ell=0}^{L} O_\ell(z_0-z_c)M_\ell(z_c) \quad (12)$$

where

$$M_\ell(z_c) = \int_{\Gamma^{\mathrm{Far}}}\frac{(z-z_c)^\ell}{\ell}\cdot q(z)|\mathrm{d}z|, \quad O_\ell(z) = \begin{cases}\log|z| & (\ell=0)\\ z^{-\ell} & (\ell\geq 1)\end{cases}. \quad (13)$$

In the case where z_0 and z satisfy the following formula : Eq. (14), the finite series of Eq. (12) is known to be sufficiently convergent by approximately 15 terms.

$$|z_0-z_c| \geq 3|z-z_c| \quad (14)$$

It means that the finite series of Eq. (12) is sufficiently convergent by a few terms in the case where the collocation point z_0 is placed in the focused domain $\Omega^{\mathrm{Focused}}$ and on the near boundary Γ^{Near} but it is not convergent in the case the collocation point is placed on the far boundary Γ^{Far}.

3.4 BIE whose Collocation Point is placed on near boundary

When the collocation point z_0 is placed on the near boundary Γ^{Near} and the field point z is placed on the far boundary Γ^{Far}, z and z_0 can satisfy Eq. (7). Therefore Eq. (8) can be transformed into the following formula:

$$c(z_0)u(z_0) \approx \mathrm{Re}\Bigg[\int_{\Gamma^{\mathrm{Near}}} u^*(z_0,z)\cdot q(z)|\mathrm{d}z| - \int_{\Gamma} q^*(z_0,z)\cdot u(z)|\mathrm{d}z| + \frac{1}{2\pi}\sum_{\ell=0}^{L} O_\ell(z_0-z_c)M_\ell(z_c)\Bigg] \tag{15}$$

Consider the case where we discretize boundary Γ by constant boundary elements and set BIEs whose collocation points are placed on elements of the near boundary Γ^{Near} only. In this case, we can't solve the simultaneous linear equations due to insufficiency of equations by the increment of multipolar moments, or L. Additional equations for this insufficiency will be demonstrated in the next subsection.

3.5 BIE whose weighting functions are harmonic functions

We set up boundary integral equations whose weighting functions are harmonic functions, that is $O_\ell(z-z_c)$ by the number of those multipole moments, or L. In this case, BIEs is the following formula:

$$\int_{\Gamma} O_\ell(z-z_c)\cdot q(z)|\mathrm{d}z| - \int_{\Gamma^{\mathrm{Near}}} P_\ell(z-z_c)\cdot u(z)|\mathrm{d}z| - \int_{\Gamma^{\mathrm{Far}}} P_\ell(z-z_c)\cdot u(z)|\mathrm{d}z| = 0 \qquad (\ell = 0,1,\cdots,L) \tag{16}$$

where

$$P_\ell(z) = \frac{\partial O_\ell(z)}{\partial n(z)} = -\frac{\ell\cdot n(z)}{z^{\ell+1}} \tag{17}$$

The process for expressing the integral in Eq. (16) which contains unknown quantities on far boundaries as these multipolar moments approximately is demonstrated below. We discretize the boundary by constant boundary elements and obtain the discretized BIE in matrix form:

$$\begin{bmatrix}\boldsymbol{K}_{\Gamma^{\mathrm{Near}}} & \boldsymbol{K}_{\Gamma^{\mathrm{Far}}}\end{bmatrix}\begin{Bmatrix}\boldsymbol{q}_{\Gamma^{\mathrm{Near}}} \\ \boldsymbol{q}_{\Gamma^{\mathrm{Far}}}\end{Bmatrix} = \boldsymbol{J}_\Gamma \boldsymbol{u}'_\Gamma, \tag{18}$$

where

$$\boldsymbol{K}_\Gamma = \begin{bmatrix}\boldsymbol{k}_{00} & \cdots & \boldsymbol{k}_{0N} \\ \vdots & \ddots & \vdots \\ \boldsymbol{k}_{L0} & \cdots & \boldsymbol{k}_{LN}\end{bmatrix} \qquad \boldsymbol{J}_\Gamma = \begin{bmatrix}\boldsymbol{j}_{01} & \cdots & \boldsymbol{j}_{0N} \\ \vdots & \ddots & \vdots \\ \boldsymbol{j}_{L0} & \cdots & \boldsymbol{j}_{LN}\end{bmatrix}, \tag{19}$$

$$\boldsymbol{k}_{\ell k} = \begin{Bmatrix} \mathrm{Re}\left[\int_{\Gamma_k} P_\ell(z-z_c)|\mathrm{d}z|\right] \\ \mathrm{Im}\left[\int_{\Gamma_k} P_\ell(z-z_c)|\mathrm{d}z|\right] \end{Bmatrix}, \quad \boldsymbol{j}_{\ell k} = \begin{Bmatrix} \mathrm{Re}\left[\int_{\Gamma_k} O_\ell(z-z_c)|\mathrm{d}z|\right] \\ \mathrm{Im}\left[\int_{\Gamma_k} O_\ell(z-z_c)|\mathrm{d}z|\right] \end{Bmatrix}. \tag{20}$$

$\mathrm{Re}[z]$ and $\mathrm{Im}[z]$ represents a real and an imaginary part of z. We discretize Eq. (13) by constant boundary elements in the same way.

$$\boldsymbol{M} = \boldsymbol{I}_{\Gamma^{\mathrm{Far}}} \boldsymbol{q}_{\Gamma^{\mathrm{Far}}}, \tag{21}$$

where

$$\boldsymbol{I}_\Gamma = \begin{bmatrix} \boldsymbol{i}_{01} & \cdots & \boldsymbol{i}_{0N} \\ \vdots & \ddots & \vdots \\ \boldsymbol{i}_{L1} & \cdots & \boldsymbol{i}_{LN} \end{bmatrix}, \qquad \boldsymbol{i}_{\ell k} = \begin{Bmatrix} \mathrm{Re}\left[\int_{\Gamma_k} \frac{(z-z_c)^\ell}{\ell}|\mathrm{d}z|\right] \\ \mathrm{Im}\left[\int_{\Gamma_k} \frac{(z-z_c)^\ell}{\ell}|\mathrm{d}z|\right] \end{Bmatrix},$$

$$\boldsymbol{M} = \begin{bmatrix} \boldsymbol{M}_0 \\ \vdots \\ \boldsymbol{M}_L \end{bmatrix}, \qquad \boldsymbol{M}_\ell = \begin{bmatrix} \mathrm{Re}[M_\ell(z_c)] \\ \mathrm{Im}[M_\ell(z_c)] \end{bmatrix}.$$

Let us assume q_j can be described as the following formula by using $\boldsymbol{I}^+_{\Gamma^{\mathrm{Far}}}$, Moore-Penrose type generalized inverse matrix of $\boldsymbol{I}_{\Gamma^{\mathrm{Far}}}$ in Eq. (21) :

$$\boldsymbol{q}_{\Gamma^{\mathrm{Far}}} \approx \boldsymbol{I}^+_{\Gamma^{\mathrm{Far}}} \boldsymbol{M} = \boldsymbol{I}^T_{\Gamma^{\mathrm{Far}}} \left(\boldsymbol{I}_{\Gamma^{\mathrm{Far}}} \cdot \boldsymbol{I}^T_{\Gamma^{\mathrm{Far}}}\right)^{-1} \boldsymbol{M}, \tag{22}$$

where $\boldsymbol{A}^T$ is the transposed matrix of A. Therefore the third left-handed term of Eq. (16) is:

$$\boldsymbol{K}_{\Gamma^{\mathrm{Far}}} \boldsymbol{q}_{\Gamma^{\mathrm{Far}}} \approx \boldsymbol{K}_{\Gamma^{\mathrm{Far}}} \boldsymbol{I}^T_{\Gamma^{\mathrm{Far}}} \left(\boldsymbol{I}_{\Gamma^{\mathrm{Far}}} \cdot \boldsymbol{I}^T_{\Gamma^{\mathrm{Far}}}\right)^{-1} \boldsymbol{M}. \tag{23}$$

3.6 Simultaneous linear equations

As mentioned above, this method drastically reduces the number of unknown quantities and the BIEs set up. We can set up the simultaneous linear equations by discretizing Eq. (15) and Eq. (16), and substituting Eq. (23) as the following:

$$\begin{bmatrix} \boldsymbol{G}_{\Gamma^{\mathrm{Near}}} & \boldsymbol{O} \\ \boldsymbol{K}_{\Gamma^{\mathrm{Near}}} & \boldsymbol{K}_{\Gamma^{\mathrm{Far}}} \boldsymbol{I}^T_{\Gamma^{\mathrm{Far}}} \left(\boldsymbol{I}_{\Gamma^{\mathrm{Far}}} \cdot \boldsymbol{I}^T_{\Gamma^{\mathrm{Far}}}\right)^{-1} \end{bmatrix} \begin{Bmatrix} \boldsymbol{q}_{\Gamma^{\mathrm{Near}}} \\ \boldsymbol{M} \end{Bmatrix} \approx \begin{bmatrix} \boldsymbol{H}_\Gamma \\ \boldsymbol{J}_\Gamma \end{bmatrix} \boldsymbol{u}'_\Gamma, \tag{24}$$

where

$$\boldsymbol{O} = \begin{bmatrix} \boldsymbol{O}_{10} & \cdots & \boldsymbol{O}_{1L} \\ \vdots & \ddots & \vdots \\ \boldsymbol{O}_{10} & \cdots & \boldsymbol{O}_{1L} \end{bmatrix}, \qquad \boldsymbol{O}_{j\ell} = \begin{Bmatrix} \mathrm{Re}[O_\ell(z_0^j - z_c)] \\ -\mathrm{Im}[O_\ell(z_0^j - z_c)] \end{Bmatrix}. \tag{25}$$

We can compute unknown quantities q on the near boundary Γ^{Near} and multipolar moments $M_l(z_c)$ by solving Eq. (24). In the case where a collocation point z_0 is placed in the focused domain $\Omega^{\mathrm{Focused}}$, $c(z_0) = 1$ in Eq. (15), hence unknown quantity u in $\Omega^{\mathrm{Focused}}$ can be computed with the same level of accuracy as the conventional BEM.

4 Numerical results

In order to examine the accuracy and efficiency of FD–EBEM, we carry out a numerical experiment with this method and the conventional BEM.

4.1 Setup boundary value problem

We consider a tube-shaped Laplace field with a square hole as shown in Fig. 5. Boundary conditions on the inner square and outer circle are Dirichlet conditions as shown in Fig. 6. The requisite unknown quantity is assumed to be potential u in focused domain $\Omega^{\mathrm{Focused}}$ shown in Fig. 5. The inner square and outer circle are far boundary Γ^{Far} and near boundary Γ^{Near}, respectively. The center of multipole moments z_c is placed at the center of the outer circle so that $\forall z_0 \in \Omega^{\mathrm{Focused}}$ satisfy Eq. (14) for $\forall z \in \Gamma^{\mathrm{Far}}$. The number of multipole moments is set to be 15.

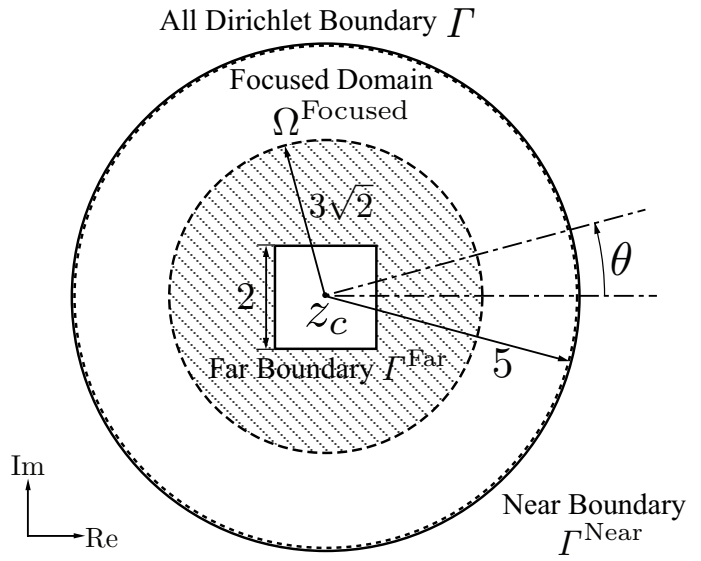

Figure 5: Model for the numerical experiment.

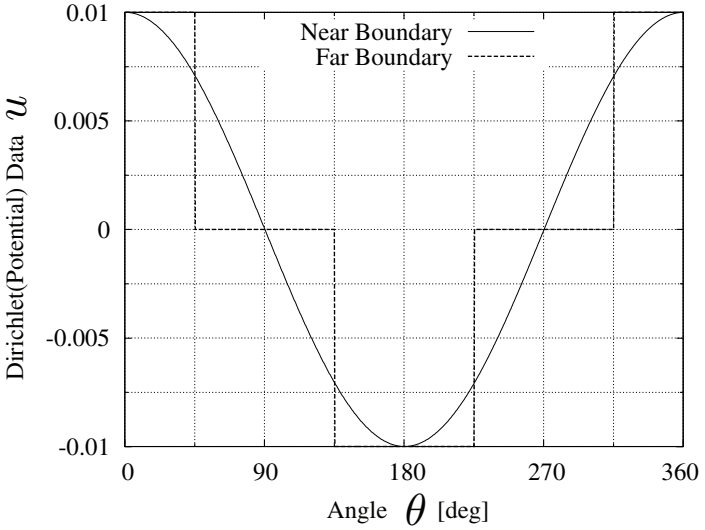

Figure 6: Boundary condition.

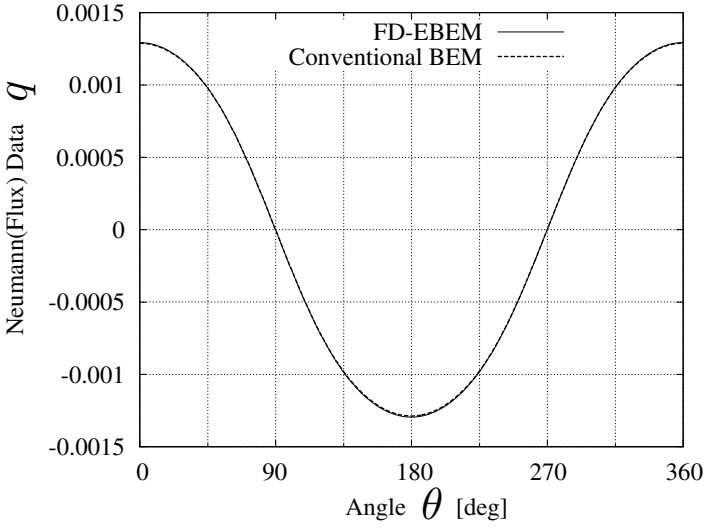

Figure 7: Neumann data (flux) q on near boundary Γ^{Near}.

4.2 Verification of accuracy

For the problem indicated in the previous subsection, we divided Γ^{Near} and Γ^{Far} into 1000 and 5000 constant line elements, respectively, and computed flux q on Γ^{Near} and potential u by this method and the conventional BEM.

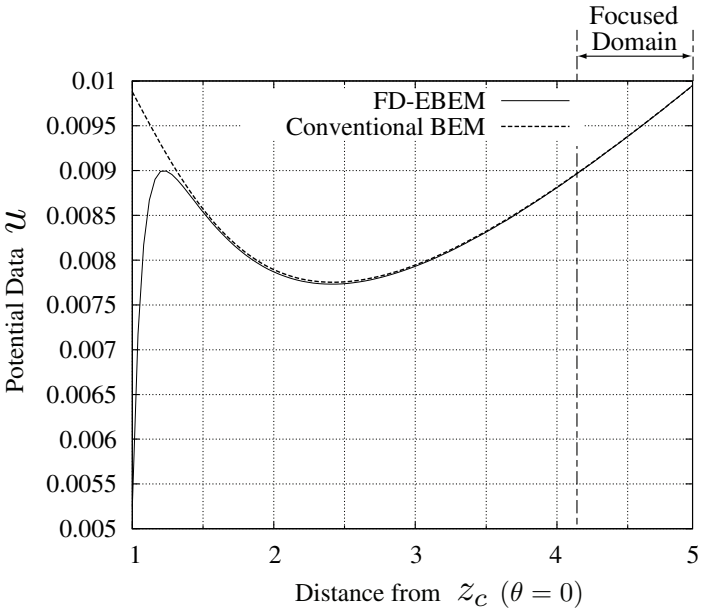

Figure 8: Potential data u in domain $\Omega(\theta = 0)$.

Fig. 7 compares this method with the conventional BEM in the computational results of flux q on the near boundary Γ^{Near}. Good agreement in computational results is observed.

Fig. 8 compares this method with the conventional BEM in the computational results of potential u on the line of parameter $\theta = 0$ within the whole domain Ω. Though this method differs from the conventional BEM in the computational results external to the focused domain $\Omega^{\mathrm{Focused}}$, they are in good agreement in the focused domain $\Omega^{\mathrm{Focused}}$.

It seems that this method is capable of computing flux q on the near boundary Γ^{Near} and potential u in the focused domain $\Omega^{\mathrm{Foacused}}$ with the same sufficient accuracy as the conventional BEM.

4.3 Verification of efficiency

For the problem indicated in the previous subsection, we divided Γ^{Near} and Γ^{Far} into constant line elements and computed unknown quantities by this method and the conventional BEM.

The number of elements on Γ^{Near} fixed at 1000 and the number of elements on Γ^{Far} is varied from 1000 to 10000. All the computations in this subsection were done on Intel(R) Core(TM) i7–965 Extreme Edition(3.2 GHz).

Fig. 9 shows the relationship between computational time and the total number of elements N. It demonstrates that the computational cost of this method is about

$O(N)$, while the cost of the conventional BEM is about $O\left(N^3\right)$. This method is more efficient as the number of elements on far boundaries Γ^{Far} is larger.

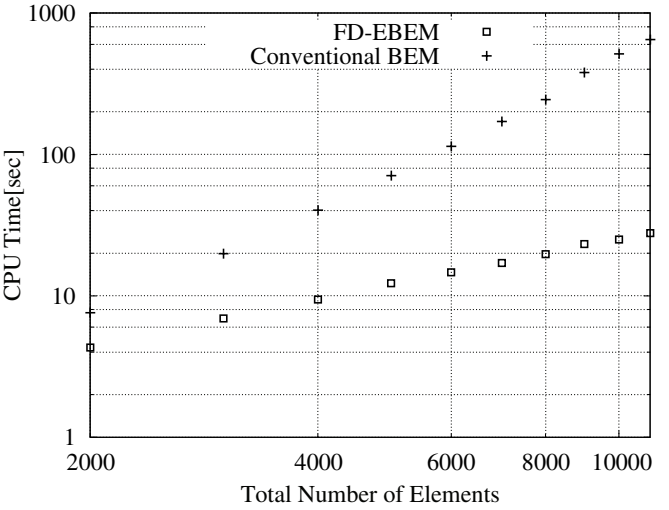

Figure 9: Comparison of CPU time between FD–EBEM and the conventional BEM.

5 Conclusions

In this paper, we presents the efficient boundary element method for the focused domain, that is the "Focused Domain Efficient Boundary Element Method (FD–EBEM)". We validated FD–EBEM in accuracy and efficiency by carrying out a numerical experiment.

There are many practical applications in which unknown quantities only in a specific domain are required. This method can extended not only to potential problems but also any other boundary value problems such as elastostatic analysis.

References

[1] Onishi, Y. & Amaya, K., A new technique for high-speed boundary element analyses of laplace equations to obtain solutions in target regions. *Engineering Analysis with Boundary Elements*, **28**, pp. 791–799, 2004.

[2] Liu, Y. & Nishimura, N., The fast multipole boundary element method for potential problems:a tutorial. *Engineering Analysis with Boundary Elements*, **30**, pp. 371–381, 2006.

Performance of GMRES for the MFS

A. Karageorghis & Y.-S. Smyrlis
Department of Mathematics and Statistics, University of Cyprus, Cyprus

Abstract

In this work we present some preliminary numerical results regarding the performance of the Generalized Minimal Residual (GMRES) method when it is applied to the solution of the linear systems arising from the discretization of certain elliptic boundary value problems in two and three dimensions by the Method of Fundamental Solutions (MFS).
Keywords: method of fundamental solutions, generalized minimal residual method, Laplace equation, iterative methods.

1 The problem and method

We consider the solution of Laplace's equation

$$\Delta u = 0 \quad \text{in} \quad \Omega \tag{1.1}$$

subject to the Dirichlet boundary condition

$$u = f \quad \text{on} \quad \partial\Omega \tag{1.2}$$

where the domain Ω is bounded in $\mathbb{R}^d,\ d = 1, 2$ and f is a given function.

In the MFS [1], the solution u of (1.1)-(1.2) is approximated by

$$u_N(\boldsymbol{c}, \boldsymbol{Q}; P) = \sum_{\ell=1}^{N} c_\ell\, K_d(P, Q_\ell), \qquad P \in \overline{\Omega}, \tag{1.3}$$

where $\boldsymbol{c} = (c_1, c_2, \ldots, c_N)^T$ and $\boldsymbol{Q}$ is a dN-vector containing the coordinates of the singularities Q_ℓ, $\ell = 1, \ldots, N$, which lie outside $\overline{\Omega}$. The function $K_d(P, Q)$ is a fundamental solution of Laplace's equation given by

WIT Transactions on Modelling and Simulation, Vol 49, © 2009 WIT Press
www.witpress.com, ISSN 1743-355X (on-line)
doi:10.2495/BE090151

$$K_d(P,Q) = \begin{cases} -\dfrac{1}{2\pi}\ \log|P-Q|, & d=2, \\ \\ \dfrac{1}{4\pi}\ \dfrac{1}{|P-Q|}, & d=3, \end{cases} \tag{1.4}$$

with $|P-Q|$ denoting the distance between the points P and Q. As recommended in [2], the singularities Q_ℓ are fixed on a pseudo-boundary $\partial\tilde{\Omega}$ similar to $\partial\Omega$ and a set of collocation points $\{P_k\}_{k=1}^N$ is placed on $\partial\Omega$.

The coefficients $\boldsymbol{c}$ are determined so that the boundary condition is satisfied at the boundary points $\{P_k\}_{k=1}^N$:

$$u_N(\boldsymbol{c}, \boldsymbol{Q}; P_k) = f(P_k), \quad k = 1, \ldots, N. \tag{1.5}$$

This yields a linear system of the form

$$G^d\,\boldsymbol{c} \ = \ \boldsymbol{f}\,, \tag{1.6}$$

for the coefficients $\boldsymbol{c}$, where the elements of the matrix G^d are given by

$$G^d_{k,\ell} = \begin{cases} -\dfrac{1}{2\pi}\log|P_k - Q_\ell|, & d=2, \\ \\ \dfrac{1}{4\pi}\ \dfrac{1}{|P_k - Q_\ell|}, & d=3, \end{cases}$$

for $k = 1, \ldots, N \quad \ell = 1, \ldots, N$.

The matrix G^d is full and, in general, not symmetric. Also, as the pseudo-boundary $\partial\tilde{\Omega}$ moves away from the boundary $\partial\Omega$ the matrix becomes very ill-conditioned resulting in loss of accuracy of the MFS approximation [3].

In most applications of the MFS so far, system (1.6) is solved using standard Gaussian elimination at a cost of $O(N^3)$ operations. The question is whether an iterative technique would lead to savings in the cost of solving the system and the effect it could have on the accuracy of the approximation. Since the matrix G^d is full and, in general, not symmetric, and as recommended in the literature (see, for example [4]) we shall experiment with the Generalized Minimal Residual (GMRES) method derived by Saad and Schultz [5].

In this work we shall try and address the following two questions:

1. When N is large the cost of solving (1.6) is obviously large. *Would the cost be reduced if one used an iterative method to solve system* (1.6)*?* In order to address this question we shall investigate the performance of GMRES.

2. When the distance of the pseudo-boundary from the boundary is large there is the additional problem that the matrix G in (1.6) becomes ill-conditioned. *Would the use of a pre-conditioner in GMRES improve the situation [6]?*

What would a suitable choice for such a pre-conditioner be? We shall experiment by taking the pre-conditioner P to be a diagonal matrix consisting of the diagonal elements of G^d. Such pre-conditioners were found to be effective when using GMRES to solve systems resulting from Boundary Element Method (BEM) discretizations [7–9].

2 Well-conditioned systems

We first consider the case when the MFS systems are (relatively) well-conditioned. This occurs when the distance of the pseudo-boundary from the boundary is small, and becomes smaller with increasing N.

2.1 Example 1

We consider the boundary value problem (1.1)–(1.2) when $\Omega \subset \mathbb{R}^2$, in particular when Ω is the square $(-1,1) \times (-1,1)$ and f corresponds to the exact solution $u(x,y) = \mathrm{e}^x \cos y$. The boundary points and the singularities are uniformly distributed around the boundary and pseudo-boundary, respectively. We calculated the maximum error on a set of uniformly distributed points on the boundary (different from the boundary collocation points) for various values of the distance of the pseudo-boundary from the boundary, ranging from 0 to 0.05. In Figures 1(a), 1(b), 1(c) and 1(d), in the upper subplots we present the maximum error on the boundary, obtained (i) with Gaussian elimination, (ii) with $4\log_2 N$, $8\log_2 N$ and $12\log_2 N$, iterations of GMRES, and (iii) preconditioned GMRES, in each case, versus the distance of the pseudo-boundary from the boundary, for $N = 400, 600, 800$ and 1000, respectively. In the lower subplots of each figure we present the 2-norm condition number κ_2 of the matrix G versus the distance of the pseudo-boundary from the boundary. The results indicate that for values of κ_2 less than 10^{20}, the results obtained with GMRES are indistinguishable from those obtained with Gaussian elimination for as few as $4\log_2 N$ GMRES iterations. When κ_2 reaches 10^{20}, $4\log_2 N$ GMRES were no longer sufficient. The number of GMRES iterations started depending on both the distance from the boundary and the value of N. For $N = 400$, $4\log_2 N$ iterations yielded better results than Gaussian elimination for a distance up to 0.04, whereas $8\log_2 N$ and $12\log_2 N$ iterations yielded better results than Gaussian elimination for a distance up to 0.05. For $N = 600$, $4\log_2 N$ iterations yielded better results than Gaussian elimination for a distance up to 0.02, whereas $8\log_2 N$ and $12\log_2 N$ iterations yielded better results than Gaussian elimination for a distance up to 0.05. For $N = 800$, $4\log_2 N$ iterations yielded better results than Gaussian elimination for a distance up to 0.01, $8\log_2 N$ iterations yielded better results than Gaussian elimination for a distance up to 0.022, whereas $12\log_2 N$ iterations yielded better results than Gaussian elimination for a distance up to 0.032. The difference in accuracy between GMRES and Gaussian elimination for $8\log_2 N$ and $12\log_2 N$ iterations was small all the way up to 0.05. Finally, for $N = 1000$, $4\log_2 N$ iterations did not yield better results than Gaussian elimination beyond the point where κ_2 reaches 10^{20}, $8\log_2 N$ iterations yielded better results than Gaussian elimination for a distance up to 0.018,

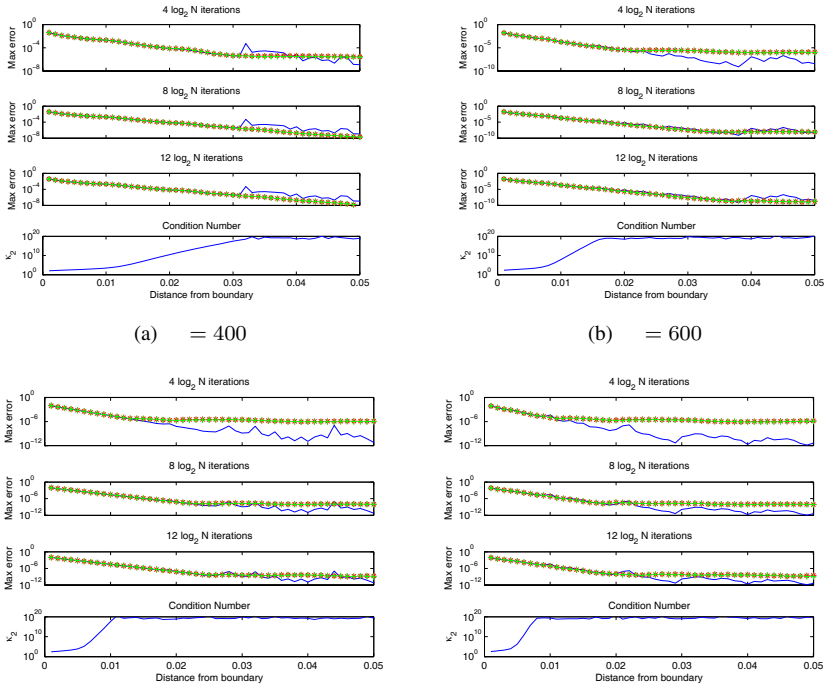

(a) $= 400$ (b) $= 600$

(c) $= 800$ (d) $= 1000$

Figure 1: Example 1: Plots with $\ell \log_2 N$ GMRES iterations $\ell = 4, 8, 12$. Key: $-$ Gaussian elimination, $*$ GMRES, $+$ preconditioned GMRES.

whereas $12 \log_2 N$ iterations yielded better results than Gaussian elimination for a distance up to 0.024. The difference in accuracy between GMRES and Gaussian elimination for $8 \log_2 N$ and, in particular, $12 \log_2 N$ iterations was small all the way up to 0.05. No particular improvement was observed for the pre-conditioned GMRES. In Figure 2 we present the timings recorded using the Matlab commands `tic` and `toc` for various values of N and iterations and using Gaussian elimination. We observe that with the exception of $12 \log_2 N$ iterations, in the other cases substantial savings are achieved using GMRES. Note that for GMRES we used the Matlab command `gmres` with the tolerance set at $\texttt{TOL} = 1.e-10$.

2.2 Example 2

We consider the boundary value problem (1.1)–(1.2) when $\Omega \subset \mathbb{R}^3$, in particular when Ω is the cube $(-1,1) \times (-1,1) \times (-1,1)$ and f corresponds to the exact solution $u(x,y) = \cosh(0.3x)\cosh(0.4y)\cos(0.5y)$. The boundary points and the singularities are uniformly distributed around the boundary and pseudo-boundary, respectively. As in Example 1, we calculated the maximum error on a

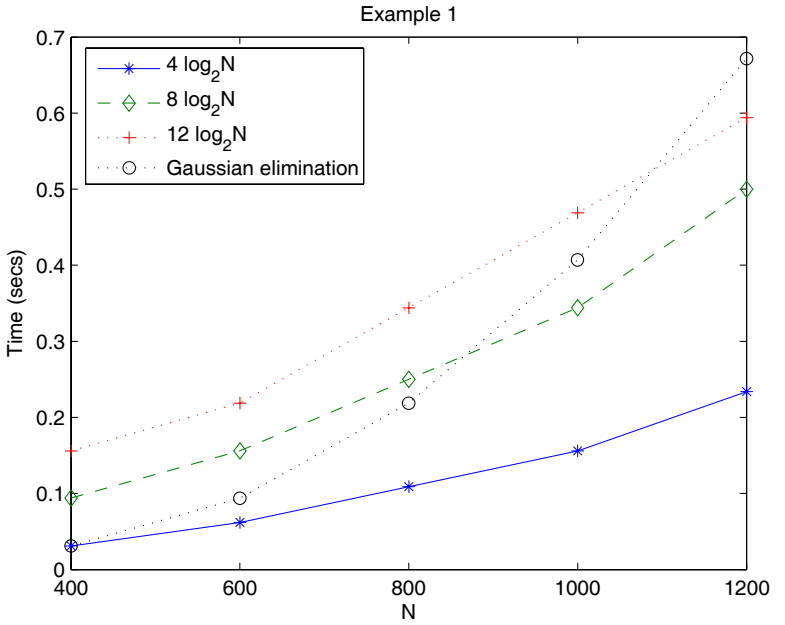

Figure 2: Example 1: Timings recorded for various numbers of degrees of freedom and iterations.

set of uniformly distributed points on the boundary (different from the boundary collocation points) for various values of the distance of the pseudo-boundary from the boundary. In Figures 3(a), 3(b) and 3(c), in the upper subplots we present the maximum error on the boundary, obtained (i) with Gaussian elimination, (ii) with $4\log_2 N$, $8\log_2 N$ and $12\log_2 N$, iterations of GMRES, and (iii) preconditioned GMRES, in each case, versus the distance of the pseudo-boundary from the boundary, for $N = 600, 864$ and 1176 (i.e. $6 \times 10^2, 6 \times 12^2$ and 6×14^2), respectively. In the lower subplots of each figure we present the 2-norm condition number κ_2 of the matrix G versus the distance of the pseudo-boundary from the boundary. The observations from these plots are similar to the ones drawn from the corresponding plots for Example 1. Interestingly, the conditioning of the MFS matrix for the three-dimensional example is considerably better that the one for the two-dimensional example, in the sense that the condition number κ_2 stays below 10^{20} for considerably longer distances of the pseudo-boundary from the boundary. As a result, the range of distances of the pseudo-boundary to the boundary was extended from 0 up to 2. For $N = 600$, $4\log_2 N$ iterations produced identical results to Gaussian elimination for a distance up to 1, while remaining very close up to 2. For both $8\log_2 N$ and $12\log_2 N$ iterations the GMRES results were identical to the results obtained with Gaussian elimination. For $N = 864$, $4\log_2 N$ iterations

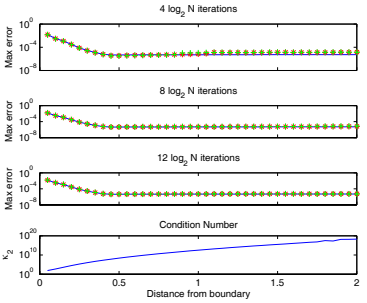

(a) $= 600$

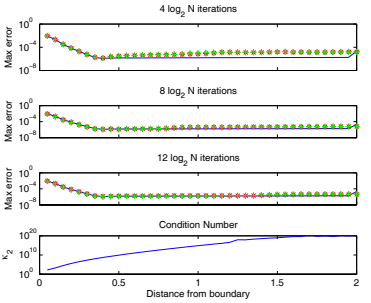

(b) $= 864$

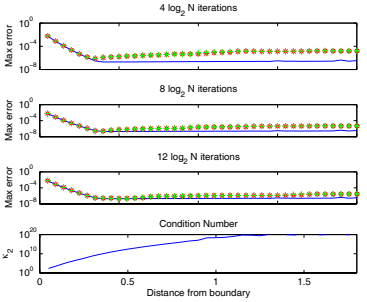

(c) $= 1176$

Figure 3: Example 2: Plots with $\ell \log_2 N$ GMRES iterations $\ell = 4, 8, 12$. Key: $-$ Gaussian elimination, $*$ GMRES, $+$ preconditioned GMRES.

yielded identical results to Gaussian elimination for a distance up to 0.5, while remaining close up to 2. For $8 \log_2 N$ iterations the GMRES results were identical to those obtained with Gaussian elimination up to 0.8 and for $12 \log_2 N$ iterations this range went up to 1.5. For both $8 \log_2 N$ and $12 \log_2 N$ iterations the GMRES results were very close to the results obtained with Gaussian elimination up to 2. For $N = 1176$, $4 \log_2 N$ iterations yielded identical results to Gaussian elimination for a distance up to 0.25. For $8 \log_2 N$ iterations the GMRES results were identical to those obtained with Gaussian elimination up to 0.5 and for $12 \log_2 N$ iterations this range went up to 0.7. For both $8 \log_2 N$ and, in particular, $12 \log_2 N$ iterations the GMRES results were very close to the results obtained with Gaussian elimination up to 2.

3 Ill-conditioned systems

We now consider the case when the MFS systems are ill-conditioned. This occurs when the distance of the pseudo-boundary from the boundary is large, and becomes the ill-conditioning becomes more severe with increasing N.

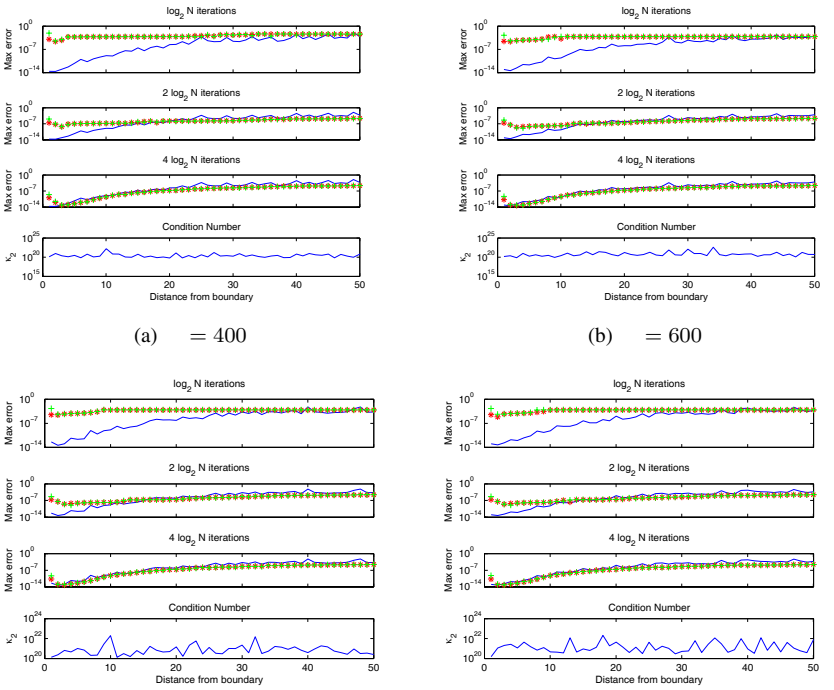

(a) (b)

(c) (d)

Figure 4: Example 1: Plots with $\ell \log_2 N$ GMRES iterations $\ell = 1, 2, 4$. Key: $-$ Gaussian elimination, $*$ GMRES, $+$ preconditioned GMRES.

3.1 Example 1

As in Section 2.1 we calculated the maximum error on a set of uniformly distributed points on the boundary (different from the boundary collocation points) for various values of the distance of the pseudo-boundary from the boundary. This time we considered the range from 0 to 50. In Figures 4(a), 4(b), 4(c) and 4(d), in the upper subplots we present the maximum error on the boundary, obtained (i) with Gaussian elimination, (ii) with $\log_2 N$, $2\log_2 N$ and $4\log_2 N$, iterations of GMRES, and (iii) preconditioned GMRES, in each case, versus the distance of the pseudo-boundary from the boundary, for $N = 400, 600, 800$ and 1000, respectively. In the lower subplots of each figure we present the 2-norm condition number κ_2 of the matrix G versus the distance of the pseudo-boundary from the boundary. The results indicate that in all cases, as few as $4\log_2 N$ GMRES iterations yield considerably more accurate results than Gaussian elimination, with the exception of the cases when the pseudo-boundary is very close to the boundary. No improvement was observed for more than $4\log_2 N$ GMRES iterations. Also, as in Section 2.1, no particular improvement was observed for the pre-conditioned GMRES.

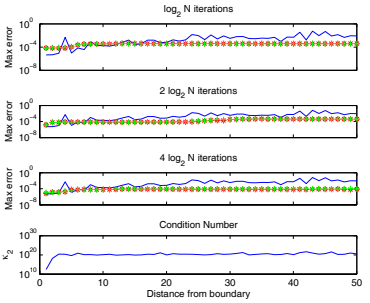

(a) $= 600$

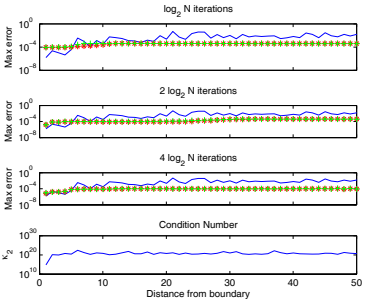

(b) $= 864$

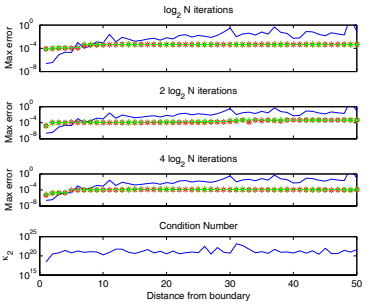

(c) $= 1176$

Figure 5: Example 2: Plots with $\ell \log_2 N$ GMRES iterations $\ell = 1, 2, 4$. Key: $-$ Gaussian elimination, $*$ GMRES, $+$ preconditioned GMRES.

3.2 Example 2

We consider the example of Section 2.2 examining the maximum error for the distance of the pseudo-boundary from the boundary ranging from 0 to 50. In Figures 5(a), 5(b) and 5(c), in the upper subplots we present, as before, the maximum error on the boundary, obtained (i) with Gaussian elimination, (ii) with $\log_2 N$, $2 \log_2 N$ and $4 \log_2 N$, iterations of GMRES, and (iii) preconditioned GMRES, in each case, versus the distance of the pseudo-boundary from the boundary, for $N = 600, 864$ and 1176, respectively. In the lower subplots of each figure we present the 2-norm condition number κ_2 of the matrix G versus the distance of the pseudo-boundary from the boundary. The observations from these plots are similar to the ones drawn from the corresponding plots for Example 1, namely that for as few as $4 \log_2 N$, GMRES iterations considerably more accurate results are obtained than using Gaussian elimination. No further improvement was observed for larger values of the number of iterations.

4 Conclusions

In this work we carried out some preliminary numerical tests on the performance of GMRES when applied to the solution of the linear systems arising from the MFS discretization of certain two- and three-dimensional elliptic boundary value problems. For the case when the pseudo-boundary is located very close to the boundary, yielding well-conditioned systems, the accuracy of the iterative solver is satisfactory, although, in general inferior to that of Gaussian elimination. Interestingly, in the case when the pseudo-boundary is located far from the boundary, yielding ill-conditioned systems, the accuracy of the iterative solver is superior to that of Gaussian elimination, even for relatively few iterations. No improvement was observed in either case by the use of a preconditioned GMRES.

References

[1] Fairweather, G. & Karageorghis, A., The method of fundamental solutions for elliptic boundary value problems. Numerical treatment of boundary integral equations. *Adv Comput Math*, **9(1-2)**, pp. 69–95, 1998.
[2] Gorzelańczyk, P. & Kołodziej, J.A., Some remarks concerning the shape of the source contour with application of the method of fundamental solutions to elastic torsion of prismatic rods. *Engng Analysis with Boundary Elements*, **37**, pp. 64–75, 2008.
[3] Smyrlis, Y.S. & Karageorghis, A., Some aspects of the method of fundamental solutions for certain harmonic problems. *J Sci Comput*, **16(3)**, pp. 341–371, 2001.
[4] Demmel, J.W., *Applied Numerical Linear Algebra*. SIAM: Philadelhia, 1997.
[5] Saad, Y. & Schultz, M.H., GMRES: A generalized minimal residual algorithm for solving non–symmetric linear systems. *SIAM J Sci Statist Comput*, **7**, pp. 856–869, 1986.
[6] Greenbaum, A., *Iterative Methods for Solving Linear Systems*. SIAM: Philadelhia, 1997.
[7] Barra, L.P.S., Coutinho, A.L.G.A., Mansur, W.J. & Telles, J.C.F., Iterative solution of BEM equations by GMRES algorithm. *Comput & Structures*, **44**, pp. 1249–1253, 1992.
[8] Guru Prasad, K., Kane, J., Keyes, D.E. & Balakrishna, C., Preconditioned Krylov solvers for BEA. *Internat J Numer Methods Engrg*, **37**, pp. 1651–1672, 1994.
[9] Marburg, S. & Schneider, S., Performance of iterative solvers for acoustic problems. Part I. Solvers and effect of diagonal preconditioning. *Engrg Anal Boundary Elem*, **27**, pp. 727–750, 2003.

This page intentionally left blank

Section 3
Computational methods

This page intentionally left blank

On the use of integrated radial basis function schemes in weighted residual statements for elliptic problems

N. Mai-Duy & T. Tran-Cong
Computational Engineering and Science Research Centre, University of Southern Queensland, Australia

Abstract

In this paper, we discuss the use of integrated radial basis functions (IRBFs) in solving elliptic differential equations. Various formulations, namely point collocation, subregion collocation, Galerkin and inverse statements, are considered. IRBFs are incorporated into these formulations to represent the field variables. Numerical results indicate that this use of IRBFs leads to a considerable improvement in accuracy and convergence rate over the case of using conventional low-order polynomials.
Keywords: integrated radial basis functions, collocation method, Galerkin method, control volume method, boundary element method.

1 Introduction

Mathematical modelling of physical processes usually leads to partial/ordinary differential equations (PDEs/ODEs). Consider a differential problem governed by

$$\mathcal{L}\bar{u} = b, \quad \mathbf{x} \in \Omega, \tag{1}$$

where $\bar{u}$ is the field variable, b a given function, $\mathcal{L}$ a differential operator, $\mathbf{x}$ the position vector and Ω the domain. A function $\bar{u}(\mathbf{x})$ can be sought in the form of truncated series

$$\bar{u}(\mathbf{x}) \approx u(\mathbf{x}) = \sum_{i=1}^{n} u^{(i)}\phi^{(i)}(\mathbf{x}) + \gamma, \quad \mathbf{x} \in \Omega, \tag{2}$$

WIT Transactions on Modelling and Simulation, Vol 49,
www.witpress.com, ISSN 1743-355X (on-line)
doi:10.2495/BE090161

where $\left\{\phi^{(i)}(\mathbf{x})\right\}_{i=1}^{n}$ is the set of basis/trial functions which are known, $\left\{u^{(i)}\right\}_{i=1}^{n}$ the set of nodal variable values to be found, and γ a known value. The weighted residuals approach tries to reduce the residual of (1) to a minimum through

$$\int_{\Omega} \psi(\mathbf{x})\,(Lu-b)\,d\Omega = 0, \quad \mathbf{x}\in\Omega, \tag{3}$$

where $\psi(\mathbf{x})$ is a weighting function. Different choices of $\psi(\mathbf{x})$ result in different discretisation formulations such as point collocation, subregion collocation, Galerkin and inverse statements. More details can be found in [1].

RBF networks (RBFNs) have emerged as a powerful approximation tool [2]. A network relies on a set of points that can be uniformly/nonuniformly distributed throughout the domain for the representation of a function. Some RBFs such as the multiquadric and Gaussian basis functions can offer an exponential rate of convergence. To avoid the problem of reduced convergence rate caused by differentiation, integrated RBFNs (IRBFNs) have been proposed [3]. In this paper we discuss the use of IRBFNs as an interpolating method for different discretisation schemes for the solution of elliptic DEs. This discussion is based on our previous works on IRBFNs reported in [4–7].

The remainder of the paper is organised as follows. Section 2 gives a brief review of IRBFNs. Section 3 is concerned with the discussion of using IRBFNs as trial functions for the solution of DEs, in which several representative examples are given. Section 4 concludes the paper.

2 Integrated radial-basis-function networks

RBFNs allow a conversion of a function f from a low-dimensional space (e.g. 1D-3D) to a high-dimensional space in which the function will be expressed as a linear combination of RBFs

$$f(\mathbf{x}) = \sum_{i=1}^{m} w^{(i)} g^{(i)}(\mathbf{x}), \tag{4}$$

where the superscript (i) is the sum index, $\mathbf{x}$ the input vector, $\{w^{(i)}\}_{i=1}^{m}$ the set of network weights to be found, and $\{g^{(i)}(\mathbf{x})\}_{i=1}^{m}$ the set of RBFs. An example of RBFs is the multiquadric (MQ) basis function $g^{(i)}(\mathbf{x}) = \sqrt{(\mathbf{x}-\mathbf{c}^{(i)})^T(\mathbf{x}-\mathbf{c}^{(i)}) + a^{(i)2}}$, where $\mathbf{c}^{(i)}$ and $a^{(i)}$ are the centre and width of the ith MQ-RBF, respectively.

IRBFNs consist in decomposing the highest-order derivatives of u in (1) into RBFs in the form of (4) ($f(\mathbf{x}) = \partial^p u(\mathbf{x})/\partial x_j^p$) and then integrating them to obtain lower-order derivatives and the function itself

$$\frac{\partial^p u(\mathbf{x})}{\partial x_j^p} = \sum_{i=1}^{m} w_{[x_j]}^{(i)} g^{(i)}(\mathbf{x}), \tag{5}$$

$$\frac{\partial^{p-1} u(\mathbf{x})}{\partial x_j^{p-1}} = \sum_{i=1}^{m+q_1} w_{[x_j]}^{(i)} H_{[x_j]}^{(i)[p-1]}(\mathbf{x}), \tag{6}$$

$$\cdots \quad \cdots \quad \cdots \quad \cdots \quad \cdots$$

$$u_{[x_j]}(\mathbf{x}) = \sum_{i=1}^{m+q_p} w_{[x_j]}^{(i)} H_{[x_j]}^{(i)[0]}(\mathbf{x}), \tag{7}$$

where the subscript $[x_j]$ is used to denote the process of integration with respect to x_j; q_1 the number of centres in a subnetwork that is employed to approximate a set of nodal integration constants, $q_2 = 2q_1, \cdots, q_p = pq_1$; and $H_{[x_j]}^{(i)[p-1]} = \int g^{(i)} dx_j, H_{[x_j]}^{(i)[p-2]} = \int H_{[x_j]}^{(i)[p-1]} dx_j, \cdots, H_{[x_j]}^{(i)[0]} = \int H_{[x_j]}^{(i)[1]} dx_j$. For convenience of presentation, we introduce another notation, $H_{[x_j]}^{(i)[p]}(\mathbf{x})$, to denote the RBF (i.e. $H_{[x_j]}^{(i)[p]}(\mathbf{x}) \equiv g^{(i)}(\mathbf{x})$) so that $H_{[x_j]}^{(i)[p-1]} = \int H_{[x_j]}^{(i)[p]} dx_j$. It is noted that the new centres and their associated known basis functions in subnetworks are also denoted by the notations $w^{(i)}$ and $H^{(i)}(\mathbf{x})$, respectively, but with $i > m$. An IRBFN is said to be of order p if its starting point is the pth-order derivative.

We seek the solution in terms of nodal variable values for the purpose of having a clear physical meaning and computational efficiency. The evaluation of (5)–(7) at a set of collocation points $\{\mathbf{x}^{(i)}\}_{i=1}^m$, which is selected to coincide with the set of centres $\{\mathbf{c}^{(i)}\}_{i=1}^m$, yields

$$\widetilde{\frac{\partial^p u}{\partial x_j^p}} = \widetilde{\mathcal{H}}_{[x_j]}^{[p]} \widetilde{w}_{[x_j]}, \tag{8}$$

$$\widetilde{\frac{\partial^{p-1} u}{\partial x_j^{p-1}}} = \widetilde{\mathcal{H}}_{[x_j]}^{[p-1]} \widetilde{w}_{[x_j]}, \tag{9}$$

$$\cdots \quad \cdots$$

$$\widetilde{u} = \widetilde{\mathcal{H}}_{[x_j]}^{[0]} \widetilde{w}_{[x_j]}, \tag{10}$$

where

$$\widetilde{w}_{[x_j]} = \left[w_{[x_j]}^{(1)}, w_{[x_j]}^{(2)}, \cdots, w_{[x_j]}^{(m+q_p)} \right]^T,$$

$$\widetilde{u} = \left[u(\mathbf{x}^{(1)}), u(\mathbf{x}^{(2)}), \cdots, u(\mathbf{x}^{(m)}) \right]^T = \left[u^{(1)}, u^{(2)}, \cdots, u^{(m)} \right]^T,$$

$$\widetilde{\frac{\partial^k u}{\partial x_j^k}} = \left[\frac{\partial^k u(\mathbf{x}^{(1)})}{\partial x_j^k}, \cdots, \frac{\partial^k u(\mathbf{x}^{(m)})}{\partial x_j^k} \right]^T = \left[\frac{\partial^k u^{(1)}}{\partial x_j^k}, \cdots, \frac{\partial^k u^{(m)}}{\partial x_j^k} \right]^T,$$

$k = \{1, \cdots, p\}$, and the matrices $\widetilde{\mathcal{H}}_{[x_j]}^{[.]}$ have entries $\left(\widetilde{\mathcal{H}}_{[x_j]}^{[.]} \right)^{(l,i)} = H_{[x_j]}^{(i)[.]}(\mathbf{x}^{(l)})$, where $1 \le l \le m$ and $1 \le i \le (m + q_p)$. In (8)–(10), the matrices, $\widetilde{\mathcal{H}}_{[x_j]}^{[p]}, \widetilde{\mathcal{H}}_{[x_j]}^{[p-1]}, \ldots, \widetilde{\mathcal{H}}_{[x_j]}^{[1]}$, are augmented using zero-submatrices so that they have the same size as the matrix $\widetilde{\mathcal{H}}_{[x_j]}^{[0]}$.

Owing to the presence of the constants of integration (extra coefficients), one can add extra equations to the conversion system that transforms the RBF space into the physical space

$$\begin{pmatrix} \widetilde{u} \\ \widehat{e}_{[x_j]} \end{pmatrix} = \begin{bmatrix} \widetilde{\mathcal{H}}^{[0]}_{[x_j]} \\ \widehat{\mathcal{K}}_{[x_j]} \end{bmatrix} \widetilde{w}_{[x_j]} = \widetilde{\mathcal{C}}_{[x_j]} \widetilde{w}_{[x_j]}, \tag{11}$$

$$\widetilde{w}_{[x_j]} = \widetilde{\mathcal{C}}^{-1}_{[x_j]} \begin{pmatrix} \widetilde{u} \\ \widehat{e}_{[x_j]} \end{pmatrix}, \tag{12}$$

where $\widetilde{\mathcal{C}}_{[x_j]}$ is the conversion matrix, $\widehat{e}_{[x_j]} = \widehat{\mathcal{K}}_{[x_j]} \widetilde{w}_{[x_j]}$ the set of extra equations. When the boundary data involve derivative values, these extra equations can be used to represent derivative boundary values in the x_j direction.

Substitution of (12) into (5)–(7) yields

$$u(\mathbf{x}) = \frac{1}{N} \sum_{j=1}^{N} \left(\left[H^{(1)[0]}_{[x_j]}(\mathbf{x}), H^{(2)[0]}_{[x_j]}(\mathbf{x}), \cdots \right] \widetilde{\mathcal{C}}^{-1}_{[x_j]} \begin{pmatrix} \widetilde{u} \\ \widehat{e}_{[x_j]} \end{pmatrix} \right), \tag{13}$$

$$\frac{\partial u(\mathbf{x})}{\partial x_j} = \left[H^{(1)[1]}_{[x_j]}(\mathbf{x}), H^{(2)[1]}_{[x_j]}(\mathbf{x}), \cdots \right] \widetilde{\mathcal{C}}^{-1}_{[x_j]} \begin{pmatrix} \widetilde{u} \\ \widehat{e}_{[x_j]} \end{pmatrix}, \tag{14}$$

$$\cdots \quad \cdots \quad \cdots \quad \cdots \quad \cdots \quad \cdots \quad \cdots$$

$$\frac{\partial^p u(\mathbf{x})}{\partial x_j^p} = \left[H^{(1)[p]}_{[x_j]}(\mathbf{x}), H^{(2)[p]}_{[x_j]}(\mathbf{x}), \cdots \right] \widetilde{\mathcal{C}}^{-1}_{[x_j]} \begin{pmatrix} \widetilde{u} \\ \widehat{e}_{[x_j]} \end{pmatrix}, \tag{15}$$

where N is the dimension of the problem and the approximate function $u(\mathbf{x})$ is taken to be the average value of the $u_{[x_j]}(\mathbf{x})$ due to numerical error.

The calculation of cross derivatives of u is based on the following relation

$$\frac{\partial^p u}{\partial x_i^r \partial x_j^s} = \frac{1}{2} \left(\frac{\partial^r}{\partial x_i^r} \left(\frac{\partial^s u}{\partial x_j^s} \right) + \frac{\partial^s}{\partial x_j^s} \left(\frac{\partial^r u}{\partial x_i^r} \right) \right), \quad p = r + s,\ i \neq j, \tag{16}$$

which reduces the computation of mixed derivatives to that of lower-order pure derivatives for which IRBFNs involve integration with respect to x_i or x_j only.

Since all integrals involved can be obtained analytically, IRBFNs only require a set of distinct points for the approximation of a function.

3 IRBFNs for PDEs

IRBFNs are employed to represent the field variable. The governing equation is discretised using various formulations, namely point-collocation, control-volume, Galerkin and boundary integral equation schemes. We implement IRBFNs with the MQ basis function. The MQ width $a^{(i)}$ is simply chosen to be the minimal distance between the centre $\mathbf{c}^{(i)}$ and its neighbours. The accuracy of a numerical

scheme is measured through the discrete relative L_2 error of the solution u, denoted by $Ne(u)$. Let h and n_{ip} be the "mesh" size and the number of interior points. Another important measure is the convergence rate of the solution u, defined by $N_e(u) \approx \theta h^{\nu} = O(h^{\nu})$ or $N_e(u) \approx \theta n_{ip}^{\nu} = O(n_{ip}^{\nu})$ where θ and ν are the exponential model's parameters. Only 1D and 2D elliptic problems are considered here.

3.1 Point-collocation schemes

For these schemes, the residual of (1) is exactly zero at certain points. There are no integrations required in discretising (1). Two versions of IRBFNs are considered.

3.1.1 Two-dimensional IRBFNs

The problem domain is discretised using a set of scattered points (Figure 1a). We employ (13)–(15) over the domain, i.e. 2D-IRBFNs. It can be seen that the 2D-IRBFN collocation technique is truly meshless. The accuracy of the technique is demonstrated through the solution of $\nabla^2 \bar{u} = \sin(\pi x_1)\sin(\pi x_2)$ on a unit square with homogeneous Dirichlet boundary conditions. Its exact solution is $\bar{u}(x_1, x_2) = -(1/2\pi^2)\sin(\pi x_1)\sin(\pi x_2)$. Four scattered data sets of interior points using $n_{ip} = \{32, 52, 89, 145\}$ are employed . We discretise the boundaries using uniformly-distributed points with $n_{x_1} = n_{x_2} = \sqrt{n_{ip}}$. The value of q_1 is taken as $3n_{x_j}$. The variable u is represented using IRBFNs of second order, where $\widehat{e}$ and $\widehat{\mathcal{K}}$ in (13)–(15) are simply set to null. For comparison purposes, the conventional (differentiated) RBFN (DRBFN) approach is also considered here. Results are displayed in Figure 2, indicating that the IRBFN approach is superior to the DRBFN approach regarding accuracy and convergence rate. The solution converges apparently as $O(n_{ip}^{-1.46})$ for IRBFN and $O(n_{ip}^{-0.51})$ for DRBFN.

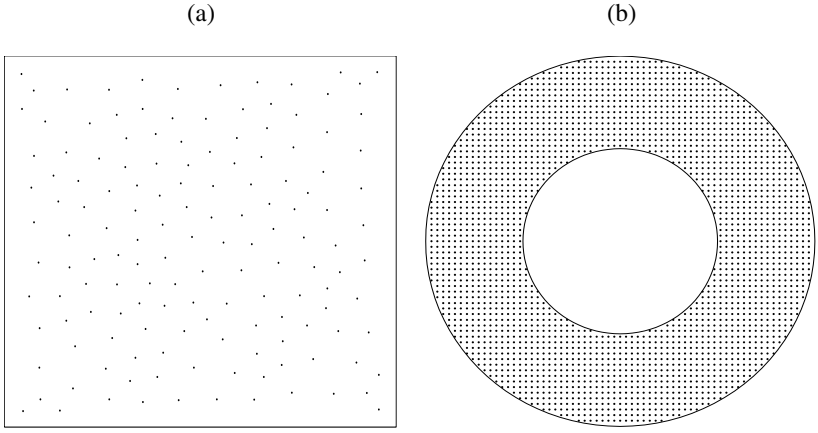

Figure 1: Point-collocation scheme: scattered point (2D-IRBFNs) and Cartesian-grid (1D-IRBFNs) discretisations.

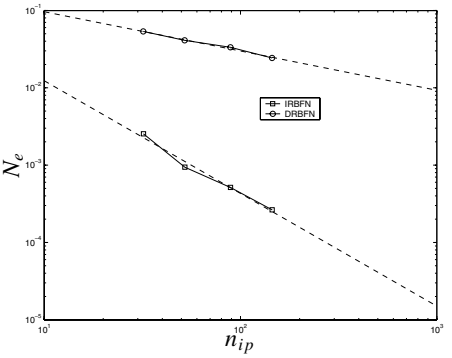

Figure 2: Point collocation scheme, 2D-IRBFNs: accuracy by the IRBFN and DRBFN methods.

3.1.2 One-dimensional IRBFNs

The problem domain is discretised using a Cartesian grid (Figure 1b). We employ (13)–(15) on grid lines, i.e. 1D-IRBFNs. The construction of the 1D-IRBFN approximations for a point $\mathbf{x}$ involves only points that lie on grid lines intersecting at $\mathbf{x}$ rather than the whole set of data points. The inversion is now conducted for a series of small matrices rather than for a large matrix. This use of 1D-IRBFNs thus leads to a considerable economy in forming the system matrix over that of 2D-IRBFNs. Consider the biharmonic equation $\nabla^4\bar{u} = 256(\pi^2 - 1)^2[\sin(4\pi x_1)\cosh(4x_2) - \cos(4\pi x_1)\sinh(4x_2)]$ defined on an annulus domain of radii $R_1 = 1/4$ and $R_2 = 1/2$ (Figure 1b) and subject to Dirichlet boundary conditions ($\bar{u}$ and $\partial\bar{u}/\partial n$). The exact solution is $\bar{u} = \sin(4\pi x_1)\cosh(4x_2) - \cos(4\pi x_1)\sinh(4x_2)$. We employ 1D-IRBFNs of fourth order, where $\widehat{e}_{[x_j]}$ is made up of the values of $\partial\bar{u}/\partial x_j$ at the two end points of a grid line. Double boundary conditions are thus incorporated into the system in an accurate manner. Table 1 shows that the proposed method produces a very high convergence rate, $O(h^{5.39})$ with relatively-low matrix condition numbers.

3.2 Boundary integral equation (BIE) schemes

These schemes are based on free-space fundamental solutions. One attractive feature of BIE schemes is that the differential equation is satisfied exactly. Consider a Dirichlet biharmonic problem. The BIE analog of $\nabla^4\bar{u} = b$ can be written as

$$C(\mathbf{y})\bar{u}(\mathbf{y}) + \int_\Gamma \frac{\partial G^H(\mathbf{y},\mathbf{x})}{\partial n}\bar{u}(\mathbf{x})d\Gamma = \int_\Gamma G^H(\mathbf{y},\mathbf{x})\frac{\partial\bar{u}(\mathbf{x})}{\partial n}d\Gamma - \int_\Gamma \left(\frac{\partial G^B(\mathbf{y},\mathbf{x})}{\partial n}\bar{v}(\mathbf{x}) - G^B(\mathbf{y},\mathbf{x})\frac{\partial\bar{v}(\mathbf{x})}{\partial n}\right)d\Gamma - \int_\Omega G^B(\mathbf{y},\mathbf{x})b(\mathbf{x})d\Omega, \quad (17)$$

Table 1: Point collocation scheme, 1D-IRBFNs: Condition number of the system matrix $\widetilde{\mathcal{A}}$ and accuracy of the solution u. Notice that $a(-b)$ means $a \times 10^{-b}$.

Grid	cond$\widetilde{\mathcal{A}}$	$N_e(u)$
11×11	2.93(1)	1.15(−2)
17×17	5.40(2)	1.05(−3)
21×21	2.12(3)	5.56(−4)
27×27	3.53(3)	4.81(−5)
31×31	1.41(4)	2.47(−5)
37×37	1.24(4)	1.46(−5)
41×41	3.41(4)	8.37(−6)
47×47	5.80(4)	1.97(−6)
51×51	8.37(4)	1.77(−6)
57×57	1.50(5)	1.37(−6)
61×61	2.29(5)	8.85(−7)
67×67	2.70(5)	5.87(−7)
		$O(h^{5.39})$

where $\mathbf{y}$ is the source point, $\mathbf{x}$ the field point, Γ the piecewise smooth boundary of a domain Ω in $\mathbf{R}^2$, $C(\mathbf{y})$ the free term coefficient, $\bar{v}$ the new variable defined as $\bar{v} = \nabla^2 \bar{u}$, n the outward normal direction at a point on the boundary, and G^H and G^B the harmonic and biharmonic fundamental solutions.

For traditional BIEMs, two BIEs are required and often solved in a coupled manner. Lagrange polynomials such as constant, linear and quadratic functions are usually employed to approximate the variations of $\bar{v}$ and $\partial \bar{v}/\partial n$ along the boundary.

A domain-type interpolation scheme is adopted here to represent the variable u, from which approximations to the unknown variables $\bar{v}$ and $\partial \bar{v}/\partial n$ are derived. From the prescribed boundary conditions $\bar{u}$ and $\partial \bar{u}/\partial n$, the values of $\partial \bar{u}/\partial x_1$ and $\partial \bar{u}/\partial x_2$ at a boundary point can be easily obtained. We implement 2D-IRBFNs of fourth order, where $\widehat{e}_{[x_j]}$ is made up of the values of $\partial \bar{u}/\partial x_j$ at the boundary points. The 2D-IRBFN BIE technique requires only one BIE, namely (17). The present unknowns are the values of u at the interior points. The algebraic system is generated by applying the BIE (17) at the interior points. It should be emphasised that the present equation system consists of the interior equations only, thus completely avoiding all difficulties in numerical computation caused by the singularity of boundary integrals.

Table 2: BIE scheme: accuracy and convergence rate.

	Linear		IRBFN-4	
	$Ne(v)$		$Ne(v)$	
$n_{x_1} = n_{x_2}$	Boundary	Interior	Boundary	Interior
5	4.6349(0)	1.7829(−1)	1.0325(−1)	2.6475(−1)
7	4.3553(0)	1.2632(−1)	2.1247(−2)	3.1643(−2)
9	4.0599(0)	9.0515(−2)	9.8104(−3)	1.0121(−2)
11	3.7946(0)	7.0285(−2)	5.6267(−3)	4.6423(−3)
13	3.5625(0)	5.7887(−2)	3.5808(−3)	2.5094(−3)
15	3.3602(0)	4.9755(−2)	2.4541(−3)	1.5060(−3)
17	3.1830(0)	4.4192(−2)	1.7799(−3)	9.7711(−4)
19	3.0262(0)	4.0332(−2)	1.3494(−3)	6.7476(−4)
21	2.8860(0)	3.7703(−2)	1.0595(−3)	4.9015(−4)
23	2.7592(0)	3.6049(−2)	8.5548(−4)	3.7082(−4)
25	2.6431(0)	3.5238(−2)	7.0667(−4)	2.8978(−4)
27	2.5356(0)	3.5226(−2)	5.9459(−4)	2.3265(−4)
29	2.4348(0)	3.6038(−2)	5.0821(−4)	1.9050(−4)
31	2.3393(0)	3.7778(−2)	4.4080(−4)	1.5844(−4)
	$O(h^{0.35})$	$O(h^{0.84})$	$O(h^{2.58})$	$O(h^{3.52})$

A test problem chosen here is $\nabla^4 u = 0$ on $-2 \leq x_1, x_2 \leq 2$ with Dirichlet boundary conditions. The exact solution of this problem is $\bar{u} = (1/2)x_1(\sin x_1 \cosh x_2 - \cos x_1 \sinh x_2)$ Results concerning Ne are shown in Table 2, together with those obtained by a linear-BIEM. The present method yields a much faster convergence rate.

3.3 Galerkin schemes

For these schemes, the residual of (1) is zero in an average sense. Galerkin schemes have a smoothing capability owing to their integral nature. Consider a rectangular domain. We use a Cartesian grid to generate the finite trial and test spaces. 1D-IRBFNs are employed on grid lines. The present solutions are constructed to satisfy the boundary conditions using the point-collocation approximation and the governing DE using the Galerkin approximation. A distinguishing feature here is that the networks are sought to satisfy a priori the derivative boundary conditions in an exact manner. Moreover, any derivative of the field variable is defined and continuous throughout the entire domain.

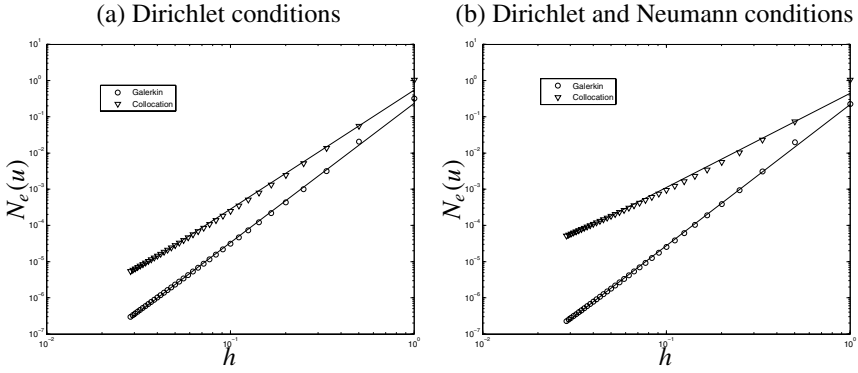

Figure 3: Galerkin scheme, 1D-IRBFNs: Error $N_e(u)$ versus the centre spacing h for the Galerkin and collocation solutions. They converge as $O(h^{3.84})$ and $O(h^{3.28})$ for (a) and $O(h^{3.89})$ and $O(h^{2.60})$ for (b).

3.3.1 Dirichlet boundary conditions

The accuracy of the 1D-IRBFN Galerkin method is demonstrated through the solution of $\nabla^2\bar{u} = -(2\pi^2/(1+2\pi^2))\cos(\pi x_1)\cos(\pi x_2)$ on $-1 \leq x_1, x_2 \leq 1$ with Dirichlet boundary conditions. Its exact solution is $\bar{u}(x_1, x_2) = (1/(1+2\pi^2))\cos(\pi x_1)\cos(\pi x_2)$. Uniform grids, $3\times 3, 5\times 5, \cdots, 71\times 71$, are employed. As shown in Figure 3a, error reduces rapidly with decreasing h for both the Galerkin and collocation solutions. The former outperforms the latter regarding accuracy and convergence rate. Condition numbers of the present system matrix are in the range of 1.0 to 1.3×10^4.

3.3.2 Neumann boundary conditions

This problem is exactly the same as the previous one, except that Dirichlet boundary conditions prescribed along the two horizontal boundaries are replaced with Neumann ones. Figure 3b indicates that the accuracy of the Galerkin solution is far superior to that of the collocation solution. The condition numbers of the Galerkin approach are relatively low, varying from 3.24×10^0 to 1.16×10^4.

Through Figures 3a (Dirichlet-type problem) and 3b (Neumann-type problem), it can be seen that the order of accuracy reduces from $O(h^{3.28})$ to $O(h^{2.60})$ for the collocation solution, but slightly increases from $O(h^{3.84})$ to $O(h^{3.89})$ for the Galerkin solution. The 1D-IRBFN Galerkin technique is able to work well for Neumann boundary conditions without the need for refining the grid near the boundaries, as is often the case with conventional techniques. This is a clear advantage of the present implementation.

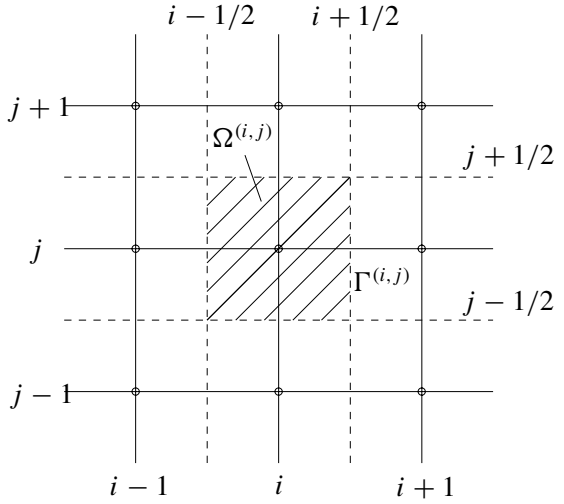

Figure 4: Control-volume scheme: Node (i, j) and its associated control volume $\Omega^{(i,j)}$. Note that the dash lines represent the faces of the control volume.

3.4 Subregion-collocation/control-volume schemes

For these schemes, the weighting function is chosen to be unity over a control volume. Control-volume (CV) formulations are based on the actual satisfaction of the physical laws (i.e. the conservations of mass, momentum and energy) rather than on the satisfaction of approximate discrete expressions controlled by means of mesh size. The accuracy of a CV technique depends on both the approximation of gradients (e.g. diffusive fluxes) and the evaluation of integrals involving these gradients. For the latter, assume that the flux evaluations are sufficiently accurate, the midpoint rule is capable of yielding second-order accuracy only. Consider the diffusion equation $\nabla \cdot \nabla u = 0$ on $0 \leq x_1, x_2 \leq \pi$. Its exact solution is $\bar{u} = (1/\sinh(\pi)) \sin(x_1) \sinh(x_2)$. The problem domain is discretised using a uniform Cartesian grid. For each grid point $(x_1^{(i)}, x_2^{(j)})$, one can construct a CV $\Omega^{(i,j)}$ with its interfaces $\Gamma^{(i,j)}$ as shown in Figure 4. There is a full CV for an interior node and only a half CV for a boundary node. The CV equation of the governing equation takes the form

$$\int_{\Gamma^{(i,j)}} \nabla u \cdot \mathbf{n} \, d\Gamma = 0, \tag{18}$$

which involves first derivatives of u only. Flux integrals over line segments of $\Gamma^{(i,j)}$ are evaluated using Gaussian quadrature which facilitates a high-order accurate solution. Two different cases of boundary conditions, namely (i) Dirichlet conditions only and (ii) Dirichlet ($x_1 = 0$ and $x_1 = \pi$) and Neumann ($x_2 = 0$ and $x_2 = \pi$) conditions, are considered. The 1D-IRBFN approximations are constructed in the same manner as in the case of Galerkin schemes. Figure 5 shows

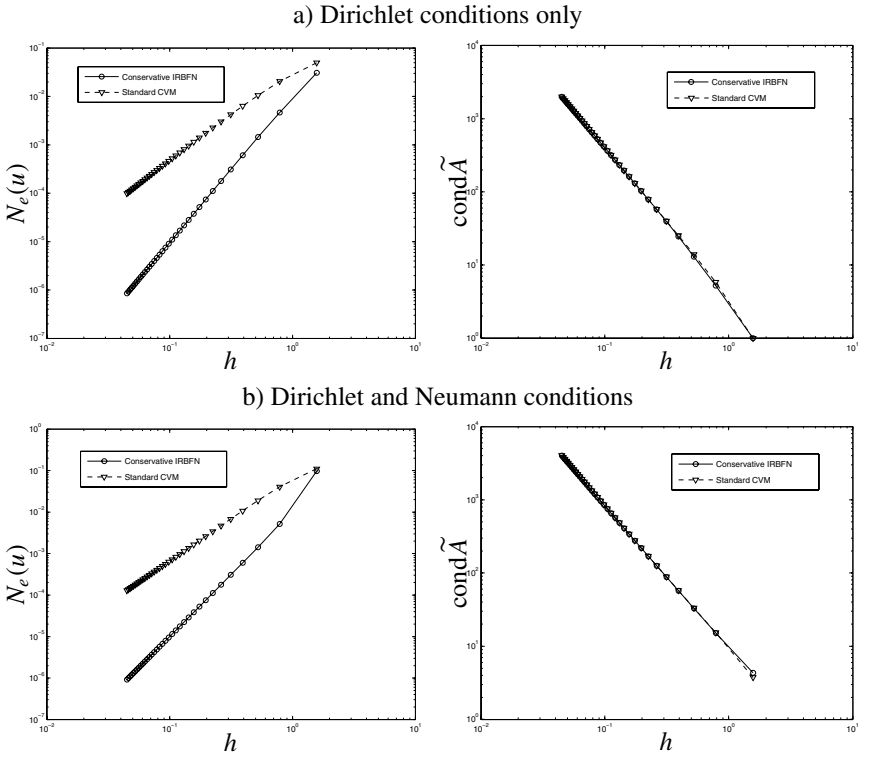

Figure 5: Control-volume scheme, $n = [9, 25, \cdots, 5041]$: Comparisons of the accuracy and condition number between the conservative IRBFN and standard CV methods.

comparisons of the condition number and accuracy of the conservative IRBFN and standard CV methods. For the case of Dirichlet conditions, their rates respectively are $O(h^{3.00})$ and $O(h^{1.84})$ for the accuracy $N_e(u)$, and $O(h^{-2.08})$ and $O(h^{-2.06})$ for the matrix condition number $\widetilde{\text{cond}}A$. For the case of Dirichlet and Neumann conditions, they are $O(h^{3.09})$ and $O(h^{1.98})$ for $N_e(u)$, and $O(h^{-1.94})$ and $O(h^{-1.96})$ for $\widetilde{\text{cond}}A$. Both techniques have similar condition numbers, but the former yields much faster convergence than the latter. Like in the case of Galerkin schemes, conservative IRBFN solutions to Dirichlet and Dirichlet-Neumann problems have similar degrees of accuracy.

4 Concluding remarks

In this paper, trial functions are implemented using IRBFNs rather than the usual low-order polynomials for the solution of elliptic DEs. Attractive features of IRBFNs include (i) to result in mesh-free methods for the collocation statement,

(ii) to provide effective treatments of irregular boundary geometries for Cartesian-grid-based methods, (iii) to offer a proper way of implementing derivative boundary conditions, (iv) to avoid the application of the BIE on the boundaries when the domain-type approach is adopted for the inverse statement, and (v) to allow the use of high-order integration schemes to evaluate flux integrals arising from a control volume discretisation. Various examples are presented to demonstrate high-order accurate solutions and accurate implementation of derivative boundary conditions of IRBFNs.

References

[1] Brebbia, C.A. & Dominguez, J., *Boundary Elements–An Introductory Course*, Computational Mechanics Publications: Southampton, 1992.
[2] Fasshauer G.E., *Meshfree Approximation Methods With Matlab*, World Scientific Publishers: Singapore, 2007.
[3] Mai-Duy, N. & Tran-Cong, T., Approximation of function and its derivatives using radial basis function networks. *Applied Mathematical Modelling*, **27**, pp. 197–220, 2003.
[4] Mai-Duy, N., Indirect RBFN method with scattered points for numerical solution of PDEs. *Computer Modeling in Engineering & Sciences*, **6(2)**, pp. 209–226, 2004.
[5] Mai-Duy, N., Tran-Cong, T. & Tanner, R.I., A domain-type boundary-integral-equation method for two-dimensional biharmonic Dirichlet problem. *Engineering Analysis with Boundary Elements*, **30(10)**, pp. 809–817, 2006.
[6] Mai-Duy, N. & Tran-Cong, T., A Cartesian-grid collocation method based on radial-basis-function networks for solving PDEs in irregular domains. *Numerical Methods for Partial Differential Equations*, **23(5)**, pp. 1192–1210, 2007.
[7] Mai-Duy, N. & Tran-Cong, T., A control volume technique based on integrated RBFNs for the convection-diffusion equation. *Numerical Methods for Partial Differential Equations*(to appear)

A time domain Galerkin boundary element method for a heat conduction interface problem

R. Vodička
Technical University of Košice, Civil Engineering Faculty, Slovakia

Abstract

A heat conduction problem with a material or other type interface is solved. The numerical method used includes a boundary element technique presented as a Galerkin boundary element method for the space variables together with convolution quadrature in time. The treatment of the interface conditions enabled them to be formulated in a weak sense, with generally curved interfaces and independent meshing of each side of the interfaces. Results of the examples present influences of non-conformingly meshed interfaces, a comparison with a known analytical solution, and the time evolution of the interface solution with different material properties of the substructures adjacent to the interface.

Keywords: boundary element method, interface problem, non-matching meshes, heat conduction, convolution quadrature.

1 Introduction

Many problems of civil engineering are modeled by initial-boundary value problems (IBVP) for partial differential equations. Numerical algorithms used for their solution may also include methods based on boundary integral equations (BIE). If, in addition, the solved problem includes an interface, e.g. due to different materials in the analyzed structure or for algorithmic reasons such as parallelization, finding an efficient solver for determining the interface solution may be rather involved. Moreover, a time-dependence may even more complicate the task.

WIT Transactions on Modelling and Simulation, Vol 49, © 2009 WIT Press
www.witpress.com, ISSN 1743-355X (on-line)
doi:10.2495/BE090171

The time-dependent problems can be successfully treated by BIE methods. A nice survey of BIE applications for time dependent problems is given by Costabel [1]. Such methods are widely and successfully being used also for numerical modeling of problems in heat conduction.

The formulation of BIEs, which leads to Symmetric Galerkin Boundary Element Method (SGBEM), has already become classical, see Bonnet *et al.* [2]. It has advantages of symmetry of used boundary integral operators and also their discretized forms – matrices used in numerical solution. It also provides nice convergence properties in energetic norms of Sobolev spaces. With time dependence, there appears a question how to resolve this aspect of the problem. It is possible to use complete space-time solution, or to treat the time variables separately, either by integral, usually Laplace, transform or by a time-stepping algorithm.

In the present paper, the approach introduced uses the Galerkin method only for space variables. The time dependence, which includes the use of convolution in the operators of the integral equations, is treated separately by calculation of the convolution quadrature as introduced by Lubich and Schneider [3], which is based on a linear multistep method and uses only the Laplace transform of the time-dependent fundamental solution.

The existence of an interface requires a split of the space domain into several parts in the solution and usually includes domain decomposition techniques to be used as described by Hsiao *et al.* [4] or Wohlmuth [5]. In the present approach, these are applied very naturally: A variational formulation, originally discussed by Carini [6], of the IBVP directly provides a BIE system with interface conditions directly included into the integral equations as an innovation of the original formulation. Moreover, these conditions are satisfied in a weak form, which has an advantage in the numerical solution for the both sides of the interfaces could be discretized separately. A similar algorithm has been presented for the use with elastic interface problems by Hsiao *et al.* [4], Langer *et al.* [7] or Vodička *et al.* [8].

Independent meshing of both sides of an interface requires a special procedure for cross-transferring of the solution, mainly when the interface is curved. The present approach uses the implementation of data transfer with an auxiliary interface mesh referred to as common-refinement mesh; nevertheless there exist also other possibilities which have been discussed, for example, in de Boer *et al.* [9].

The paper is divided into four main parts. In the first one, Section 2, the solved problem of heat transfer is briefly described. Then, in Section 3, the variational solution leading to a system of BIEs is presented and numerically solved in Section 4 by convolution quadrature in time and by a Galerkin method in space. Finally, Section 5 presents two examples with their solution by suggested approach. One of the examples includes a problem with known analytical solution, so that a comparison can be shown. The other example, although without an analytical solution, even defines different materials for sub-domains and jumps in initial conditions along the interfaces.

2 A heat transfer problem with an interface

Let us consider a body defined by a domain $\Omega \subset R^d$ in a fixed Cartesian coordinate system x_i, $i=1,\ldots,d$, with a bounded Lipschitz boundary $\Gamma=\partial\Omega$. Let $\Gamma_S \subset \Gamma$ denote the smooth part of Γ, i.e. excluding corners, edges, points of curvature jumps, etc. Let n denote the outward unit normal vector defined on Γ_S.

The presence of interfaces causes the domain Ω to be split into several parts. For the sake of simplicity, let us divide Ω into two non-overlapping parts Ω^A and Ω^B whose respective boundaries we denote Γ^A and Γ^B. There also exists a common part of both boundaries, let us denote this coupling boundary by Γ_c.

Let us denote the temperature solution of an initial-boundary value heat conduction problem with an interface in each sub-domain Ω^η as $u^\eta(x;t)$ (the superscript η distinguishes the sub-domains, here it can be either A or B), obtained during a time interval $t \in \langle 0;\bar{t} \rangle$. If neither volume heat sources nor convective boundary conditions are considered and each Ω^η is homogeneous, the problem can be formulated as follows:

$$\begin{gathered}
\frac{\partial u^\eta(x;t)}{\partial t} - \alpha^\eta \, \Delta u^\eta(x;t) = 0, \quad x \in \Omega^\eta, \, t \in \langle 0;\bar{t} \rangle, \quad \eta = A, B, \\
u^\eta(x;0) = u_0^\eta(x), \quad x \in \Omega^\eta, \\
u^\eta(x;t) = g^\eta(x;t), \quad x \in \Gamma_u^\eta, \, t \in \langle 0;\bar{t} \rangle, \\
q^\eta(x;t) = -k^\eta \frac{\partial u^\eta(x;t)}{\partial n^\eta} = h^\eta(x;t), \quad x \in \Gamma_q^\eta, \, t \in \langle 0;\bar{t} \rangle, \\
u^A(x;t) - u^B(x;t) = 0, \quad x \in \Gamma_c, \, t \in \langle 0;\bar{t} \rangle, \\
q^A(x;t) + q^B(x;t) = 0, \quad x \in \Gamma_c, \, t \in \langle 0;\bar{t} \rangle.
\end{gathered} \tag{1}$$

The equations include diffusivity coefficient $\alpha^\eta = k^\eta/(\gamma^\eta \rho^\eta)$ defined by specific heat γ^η, mass density ρ^η and thermal conductivity k^η. The function $q^\eta(x;t)$ determined by the normal derivative of the temperature field introduces heat flux density along the boundary. The split of each boundary Γ^η into three non-overlapping parts due to the boundary and interface conditions can be written as $\Gamma^\eta = \Gamma_u^\eta \cup \Gamma_q^\eta \cup \Gamma_c$. The functions $g^\eta(x;t)$ and $h^\eta(x;t)$ introduce given boundary conditions, while the function $u_0^\eta(x)$ defines the initial condition.

When a problem of heat conduction is to be solved by BIEs, the fundamental solution of the pertinent differential equation eqn. $(1)_1$ is required. This is the solution of eqn. $(1)_1$ at the point x of the equation, where the right hand side contains a point pulse at y and time instance τ, instead of zero. The function and its normal derivatives are given as follows:

$$\begin{gathered}
U^\eta(x,y;t-\tau) = \frac{\alpha^\eta \exp\left(-\frac{|x-y|^2}{4\alpha^\eta(t-\tau)}\right)}{k^\eta \left(4\pi\alpha^\eta(t-\tau)\right)^{\frac{d}{2}}}, \; t \geq \tau, \\
Q^\eta(x,y;t-\tau) = Q^{\eta *}(y,x;t-\tau) = -k^\eta \frac{\partial U^\eta(x,y;t-\tau)}{\partial n_y^\eta}, \quad D^\eta(x,y;t-\tau) = k^{\eta 2} \frac{\partial^2 U^\eta(x,y;t-\tau)}{\partial n_x^\eta \partial n_y^\eta}.
\end{gathered} \tag{2}$$

They will be used in the next section to introduce the energy functional and the kernels of the resulting BIEs.

3 Variational formulation

The SGBEM approach is usually connected with a variational principle based on a boundary saddle-point quadratic functional, the time dependent problems need it to be convolutive in time, see Bonnet *et al.* [2]. Let us introduce the boundary energy functional Π, established by Carini *et al.* [6] and modified here for a different treatment of the interface conditions, as a function of boundary temperatures and flux densities

$$\begin{aligned}\Pi\left(u^A,u^B,q^A,q^B\right)=&-\sum_{\eta=A,B}\left\{\frac{1}{2}\int\limits_{\Gamma_{uc}^{\eta}}\int\limits_{0}^{\bar{t}}q^{\eta}\left(x;\bar{t}-t\right)\int\limits_{\Gamma_{uc}^{\eta}}U^{\eta}\left(x,y;t\right)*q^{\eta}\left(y;t\right)\mathrm{d}S_y\mathrm{d}t\mathrm{d}S_x+\right.\\&+\tfrac{1}{2}\int\limits_{\Gamma_{qc}^{\eta}}\int\limits_{0}^{\bar{t}}u^{\eta}\left(x;\bar{t}-t\right)\int\limits_{\Gamma_{qc}^{\eta}}D^{\eta}\left(x,y;t\right)*u^{\eta}\left(y;t\right)\mathrm{d}S_y\mathrm{d}t\mathrm{d}S_x-\\&\left.-\int\limits_{\Gamma_{uc}^{\eta}}\int\limits_{0}^{\bar{t}}q^{\eta}\left(x;\bar{t}-t\right)\int\limits_{\Gamma_{qc}^{\eta}}Q^{\eta}\left(x,y;t\right)*u^{\eta}\left(y;t\right)\mathrm{d}S_y\mathrm{d}t\mathrm{d}S_x\right\}-\\&-\frac{1}{2}\int\limits_{\Gamma_c}\int\limits_{0}^{\bar{t}}\left[q^A\left(x;\bar{t}-t\right)\left(u^A\left(x;t\right)-u^B\left(x;t\right)\right)-u^B\left(x;\bar{t}-t\right)\left(q^A\left(x;t\right)+q^B\left(x;t\right)\right)\right]\mathrm{d}t\mathrm{d}S_x-\\&-\sum_{\eta=A,B}\left\{\int\limits_{\Gamma_{uc}^{\eta}}\int\limits_{0}^{\bar{t}}q^{\eta}\left(x;\bar{t}-t\right)\hat{g}^{\eta}\left(x;t\right)\mathrm{d}t\mathrm{d}S_x+\int\limits_{\Gamma_{qc}^{\eta}}\int\limits_{0}^{\bar{t}}u^{\eta}\left(x;\bar{t}-t\right)\hat{h}^{\eta}\left(x;t\right)\mathrm{d}t\mathrm{d}S_x\right\}.\end{aligned}\tag{3}$$

The terms $\hat{g}^{\eta}$ and $\hat{h}^{\eta}$ are defined by the prescribed boundary values, eqns. $(1)_{2,3,4}$,

$$\begin{aligned}\hat{g}^{\eta}\left(x;t\right)=&\int\limits_{\Gamma_q^{\eta}}U^{\eta}\left(x,y;t\right)*h^{\eta}\left(y;t\right)\mathrm{d}S_y-\mathrm{p.v.}\int\limits_{\Gamma_u^{\eta}}Q^{\eta}\left(x,y;t\right)*g^{\eta}\left(y;t\right)\mathrm{d}S_y\\&+\rho\gamma\int\limits_{\Omega^{\eta}}U^{\eta}\left(x,y;t\right)u_0^{\eta}\left(y\right)\mathrm{d}y-c_u^{\eta}\left(x\right)g^{\eta}\left(x;t\right),\\\hat{h}^{\eta}\left(x;t\right)=&-\mathrm{p.v.}\int\limits_{\Gamma_q^{\eta}}Q^{\eta*}\left(x,y;t\right)*h^{\eta}\left(y;t\right)\mathrm{d}S_y+\mathrm{f.p.}\int\limits_{\Gamma_u^{\eta}}D^{\eta}\left(x,y;t\right)*g^{\eta}\left(y;t\right)\mathrm{d}S_y\\&-\rho\gamma\int\limits_{\Omega^{\eta}}Q^{\eta*}\left(x,y;t\right)u_0^{\eta}\left(y\right)\mathrm{d}y+c_q^{\eta}\left(x\right)h^{\eta}\left(x;t\right).\end{aligned}\tag{4}$$

If $x\in\Gamma_S^{\eta}$, the free term $c_r^{\eta}(x)$ is equal to one half along Γ_r^{η} and vanishes elsewhere on Γ^{η} for any $r=u,q,c$ or their combination. The marks 'p.v.' and 'f.p.' refer to the Cauchy principle value and the Hadamard finite part, respectively, the methods of strongly and hyper singular integral evaluation.

The weak solution of eqn. (1) can be obtained from the first variation of the energy functional Π, it may provide the BIEs and also the interface conditions. A

slight rearrangement of the terms appearing in the first variation renders the relation

$$
\begin{aligned}
&\delta\Pi\left(u^A,u^B,q^A,q^B;\delta u^A,\delta u^B,\delta q^A,\delta q^B\right)=\\
&-\sum_{\eta=A,B}\left\{\int_{\Gamma_{uc}^{\eta}}\int_0^{\bar t}\delta q^{\eta}\left(x;\bar t-t\right)\left(\int_{\Gamma_{uc}^{\eta}}U^{\eta}\left(x,y;t\right)*q^{\eta}\left(y;t\right)\mathrm{d}S_y-\int_{\Gamma_{qc}^{\eta}}Q^{\eta}\left(x,y;t\right)*u^{\eta}\left(y;t\right)\mathrm{d}S_y\right)\mathrm{d}t\mathrm{d}S_x+\right.\\
&\left.+\int_{\Gamma_{qc}^{\eta}}\int_0^{\bar t}\delta u^{\eta}\left(x;\bar t-t\right)\left(-\int_{\Gamma_{uc}^{\eta}}Q^{\eta*}\left(x,y;t\right)*q^{\eta}\left(y;t\right)\mathrm{d}S_y+\int_{\Gamma_{qc}^{\eta}}D^{\eta}\left(x,y;t\right)*u^{\eta}\left(y;t\right)\mathrm{d}S_y\right)\mathrm{d}t\mathrm{d}S_x\right\}-\\
&-\int_{\Gamma_c}\int_0^{\bar t}\left[\delta q^A\left(x;\bar t-t\right)\left(\tfrac{1}{2}u^A\left(x;t\right)-u^B\left(x;t\right)\right)+\tfrac{1}{2}\delta u^A\left(x;\bar t-t\right)q^A\left(x;t\right)\right]\mathrm{d}t\mathrm{d}S_x+\\
&+\int_{\Gamma_c}\int_0^{\bar t}\left[\delta u^B\left(x;\bar t-t\right)\left(q^A\left(x;t\right)+\tfrac{1}{2}q^B\left(x;t\right)\right)+\tfrac{1}{2}\delta q^B\left(x;\bar t-t\right)u^B\left(x;t\right)\right]\mathrm{d}t\mathrm{d}S_x-\\
&-\sum_{\eta=A,B}\left\{\int_{\Gamma_{uc}^{\eta}}\int_0^{\bar t}\delta q^{\eta}\left(x;\bar t-t\right)\hat g^{\eta}\left(x;t\right)\mathrm{d}t\mathrm{d}S_x+\int_{\Gamma_{qc}^{\eta}}\int_0^{\bar t}\delta u^{\eta}\left(x;\bar t-t\right)\hat h^{\eta}\left(x;t\right)\mathrm{d}t\mathrm{d}S_x\right\}.
\end{aligned}
\tag{5}
$$

The stationary point of the functional Π determined by its vanishing first variation provides the BIEs:

$$
\begin{aligned}
0&=\int_{\Gamma_{uc}^{\eta}}U^{\eta}\left(x,y;t\right)*q^{\eta}\left(y;t\right)\mathrm{d}S_y-\text{p.v.}\int_{\Gamma_{qc}^{\eta}}Q^{\eta}\left(x,y;t\right)*u^{\eta}\left(y;t\right)\mathrm{d}S_y-c_c^{\eta}\left(x\right)u^{\eta}\left(x;t\right)+\hat g^{\eta}\left(x;t\right),\\
0&=-\text{p.v.}\int_{\Gamma_{uc}^{\eta}}Q^{\eta*}\left(x,y;t\right)*q^{\eta}\left(y;t\right)\mathrm{d}S_y+\text{f.p.}\int_{\Gamma_{qc}^{\eta}}D^{\eta}\left(x,y;t\right)*u^{\eta}\left(y;t\right)\mathrm{d}S_y+c_c^{\eta}\left(x\right)q^{\eta}\left(x;t\right)+\hat h^{\eta}\left(x;t\right).
\end{aligned}
\tag{6}
$$

Notice that for points x from to the interface Γ_c the free term contains an unknown function, while the terms $\hat g^{\eta}$ and $\hat h^{\eta}$ defined in eqn. (4) do not contain this free term for interface points. It also makes true a weak representation of interface conditions eqns. $(1)_{5,6}$

$$
\begin{aligned}
0&=\int_{\Gamma_c}\int_0^{\bar t}\delta q^A\left(x;\bar t-t\right)\left(u^A\left(x;t\right)-u^B\left(x;t\right)\right)\mathrm{d}t\mathrm{d}S_x,\\
0&=\int_{\Gamma_c}\int_0^{\bar t}\delta u^B\left(x;\bar t-t\right)\left(q^A\left(x;t\right)+q^B\left(x;t\right)\right)\mathrm{d}t\mathrm{d}S_x.
\end{aligned}
\tag{7}
$$

This weak form of the interface conditions should be seen in view of Vodička *et al.* [8]: the compatibility condition eqn. $(7)_1$ is satisfied with respect to sub-domain Ω^A, $u^B\left(x;t\right)$ being assumed as a known function, on the contrary, the flux equilibrium condition eqn. $(7)_2$ is satisfied with respect to sub-domain Ω^B and with $q^A\left(x;t\right)$ supposed to be given.

4 Numerical solution

The time variable will be treated in a way different from that one used for space variables. Therefore, there appears a difference also in the treatment of the weight functions in eqn. (5). First, let us suppose that the test function includes

an impulse at the time $\tau \in \langle 0;\bar{t}\rangle$, so that it can be rewritten in a weak form with respect only to the space variables

$$
\begin{aligned}
0 = &\int_{\Gamma_u^A} \delta q^A(x)\left(\int_{\Gamma_{uc}^A} U^A(x,y;\tau) * q^A(y;\tau)\,\mathrm{d}S_y - \int_{\Gamma_{qc}^A} Q^A(x,y;\tau) * u^A(y;\tau)\,\mathrm{d}S_y + \hat{g}^A(x;\tau)\right)\mathrm{d}S_x + \\
&+\int_{\Gamma_q^A} \delta u^A(x)\left(-\int_{\Gamma_{uc}^A} Q^{A*}(x,y;\tau) * q^A(y;\tau)\,\mathrm{d}S_y + \int_{\Gamma_{qc}^A} D^A(x,y;\tau) * u^A(y;\tau)\,\mathrm{d}S_y + \hat{h}^A(x;\tau)\right)\mathrm{d}S_x + \\
&+\int_{\Gamma_c} \delta q^A(x)\left(\int_{\Gamma_{uc}^A} U^A(x,y;\tau) * q^A(y;\tau)\,\mathrm{d}S_y - \right. \\
&\qquad \left. - \int_{\Gamma_{qc}^A} Q^A(x,y;\tau) * u^A(y;\tau)\,\mathrm{d}S_y + \tfrac{1}{2}u^A(x;\tau) - u^B(x;\tau) + \hat{g}^A(x;\tau)\right)\mathrm{d}S_x + \\
&+\int_{\Gamma_c} \delta u^A(x)\left(-\int_{\Gamma_{uc}^A} Q^{A*}(x,y;\tau) * q^A(y;\tau)\,\mathrm{d}S_y + \tfrac{1}{2}q^A(x;\tau) + \right. \\
&\qquad \left. + \int_{\Gamma_{qc}^A} D^A(x,y;\tau) * u^A(y;\tau)\,\mathrm{d}S_y + \hat{h}^A(x;\tau)\right)\mathrm{d}S_x + \\
&+\int_{\Gamma_u^B} \delta q^B(x)\left(\int_{\Gamma_{uc}^B} U^B(x,y;\tau) * q^B(y;\tau)\,\mathrm{d}S_y - \int_{\Gamma_{qc}^B} Q^B(x,y;\tau) * u^B(y;\tau)\,\mathrm{d}S_y + \hat{g}^B(x;\tau)\right)\mathrm{d}S_x + \\
&+\int_{\Gamma_q^B} \delta u^B(x)\left(-\int_{\Gamma_{uc}^B} Q^{B*}(x,y;\tau) * q^B(y;\tau)\,\mathrm{d}S_y + \int_{\Gamma_{qc}^B} D^B(x,y;\tau) * u^B(y;\tau)\,\mathrm{d}S_y + \hat{h}^B(x;\tau)\right)\mathrm{d}S_x + \\
&+\int_{\Gamma_c} \delta q^B(x)\left(\int_{\Gamma_{uc}^B} U^B(x,y;\tau) * q^B(y;\tau)\,\mathrm{d}S_y - \right. \\
&\qquad \left. - \int_{\Gamma_{qc}^B} Q^B(x,y;\tau) * u^B(y;\tau)\,\mathrm{d}S_y - \tfrac{1}{2}u^B(x;\tau) + \hat{g}^B(x;\tau)\right)\mathrm{d}S_x + \\
&+\int_{\Gamma_c} \delta u^B(x)\left(-q^A(x;\tau) - \int_{\Gamma_{uc}^B} Q^{B*}(x,y;\tau) * q^B(y;\tau)\,\mathrm{d}S_y - \tfrac{1}{2}q^B(x;\tau) + \right. \\
&\qquad \left. + \int_{\Gamma_{qc}^B} D^B(x,y;\tau) * u^B(y;\tau)\,\mathrm{d}S_y + \hat{h}^B(x;\tau)\right)\mathrm{d}S_x .
\end{aligned}
\tag{8}
$$

The convolution can be evaluated numerically, see Lubich [3], by a quadrature formula whose weights are determined with the help of Laplace transform $\mathcal{L}(f)$ of a function f

$$
\mathcal{L}\left(f(t)\right)(s) = \int_0^{+\infty} f(t)\exp(-st)\,\mathrm{d}t \tag{9}
$$

and a backward difference formula of order $p \le 6$ for ordinary differential equations with the generating function δ, see below eqn. (11).

Let us rewrite the space double integrals in eqn. (8), using a mask integral kernel Z^{η} instead of the pertinent fundamental kernels U^{η}, Q^{η}, D^{η}. The approximation of the convolution at time $\tau=nt_h$, where $t_h=\bar{t}/N_t$ is a time step and N_t is the total number of time steps, renders

$$\int_{\Gamma_s^{\eta}} \delta v^{\eta}(x) \int_{\Gamma_r^{\eta}} Z^{\eta}(x,y;\tau) * w^{\eta}(y;\tau)\,\mathrm{d}S_y\,\mathrm{d}S_x \cong \int_{\Gamma_s^{\eta}} \int_{\Gamma_r^{\eta}} \delta v^{\eta}(x) \sum_{j=0}^{n} \mathcal{Z}_{n-j}^{\eta}(x,y)\, w_j^{\eta}(y)\,\mathrm{d}S_y\,\mathrm{d}S_x . \tag{10}$$

The quadrature weight functions $\mathcal{Z}_n^{\eta}$ are the coefficients of the power series expansion associated to the Laplace transform of the pertinent integral kernel Z^{η} evaluated at a point depending on the used backward difference formula

$$\sum_{n=0}^{+\infty} \mathcal{Z}_n^{\eta}(x,y)\,\xi^n = \mathcal{L}\left(Z^{\eta}(x,y;\tau)\right)\left(\frac{\delta(\xi)}{t_h}\right), \quad |\xi|<1, \quad \delta(\xi)=\sum_{m=1}^{p}\frac{(1-\xi)^m}{m}. \tag{11}$$

The details of the quadrature weight function calculation can be found in [3]. The solution (either $u^{\eta}(x;t)$ or $q^{\eta}(x;t)$) at j-th time step is denoted by the mask function $w_j^{\eta}(y)=w^{\eta}(y;jt_h)$.

The numerical solution of eqn. (8) by the Symmetric Galerkin Boundary Element Method includes division of the boundaries Γ^{η} into boundary elements. The simplest way of discretization suggests conforming isoparametric elements. The approximation of the functions $w_j^{\eta}(x)$ and the choice of weight functions in eqn. (8) can be written in the following form

$$w_j^{\eta}(x) \cong \sum_{k=1}^{N_w^{\eta}} \phi_w^{\eta k}(x)\,\mathrm{w}_{\mathrm{j}}^{\eta k}, \quad \delta v^{\eta}(x)=\phi_v^{\eta l}(x), l=1,\ldots,N_v^{\eta}. \tag{12}$$

The functions $\varphi_w^{\eta k}(x)$ are the nodal shape functions, according to the discretization made, for the approximation $\mathrm{w}_j^{\eta k}$ of the nodal values of the function $w_j^{\eta}(x)$, N_w^{η} is the number of nodal unknowns pertinent to function $w_j^{\eta}(x)$. The eqn. (8) can be written, after an appropriate reordering of the terms according to given and unknown data in the n-th temporal step, as follows:

$$\begin{aligned}
&-\left(\mathbf{U}_{uu}^{\eta}\right)_0\left(\mathbf{q}_u^{\eta}\right)_n+\left(\mathbf{Q}_{uq}^{\eta}\right)_0\left(\mathbf{u}_q^{\eta}\right)_n-\left(\mathbf{U}_{uc}^{\eta}\right)_0\left(\mathbf{q}_c^{\eta}\right)_n+\left(\mathbf{Q}_{uc}^{\eta}\right)_0\left(\mathbf{u}_c^{\eta}\right)_n=\\
&\quad=e_n\left(\hat{\mathbf{g}}_u^{\eta}\right)_n-\sum_{j=0}^{n-1}\left[-\left(\mathbf{U}_{uu}^{\eta}\right)_{n-j}\left(\mathbf{q}_u^{\eta}\right)_j+\left(\mathbf{Q}_{uq}^{\eta}\right)_{n-j}\left(\mathbf{u}_q^{\eta}\right)_j-\left(\mathbf{U}_{uc}^{\eta}\right)_{n-j}\left(\mathbf{q}_c^{\eta}\right)_j+\left(\mathbf{Q}_{uc}^{\eta}\right)_{n-j}\left(\mathbf{u}_c^{\eta}\right)_j\right],\\
&\left(\mathbf{Q}_{qu}^{\eta*}\right)_0\left(\mathbf{q}_u^{\eta}\right)_n-\left(\mathbf{D}_{qq}^{\eta}\right)_0\left(\mathbf{u}_q^{\eta}\right)_n+\left(\mathbf{Q}_{qc}^{\eta*}\right)_0\left(\mathbf{q}_c^{\eta}\right)_n-\left(\mathbf{D}_{qc}^{\eta}\right)_0\left(\mathbf{u}_c^{\eta}\right)_n=\\
&\quad=e_n\left(\hat{\mathbf{h}}_q^{\eta}\right)_n-\sum_{j=0}^{n-1}\left[\left(\mathbf{Q}_{qu}^{\eta*}\right)_{n-j}\left(\mathbf{q}_u^{\eta}\right)_j-\left(\mathbf{D}_{qq}^{\eta}\right)_{n-j}\left(\mathbf{u}_q^{\eta}\right)_j+\left(\mathbf{Q}_{qc}^{\eta*}\right)_{n-j}\left(\mathbf{q}_c^{\eta}\right)_j-\left(\mathbf{D}_{qc}^{\eta}\right)_{n-j}\left(\mathbf{u}_c^{\eta}\right)_j\right],
\end{aligned}$$

$$
\begin{aligned}
&-\left(\mathbf{U}_{cu}^{A}\right)_0\left(\mathbf{q}_u^A\right)_n+\left(\mathbf{Q}_{cq}^{A}\right)_0\left(\mathbf{u}_q^A\right)_n-\left(\mathbf{U}_{cc}^{A}\right)_0\left(\mathbf{q}_c^A\right)_n+\left[\left(\mathbf{Q}_{cc}^{A}\right)_0-\tfrac{1}{2}\mathbf{M}_c^{AA}\right]\left(\mathbf{u}_c^A\right)_n+\mathbf{M}_c^{AB}\left(\mathbf{u}_c^B\right)_n=\\
&\qquad=e_n\left(\hat{\mathbf{g}}_c^A\right)_n-\sum_{j=0}^{n-1}\left[-\left(\mathbf{U}_{cu}^{A}\right)_{n-j}\left(\mathbf{q}_u^A\right)_j+\left(\mathbf{Q}_{cq}^{A}\right)_{n-j}\left(\mathbf{u}_q^A\right)_j-\left(\mathbf{U}_{cc}^{A}\right)_{n-j}\left(\mathbf{q}_c^A\right)_j+\left(\mathbf{Q}_{cc}^{A}\right)_{n-j}\left(\mathbf{u}_c^A\right)_j\right],\\
&\left(\mathbf{Q}_{cu}^{A*}\right)_0\left(\mathbf{q}_u^A\right)_n-\left(\mathbf{D}_{cq}^{A}\right)_0\left(\mathbf{u}_q^A\right)_n+\left[\left(\mathbf{Q}_{cc}^{A*}\right)_0-\tfrac{1}{2}\mathbf{M}_c^{AA}\right]\left(\mathbf{q}_c^A\right)_n-\left(\mathbf{D}_{cc}^{A}\right)_0\left(\mathbf{u}_c^A\right)_n=\\
&\qquad=e_n\left(\hat{\mathbf{h}}_c^A\right)_n-\sum_{j=0}^{n-1}\left[\left(\mathbf{Q}_{cu}^{A*}\right)_{n-j}\left(\mathbf{q}_u^A\right)_j-\left(\mathbf{D}_{cq}^{A}\right)_{n-j}\left(\mathbf{u}_q^A\right)_j+\left(\mathbf{Q}_{cc}^{A*}\right)_{n-j}\left(\mathbf{q}_c^A\right)_j-\left(\mathbf{D}_{cc}^{A}\right)_{n-j}\left(\mathbf{u}_c^A\right)_j\right],\\
&-\left(\mathbf{U}_{cu}^{B}\right)_0\left(\mathbf{q}_u^B\right)_n+\left(\mathbf{Q}_{cq}^{B}\right)_0\left(\mathbf{u}_q^B\right)_n-\left(\mathbf{U}_{cc}^{B}\right)_0\left(\mathbf{q}_c^B\right)_n+\left[\left(\mathbf{Q}_{cc}^{B}\right)_0+\tfrac{1}{2}\mathbf{M}_c^{BB}\right]\left(\mathbf{u}_c^B\right)_n=\\
&\qquad=e_n\left(\hat{\mathbf{g}}_c^B\right)_n-\sum_{j=0}^{n-1}\left[-\left(\mathbf{U}_{cu}^{B}\right)_{n-j}\left(\mathbf{q}_u^B\right)_j+\left(\mathbf{Q}_{cq}^{B}\right)_{n-j}\left(\mathbf{u}_q^B\right)_j-\left(\mathbf{U}_{cc}^{B}\right)_{n-j}\left(\mathbf{q}_c^B\right)_j+\left(\mathbf{Q}_{cc}^{B}\right)_{n-j}\left(\mathbf{u}_c^B\right)_j\right],\\
&\left(\mathbf{Q}_{cu}^{B*}\right)_0\left(\mathbf{q}_u^B\right)_n-\left(\mathbf{D}_{cq}^{B}\right)_0\left(\mathbf{u}_q^B\right)_n+\left[\left(\mathbf{Q}_{cc}^{B*}\right)_0+\tfrac{1}{2}\mathbf{M}_c^{BB}\right]\left(\mathbf{q}_c^B\right)_n-\left(\mathbf{D}_{cc}^{B}\right)_0\left(\mathbf{u}_c^B\right)_n+\mathbf{M}_c^{BA}\left(\mathbf{q}_c^A\right)_n=\\
&\qquad=e_n\left(\hat{\mathbf{h}}_c^B\right)_n-\sum_{j=0}^{n}\left[\left(\mathbf{Q}_{cu}^{B*}\right)_{n-j}\left(\mathbf{q}_u^B\right)_j-\left(\mathbf{D}_{cq}^{B}\right)_{n-j}\left(\mathbf{u}_q^B\right)_j+\left(\mathbf{Q}_{cc}^{B*}\right)_{n-j}\left(\mathbf{q}_c^B\right)_j-\left(\mathbf{D}_{cc}^{B}\right)_{n-j}\left(\mathbf{u}_c^B\right)_j\right].
\end{aligned}
\tag{13}
$$

The symbols $\left(\mathbf{Z}_{sr}^{\eta}\right)_i, \mathbf{M}_{sr}^{\eta\sigma}$ denote matrices, whose elements are defined respectively by the relations

$$
\left(Z_{sr}^{\eta}\right)_i^{lk}=\int_{\Gamma_s^\eta}\int_{\Gamma_r^\eta}\phi_v^{\eta\,l}(x)\mathcal{Z}_i^{\eta}(x,y)\phi_w^{\eta\,k}(y)\,\mathrm{d}S_y\,\mathrm{d}S_x,\quad \left(\mathrm{M}_s^{\eta\sigma}\right)^{lk}=\int_{\Gamma_s^\eta}\phi_v^{\eta\,l}(x)\phi_w^{\sigma\,k}(x)\,\mathrm{d}S_x.
\tag{14}
$$

The nodal values either prescribed or not are gathered into vectors $\left(\mathbf{w}_r^{\eta}\right)_j$, with subscripts $s,r=u,t,c$ introduced according to boundaries' splits.

It should be clearly seen that the solution at each time step uses the same left hand side matrix with index 0 which is symmetric. Therefore, matrix factorization has to be performed only once. However, at each time step, the right hand side has to be evaluated from the results of the previous steps. The vectors $\left(\hat{\mathbf{g}}_r^{\eta}\right)_j$ and $\left(\hat{\mathbf{h}}_r^{\eta}\right)_j$ contain nodal data given by the boundary conditions and appropriately evaluated by eqn. (4). The numbers e_n are the end-point correction weights of the p-th order Newton-Gregory quadrature formula introduced in order to obtain the convergence property according to [3]. Otherwise they can be set to unity.

5 Examples

Although the developed formulation is valid in 3D space as well, for the sake of simplicity we confine ourselves only to the 2D examples. Nevertheless, the algorithm presented here only for a split of the solution domain into two parts can be applied also for domains containing more sub-domains. An example therefore contains three sub-domains to demonstrate this possibility.

First, let us consider a square divided into two parts as shown on the left picture in Figure 1. This example has been taken to demonstrate the properties of the solution transfer across the interface. The material parameters have been set to unity and all calculations have been done without units. The initial and boundary conditions have been set according to the relations

$$u\left(\left(x_1,x_2\right);0\right)=0,\quad u\left(\left(x_1,0\right);t\right)=0,\quad q\left(\left(0,x_2\right);t\right)=0,$$
$$q\left(\left(2,x_2\right);t\right)=-4x_2^2\left(1-\exp\left(-t\right)\right),\quad q\left(\left(x_1,2\right);t\right)=-4x_1^2\left(1-\exp\left(-t\right)\right). \tag{15}$$

The problem is solved up to the unit total time $\bar{t}$.

The analytical solution is known, at least in the form of a series-expansion so that a comparison of analytical and numerical solutions has been enabled. The interface has been defined by a cubic spline passing through the points E, S_i and F, with: S_1[0.5;0.4], S_2[1.0;1.1], S_3[1.5;1.6]. Numerical solutions have been compared for three boundary element meshes. The coarsest mesh consists of four linear elements along the long segments of the outer contour of each sub-domain and one along the short ones. Five elements have been put along both sides of the interface meshed conformingly and a five-to-six non-conforming interface mesh has been chosen in the other case. The mesh has been then two times refined doubling at each step the number of elements. With respect to the time variable, the total time $\bar{t}$ has been split into four equal time-steps for the first boundary element mesh. The time step has been also halved for the subsequent meshes. The order p of the backward difference formula, see also eqn. (11), has been two.

In this example, the behavior of the errors with respect to the refinement can be studied as long as the analytical solution can be calculated, too. The graphs of Figure 2 and Figure 3 show the distribution of errors relatively to the magnitude of the overall analytical solution obtained for conforming and non-conforming interface meshes, respectively, of temperatures u and heat fluxes q plotted against the arc length l of the interface measured from the point E. The letters in the legends refer to the letters which distinguish the sub-domains on Figure 1 (left) and the numbers denote the smallest number of the elements used in the interface meshes. The superscripts 'num' and 'ex' refer to numerical and analytical results, respectively.

The results of conforming meshes are naturally smoother than those of non-conforming meshes, their magnitudes, however, do not differ significantly.

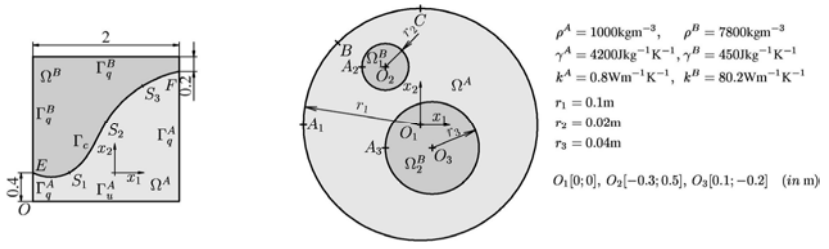

Figure 1: Geometry of the examples.

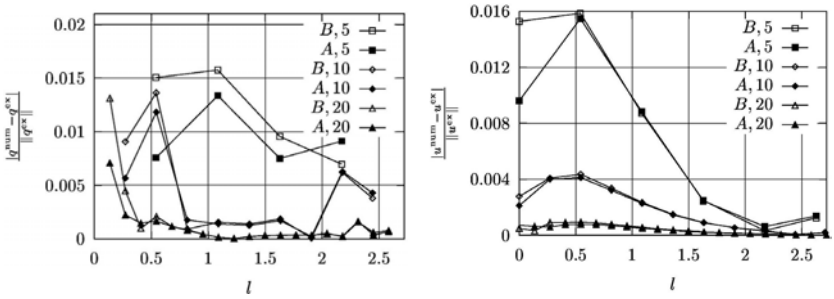

Figure 2: Errors for $t = \overline{t}$, conforming meshes.

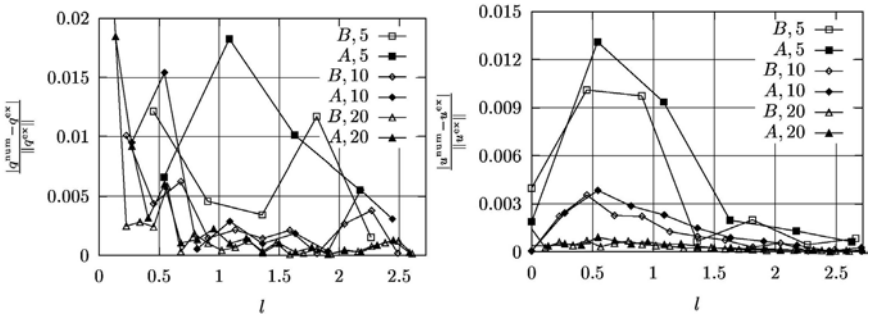

Figure 3: Errors for $t = \overline{t}$, non-conforming meshes.

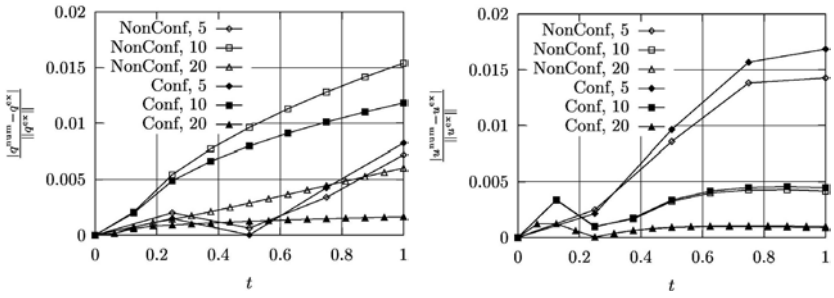

Figure 4: Errors at the point S_3.

Moreover, it can be seen that the errors diminish approximately four times for each refinement, especially for temperatures, which confirms the expected quadratic convergence of the errors, see Lubich and Schneider [3]. The equilibrium and compatibility of the data, supposed to be satisfied in a weak form, eqn. (5), are satisfied, with an excellent agreement for conforming meshes and a quite good fit also for the non-conforming meshes.

The evolution of the errors in time at the point S_3 is shown on Figure 4, where both conforming and non-conforming mesh results are presented. The convergence observations from the previous paragraph can be repeated. The quadratic convergence can be observed, here caused by the choice p=2, see

Lubich and Schneider [3], a bit lower order appeared for the heat fluxes, especially non-conforming mesh. Notice that the coarsest mesh behaves differently in heat fluxes, probably due to the fact that it is actually rather coarse, with respect to the curvature of the interface and its approximation by linear isoparametric space elements.

In the second example, let us consider more realistic material parameters and real units, see Figure 1 (right). The initial and boundary conditions have been set as follows: the initial conditions have been given by different constant temperatures in each of the sub-domains: u_0^A=290K, u_0^{B1}=280K, u_0^{B2}=320K with vanishing flux prescribed along the outer contour. The problem is solved up to the total time $\bar{t}$=1h.

The boundary element mesh contains equally distributed 32 linear elements along each circle of the boundary or the interface, with an exception of the upper half circles of the interfaces with respect to B sub-domains, which contain 20 elements. The time step has been taken such that 16 steps have been done to reach $\bar{t}$ with the order p=2 in the algorithm of the convolution quadrature.

The results shown on Figure 5 demonstrate the evolution of both calculated functions along the interfaces evaluated with respect to the inclusions at the time instances $t=\alpha\bar{t}$. The data are plotted starting respectively from points A_2, A_3 counter-clockwise, the arc angle is denoted by φ. No difference in the solution appeared between the upper and lower half circles, possibly caused by the different meshing properties supposed.

The graphs confirm expected behavior of the solution, where the heat flux shows the concentration at inclusion points which are closest to each other. The

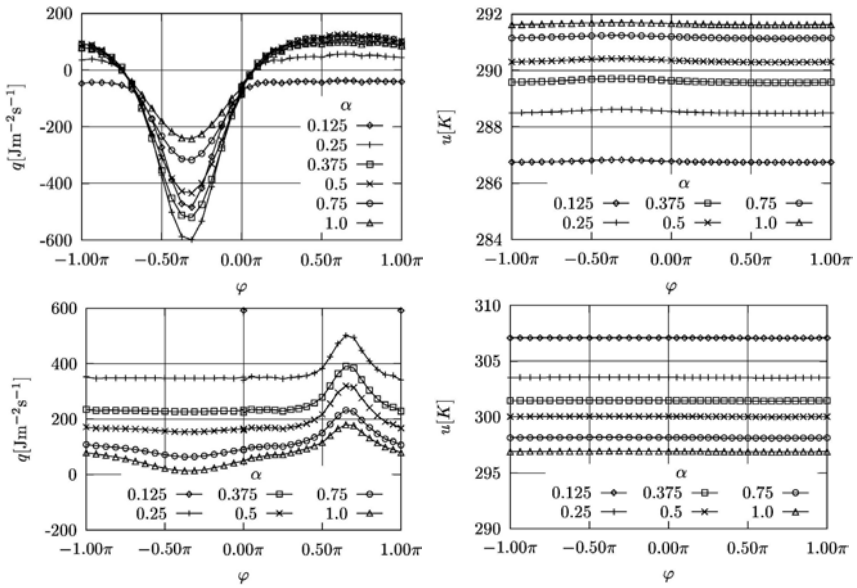

Figure 5: Solutions along the interfaces: $\Omega^A \leftrightarrow \Omega^B{}_1$ (top), $\Omega^A \leftrightarrow \Omega^B{}_2$ (bottom).

evolution of temperature is also natural, as depending on the size of the inclusion and its position they tend towards the expected values of a stationary solution.

6 Conclusions

A solution of interface heat conduction IBVP by a Galerkin boundary element technique has been discussed. In the proposed method, the two crucial points of the solution, treatment of the interface relations and time dependence, have been resolved satisfactorily by applying a variational principle to obtain a weak form of the interface conditions for the former crucial point and by utilizing a convolution quadrature method for obtaining a time-domain solution as the latter one. It was demonstrated by two simple but problem describing examples. The results provoke the further demonstration of the method in a wider range of problems with interfaces in a forthcoming paper.

Acknowledgement

The work has been supported by the grants VEGA No 1/4198/07 and 1/4160/07.

References

[1] Costabel, M., Time-dependent problems with boundary integral equation method (Chapter 25). *Encyclopedia of Computational Mechanics*, John Wiley & Sons, Eds. Stein, de Borst, Hughes. vol. 1, 2004.
[2] Bonnet, M., Maier, G., Polizzotto, C., Symmetric Galerkin boundary element method. *Applied Mechanics Review,* **5**, pp.669–704, 1998.
[3] Lubich, C., Schneider R., Time discretization of parabolic boundary integral equations. *Numerishe Mathematik,* **63**, pp. 455—481, 1992.
[4] Hsiao, G.C., Steinbach, O., Wendland, W.L., Domain decomposition methods via boundary integral equations. *Journal of Computations and Applied Mathematics,* **125**, pp.521–537, 2000.
[5] Wohlmuth, B.I., Discretization Methods and Iterative Solvers Based on Domain Decomposition. *Lecture Notes in Computational Science and Engineering,* vol.17, Springer: Berlin, 2001.
[6] Carini, A., Diligenti, M., Maier, G., Symmetric boundary integral formulations of transient heat conduction: saddle-point theorems for BE analysis and BE-FE coupling. *Archives of Mechanics*, **49**, pp. 253–283, 1997.
[7] Langer, U., Steinbach, O., Boundary element tearing and interconnecting method. *Computing*, **71**, pp. 205–228, 2003.
[8] Vodička, R., Mantič, V., París, F., Symmetric variational formulation of BIE for domain decomposition problems in elasticity - an SGBEM approach for nonconforming discretizations of curved interfaces. *CMES – Computer Modeling in Engineering and Science,* **17**, pp. 173–203, 2007.
[9] Boer, A. de, Zuijlen, A.H. van, Bijl, H., Review of coupling methods for non-matching meshes. *Computational Methods in Applied Mechanics and Engineering,* ***196***, pp.1515–1525, 2007.

Hierarchical matrices and adaptive cross approximation applied to the boundary element method with multi-domain governed by iterative coupling

T. Grytsenko & A. Peratta
Wessex Institute of Technology, Southampton, UK

Abstract

The approach presented in this paper is based on the Adaptive Cross Approximation (ACA) applied to the matrices coming from the Boundary Element Method (BEM) with multi-domain. The algorithm uses a hierarchical matrix (H-matrix) storage approach splitting the coefficient matrices representing the interactions inside the sub-domains into many blocks where rank of the off-diagonal blocks is reduced with the help of ACA approximation. The sub-domains are then coupled through the iterative process. These optimisations of the coefficient matrices in conjunction with highly effective algorithms for manipulation with H-matrices allow one to perform the operation of matrix-vector multiplication with almost linear complexity $O(NlogN)$. The approach allows one to solve the linear systems of equations for BEM with multi-domain having nearly 100.000 DOFs using the usual PC. This paper formulates the approach and demonstrates its numerical properties by means of a theoretical example involving a cube with 27 sub-domains.

1 Introduction

The Boundary Element Method (BEM) with multi-domain [1–3] produces as many coefficient matrices as the number of sub-domains in the system. Those coefficient matrices can be coupled within either one matrix or unified into one system through the iterative process [4].

The former approach works well if the neighboring sub-domains are coupled exploiting the continuity of potentials and normal fluxes. However, if this is not

WIT Transactions on Modelling and Simulation, Vol 49, © 2009 WIT Press
www.witpress.com, ISSN 1743-355X (on-line)
doi:10.2495/BE090181

the case and the relationship between the sub-domains have to be expressed using the constraint equations, the latter approach has to be used [4].

In the case with iterative coupling of the sub-domains, each sub-domain produces a dense coefficient matrix having $O(N^2)$ storage requirement. The solution of such matrices forces the usage of direct LU-based methods requiring $O(N^3)$ of floating point operations.

In this way the calculation becomes too expensive from a computational point of view thus representing a big obstacle for solving large scale BEM problems involving more than 20.000 unknowns.

The method presented in this paper allows to compresses the dense matrices using the Adaptive Cross Approximation (ACA) [5] algorithm. The method uses a hierarchical matrix (H-matrix) storage approach [6] where each sub-domain of the model is split into many blocks classified into two categories, weakly and strongly coupled. The formers are off-diagonal blocks which represent remote interactions between the source points and field elements, and therefore can be approximated by low-rank matrices using the ACA approach [5]. These blocks are stored in a special Rk-format [6]. The latter blocks describing close interactions between the source points and field elements are stored without any changes in a full-matrix format [6].

This reorganisation of the LSE, implemented in conjunction with algorithms for manipulation with H-matrices reduces the calculation complexity of matrix-vector multiplication to approximately $O(NlogN)$. The simplification of MVM reduces considerably the computational burden of the solving stage and shows much better solution time in comparison with standard iterative solvers such as preconditioned GMRES, CG etc.

This paper formulates the approach and comments on the performance of BEM with multi-domain using the hierarchical matrices and ACA. The theoretical example involving nearly 100.000 DOFs is solved on a usual desktop PC.

The paper is organised as follows: in Section 2, the BEM with multi-domain method formulation for Laplace equation is considered; Section 3 formulates the method for iterative coupling of the sub-domains; Section 4 demonstrates the numerical results of application to the theoretical example involving a model with 27 sub-domains and finally Section 5 makes the conclusions.

2 Boundary Element Method formulation

Consider solving the potential equation for the unknown scalar field $u(\mathbf{x})$ given by:

$$\nabla \cdot [-k\nabla u(\mathbf{x})] = 0, \quad \mathbf{x} \in \Omega \subseteq R^3 \tag{1}$$

where k is conductivity, Ω is the integration domain with boundary $\Gamma = \partial(\Omega)$ of outward unit normal $\hat{\mathbf{n}}$, and proper boundary conditions are applied to Γ, i.e. Dirichlet or Neumann type. Then, the boundary integral formulation for eq. (1)

can be expressed in the following way [7, 8]:

$$c_i u(\mathbf{x}_i) + \int_\Gamma q^*(\mathbf{x}, \mathbf{x}_i) u(\mathbf{x})\, d\Gamma - \int_\Gamma u^*(\mathbf{x}, \mathbf{x}_i) q(\mathbf{x})\, d\Gamma = 0, \tag{2}$$

where u is the unknown field, q its normal derivative in $\hat{\mathbf{n}}$ direction, u^* the Green's function of Laplace equation such that $\nabla^2 u^* + \delta(\mathbf{x}_i, \mathbf{x}) = 0$, q^* its normal derivative in $\hat{\mathbf{n}}$ direction, and c_s is the self-interaction coefficient. In 3D problems u^* and q^* become: $u^* = 1/(4\pi r)$ and $q^* = -\mathbf{r}\cdot\hat{\mathbf{n}}/(4\pi r^3)$, respectively, where $\mathbf{r} = \mathbf{x} - \mathbf{x}_i$ and $r = |\mathbf{r}|$ is the distance between the field ($\mathbf{x}$) and source ($\mathbf{x}_i$) points.

In order to solve eq.(2), Γ is discretised into N_e constant triangular boundary elements Γ. Thus, the discretised boundary integral equation becomes:

$$c_i u_i + \sum_{j=1}^{N_e} h_j u_j - \sum_{j=1}^{N_e} g_j q_j = 0, \tag{3}$$

where u_e is the potential at the CFN in the j-th element, q_j is the mean normal flux at central DFN of j-th element, and q_j and h_j are the following integrals:

$$g_j = \frac{1}{4\pi} \int_{\Gamma_j} \frac{1}{r} d\Gamma_j \tag{4}$$

$$h_j = -\frac{1}{4\pi} \int_{\Gamma_j} \frac{\mathbf{r}\cdot\hat{n}}{r^3} d\Gamma_j \tag{5}$$

The assembly scheme consists in appending one equation (2) per each selected source point $\mathbf{x}_i$ per sub-domain to the appropriate system of equations ($\mathbf{A}\,\mathbf{x} = \mathbf{b}$), where $\mathbf{A} \in R^{n\times m}$ contains the coefficients h_j and g_j, $\mathbf{x}$ is a 1-column array with the unknown u and q, $\mathbf{b}$ is the right hand side 1-column array formed by the boundary conditions. The matrix A will be presented in hierarchical format [6].

3 The method formulation

An initial BEM 3D model is decoupled into a number of independent sub-domains $\{\Omega_1, \Omega_2, \cdots, \Omega_N\}$ each of which usually has different material properties. Those sub-domains form the appropriate linear systems of equations $A_i x_i = b_i$ according to Section 2, where i is an index of sub-domain. The matrices $\{A_1, A_2, \ldots, A_N\}$ that correspond to the sub-domains $\Omega_1, \Omega_2, \ldots, \Omega_N$ are represented in hierarchical format [6]. Each sub-domain is solved independently taking into account the results from all its neighbors, i.e. each iteration includes the following stages:

1. The method forms an initial guess for q that is located on the interfaces between the current sub-domain A and all its adjacent neighbors. In general, as an initial guess either u or q can be considered, but for this particular explanation it is assumed that the initial guess is always q. In order to refresh the right-hand side vector $\mathbf{RHS}$, the initial guess has to be applied as the artificial Neumann boundary conditions. For the sake of simplicity, the part

of the coefficient matrix corresponding to the imposed artificial Neumann boundary conditions is allocated as a separate structure called refreshing matrix $\mathbf{R}$. Thus, each sub-domain forms the local LSE: $\mathbf{A\ x} + \mathbf{R\ Guess} = \mathbf{RHS}$.

2. Update the $\mathbf{RHS}$ vector of a local LSE with the current value of $\mathbf{Guess}$ vector.
3. Solve the system of equation $\mathbf{A_i\ x_i} + \mathbf{R_i\ Guess_i} = \mathbf{RHS_i}$ for the current sub-domain and obtain the fluxes and the potentials at each freedom node.
4. The potentials that are the result of previous step are imposed as the artificial Dirichlet boundary conditions to all adjacent neighbors. Consequently, all adjacent sub-domains have the new values for the potentials u.
5. For each sub-domain the following steps has to be performed: update the right hand side term with either artificial boundary conditions or imposed initial guess or both; solve the system of equations to get the normal fluxes at the freedom nodes.
6. Update the normal fluxes $q^*_{\Omega_1} = q_{\Omega_1} + (q_{\Omega_1} - q_{\Omega_2})/r$, where r is a relaxation factor $r > 1$.
7. Test the convergence

$$MAX(u_{n+1} - u_n)/u_n < error \tag{6}$$

where u_{n+1} is a value of the potential at $n+1$ iteration whereas u_n is at iteration n;

$$MAX(q_{\Omega_1} - q_{\Omega_2})/q_{\Omega_1} < error \tag{7}$$

where q_{Ω_1} is a value of a normal flux for the sub-domain Ω_1 and q_{Ω_2} is a value of the corresponding normal flux in sub-domain Ω_2. if (6-7) are not achieved return to step 2.

The system of equations for each sub-domain is computed and approximated only once at the very beginning of iterative scheme whereas the RHS is refreshed with every iteration.

An example (see Figure 1) shows how the iterative technique is applied.

The sub-domain Ω_1 has 6 surfaces and only 4 which the boundary conditions are known for, i.e. there are two surfaces with unknown boundary conditions. At the very beginning of iterative scheme, an initial guess has to be formed for those two surfaces, i.e. the boundary conditions for the normal flux over those surfaces have to be imposed. Hence, after this operation, the sub-domain Ω_1 has the boundary conditions for all surfaces. The coefficient matrix A^1_H can now be built and the RHS can be computed taking into account imposed boundary conditions q^1_1 and q^1_2. Once the system $A^1_H x_1 = RHS_1$ is solved and appropriate values for u^1_1 and u^1_2 are known, they can be applied as temporary Dirichlet-type boundary conditions to the sub-domains Ω_2 and Ω_3 appropriately. Then, the sub-domain Ω_2 has the boundary conditions for all surfaces excluding the only one, where an initial guess q^2_2 has to be applied again. Once the system $A^2_H x_2 = RHS_2$ is solved it will produce the BC for the sub-domain Ω_4. In this way, an initial guess q^3_2 has to be applied in order to produce the integrity of the whole system. The iterative scheme

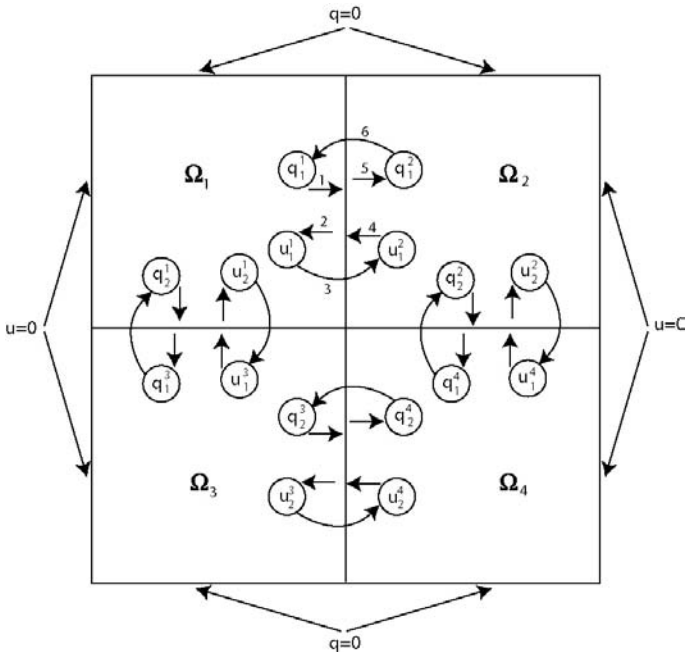

Figure 1: Iterative technique for BEM with multi-domain. The strategy for coupling two sub-domains consists of six steps: 1 - to solve the LSE for a local sub-domain taking into account the initial guess for the normal fluxes distributed over the interface, 2 - to get the solution for the potentials located on the same interface, 3 - use the solution for the potentials as the artificial BC which is at the same time the initial guess for the connected sub-domain (4), 5 - solve the LSE for the next sub-domain and get the solution for the normal fluxes, 6 - compare the solution for the normal fluxes with the initial guess for the first sub-domain.

for the sub-domain Ω_1 of the model demonstrated in Figure 1 is shown in Figure 2. At the next stage of iterative scheme, the new values for q_1^1, q_2^1, q_2^2 and q_2^3 has to be computed and appropriate RHS are refreshed. In order to do so, let's consider the sub-domains Ω_1 and Ω_2. Once the system $A_H^2 x_2 = RHS_2$ is solved taking into account an enforced value for u_1^2, an appropriate value for q_1^2 will be computed. In fact, q_1^1 and q_1^2 correspond to the normal flux of the same element and therefore they have to be compared in order to be adjusted for the next iteration. Having an initial value for q_1^1 from Ω_1 as well as a new one q_1^2 from Ω_2, those two values can be prepared for the next iteration according to the following expression:

$$q_1^{1^*} = q_1^1 + (q_1^1 - q_1^2)/r \tag{8}$$

where r is a relaxation factor $r > 1$, $q_1^{1^*}$ is a new value for q_1^1 from the sub-domain Ω_1.

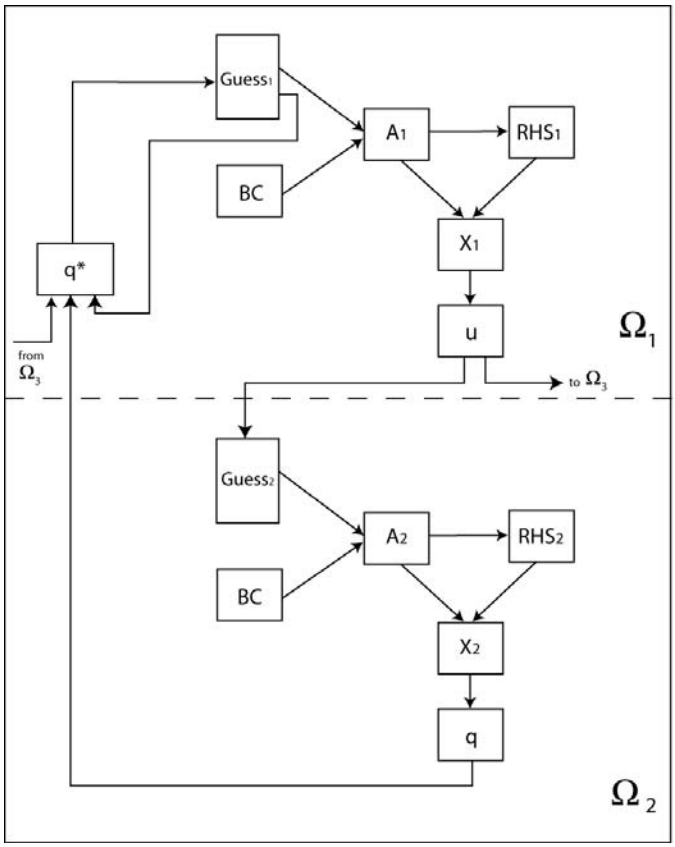

Figure 2: Coupling the sub-domains Ω_1 and Ω_2 of the model shown in Figure 1: $\mathbf{A}$ is the entire coefficient matrix, $\mathbf{RHS}$ is the corresponding right hand side, $\mathbf{BC}$ is the vector of known boundary conditions, $\mathbf{Guess}$ is the vector of the initial guess, $\mathbf{X}$ is the result vector and $\mathbf{u}$ and $\mathbf{q}$ are the vectors with the current results for the potentials and normal flux respectively.

In this way, all imposed BC has to be updated and the RHS refreshed. Once this is done, the next iteration starts. At the end of each iteration the convergence has to be tested in order to make a decision if more iterations are needed see eq.(6), i.e. if the maximal relative difference between the potential at current iteration and at the previous one is less than an appropriate $error$ which is set up in advance, then the scheme must stop. Instead of the potentials, the normal fluxes can be used.

Another expression (7) is for the normal fluxes only, i.e. if the maximal relative difference between all corresponding normal fluxes over the all interfaces shared between two volumes (in this case Ω_1 and Ω_2) is less than an appropriate $error$ which is set up in advance, then the scheme must stop. Both expressions (6-7) are used at the same time in order to secure the precision of iterative scheme.

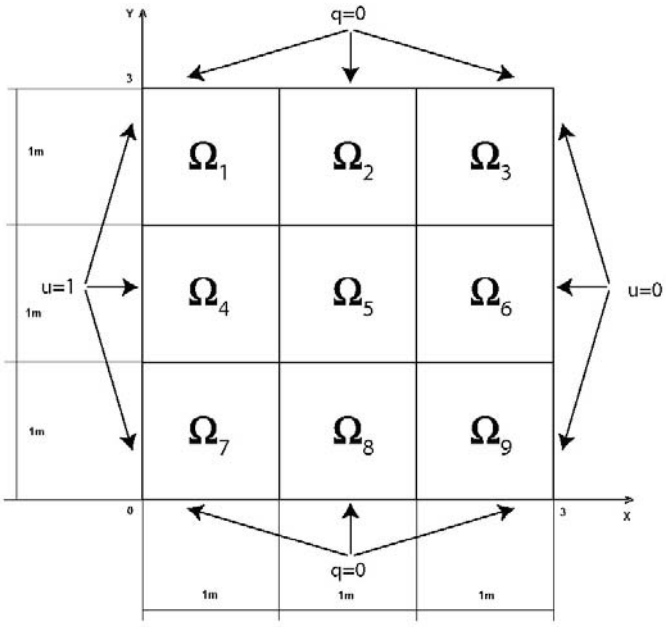

Figure 3: The front 2D representation of 3D BEM with a multi-domain model consisting of 27 sub-domains with uniformly distributed conductivity $k = 1$.

4 Case study

This section examines the theoretical example in order to verify the accuracy, storage requirements and the complexity of the solution of LSE for BEM with multi-domain using the ACA-based approach and iterative coupling.

4.1 The model description

The problem represents a Laplacian equation in a cube consisting of 27 sub-cubes coupled together as shown in Figure 3. The model is meshed with triangular constant elements involving different level of mesh refinement yielding up to 95504 BEs.

Despite the ability of the developed method to deal with the models where the sub-domains have different material properties, the conductivity of the sub-domains is selected to be the same everywhere $k = 1$. This allows to check the accuracy of the numerical solution against the analytical one which is known for the 'Cube-like' and in this particular case is defined as $u^{\mathbf{x}} = 1 - \mathbf{x}/3$ for the potentials, where $\mathbf{x}$ is the $\mathbf{x}$-component in 3D-coordinates $(\mathbf{x}, \mathbf{y}, \mathbf{z})$ of the DOF (see Figure 3).

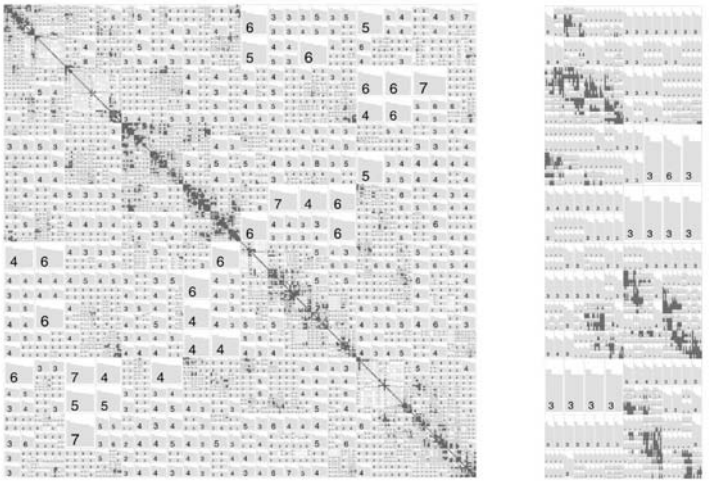

Figure 4: The coefficient H-matrix (to the right) and the refreshing H-matrix (to the left) for the sub-domain Ω_1 of the model shown in Figure 3 meshed with 22566 triangular BEs: dark blocks are Full-matrices and the grey ones are Rk-blocks.

Figure 4 demonstrates how the coefficient and refreshing matrix looks for a sub-domain Ω_1 of the model introduced in Figure 3 if it is meshed with 22566 BEs.

4.2 The numerical properties

Tables 1-4 demonstrate the numerical properties of the developed approach.

Table 1: The memory consumption (in Mb) required to store the coefficient and refreshing matrices depending on the ACA-error ε_{ACA} and N.

N/ε_{ACA}	1e-01	1e-02	1e-03	1e-04	1e-05
1944	3.1	3.1	3.1	3.1	3.1
5616	28.3	30.1	32.2	34.6	36.9
10604	63.2	75.9	89.4	105.9	113.4
22566	157.4	203.9	255.5	319.4	390.6
47568	275.5	462.2	649.5	882	1128
95504	833	1156	1509.2	-	-

Table 2: The CPU time (in sec) required to solve the LSE depending on the ACA-error ε_{ACA} and N.

N/ε_{ACA}	1e-01	1e-02	1e-03	1e-04	1e-05
1944	14	14	14	14	14
5616	19	20	23	25	26
10604	23	25	28	40	42
22566	63	68	77	98	119
47568	153	178	224	282	366
95504	390	425	-	-	-

Table 3: The second norm of the difference between the analytical S_{an} and numerical S_{num} solution $\varepsilon_{AN} = ||S_{an} - S_{num}||_2$ in function of both the number of DOFs N and ε_{ACA}.

N/ε_{ACA}	1e-01	1e-02	1e-03	1e-04	1e-05
1944	0.0071	0.0071	0.0071	0.0071	0.0071
5616	0.014	0.0037	0.0032	0.0032	0.0032
10604	0.024	0.0029	0.0026	0.0026	0.0026
22566	0.034	0.0029	0.0024	0.0024	0.0024
47568	0.051	0.011	0.01	0.01	0.01
95504	0.049	0.008	-	-	-

5 Conclusions

The memory consumption grows as the ε_{ACA} decreases as well as grows proportionally to the increase of N as shown in Table 1.

As it is observed, the compression ratio increases as the number of unknowns increases. Thus, the same model meshed with nearly 100.000 BEs has higher compression ratio (8.7%) than the model meshed with 10.000 of BEs (46.6%).

The method requires more CPU time if ε_{ACA} decreases as well as when the number of unknowns increases (see Table 2).

As is shown in Table 3, ε_{AN} decreases as the number of BEs increases. However, if the ACA-error ε_{ACA} is high, the error ε_{AN} may grow due to the fact that the off-diagonal blocks of the coefficient matrix are heavily approximated

Table 4: The compression ratio of the coefficient and refreshing matrices depending on the ACA-error ε_{ACA} and N.

N/ε_{ACA}	1e-01	1e-02	1e-03	1e-04	1e-05
1944	101.6	101.6	101.6	101.6	101.6
5616	82.6	89	96.4	104.8	113
10604	46.6	59.8	73.2	89.9	107.2
22566	27.2	36.5	46.8	59.4	73.4
47568	11.7	19.6	27.6	37.3	47.7
95504	8.7	12.1	15.8	-	-

causing the serious damage to the coefficient matrix. Nevertheless, in general case the higher level of mesh refinement improves the precision of the solution against the analytical one.

References

[1] Erhart K., Divo E., and Kassab A.J. A parallel domain decomposition boundary element method technique for large-scale transient heat conduction problems. *Numerical Heat Transfer*, 2006.

[2] P. Skerget M. Ribersek and I. Zagar. Boundary-domain integral method with subdomain technique for time dependent viscous flow. *Z. Angew Math. Mech*, 73:935–939, 1993.

[3] W. Florez, H. Power, and F. Chejne. Numerical solution of thermal convection problems using the multidomain boundary element method. *J. Num. Meth. for Partial Differential Equations*, 18(4):469–489, 2002.

[4] A. Peratta and V. Popov. A new scheme for numerical modelling of flow and transport processes in 3D fractured porous media. *Advances in Water Resources*, 29:42–61, 2006.

[5] M. Bebendorf and S. Rjasanov. Adaptive low-rank approximation of collocation matrices. *Computing*, 70:1–24, 2003.

[6] Lars Grasedyck Stefen Borm and Wolfgang Hackbusch. Hierarchical matrices. April 2005.

[7] C. Brebbia, J. Telles, and L. Wrobel. *Boundary Elements Techniques*. Splinger-Verlag, Berlin, Heidelberg, New York and Tokio, 1984.

[8] C. Brebbia and J.Dominguez. *Boundary Elements, an Introductory Course*. Computational Mechanics Publications. McGraw-Hill, New York, Colorado, San Francisco, Mexico, Toronto, 2nd edition, 1992.

Section 4
Advanced structural applications

This page intentionally left blank

Boundary element modelling of non-linear buckling for symmetrically laminated plates

S. Syngellakis[1] & N. Cherukunnath[2]
[1]*University of Southampton, UK*
[2]*Rolls Royce plc, UK*

Abstract

The non-linear buckling of composite laminates, triggered by geometric imperfections, is here analysed adopting a boundary element methodology. The non-linear theory for thin anisotropic plates couples in-plane forces causing buckling with the consequent bending deformation. The adopted formulation for in-plane forces in terms of the stress function is mathematically identical to that for the bending problem, thus boundary integral equations and fundamental solutions of the same form are used. Differential equations governing increments of the stress function and the deflection are obtained; the resulting integral equations include irreducible domain integrals depending on powers or products of the second derivatives of the stress function and the deflection. The latter are calculated through complementary integral equations obtained from the original ones by differentiating the field variables in the domain. The solution process accounts for the domain integrals through an iterative scheme; thus there is no need for modelling any field variables in the plate domain although domain meshing is necessary for performing numerical integrations. The boundary is meshed into quadratic discontinuous elements while the domain is divided into triangular cells with linear discontinuous variation of the relevant field variables for integration purposes. The analysis is implemented through a suit of C codes and applied to a rectangular symmetrically laminated plate. Its predictions are compared with published results obtained by other methods. The accuracy and limitations of the formulation are discussed and alternative approaches for expanding its scope pointed out.

Keywords: boundary elements, composites, laminates, postbuckling, initial imperfections, irreducible domain integrals.

WIT Transactions on Modelling and Simulation, Vol 49, © 2009 WIT Press
www.witpress.com, ISSN 1743-355X (on-line)
doi:10.2495/BE090191

1 Introduction

Laminated plate structures are used for a variety of functions in aerospace and other industries due to their favourable strength-to-weight ratio. During the fabrication of such structures, it is possible that small deviations from the intended, perfectly flat shapes may occur. These deviations, known as geometric imperfections, may alter significantly the buckling behaviour of a plate. The plate response to in-plane loads in the presence of imperfections is governed by a non-linear thin-plate theory which can predict the large deflections occurring at or above the critical buckling load.

Early numerical studies on the post-buckling behaviour of perfectly flat, rectangular orthotropic plates were based on series solutions for the deflection and the stress function [1–3]. This approach was extended to include the flexure-extension coupling terms as well as the effects of transverse shear and initial imperfections [4]. Shear deformation effects have also been studied through finite element analyses based on higher-order theories [5]. Such analyses have also allowed the assessment of boundary conditions [6]. Stiffened laminated panels have been analysed by a spline finite strip method also accounting for shear deformation [7].

The boundary element method (BEM) had originally been applied to the analysis of non-linear isotropic plate behaviour induced by high lateral loads [8]. Other incremental and iterative approaches extended the scope of BEM to predict the non-linear plate response to in-plane edge loading. Such a response can either be generated as a bifurcation from the fundamental equilibrium path at the critical load [9, 10] or initiated by imperfections [11]. There has not been any known attempt at analysing the post-buckling behaviour of anisotropic laminated plates using a BEM-based technique.

An analytical procedure is presented here whereby BEM modelling, based on classical plate theory, is combined with irreducible domain integrals involving the deflection curvatures and the membrane stresses. The non-linear plate response to in-plane loading initiated by imperfections is determined incrementally with the non-linear terms taken into account through iterations within each loading step. The proposed boundary element formulation for the post-buckling analysis of symmetrically laminated plates has the advantage of using the same type of fundamental solution and its derivatives for both the membrane stress and buckling analyses. This allows the use of non-uniform edge loads for the analysis while facilitating the programming effort.

2 Non-linear plate theory

The orientation of a plate is assumed such that its mid-plane coincides with the x_1-x_2 plane of a two-dimensional Cartesian frame of reference. Greek indices for the range from 1 to 2 and the summation convention for terms with repeated indices are adopted. Plates with initial imperfections $w^i(x_\alpha)$, when loaded in their plane, undergo some deflection $w(x_\alpha)$ before the theoretical critical buckling load is reached. The total plate deflection is given by

$$\hat{w} = w + w^i$$

The developing in-plane forces $N_{\alpha\beta}$ and bending moments $M_{\alpha\beta}$ satisfy the equations of equilibrium

$$N_{\alpha\beta,\beta} + f_\alpha = 0 \tag{1}$$

$$M_{\alpha\beta,\alpha\beta} + (N_{\alpha\beta}\,\hat{w}_{,\alpha})_{,\beta} + q = 0 \tag{2}$$

where $q(x_\alpha)$ is a lateral distributed force acting on the middle plane and f_α the body force, which may be derivable from a potential function V according to

$$f_\alpha = -V_{,\alpha} \tag{3}$$

The solution of eqns (1) and (2) should satisfy the boundary conditions

$$n_\beta N_{\alpha\beta} = \tilde{p}_\alpha \quad \text{or } u_\alpha = \tilde{u}_\alpha \tag{4}$$

$$n_\alpha M_{\alpha\beta,\beta} + s_\alpha s_\beta n_\kappa M_{\alpha\kappa,\beta} + \phi s_\alpha s_\beta M_{\alpha\beta} + n_\beta N_{\alpha\beta}\,\hat{w}_{,\alpha} = \tilde{V}_n + \tilde{p}_\alpha \hat{w}_{,\alpha} \quad \text{or } w = \tilde{w} \tag{5}$$

$$n_\alpha n_\beta M_{\alpha\beta} = \tilde{M}_n \quad \text{or } n_\alpha w_{,\alpha} = \tilde{\theta}_n \tag{6}$$

$$\left[\!\left[s_\alpha n_\beta M_{\alpha\beta} \right]\!\right]_j = \tilde{C}_j \quad \text{or } w_j = \tilde{w}_j \tag{7}$$

where u_α are the in-plane displacements, n_α, s_α are, respectively, the direction cosines of unit vectors normal and tangent to the plate boundary, ϕ is the boundary curvature; $\tilde{u}_\alpha$, $\tilde{w}$, $\tilde{\theta}_n$ are, respectively, prescribed boundary values of the in-plane displacements, deflection and deflection gradient relative to the boundary normal; $\tilde{p}_\alpha$, $\tilde{V}_n$, $\tilde{M}_n$, $\tilde{C}_j$ are, respectively, prescribed boundary values of the traction, shear force, bending moment in the plane of the boundary normal, force at boundary corner j.

The constitutive equations for symmetrically laminated plates are

$$N_{\alpha\beta} = A_{\alpha\beta\gamma\delta}\varepsilon_{\gamma\delta} \tag{8}$$

$$M_{\alpha\beta} = D_{\alpha\beta\gamma\delta}\kappa_{\gamma\delta} \tag{9}$$

where the mid-plane strains $\varepsilon_{\alpha\beta}$ and deflection curvatures $\kappa_{\alpha\beta}$ are related to the displacements by

$$\varepsilon_{\alpha\beta} = \frac{1}{2}(u_{\alpha,\beta} + u_{\beta,\alpha} + \hat{w}_{,\alpha}\,\hat{w}_{,\beta} - w^i{}_{,\alpha}\,w^i{}_{,\beta}) \tag{10}$$

$$\kappa_{\alpha\beta} = -w_{,\alpha\beta} \tag{11}$$

The compatibility condition is obtained by eliminating the in-plane displacements from eqn (10). This is accomplished by defining the operator

$$L_{\alpha\beta} = \delta_{\alpha\beta}\nabla^2 - \partial_\alpha \partial_\beta \tag{12}$$

and applying it to both sides of eqn (10) leading to:

$$L_{\alpha\beta}\varepsilon_{\alpha\beta} = \frac{1}{2}[\, L_{\alpha\beta}(\,\hat{w},_{\alpha}\ \hat{w},_{\beta}\,) - L_{\alpha\beta}(\,w^{i},_{\alpha}\ w^{i},_{\beta}\,)] \tag{13}$$

It can be shown that

$$L_{\alpha\beta}(w,_{\alpha}\, w,_{\beta}) \ = -\,(L_{\alpha\beta}\, w)w,_{\alpha\beta} \tag{14}$$

Hence the compatibility condition, eqn (13), becomes

$$L_{\alpha\beta}\varepsilon_{\alpha\beta} = -\frac{1}{2}\,[L_{\alpha\beta}(\,\hat{w}\,)\,\hat{w},_{\alpha\beta} - L_{\alpha\beta}(\,w^{i}\,)\,w^{i},_{\alpha\beta}\,] \tag{15}$$

Defining $A^{-1}_{\alpha\beta\gamma\delta}$ as the inverse of $A_{\alpha\beta\gamma\delta}$:

$$A^{-1}_{\alpha\beta\gamma\delta}\, A_{\gamma\delta\lambda\mu} = \delta_{\alpha\lambda}\delta_{\beta\mu}, \tag{16}$$

constitutive eqn (8) is re-arranged to

$$\varepsilon_{\alpha\beta} \ = A^{-1}_{\alpha\beta\gamma\delta}\, N_{\gamma\delta}. \tag{17}$$

Introducing the stress function F such that

$$N_{\alpha\beta} = \ L_{\alpha\beta}F + \delta_{\alpha\beta}\, V, \tag{18}$$

compatibility eqn (15) can be expressed in terms of F and w:

$$L_{\alpha\beta}[\ A^{-1}_{\alpha\beta\gamma\delta}\ (L_{\gamma\delta}F + \delta_{\gamma\delta}\, V) = -\frac{1}{2}\,[L_{\alpha\beta}(\,\hat{w}\,)\,\hat{w},_{\alpha\beta} - L_{\alpha\beta}(\,w^{i}\,)\,w^{i},_{\alpha\beta}\,] \tag{19}$$

Using constitutive eqn (9), curvature-deflection relation (11) and expressing the in-plane forces in terms of the stress function according to eqn (18), equilibrium eqn (2) can also be written in terms of F and w:

$$-\,D_{\alpha\beta\gamma\delta}\, w,_{\alpha\beta\gamma\delta} + [(L_{\alpha\beta}F + \delta_{\alpha\beta}\, V)\,\hat{w},_{\alpha}\ ],_{\beta} + q = 0 \tag{20}$$

In the absence of body forces and lateral pressure, the only external action is that due to in-plane tractions causing non-linear buckling. Thus, field equations (19) and (20) are reduced to

$$\hat{A}_{\alpha\beta\gamma\delta}\, F,_{\alpha\beta\gamma\delta} = -\frac{1}{2}\,[L_{\alpha\beta}(\,\hat{w}\,)\,\hat{w},_{\alpha\beta} - L_{\alpha\beta}(\,w^{i}\,)\,w^{i},_{\alpha\beta}\,] \tag{21}$$

$$D_{\alpha\beta\gamma\delta}\, w,_{\alpha\beta\gamma\delta} = (L_{\alpha\beta}F)\ \ \hat{w},_{\alpha\beta} \tag{22}$$

where

$$\hat{A}_{\alpha\beta\gamma\delta} \ = \ A^{-1}_{\kappa\kappa\lambda\lambda}\ \delta_{\alpha\beta}\delta_{\gamma\delta} - \ A^{-1}_{\alpha\beta\kappa\kappa}\ \delta_{\gamma\delta} - \ A^{-1}_{\kappa\kappa\gamma\delta}\ \delta_{\alpha\beta} + A^{-1}_{\alpha\beta\gamma\delta} \tag{23}$$

An incremental procedure is adopted for the solution of the non-linear system of eqns (21) and (22). The two field variables are incremented by small amounts

such that $F \rightarrow F + \delta F$, $w \rightarrow w + \delta w$ and the field equations governing the increments are derived as follows

$$\hat{A}_{\alpha\beta\gamma\delta}\,\delta F_{,\alpha\beta\gamma\delta} = -L_{\alpha\beta}(\hat{w})\delta w_{,\alpha\beta} + \frac{1}{2}L_{\alpha\beta}(\delta w)\delta w_{,\alpha\beta} \tag{24}$$

$$D_{\alpha\beta\gamma\delta}\,\delta w_{,\alpha\beta\gamma\delta} = (L_{\alpha\beta}\,\hat{w})\delta F_{,\alpha\beta} + (L_{\alpha\beta}F)\delta w_{,\alpha\beta} + (L_{\alpha\beta}\delta F)\delta w_{,\alpha\beta} \tag{25}$$

The field variable increments should also satisfy the boundary conditions

$$\delta p_\alpha = n_\beta \delta N_{\alpha\beta} = \delta \tilde{p}_\alpha \text{ or } \delta u_\alpha = \delta \tilde{u}_\alpha \tag{26}$$

$$\delta V_n + \delta p_\alpha \hat{w}_{,\alpha} + (p_\alpha + \delta p_\alpha)\delta w_{,\alpha} = \delta \tilde{V}_n \text{ or } \delta w = \delta \tilde{w} \tag{27}$$

$$\delta M_n = \delta \tilde{M}_n \text{ or } \delta \theta_n = \delta \tilde{\theta}_n \tag{28}$$

$$\delta C_j = [\![\delta M_{ns}]\!]_j = \delta \tilde{C}_j \text{ or } \delta w_j = \delta \tilde{w}_j \tag{29}$$

which are derived from eqns (4)-(7).

3 Boundary integral equations for the linear operators

The left-hand sides of both field eqns (21) and (22) or both incremental eqns (24) and (25) involve linear operators in the form

$$\Lambda^c(u) = C_{\alpha\beta\gamma\delta}\,u_{,\alpha\beta\gamma\delta} \tag{30}$$

where $C_{\alpha\beta\gamma\delta}$ is a symmetric fourth-order constant tensor and $u(x_1,x_2)$ a function defined in the two-dimensional domain Ω bounded by contour Γ. Due to the symmetry of $C_{\alpha\beta\gamma\delta}$, the reciprocity relation

$$\int_\Omega C_{\alpha\beta\gamma\delta} u_{,\alpha\beta}\, u^*_{,\gamma\delta}\, \mathrm{d}\Omega = \int_\Omega C_{\alpha\beta\gamma\delta} u^*_{,\alpha\beta}\, u_{,\gamma\delta}\, \mathrm{d}\Omega \tag{31}$$

can be derived, where $u^*(x_1,x_2)$ is a second function, also defined in Ω. Integrating by parts both sides of eqn (31), applying Green's theorem and defining the operators

$$M_n^c(u) = -C_{\alpha\beta\gamma\delta} n_\alpha n_\beta u_{,\gamma\delta} \tag{32}$$

$$M_{ns}^c(u) = -C_{\alpha\beta\gamma\delta} n_\alpha s_\beta u_{,\gamma\delta} \tag{33}$$

$$V^c(u) = -(C_{\alpha\beta\gamma\delta} n_\alpha + C_{\alpha\kappa\gamma\delta} s_\alpha s_\beta n_\kappa)\, u_{,\beta\gamma\delta} - \phi\, C_{\alpha\beta\gamma\delta} s_\alpha s_\beta u_{,\gamma\delta}, \tag{34}$$

eqn (31) is transformed to:

$$\int_\Omega [u^* \Lambda^c(u) - u \Lambda^c(u^*)]\mathrm{d}\Omega + I_b^c(u,u^*) + J^c(u,u^*) = 0 \tag{35}$$

where ϕ is the curvature of the boundary contour Γ and

$$I_b^c(u,u^*) = \int_\Gamma [u^* V^c(u) - M_n^c(u)\theta_n(u^*) + M_n^c(u^*)\theta_n(u) - uV^c(u^*)]\mathrm{d}\Gamma \tag{36}$$

$$J^c(u,u^*) = \sum_{j=1}^{K} \left\{ \left[\!\left[M_{ns}^c(u) \right]\!\right]_j u_j^* - \left[\!\left[M_{ns}^c(u^*) \right]\!\right]_j u_j \right\} \tag{37}$$

where K is the number of corners along a non-smooth boundary Γ. Relative to the local **n**-**s** frame of reference relative to Γ:

$$M_n^c(u) = -C_{\alpha\beta\gamma\delta} n_\alpha n_\beta (n_\gamma n_\delta \frac{\partial u^2}{\partial n^2} + 2n_\gamma s_\delta \frac{\partial u^2}{\partial n \partial s} + s_\gamma s_\delta \frac{\partial u^2}{\partial s^2})$$

$$= -(C_{nnnn} \frac{\partial u^2}{\partial n^2} + 2C_{nnns} \frac{\partial u^2}{\partial n \partial s} + C_{nnss} \frac{\partial u^2}{\partial s^2}) \tag{38}$$

$$M_{ns}^c(u) = -C_{\alpha\beta\gamma\delta} n_\alpha s_\beta (n_\gamma n_\delta \frac{\partial u^2}{\partial n^2} + 2n_\gamma s_\delta \frac{\partial u^2}{\partial n \partial s} + s_\gamma s_\delta \frac{\partial u^2}{\partial s^2})$$

$$= -(C_{nsnn} \frac{\partial u^2}{\partial n^2} + 2C_{nsns} \frac{\partial u^2}{\partial n \partial s} + C_{nsss} \frac{\partial u^2}{\partial s^2}) \tag{39}$$

Eqn (35) is transformed into a pair of boundary integral equations if u^* is replaced by the fundamental solutions u_λ^*; $\lambda = 1,2$, satisfying

$$C_{\alpha\beta\gamma\delta} u_{\lambda,\alpha\beta\gamma\delta}^* = \delta_\lambda(\mathbf{x} - \boldsymbol{\xi}) \tag{40}$$

with

$$\delta_1(\mathbf{x} - \boldsymbol{\xi}) = \delta(\mathbf{x} - \boldsymbol{\xi}) \tag{41}$$

$$\delta_2(\mathbf{x} - \boldsymbol{\xi}) = \partial\delta(\mathbf{x} - \boldsymbol{\xi})/\partial m(\boldsymbol{\xi}) \tag{42}$$

where $\delta(\mathbf{x} - \boldsymbol{\xi})$ is the delta function representing a unit action at the source point $\boldsymbol{\xi}$ and **m** a unit vector of arbitrary direction emanating from the source point. Substituting u_λ^* in eqn (35) and taking $\boldsymbol{\xi}$ to the boundary so that **m** becomes normal to it, gives

$$\int_\Omega (\Lambda_C u) u_\lambda^* \mathrm{d}\Omega - k u_\lambda(\boldsymbol{\xi}) + I_C^b(u,\, u_\lambda^*) + J_C(u,\, u_\lambda^*) = 0 \tag{43}$$

where $u_1 = u$, $u_2 = \partial u/\partial m$ and $k = 0.5$ along a smooth boundary. Expressions for u_λ^* can be found in earlier, linear BEM analyses of laminated plates [12].

4 Integral equations for the non-linear problem

Integral eqn (43) is applied to both extensional and flexural problems governed, respectively, by incremental eqns (24) and (25):

$$-k\delta F_\lambda(\boldsymbol{\xi}) + I_A^b(\delta F,\ F_\lambda^*) + J_A(\delta F,\ F_\lambda^*) + I_F^d(w_{,\alpha\beta},\ \delta w_{,\alpha\beta},\ F_\lambda^*) = 0 \tag{44}$$

$$-k\delta w_\lambda(\boldsymbol{\xi}) + I_D^b(\delta w,\ w_\lambda^*) + J_D(\delta w,\ w_\lambda^*) + I_w^d(F_{,\alpha\beta},\ \delta F_{,\alpha\beta},\ w_{,\alpha\beta},\ \delta w_{,\alpha\beta},\ w_\lambda^*) = 0 \tag{45}$$

where

$$I_F^d(w_{,\alpha\beta},\ \delta w_{,\alpha\beta},\ F_\lambda^*) = \int_\Omega (-L_{\alpha\beta}\hat{w} + \frac{1}{2}L_{\alpha\beta}\delta w)\delta w_{,\alpha\beta}\ F_\lambda^* \mathrm{d}\Omega$$

$$I_w^d(F_{,\alpha\beta},\ \delta F_{,\alpha\beta},\ w_{,\alpha\beta},\ \delta w_{,\alpha\beta},\ w_\lambda^*) = \int_\Omega [L_{\alpha\beta}\hat{w}\delta F_{,\alpha\beta} + L_{\alpha\beta}(F+\delta F)\delta w_{,\alpha\beta}]w_\lambda^* \mathrm{d}\Omega$$

The domain values of the stress function and deflection increments are obtained by setting $k = \lambda = 1$ in eqns (44) and (45) and recalling that $F_1 = F,\ F_1^* = F^*$, $w_1 = w,\ w_1^* = w^*$, so that

$$\delta F(\boldsymbol{\xi}) = I_A^b(\delta F,\ F^*) + J_A(\delta F,\ F^*) + I_F^d(w_{,\alpha\beta},\ \delta w_{,\alpha\beta},\ F^*) \tag{46}$$

$$\delta w(\boldsymbol{\xi}) = I_D^b(\delta w,\ w^*) + J_D(\delta w,\ w^*) + I_w^d(F_{,\alpha\beta},\ \delta F_{,\alpha\beta},\ w_{,\alpha\beta},\ \delta w_{,\alpha\beta},\ w^*) \tag{47}$$

Thus, the incremental 2nd order derivatives of the stress function and deflection are obtained from

$$\delta F_{,\gamma\delta}(\boldsymbol{\xi}) = I_A^b(\delta F,\ F^*{}_{,\gamma\delta}) + J_A(\delta F,\ F^*{}_{,\gamma\delta}) + I_F^d(w_{,\alpha\beta},\ \delta w_{,\alpha\beta},\ F^*{}_{,\gamma\delta}) \tag{48}$$

$$\delta w_{,\gamma\delta}(\boldsymbol{\xi}) = I_D^b(\delta w,\ w^*{}_{,\gamma\delta}) + J_D(\delta w,\ w^*{}_{,\gamma\delta}) + I_w^d(F_{,\alpha\beta},\ \delta F_{,\alpha\beta},\ w_{,\alpha\beta},\ \delta w_{,\alpha\beta},\ w^*{}_{,\gamma\delta}) \tag{49}$$

5 Solution procedure

Boundary element modelling of the plate contour, introduced to integral eqns (44) and (45) as well as (48) and (49) leads to the incremental solution of the problem governing the post-buckling behaviour of a symmetrically laminated plate. The variables δF and $\partial(\delta F)/\partial n$ in boundary integrals $I_A^b(\delta F, F_\lambda^*;\ \lambda = 1,2)$ on the right-hand side of eqns (44) and (48) are functions of the edge traction increments $\delta\tilde{p}_\alpha$ [12]. The distribution of the other two boundary variables $M_n(\delta F)$ and $V_n(\delta F)$ in the same integrals are unknown.

The deflection-related unknown boundary variables in boundary integrals $I_D^b(\delta w, w_\lambda^*;\ \lambda = 1,2)$ on the right-hand side of eqns (45) and (49) are consistent with the specified boundary conditions among eqns (27)-(29). The boundary is discretised into quadratic discontinuous elements for evaluating the boundary integrals and the domain is discretised into linear discontinuous cells for the evaluation of domain integrals. The incremental membrane stresses and curvatures at points inside the domain are obtained using eqns (48) and (49).

All the incremental values are assumed zero at the beginning of each step. At the first step and first iteration, an assumed pattern of very small initial imperfection w^i is considered as the total deflection $\hat{w}$ over the domain. The unknown boundary distributions of $M_n(\delta F)$ and $V_n(\delta F)$ are obtained for an increment of edge traction $\delta \tilde{p}_\alpha$ by solving eqns (44) with $I_F^d(w_{,\alpha\beta}, \delta w_{,\alpha\beta}, F_\lambda^*; \lambda = 1,2)$ set equal to zero. The incremental membrane stresses at domain cell nodes are obtained using eqn (48). The distributions of unknown deflection-related variables on the boundary are obtained by solving eqns (45). The domain integrals $I_w^d(F_{,\alpha\beta}, \delta F_{,\alpha\beta}, w_{,\alpha\beta}, \delta w_{,\alpha\beta}, w_\lambda^*; \lambda = 1,2)$ are evaluated using the incremental membrane stresses obtained previously. The incremental deflections and curvatures at domain cell nodes are obtained using eqns (47) and (49), respectively. Replacing the incremental values of membrane stresses and curvatures by the new values, the procedure is repeated in an iterative manner until the specified convergence criteria are satisfied. The adopted convergence criterion for the deflection after j^{th} iterations is:

$$\frac{\sum_{i=1}^{N_d} \left| (\delta w_i)^j - (\delta w_i)^{j-1} \right|}{\sum_{i=1}^{N_d} \left| (\delta w_i)^j \right|} \le 0.0005 \tag{50}$$

where N_d is the number of domain cell nodes. Similar criteria for the incremental membrane stresses are also imposed in order to reduce the error accumulated at each step. The final incremental values of the last iteration in the previous step are added to the membrane stresses, deflections and curvatures for the next step. The solution procedure is carried out in a similar manner for further steps. The procedure at $(i+1)^{\text{th}}$ step is summarised as follows:

(1) From step i, $\hat{w}$, $\hat{w}_{,\alpha\beta}$ and $N_{\alpha\beta}$ are known.

(2) For step $(i+1)$, $\delta w_{,\alpha\beta}$ are set equal to zero for the 1st iteration, otherwise taken from the previous iteration.

(3) Domain integrals $I_F^d(w_{,\alpha\beta}, \delta w_{,\alpha\beta}, F_\lambda^*; \lambda = 1,2)$ are evaluated using the curvatures of the i^{th} step and the incremental curvatures from the previous iteration within the $(i+1)^{\text{th}}$ step.

(4) Eqns (44) are solved for the unknown boundary variables and then the incremental membrane stresses are evaluated at domain cell nodes using eqn (48).

(5) Domain integrals $I_w^d(F_{,\alpha\beta}, \delta F_{,\alpha\beta}, w_{,\alpha\beta}, \delta w_{,\alpha\beta}, w_\lambda^*; \lambda = 1,2)$, are evaluated using membrane stresses and curvatures from the i^{th} step and the incremental membrane stresses and curvatures from the previous iteration within the $(i+1)^{\text{th}}$ step.

(6) Eqns (45) are solved for unknown boundary variables and then the incremental deflection and curvatures are evaluated at domain cell nodes using eqns (47) and (49), respectively.

(7) Convergence criteria are applied.

(8) If the convergence criteria are satisfied, the procedure moves to the next step, otherwise steps 2 to 6 are repeated.
(9) Before moving to the next step (i+2), the values of $\hat{w}$, $\hat{w}_{,\alpha\beta}$ and $N_{\alpha\beta}$ are updated by adding the incremental values from the last iteration within step (i+1).

6 Results

The proposed BEM formulation for the post-buckling analysis of laminated plates was implemented through a suite of C codes. The analysis was applied to a simply-supported square plate with a side length of 1.0 m and a thickness of 10 mm, subjected to uni-axial, uniformly distributed compressive loads along the stiffer direction. Two cases were analysed corresponding to different initial imperfection patterns with maximum values of 0.5 and 5 mm. The flexural rigidities and extensional stiffness of the plate were

D_{11} = 16692.7 Nm D_{22} = 417.319 Nm
D_{66} = 250.0 Nm D_{12} = 417.319 Nm
$A_{11} = 2.00313\times10^{9}$ N/m $A_{22} = 5.00782\times10^{7}$ N/m
$A_{12} = 1.25196\times10^{7}$ N/m $A_{66} = 3.0\times10^{7}$ N/m

The boundary was discretised into 80 quadratic discontinuous elements with 50 linear domain cells over the plate. The results were compared with the corresponding solution for a perfectly flat plate given by Prabhakara and Chia [1], which was based on a double Fourier series for the transverse deflection and a double series for the stress function consisting of appropriate beam functions. The results are in good agreement for the range of post-buckling deflection shown in Figure 1. The present method relies heavily on iterations and its performance depends upon various factors like step size, the degree of non-linearity, the convergence criteria and the rate change of slope of load-deflection curve. Thus, further parametric studies are required for identifying an optimised procedure for the solution. Alternative solution procedures whereby iterations may be avoided or their number significantly reduced are described in the next section.

7 Concluding remarks

A large deformation analysis leading to the prediction of the post-buckling behaviour was developed as an expansion and coupling of the formulations for linear analyses [12]. This problem is of considerable design interest since its output is linked more closely than the critical load to the strength limits of stiffened composite panels. The analysis performed shows that the present procedure is highly dependent on the size of load step, the number of iterations within each step, which is controlled by convergence criteria, and the degree of non-linearity. The size of load step should be reduced near the critical load and within the post-buckling region. Further validation of the proposed procedure is

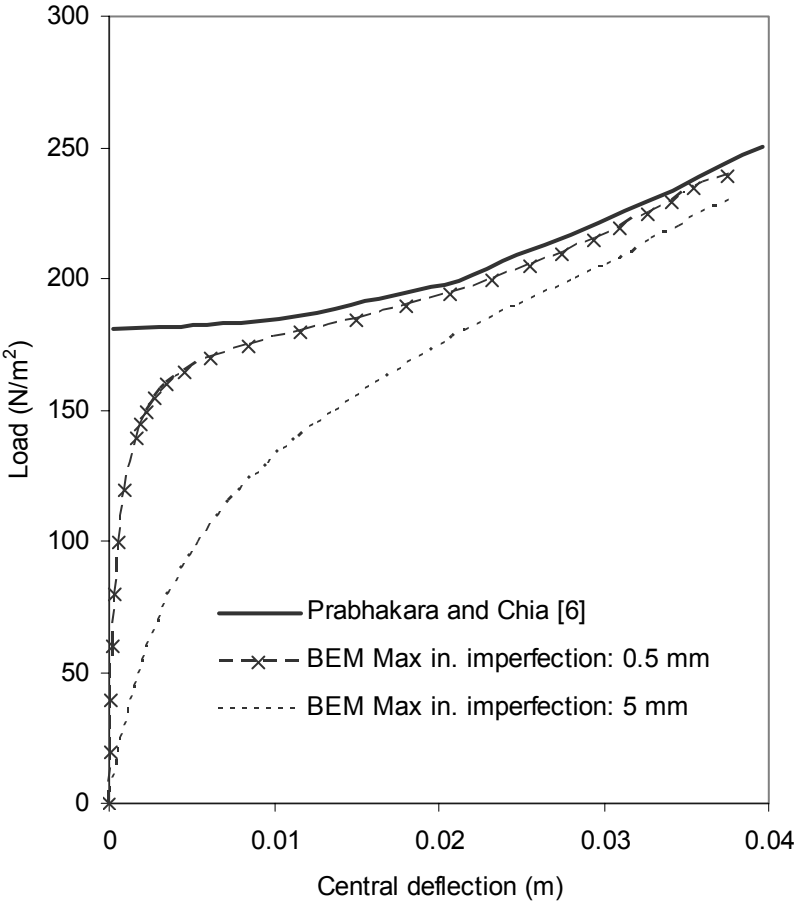

Figure 1: Non-linear load-deflection curves for different initial imperfections for a simply supported plate under uni-axial uniform loading.

required for developing an optimised, efficient analysis in terms of computational cost.

The advantage of the boundary element method relies on the existence of a boundary integral equation that reduces the dimensions of a problem by one thus leading to its more efficient formulation and solution. This basic advantage of BEM is to a certain extent compromised by the presence of irreducible domain integrals in the integral equations governing the plate post-buckling problem. Transformation of such integrals into boundary ones is therefore desirable and could be achieved by adopting suitable approximate representations of the domain unknowns.

The performance of the proposed scheme may be improved by dividing each step into two sub-steps. Within the first of those sub-steps, the solution is carried out without considering the quadratic terms in the unknown increments appearing in the domain integrals of eqns (44) and (45). This will allow the direct solution of eqns (44) and the determination of the incremental membrane stresses over the domain from eqn (48). A consistent system of equations, containing the deflection-related boundary unknowns and the domain curvatures, is also obtained from integral eqns (45) and (49). After determining all incremental quantities, the result is further corrected by including the quadratic terms in the domain integrals and solving the system iteratively within the second sub-step of the current load step.

An alternative scheme would rely on a model for the deflection that would allow the numerical evaluation of the curvatures on which the domain integrals in the post-buckling eqns (44) and (45) depend. This can be achieved by adopting non-linear interpolation models in the form of higher order polynomials or trigonometric functions. The curvatures can be obtained by differentiating these models, which leads to a direct relationship between nodal cell curvatures and deflections. An additional system of equations for the deflections can be obtained from integral eqn (47). By eliminating the membrane stresses and the curvatures over the plate domain, the final system of equations would contain only the deflection-related boundary variables and domain deflections as unknowns. As with the previously described scheme, the solution can be initially carried out neglecting the quadratic terms in the domain integrals. After the determination of all incremental quantities, the result can be further corrected by including these quadratic terms and solving the system iteratively within the current load step. This approach may lead to a reduction and a more efficient use of iterations towards an accurate and stable solution.

References

[1] Prabhakara, M.K. & Chia, C.Y., Post-buckling behaviour of rectangular orthotropic plates. *Journal of Mechanical Engineering Science*, **15(1)**, pp. 25-33, 1973.

[2] Stein, M., Postbuckling of orthotropic composite plates loaded in compression. *AIAA Journal*, **21(12)**, pp. 1729-1735, 1983.

[3] Stein, M., Postbuckling of long orthotropic plates under combined loading. *AIAA Journal*, **23(8)**, pp. 1267-1272, 1985.

[4] Minguet, P.J., Dugundji, J. & Lagace, P., Postbuckling behavior of laminated plates using a direct energy-minimization technique. *AIAA Journal*, **27(12)**, pp. 1785-1792, 1989.

[5] Shiau, L.C. & Wu, T.Y., Application of the finite-element method to postbuckling analysis of laminated plates. *AIAA Journal*, **33(12)**, pp. 2379-2385, 1995.

[6] Carrera, E. & Villani, M., Effects of boundary conditions on postbuckling of compressed, symmetrically laminated thick plates. *AIAA Journal*, **33(8)**, pp. 1543-1546, 1995.

[7] Dawe, D.J. & Wang, S., Postbuckling analysis of composite laminated panels. *AIAA Journal*, **38(11)**, pp. 2160-2170, 2000.
[8] Tanaka, M., Integral equation approach to small and large displacement of thin elastic plates. *Boundary Element Methods in Engineering: Proc. of the 4th International Seminar*, ed. C.A. Brebbia, Springer-Verlag: Berlin, pp. 526-539, 1983.
[9] Qin, Q. & Huang, Y., BEM of post-buckling analysis of thin plates. *Applied Mathematical Modelling*, **14**, pp. 544-548, 1990.
[10] Tanaka, M., Matsumoto, T. & Zheng, Z., An incremental approach to the pre/post buckling problem of thin elastic plates via boundary-domain element method. *Boundary Element Methods*, ed. M. Tanaka & Z. Yao, Elsevier Science: Oxford, pp. 3-14, 1996.
[11] Elzein, A. & Syngellakis, S., High-order elements for the BEM stability analysis of imperfect plates. *Advances in Boundary Elements, Vol. 3: Stress Analysis*, ed. C.A. Brebbia & J.J. Connor, Springer-Verlag: Berlin, pp. 269-289, 1989.
[12] Syngellakis, S. & Cherukunnath, N., Boundary element analysis of symmetrically laminated plates. *Engineering Analysis with Boundary Elements*, **28(9)**, pp. 1005-1016, 2004.

Effective properties of fibers with various ratios of phase stiffness

P. Procházka
CTU Prague, Civil Engineering, Prague, Czech Republic

Abstract

In the paper a new procedure for effective properties of nonlinear composites will be proposed. Based on boundary element method various ratios of phase stiffnesses are studied. Special properties of the stress distribution (or concentration factors) on a unit cell are utilized. The overall properties start with Hashin-Shtrikman idea, which is transformed to a numerical framework. Without loss of generality geometrical boundary conditions on the boundary of a unit cell are prescribed in this study. A special case of the presented approach is the effect of pore pressure, occurring in fiber reinforced concrete, for example. Also nonlinear behavior of the phases is taken into consideration, especially the von Mises-Huber-Hencky criterion is adopted in the model of matrix. The examples are exclusively prepared for two-phase materials.

Keywords: boundary element method, various stiffness of phases, plasticity, Hashin-Shtrikman variational principle.

1 Introduction

Eigenstresses and eigenstrains play a very important role in many branches of applied mechanics, e.g., in composites, geotechnics, concrete structures, etc. In previous papers, the authors have formulated an effective approach to the analysis and optimization of inhomogeneous bodies with prescribed boundary displacements or tractions and have used the transformation field analysis for relating the components of stress or strain tensors and of eigenstrains or eigenstresses. The transformation field analysis established by Dvorak and Procházka in [1] has been applied to localization of stresses and strains in two-phase composites. The eigenstresses stood for relaxation stresses while eigenstrains represented plastic strains. This idea was extended in [2], where

WIT Transactions on Modelling and Simulation, Vol 49, © 2009 WIT Press
www.witpress.com, ISSN 1743-355X (on-line)
doi:10.2495/BE090201

applications of a large scale of combinations of internal material situations using boundary element method with eigenstress of composite structures were considered.

In [3] an attempt for obtaining effective material properties of a nonlinear isotropic composite has been made, using the basic ideas of Hashin and Shtrikman, [4]. A new variational approach was proposed that provides the effective energy potentials of nonlinear composites in terms of the corresponding energy potentials for linear composites with the same microstructural distributions.

Our approach is based on the idea of extended Hashin-Shtrikman variational principles for nonhomogeneous bodies. By means of internal parameters, eigenstrains or eigenstresses, involved in H-S principles, it is possible to obtain new bounds on mechanical properties of the trial material, increase the bearing capacity of structures, and to minimize the stress excesses.

2 Basic relations

We start with basic relations which are valid in mechanics of continuum and are appropriate for our next considerations. Denote by Ω a bounded domain, $\Gamma \equiv \Gamma_u \cup \Gamma_p, \Gamma_u \cap \Gamma_p = 0$, being its Lipschitz's boundary, both representing the trial body. On Γ_u the displacement vector $\boldsymbol{u} = \{u_1, u_2, u_3\}$ is prescribed, and on Γ_p the vector of tractions $\boldsymbol{p} = \{p_1, p_2, p_3\}$ is given. Recall the relation stresses-tractions on the boundary $\Gamma_p : p_i = \sigma_{ij} n_j$, where $\boldsymbol{n} \equiv \{n_1, n_2, n_3\}$ is the outward unit normal to the boundary, $\sigma_{ij}, \varepsilon_{ij}$ are components of stress and strain tensors, respectively.

Hooke's law for anisotropic and inhomogeneous field is introduced in the form

$$\sigma_{ij}(\boldsymbol{x}) = L_{ijkl}(\boldsymbol{x})\varepsilon_{kl}(\boldsymbol{x}) + \lambda_{ij}(\boldsymbol{x}), \quad \varepsilon_{ij}(\boldsymbol{x}) = M_{ijkl}(\boldsymbol{x})\sigma_{kl}(\boldsymbol{x}) + \mu_{ij}(\boldsymbol{x}) \tag{1}$$

where λ_{ij} are components of the eigenstress tensor, μ_{ij} are the components of the eigenstrain tensor, $\boldsymbol{x}$ is a position at which the material relations are studied, L_{ijkl} are components of the material stiffness tensor and M_{ijkl} describe its compliance material tensor, both with the standard symmetry; the subscripts i, j, k, l run the set {1, 2, 3},

Moreover, we have

$$L_{ijkl} M_{klmn} = I_{ijmn}, \qquad I_{ijmn} = \frac{1}{2}(\delta_{im}\delta_{jn} + \delta_{in}\delta_{jm}) \tag{2}$$

where I_{ijmn} characterises the fourth-order unit tensor, δ_{ij} is the Kronecker delta being equal to one for $i = j$ and zero otherwise.

Note that for a homogeneous and isotropic material the material stiffness matrix has the form

$$L_{ijkl} = \lambda\delta_{ij}\delta_{kl} + 2\mu I_{ijkl} \tag{3}$$

where λ and μ are Lame's constants. Instead of μ, the shear modulus G is sometimes introduced.

Comparing both equations (1), we get

$$\lambda_{ij} = -L_{ijkl}\mu_{kl}, \quad \mu_{ij} = -M_{ijkl}\lambda_{kl} \tag{4}$$

Kinematic equations may be written as

$$\varepsilon_{ij} = \frac{1}{2}\left(\frac{\partial u_i}{\partial x_j} + \frac{\partial u_j}{\partial x_i}\right) \tag{5}$$

Note that displacements are said to be kinematically admissible if the relation (5) holds.

Eventually, static equations or equations of equilibrium yield

$$\frac{\partial \sigma_{ij}}{\partial x_j} = 0 \tag{6}$$

provided no volume weight forces are taken into account. The last relation has to be taken in the sense of distributions.

Note that one says that the stress tensor is statically admissible or its components are statically admissible, if statistical boundary conditions on Γ_p are prescribed and (6) is fulfilled.

Substituting the kinematical equations into the equations of equilibrium leads to Lame's equations for the unknown displacement vector $\boldsymbol{u}$, which are written in the sense of distributions:

$$\frac{\partial}{\partial x_j}\left[L_{ijkl}\left(\frac{\partial u_k}{\partial x_l} + \frac{\partial u_l}{\partial x_k} - 2\mu_{kl}\right)\right] = 0 \quad \text{in } \Omega, \tag{7}$$

or alternatively

$$\frac{\partial}{\partial x_j}\left[L_{ijkl}\left(\frac{\partial u_k}{\partial x_l} + \frac{\partial u_l}{\partial x_k} - 2\lambda_{kl}\right)\right] = 0 \quad \text{in } \Omega \tag{8}$$

for a given field μ_{kl}, or λ_{kl}.

Recall that on the part Γ_u of the boundary Γ the displacement vector $\boldsymbol{u} = \overline{\boldsymbol{u}}$ is prescribed, and the traction field $\boldsymbol{p} = \overline{\boldsymbol{p}}$ is given on Γ_p.

3 Localization using the BEM

In this section we use extend Hashin-Shtrikman variational principle [4], by introducing both the eigenstrain and eigenstress fields into the formulation. For the sake of simplicity assume that no body forces are present.

The idea of Hashin and Shtrikman consists in introducing new variables τ_{ij} (components of the polarization tensor). Let us consider again a bounded domain Ω with its bounded Lipschitz's boundary Γ and with subdomains Ω_i, i = 1,…,n, describing local inhomogeneities.

The overall strain E_{ij} is assumed to be given independently of the shape of the unit cell and of the shape of the fiber. The loading of this unit cell will be given by unit impulses of E_{ij}, i.e. we successively select $E_{i_0 j_0} = E_{j_0 i_0} = 1; E_{ij} = 0$ for either $i_0 \neq i$ or $j_0 \neq j$. How to select the unit impulses of the overall strain components will be discussed later on.

Now we concentrate our attention on the approach of computing the concentration factors, which play the most important role in our solution of the optimal problem. The idea is adapted to the computation of the concentration factors. Note that approximate estimates of the concentration factors can be done using several formulas (Mori-Tanaka, self/consistent method, etc.). We are going to show in this paper relatively simple calculation of the factors using the boundary elements.

First let us specify the boundary conditions, being equivalent to the unit impulses of the overall strain components. In elasticity it is possible to prescribe the overall strain field all over the domain Ω of the unit cell. Then the solution of responses to the unit impulses is given by the periodicity conditions and tractions along the interfacial surface Γ between fibers and matrix. This approach is little bit cumbersome in case of debonding is admitted. The latter case is not considered here, but we apply more general form of introducing the unit impulses. It is well known that because of identity; see (2_3) and Green's theorem:

$$E_{ij} = \int_{\Omega} \varepsilon_{ij}(\boldsymbol{y})\,\mathrm{d}\Omega = \frac{1}{2}\int_{\Omega}\left[\frac{\partial u_i}{\partial y_j}(\boldsymbol{y}) + \frac{\partial u_j}{\partial y_i}(\boldsymbol{y})\right]\mathrm{d}\Omega = \\ = -\frac{1}{2}\int_{\partial\Omega}[u_i(\boldsymbol{y})n_j(\boldsymbol{y}) + u_j(\boldsymbol{y})n_i(\boldsymbol{y})]\,\mathrm{d}\gamma(\boldsymbol{y}) \tag{9}$$

From (9) it immediately follows that the unit responses are given by prescribed displacements along the boundary of the unit cell.

The procedure is split into two steps. Assume the above described surface displacements to be prescribed along the entire boundary $\partial\Omega$ and there are no body forces here. In the first step, the unit cell obeys static equilibrium equations and linear homogeneous Hooke's law (homogeneous and isotropic medium):

$$\sigma_{ij}^0 = L_{ijkl}^0 \varepsilon_{kl}^0, \text{ in } \Omega, \quad \text{given boundary conditions are fulfilled on } \partial\Omega. \tag{10}$$

L_{ijkl}^0 are components of a not yet determined material stiffness matrix (stiffness tensor). These components will be stated later. Such a medium is called comparative one.

The solution of (10) is easy, as the comparative medium is homogeneous and isotropic:

$$u_i^0 = E_{ij} y_j, \quad \varepsilon_{ij}^0 = E_{ij} \quad \text{in } \Omega, \quad p_i^0 = \sigma_{ij}^0 n_j = L_{ijkl}^0 E_{kl} n_j \quad \text{on } \partial\Omega$$

In the second step a geometrically identical unit cell is considered. Also the loading and boundary conditions on $\partial\Omega$ remain valid. Define

$$\begin{aligned} &\bar{u}_i = u_i - u_i^0 = u_i - E_{ij} y_j, \ \bar{\varepsilon}_{ij} = \varepsilon_{ij} - \varepsilon_{ij}^0 = \varepsilon_{ij} - E_{ij}, \\ &\bar{\sigma}_{ij} = \sigma_{ij} - \sigma_{ij}^0 = \sigma_{ij} - L_{ijkl}^0 E_{kl} \ \text{ in } \Omega \quad \bar{u}_i = 0 \ \text{ on } \ \Gamma_u, \ \ \bar{p}_i = 0 \ \text{ on } \ \Gamma_p \end{aligned} \tag{11}$$

Our next aim is to determine primed quantities, components of displacement vector $\bar{u}_i$ and components of strain and stress tensors $\bar{\varepsilon}_{ij}$ and $\bar{\sigma}_{ij}$. In order to do so, system of fifteen equations of elasticity (2) has to be formulated for the primed set. We start with Hooke's law, which is valid for heterogeneous medium:

$$\sigma_{ij}(\boldsymbol{y}) = L_{ijkl}(\boldsymbol{y}) \varepsilon_{kl}(\boldsymbol{y}) \quad \text{in } \Omega \tag{12}$$

Since the material stiffness tensor appears to be nonhomogeneous and unisotropic, idea used in [4], among others, will be adapted also here:

$$\sigma_{ij}(\boldsymbol{y}) = L_{ijkl}^0 \varepsilon_{kl}(\boldsymbol{y}) + \tau_{ij}(\boldsymbol{y}) \quad \text{in } \Omega \tag{13}$$

where τ_{ij} are components of the polarization tensor and the direct relation between stresses and strains becomes homogeneous and isotropic, so that integral formulation of elastic problem may be formulated. Subtracting (13) and (12) yields:

$$\tau_{ij} = [L_{ijkl}] \varepsilon_{kl}, \qquad [L_{ijkl}] = L_{ijkl} - L_{ijkl}^0 \tag{14}$$

which can be considered a definition of polarization tensor. Moreover, transformation to the primed system will not disturb the direct relation stresses – strains, as after substituting (13) to (11_3) gives:

$$\bar{\sigma}_{ij} = \sigma_{ij} - \sigma_{ij}^0 = L_{ijkl}^0 \varepsilon_{kl} + \tau_{ij} - \sigma_{ij}^0 = L_{ijkl}^0 \varepsilon_{kl} + \tau_{ij} - L_{ijkl}^0 E_{kl} = L_{ijkl}^0 \bar{\varepsilon}_{kl} + \tau_{ij} \tag{15}$$

Since both σ_{ij} and σ_{ij}^0 are statically admissible, it holds (the following equations must be defined in the sense of distributions):

$$\frac{\partial (L_{ijkl}^0 \bar{\varepsilon}_{kl} + \tau_{ij})}{\partial y_j} = 0 \quad \text{in } \Omega, \quad \bar{u}_i = u_i - u_i^0, \quad \bar{p}_i = p_i - p_i^0 \quad \text{on } \partial\Omega \tag{16}$$

Following the assumption of the same prescribed boundary conditions, some of the terms in (16) disappear.

Owing to constant distribution of L^0_{ijkl} in Ω, the equivalent integral formulation can be written as:

$$\bar{u}_m(\boldsymbol{\xi}) = \int_{\partial\Omega} p^*_{mi}(\boldsymbol{y},\boldsymbol{\xi})\bar{u}_i(\boldsymbol{y})\,\mathrm{d}\gamma(\boldsymbol{y}) - \int_{\partial\Omega} u^*_{mi}(\boldsymbol{y},\boldsymbol{\xi})\bar{p}_i(\boldsymbol{y})\,\mathrm{d}\gamma(\boldsymbol{y}) + \\ + \left([L^{\mathrm{f}}_{ijkl} - L^0_{ijkl}] \int_{\Omega^{\mathrm{f}}} + [L^{\mathrm{m}}_{ijkl} - L^0_{ijkl}] \int_{\Omega^{\mathrm{m}}} \right) \varepsilon^*_{mij}(\boldsymbol{y},\boldsymbol{\xi})\bar{\varepsilon}_k(\boldsymbol{y})\,\mathrm{d}\Omega \qquad \boldsymbol{\xi} \in \Omega \quad (17)$$

$$c_{mn}(\boldsymbol{\xi})\bar{u}_n(\boldsymbol{\xi}) = \int_{\partial\Omega} p^*_{mi}(\boldsymbol{y},\boldsymbol{\xi})\bar{u}_i(\boldsymbol{y})\,\mathrm{d}\gamma(\boldsymbol{y}) - \int_{\partial\Omega} u^*_{mi}(\boldsymbol{y},\boldsymbol{\xi})\bar{p}_i(\boldsymbol{y})\,\mathrm{d}\gamma(\boldsymbol{y}) + \\ + \left([L^{\mathrm{f}}_{ijkl} - L^0_{ijkl}] \int_{\Omega^{\mathrm{f}}} + [L^{\mathrm{m}}_{ijkl} - L^0_{ijkl}] \int_{\Omega^{\mathrm{m}}} \right) \sigma^*_{mij}(\boldsymbol{y},\boldsymbol{\xi})\bar{\varepsilon}_k(\boldsymbol{y})\,\mathrm{d}\Omega \qquad \boldsymbol{\xi} \in \partial\Omega \quad (18)$$

where c_{mn} are components of a tensor depending on position $\boldsymbol{\xi} \in \partial\Omega$ and the quantities with asterisks are given kernels.

Differentiating (17) by ξ_n and putting $\boldsymbol{\xi} \in \partial\Omega$ provides

$$\bar{\varepsilon}_{mn}(\boldsymbol{\xi}) = \int_{\partial\Omega} P^*_{mi}(\boldsymbol{y},\boldsymbol{\xi})\bar{u}_i(\boldsymbol{y})\,\mathrm{d}\gamma(\boldsymbol{y}) - \int_{\partial\Omega} U^*_{mi}(\boldsymbol{y},\boldsymbol{\xi})\bar{p}_i(\boldsymbol{y})\,\mathrm{d}\gamma(\boldsymbol{y}) + \\ + \left([L^{\mathrm{f}}_{ijkl} - L^0_{ijkl}] \int_{\Omega^{\mathrm{f}}} + [L^{\mathrm{m}}_{ijkl} - L^0_{ijkl}] \int_{\Omega^{\mathrm{m}}} \right) \Sigma^*_{mij}(\boldsymbol{y},\boldsymbol{\xi})\bar{\varepsilon}_k(\boldsymbol{y})\,\mathrm{d}\Omega + \text{convected term} \quad (19)$$

First, let $L^0_{ijkl} \equiv L^{\mathrm{f}}_{ijkl}$. Eliminating unknown boundary values from (18) and (19) we obtain the relation

$$\varepsilon^{\mathrm{m}}_{ij}(\bar{\boldsymbol{u}}(\boldsymbol{y})) = \beta^{\mathrm{m}}_{ijkl}(\boldsymbol{y})E_{kl} \quad (20)$$

and if $L^0_{ijkl} \equiv L^{\mathrm{m}}_{ijkl}$ then

$$\varepsilon^{\mathrm{f}}_{ij}(\bar{\boldsymbol{u}}(\boldsymbol{y})) = \beta^{\mathrm{f}}_{ijkl}(\boldsymbol{y})E_{kl} \quad (21)$$

This process leads to a fourth-order "concentration factor tensor" A_{ijkl} defined as

$$\varepsilon^p_{ij}(\boldsymbol{u}(\boldsymbol{y})) = (I_{ijkl} + \beta^p_{ijkl}(\boldsymbol{y}))E_{kl} = A^p_{ijkl}(\boldsymbol{y})E_{kl} \quad (22)$$

where the superscript $p \equiv \mathrm{f}$ for $\boldsymbol{y} \in \Omega^{\mathrm{f}}$ and $p \equiv \mathrm{m}$ for $\boldsymbol{y} \in \Omega^{\mathrm{m}}$.

Since it obviously holds

$$< A^{\mathrm{f}}_{ijkl} >_{\mathrm{f}} + < A^{\mathrm{m}}_{ijkl} >_{\mathrm{m}} = 1 \quad (23)$$

one does not need to compute both concentration factors. It is sufficient to draw a concentration on fiber, when dealing with concrete composites (the fiber ratio is very small), or on matrix, if the matrix volume ratio is large and the material behavior of stresses on matrix is nearly uniformly distributed.

4 Inelastic behavior of one phase

Assume that in the domain of elastic stresses a set

$$F(\sigma_{ij}) < 0 \tag{24}$$

Is given and the domain of the plastic surface is defined by the equality:

$$F(\sigma_{ij}) = 0 \tag{25}$$

Here σ_{ij} are components of the symmetric stress tensor. Function F is convex and continuous with respect to the arguments σ_{ij} as in $\Re_6$ the admissible set $F(\sigma_{ij}) \le 0$ is closed convex and $F(\sigma_{ij})$ involves only deviatoric stresses $\sigma_{ij}^{\mathrm{D}} = \sigma_{ij} - \dfrac{\delta_{ij}}{3}(\sigma_{kk})$, so that the deviatoric stress tensor possesses zero trace. Namely, for the von Mises-Huber-Hencky it holds:

$$F(\sigma_{ij}) = \frac{1}{2}\sigma_{ij}^{\mathrm{D}}\sigma_{ij}^{\mathrm{D}} - k^2 \tag{26}$$

where k is another material constant. Formulating a set

$$K = \{\boldsymbol{\sigma};\quad \boldsymbol{\sigma} = \{\sigma_{ij}\} \in \Re_6,\quad \sigma_{ij} = \sigma_{ji},\quad F(\sigma_{ij}) \le 0\} \tag{27}$$

the constitutive equations are written as:

$$\varepsilon_{ij}(\dot{\boldsymbol{u}}) = M_{ijkl}\dot{\sigma}_{kl} + \lambda_{ij} \tag{28}$$

where ε_{ij} are components of the strain tensor, M_{ijkl} is the compliance tensor of elastic parameters, overdot means time derivative (response of and increment of loading), λ_{ij} are components of the eigenstress tensor, here standing for components of the relaxation stress being defined as:

$$\lambda_{ij} = \begin{cases} 0, & \text{if } F(\boldsymbol{\sigma}) < 0 \\ \dfrac{1}{2\mu}[\sigma_{ij} - (P_K\boldsymbol{\sigma})_{ij}] & \text{if } F(\boldsymbol{\sigma}) \ge 0 \end{cases} \tag{29}$$

and a mapping $\boldsymbol{\sigma} \to P_K(\boldsymbol{\sigma})$ is an orthogonal projection in the domain of Euclidean structure $\boldsymbol{\sigma} \in \Re_6$ on a convex set K. Coefficient μ is possible to consider as the coefficient of viscosity in describing fluid movement and is identified as shear modulus G in solid materials. If only constant σ_{ij} appear in the development of material stages, i.e. $\dot{\sigma}_{ij} = 0$, the latter equations turn to

$\sigma_{ij} = (P_K \boldsymbol{\sigma})_{ij} + 2\mu\varepsilon_{ij}(\dot{\boldsymbol{u}})$ and for fluids their movement is described by the Navier-Stokes equations it holds:

$$\sigma_{ij} = -p\delta_{ij} + 2\mu\varepsilon_{ij}(\dot{\boldsymbol{u}}) \tag{30}$$

In case Mises condition is allowed for the relaxation stresses are derived as:

$$\lambda_{ij} = \begin{cases} 0, & \text{if } F(\boldsymbol{\sigma}) < 0 \\ \dfrac{1}{2\mu}\dfrac{\sqrt{\sigma_{\mathrm{II}}} - k}{\sqrt{\sigma_{\mathrm{II}}}}\sigma_{ij}^{\mathrm{D}} & \text{if } F(\boldsymbol{\sigma}) \geq 0 \end{cases} \tag{31}$$

where $\sigma_{\mathrm{II}} = \dfrac{1}{2}\sigma_{ij}^{\mathrm{D}}$.

5 Conclusions

In this paper combustion of the concrete lining and the rock surrounding the tunnel is solved by Smooth Particle Hydrodynamics Method. The results are partly compared with experiments on concrete slabs burned in a furnace. Particularly, influences of fibers from fused basalt are observed and the composite with concrete matrix is evaluated after carrying out tests in Innsbruck University. The basalt material seems to be quite suitable for this case of endangered concrete linings. The reason is that at lower temperatures it behaves as stiffener of the concrete matrix and overcoming the temperature of 1000^0C it becomes melting and enables vapor to escape from the concrete not to cause any larger damage. Consequently, in comparison to other types of fibers fused basalt serves in a proper way. Natural fibers are very suitable for high temperatures (they burn out and the vapor can freely dilute in the air) and stiff fibers like steel serve a good reinforcement but too troublesome in he case of influence of high temperature.

The SPH method is perfectly suitable for solving such a problem. This method shows very promising time consumption of computer (it is basically low in comparing it with other numerical methods), but generally it suffers from one unpleasant property: inhomogeneous geometrical boundary conditions can be respected in the calculus in complicated way. In our case this type of boundary conditions does not play any decisive role. The boundary conditions are declared by time changing source of heat, and the damage in the material is calculated at the time-stage.

Acknowledgement

Work on this project has been financially supported by GACR, project No. 103/07/0304. Sponsorship of CIDEAS is also acknowledged.

References

[1] Dvorak, G.J., Procházka, P.P. Thin-walled composite cylinders with optimal fiber prestress. Composites Part B, 27B, 1996, 643-649
[2] Procházka, P.P., Sejnoha, J. Behavior of composites on bounded domain. BE Communications 7, 1996, 6-8
[3] Procházka, P.P., Sejnoha, J. Extended Hashin-Shtrikman variational principles. Applications of Mathematics, No. 4, 49, 2004, 357-372
[4] Hashin, Z., Shtrikman, S. A variational approach to the theory of the elastic behaviour of polycristals. J. Mech. Phys. Solids 10, 1962, 343-352
[5] Duvant, G., Lions, J-L. Les inéquations en méchanique et en physique. DUNOD, Paris 1972.
[6] Suquet, P.M. Elements of homogenization for inelastic solid mechanics. Lecture Notes in Physics 272: Homogenization Techniques for Composite Media, Eds E. Sanches.Palencia and A. Zaoui, Springer-Verlag 1987.

This page intentionally left blank

Hybrid finite element method in supersonic flutter analysis of circular cylindrical shells

F. Sabri[1], A. A. Lakis[1] & M. H. Toorani[2]
[1]*Department of Mechanical Engineering, Ecole Polytechnique of Montreal, Canada*
[2]*Nuclear Engineering Department, Babcock & Wilcox Canada, Canada*

Abstract

This study is focused on the aeroelastic behaviour of circular cylindrical shells in a supersonic airflow. The development is based on a combination of Sanders' thin shell theory and the classical finite element method. Potential and piston theory with and without the correction factor for shell curvature is applied to derive the aerodynamic damping and stiffness matrices. The influence of stress stiffness due to the shell internal pressure and axial loading is also taken into account. Aeroelastic equations in hybrid finite formulation are derived and solved numerically. The effect of shell boundary conditions; geometry and flow parameters on the structure response is investigated. In all study cases, the shell loses its stability by coupled-mode flutter where a travelling wave is observed during this dynamic instability. The results are compared with existing experimental data, other analytical and finite element solutions. The present study shows efficient and reliable results that can be applied for the aeroelastic design of shell structures used for aerospace vehicles.

Keywords: FSI, hybrid element, flutter, cylindrical shells.

1 Introduction

Shells and plates are among the key structures in aerospace vehicles. For instance, these elements are used numerously in the fuselage and engine nacelles of airplanes and in space shuttles' skin. As they are exposed to the external air flow and particularly supersonic flow, dynamic instability (flutter) is one of the practical considerations in the design and analysis of skin panels that may occur. Cylindrical shells could also show this kind of aeroelastic instability where

WIT Transactions on Modelling and Simulation, Vol 49, © 2009 WIT Press
www.witpress.com, ISSN 1743-355X (on-line)
doi:10.2495/BE090211

prevention of that behaviour is one of the primary design criterions, which is something that aeronautical engineers are challenged with. After introducing the application of piston theory in the aeroelastic modelling proposed by Ashley and Zartarian [1], many interesting experimental and theoretical studies started to investigate supersonic flutter of a cylindrical shell. Most of these researches are concerned with the development of analytical relations to investigate the effect of the shell and flow parameters on the critical flutter frequency. The aeroelastic models have been developed on the basis of the shell and piston theory to establish the coupled fluid-structure system. Olson and Fung [2] examined the effect of the shell boundary conditions and initial strain state, due to the internal pressure and axial load, on the dynamic behaviour of the given structure. They observed that the pressurized cylindrical shell fluttered at a lower level of freestream static pressure than predicted by theory [3]. Evensen and Olson [4] presented a non-linear analysis for calculating the limit cycle amplitude of a cylindrical shell. Dowell [5] investigated the behaviour of a cylindrical shell in a supersonic flow for different flow and shell parameters; an extensive description of panel flutter modelling has been addressed in his monograph [6]. Amabili and Pellicano [7] developed a model considering the geometric nonlinearities to study the supersonic flutter of the circular cylindrical shell. They also applied the nonlinear piston theory with the shell imperfection to reproduce the experimental data for a pressurized cylindrical shell [8].

The present study is focused on the development of a circumferential hybrid element for a circular cylindrical shell in a supersonic flow. The procedure is similar to the finite element development done for a vertical shell by Lakis and Paidoussis [9] and for a horizontal open shell by Selmane and Lakis [10]. Those developments resulted in a precise and fast convergence with less numerical difficulties. The element is a cylindrical frustum instead of the usual rectangular shell element. Linear Sanders' shell theory; in which all the strains vanish for rigid body motions; is coupled with the linearized first-order of piston theory (including the curvature correction term) and also the potential theory to carry out the fluid-structure interaction model. The initial stress stiffening in the presence of shell internal pressure and axial compression is also applied into the formulation. Finally the linear mass, damping and stiffness matrix of the aeroelastic system are obtained and solved numerically.

2 Structural model

2.1 Structural mass and stiffness

The equilibrium equations of cylindrical shells according to the Sanders' shell theory are developed in [10] and [11]. The strain-displacement equations as a function of three infinitesimal displacements in axial (U), radial (W), and circumferential (V) directions are derived and given in [10] and [11]. The system of equilibrium equations described as a function of the displacement components and material properties are defined as:

$$L_J(U, W, V, P_{ij}) = 0 \tag{1}$$

where L_J ($J = 1,2,3$) are three partial differential equations and can be found in [10] and [11]. Matrix [P] is the elasticity matrix for anisotropic shell [11]. A circumferential cylindrical frustum based on the development done by Lakis and Paidoussis [9] is applied to generate the mass and stiffness matrix of the structural model. This element type (see Fig. 1) has two nodal circle with two nodal points i and j.

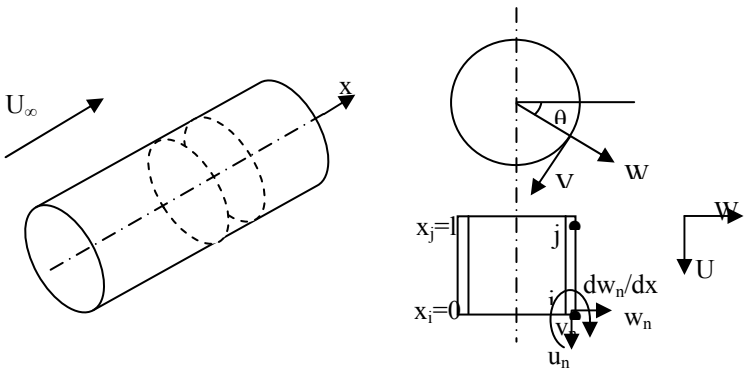

Figure 1: Geometry of cylindrical frustum element.

There are four degrees of freedom at each node; axial, radial, circumferential displacement, and rotation. This kind of element makes it possible to use thin shell equation easily in order to find the exact solution of displacement functions rather than the approximation with the polynomial functions in the classical finite element method. This element selection results in a hybrid element where a convergence criterion of the finite element method is provided with greater accuracy. Consider the displacement components in the normal manner as:

$$\begin{aligned} U(r,x,\theta) &= u_n(x)\cos(n\theta) \\ W(r,x,\theta) &= w_n(x)\cos(n\theta) \\ V(r,x,\theta) &= v_n(x)\sin(n\theta) \end{aligned} \tag{2}$$

where n is the circumferential wave number. Lakis and Paidoussis [9] derived the exact analytical relations for the displacement shape functions based on the equations of motion of shell associated with the system of equations (2). The final form of displacement functions is defined as:

$$\begin{Bmatrix} U(x,r,\theta) \\ W(x,r,\theta) \\ V(x,r,\theta) \end{Bmatrix} = [N] \begin{Bmatrix} \delta_i \\ \delta_j \end{Bmatrix} \tag{3}$$

where the nodal displacements vector $\{\delta\}$ and displacement shape function matrix $[N]$ are given in [9]. Now the stress resultant can be defined as:

$$\{\sigma\} = [P][B] \begin{Bmatrix} \delta_i \\ \delta_j \end{Bmatrix} \tag{4}$$

Therefore, the mass and stiffness matrix for each element are derived as:

$$[m] = \rho h \iint [N]^T [N] dA; [k] = \iint [B]^T [P][B] dA \tag{5}$$

where ρ is the shell density and $dA = rdxd\theta$. For the entire shell geometry, using the standard assembly technique in FEM and applying the appropriate boundary conditions, the global mass and stiffness matrices are found.

2.2 Initial stress stiffness

The influence of membrane forces on the dynamic stability of a cylindrical shell in the presence of the supersonic airflow is investigated. These membrane forces are due to the pressure differential across the shell P_m, and axial compression P_x. It is assumed that the shell is under equilibrium condition and also it has not reached its buckling state. The initial in-plane shear, static bending and transverse shear are not considered either. The stress resultant due to the internal pressure P_m and the axial compression P_x are defined as:

$$\overline{N}_x = -\frac{P_x}{2\pi R}; \qquad \overline{N}_\theta = P_m R \tag{6}$$

The potential energy due to this initial strain is equal to:

$$U_i = 1/2 \int_0^l \int_0^{2\pi} [\overline{N}_x \phi_{\theta\theta}^2 + \overline{N}_\theta \phi_{xx}^2 + (\overline{N}_x + \overline{N}_\theta)\phi_n^2] R d\theta dx \tag{7}$$

where l is the element length, ϕ_{xx} is the strain rotation about the x axis, $\phi_{\theta\theta}$ is the rotation about normal to the $x\theta$ plane, and ϕ_n is the rotation about normal to the shell element. The rotation vector is given by:

$$\phi_{\theta\theta} = -\frac{\partial W}{\partial x}; \qquad \phi_{xx} = \frac{1}{R}(V - \frac{\partial W}{\partial \theta}); \qquad \phi_n = \frac{1}{2}(-\frac{1}{R}\frac{\partial U}{\partial \theta} + \frac{\partial V}{\partial x}) \tag{8}$$

If the displacements are replaced by equation (3), the potential energy in terms of nodal degrees of freedom is generated as:

$$U_i = 1/2 \int_0^l \int_0^{2\pi} \{r\}^T \begin{bmatrix} \overline{N}_x & 0 & 0 \\ 0 & \overline{N}_\theta & 0 \\ 0 & 0 & \overline{N}_x + \overline{N}_\theta \end{bmatrix} \{r\} R d\theta dx \tag{9}$$

where vector $\{r\}$ is defined as:

$$\{r\} = \begin{bmatrix} 0 & -\frac{\partial}{\partial x} & 0 \\ 0 & -\frac{1}{R}\frac{\partial}{\partial \theta} & 0 \\ -\frac{1}{2R}\frac{\partial}{\partial \theta} & 0 & \frac{1}{2}\frac{\partial}{\partial x} \end{bmatrix} \begin{Bmatrix} U \\ W \\ V \end{Bmatrix} = [C_0][N] \begin{Bmatrix} \delta_i \\ \delta_j \end{Bmatrix} \tag{10}$$

Therefore, the initial stiffness matrix for each element becomes:

$$[k_I] = \int_0^l \int_0^{2\pi} [N]^T [C_0]^T \begin{bmatrix} \overline{N}_x & 0 & 0 \\ 0 & \overline{N}_\theta & 0 \\ 0 & 0 & \overline{N}_x + \overline{N}_\theta \end{bmatrix} [C_0]^T [N]^T R d\theta dx \tag{11}$$

With the help of Maple software, the analytical integration of equation (11) for each element is carried out. The initial stuffiness matrix is superimposed to the global stiffness matrix calculated in equation (5).

3 Aerodynamic modelling

Piston theory is a powerful tool for aerodynamic modelling in aeroelasticity. For a cylinder subjected to an external supersonic airflow parallel to the centreline of the shell, the fluid-structure effect due to external pressure loading can be taken into account by linearized first-order potential theory with (or without) the curvature correction term:

$$P_a = \frac{\gamma p_\infty M^2}{(M^2-1)^{1/2}}\left[\frac{\partial W}{\partial x}+\frac{M^2-2}{M^2-1}\frac{1}{U_\infty}\frac{\partial W}{\partial t}-\frac{W}{2R(M^2-1)^{1/2}}\right] \tag{12}$$

where p_∞, U_∞, M and γ are freestream static pressure, freestream velocity, the Mach number and the adiabatic exponent of air, respectively. At a sufficiently high Mach number ($M \geq 2$) and neglecting the curvature term $\frac{W}{2R(M^2-1)^{1/2}}$, equation (12) is simplified to the so-called linear piston theory as:

$$P_a = -\gamma p_\infty\left[M\frac{\partial W}{\partial x}+\frac{1}{a_\infty}\frac{\partial W}{\partial t}\right] \tag{13}$$

where a_∞ is the sound speed. In order to show the compatibility and power of this development compared with different loading theories, the potential solution proposed by Lakis and Laveau [12] is also applied to account for the pressure field. They have developed an exact expression for the nonlinearized aerodynamic pressure acting on the cylindrical shell that is exposed to external or internal incompressible flow. In this study, the effect of compressibility has been taken into account. This effect is entered through the calculation of Bessel's functions for finding the velocity potential. Using the Laplace equation for the potential flow accompany with boundary conditions defined by impermeability and Bernoulli's equation, the linear pressure load on the shell wall is given by:

$$P_a = -\rho_f Z\left[\frac{\partial^2 W}{\partial t^2}+2U_\infty\frac{\partial^2 W}{\partial x\partial t}+U_\infty^2\frac{\partial^2 W}{\partial x^2}\right] \tag{14}$$

where ρ_f is fluid density and Z is expressed in terms of Bessel's functions of the first and second kind [9]. The radial displacement is defined in terms of the analytical solution of λ_j (the complex roots of a characteristic equation related to the equations of motion and oscillation frequency of the shell) and the circular frequency ω as:

$$W = \sum_{j=1}^{8} e^{i(\lambda_j \frac{x}{R}+\omega t)}\cos(n\theta) = \sum_{j=1}^{8} W_j \tag{15}$$

In the following subsection, the pressure field for each aerodynamic loading is expressed in terms of nodal displacements.

3.1 Piston theory

The pressure field expressed by equation (13) can be rewritten as:

$$P_a = -\gamma p_\infty \sum_{j=1}^{8} \left(\frac{1}{a_\infty}\frac{\partial W_j}{\partial t} + M\frac{\partial W_j}{\partial x}\right) \tag{16}$$

Substituting equations (3) and (15) into equation (16), aerodynamic pressure may be defined as:

$$\{P_a\} = \begin{Bmatrix} 0 \\ p_{radial} \\ 0 \end{Bmatrix} = -\gamma \frac{p_\infty}{a_\infty}[T][R_f][A^{-1}]\begin{Bmatrix}\dot{\delta}_i \\ \dot{\delta}_j\end{Bmatrix} - (i\frac{\lambda_j}{R})\gamma p_\infty M[T][R_f][A^{-1}]\begin{Bmatrix}\delta_i \\ \delta_j\end{Bmatrix} \tag{17}$$

where the elements of matrix $[R_f]$ are defined in terms of shell radius (R), longitudinal coordinate (x), and the characteristic equation's roots (λ).

3.2 Piston theory with curvature term

The aerodynamic pressure field for the case of applying equation (12) will become as:

$$\{P_a\} = \begin{Bmatrix} 0 \\ p_{radial} \\ 0 \end{Bmatrix} = \frac{-\rho_\infty U_\infty^2}{(M^2-1)^{1/2}}\frac{1}{U_\infty}\left(\frac{M^2-2}{M^2-1}\right)[T][R_f][A^{-1}]\begin{Bmatrix}\dot{\delta}_i \\ \dot{\delta}_j\end{Bmatrix} + (i\frac{\lambda_j}{R})\frac{-\rho_\infty U_\infty^2}{(M^2-1)^{1/2}}[T][R_f][A^{-1}]\begin{Bmatrix}\delta_i \\ \delta_j\end{Bmatrix} -$$
$$-\frac{-\rho_\infty U_\infty^2}{(M^2-1)^{1/2}}\left(\frac{1}{2(M^2-1)^{1/2}R}\right)[T][R_f][A^{-1}]\begin{Bmatrix}\delta_i \\ \delta_j\end{Bmatrix} \tag{18}$$

where ρ_∞ is the freestream air density. It is seen that the freestream static pressure and velocity can be related together through the following equations:

$$U_\infty = M.a_\infty, \qquad a_\infty = \sqrt{\gamma\frac{p_\infty}{\rho_\infty}} \tag{19}$$

3.3 Potential theory

Considering the potential theory, the final form for pressure field is given as:

$$\{P_a\} = \begin{Bmatrix} 0 \\ p_{radial} \\ 0 \end{Bmatrix} = -\rho_\infty Z[T][R_f]\begin{Bmatrix}\ddot{\delta}_i \\ \ddot{\delta}_j\end{Bmatrix} - 2(i\frac{\lambda_j}{R})\rho_\infty U_\infty Z[T][R_f]\begin{Bmatrix}\dot{\delta}_i \\ \dot{\delta}_j\end{Bmatrix} + (\frac{\lambda_j}{R})^2\rho_\infty U_\infty^2 Z[T][R_f]\begin{Bmatrix}\delta_i \\ \delta_j\end{Bmatrix} \tag{20}$$

3.4 Aerodynamic damping and stiffness

The general force vector due to the pressure field is defined as:

$$\{F_p\} = \iint [N]^T \{p_a\} dA \tag{21}$$

Substituting the displacement shape functions (eq. (3)) and the calculated dynamic pressure (eq. (17)) and integrating over the fluid-structure contact

surface, the aerodynamic damping $[c_f]$, and stiffness $[k_f]$ are determined for each element as:

$$[c_f] = [A^{-1}]^T [D_f][A^{-1}]; [k_f] = [A^{-1}]^T [G_f][A^{-1}] \tag{22}$$

where

$$[D_f] = -\frac{\gamma}{a_\infty} p_\infty \pi r \int_0^l [R]^T [R_f] dx; [G_f] = -i \frac{\lambda_j}{r} \gamma p_\infty M \pi r \int_0^l [R]^T [R_f] dx \tag{23}$$

The same procedure can be done by substituting the different pressure fields as given in equations (18 and 20) into equation (21) to derive those local damping and stiffness matrices. Finally, global aerodynamic damping $[C_f]$ and aerodynamic stiffness $[K_f]$ matrices are found through assembling procedure.

4 Aeroelastic model in FEM

The governing equations of motion in the global system of a cylindrical shell exposed to an external supersonic flow are found as:

$$[M_s]\begin{Bmatrix} \ddot{\delta}_i \\ \ddot{\delta}_j \end{Bmatrix} - [C_f]\begin{Bmatrix} \dot{\delta}_i \\ \dot{\delta}_j \end{Bmatrix} + [\,[K_s] + [K_I] - [K_f]\,]\begin{Bmatrix} \delta_i \\ \delta_j \end{Bmatrix} = 0 \tag{24}$$

where subscripts *s* and *f* refer to shell in vacuo and fluid, respectively. It should be noted that in the case of applying potential theory to account for aerodynamic loading, the mass matrix is modified by considering the fluid added mass. In order to find the aeroelastic behaviour of the shell, eigenvalues and eigenvectors of equation (24) are found by means of equation reduction method technique. Dynamic stability of the shell is investigated by studying the eigenvalues in the complex plane. The flutter onset is found when the imaginary part of the eigenvalue changes from positive to negative.

5 Numerical results and discussions

Following shell geometry and flow parameters are used for the given examples.

$$E = 16 \times 10^6 \ lb/in; \upsilon = 0.35; \rho_s = 0.000833 \ lb - s^2/in^4$$
$$h = 0.0040 \ in; L = 15.4 \ in; R = 8.00 \ in$$
$$M = 3.00; a_\infty = 8400 \ \ in/s; T_{t\infty} = 120^\circ \ F$$

where $T_{t\infty}$ is the freestream stagnation temperature, and ρ_s is the shell density. A set of calculation is carried out to find the appropriate number of elements for shell discretization. It is found that the present model results in a very good accuracy of results using 20 elements. The first set of results along with those of experiment and other theories are presented in Table 1. In all of the cases, the instability is raised in the form of coupled-mode flutter. The proposed method shows a very good agreement with experimental and analytical results.

Table 1: Comparison of shell flutter boundary at $M = 3$ and $p_x = p_m = 0$.

	p_∞ (psi)	$n_{critical}$	L (in)	υ	$E(lb/in^2)$
Experimental results[2]	0.380-0.420	20	15.40	0.35	16×10^6
Analytical results[13]	0.420	24	16.00	0.33	13×10^6
Analytical results[3]	0.550	25	15.40	0.35	16×10^6
Analytical results[7]	0.330	27	15.40	0.35	16×10^6
FEM results[14]	0.5621	34	16.00	0.33	13×10^6
FEM results[15]	0.5621	25	16.00	0.33	13×10^6
FEM results[15]	0.5621	26	15.40	0.35	16×10^6
Present results	0.522	26	15.40	0.35	16×10^6
Present results	0.382	25	16.00	0.33	13×10^6

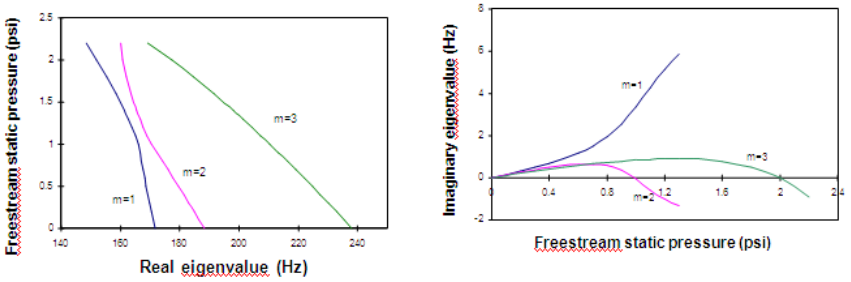

Figure 2: The real and imaginary part of the eigenvalue of system versus freestream static pressure (n=20, P_m=P_x=0.0 psi).

The complex frequencies of an unpressurized shell, P_m=0 and n=20, are determined using the potential theory and plotted in fig. 2. It is shown that the flutter occurs at the second axial mode where the imaginary part of eigenvalue, representing the damping of system, passes through zero at high freestream static pressure. The same behaviour was found by Olson and Fung [3].

The effect of the curvature term appearing in the piston theory is examined through the following example. The real and imaginary parts of system eigenvalues are plotted at the first two modes versus freestream pressure as shown in fig. 3. This figure shows that the real parts eventually merge into a single mode. For the further increasing the pressure, the shell loses stability by coupled-mode flutter once the imaginary part of complex frequency crosses the zero value. Prediction of critical freestream static pressure by using equation (12) is closer to the experimental results than evaluating pressure field by equation (13). The complex frequencies for the case that aerodynamic pressure is evaluated using equation (13) are plotted in fig. 4. It is stated that the piston theory including the shell curvature effect results in a better approximation to evaluate the pressure loading on a shell exposed to a supersonic flow. In order to investigate the effect of shell internal pressure, the complex eigenvalues for the critical circumferential wave number n=23, with the shell internal pressure

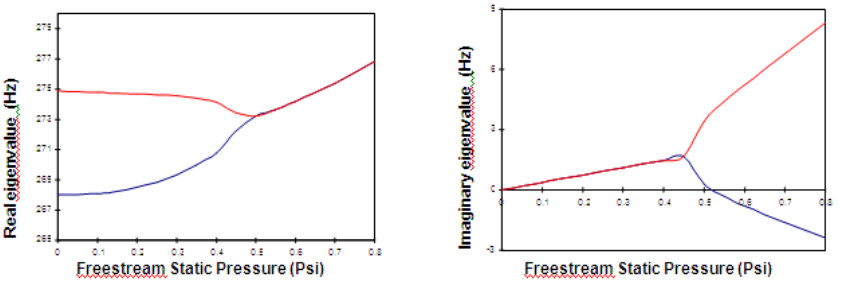

Figure 3: System eigenvalue versus freestream static pressure when the curvature term is included in the piston theory (n=25, P_m=P_x=0.0 psi).

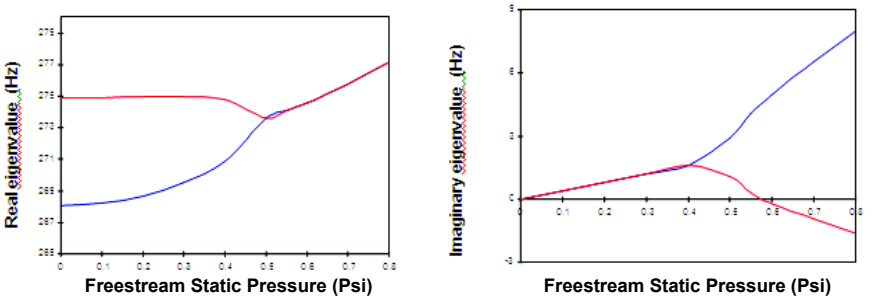

Figure 4: System eigenvalue versus freestream static pressure without considering the shell curvature effect (n=25, P_m=P_x=0.0 psi).

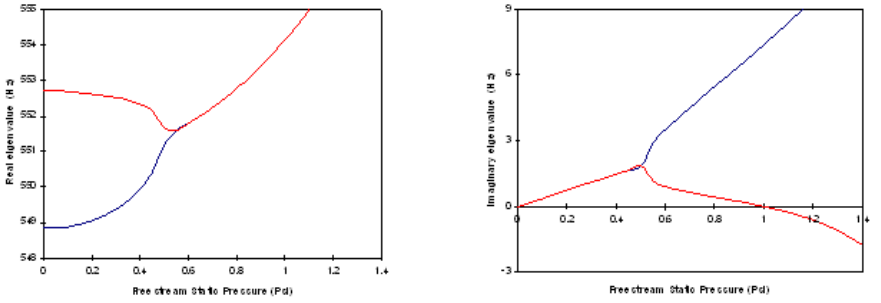

Figure 5: System eigenvalue versus freestream static pressure considering the shell internal pressure (n=23, P_m=0.5psi, P_x=0.0 psi).

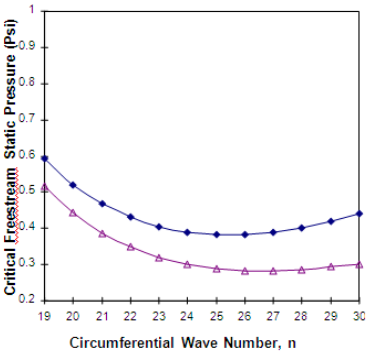

Figure 6: Flutter boundaries for stressed shell, ♦ $p_x = 0.0\ lb$; Δ: $p_x = 30\ lb$.

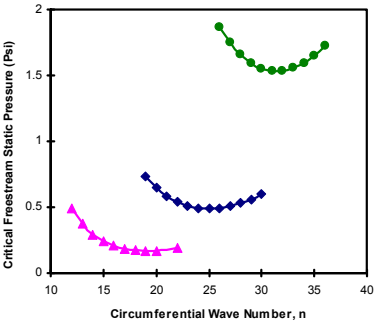

Figure 7: Flutter boundaries for different L/R ratios, ▲ $L/R = 4$; ♦ $L/R = 2$; ● $L/R = 1$.

pm=0.50psi, are shown in fig. 5. In this case, the flutter occurs at higher value of freestream static pressure ($p_\infty = 1.00\,\text{psi}$) since the shell stiffness increases due to applied internal pressure.

The effect of axial compression on the flutter boundary is also shown in fig. 6. The axial load, P_x, decreases the stiffness of the shell, which results in lower critical freestream pressure compared to the unstressed shell.

Figure 7 presents the effect of length-to-radius ratio (L/R) on the critical static pressure. For L/R=1, the shell loses its stability at $n=18$ and $P_\infty=0.171$ psi while for L/R=4 onset flutter occurs at $n=31$ and $P_\infty=1.535$ psi.

6 Conclusions

An efficient hybrid finite element method is used to deal with the dynamic stability of circular cylindrical shell subjected to an external supersonic flow. Linear Sanders' shell theory is coupled with two different potential and piston

theory to account for aerodynamic pressure field to derive the aeroelastic equations of motion. It is observed that the piston theory has a better approximation in describing the fluid–structure interaction phenomenon in a supersonic airflow. There is a good agreement for prediction of flutter onset with existed results of experiment, other analytical approaches and FEM analysis. In all cases, only one type of instability is found (known as coupled-mode flutter in form of travelling wave flutter) mostly in the first and second longitudinal modes. Shell internal pressure has stabilizing effect while the axial compression leads to the lower flutter boundary. The developed model is capable to provide reliable results with less computational cost compare to the commercial FEM software where for such analysis, they have some restrictions.

Acknowledgement

The authors acknowledge the financial support of NSERC of Canada, grant No. A8814.

References

[1] Ashley, H. & Zartarian G., *Piston Theory-New Aerodynamic Tool for Aeroelastician*, *Journal of the Aeronautical Sciences*, **23(12)**, pp. 1109-1118, 1956.

[2] Olson, M.D. & Fung Y. C., *Supersonic Flutter of Circular Cylindrical Shells Subjected to Internal Pressure and Axial Compression*, *AIAA Journal*, **4(5)**, pp. 858-864, 1966.

[3] Olson, M. D. and Fung, Y. C., *Comparing Theory and Experiment for Supersonic Flutter of Circular Cylindrical Shells*, AIAA Journal, **5(10)**, pp. 1849-1856, 1967.

[4] Evensen, D.A. & Olson M. D., *Nonlinear Flutter of a Circular Cylindrical Shell in Supersonic Flow*, NASA TN D-4265, 1967.

[5] Dowell, E. H., *Flutter of Infinitely Long Plates and Shells. Part II*, *AIAA Journal*, **4(9)**, pp. 1510-1518, 1966.

[6] Dowell, E.H., *Aeroelasticity of Plates and Shells*, Noordhoff International Publishing, Leyden, 1975.

[7] Amabili, M. & F. Pellicano, *Nonlinear Supersonic Flutter of Circular Cylindrical Shells*, *AIAA Journal*, **39(4)**, pp. 564-573, 2001.

[8] Amabili, M. & F. Pellicano, *Multimode Approach to Nonlinear Supersonic Flutter of Imperfect Circular Cylindrical Shells*, *Journal of Applied Mechanics, Transactions ASME*, **69(2)**, pp. 117-129, 2002.

[9] Lakis, A. A. & Paidoussis, M. P., *Dynamic Analysis of Axially Non-Uniform Thin Cylindrical Shells*, *Journal of Mechanical Engineering Science*, **14(1)**, pp. 49-71, 1972.

[10] Selmane, A. & Lakis, A. A., *Non-Linear Dynamic Analysis of Orthotropic Open Cylindrical Shells Subjected to a Flowing Fluid*, *Journal of Sound and Vibration*, **202 (1)**, pp. 67-93, 1997.

[11] Toorani, M. H. & Lakis, A. A., *General Equations of Anisotropic Plates and Shells Including Transverse Shear Deformations, Rotary Inertia and Initial Curvature Effects*, Journal of Sound and Vibration, **237(4)**, pp. 561-615, 2000.
[12] Lakis, A. A. & Laveau, A., *Non-Linear Dynamic Analysis of Anisotropic Cylindrical Shells Containing a Flowing Fluid*, International Journal of Solids and Structures, **28(9)**, pp. 1079-1094, 1991.
[13] Carter, L. L., & Stearman, R. O., Some aspects of cylindrical shell panel flutter, AIAA Journal, **6(1)**, pp. 37-43, 1968.
[14] Bismark-Nasr, M. N., *Finite element method applied to the supersonic flutter of circular cylindrical shells*, International Journal for Numerical Methods in Engineering, **10(2)**, pp. 423-435, 1976.
[15] Ganapathi, M., Varadan, T. K., Jijen, J., *Field-consistent element applied to flutter analysis of circular cylindrical shells*, Journal of Sound and Vibration, **171(4)**, pp. 509-527, 1994.

Section 5
Damage mechanics and fracture

This page intentionally left blank

Cohesive crack propagation using a boundary element formulation with a tangent operator

E. D. Leonel & W. S. Venturini
Department of Structural Engineering,
São Carlos School of Engineering, University of São Paulo, Brazil

Abstract

In this work, a BEM formulation is proposed to analyse cohesive crack using the dual reciprocity method. The solution of the non-linear system of equations is based on the Newton–Raphson process for which the consistent tangent operator is derived. The cohesive crack model is the criterion adopted to describe crack growth particularly for quasi-brittle material problems. The solution is very stable and accurate and can be easily applied to solids that exhibit many crack or micro-cracks. Examples are shown to illustrate the applicability of the formulation.

Keywords: boundary elements, crack growth, cohesive crack model.

1 Introduction

The boundary element method (BEM) has already been recognized as an accurate and efficient numerical technique to deal appropriately with many problems in engineering. In particular, the method is recommended to analyse crack problems. For this kind of problems the dimensionality reduction of BEM is clear, as only boundary discretization is required. Internal points are needed only to approximate the crack line, but without requiring remeshing. Among the crack models the Hillerborg cohesive model is an idealization that represents well the dissipation process occurring in a small region ahead the crack tip [1]. The dissipation zone is approximated by a crack line since the process begins. This model is particularly recommended for the analysis of quasi-brittle materials.

The Dual Boundary Element Method (DBEM), proposed by Portela *et al*. [2], is nowadays the most used technique to model linear and non-linear fracture

WIT Transactions on Modelling and Simulation, Vol 49, © 2009 WIT Press
www.witpress.com, ISSN 1743-355X (on-line)
doi:10.2495/BE090221

processes. The method is based on the use of singular and hyper-singular integral equations written for collocations along the crack line. This scheme allows writing four independent relations for each node defined on the crack line and avoids the division of the solid into sub-regions. Besides these works we want to cite some alternative procedures proposed by the senior author: Venturini [3] has used dipoles to enforce crack discontinuities governed by a cohesive model; Manzoli and Venturini [4] have modelled cracks by using strong discontinuities similar to the technique used for the enhanced finite element methods, and Leite and Venturini [5] adopting narrow sub-regions with rigidity going to zero for the simulation of cracks.

The solution techniques for the majority of the proposed works to analyse crack problems using BEM are based on iterative schemes that corrects the forces between the crack faces that satisfy the criterion adopted (see for instance Saleh and Aliabadi [6]). These processes are simple and the relevant matrices are also kept constant during the process. This kind of technique requires a large number of iterations to achieve the equilibrium for a single load increment. Moreover, for the cases of more complex pattern of cracks, for instance with a solid containing many micro-crack, this process can be either inaccurate or instable.

In this work, we are analysing quasi-brittle two-dimensional domains using the cohesive crack model. Two solution techniques are proposed: the classical procedure based on the corrections of the crack surface forces and a more elaborated scheme for which the consistent tangent operator has been derived. for the second procedure the system of equations is solved by using the Newton–Raphson method. Numerical examples are shown to compare the accuracy and efficiency of the two procedures.

2 Cohesive crack model

The cohesive crack models, in which the dissipation zone was reduced either to a line for 2D problems or to a surface for 3D problems, appropriate to quasi-brittle materials are due to Hillerborg *et al*. [1]. In this work a softening region just behind the crack tip is defined along which a relation between the crack surface tensile forces, or cohesive forces f_t, and the crack opening displacement Δu is defined to govern the dissipative process. The cohesive forces disappear after a crack opening critical value, Δu_c. The crack starts opening when the cohesive forces reaches a tensile critical value f_t^c. For values of the tensile stresses less than f_t^c the crack does not open. For values of the crack opening displacement larger than Δu_c the cohesive force is zero.

Several relations between cohesive forces and crack opening displacement have already been tested. Three of them are often employed to carry out crack analysis for quasi-brittle materials: linear model; bi-linear model; and exponential model (a) linear model; b) bi-linear model; and c) exponential model (Figure 1).

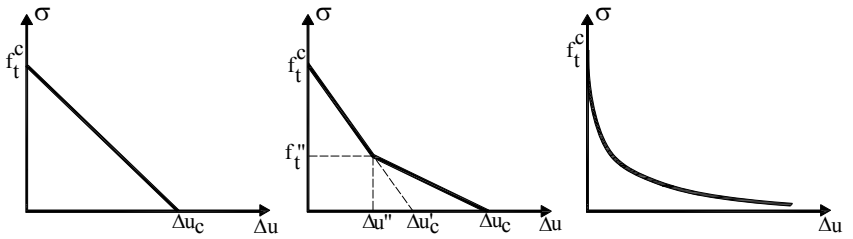

Figure 1: Cohesive force models. a) linear model ; b) bi-linear model; and c) exponential model.

For the linear case the cohesive model is given by the following relations:

$$\sigma = E\varepsilon \qquad if \quad \varepsilon \le \varepsilon_c \tag{1a}$$

$$f_t\left(\Delta u\right) = f_t^c\left(1 - \Delta u / \Delta u_c\right) \qquad if \quad 0 \le \Delta u \le \Delta u_c \tag{1b}$$

$$f_t\left(\Delta u\right) = 0 \qquad if \quad \Delta u > \Delta u_{cr} \tag{1c}$$

3 Dual Boundary Element Method

For an elastic domain Ω, with boundary Γ, one can easily derive the integral representation of displacements as follows:

$$c_{il}(f)u_l(f) + \int_\Gamma P_{il}^*(f,c)u_l(c)\,d\Gamma = \int_\Gamma P_l(c)u_{il}^*(f,c)\,d\Gamma \tag{2}$$

where u_{ij}^* and p_{ij}^* are the Kelvin's fundamental solutions for displacement and tractions, u_j and p_j are boundary displacements and tractions and c_{il} the well known free term for elastic problems; it is equal to δ_{il} for internal points, zero for outside points and $\delta_{il}/2$ for smooth boundary nodes and also nodes defined along the crack surfaces.

To obtain this integral representation one has to differentiate equation (6) to obtain the strain integral equation, apply the Hooke's law to achieve the stress integral representation and then multiply this equation by the director cosines of the crack surfaces to obtain the traction representation for smooth collocations as follows:

$$\frac{1}{2}p_j(f) + \eta_k\int_\Gamma S_{kij}(f,c)u_k(c)d\Gamma = \eta_k\int_\Gamma D_{kij}(f,c)p_k(c)d\Gamma \tag{3}$$

where the kernels S_{kij} and D_{kij} are derived from the traction and displacement fundamental values following the steps above described.

Equations (2) and (3) are, as usual, transformed to algebraic relations by dividing the boundary and the crack surfaces into elements along which displacements and tractions are approximated. Besides that one has to select a convenient number of collocation points to obtain the algebraic representations. In this work we are using boundary collocation points either at the element ends, therefore coincident with nodes, or along the element when displacement and traction discontinuities are recommended. Using the discretized form of equation (2) applied only to boundary collocation points one can obtain the usual system of algebraic equations, relating boundary values, as follows:

$$H_b^b U_b + H_b^f U_f = G_b^b P_b + G_b^f f \tag{4}$$

where U_b, U_f, are displacements assigned to boundary (*b*) and to crack surface nodes (*f*), P_b gives the boundary tractions, while *f* represents the tractions applied along the crack surfaces; H_b^b, H_b^f, G_b^b and G_b^f are the corresponding matrices to take into account displacement and traction effects, the subscript *b* indicates that the collocation is on the boundary and the superscripts specify the boundary (*b*) or crack surface (*f*) values.

For the crack surfaces we need two opposite collocations for each discretization node to obtain four algebraic independent relations, corresponding to four unknown crack surface values, two displacements and two tractions. As we are dealing with hyper-singular equations (3), it is convenient to use collocation points defined along the element and not coincident with the discretization node. The node values of crack displacements and tractions are however kept at the element end. Thus, from the discretized forms of equations (2) and (3), one can write the following set of algebraic equations:

$$H_f^b U_b + H_f^f U_f = G_f^b P_b + G_f^f f \tag{5}$$

where the subscript *f* in the matrices H_f^x and G_f^x indicates equation written for collocation along the crack line.

Using equations (4) and (5) together with the cohesive crack model described in the previous section one can develop an appropriate algorithm to analyze crack problems as will be shown in the next section.

4 Solution technique

In the context of BEM a non-linear crack problem can be solved by simple schemes, in which the relevant matrices are kept constant and the corrections are applied to the crack surface forces according to the chosen criterion [6]. This technique is simple, but usually requires a large number of iterations to find the equilibrium within a load increment.

Non-linear implicit BEM formulations, employing tangent operators, have shown to give more accurate and stable results [7, 8]. In what follows, this

scheme is employed as an alternative technique to solve crack problems.

To derive the crack BEM approach using tangent operator let us modify the equilibrium equations (4) and (5) as follows

$$H_b^b U_b + H_b^r U_r + H_b^\ell U_\ell = G_b^b P_b + G_b^r P_r + G_b^\ell P_\ell \tag{6}$$

$$H_f^b U_b + H_f^r U_r + H_f^\ell U_\ell = G_f^b P_b + G_f^r P_f^r + G_f^\ell P_\ell \tag{7}$$

where the subscripts r and ℓ are related to the right and left crack surfaces.

Crack surface displacements and tractions in Equations (6) and (7) have to be modified to be given in local coordinates (n, s), in which n and s are coordinate axes perpendicular and parallel to the crack line, respectively. Then, one can define the crack opening displacements u_s and u_n as follows

$$U_{\ell s} = u_s - U_{rs} \qquad U_{\ell n} = u_n - U_{rn} \tag{8a,b}$$

After these modifications equations (6) and (7) read

$$\begin{aligned} &H_b^b U_b + \left(H_b^{rs} - H_b^{\ell s}\right) U_{rs} + \left(H_b^{rn} - H_b^{\ell n}\right) U_{rn} + H_b^{\ell s} u_s + \\ &H_b^{\ell n} u_n = G_b^b P_b + G_b^{rs} f_{rs} + G_b^{rn} f_{rn} + G_b^{\ell s} f_{\ell s} + G_b^{\ell n} f_{\ell n} \end{aligned} \tag{9}$$

$$\begin{aligned} &H_f^b U_b + \left(H_f^{rs} - H_f^{\ell s}\right) U_{rs} + \left(H_f^{rn} - H_f^{\ell n}\right) U_{rn} + H_f^{\ell s} u_s + \\ &H_f^{\ell n} u_n = G_f^b P_b + G_f^{rs} f_{rs} + G_f^{rn} f_{rn} + G_f^{\ell s} f_{\ell s} + G_b^{\ell n} f_{\ell n} \end{aligned} \tag{10}$$

Equations (9) and (10) have to be written and solved within the context of incremental problems. Thus, for a given increment of load one has to replace the boundary and crack values by the corresponding increments. Then, after applying the boundary conditions, as usual we have to store all unknown boundary increments into the vector ΔX and cumulate the known boundary value effects into the independent vectors ΔF_b and ΔF_f. Thus, equations (9) and (10) become

$$Y_b = A_b \Delta X + H_b^{\ell n} \Delta u_n - \Delta F_b - (G_b^{rn} - G_b^{\ell n}) \Delta f_{rn} = 0 \tag{11}$$

$$Y_f = A_f \Delta X + H_f^{\ell n} \Delta u_n - \Delta F_f - (G_f^{rn} - G_f^{\ell n}) \Delta f_{rn} = 0 \tag{12}$$

where A_b and A_f contain the coefficients of matrices referred to unknown boundary and crack surface displacement increments (ΔU_b, ΔU_{rs} and ΔU_{rn}), unknown boundary traction increments (ΔP_b), and the fictitious crack opening increments in the direction s (Δu_s). The traction increments in the direction s are neglected according to the adopted cohesive crack model. Moreover, the left

surface crack tractions $\Delta f_{\ell n}$ are replaced by minus right surface crack tractions, $-\Delta f_{rn}$.

To find the solution of equations (11) and (12) one has to linearize these equations using only the first term of the Taylor's expansion, as follows

$$Y_b\left(\Delta u_{nk}^{\ i}\right)+\frac{\partial Y_b\left(\Delta X_k^i,\Delta u_n^i...\right)}{\partial \Delta X_k^i}\delta\Delta X_k^i+\frac{\partial Y_b\left(\Delta X_k^i,\Delta u_n^i...\right)}{\partial \Delta u_{nk}^{\ i}}\delta\Delta u_{nk}^{\ i}=0 \tag{13}$$

$$Y_f\left(\Delta u_{nk}^{\ i}\right)+\frac{\partial Y_f\left(\Delta X_k^i,\Delta u_n^i...\right)}{\partial \Delta X_k^i}\delta\Delta X_k^i+\frac{\partial Y_f\left(\Delta X_k^i,\Delta u_n^i...\right)}{\partial \Delta u_{nk}^{\ i}}\delta\Delta u_{nk}^{\ i}=0 \tag{14}$$

Carrying out all indicated derivatives in equations (13) and (14) the following consistent tangent matrix is derived,

$$[C]=\begin{bmatrix} A_b & \left[H_b^{\ell n}-(G_b^{rn}-G_b^{\ell n})\partial\Delta f_{rn}/\partial\Delta u_{nk}^{\ i}\right] \\ A_f & \left[H_f^{\ell n}-(G_f^{rn}-G_f^{\ell n})\partial\Delta f_{rn}/\partial\Delta u_{nk}^{\ i}\right] \end{bmatrix} \tag{15}$$

where the derivatives $\partial\Delta f_{rn}/\partial\Delta u_{nk}^{\ i}$ are obtained by differentiating properly the adopted cohesive crack law.

Thus, the corrections $\delta\Delta X_k^i$ $\delta\Delta u_{nk}^{\ i}$, obtained from equations (13) and (14), is given by

$$\begin{Bmatrix}\delta\Delta X_k^i \\ \delta\Delta u_{nk}^{\ i}\end{Bmatrix}=-[C]^{-1}\begin{Bmatrix}Y_b\left(\Delta u_{nk}^{\ i}\right) \\ Y_f\left(\Delta u_{nk}^{\ i}\right)\end{Bmatrix} \tag{16}$$

Within a given load increment *k* the solution is obtained by cumulating the corrections computed by using equations (16) as follows

$$\Delta X_k^{i+1}=\Delta X_k^i+\delta\Delta X_k^i \tag{17}$$

$$\Delta u_{nk}^{\ i+1}=\Delta u_{nk}^{\ i}+\delta u_{nk}^{\ i} \tag{18}$$

The tolerance of this non-linear process is applied on the variation of the crack opening corrections, i.e., $u_i-u_{i-1}\le tolerance$.

5 Examples

In this section one example is presented to illustrate the efficiency of the proposed numerical model to analyse crack growth. In this example, we are analysing the crack propagation in a concrete four point-bending beam proposed by Galvez *et al*. [9]. The analysed beam is defined in Figure 2. The geometry is given by the beam length of 675mm, its height of 150mm and a central notch 75mm deep. The material properties were taken from Galvez *et al*. [9], who have

performed a laboratory test: tensile strength $f_t^{'} = 3.0\,MPa$, Young's modulus $E = 37000\,MPa$, Poisson ratio $\upsilon = 0.20$, and the fracture energy $G_f = 69N/m$.

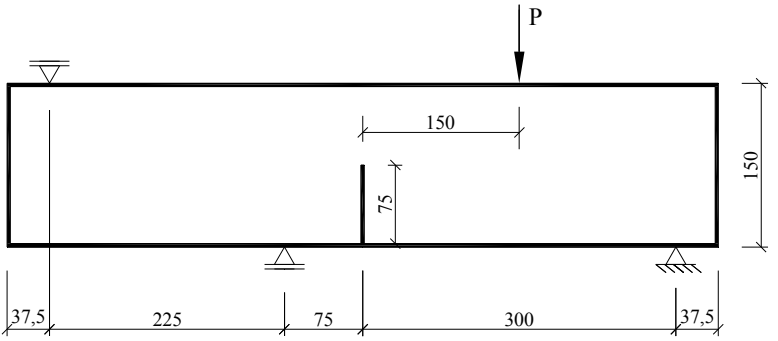

Figure 2: Analysed four-point beam. Dimensions in mm.

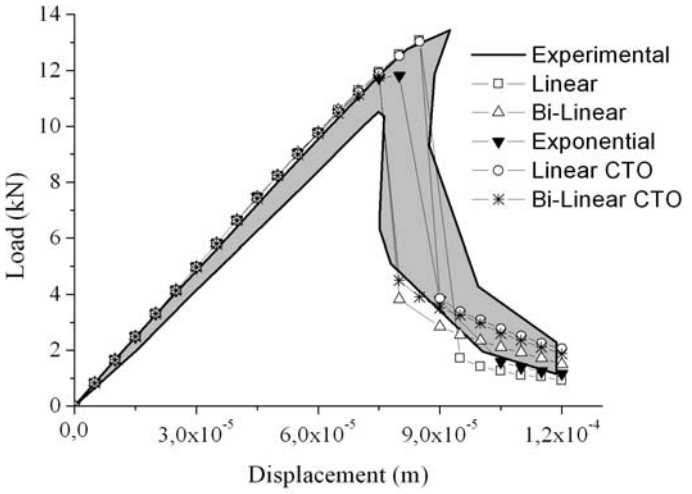

Figure 3: Load × displacement curves.

For the present analysis three cohesive laws were used: linear, bi-linear and exponential. For all analysed cases, the load was applied in 24 increments. The adopted tolerance within each increment was 10^{-5}. We have tested both non-linear system solution schemes discussed previously: a) based on the use of constant operator; b) based on the use of the consistent tangent operator. The obtained results are given in Figure 3, in which the tangent operator is identified

by the symbol CTO. The other curves are obtained by using the constant operator. Figure 4 illustrates the crack growth process during the beam loading, leading to rupture surfaces similar than the one experimentally obtained.

Although all the results are in accordance with the experimental results, it seems that the solutions obtained by using the tangent operator is more accurate. Moreover, the tangent operator give always more stable solution requiring a reduced number of iterations at each load increment. We can see that the descendent branch obtained by using constant operator is slightly different due to the cumulated errors coming from the large number of required post-pick iterations.

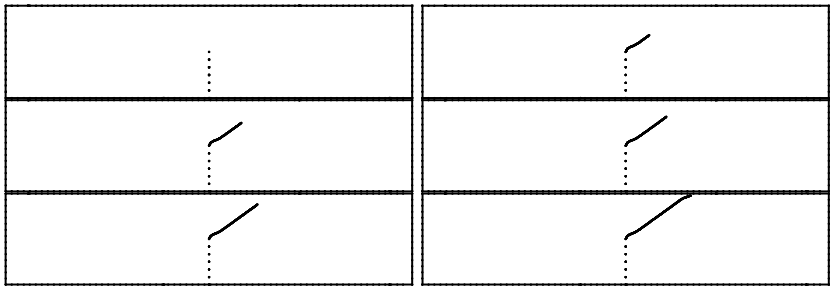

Figure 4: Crack growth profile during the load process.

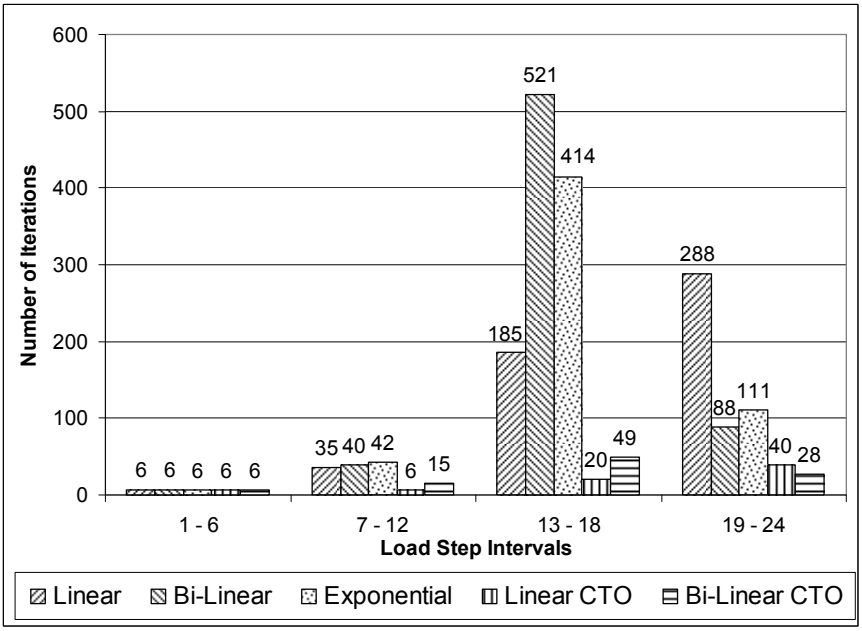

Figure 5: Number of iterations during some load increment intervals.

To emphasize the great differences between these two system solution schemes, the iteration number to reach the equilibrium at some specific load increments are given in Figure 5. It is important to see that the constant operator scheme require very large numbers of iterations after pick what may led to more inaccurate solutions.

6 Conclusions

We have derived and implemented a BEM formulation to analyse cohesive crack propagation based on using consistent tangent operator. The standard procedure based on constant operator to model crack propagation has also been implemented for comparison. The formulation based on the use of tangent operator has shown to be more stable and lead to more accurate results in comparison with the standard procedure. The use of tangent operator has shown to be always recommended to analyse crack propagations, particularly for the analysis that reach the after pick region.

References

[1] Hillerborg, A., Modeer, M. & Peterson, P.E., Analysis of crack formation and crack growth in concrete by mean of failure mechanics and finite elements. *Cement Concrete Research*, **6**, pp. 773-782, 1976.
[2] Portela, A., Aliabadi, M.H. & Rooke, D.P., Dual boundary element method: Efficient implementation for cracked problems. *International Journal for Numerical Methods in Engineering*, **33**, pp. 1269-1287, 1992.
[3] Venturini, W.S., A new boundary element formulation for crack analysis. In: Brebbia, C.A., (ed.) *Boundary element method XVI*, Computational Mechanics Publications, Southampton and Boston, pp. 405-412, 1994.
[4] Manzoli, O.L. & Venturini, W.S., An Implicit BEM formulation to model discontinuities in solids. *Computational Mechanics*, **40**, pp. 901-909, 2007.
[5] Leite, L.G.S. & Venturini, W.S., Stiff and soft thin inclusions in two-dimensional solids by the boundary element method. *Engineering analysis with boundary elements*, **29(3)**, pp. 257-267, 2005.
[6] Saleh, A.L. & Aliabadi, M.H., Crack-growth analysis in concrete using boundary-element method. *Engineering Fracture Mechanics*, **51 (4)**, pp. 533-545, 1995.
[7] Benallal, A., Fudoli, C.A. & Venturini, W.S., An implicit BEM formulation for Gradient plasticity and localization phenomena. *International Journal for Numerical Methods in Engineering*, **53**, pp. 1853-1869, 2002.
[8] Benallal, A., Botta, A.S. & Venturini, W.S., On the description of localization and failure phenomena by the boundary element method. *Computer Methods in Applied Mechanics and Engineering*, **195**, pp. 5833-5856, 2006.
[9] Galvez, J.C., Elices, M. Guinea, G.V. and Planas, J., Mixed mode fracture of concrete under proportional and nonproportional loading. *International Journal of Fracture*, **94**, pp. 267-284, 1998.

This page intentionally left blank

Stress field in the Antarctic tectonic plate: elastic and plastic models

P. Haderka[1], A. N. Galybin[1] & Sh. A. Mukhamediev[2]
[1]*Wessex Institute of Technology, Southampton, UK*
[2]*Institute of Physics of the Earth, Moscow, Russia*

Abstract

The purpose of this study is to compare different rheological models of tectonic plates for the same set of input data. First, the 2D elastic tectonic stress field in Antarctic plate is modelled by employing experimental data on principal stress orientations. Then the determination of the 2D stress field by assuming the Antarctic lithospheric plate to be in fully plastic state follows. Boundary conditions for the plastic model are specified from the elastic solution. A finite-difference type approach based of alternation of the Cauchy boundary value problems for the construction of the slip lines and the principal stress trajectories is applied to obtain distribution of the mean stress within Antarctic plate. The significance of rheology is underpinned by comparing the elastic and plastic fields of the mean stress.

Keywords: stress field, elasticity, plasticity, geodynamics, tectonics.

1 Introduction

Antarctica is a key element in Earth's geodynamic and climatic systems for a variety of reasons:

- Antarctica continues to be tectonically active, Torsvik *et al.* [1].
- Antarctica is significant in the global relative plate motion circuit and the quantification of internal deformation of Antarctica is an essential part of any global relative-plate-motion model, [2, 3].
- Antarctica plays a central role in shaping the present global environment.

Despite this importance the first-order characteristics of the lithosphere remain poorly described over large portions of the continent.

WIT Transactions on Modelling and Simulation, Vol 49, © 2009 WIT Press
www.witpress.com, ISSN 1743-355X (on-line)
doi:10.2495/BE090231

To the best of our knowledge, no papers devoted to mathematical modelling of the regional tectonic stress field caused by driving forces applied at the Antarctic plate (AP) boundaries have been published. This can be explained by the absence of data on principal stress orientations within the plate, that is vital for obtaining the plate-scale solutions by conventional methods as it has been done for several regions, among others, for the Indo-Australian, African, West European, and North American plates [4–8]. The cited papers employ the traditional approach of the 2D elasticity and make use of experimentally obtained data on orientations of the principal stresses (mainly from World Stress Map Project database, Reinecker *et al* [9]) as constraints imposed on the solutions. The stress fields are calculated by solving a number of boundary value problems of elasticity often posed in terms of stresses. This presumes that the boundary stresses are chosen either hypothetically or from model considerations such that the calculated orientations of the principal stresses fit the observed stress orientations. Such an approach always leads to crucial uncertainness in the stress tensor determination because similar stress orientations can be obtained for different magnitudes of boundary stresses.

In the present study this peculiarity is overcome by the direct use of the data available without any assumptions on stress magnitudes. Analysis of the elastic constitutive equations then enables to recover the fields of mean stress and maximum shear stress. Boundary values of the former then serve as one of the boundary conditions (BC) for the plastic problem.

Solution of the 2D ideal plastic problem where the boundary values are propagated along slip lines is well known and available in works of Hill [10] or Kachanov [11]. The solution of the Cauchy problem however is constrained inside a triangular region the legs of which are the characteristics of the 2D problem's equations. The main target now becomes to propagate the solution beyond the boundaries of the initial triangle in order to extend the solution surface. The concept of stress trajectories is employed for this purpose as will be shown in the text.

Important aspects of our study are as follows:

- The use of a special numerical procedure which recasts the WSMP experimental data in the form of BC formulated in terms of principal stress orientations specified on contour (with regard to AP).
- Development of the method of alternation of the principal stress trajectories grid and the slip lines grid while integrating the plasticity equations.

2 Mathematical models in elasticity and plasticity

2.1 Data and assumptions used in modelling

The data of A-C quality on orientations of principal stresses from the 2005 release of the WSMP database (in [9]) are used. Due to low seismic activity of AP almost all data are concentrated on the AP margins suggesting that inclination, φ, of the maximum horizontal compression within AP has a limiting values $\varphi^{\pm}$ on the contour Γ associated with the AP boundary and these are the

only boundary data available from observations. Other BC are needed for proper formulation of an elastic boundary value problem, and these can assume continuity of the stress vector across the boundary, see Galybin [12] for detail.

Basal shear stresses acting beneath the lithosphere are neglected, which can be justified by the fact that AP has a low absolute velocity with respect to the deeper mantle, as introduced in [13–14]. Therefore a 2D model reflecting driving forces applied at the AP boundary can be considered separately, while the complete 3D stress tensor can be obtained by superimposing the stresses caused by the rock weight and ice sheet load on the continental part of the plate. Gravitational potential energy differences which produce lateral body forces and have been recognised as an important source for intraplate stresses in AP, see Kreemer and Holt [15], in the elastic problem affect neither principal stress orientations nor deviatoric stresses if potential of body forces is approximated by harmonic function, as explained in Mukhamediev *et al* [16]. Lateral body forces caused by harmonic potential only influence the magnitudes of principal stresses by adding to them the same amount which can be different from point to point.

For simplicity it is assumed that the region (Antarctic tectonic plate) is planar, that is, Earth's curvature is neglected and the plate is projected on the equatorial plane (plane stress conditions may be adopted). It has also been assumed that the adjacent regions are isotropic.

Body forces will be absent in the computations, however they are accounted for in the BC (data on stress orientations). For the plastic solution it is assumed that the entire domain is in the state of limiting equilibrium. The model of ideal plasticity is adopted, however, this simplification is not vital and can be extended to take friction and cohesion into account.

2.2 Mathematical model in elasticity

The mathematical model for elastic rheology has been introduced in detail e.g. in Galybin and Mukhamediev [17]. The differential equations of equilibrium (DEE) in complex form are used further on:

$$\frac{\partial P(z,\bar{z})}{\partial z} = \frac{\partial D(z,\bar{z})}{\partial \bar{z}}, \quad \frac{\partial^2 P(z,\bar{z})}{\partial z \partial \bar{z}} = 0 \tag{1}$$

where the stress functions P and D represent the mean and deviatoric stress, respectively. Using the Kolosov–Muskhelishvili formulae one can present the general solution of plane elasticity as follows:

$$P(z,\bar{z}) = \Phi(z) + \overline{\Phi(z)}, \quad D(z,\bar{z}) = \bar{z}\Phi'(z) + \Psi(z) \tag{2}$$

Here P and D are functions of complex variables $z = x - iy$, $\bar{z} = x - iy$ expressed by two holomorphic functions $\Phi(z)$, $\Psi(z)$ of the complex variable z. It is evident from (2) that the stress deviator satisfies the following equation:

$$\frac{\partial^2 D(z,\bar{z})}{\partial^2 \bar{z}} = 0 \tag{3}$$

and therefore the elastic problem can be formulated in terms of the stress function D alone. As soon as this function becomes known one can also obtain the mean stress by integration of the equations of equilibrium. This operation introduces an additive constant that cannot be found from the data on orientations of principal stresses.

It should be noted that the deviatoric stress in complex exponential form is:

$$D(z,\bar{z}) = \tau(z,\bar{z})e^{i\alpha(z,\bar{z})} \tag{4}$$

where the modulus $\tau(z,\bar{z})$ is associated with the maximum shear stress τ_{max} while the argument $\alpha(z,\bar{z})$ is associated with the principal direction φ as $\alpha(z,\bar{z}) = -2\varphi(z,\bar{z})$ (in accordance with the geomechanical convention).

The first set of boundary conditions is represented by the argument of the deviatoric stress ($\arg(D(z,\bar{z})) = \alpha(z,\bar{z})$), which can be expressed in the following form:

$$\mathrm{Im}\left(e^{-i\alpha^{\pm}(z,\bar{z})} D^{\pm}(\zeta,\overline{\zeta}) \right) = 0, \quad \zeta \in \Gamma \tag{5}$$

Hereafter the sings ± distinguish the boundary values for different sides of the domain's boundary.

To complete the formulation of the problem another BC has to be specified. It assumes continuity of tractions along the margins of the domain:

$$N^{+}(\zeta) + iT^{+}(\zeta) = N^{-}(\zeta) + iT^{-}(\zeta) \tag{6}$$

N, T are normal and shear components of the stress vector on Γ.

The following procedure is further applied for numerical calculations. The complex potentials Φ, Ψ are sought as polynomials with unknown complex coefficients c_k:

$$\Psi(z) = \sum_{k=0}^{n} c_k z^k , \quad \Phi(z) = \sum_{k=0}^{n} c_{k+n+1} z^k \tag{7}$$

After substitution of (7) into (2) followed by further substitution of the latter into (5) and (6) one obtains a system of linear algebraic equations with respect to unknown coefficients c_k:

$$\mathbf{AX} = \mathbf{B} \tag{8}$$

Here it should be noted that this system is not fully homogeneous, it has been complemented by a non-homogeneous equation that assumes that the average value of the maximum shear stress over the entire domain is unity. The system is redundant and therefore it is solved by the least squares method

$$\mathbf{X} = \left(\mathbf{A}^T\mathbf{A}\right)^{-1}\mathbf{A}^T\mathbf{B} \tag{9}$$

The identified coefficients c_k are then inserted back to (7) and further to (2) which gives the sought stress functions.

2.3 Mathematical model in plasticity

Plastic model is based on classical formulations and numerical approaches developed in [10, 11] and complemented by an approach reported recently in Haderka and Galybin [18] that allows extending the solution of the Cauchy boundary value problem beyond the characteristic triangle formed by the slip lines emanating from the boundary. This approach is briefly explained further on.

Based on the Tresca's yield criterion for an ideally plastic material:

$$\tau = \frac{\sigma_1 - \sigma_2}{2} = const = c \tag{10}$$

one can present the Lamé-Maxwell DEE along stress trajectories s_1 and s_2 in the following simple form:

$$\frac{\partial \psi}{\partial s_1} + \frac{\partial \varphi}{\partial s_2} = 0\,, \quad \frac{\partial \psi}{\partial s_2} + \frac{\partial \varphi}{\partial s_1} = 0 \tag{11}$$

where $\psi = P/2c$ and will be referred to as normalised mean stress.

Classical boundary value problem of plasticity assumes that the mean stress P and orientations of principal stresses φ can be found by the given stress vector, $N+iT$, on the boundary, and therefore DEE can be easily integrated by the finite difference method. In this study we modified the procedure of numerical integration by using curvilinear net of the stress trajectories instead of the regular grid in Cartesian coordinates that is often used in conventional approaches.

Integration of the equations is performed layer by layer, the first layer being the initial boundary of the problem (L in Fig. 1). Individual layers are denoted by index k and the position on the layer by j.

In order to build the solution along the stress trajectories the Taylor's expansion is used. Accepting the notation in Fig. 1, the orientations and stresses in the layer z_j^{k+1} next to the boundary z_j^k, can be written as follows:

$$\varphi_j^{k+1} = \varphi_j^k + \left| s_{1,j}^k \right| \left| \frac{\partial \varphi}{\partial s_1} \right|_j^k \qquad \psi_j^{k+1} = \psi_j^k + \left| s_{1,j}^k \right| \left| \frac{\partial \psi}{\partial s_1} \right|_j^k \tag{12}$$

The derivatives in (12) are determined from DEE (11). However, they still remain unknown. In order to find them, decomposition to the tangential and normal part is necessary which has the form:

$$\frac{\partial}{\partial s_1} = \cos\gamma \frac{\partial}{\partial t} + \sin\gamma \frac{\partial}{\partial n} \qquad \frac{\partial}{\partial s_2} = -\sin\gamma \frac{\partial}{\partial t} + \cos\gamma \frac{\partial}{\partial n} \tag{13}$$

Transformation (13) introduces new unknowns, namely, the normal derivatives of normalised mean stress and of principal orientation which are connected with the contour derivatives as follows:

$$\begin{bmatrix} \left.\frac{\partial \psi}{\partial n}\right|_j^k \\ \left.\frac{\partial \varphi}{\partial n}\right|_j^k \end{bmatrix} = -\begin{bmatrix} \sin\gamma_j^k & \cos\gamma_j^k \\ \cos\gamma_j^k & \sin\gamma_j^k \end{bmatrix}^{-1} \begin{bmatrix} \cos\gamma_j^k & -\sin\gamma_j^k \\ -\sin\gamma_j^k & \cos\gamma_j^k \end{bmatrix} \begin{bmatrix} \left.\frac{\partial \psi}{\partial t}\right|_j^k \\ \left.\frac{\partial \varphi}{\partial t}\right|_j^k \end{bmatrix} \tag{14}$$

Here the tangential derivatives are found from the values at nodes z_j^k. Finally the tangential and normal derivatives may be introduced in (12) to give the orientations and stresses in the nodes z_j^{k+1}:

$$\begin{bmatrix} \varphi_j^{k+1} \\ \psi_j^{k+1} \end{bmatrix} = \begin{bmatrix} \varphi_j^k \\ \psi_j^k \end{bmatrix} + \frac{\left|s_{1,j}^k\right|}{\cos 2\gamma_j^k} \begin{bmatrix} \cos\gamma_j^k & -\sin\gamma_j^k \\ -\sin\gamma_j^k & \cos\gamma_j^k \end{bmatrix} \begin{bmatrix} \left.\frac{\partial \varphi}{\partial t}\right|_j^k \\ \left.\frac{\partial \psi}{\partial t}\right|_j^k \end{bmatrix} \tag{15}$$

Equations (15) are solved by employing the forward finite difference scheme. The solution is less stable in the regions where the local angle γ is close to $\pm n\pi/4$, $n = 1,2,\ldots$. Nodes z_j^{k+1} have to be determined prior to the solution of φ and ψ as these coordinates enter the calculations. The basic property of stress trajectories is used here which states that they form an orthogonal grid (different families of stress trajectories intersect at right angles). However, only a linear approximation of stress trajectories is used and tangents, see Fig. 1, to them are used instead the real trajectories (same type of approximation is utilized in classical solution).

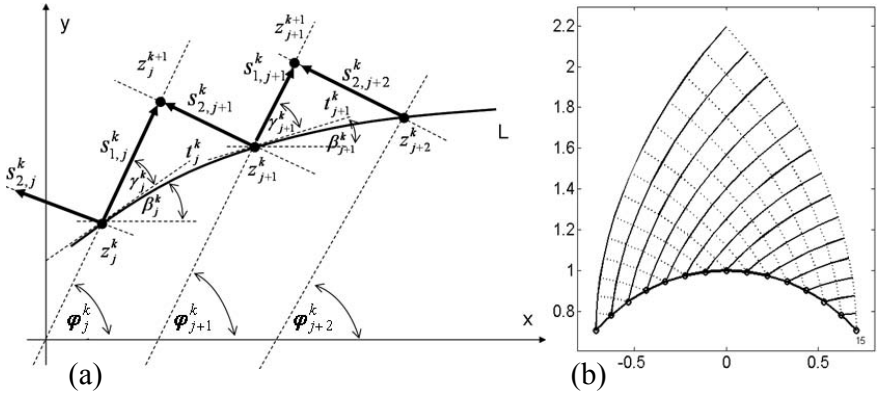

Figure 1: Determination of the coordinates and visualization of angles (a). Typical solution (characteristic triangle) (b).

2.4 Plastic model and the alternations of Cauchy's problems

The idea is based on the relation between lines of slip and stress trajectories which, according to the classical stress theory, are inclined at angles $\pi/4$ (see Fig. 2(a)). The main reason for the development of the concept of alternations is

to eliminate the drawback of the classical solutions which is the impossibility to construct solution beyond the initial characteristic triangle (unless some special conditions are imposed, e.g. in Martin [19]).

Let a characteristic triangle be obtained by means of classical methods using the slip lines. Then the principal directions are obtained within this triangle by the rotation of the tangents to the slip lines at the nodes (Fig. 2(b)). Now a new boundary can be formed for the solution along stress trajectories and the numerical scheme, described is subsection 2.3, may be employed. The same procedure can be applied to the solution obtained for the stress trajectories in a different characteristic triangle in order to recover the slip lines.

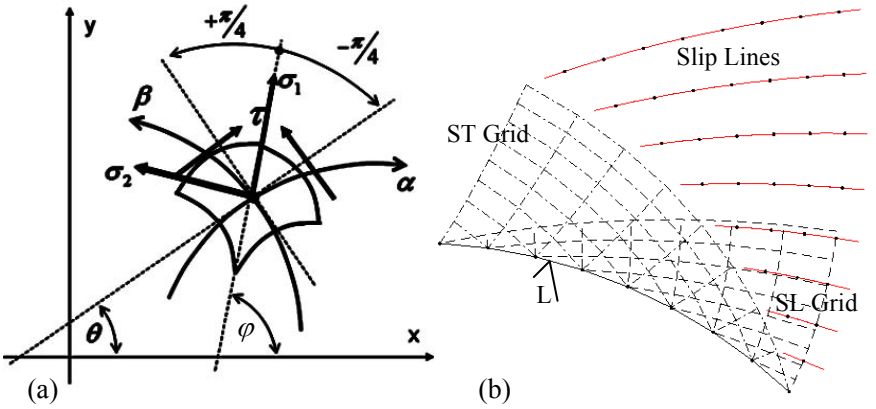

Figure 2: Slip element under normal and shear load (a). Alternations of Cauchy's problems (b).

It is required to modify the BC properly as the classical methods require the angle of slip as the boundary condition while for building stress trajectories the principal orientations are employed as the BC.

Fig. 2(b) shows a boundary L for which the stress trajectories grid (ST grid) and the slip lines grid (SL grid) have been obtained. It should be mentioned that the results in the area where the triangles intersect correspond perfectly. Moreover the idea of alternations can be noticed from the same picture. The area labelled as Slip Lines is reconstructed by taking the right leg of the ST triangle as a new contour. Note the agreement of the results where the slip lines and SL grid overlaps.

3 Computational model of Antarctic tectonic plate and results of numerical analysis

The computational domain for the 2D elastic problem was built according to Bird's [20] digital model which includes 353 points presenting the margins of the plate. For the purposes of the computations the data which are originally scattered along the margin of the plate had to be separated into internal and external ones. The numerical procedure designed for this objective revealed that

there are 170 internal data on stress orientations available for the solution. Moreover, data of highest quality were only chosen (quality ranks A-C; according to the WSMP ranking scheme, taken from Reinecker *et al* [9], these record data to within ±10°- 25° precision).

For the plane strain perfectly plastic problem the necessary boundary conditions were taken from the results of the previous elastic analysis (Galybin [12]). The scattered data were approximated along the model's boundary and their number was set to 90 (number of boundary nodal points with mean stress and orientations of principal stress available in them). This allows the comparison of elastic and plastic solutions inside the plate for the same set of boundary conditions.

Fig. 3(a) shows the computational domain, Antarctic tectonic plate, together with the continent of Antarctica and the available data on stress orientations which are clearly scattered along the margins. Fig. 3(b) presents the profiles of the boundary conditions used for plastic analysis (mean stress and orientations of principal stresses).

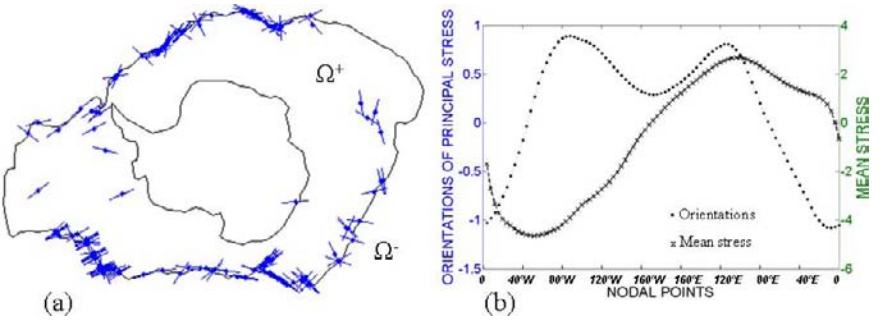

Figure 3: Antarctic tectonic plate with the data on orientations (a). Smoothened data for plastic solution (b).

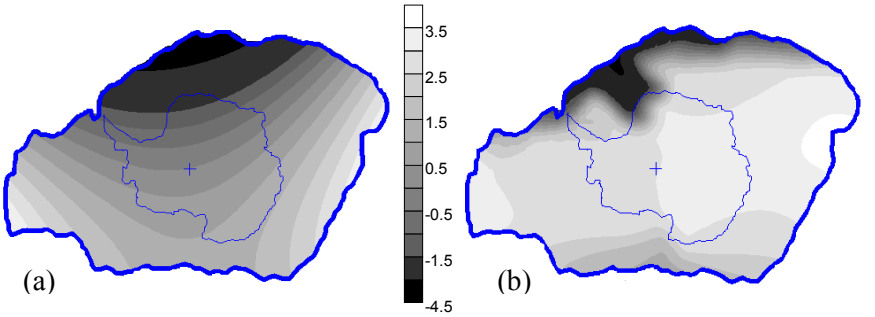

Figure 4: Map of reconstructed stress fields, function *F*, for elastic (a) and plastic (b) rheologies.

For both elastic and plastic problems the maps of mean stresses have been compiled. However, it is necessary to state that only the scaled mean stress

function F has been recovered which is related to the mean stress as $P=aF+b$ ($a>0$, and b are free constant parameters of the problem). The maps of this function for both the elastic and plastic cases are shown in Fig. 4.

It is evident from Fig. 4 that the maps are essentially different even for the same boundary values. The reconstructed function F is strongly affected by the type of the rheology selected for the analysis. Thus, in the case of the elastic solution the distribution of mean stresses in the eastern part of the continental lithosphere is more non-uniform as compare to homogeneous one for the plastic case.

4 Conclusions

In contrast to other lithospheric plates no attempts have been made so far to determine the stress field in the AP. This is due to the nature of experimental data on stress orientations the majority of which are concentrated at the AP boundaries causing non-applicability of standard approach that needs stress orientations to be known inside a region to constrain solution.

In the present paper two models of the AP stress field have been developed based on the stress orientation concept. They presume either elastic or ideal plastic rheology for the entire AP tectonic plate. It is evident from the results in Fig. 4 that different rheologies lead to essentially different results in modelling tectonic stresses. Therefore the use of purely statistical or interpolation methods, widely applied for studying stresses in the lithosphere, should be avoided and replaced by proper mechanical models that take the rheology into account.

The elastic model is based on numerical solution of the optimisation problem for the data fitting complemented by mechanically justified conditions of continuity of the stress vector across the margins of the adjacent tectonic plates.

The plastic model is investigated by using the concept of alternations of the Cauchy problems for the construction the slip lines and stress trajectories. It is shown that such approach is capable to handle quite complex plane regions, however, verifications regarding convergence and accuracy are still necessary.

Acknowledgement

The authors acknowledge the support of EPSRC through Research Grant EP/E032494/1.

References

[1] Torsvik, T. H., Gaina, C., Redfield, T. F., Antarctica and global paleogeography: From Rodinia, through Gondwanaland and Pangea, to the birth of the Southern Ocean and the opening of Gateways, –In: Cooper A.K. et al., eds. Antarctica: A keystone in a changing world, Proceedings of the 10th International Symposium on Antarctic Earth Sciences, Washington, DC: The National Academies Press, p. 125-140, 2008.

[2] Gordon, R. G., The Antarctic connection, Nature, **404**, p 139-140, 2000.
[3] Sutherland, R., The significance of Antarctica for studies of global geodynamics, –In: Cooper A.K. et al., eds. Antarctica: A keystone in a changing world, Proceedings of the 10th International Symposium on Antarctic Earth Sciences, Washington, DC: The National Academies Press, p. 115-124, 2008.
[4] Cloetingh, S., Wortel, R., Regional stress field of the Indian plate, Geophys. Res. Lett., **12**, p. 77-80, 1985.
[5] Coblentz, D. D., Sandiford, M., Richardson, R. M., Zhou S and Hillis, R., The origins of the intraplate stress field in continental Australia. Earth Planet. Sci. Lett., **133**, p. 299-309, 1995.
[6] Coblentz, D. D., Sandiford, M., Tectonic stresses in the African plate: Constraints on the ambient lithospheric stress state, Geology, **22**, p. 831-834, 1994.
[7] Gölke, M., Coblenz, D., Origins of the European regional stress field, Tectonophysics, **266**, p. 11-24, 1996.
[8] Humphreys, E. D., Coblentz, D. D., North American dynamics and western U.S. tectonics, Rev. Geophys, v. 45, RG3001, doi:10.1029/2005RG000181, 2007.
[9] Reinecker, J., Heidbach, O., Tingay, M., Sperner, B., Müller, B., The release 2005 of the World Stress Map // 2005, available online at www.world-stress-map.org.
[10] Hill, R., The Mathematical Theory of Plasticity, Oxford: Clarendon Press, 1950.
[11] Kachanov, L. M., Fundamentals of Theory of Plasticity, Published: Foundations of the theory of plasticity, Amsterdam, 1971.
[12] Galybin, A. N., Stress fields in joined elastic regions: Modelling based on discrete stress orientations, In Situ Rock Stress – Lu, Li, Kjerholt & Dahle (eds), Taylor & Francis/Balkema, Leiden, p. 193-199, 2006.
[13] Sykes, L., Intraplate seismicity, reactivation of pre-existing zone of weakness, alkaline magmatism and other tectonism postdating continental fragmentation, J. Geophys. Res., **16 (B)**, p. 621-687, 1978.
[14] Okal, E. A., The Bellingshausen sea earthquake of February 5, 1977: Evidence for ridge-generated compression in the Antarctic plate, Earth Planet. Sci. Lett., **46**, p. 306-310, 1980.
[15] Kreemer, C., Holt, W. E., What Caused the March 25, 1998 Antarctic Plate Earthquake?: Inferences from Regional Stress and Strain Rate Fields, Geophys. Res. Lett., **27**, p. 2297-2300, 2000.
[16] Mukhamediev, Sh. A., Galybin, A. N., Brady, B. H. G., Determination of stress fields in the elastic lithosphere by methods based on stress orientations, Int. J. of Rock Mech. & Mining Sci., **43**, p. 66-88, doi:10.1016/j.ijrmms.2005.04.008, 2006.
[17] Galybin, A. N., Mukhamediev Sh. A., Determination of Elastic Stresses from Discrete Data on Stress Orientations, Int. J. of Sol. and Struc., **41**, 5125-5142, 2004.

[18] Haderka P., Galybin A. N., Damage zones near excavations: Plastic solution by means of stress trajectories, First international conference on underground spaces – design, engineering and environmental aspects, **1**, 109-119, 2008.
[19] Martin, C. M., Exact bearing capacity calculations using the method of characteristics, Proc. 11th Int. Conf. of IACMAG, Turin, **4**, pp 441-450, 2005
[20] Bird, P., An updated digital model for plate boundaries, Geochem. Geophys. Geosyst., **4(3)**, 1027, doi: 10.1029/2001GC000252, 2003.

This page intentionally left blank

Section 6
Dynamics and vibrations

This page intentionally left blank

Velocity-based boundary integral equation formulation in the time domain

G. D. Manolis & C. G. Panagiotopoulos
Department of Civil Engineering, Aristotle University of Thessaloniki, Thessaloniki, Greece

Abstract

In this work, we present a reciprocal theorem of linear elastodynamics derived in terms of velocities instead of displacements, which seems to be better suited in relating two different elastodynamic states of an elastic region for several reasons that will be discussed latter on. As with the conventional displacement integral equation representation, using this alternative reciprocal theorem we can produce a velocity integral equation representation and then formulate a novel numerical approximation based on the boundary element method (BEM). Furthermore, a thorough stability performance analysis of the formulations arise utilizing displacement and/or velocity reciprocal theorems is presented.

Keywords: boundary elements, convolution integrals, transient elastodynamics, reciprocal theorems, velocities.

1 Introduction

In linear elastodynamics and their numerical approximations based on the boundary integral equation method (BIEM), a common starting point is Graffi's reciprocal theorem relating the displacement and traction fields in a given solid body [1]. Furthermore, either a variational or a weighted residual statement that leads to the above reciprocal theorem can also serve as the starting point [2].

In general, reciprocal theorems in elasticity provide a relation between displacements, tractions and body forces for two different loading states pertaining to the same solid. Assuming that the one loading state is the one sought, and another is that corresponding to a unit impulse applied at zero time and at fixed source point ξ in the infinite region and in the direction of the coordinate axes, it is possible to obtain what is called an integral representation for displacements in elastodynamics. A drawback, however, of the reciprocal

WIT Transactions on Modelling and Simulation, Vol 49, © 2009 WIT Press
www.witpress.com, ISSN 1743-355X (on-line)
doi:10.2495/BE090241

relation is that it does not include the purely elastostatics case; also, the numerical formulations derived from its use are known to present stability problems unless special precautions are taken.

The advantage of this velocity-based reciprocal theorem, as well as of the numerical approximation that derives from it is as follows:

- It includes the case of elastostatics from which the well-known Betti's reciprocal theorem may be derived.
- Problems for which the prescribed boundary data of Dirichlet-type and given as velocities at discrete time intervals may be countered without the need of time integration to recover the corresponding displacement input data.
- More stable numerical methods than those produced by the conventional displacement formulation.

It is important here to mention that velocity integral representation formula has also been presented and utilized elsewhere [3, 4] but not as an outgrowth of the respective reciprocal theorem and also used for other purposes, *i.e.* discontinuous traction field, than for these presented here that are theoretical consistency of reciprocal statement in elastodynamics and numerical stability of BIEM formulations derived.

2 Reciprocal theorems in terms of displacements

The reciprocal theorem first specifies a regular region V in the sense of Kellog with boundary S and material properties ρ, c_1, c_2 as the mass density, the pressure and shear velocity of propagation respectively. Considering two distinct elastodynamic states $A=[u_i, t_i, b_i]$ and $B=[u'_i, t'_i, b'_i]$ defined in that region and with initial conditions,

$$u_i(x,0)=u_i^0(x), v_i(x,0)=v_i^0(x) \tag{1a}$$

$$u'_i(x,0)=u_i'^0(x), v'_i(x,0)=v_i'^0(x) \tag{1b}$$

where u_i, t_i, b_i are the displacement field, the tractions and body forces respectively, while v_i is the velocity field defined as the first time derivative of displacements. Then for time $t \geq 0$

$$\int_S t_i * u'_i \, dS + \int_V \rho\left(b_i * u'_i + v_i^0 u'_i + u_i^0 v'_i\right) dV = \int_S t'_i * u_i \, dS + \int_V \rho\left(b'_i * u_i + v_i'^0 u_i + u_i'^0 v_i\right) dV \tag{2}$$

holds true, where operation $*$ denotes Riemann's convolution, *i.e.*,

$$f * g = \int_0^t f(x, t-\tau) g(x,\tau)\, d\tau \tag{3}$$

for $t \geq 0$ and for two arbitrary functions f and g. As it is well known the basic approach for considering static conditions in an elastic body is to take zero values for time derivatives of the displacements. Under this consideration eqn (2) would led to the following form:

$$\int_S t_i * u_i' \, dS + \int_V \rho b_i * u_i' \, dV = \int_S t_i' * u_i \, dS + \int_V \rho b_i' * u_i \, dV \tag{4}$$

which goes on being convoluted type relation between displacement, traction fields and body forces and it can not lead to the classical Betti's reciprocal theorem for linear elastodynamics.

3 Reciprocal theorems in terms of velocities

There are several ways to proceed with higher order time derivatives reciprocal theorems, *e.g.* variational approaches, here we adopt the simplest one which is the direct differentiation in time of eqn (2). To proceed further we utilize the Leibniz's general rule for differentiation under the integral sign, or the time-differentiation property of convolutions, which states that:

$$\frac{d\left(f * g\right)}{dt} = \frac{df}{dt} * g + f^0 g = f * \frac{dg}{dt} + f\, g^0 \tag{5}$$

where f^0 and g^0 stand for f and g at time $t = 0$. We focus here at the first time derivative of eqn (2) which will provide us with the reciprocal theorem of elastodynamics in terms of velocities,

$$\begin{aligned} &\int_S t_i * v_i' + t_i u_i'^0 \, dS + \int_V \rho\left(b_i * v_i' + b_i u_i'^0 + v_i^0 v_i' + u_i^0 a_i'\right) dV = \\ &\qquad \int_S t_i' * v_i + t_i' u_i^0 \, dS + \int_V \rho\left(b_i' * v_i + b_i' u_i^0 + v_i'^0 v_i + u_i'^0 a_i\right) dV \end{aligned} \tag{6}$$

where a_i denotes the second time derivative of u_i component, namely the acceleration's i^{th} component. Also notice here that in order to achieve eqn (6) the property of convolution given by eqn (5) has been utilized. Reciprocal statement given by eqn (6) is one of convolution type relating velocities and tractions on the boundaries of two distinct elastodynamic states as well as displacements, velocities, accelerations and body forces inside the domain V. For the above reciprocal relation if someone assumes static conditions, *i.e.* zero time derivatives for displacements, would lead directly to:

$$\int_S t_i u_i'^0 \, dS + \int_V \rho b_i u_i'^0 \, dV = \int_S t_i' u_i^0 \, dS + \int_V \rho b_i' u_i^0 \, dV \tag{7}$$

which is the well-known Betti's reciprocal theorem for linear elastostatics. It is also interesting to notice that like eqn (2), which may be seen as a "convoluted" form of the principle of virtual work produced by the displacements of one state with the tractions of the other state, eqn (6) represent a "convoluted" form of the principle of virtual power produced by velocities of one state with the tractions of the other.

4 Axial waves in the 1D rod

In order to investigate at least the temporal properties of algorithms derived by displacement and velocity reciprocal theorems and in an effort to avoiding the spatial discretization and integration we deal here with the simplest case

consisting of the case of axial waves in one-dimensional finite rods (homogeneous or piecewise homogeneous).

The governing equations of the problem under consideration are the equilibrium equation plus the boundary conditions at the two end of a rod with elasticity modulus E, mass density ρ and section A:

$$EA\frac{\partial^2 u}{\partial x^2} - \rho A\frac{\partial^2 u}{\partial t^2} = 0 \tag{8}$$

$$\begin{aligned} u(x,t) &= \tilde{u}(x,t) \quad on \quad \Gamma_u \\ f(x,t) &= \tilde{f}(x,t) \quad on \quad \Gamma_t \end{aligned} \tag{9}$$

The fundamental solution as well as its derivatives (temporal or spatial) for this simple problem can be achieved with standard procedures like those described in [5] and are given below.

$$u^* = -\frac{c}{2EA}H\left(t - \frac{|x-\xi|}{c}\right) \tag{10}$$

$$\frac{\partial u^*}{\partial x} = \frac{1}{2EA}\frac{|x-\xi|}{x-\xi}\delta\left(-t + \frac{|x-\xi|}{c}\right) \tag{11}$$

$$\frac{\partial u^*}{\partial t} = -\frac{c}{2EA}\delta\left(t - \frac{|x-\xi|}{c}\right) \tag{12}$$

In the above solutions $c = \sqrt{E/\rho}$ is the velocity of wave propagation, δ is the Dirac's delta and H is the Heaviside function. Although the simplicity of eqn (8) it is very suitable in order to investigate the numerical behaviour of algorithms arise applying boundary integral methodology utilizing reciprocal theorems and also has a practical rate. A boundary integral formulation in order to numerically solve eqn (30) is also presented in [6] for the exploration of 1D wave propagation analysis in layered media.

4.1 Time discretization and BIEM formulation

Following standard procedures of the BIEM formulations that due to space limitations are ignored, we may derive the displacement and velocity integral representation based on reciprocal theorems in terms of displacements and velocities respectively, for a rod of length L:

$$\begin{aligned} u(\xi,t) = &\int_0^t EAu(L,\tau)u'^*(L-\xi,t-\tau)\,d\tau - \int_0^t EAu'(L,\tau)u^*(L-\xi,t-\tau)\,d\tau \\ &- \int_0^t EAu(0,\tau)u'^*(-\xi,t-\tau)\,d\tau + \int_0^t EAu'(0,\tau)u^*(-\xi,t-\tau)\,d\tau \end{aligned} \tag{13}$$

$$\begin{aligned} v(\xi,t) = &\int_0^t EAv(L,\tau)u'^*(L-\xi,t-\tau)\,d\tau - \int_0^t EAu'(L,\tau)v^*(L-\xi,t-\tau)\,d\tau \\ &- \int_0^t EAv(0,\tau)u'^*(-\xi,t-\tau)\,d\tau + \int_0^t EAu'(0,\tau)v^*(-\xi,t-\tau)\,d\tau \end{aligned} \tag{14}$$

The $(\ )'$ symbol represents a spatial derivative, and u^*, u'^*, v^* are the fundamental solutions of the displacement as well as its spatial and time derivatives as given by eqs (10) and (12), respectively. In order to further proceed with the numerical implementation of integral equations (13) or (14) we divide the time interval (0, t) into N equal time steps of length h and assume, for the displacement, velocity and the spatial derivative of displacements, an approximation in terms of linear basis functions. The temporal approximation of any of these fields it is given as,

$$q(t) = \sum_{n=1}^{N} \left(H\left(t - t_{n-1}\right) - H\left(t - t_n\right) \right) \left(\frac{t_n - t}{h} q_{n-1} + \frac{t - t_{n-1}}{h} q_n \right) \tag{15}$$

where H is the Heaviside function and $t_n = n\,h$. Collocating point ξ over the boundary of the domain, that is points $\xi = 0$ and $\xi = L$, each one of the integral equations (13) and (14) provides us with two equations. Note also that in these integral equations we have also assumed initial conditions to be zero so that respective terms to be vanished; however it is not difficult to also include these terms. Introducing temporal approximation of the type presented in eqn (15) in integrals of eqn (13) and (14), and also accomplishing analytical temporal integrations we derive equations needed in order to have a BIEM time marching formulation of the problem. Note also here that in the case of a homogeneous 1D rod of constant cross section, internal force as well as the normal stress is given as below.

$$\begin{aligned} \sigma_x(t) &= E\varepsilon_x(t) = Eu_{,x}(t) \\ N(t) &= A\sigma_x(t) = EAu_{,x}(t) \end{aligned} \tag{16}$$

From eqn (16) it is clear that for this case is near the same, from a numerical point of view, when referring to force, stress, traction or the spatial displacement derivative since all these variables are derived from the displacement's spatial derivative.

4.2 Stability analysis

The unstable behaviour of boundary integral equation method is well documented and has been remarked since the early appearance of time domain boundary integral equations formulations [7]. In [8] a procedure in order to investigate the stability characteristics of such equations is given, based on the z-Transformation and some answers are provided for the "intermittent instability" phenomenon. Here we will investigate the stability of such equations utilizing a method similar to the one referred as the matrix method [9] frequently utilized in order to exploit stability properties of finite differences schemes in time. According to the matrix method, if q_n is the vector of the unknown boundary variables at discrete time $t_n = nh$ then it may be written as,

$$q_n = c_n q_0 \tag{17}$$

where c_n is the amplification matrix of step n. Assuming an error in the initial data q_0 we may establish the error vector $\overline{q}_0$. The evolution of that error in time is given similar to eqn (17) as follows.

$$\overline{q}_n = c_n \overline{q}_0 \tag{18}$$

In the regime of BIEM time marching formulation this c_n amplification matrix depends on time step n and it is difficult to establish an explicit form of it. Instead of exploit the evolution of the error utilizing properties of the amplification matrix, *e.g.* spectral radius, we proceed further in a numerical manner. That is we introduce an error in initial data and we explore this error's evolution in time computed by BIEM procedures resulted utilizing displacement and velocity reciprocal theorems. Beneficial factor of this procedure is that the only parameter manifests the stability performance for the case of 1D wave propagation in a rod is the non-dimensional ratio sometimes encountered as the Courant-Friedrichs-Lewy (**CFL**) parameter and given as

$$\beta = \frac{c\,h}{L} \tag{19}$$

Consequently results produced are problem independent. In Table 1, stability regions are given explicitly, for various combinations of boundary conditions, in terms of parameter β.

Table 1: Stability properties for varying β parameter.

prescribed variable on i (start) boundary	prescribed variable on j (end) boundary	stability on region $0 \le \beta < 1$	stability on region $1 < \beta \le 2$
u	u	unstable for any $\beta \ne \frac{1}{z}$	unstable for any β
u	u'	stable for small regions of β	stable for any β
u' or v	u' or v	stable for any $\beta \ne \frac{1}{z}$	stable for any β

Variable z appeared in table (1) stands for the positive integer numbers. As it may observed in table (1), in formulations where only velocities and/or tractions used, that means that the velocity reciprocal theorem has been utilised, the behaviour is in general stable except for the cases where the parameter β has been chosen such to be equal to a ratio of unity with an integer number. Regarding formulations based on the displacement reciprocal theorem it seems, as it can also be seen in table (1), that are most prone to numerical instabilities. For the case of Dirichlet problems formed in terms of displacements there is appeared a "stable" behaviour for discrete values of β, however stability can

not be guaranteed since it is almost difficult to define these values due to computer's numerical precision. Regarding the stability regions presented in the case of mixed problem when utilizing displacement formulation these are shown to have a finite range near to $\beta = 1/(z+0.5)$ and also near but not equal to the value of $1/z$. For increasing z, and furthermore for decreasing β and time step value h these finite stability region are decrease and tend to degenerate to discrete values.

5 Numerical examples

In this section there are presented some numerical examples in order to verify the results obtained on the stability performance of algorithms utilizing the displacement as well as velocity reciprocal theorems. In the case of a single 1D rod we present a set of examples in order to cover the Dirichlet, as also the mixed type of problems. Both examples consider a rod of elasticity modulus $E = 1000\,{kN}/{m^2}$, mass density $\rho = 1.0\,{t}/{m^3}$, a cross section of area $A = 16\,m^2$ and a length $L = 4\,m$.

5.1.1 A Dirichlet problem

As a first example a Dirichlet type of problem is solved utilizing both the displacement as well as the velocity formulations. The rod is constrained on the i and j boundary points to prescribed motion given as

$$u_i(t) = \cos(24t) - 1$$
$$u_j(t) = 1.5u_i(t)$$

with the respective velocities give as

$$v_i(t) = -24\sin(24t)$$
$$v_j(t) = 1.5v_i(t)$$

As a frequency of the prescribed motion have been chosen one near the first natural frequency of the constrained rod which is $\omega_q = q\pi c/L$ with q equal to unit. In fig (1) numerical solution of the spatial derivative of displacement is plotted utilizing velocities formulation for parameter $\beta = 1/30$ which is the unstable solution and also for $\beta = 1/30.1$ which is the stable one.

5.1.2 A mixed problem for wave propagation

A benchmark problem which is very frequently utilized in order to test the performance of boundary integral equation methods in time is presented here. It consists of a rod with its i boundary point constrained to have a zero motion in time while its j boundary point excited by a constant force in time. First we consider the solutions computed utilizing the velocity formulation which, as could be seen in fig (2), are stable and really accurate for values of parameter β equal to 1/101.50 as well as 1/101.25 but not for that of β = 1/101. Contrary to

the velocity formulation, the respective one utilizing the displacement reciprocity gives stable results only for the case where β equals to 1/(z+0.5), or to values very close to that according also the notes given in sec (4.2). This can be ascertained by results in time, plotted in fig (2) where the unstable performance for β equal to 1/101.25 and 1/101.00 are shown together with those of β equal to 1/101.5.

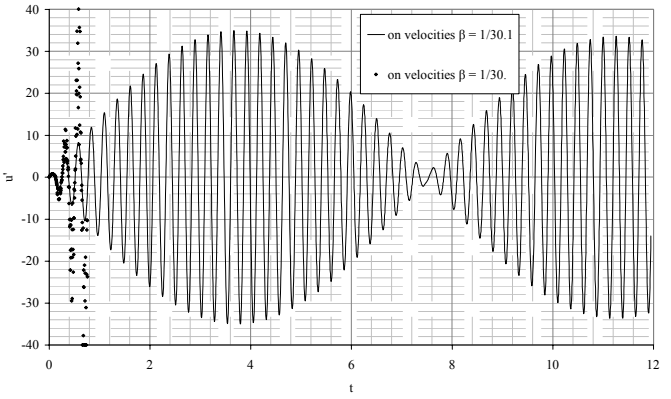

Figure 1: Displacement's spatial derivative of boundary point i in time utilizing velocity formulation.

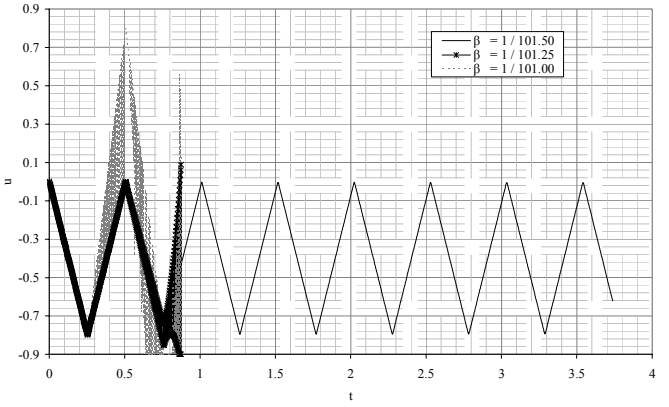

Figure 2: Plots of computed displacement utilizing velocity formulation.

As further verification for these almost discrete stability conditions in reference to β parameter for the case of displacement formulation in fig (3) there is a series of solutions for various z integer values. In this plot, someone may also notice the numerical damping introduced for increasing β. As also

someone may observe in fig.(3), contrary to other 1D formulations reported elsewhere, *e.g.* [6], there are not presented difficulties to accurately describe discontinuous variations in time, *e.g.* that of tractions. Also inaccurate results as reported in [3] have as origin the discontinuity of tractions that generates an error, but their raising in time is due to unstable behaviour of the formulations.

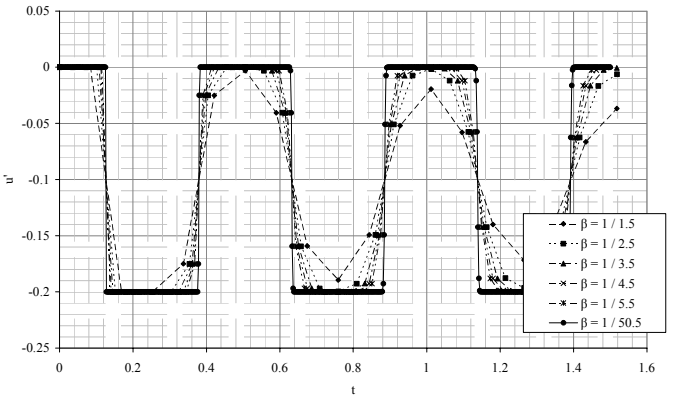

Figure 3: Displacement's spatial derivative results utilizing displacement formulation for various "stable" values of β .

6 Conclusions

In this work the classical Graffi's reciprocal theorem in term of displacements is re-examined as a counterpart of that of Betti's in the case of elastostatics. It is shown that, despite the doubtless validity of Graffi's theorem, nevertheless a similar reciprocal statement involving velocity field which also is valid in the case of elastodynamics, is also includes the elastostatic case as a limit case. After introducing this theorem, it is shown that it is straightforward to establish the integral representation of velocities. Furthermore utilizing this reciprocal theorem in terms of velocities, boundary integral equation methods type of formulations are established and tested on simple model problems. Also results obtained are compared to those computed utilizing conventional BIEM formulations based on the classical reciprocal theorem in terms of displacements. It is found that formulations based on velocities present a superiority regarding stability performance and considered more compatible for the case of transient elastodynamics. Also extension of the fully three-dimensional elastodynamics case with boundary elements is an ongoing research, undertaken by the authors.

References

[1] Graffi, D., Sul teorema di reciprocita nella dinamica dei corpi elastici. *Memoric della Reale Accademia delle Scinze dell'Istituto di Bologna*, **10**, pp. 103-111, 1946.

[2] Dominguez, J., *Boundary Elements in Elastodynamics*, Computational Mechanics Publications, Elsevier Applied Science, UK, 1993.
[3] Carrer, J.A.M., Mansur, W.J., Time discontinuous linear traction approximation in time-domain bem: 2-D elastodynamics. *International Journal for Numerical Methods in Engineering*, **49**, pp. 833-848, 2000.
[4] Frangi, A., "Causal" shape functions in the time domain boundary element method, *Computational Mechanics*, **25**, pp. 533-541, 2000.
[5] Greenberg, M.D., Applications of Green's Functions in Science and Engineering, Prentice-Hall, Inc. Englewood Cliffs, New Jersey, 1971.
[6] Moser, W., Antes, H., Beer, G., A Duhamel integral based approach to one-dimensional wave propagation analysis in layered media, *Computational Mechanics*, **35**, pp. 115-126, 2005.
[7] Mansur, W.J., *A time-stepping technique to solve wave propagation problems using the boundary element method*, Ph.D. thesis, University of Southampton, 1983.
[8] Pierce, A., Siebrits, E., Stability Analysis of Model Problems for Elastodynamic Boundary Element Discretizations, *Numerical Methods for Partial Differential Equation*, **12**, pp. 585-613, 1996.
[9] Mitchell, A.R.M, Griffiths, D.F., *The finite Difference Method in Partial Differential Equations*, John Willey and Sons Ltd., 1988.

Trefftz collocation for frequency domain elastodynamic problems

V. M. A. Leitão[1], B. Sensale[2] & B. S. Rodriguez[2]
[1]*DECivil-ICIST, Instituto Superior Técnico, TULisbon, Portugal*
[2]*Facultad de Ingeniería, Universidad de la República, Uruguay*

Abstract

A Trefftz collocation method is proposed for the analysis of two-dimensional elastodynamic problems subjected to steady-state time-harmonic loads. Trefftz methods are characterized by the use of a superposition of a number of actual solutions of the homogeneous part of governing equations, the so-called T(Trefftz)-functions. This leads to high quality approximations where the unknowns are the weights of each of the T-functions considered. The unknowns are found by matching the approximations to the boundary conditions by following a standard collocation approach.

The numerical implementation of the method is briefly described and results are obtained for two anti-plane elastodynamic problems. The results compare quite favourably to other results available in the literature whereby Galerkin and collocation boundary element methods were used.

Keywords: Trefftz method, elastodynamics, collocation.

1 Introduction

The Trefftz method (Trefftz [1]), consists essentially in building an approximation by resorting to a set of actual solutions of the homogeneous system of partial differential equations that governs the boundary value problem. As the homogeneous part of the equations is well taken care of, all that remains to be done is the (approximate) enforcement of the boundary conditions. The traditional way to achieve this is by collocation (Leitão [2, 3], Sensale and Rodriguez [4]). This means selecting a set of (boundary) points and forcing the approximation to satisfy, locally, the boundary conditions.

The use of the Trefftz concept is not restricted to boundary solution methods. Galerkin approaches typical of the conventional formulations of the finite

WIT Transactions on Modelling and Simulation, Vol 49, © 2009 WIT Press
www.witpress.com, ISSN 1743-355X (on-line)
doi:10.2495/BE090251

element methods may also be used to implement the Trefftz method (Freitas [5]) but this will not be addressed here.

The solutions for the homogeneous differential equations of a given problem are, in the Trefftz approach, obtained in the form of an infinite series of regular functions centered at a given point and well defined everywhere. Solutions for the homogeneous differential equations may also be obtained in the form of fundamental (singular) solutions. This is the approach followed by the Boundary Element Method (BEM) (see Brebbia *et al.* [6]) and by the Method of Fundamental Solutions (MFS) (see Fairweather and Karageorghis [7]).

In what follows the "Trefftz method" is characterized by the following: 1) each function of the approximation basis is a non-singular term of an infinite series (although singular functions may be added to the basis when necessary); 2) the collocation approach is used (even though the more general setting of weighted least squares may also be used).

The range and scope of applications of the Trefftz method, be it the collocation or the Galerkin-based approaches, has seen a strong increase in the last decade. Reviews on the subject may be found in Kita and Kamya [8], Jirousek and Zielinski [9] and Li *et al.* [10].

In this work the Trefftz collocation method is applied to the analysis of two-dimensional elastodynamic problems subjected to steady-state time-harmonic loads. As will be later shown this problem may be simplified in a way that leads to the Helmholtz equation, which is the equation that models the scattering of acoustic waves. Trefftz methods are particularly suited for this type of problems because, contrary to the finite element method and, in a certain way, the boundary element method the discretization requirements are not dependent on the wavelength considered. Trefftz collocation methods have essentially been applied to the case of acoustics, that is, the scalar Helmholtz case (see Li [11]). Galerkin type Trefftz methods have been applied to the acoustic case (see Pluymers *et al.* [12], Cheung *et al.* [13]) but also to the elastodynamic case (Freitas and Cismasiu [14]) amongst others.

The numerical validation of the proposed method is achieved by the application to a set of anti-plane elastodynamic problems for which analytic (Kitahara [15]) as well as other numerical solutions are available (Dominguez [16] and Perez-Gavilan and Aliabadi [17].)

2 The Navier equations

The motion, with respect to time, of homogeneous, isotropic, linear elastic bodies is described by the Navier equations. These are obtained by appropriately replacing the compatibility (kinematic) description (and the strains are assumed to be infinitesimal for the sake of simplicity) into the constitutive relationship followed by the substitution into the equilibrium (static) equation. The resulting equation, written in terms of displacements, has to be satisfied everywhere in the domain together with the satisfaction of the boundary and initial conditions of the problem.

A starting assumption that will be made here is that the main variables of the problem vary harmonically in time, that is, all variables depending on time are functions of $\sin \omega t$ and $\cos \omega t$ where ω is the (angular) frequency. This assumption allows the problem to be stated in the frequency domain by means of a Fourier transform.

When dealing with problems that may exhibit some form of damping it is convenient to resort to the more general setting of viscoelasticity, that is, to the case when the material characteristics vary with time. In this case the following two independent complex-valued Lamé type coefficients may be obtained:

$$\mu(\omega) = \frac{1}{2(1+\nu)} E^*(\omega)$$
$$\lambda(\omega) = \frac{\nu}{(1+\nu)(1-2\nu)} E^*(\omega) \tag{1}$$

where $E^*(\omega)$ is the complex modulus and ν is the time independent (for the sake of simplicity) Poisson coefficient.

When damping effects are present these Lamé type coefficients take the form:

$$\mu = \mathrm{Re}[\mu(\omega)](1+2i\beta_\mu)$$
$$\lambda = \mathrm{Re}[\lambda(\omega)](1+2i\beta_\lambda) \tag{2}$$

By expressing the constants in this convenient form there are no differences between the governing equations for the elastic or the viscoleastic case when treating time-harmonic problems in the frequency domain.

In the expressions above β_μ and β_λ are damping factors. It is usual to consider $\beta = \beta_\mu = \beta_\lambda$, and refer to β as being the viscous damping factor.

3 Formulation of the elastodynamic equation

The general form of the elastodynamic governing equation for viscoelastic materials in the time domain is (Christensen [18]):

$$c_S^2(t,\tau) * \Delta\vec{u}(X,t) + (c_P^2(t,\tau) - c_S^2(t,\tau)) * \nabla\left(\nabla \cdot \vec{u}(X,t)\right) + \\ + \vec{b}(X,t) = \ddot{\vec{u}}(X,t), \quad \forall X \in \Omega \tag{3}$$

where $\vec{b}(X,t)$ is the body force load vector, and

$$c_S^2(t,\tau)* = \frac{1}{2(1+\nu)\rho} R_E(t,\tau)*$$
$$c_P^2(t,\tau)* = \frac{1-\nu}{(1+\nu)(1-2\nu)\rho} R_E(t,\tau)* \tag{4}$$

are, respectively, the square of the S-wave velocity and the square of the P-wave velocity in the viscoelastic case, ν is the Poisson coefficient, ρ is the density of the material and $R_E(t,\tau)$ is its relaxation function.

For the sake of simplicity let us assume that the boundary conditions (displacements $\vec{u}(X,t)$ and tractions $\vec{p}(X,t)$) vary harmonically in time as follows:

$$\begin{aligned} \vec{u}(X,t) &= \vec{u}_o(X)e^{i\omega_o t}, \quad \forall X \in \partial\Omega_u \\ \vec{p}(X,t) &= \vec{p}_o(X)e^{i\omega_o t}, \quad \forall X \in \partial\Omega_p \end{aligned} \tag{5}$$

and that the body forces are not present.

In these conditions, that is, for time-harmonic problems, a description of the governing equation in the frequency domain is achieved by applying the Fourier transform to the general equation in time. The result may be written as:

$$\begin{aligned} \overline{c}_S^2(\omega)\Delta\vec{\overline{u}}(X,\omega) + (\overline{c}_P^2(\omega) - \overline{c}_S^2(\omega))\nabla\left(\nabla\cdot\vec{\overline{u}}(X,\omega)\right) - \\ - \omega^2\vec{\overline{u}}(X,\omega) = 0, \quad \forall X \in \Omega \end{aligned} \tag{6}$$

where the bar over the displacement and traction denotes the transformed variables and:

$$\begin{aligned} \overline{c}_S^2(\omega) &= \frac{1}{2(1+\nu)\rho}E^*(\omega) \\ \overline{c}_P^2(\omega) &= \frac{1-\nu}{(1+\nu)(1-2\nu)\rho}E^*(\omega) \end{aligned} \tag{7}$$

The boundary conditions now read:

$$\begin{aligned} \vec{\overline{u}}(X,\omega) &= \vec{u}_o(X)\,\delta(\omega-\omega_o), \quad \forall X \in \partial\Omega_u \\ \vec{\overline{p}}(X,\omega) &= \vec{p}_o(X)\,\delta(\omega-\omega_o), \quad \forall X \in \partial\Omega_p \end{aligned} \tag{8}$$

The above description is a three-dimensional one. The displacement field has, therefore, three components:

$$\vec{u}(X,t) = u_1\vec{e}_1 + u_2\vec{e}_2 + u_3\vec{e}_3 \tag{9}$$

In this work the three-dimensional field will be restricted to the anti-plane case only.

The geometry of the anti-plane case is a two-dimensional one and displacements only occur in the x_3 direction, that is:

$$\begin{aligned} u_1 &= u_2 = 0 \\ u_3 &= u_3(x_1,x_2,t) \end{aligned} \tag{10}$$

The only non-null components of the stress tensor are σ_{13} and σ_{23}.

Due to these simplifications u_3 is governed by a simplified version of the elastodynamic equation, the scalar wave equation:

$$\overline{c}_S^2 \Delta \overline{u}_3(x_1, x_2, \omega) + \omega^2 \overline{u}_3(x_1, x_2, \omega) = 0 \tag{11}$$

where only the S-wave velocity is considered.

4 Helmholtz decomposition

Helmholtz theorem (see Pak and Eskandari-Ghadi [19]) states that any twice differentiable vector field $\vec{u}$ may be, uniquely, decomposed into a sum of two field vectors, an irrotational one $\vec{u}_P$ not present in the anti-plane case) and a solenoidal one $\vec{u}_S$.

The application of the Helmholtz decomposition to the Navier equation in the frequency domain as shown above leads to:

$$\begin{aligned}
&\overline{c}_S^2 \Delta\left[\vec{u}_P(\omega) + \vec{u}_S(\omega)\right] + \left(\overline{c}_S^2 - \overline{c}_P^2\right) \nabla(\nabla \cdot \left[\vec{u}_P(\omega) + \vec{u}_S(\omega)\right]) + \\
&\qquad + \omega^2 \left[\vec{u}_P(\omega) + \vec{u}_S(\omega)\right] = 0 \\
&\Delta \vec{u}_P(\omega) = \nabla(\nabla \cdot \vec{u}_P(\omega)) - rot\ (rot\ \vec{u}_P(\omega)) = \nabla(\nabla \cdot \vec{u}_P(\omega)) \\
&\Delta \vec{u}_S(\omega) = \nabla(\nabla \cdot \vec{u}_S(\omega)) - rot\ (rot\ \vec{u}_S(\omega)) = -rot\ (rot\ \vec{u}_S(\omega)) \\
&\overline{c}_P^2 \Delta \vec{u}_P(\omega) + \overline{c}_S^2 \Delta \vec{u}_S(\omega) + \omega^2 \vec{u}_P(\omega) + \omega^2 \vec{u}_S(\omega) = 0
\end{aligned} \tag{12}$$

Looking only at the solenoidal field and considering a vector potential $\vec{\psi}$

$$\vec{\psi} = \psi_1 \vec{e}_1 + \psi_2 \vec{e}_2 + \psi_3 \vec{e}_3 \tag{13}$$

the following form is obtained:

$$\begin{aligned}
\vec{u}_S = rot\, \vec{\psi} \quad &\Rightarrow \quad rot\left[\overline{c}_S^2 \Delta \vec{\psi} + \omega^2 \vec{\psi}\right] = 0 \\
&\Rightarrow \quad \overline{c}_S^2 \Delta \vec{\psi} + \omega^2 \vec{\psi} = 0
\end{aligned} \tag{14}$$

where, for the anti-plane case, only the $\psi_3 \vec{e}_3$ matters.

5 The Trefftz collocation approach

The starting point in any Trefftz approach is the approximation of the variable of interest, in this case the displacement field, by a superposition of an infinite number of functions each of them solution of the homogeneous governing equation, that is:

$$\vec{u}_d(X, \omega) = \sum_{i=1}^{N} \vec{a}_i \vec{u}_i^*(X, \omega) \tag{15}$$

where the $\vec{a}_i \in \mathbb{R}^3$ represent the unknowns, that is, the weights affecting each of the $\vec{u}_i^*$ functions. The full series of functions is usually referred to as the T-

complete series in the sense that any solution of the actual problem under consideration is included in the space spanned by the T-complete series.

Applying the collocation approach, at selected X_i points located at the boundary $\partial\Omega$, the following system arises:

$$\begin{aligned} \vec{u}_d(X_i) &= \vec{u}(X_i) \qquad \forall\, X_i \in \partial\Omega_u \\ \vec{p}_d(X_i) &= \vec{p}(X_i) \qquad \forall\, X_i \in \partial\Omega_p \end{aligned} \tag{16}$$

where the left-hand side contains the Trefftz approximation and the right-hand side represents the (known) boundary conditions.

6 Trefftz functions for the anti-plane case

The governing equation is of the scalar Helmholtz type. The displacement component of interest in the anti-plane case is described by the following T-complete series (Qin [20]):

- for a bounded region:

$$\begin{aligned} \vec{u}_d(X) = u_3(X) = c_0 J(kr) + \\ + \sum_{m=1}^{N^*} \left[c_{2m} J_m(kr)\cos(m\theta) + c_{2m+1} J_m(kr)\sin(m\theta) \right] \end{aligned} \tag{17}$$

- for an unbounded region:

$$\begin{aligned} \vec{u}_d(X) = u_3(X) = c_0 J(kr) + \\ + \sum_{m=1}^{N^*} \left[c_{2m} H_m(kr)\cos(m\theta) + c_{2m+1} H_m(kr)\sin(m\theta) \right] \end{aligned} \tag{18}$$

The surface stress vector at point X of the boundary of normal $\vec{n}(X) = n_1\vec{e}_1 + n_2\vec{e}_2$ is:

$$\vec{p}_d(X) = p_3(X) = \frac{E^*(\omega)}{2(1+\nu)} \left(\frac{\partial u_3(X)}{\partial x_1} n_1 + \frac{\partial u_3(X)}{\partial x_2} n_2 \right) \tag{19}$$

7 Calculation of the natural frequencies

The above representations can be immediately applied to obtain the displacements and stresses but one aspect of interest in this type of elastodynamic problems is the calculation of the natural or resonance frequencies.

The procedure used in this work to determine the natural frequencies starts by evaluating a measure (a norm) of the solution of the problem at a given set of domain points for a range of frequencies.

A search method, in this case the Nelder-Mead Simplex Method, is then applied to fine tune the capture of the natural frequencies as those for which the norm of the solution takes the highest value.

8 Numerical results

The set of examples tested were previously analysed in the works of Domínguez [16], Kitahara [15] and Perez-Gavilan [17].

In all cases the natural frequencies points are calculated and compared to analytic results and to the numerical results shown in the above references.

8.1 Square region under uniform anti-plane shear

A 6m x 6m square region, clamped on one side, free on all others, is subjected to a uniform anti-plane shear load $p = 100\,\mathrm{N/m^2}$ on the opposite side.

The material properties are: shear modulus $\mu = 10^6\ \mathrm{N/m^2}$; specific mass $\rho = 100\,\mathrm{Kg/m^3}$; damping coefficient $\beta = 0.05$.

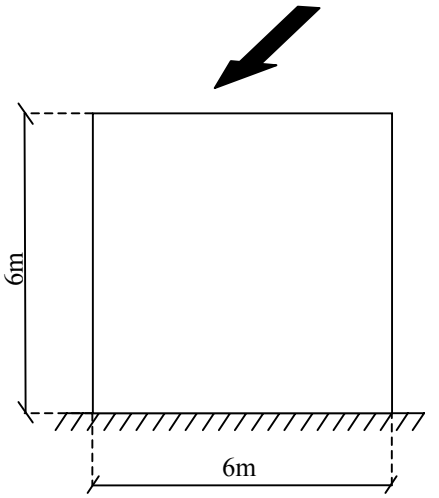

Figure 1: Square region under uniform shear.

An analytical solution of this square domain (in fact, a one dimensional) problem exists for the case of perfectly elastic material, that is, for the case of a material with null damping. The resonance frequencies are $\omega_n = (2n-1)\pi c_S / (2a)$ for a $a \times a$ square region. In this case, for which the shear-wave velocity is $c_S = 100\ \mathrm{m/s}$, and $a = 6$ the first frequencies are 26.18 $\mathrm{s^{-1}}$, 78.54 $\mathrm{s^{-1}}$, 130.90 $\mathrm{s^{-1}}$, ...

The differences when a 5% material damping is considered are negligible. These values, shown in figure 2 for the square region under uniform shear, are exactly reproduced by the present method.

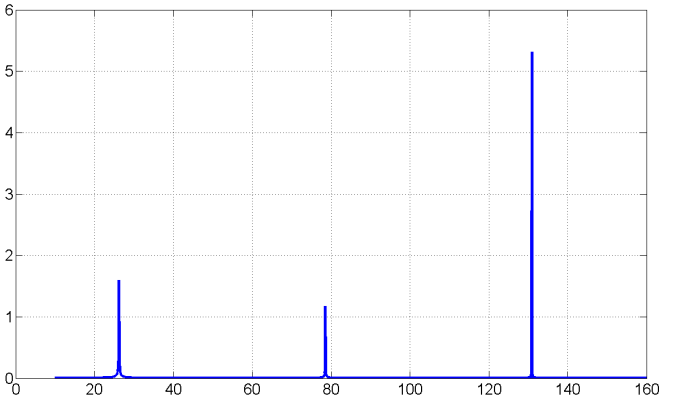

Figure 2: Norm of the solution for a range of frequencies.

8.2 Infinite cylinder under uniform axial load/displacement on the surface

This is an anti-plane problem now with a circular cross-section of radius 6m. The material properties are the same as for the previous examples.

The boundary conditions are:

- unit uniform axial displacement;
- uniform axial load on the surface $p = 100\,\mathrm{N/m^2}$.

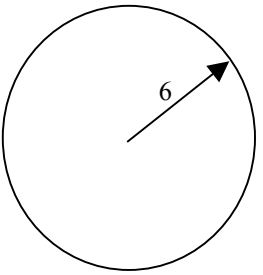

Figure 3: Cross-section of infinite cylinder under uniform load.

The first two resonance frequencies for the case of unit uniform axial displacement, $\omega = 40.08, 92.00$, match the analytical ones.

And the same for the case of uniform axial load, the first two resonance frequencies, $\omega = 63.87, 116.93$, match the analytical ones.

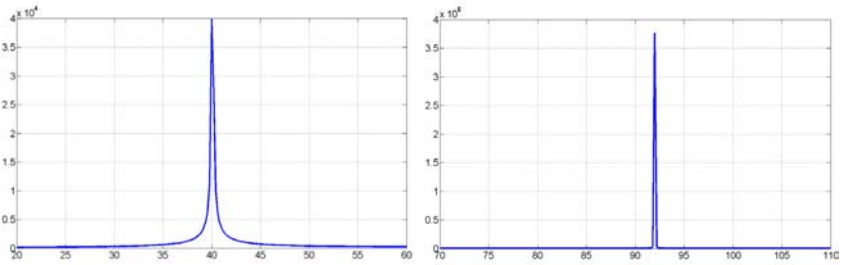

Figure 4: First two resonance frequencies for the case of unit uniform axial displacement.

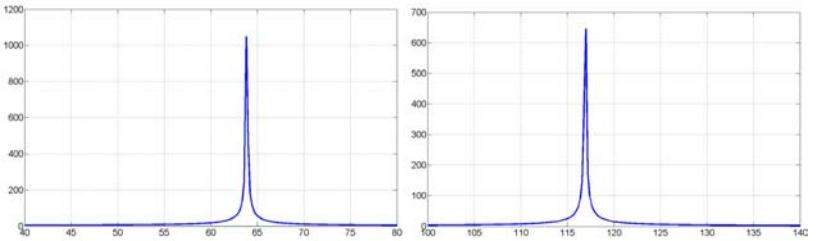

Figure 5: First two resonance frequencies for the case of unit uniform axial load.

9 Conclusions

In this work a Trefftz collocation method has been presented and applied to the analysis of elastodynamic problems in the frequency domain.

The method relies on the use of actual solutions of the homogeneous governing equation which are seen to be scalar and vector potentials satisfying the Helmholtz equation. A solution is found by superposing an appropriate number of terms of the infinite series representing the solution of the homogeneous governing equation followed by the enforcement of the boundary conditions using the collocation approach.

The results obtained in this manner for a set of representative problems compare very well with analytical and numerical results available in the literature thus showing the potential of this technique.

References

[1] Trefftz, E., (1926), "Ein Gegenstuck zum Ritzschen Verharen", paper presented at *2nd Int. Cong. Appl. Mech.,* Zurich, pp. 131-137.

[2] Leitão, V.M.A., (1997), "On the implementation of a multi-region Trefftz-collocation formulation for 2-D potential problems", *Engineering Analysis with Boundary Elements,* Vol. 20, pp. 51-61.
[3] Leitão, V.M.A., (1998) "Application of multi-region Trefftz-collocation to fracture mechanics", *Engineering Analysis with Boundary Elements*, Vol 22, pp. 251-256.
[4] Sensale, B., Sensale Rodriguez, B., (2007), "The Trefftz Boundary Method in Viscoelasticity", *CMES: Computer Modeling in Engineering & Sciences*, Vol.20, Nº1, pp. 21-33.
[5] Freitas, J.A.T., (1998), "Formulation of elastostatic hybrid-Trefftz stress elements", *Comp. Meth. Appl. Mech. Eng*. 153, pp. 127-151.
[6] Brebbia, C.A., Telles, J.C.F., Wrobel, L.C., (1984), *Boundary Element Techniques. Theory and Applications in Engineering*, Springer-Verlag, Berlin.
[7] Fairweather, G., Karageorghis, A., (1998), "The method of fundamental solutions for elliptic boundary value problems", *Adv. Comp. Math*. **9**, pp. 69–95.
[8] Kita, E., Kamiya, N., (1995), "Trefftz method, An overview", *Adv. Engrg. Softw.,* v24, pp. 3-12.
[9] Jirousek, J., Zielinski, A.P., (1997), "Survey of Trefftz-type element formulations", *Computers & Structures*, 63(2), pp. 225-242.
[10] Li, Z.C., Lu, T.T., Hu, H.Y., Cheng, A., (2008), *Trefftz and Collocation Methods*, WIT Press.
[11] Li, Z.C., (2008), "The Trefftz method for the Helmholtz equation with degeneracy", Applied Numerical Mathematics, Vol. 58, pp. 131–159.
[12] Pluymers, B., van Hal, B., Vandepitte, D., Desmet, W., (2007), "Trefftz.based methods for time-harmonic acoustics", Arch. Comput. Methods Eng., Vol. 14, pp. 343-381.
[13] Cheung, Y.K., Jin, W.G., Zienkiewicz, O.C., (1991), "Solution of Helmholtz equation by Trefftz method", *International Journal For Numerical Methods in Engineering*, Vol. 32, pp.63-78.
[14] Freitas, J.A.T., Cismasiu, C., (2003), "Hybrid-Trefftz displacement element for spectral analysis of bounded and unbounded media", *International Journal of Solids and Structures,* Vol.40, pp. 671–699.
[15] Kitahara, M., (1985), *Applications of boundary integral equation methods to eigenvalue problems of elastodynamic and thin plates*, Elsevier, Amsterdam.
[16] Dominguez, J., (1993), *Boundary Elements in dynamics,* Computational Mechanics Publication, Elsevier Applied Science, Amsterdam.
[17] Perez-Gavilán, J.J., Aliabadi, M.H., (2001), "A symmetric Galerkin boundary element method for dynamic frequency domain viscoelastic problems", *Computers and Structures*, Vol.79, pp.2621-2633
[18] Christensen, R.M., (1982), *Theory of Viscoelasticity, An Introduction*, 2nd edn., Academic Press, New York.

[19] Pak, R.Y.S., Eskandari-Ghadi, M., (2007), "On the completeness of a method of potentials in elastodynamics", *Quarterly of Applied Mathematics* Vol.LXV, Nº4, pp. 789-797.
[20] Qin, Q.H., (2000), *The Trefftz Finite and Boundary Element Method*, WIT Press, Southampton.

This page intentionally left blank

On the breathing frequencies computation using the Reissner and the Mindlin model

L. Palermo Jr.
Faculty of Civil Engineering, Architecture and Urban Design,
State University of Campinas, Brazil

Abstract

The breathing frequencies of plates were computed using the frequency domain solution in conjunction with direct boundary integral equations (DBIEs) for plate bending including the shear deformation effect and the influence of rotatory inertia according to Reissner and Mindlin models. The formulation for the Reissner model takes into account the linearly weighted average effect of the normal stress component in the thickness direction with reference to that for the Mindlin model. Furthermore, the irrotational approach on the bending model containing the shear deformation effect to obtain the classical model is revisited taking into account the Reissner and the Mindlin model. Flexural and breathing frequencies for both models including the shear deformation effect and the influence of rotatory inertia were obtained and compared with available results in the literature to show the accuracy of the formulation.
Keywords: natural frequencies, breathing frequencies, frequency domain solution, classical bending model, reissner bending model, mindlin bending model, rotatory inertia.

1 Introduction

The classical model was the first and well-known approach derived from the three-dimensional theory of elasticity for solid bodies to study plate-bending problems. The model is widely employed when global responses are required but it is not efficient even in static analyses when stresses are assessed in the edge zone of the plate or around holes that have a diameter not larger than eight times the plate thickness [1]. The discrepancy in results of dynamic analyses with the classical model with reference to the three-dimensional theory appears when

WIT Transactions on Modelling and Simulation, Vol 49, © 2009 WIT Press
www.witpress.com, ISSN 1743-355X (on-line)
doi:10.2495/BE090261

wavelengths become less than ten times the plate thickness and an inconsistency is verified for wavelengths approaching to zero when a limit for the velocity of propagation cannot be established [2]. The plate-bending model including the shear deformation effect proposed by Reissner [3] has fixed the main shortcomings verified in the classical model. An assumed distribution for stresses on the plate thickness and a fixed value for the parameter related to the shear deformation in the constitutive equations were the main features observed in the Reissner model. A similar model for plate-bending including the shear deformation effect but using an assumed distribution for strains with reference to the mid-surface of the plate was presented by Mindlin [2] to perform dynamic analyses. A correction of the parameter related to the shear deformation according to the Poisson ratio was proposed as a result from the analysis of the propagation of straight-crested waves into an infinite domain. On the other hand, a fixed value for this parameter and very close to Reissner's value was obtained when a particular solution was introduced by Mindlin to represent one for the circular frequency of the first anti-symmetric mode of the thickness-shear vibration in a three-dimensional model. Years later, Mindlin has shown in the study of flexural vibration of rectangular plates [4] that three types of vibration modes could be identified when the shear deformation effect was considered: the flexural, the thickness-shear and the thickness-twist mode. The thickness-twist mode is similar to the wave motion employed in [2] to get the fixed value for the parameter related to the shear deformation. The frequencies obtained with the thickness-twist mode were called breathing frequencies by Levinson [5].

The static or the frequency domain solutions have been employed for dynamic analyses of plates using the Boundary Element Method (BEM) beyond special formulations applied to specific problems [6]. The harmonic analyses of plates in this paper were carried out for Reissner and Mindlin models employing the frequency domain fundamental solution presented in [7, 8], which was not the same used in [9] where the formulation was only based on the real part of the solution and a limit for angular frequencies had to be introduced. The effect of the shear deformation and the influence of rotatory inertia can be considered alone or coupled in the present formulation. The linearly weighted average effect of the normal stress component in the thickness direction of the Reissner model is considered in the DBIE as an additional domain integral when distributed loads are considered. Analyses according to the classical model with or without the influence of rotatory inertia can be obtained when the shear deformation effect is disregarded in the formulations for both models.

2 Direct boundary integral equations

The equations of motion in time-harmonic problems for an infinitesimal plate element under a transverse distributed loading $q(t, x_i)$ are next written with Latin indices taking values {1, 2 and 3} and Greek indices taking values {1, 2}:

$$M_{\alpha\beta,\beta} - Q_\alpha = \frac{\rho h^3}{12}\frac{\partial^2 \psi_\alpha}{\partial t^2} \tag{1}$$

$$Q_{\alpha,\alpha} + q = \rho h \frac{\partial^2 w}{\partial t^2} \tag{2}$$

The plate has a uniform thickness h and the mass density ρ. The transverse acceleration $\partial^2 w/\partial t^2$ and the angular acceleration $\partial^2 \psi_\alpha/\partial t^2$ are functions of the deflection w and the components of changes of slope ψ_α (plate rotations), respectively. The constitutive relations are next written using a unified notation for the Reissner and the Mindlin models:

$$M_{\alpha\beta} = D\frac{1-\nu}{2}\left(\psi_{\alpha,\beta} + \psi_{\beta,\alpha} + \frac{2\nu}{1-\nu}\psi_{\gamma,\gamma}\delta_{\alpha\beta}\right) + RE \tag{3}$$

$$Q_\alpha = D\frac{1-\nu}{2}\lambda^2\left(\psi_\alpha + w_{,\alpha}\right) \tag{4}$$

with

$$\lambda^2 = 12\frac{\kappa^2}{h^2} \tag{5}$$

$$RE = \frac{\nu}{\lambda^2(1-\nu)}q \tag{6}$$

D is the flexural rigidity, ν is the Poisson ratio, RE is zero for the Mindlin model because it corresponds to the linearly weighted average effect of the normal stress component in the thickness direction. The shear parameter κ^2 is equal to 5/6 and $\pi^2/12$ for the Reissner and the Mindlin models, respectively. An alternate value for κ^2 according to the Poisson ratio can be calculated with the following equation [2, 8]:

$$4\sqrt{(1-\alpha\kappa^2)(1-\kappa^2)} = (2-\kappa^2)^2 \tag{7}$$

with

$$\alpha = \frac{1-2\nu}{2(1-\nu)} \tag{8}$$

The static like form of the equations of motion for harmonic problems and the unified notation for the constitutive equations carry to a unified DBIE for the Reissner and the Mindlin model similar to that presented by Weeën in [10] but used in conjunction with the elastodynamic fundamental solution instead:

$$\frac{1}{2}C_{ij}u_j + \int_\Gamma \left(T^i_j u_j - U^i_j t_j\right)d\Gamma = \iint_\Omega \left(U^i_3 q - U^i_{\alpha,\alpha} RE\right)d\Omega \tag{9}$$

where u_α is ψ_α, u_3 is w, t_α is the product $M_{\alpha\beta}.n_\beta$, t_3 is the product $Q_\alpha.n_\alpha$. U^i_j represents the rotation (j=1,2) or the deflection (j=3) due to a unit couple (i=1,2) or a unit point force (i=3). C_{ij} is an element of the matrix C related to the boundary at the source point and it is a diagonal matrix when a smooth boundary is considered: c_{11} and c_{22} are equal to $(1+0.5RS\delta_0{}^4)$, c_{33} is equal to 1. C becomes the Kronecker delta when the rotatory inertia effect is disregarded. The integrand of the domain integral in equation (9) contains the factor RE related to the linearly weighted average effect of the normal stress component in the thickness direction, which should be cut off for analyses using the Mindlin model.

The fundamental solution was presented in [7, 8] in terms of Hankel functions of the first kind of order zero or using modified Bessel functions with complex arguments. The vector of plate rotations (ψ_α) in the fundamental solution was written in terms of its scalar ($\phi_\alpha(x_\alpha, \omega)$) and vector potentials (0, 0, $H(x_\alpha, \omega)$):

$$\psi_\alpha = \frac{\partial}{\partial x_\alpha}\left[\phi_1(\delta_1 r) + \phi_2(\delta_2 r)\right] + e_{3\alpha\beta}\frac{\partial}{\partial x_\beta}\left[H(\delta_3 r)\right] \tag{10}$$

$e_{3\alpha\beta}$ is the permutation symbol and the following relations were used in terms of the rotatory inertia (R), the shear deformation (S) and the classical dynamic factors for plates (δ_0^4):

$$\delta_1^2 = \frac{1}{2}\delta_0^4\left(R + S + \sqrt{(R-S) + \frac{4}{\delta_0^4}}\right); \quad \delta_2^2 = \frac{1}{2}\delta_0^4\left(R + S - \sqrt{(R-S) + \frac{4}{\delta_0^4}}\right)$$

$$\delta_3^2 = \frac{2}{1-\nu}\left(R\delta_0^4 - \frac{1}{S}\right) = \lambda^2\left(RS\delta_0^4 - 1\right)$$

$$R = \frac{h^2}{12}; \quad S = \frac{1}{\lambda^2}\frac{2}{1-\nu}; \quad \delta_0^4 = \frac{\omega^2\rho h}{D} \tag{11}$$

The deflection w was related to the scalar potential functions (ϕ_α) [7, 8]:

$$w = -(\beta_1 + 1)\phi_1(\delta_1 r) - (\beta_2 + 1)\phi_2(\delta_2 r) \tag{12}$$

and

$$\beta_1 = S\left(\delta_1^2 - \delta_0^4 R\right); \quad \beta_2 = S\left(\delta_2^2 - \delta_0^4 R\right)$$

The expressions for the scalar and the vector potential functions of the fundamental solution are next written using modified Bessel functions with complex arguments and according to singular loads used:

a) The solution for the unit point force (F_3):

$$\phi_1 = \frac{1}{2\pi D}\frac{-K_0(i\delta_1 r)}{\sqrt{\delta_0^8(R-S) + 4\delta_0^4}} = \frac{1}{2\pi D}\frac{-K_0(i\delta_1 r)}{\left(\delta_1^2 - \delta_2^2\right)};$$

$$\phi_2 = \frac{1}{2\pi D}\frac{K_0(i\delta_2 r)}{\sqrt{\delta_0^8(R-S) + 4\delta_0^4}} = \frac{1}{2\pi D}\frac{K_0(i\delta_2 r)}{\left(\delta_1^2 - \delta_2^2\right)};$$

$$H = 0$$

b) The solution for the unit couple in the α direction (F_α):

$$\phi_1 = \frac{1}{2\pi D}\frac{-1}{\left(\delta_1^2 - \delta_2^2\right)}\frac{\partial}{\partial x_\alpha}\left[K_0(i\delta_1 r)\right]; \quad \phi_2 = \frac{1}{2\pi D}\frac{1}{\left(\delta_1^2 - \delta_2^2\right)}\frac{\partial}{\partial x_\alpha}\left[K_0(i\delta_2 r)\right];$$

$$H = e_{3\alpha\beta}\frac{S}{2\pi D}\frac{\partial}{\partial x_\beta}\left[K_0(i\delta_3 r)\right]$$

The solution becomes equal to that obtained for the classical bending model [11] when the shear deformation (S) and rotatory inertia (R) effects are set equal to zero. Furthermore, the plate rotations turn directly defined from the deflection function derivatives as a result from the classical model because the constants β_α and the function H are equal to zero in the absence of the shear deformation

effect (S). The field decomposition can be introduced in the plate rotations and their derivatives of the constitutive equations (3, 4) as it was done to the plate rotations of the fundamental solutions (equation (10)). After the introduction of the scalar and the vector potential functions in the constitutive equations, the equations of the classical model can be obtained when the function of the vector potential field is set equal to zero and the scalar potential function uses the deflection function (w). It can be also extended to the DBIE yielding a boundary formulation based on the classical model hypotheses [7, 8].

The domain integral including the Reissner effect (RE) of equation (9) can be simplified when the field decomposition is introduced in rotations U^i_α according to equation (10) and employing the first Green identity to get the final relation:

$$\int\!\!\int_\Omega U^i_{\alpha,\alpha}\,RE\,d\Omega = \oint_\Gamma \left(\phi_1+\phi_2\right)^i_{,n} RE\,d\Gamma - \int\!\!\int_\Omega \left(\phi_1+\phi_2\right)^i_{,\alpha} RE_{,\alpha}\,d\Omega \tag{13}$$

The result from equation (13) shows the linearly weighted average effect of the normal stress component in the thickness direction (RE) is only multiplied by the scalar potential function or the irrotational component of the rotation field. The effect reduces to an additional boundary integral when a uniform loading (q) is considered because it is directly related to RE according to equation (6).

The irrotational approach on the present formulation to perform analyses according to the classical bending model is similar to that shown in [12] for static loads using the Mindlin model. The first step is writing the DBIE (9) with reference to the normal and the tangential directions (**nt**) at the boundary. It is not a necessary step but the approach can be easily visualized in this way:

$$\begin{aligned} &\frac{1}{2}C_{ij}u_j + \oint_\Gamma \left(Q^i_n w + M^i_n \theta_n + M^i_{nt}\theta_t - Q_n w^i - M_n \theta^i_n - M_{nt}\theta^i_t\right)d\Gamma = \ldots \\ &\ldots = \int\!\!\int_\Omega \left[w^i q + \left(\phi_1+\phi_2\right)^i_{,\alpha} RE_{,\alpha}\right]d\Omega - \oint_\Gamma \left(\phi_1+\phi_2\right)^i_{,n} RE\,d\Gamma \end{aligned} \tag{14}$$

With i relating to the fundamental solution used, corresponding to a unit point load (i=3) or a unit couple (i=1 or 2); u_j represents the deflection (j=3) or the rotation (j=1 or 2). θ_n and θ_t stand for ψ_n and ψ_t, respectively. M_n and M_{nt} are the bending and twisting moments, respectively. Q_n is the distributed shear.

The irrotational approach is equivalent to disregarding the field component related to the vector potential function. The simplification in the presented formulation corresponds to set the shear deformation effect (S) equal to zero in the fundamental solution and assuming plate rotations θ_n and θ_t equal to $-w_{,n}$ and $-w_{,t}$, respectively, as well as releasing the twisting moments M_{nt} on the boundary ($M_{nt} = 0$). The classical hypotheses are satisfied with these assumptions. The resultant DBIE allows dynamic analyses of plates by applying the rotatory inertia correction on the classical model and is analogous to the well-known DBIE used for static analyses within classical plate theory, including an additional degree of freedom for the tangential boundary rotation [12].

$$\frac{1}{2}C_{ij}u_j + \int_{\Gamma} \left(Q_n^i w - M_n^i w_{,n} - M_{nt}^i w_{,t} - Q_n w^i + M_n w_{,n}^i \right) d\Gamma = \iint_{\Omega} w^i q d\Omega \qquad (15)$$

The DBIE for the classical bending model without the rotatory inertia correction is obtained when the parameter R is set equal to zero in the elastodynamic solution used in equation (15).

The absence of the shear deformation effect (S=0) corresponds to assume the shear parameter κ^2 approaching to infinite (or λ^2, see equation 5) and an orthotropic material replaces the actual material of the plate, supposed to be isotropic, as explained by Timoshenko and Woinowsky-Krieger [1] on the classical hypotheses. The factor RE was not included in equation (15) because it contains the shear parameter λ^2. The effect (RE) approaches to zero when the parameter (λ^2) approaches to infinite, which shows that an irrotational approach on the Reissner model carries to the same result obtained with the Mindlin model.

3 Numerical example

The dynamic analyses of plates considering the Reissner and the Mindlin models show similar results and the difference appeared in values obtained for displacements related to the linearly weighted average effect of the normal stress component in the thickness direction, which is dependent to the pressure of the surface loading. The difference in values for displacements is shown in Figure 1 using the frequency response of a square plate simply supported on all sides and 30 cm for thickness (h). A uniform loading (q) equal to 150 $N.m^{-2}$ was applied over the plate surface which side (a) is equal to 50 cm, Young's modulus was 206.9 GPa, the Poisson ratio (ν) was 0.3, the mass density (ρ) was 7860 $kg.m^{-3}$. Linear shape functions were employed to approximate displacements and efforts in the boundary elements. All nodal parameters were positioned at the ends of the elements and the collocation points were placed on the boundary. The collocation points were shifted to the interior of the element at a distance of a quarter of its length from the end, for discontinuous boundary elements, and shifted to the center of the element for continuous boundary elements. The integrations were performed with analytical expressions for the case of collocation points belonging to the boundary element and the Gauss-Legendre quadrature for other cases.

The values of natural frequencies were not changed independently of the adopted model. The natural frequency could be identified in the harmonic excitation using the value of a displacement (deflection or rotation) at an internal point but others features could be employed as the reference parameter, such as the phase angle or the determinant of the system matrix. A first evaluation with 20 incremental steps was carried out in this study to find the interval of interest. The interval to be focused, containing 2 incremental steps, was picked up when the sign of the real part of the deflection changed as shown in Figure 1. The focused interval was analyzed again with a refinement equals to 40 incremental steps and two peaks with opposite signs could be identified in the response curve

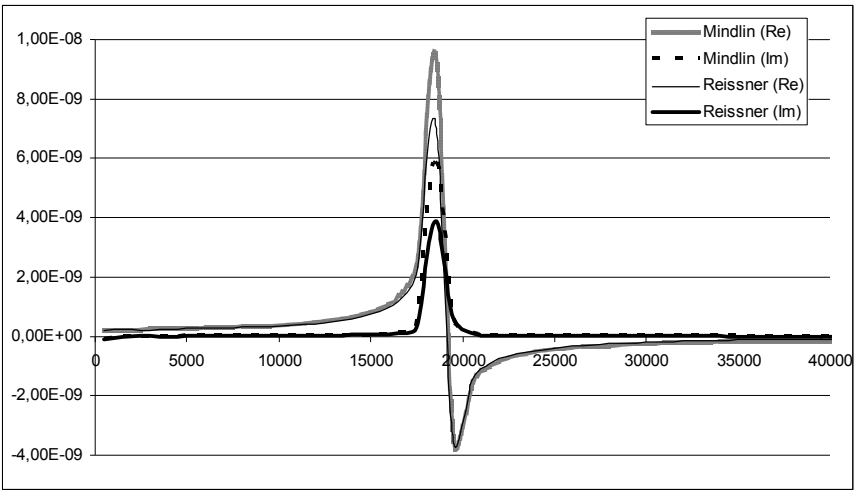

Figure 1: Responses using the Reissner and the Mindlin model for h/a= 0.6 and including the rotatory and the shear deformations effects.

Table 1: Angular frequencies of the flexural mode (rad/s).

Ratio h/a	Lim. Freq.	Elasticity [5]	Mindlin [4]	Equation (14)	
	λc_s [8]			Mindlin	Reissner
0.05	199923	3016	3049	3015	3015
0.1	99961	5906	5918	5825	5825
0.2	49980	10880	10820	10380	10380
0.4	24990	17315	17073	15760	15760
0.6	16660	20734	20306	18910	18910
0.8	12495	22653	22079	21480	21480
1.0	9996	23805	23125	23570	23570

of the real part of the deflection. The frequency responses were studied for several ratios (h/a) of the plate simply supported on all sides and using the hard restraint condition. The first natural frequencies obtained by using the numerical implementation for the Reissner and the Mindlin model are listed in Table 1 and compared to values available in the literature, obtained by the Mindlin model [4] and employing three-dimensional elasticity theory [5].

The next frequencies could be identified by using the same loading but increasing the scanned range. It is important to note the natural frequencies can be easily identified when their vibration modes are not damped due to a particular loading condition or the internal point position, as explained in [13]. The vibration modes of natural frequencies shown in Table 1 have curvatures with same sign and are related to flexural vibration modes [4].

The flexural and the thickness-shear modes are related to the scalar potential field whereas the thickness-twist mode is related to the vector potential field [4]. The rotation field of the thickness-twist mode is similar to that obtained from an anticlastic vibration surface, which contains curvatures with opposite signs [1]. Levinson [5] called the natural frequency of the thickness-twist mode as breathing frequency. The distributed loading (q) was set equal to zero in the numerical implementation to scan the first breathing frequency and the DBIEs (14) turn the same for the Reissner or the Mindlin model. A bending moment in the normal direction was applied on the node placed at the center of each side of the plate. The moments had same sign on opposite edges and opposite signs on adjacent edges. The domain was contained in the intervals $0<x_1<0.5$ and $0<x_2<0.5$, and the value of the rotation ψ_2 at the point (0.1875, 0.1875) was used to scan the natural frequencies. The breathing frequencies listed in Table 2 were obtained with the influence of rotatory inertia. The values obtained for breathing frequencies using the Mindlin model and the three-dimensional elasticity theory are close from medium to high ratios (h/a) but they are divergent for low ratios [5] where a limiting value for the frequency is obtained in the three dimensional elasticity theory as shown in Table 2.

Figure 2 shows an example of the frequency response curves to find breathing frequencies for ratios (h/a) in the range (0.4, 1.0). There are few natural frequencies lower than the first breathing frequency for plates with ratio (h/a) in that range. The loading condition with bending moments in the same directions of rotations of the first thickness-twist vibration mode was efficient to obtain the requested frequencies. On the other hand, there are several natural frequencies lower than the first breathing frequency when the ratio (h/a) is 0.2 or lower and several peaks with opposite signs are identified in the frequency response as shown in Figure 3 and the lower frequencies are related to flexural vibration modes. In spite of a frequency close the value 103870 rad/s appeared in the analysis of Figure 3, the visualization was not clear to identify the natural frequency without using theoretical values. It was the reason to do not include a value in Table 2 for ratios lower than 0.4.

Table 2: Angular frequencies of the thickness-twist mode (rad/s).

Ratio h/a	Elasticity [5]	Mindlin [4]	Equation (14)
0.05	47750	400790	-
0.1	47700	201880	-
0.2	47460	103870	-
0.4	46230	57415	53000
0.6	42860	43693	42100
0.8	37410	37729	36800
1.0	33094	34263	33750

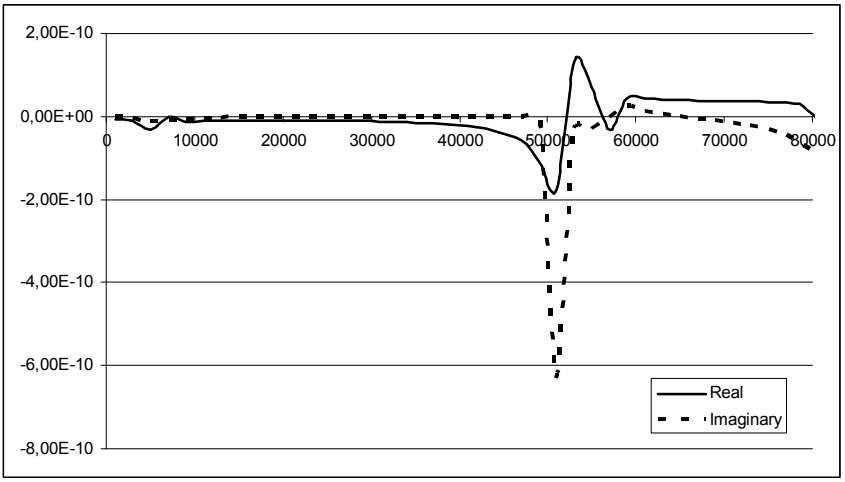

Figure 2: Rotation ψ_2 at (0.1875, 0.1875) for h/a= 0.4.

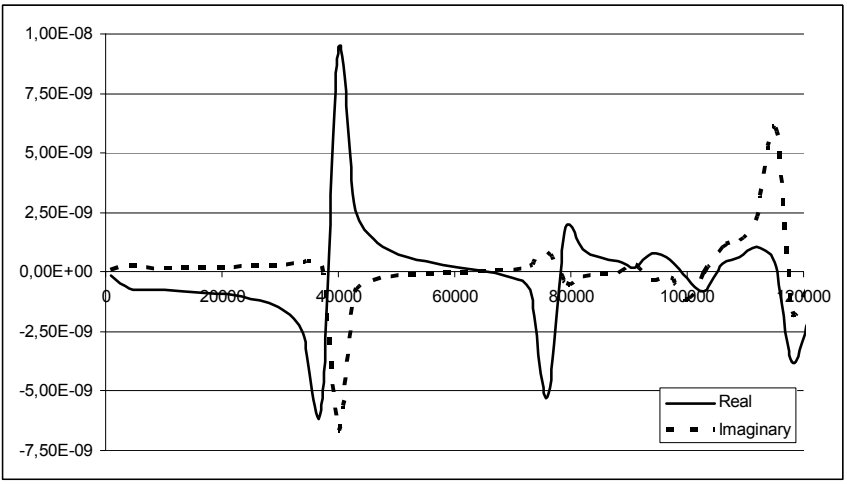

Figure 3: Rotation ψ_2 at (0.1875, 0.1875) for h/a = 0.2.

4 Conclusions

The linearly weighted average effect of the normal stress component in the thickness direction of the Reissner model introduced a little reduction on the obtained deflection with reference to that using the Mindlin model. The difference can be significant or not according to the thickness value and the boundary conditions. It is important to note the natural frequencies were not changed according to Reissner's or Mindlin's model and the differences were identified in values for displacements. The existence of three types of vibration modes and corresponding frequencies for each mode, including those with high

frequencies, justifies the present formulation employing modified Bessel functions of the second kind with complex arguments for a general treatment of vibration problems of plates. The limiting frequency λc_s [8], where c_s is the equivolumial wave velocity, that defines complex or real arguments of modified Bessel functions were exceeded in the natural frequencies of the Table 1 for ratios in the range (0.6, 1.0).

Acknowledgements

The author is grateful to CNPq and FAPESP for support for the development of research on plates.

References

[1] Timoshenko, S. P., Woinowsky-Krieger, S., Theory of Plates and Shells, McGraw-Hill Book Company, New York, 2nd Ed., 1959
[2] Mindlin, R.D., Influence of rotatory inertia and shear on flexural motions of isotropic elastic plates, Journal of Applied Mechanics, 1951.
[3] Reissner, E., The Effect of Transverse Shear Deformation on the Bending of Elastic Plates, Journal of Applied Mechanics, 1945.
[4] Mindlin, R.D., Schacknow A., Deresiewicz, H., Flexural vibrations of rectangular plates, Journal of Applied Mechanics, 23, 430-436, 1956.
[5] Levinson, M., Free vibrations of a simply supported rectangular plate: an exact elasticity solution, Journal of Sound and Vibration, 98(2), 289-298, 1985.
[6] Providakis CP, Beskos DE. Dynamic analysis of plates by the boundary elements. Appl Mech Rev.;52(7) ASME, 1999.
[7] Palermo Jr., L., On the fundamental solution to perform the dynamic analysis of Reissner-Mindlin's plates, Boundary Element Technology XV, Editors C.A. Brebbia, R.E. Dippery, 2003
[8] Palermo Jr., L., On the harmonic response of plates with the shear deformation effect using the elastodynamic solution in the boundary element method, Engineering Analysis with Boundary Elements, 2007.
[9] Antes, H., Static and Dynamic Analysis of Reissner-Mindlin Plates, Boundary Element Analysis of Plates and Shells, Editor: D.E. Beskos, Springer Series in Computational Mechanics Edited by S.N. Atluri, Springer-Verlag, 1991.
[10] Weeën, F., Application of the direct boundary element method to Reissner's plate model, International Journal for Numerical Methods in Engineering, 1982.
[11] Vivoli J, Filippi P. Eigenfrequencies of thin plates and layer potentials. J Acoust Soc Am; 55:562–7, 1974.
[12] Palermo Jr., L., Plate Bending analysis using the classical or the Reissner-Mindlin models, Engineering Analysis with Boundary Elements, 2003.
[13] Warburton, G. B., The dynamical behavior of structures, Pergamon Press, Oxford, 1976.

Free vibration analysis of a circular plate with multiple circular holes by using the addition theorem and direct BIEM

W. M. Lee[1] & J. T. Chen[2]
[1]*Department of Mechanical Engineering, China Institute of Technology, Taiwan*
[2]*Department of Harbor and River Engineering, National Taiwan Ocean University, Taiwan*

Abstract

The purpose of this paper is to propose an analytical method to solve natural frequencies and natural modes of a circular plate with multiple circular holes by using the null field integral formulation, the addition theorem and complex Fourier series. Owing to the addition theorem, all kernel functions are represented in the degenerate form and further transformed into the same polar coordinate from each local coordinate at center of all circles. Not only avoiding the computation of the principal value but also the calculation of higher-order derivatives in the plate problem can be easily determined. According to the specified boundary conditions, a coupled infinite system of simultaneous linear algebraic equations is derived and its solution can be obtained in an analytical way. The direct searching approach is adopted to determine the natural frequency through singular value decomposition (SVD). After determining the unknown Fourier coefficients, the corresponding mode shapes are obtained by using the direct boundary integral equations for domain points. Some numerical results are presented. Moreover, the inherent problem of spurious eigenvalue using integral formulation is investigated and the SVD updating technique is adopted to suppress the occurrence of spurious eigenvalues. Excellent accuracy, fast rate of convergence and high computational efficiency are the main features of the present method.

Keywords: direct boundary integral equation, null-field integral equation, addition theorem, complex Fourier series, vibration, spurious eigenvalue, SVD updating technique.

WIT Transactions on Modelling and Simulation, Vol 49, © 2009 WIT Press
www.witpress.com, ISSN 1743-355X (on-line)
doi:10.2495/BE090271

1 Introduction

Circular plates with multiple circular holes are widely used in engineering structures [1], e.g. missiles, aircraft, etc. These holes usually cause the change of natural frequency as well as the decrease of load carrying capacity. It is important to comprehend the associated effects in the work of mechanical design or flight control of the structure. As quoted by Leissa and Narita [2]: "the free vibrations of circular plates have been of practical and academic interest for at least a century and a half", we revisit this problem by proposing an analytical method.

Over the past few decades, most of the researches have focused on the analytical solutions for natural frequencies of the circular or annular plates [3–6]. Recently some researchers intended to extend an annular plate [7, 8] to the plate with an eccentric hole. Lee *et al.* [9, 10] proposed a semi-analytical approach to solve the free vibration analysis of a circular plate with multiple holes and pointed out some insufficient accurate results in [8] after careful comparisons.

It is clear that the number of variables can be dramatically decreased by using boundary element method (BEM) or boundary integral equation method (BIEM). For BEM applications to plate problems, readers may consult with the review article [11]. By using the BIEM to analytically solve the problem of plate with multiple holes, two questions need to be solved. One is the improper integral in the boundary integral equation; the other is that both field point and source point are located on different circular boundaries. These problems have been treated by using the degenerate kernel and tensor transformation [9, 10], respectively. But tensor transformation accompanied with the higher order derivative increases the complexity of computation and then affect the accuracy of its solution [9]. In addition, the collocation method in [9, 10] belongs to point-matching approach instead of analytical derivation. It also increases the effort of computation since boundary nodes for collocation are required.

This paper presents an analytical approach to solve the multiple-connected domain plate problem by using the null field integral formulation, addition theorem and complex Fourier series. Some numerical computations are presented. Moreover, the SVD updating technique [10] is employed to suppress the appearance of spurious eigenvalues.

2 Problem statement and direct boundary integral formulations

2.1 Problem statement of plate eigenproblem

As shown in fig.1, a uniform thin circular plate with H circular holes centred at O_k (k=0,1,…,H) has a domain Ω which is enclosed with boundary

$$B=\bigcup_{k=0}^{H} B_k \tag{1}$$

where R_k denotes the radius of the kth circle and O_0 is the position vector of the outer circular boundary of the plate. The governing equation of the free flexural vibration for this plate is expressed as:

$$\nabla^4 u(x) = \lambda^4 u(x), \qquad x \in \Omega \tag{2}$$

where ∇^4 is the biharmonic operator, u is the lateral displacement, $\lambda^4 = \omega^2 \rho_0 h / D$, λ is the dimensionless frequency parameter, ω is the circular frequency, ρ_0 is the volume density, h is the plate thickness, $D = Eh^3/12(1-\mu^2)$ is the flexural rigidity of the plate, E denotes the Young's modulus and μ is the Poisson's ratio

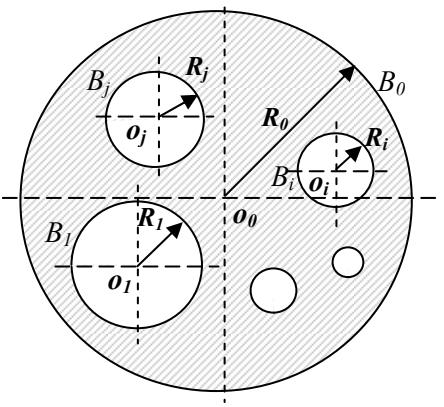

Figure 1: Problem statement for an eigenproblem of a circular plate with multiple circular holes.

2.2 Direct boundary integral formulation

The integral representation for the plate problem can be derived from the Rayleigh-Green identity [12] as follows:

$$u(x) = \int_B U(s,x) v(s) dB(s) - \int_B \Theta(s,x) m(s) dB(s) + \int_B M(s,x) \theta(s) dB(s) - \int_B V(s,x) u(s) dB(s), \qquad x \in \Omega \tag{3}$$

where B is the boundary of the domain Ω, $u(x)$ is the displacement, s and x mean the source and field points, respectively. $U(s, x)$, $\Theta(s, x)$, $M(s, x)$ and $V(s, x)$ in eqn. (3) are kernel functions. The kernel function $U(s, x)$ in eqn. (3),

$$U(s,x) = \frac{1}{8\lambda^2 D}\left[Y_0(\lambda r) - iJ_0(\lambda r) + \frac{2}{\pi} K_0(\lambda r)\right], \tag{4}$$

is the fundamental solution which satisfies

$$\nabla^4 U(s,x) - k^4 U(s,x) = \delta(s-x) \tag{5}$$

where $\delta(s-x)$ is the Dirac-delta function, $J_0(\lambda r)$, $Y_0(\lambda r)$ and $K_0(\lambda r)$ are Bessel functions, $r \equiv |s-x|$ and $i^2=-1$. The other three kernel functions, $\Theta(s, x)$, $M(s, x)$ and $V(s, x)$, in eqn. (3) can be obtained by applying the following slope, moment and effective shear operators defined by

$$K_{\Theta} = \frac{\partial(\cdot)}{\partial n} \tag{6}$$

$$K_{\mathrm{M}} = -D\left[\mu\nabla^2(\cdot) + (1-\mu)\frac{\partial^2(\cdot)}{\partial n^2}\right] \tag{7}$$

$$K_{\mathrm{V}} = -D\left[\frac{\partial}{\partial n}\nabla^2(\cdot) + (1-\mu)\frac{\partial}{\partial t}\left(\frac{\partial}{\partial n}\left(\frac{\partial}{\partial t}(\cdot)\right)\right)\right] \tag{8}$$

to the kernel $U(s, x)$ with respect to the source point, where $\partial/\partial n$ and $\partial/\partial t$ are the normal and tangential derivatives, respectively, ∇^2 means the Laplacian operator.

2.3 Null-field integral equations

The null-field integral equation for displacement can be derived from eqn. (3) and by moving the field point outside the domain. It is expressed as follows:

$$\begin{aligned} 0 = &\int_B U(s,x)v(s)dB(s) - \int_B \Theta(s,x)m(s)dB(s) \\ &+ \int_B M(s,x)\theta(s)dB(s) - \int_B V(s,x)u(s)dB(s), \quad x \in \Omega^C \cup B, \end{aligned} \tag{9}$$

where Ω^C is the complementary domain of Ω. It is noted that once kernel functions are expressed in proper degenerate forms, the field points can be exactly located on the real boundary, that is $x \in \Omega^C \cup B$.

2.4 Degenerate kernels and Fourier series for boundary densities

In the polar coordinate, the field point and source point can be expressed as (ρ,ϕ) and (R,θ), respectively. By employing the addition theorem [13], the kernel function $U(s, x)$ is expanded in the series form as follows:

$$U: \begin{cases} U^I(s,x) = \dfrac{1}{8\lambda^2 D}\displaystyle\sum_{m=-\infty}^{\infty}\{J_m(\lambda\rho)[Y_m(\lambda R) - iJ_m(\lambda R)] + \frac{2}{\pi}I_m(\lambda\rho)K_m(\lambda R)\}e^{im(\varphi-\theta)}, & \rho < R \\ U^E(s,x) = \dfrac{1}{8\lambda^2 D}\displaystyle\sum_{m=-\infty}^{\infty}\{J_m(\lambda R)[Y_m(\lambda\rho) - iJ_m(\lambda\rho)] + \frac{2}{\pi}I_m(\lambda R)K_m(\lambda\rho)\}e^{im(\varphi-\theta)}, & \rho \geq R \end{cases} \tag{10}$$

where the superscripts "I" and "E" denote the interior and exterior cases for $U(s, x)$ degenerate kernel to distinguish $\rho < R$ and $\rho > R$, respectively, as shown in fig. 2.

The displacement $u(s)$, slope $\theta(s)$, moment $m(s)$ and shear force $v(s)$ along the circular boundaries in the null-field integral equations can be expanded in terms of complex Fourier series, respectively, as shown below:

$$u^k(s_k) = \sum_{n=-\infty}^{\infty} a_n^k e^{in\theta_k} \quad , \qquad s_k \in B_k, \quad k = 0,...,H \tag{11}$$

$$\theta^k(s_k) = \sum_{n=-\infty}^{\infty} b_n^k e^{in\theta_k} \quad , \qquad s_k \in B_k, \quad k = 0,...,H \tag{12}$$

$$m^k(s) = \sum_{n=-\infty}^{\infty} c_n^k e^{in\theta_k} \quad , \qquad s_k \in B_k, \quad k = 0,...,H \tag{13}$$

$$v^k(s) = \sum_{n=-\infty}^{\infty} d_n^k e^{in\theta_k} \quad , \qquad s_k \in B_k, \quad k = 0,...,H \tag{14}$$

where a_n^k, b_n^k, c_n^k and d_n^k are the complex Fourier coefficients of the kth circular boundary and θ_k is its polar angle.

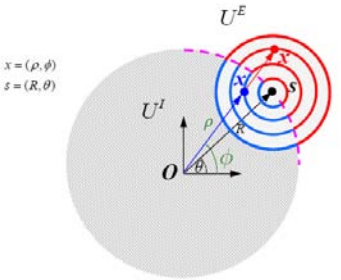

Figure 2: Degenerate kernel for $U(s, x)$.

3 Analytical eigensolution for a circular plate with multiple circular holes

To present formulation clearly and without loss of geniality, a clamped circular plate ($u^0 = \theta^0 = 0$) with H circular holes subject to free edge ($m^k = v^k = 0$; $k=1,\ldots,H$) is considered. Considering the null field near the circular boundary B_0, eqn. (9) can be explicitly expressed as:

$$\begin{aligned} 0 = &\int_{B_0} U^E(s_0, x_0) v^0(s_0) dB_0(s_0) - \int_{B_0} \Theta^E(s_0, x_0) m^0(s_0) dB_0(s_0) \\ &- \left[\sum_{k=1}^{H} \int_{B_k} M^E(s_k, x_k) \theta^k(s_k) dB_k(s_k) - \int_{B_k} V^E(s_k, x_k) u^k(s_k) dB_k(s_k) \right] \end{aligned} \tag{15}$$

By substituting the degenerate kernels, such as eqn. (10), and eqns. (11)-(14) into the eqn. (15), employing the analytical integration along each circular boundary and applying the orthogonal property, eqn. (15) yields

$$
\begin{aligned}
0 = {} & \frac{\pi R_0}{4\lambda^2 D}\sum_{m=-\infty}^{\infty}\{J_m(\lambda R_0)[Y_m(\lambda\rho_0)-iJ_m(\lambda\rho_0)]+\frac{2}{\pi}I_m(\lambda R_0)K_m(\lambda\rho_0)\}d_m^0 e^{im\phi_0} \\
& -\frac{\pi R_0}{4\lambda D}\sum_{m=-\infty}^{\infty}\{J'_m(\lambda R_0)[Y_m(\lambda\rho_0)-iJ_m(\lambda\rho_0)]+\frac{2}{\pi}I'_m(\lambda R_0)K_m(\lambda\rho_0)\}c_m^0 e^{im\phi_0} \\
& -\sum_{k=1}^{H}\left[-\frac{\pi R_k}{4\lambda^2}\sum_{m=-\infty}^{\infty}\{J_m(\lambda\rho_k)[\alpha_m^Y(\lambda R_k)-i\alpha_m^J(\lambda R_k)]+\frac{2}{\pi}I_m(\lambda\rho_k)\alpha_m^K(\lambda R_k)\}b_m^k e^{im\phi_k}\right. \\
& \left.+\frac{\pi R_k}{4\lambda^2}\sum_{m=-\infty}^{\infty}\{J_m(\lambda\rho_k)[\beta_m^Y(\lambda R_k)-i\beta_m^J(\lambda R_k)]+\frac{2}{\pi}I_m(\lambda\rho_k)\beta_m^K(\lambda R_k)\}a_m^k e^{im\phi_k}\right]
\end{aligned}
\tag{16}
$$

where the (ρ_0,ϕ_0), (ρ_1,ϕ), …, (ρ_H,ϕ_H) are the coordinates for the field point x with respect to each center of circles. From eqns. (7) and (8), the moment and the effective shear operators, $\alpha_m^X(\lambda\rho)$ and $\beta_m^X(\lambda\rho)$ are defined as, respectively,

$$
\alpha_m^X(\lambda\rho) = D\left\{(1-\mu)\frac{X'_m(\lambda\rho)}{\rho}-\left[(1-\mu)\frac{m^2}{\rho^2}\mp\lambda^2\right]X_m(\lambda\rho)\right\} \tag{17}
$$

$$
\beta_m^X(\lambda\rho) = D\left\{\left[m^2(1-\mu)\pm(\lambda\rho)^2\right]\frac{X_m{}'(\lambda\rho)}{\rho^2}-m^2(1-\mu)\frac{X_m(\lambda\rho)}{\rho^3}\right\} \tag{18}
$$

where the upper (lower) signs refer to $X = J$, Y, (I, K), respectively. The Bessel's differential equations have been used to simplify $\alpha_m^X(\lambda\rho)$ and $\beta_m^X(\lambda\rho)$.

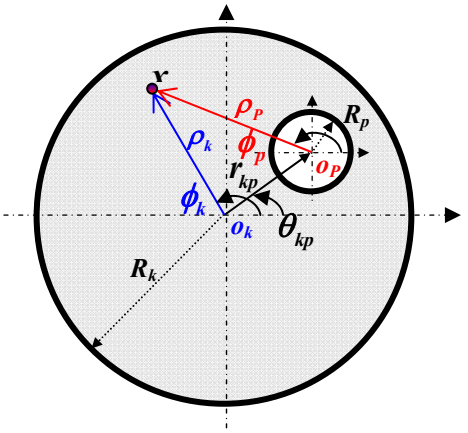

Figure 3: Notation of Graf's addition theorem for Bessel functions.

Based on the Graf's addition theorem for Bessel functions given in [13, 14], we can express the theorem in the following form

$$
J_m(\lambda\rho_p)e^{im\phi_p} = \sum_{n=-\infty}^{\infty} J_{m-n}(\lambda r_{pk})e^{i(m-n)\theta_{pk}}J_n(\lambda\rho_k)e^{in\phi_k} \tag{19}
$$

$$
I_m(\lambda\rho_p)e^{im\phi_p} = \sum_{n=-\infty}^{\infty} I_{m-n}(\lambda r_{pk})e^{i(m-n)\theta_{pk}}I_n(\lambda\rho_k)e^{in\phi_k} \tag{20}
$$

$$Y_m(\lambda\rho_p)\mathrm{e}^{im\phi_p}=\begin{cases}\displaystyle\sum_{n=-\infty}^{\infty}Y_{m-n}(\lambda r_{pk})\mathrm{e}^{i(m-n)\theta_{pk}}J_n(\lambda\rho_k)e^{in\phi_k}, & \rho_k<r_{pk}\\ \displaystyle\sum_{n=-\infty}^{\infty}J_{m-n}(\lambda r_{pk})\mathrm{e}^{i(m-n)\theta_{pk}}Y_n(\lambda\rho_k)e^{in\phi_k}, & \rho_k>r_{pk}\end{cases} \tag{21}$$

$$K_m(\lambda\rho_p)\mathrm{e}^{im\phi_p}=\begin{cases}\displaystyle\sum_{n=-\infty}^{\infty}(-1)^n K_{m-n}(\lambda r_{pk})\mathrm{e}^{i(m-n)\theta_{pk}}I_n(\lambda\rho_k)e^{in\phi_k}, & \rho_k<r_{pk}\\ \displaystyle\sum_{n=-\infty}^{\infty}(-1)^{m-n}I_{m-n}(\lambda r_{pk})\mathrm{e}^{i(m-n)\theta_{pk}}K_n(\lambda\rho_k)e^{in\phi_k}, & \rho_k>r_{pk}\end{cases} \tag{22}$$

where (ρ_p,ϕ_p) and (ρ_k,ϕ_k) shown in fig. 3 are the polar coordinates of a general field point $\boldsymbol{x}$ with respect to O_p and O_k, which are origins of two polar coordinate system and (r_{pk},θ_{pk}) are the polar coordinates of O_k with respect to O_p.

By using the addition theorem for Bessel functions $J_m(\lambda\rho_k)$, $Y_m(\lambda\rho_k)$ and $K_m(\lambda\rho_k)$, eqn. (16) near the circular boundary B_0 under the condition of $\rho_0>r_{k0}$ can be expanded as follows:

$$\begin{aligned}0=&\frac{\pi R_0}{4\lambda^2 D}\sum_{m=-\infty}^{\infty}\{J_m(\lambda R_0)[Y_m(\lambda\rho_0)-iJ_m(\lambda\rho_0)]+\frac{2}{\pi}I_m(\lambda R_0)K_m(\lambda\rho_0)\}d_m^0\mathrm{e}^{im\phi_0}\\ &-\frac{\pi R_0}{4\lambda D}\sum_{m=-\infty}^{\infty}\{J'_m(\lambda R_0)[Y_m(\lambda\rho_0)-iJ_m(\lambda\rho_0)]+\frac{2}{\pi}I'_m(\lambda R_0)K_m(\lambda\rho_0)\}c_m^0\mathrm{e}^{im\phi_0}\\ &+\sum_{k=1}^{H}\Bigg[\frac{\pi R_k}{4\lambda^2}\sum_{m=-\infty}^{\infty}\{[\alpha_m^Y(\lambda R_k)-i\alpha_m^J(\lambda R_k)]\sum_{n=-\infty}^{\infty}J_{m-n}(\lambda r_{k0})\mathrm{e}^{i(m-n)\theta_{k0}}J_n(\lambda\rho_0)\\ &\qquad+\frac{2}{\pi}\alpha_m^K(\lambda R_k)\sum_{n=-\infty}^{\infty}I_{m-n}(\lambda r_{k0})\mathrm{e}^{i(m-n)\theta_{k0}}I_n(\lambda\rho_0)\}\mathrm{e}^{in\phi_0}b_m^k\\ &\quad-\frac{\pi R_k}{4\lambda^2}\sum_{m=-\infty}^{\infty}\{[\beta_m^Y(\lambda R_k)-i\beta_m^J(\lambda R_k)]\sum_{n=-\infty}^{\infty}J_{m-n}(\lambda r_{k0})\mathrm{e}^{i(m-n)\theta_{k0}}J_n(\lambda\rho_0)\\ &\qquad+\frac{2}{\pi}\beta_m^K(\lambda R_k)\sum_{n=-\infty}^{\infty}I_{m-n}(\lambda r_{k0})\mathrm{e}^{i(m-n)\theta_{k0}}I_n(\lambda\rho_0)\}\mathrm{e}^{in\phi_0}a_m^k\Bigg]\end{aligned} \tag{23}$$

Furthermore, eqn. (23) can be rewritten as

$$0=\sum_{m=-\infty}^{\infty}\mathrm{e}^{im\phi_0}\left\langle A_m^0(\lambda\rho_0)d_m^0+B_m^0(\lambda\rho_0)c_m^0+\sum_{k=1}^{H}\left[\sum_{n=-\infty}^{\infty}A_{mn}^k(\lambda\rho_0)b_n^k+\sum_{n=-\infty}^{\infty}B_{mn}^k(\lambda\rho_0)a_n^k\right]\right\rangle \tag{24}$$

where

$$A_m^0(\lambda\rho_0)=\frac{\pi R_0}{4\lambda^2 D}\{J_m(\lambda R_0)[Y_m(\lambda\rho_0)-iJ_m(\lambda\rho_0)]+\frac{2}{\pi}I_m(\lambda R_0)K_m(\lambda\rho_0)\} \tag{25}$$

$$B_m^0(\lambda\rho_0)=-\frac{\pi R_0}{4\lambda D}\{J'_m(\lambda R_0)[Y_m(\lambda\rho_0)-iJ_m(\lambda\rho_0)]+\frac{2}{\pi}I'_m(\lambda R_0)K_m(\lambda\rho_0)\} \tag{26}$$

$$\begin{aligned}A_{mn}^k(\lambda\rho_0)=&\frac{\pi R_k}{4\lambda^2}\mathrm{e}^{i(n-m)\theta_{k0}}\{J_{n-m}(\lambda r_{k0})\alpha_n^J(\lambda R_k)[Y_m(\lambda\rho_0)-iJ_m(\lambda\rho_0)]\\ &+\frac{2}{\pi}(-1)^{n-m}I_{n-m}(\lambda r_{k0})\alpha_n^I(\lambda R_k)K_m(\lambda\rho_0)\}\end{aligned} \tag{27}$$

$$B_{mn}^{k}(\lambda\rho_0) = -\frac{\pi R_k}{4\lambda^2}\mathrm{e}^{i(n-m)\theta_{k0}}\{J_{n-m}(\lambda r_{k0})\beta_n^J(\lambda R_k)[Y_m(\lambda\rho_0) - iJ_m(\lambda\rho_0)] + \frac{2}{\pi}(-1)^{n-m}I_{n-m}(\lambda r_{k0})\beta_n^I(\lambda R_k)K_m(\lambda\rho_0)\} \tag{28}$$

By differentiating eqn. (24) with respect to ρ_0, the equation for the slope θ near the circular boundary B_0 is given as

$$0 = \sum_{m=-\infty}^{\infty}\mathrm{e}^{im\phi_0}\left\langle C_m^0(\lambda\rho_0)d_m^0 + D_m^0(\lambda\rho_0)c_m^0 + \sum_{k=1}^{H}\left[\sum_{n=-\infty}^{\infty}C_{mn}^k(\lambda\rho_0)b_n^k + \sum_{n=-\infty}^{\infty}D_{mn}^k(\lambda\rho_0)a_n^k\right]\right\rangle \tag{29}$$

where $C_m^0(\lambda\rho_0)$, $D_m^0(\lambda\rho_0)$, $C_{mn}^k(\lambda\rho_0)$ and $D_{mn}^k(\lambda\rho_0)$ can be obtained by differentiating $A_m^0(\lambda\rho_0)$, $B_m^0(\lambda\rho_0)$, $A_{mn}^k(\lambda\rho_0)$ and $B_{mn}^k(\lambda\rho_0)$ in eqns. (25-28) with respective to ρ_0.

Similarly, considering the null field points near the circular boundary B_p ($p=1,\ldots,H$), eqn. (9) can be explicitly expressed as:

$$0 = \int_{B_0}U^I(s_0,x_0)v^0(s_0)dB_0(s_0) - \int_{B_0}\Theta^I(s_0,x_0)m^0(s_0)dB_0(s_0) - \left[\sum_{k=1}^{H}\int_{B_k}M^\gamma(s_k,x_k)\theta^k(s_k)dB_k(s_k) - \int_{B_k}V^\gamma(s_k,x_k)u^k(s_k)dB_k(s_k)\right] \tag{30}$$

where $\gamma = I$, $k=p$; $\gamma = E$, $k\neq p$.

By substituting degenerate kernel functions and complex Fourier series into eqn. (30) and then applying the addition theorem, eqn. (30) yields

$$0 = \sum_{m=-\infty}^{\infty}\mathrm{e}^{im\phi_p}\left\langle E_m^p(\lambda\rho_p)d_m^p + F_m^p(\lambda\rho_p)c_m^p + \sum_{\substack{k=0\\k\neq p}}^{H}\left[\sum_{n=-M}^{M}E_{mn}^k(\lambda\rho_p)b_n^k + \sum_{n=-\infty}^{\infty}F_{mn}^k(\lambda\rho_p)a_n^k\right]\right\rangle \tag{31}$$

where

$$E_m^p(\lambda\rho_p) = \frac{\pi R_p}{4\lambda^2}\{J_m(\lambda\rho_p)[\alpha_m^Y(\lambda R_p) - i\alpha_m^J(\lambda R_p)] + \frac{2}{\pi}I_m(\lambda\rho_p)\alpha_m^K(\lambda R_p)\} \tag{32}$$

$$F_m^p(\lambda\rho_p) = -\frac{\pi R_p}{4\lambda^2}\{J_m(\lambda\rho_p)[\beta_m^Y(\lambda R_p) - i\beta_m^J(\lambda R_p)] + \frac{2}{\pi}I_m(\lambda\rho_p)\beta_m^K(\lambda R_p)\} \tag{33}$$

$$E_{mn}^k(\lambda\rho_p) = \begin{cases} \dfrac{\pi R_k}{4\lambda^2 D}\mathrm{e}^{i(n-m)\theta_{kp}}\{J_{n-m}(\lambda r_{kp})J_m(\lambda\rho_p)[Y_n(\lambda R_k) - iJ_n(\lambda R_k)] + \dfrac{2}{\pi}I_{n-m}(\lambda r_{kp})I_m(\lambda\rho_p)K_n(\lambda R_k)\}, & k=0 \\ \dfrac{\pi R_k}{4\lambda^2}\mathrm{e}^{i(n-m)\theta_{kp}}\{J_m(\lambda\rho_p)\alpha_n^J(\lambda R_k)[Y_{n-m}(\lambda r_{kp}) - iJ_{n-m}(\lambda r_{kp})] + \dfrac{2}{\pi}(-1)^m I_m(\lambda\rho_p)\alpha_n^I(\lambda R_k)K_{n-m}(\lambda r_{kp})\}, & k\neq 0,p \end{cases} \tag{34}$$

$$F_{mn}^{k}(\lambda\rho_p)=\begin{cases}-\dfrac{\pi R_k}{4\lambda D}\mathrm{e}^{i(n-m)\theta_{kp}}\{J_{n-m}(\lambda r_{kp})J_m(\lambda\rho_p)[Y_n'(\lambda R_k)-iJ_n'(\lambda R_k)] \\ \qquad +\dfrac{2}{\pi}I_{n-m}(\lambda r_{kp})I_m(\lambda\rho_p)K_n'(\lambda R_k)\}, \qquad k=0 \\ -\dfrac{\pi R_k}{4\lambda^2}\mathrm{e}^{i(n-m)\theta_{kp}}\{J_m(\lambda\rho_p)\beta_n^J(\lambda R_k)[Y_{n-m}(\lambda r_{kp})-iJ_{n-m}(\lambda r_{kp})] \\ \qquad +\dfrac{2}{\pi}(-1)^m I_m(\lambda\rho_p)\beta_n^I(\lambda R_k)K_{n-m}(\lambda r_{kp})\}, \qquad k\neq 0,p\end{cases} \tag{35}$$

By differentiating eqn. (31) with respect to ρ_p, the equation of the slope θ near the circular boundary B_p is given as

$$0=\sum_{m=-\infty}^{\infty}\mathrm{e}^{im\phi_p}\left\langle G_m^p(\lambda\rho_p)d_m^p+H_m^p(\lambda\rho_p)c_m^p+\sum_{\substack{k=0\\k\neq p}}^{H}\left[\sum_{n=-M}^{M}G_{mn}^k(\lambda\rho_p)b_n^k+\sum_{n=-\infty}^{\infty}H_{mn}^k(\lambda\rho_p)a_n^k\right]\right\rangle \tag{36}$$

where $G_m^p(\lambda\rho_p), H_m^p(\lambda\rho_p), G_{mn}^k(\lambda\rho_p)$ and $H_{mn}^k(\lambda\rho_p)$ can be obtained by differentiating $E_m^p(\lambda\rho_p), F_m^p(\lambda\rho_p)$, $E_{mn}^k(\lambda\rho_p)$ and $F_{mn}^k(\lambda\rho_p)$ in eqns. (32-35) with respective to ρ.

By setting ρ_p to R_p and applying the orthogonal property of $\{\mathrm{e}^{im\phi_p}\}$ (p =0, 1,…,H), eqns.(24), (29), (31) and (36) yield , for m=0, ±1, ±2, …; n=0, ±1, ±2, …; p =1,…,H,

$$\begin{cases}A_m^0(\lambda R_0)d_m^0+B_m^0(\lambda R_0)c_m^0+\sum_{k=1}^{H}\left[\sum_{n=-\infty}^{\infty}A_{mn}^k(\lambda R_0)b_n^k+\sum_{n=-\infty}^{\infty}B_{mn}^k(\lambda R_0)a_n^k\right]=0 \\ C_m^0(\lambda R_0)d_m^0+D_m^0(\lambda R_0)c_m^0+\sum_{k=1}^{H}\left[\sum_{n=-\infty}^{\infty}C_{mn}^k(\lambda R_0)b_n^k+\sum_{n=-\infty}^{\infty}D_{mn}^k(\lambda R_0)a_n^k\right]=0 \\ E_m^p(\lambda R_p)d_m^p+F_m^p(\lambda R_p)c_m^p+\sum_{\substack{k=0\\k\neq p}}^{H}\left[\sum_{n=-M}^{M}E_{mn}^k(\lambda R_p)b_n^k+\sum_{n=-\infty}^{\infty}F_{mn}^k(\lambda R_p)a_n^k\right]=0 \\ G_m^p(\lambda R_p)d_m^p+H_m^p(\lambda R_p)c_m^p+\sum_{\substack{k=0\\k\neq p}}^{H}\left[\sum_{n=-M}^{M}G_{mn}^k(\lambda R_p)b_n^k+\sum_{n=-\infty}^{\infty}H_{mn}^k(\lambda R_p)a_n^k\right]=0\end{cases} \tag{37}$$

eqn. (37) results in a couple infinite system of simultaneous linear algebraic equations for the coefficients a_m^k, b_m^k, c_m^k and d_m^k, k=0,…, H. In the following computation, only the finite M terms are used in eqn. (37). According to the direct-searching scheme [12], the eigenvalue are obtained by applying the SVD technique [15] to the matrix from eqn. (37). Once the eigenvalues are found, the associated mode shapes can be obtained by substituting the corresponding boundary eigenvectors (i.e. the complex Fourier series representing the fictitious boundary density) into the boundary integral equations.

4 Spurious eigenvalue for multiply-connected plate eigenproblem using BEM

In this section, SVD updating technique is adopted to suppress the appearance of spurious eigenvalue which cause the present method fail. The concept of this technique is to provide sufficient constrains to overcome the rank deficiency of the system. Since four null field integral equations for the plate formulation are provided [10], there are 6 (C (4,2)) options for choosing any two equations to solve the eigenproblem. The $U\Theta$ formulation in section 3 uses the first and the second equations. To provide sufficient constrains, the *UM* formulation is alternative, which uses the first and the third equations. Applying the moment operator of eqn. (17), to eqns. (24) and (31), respectively, yield

$$0=\sum_{m=-\infty}^{\infty} e^{im\phi_0}\left\langle P_m^0(\lambda\rho_0)d_m^0+Q_m^0(\lambda\rho_0)c_m^0+\sum_{k=1}^{H}\left[\sum_{n=-\infty}^{\infty}P_{mn}^k(\lambda\rho_0)b_n^k+\sum_{n=-\infty}^{\infty}Q_{mn}^k(\lambda\rho_0)a_n^k\right]\right\rangle \tag{38}$$

$$0=\sum_{m=-\infty}^{\infty} e^{im\phi_p}\left\langle S_m^p(\lambda\rho_p)d_m^p+T_m^p(\lambda\rho_p)c_m^p+\sum_{\substack{k=0\\k\neq p}}^{H}\left[\sum_{n=-M}^{M}S_{mn}^k(\lambda\rho_p)b_n^k+\sum_{n=-\infty}^{\infty}T_{mn}^k(\lambda\rho_p)a_n^k\right]\right\rangle \tag{39}$$

where $P_m^0(\lambda\rho_0)$, $Q_m^0(\lambda\rho_0)$, $P_{mn}^k(\lambda\rho_0)$, $Q_{mn}^k(\lambda\rho_0)$, $S_m^p(\lambda\rho_p)$, $T_m^p(\lambda\rho_p)$, $S_{mn}^k(\lambda\rho_p)$ and $T_{mn}^k(\lambda\rho_p)$ can be obtained by applying the moment operator to $A_m^0(\lambda\rho_0)$, $B_m^0(\lambda\rho_0)$, $A_{mn}^k(\lambda\rho_0)$, $B_{mn}^k(\lambda\rho_0)$, $E_m^p(\lambda\rho_p)$, $F_m^p(\lambda\rho_p)$, $E_{mn}^k(\lambda\rho_p)$ and $F_{mn}^k(\lambda\rho_p)$ with respect to ρ.

By setting ρ_P to R_P and applying the orthogonal property of $\{e^{im\phi_P}\}$ ($p=0, 1,\ldots,H$), eqns.(24), (38), (31) and (39) yield , for m=0, ±1, ±2, …; n=0, ±1, ±2, …; $p=1,\ldots,H$,

$$\begin{cases} A_m^0(\lambda R_0)d_m^0+B_m^0(\lambda R_0)c_m^0+\sum_{k=1}^{H}\left[\sum_{n=-\infty}^{\infty}A_{mn}^k(\lambda R_0)b_n^k+\sum_{n=-\infty}^{\infty}B_{mn}^k(\lambda R_0)a_n^k\right]=0 \\ P_m^0(\lambda R_0)d_m^0+Q_m^0(\lambda R_0)c_m^0+\sum_{k=1}^{H}\left[\sum_{n=-\infty}^{\infty}P_{mn}^k(\lambda R_0)b_n^k+\sum_{n=-\infty}^{\infty}Q_{mn}^k(\lambda R_0)a_n^k\right]=0 \\ E_m^p(\lambda R_p)d_m^p+F_m^p(\lambda R_p)c_m^p+\sum_{\substack{k=0\\k\neq p}}^{H}\left[\sum_{n=-M}^{M}E_{mn}^k(\lambda R_p)b_n^k+\sum_{n=-\infty}^{\infty}F_{mn}^k(\lambda R_p)a_n^k\right]=0 \\ S_m^p(\lambda R_p)d_m^p+T_m^p(\lambda R_p)c_m^p+\sum_{\substack{k=0\\k\neq p}}^{H}\left[\sum_{n=-M}^{M}S_{mn}^k(\lambda R_p)b_n^k+\sum_{n=-\infty}^{\infty}T_{mn}^k(\lambda R_p)a_n^k\right]=0 \end{cases} \tag{40}$$

which is called the *UM* formulation. By using the concept of SVD technique of updating terms, combing eqns. (37) and (40) can filter out spurious eigenvalues.

5 Numerical results and discussions

To demonstrate the proposed method, the FORTRAN code was implemented to determine natural frequencies and modes of a circular plate with multiple circular holes. The same problem was independently solved by using FEM (the ABAQUS software [16]) for comparison. The thickness of plate is 0.002m and the Poisson ratio μ=1/3. The general-purpose linear triangular elements of type S3 were employed to model the plate problem by using ABAQUS. Although the thickness of the plate is 0.002 m, these elements do not suffer from transverse shear locking based on the theoretical manual of ABAQUS [16].

A circular plate with three holes [10] is considered. The radii of holes are 0.4m, 0.2m and 0.2m and the coordinates of the center are (0.5,0), (−0.3,0.4) and (−0.3, −0.4), respectively. Fig. 4 shows the former six natural frequency parameters versus the number of terms of Fourier series *N*. It indicates that the proposed solution promptly converges with few terms of Fourier series. By taking thirteen terms of Fourier series (*N*=13), fig. 5 shows the minimum singular value versus the frequency parameter by using the $U\Theta$ formulation, *UM* formulation and SVD updating technique for a circular clamped plate with three circular holes. Since the direct-searching scheme is used, the drop location indicates the eigenvalue. The spurious eigenvalues of 5.5811 and 7.9906 occur when using the *UM* and $U\Theta$ formulation, respectively. They are found to be the true eigenvalue of simply supported and clamped circular plate with a radius of 0.4 m, respectively. It demonstrates that the spurious eigenvalue can be filtered out by using the SVD updating technique. The same problem is also solved by using ABAQUS and its model has 308960 elements in order to obtain comparable results for comparison. The former five natural frequency parameters and modes by using the present method, the semi-analytical method [10] and FEM are shown in fig. 6. Good agreement between the results of the present method and those of ABAQUS is observed.

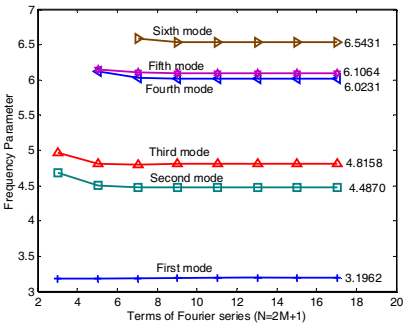

Figure 4: Natural frequency parameter versus the number of terms of Fourier series.

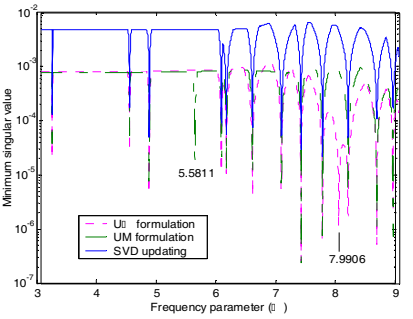

Figure 5: The minimum singular value versus the frequency parameter by using different methods.

.

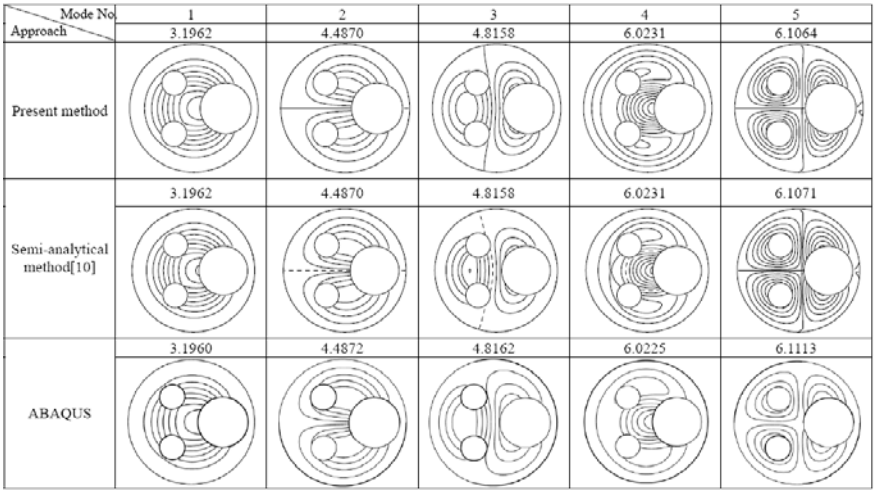

Figure 6: The former five natural frequency parameters and mode shapes by using the present method, semi-analytical method and FEM.

6 Concluding remarks

Natural frequencies and natural modes of a circular plate with multiple circular holes have been obtained by using the null field integral formulation and the addition theorem. Based on the addition theorem, two critical problems of improper integrals in the boundary integration and the higher derivative in the multiply-connected domain problems were successively treated in a novel way. By matching the specified boundary conditions, an analytical solution can be derived from a coupled infinite systems of simultaneous linear algebraic equations. By using the direct-searching method, numerical eigensolutions were given from the corresponding truncated finite system. The proposed results match well with those provided by the FEM using many elements to obtain acceptable data for comparison. In addition, the SVD technique of updating terms was employed to filter out spurious eigenvalues. Numerical results show good accuracy and fast rate of convergence thanks to the analytical method.

References

[1] Khurasia, H. B. & Rawtani, S., Vibration analysis of circular plates with eccentric hole. ASME *Journal of Applied Mechanics*, **45**, pp. 215-217, 1978.

[2] Leissa A. W. & Narita, Y., Natural frequencies of simply supported circular plates. *Journal of Sound and Vibration*, **70**, pp. 221-229, 1980.

[3] Vogel, S. M. & Skinner, D. W., Natural frequencies of transversely vibrating uniform annular plates. ASME *Journal of Applied Mechanics*, **32**, pp. 926-931, 1965.
[4] Vega, D. A., Vera, S. A., Sanchez, M. D. & Laura, P. A. A., Transverse vibrations of circular, annular plates with a free inner boundary, *Journal of the Acoustical Society of America*, **103**, pp. 1225-1226, 1998.
[5] Vera, S. A., Sanchez, M. D., Laura, P. A. A. & Vega, D. A., Transverse vibrations of circular, annular plates with several combinations of boundary conditions. *Journal of Sound and Vibration*, **213**(4), pp.757-762, 1998.
[6] Vera, S. A., Laura, P. A. A. & Vega, D. A., Transverse vibrations of a free-free circular annular plate. *Journal of Sound and Vibration*, **224**(2), pp. 379-383, 1999.
[7] Cheng L., Li, Y. Y. & Yam, L. H., Vibration analysis of annular-like plates. *Journal of Sound and Vibration*, **262**, pp.1153-1170, 2003.
[8] Laura, P. A. A., Masia, U. & Avalos, D. R., Small amplitude, transverse vibrations of circular plates elastically restrained against rotation with an eccentric circular perforation with a free edge. *Journal of Sound and Vibration,* **292**, pp. 1004-1010, 2006.
[9] Lee, W. M., Chen, J. T. & Lee, Y. T., Free vibration analysis of circular plates with multiple circular holes using indirect BIEMs. *Journal of Sound and Vibration,* **304**, pp.811-830, 2007.
[10] Lee, W. M. & Chen, J. T., Null-field integral equation approach for free vibration analysis of circular plates with multiple circular holes. *Computational Mechanics*, **42**, pp.733–747, 2008.
[11] Providatis, C. P. & Beskos, D. E., Dynamic analysis of plates by boundary elements. ASME *Applied Mechanics Reviews*, **52**(7), pp. 213-236, 1999.
[12] Kitahara, M., *Boundary Integral Equation Methods in Eigenvalue Problems of Elastodynamics and Thin Plates*. Elsevier: Amsterdam, 1985.
[13] Watson, G. N., *A treatise on the theory of Bessel Functions*, second edition. Cambridge: Cambridge Library edition, 1995.
[14] Gradshteyn, I. S. & Ryzhik, I. M., *Table of integrals, series, and products*, 5th edition, Academic Press, New York, 1996.
[15] IMSL, Math/Library Volumes 1 and 2 version 4.01 Visual Numerics, Inc., 1999.
[16] ABAQUS 6.5, Hibbitt, Karlsson and Sorensen, Inc., RI, 2004.

This page intentionally left blank

Free vibration analysis of thin circular plates by the indirect Trefftz method

A. Ghannadi-Asl[1] & A. Noorzad[2]
[1]*Sama Organization (Affiliated with Islamic Azad University) – Ardabil Branch, Iran*
[2]*School of Civil Engineering, University of Tehran, Iran*

Abstract

The vibration of plates is important in many applications pertaining to mechanical, civil and aerospace engineering. Therefore, the vibration of plates is an important research area that has been studied by many researchers. To date, there are abundant plate vibration solutions available in the open literature based on Kirchhoff assumptions. The purpose of the present paper is free vibration analysis of thin circular plates by the indirect Trefftz method. In thin plate vibration problems, we will deal with the governing equation with the homogeneous boundary conditions. The Trefftz method basically employs the complete set of solutions satisfying the governing equation as the first step. To derive the boundary integral equation, either the reciprocity law, which is similar to those used in conventional BEMs, or the weight residual method can be used. The proposed approach has some merits when compared with other regular boundary element formulations reported so far. A main benefit for the Trefftz method is that it does not involve singular integrals due to the properties of its solution basis functions (T functions); thus, it can be categorized into the regular boundary element method. Besides, this advocated approach yields a solution that offers simultaneously the advantages of the classical FEM and BEM solutions, without having their drawbacks. Finally, several numerical examples are demonstrated to show the validity of the current approach.

Keywords: indirect Trefftz method, boundary-type solution, free vibration, thin circular plates.

WIT Transactions on Modelling and Simulation, Vol 49, © 2009 WIT Press
www.witpress.com, ISSN 1743-355X (on-line)
doi:10.2495/BE090281

1 Introduction

Plates with various boundary conditions are common components in many fields of engineering, especially in civil and mechanical engineering. With the wide application of plate structures, static and dynamic analyses of plates become very important. We consider various kinds of motion of plates. There is a free vibration, which occurs in the absence of applied loads but may be initiated by applying initial conditions to the plate. The free vibration deals with natural characteristics of the plates, and these natural vibrations occur at discrete frequencies, depending only on the geometry and material of the plates. Then, there is a forced vibration, which results from an application of time-dependent loads. Forced vibrations come in two kinds: a harmonic response, when a periodic force is applied to the plate; and a transient response, when the applied force is not a periodic force. The dynamic characteristics of the plate have a considerable effect on the overall structure performance. When the frequency of the external load matches the natural frequency of the plate, damage or destruction may occur. With this respect, the natural frequencies of the plates have been studied extensively for more than a century. Therefore, vibration of the plate is an important research area that has been studied by many researchers.

For the solution of a free-vibration problem, many well-developed numerical techniques such as the finite element method (FEM), finite difference method (FDM) and boundary element method (BEM) can be adopted. This paper is concerned with the free vibration analysis of thin circular plates by using of the indirect Trefftz boundary approach [1]. In the indirect formulation, the solutions of the problems to be solved are approximated by the superposition of the T-complete functions. Then, the unknown parameters are determined so that the approximate solutions satisfy the boundary conditions. Although in recent years various boundary solution methods have been applied to the thick plate bending problem [2-4], in the present work, we will restrict ourselves to the indirect Trefftz boundary approach and extend the method to free vibration analysis of thin circular plate problems.

Basically, the Trefftz method consists in the solution of a partial differential equation by the superposition of a number of functions, themselves solutions of the homogeneous governing equation, appropriately scaled by a number of unknown parameters. These unknowns are then obtained from the approximate satisfaction of the boundary conditions by means of collocation or in a weighted residual sense. Trefftz-based formulations have been studied by several authors, such as Jirousek and co-workers (of which Jirousek and Wrobleski [5] give a thorough account), Cheung et al. [6], Jin et al. [7], Zielinski and Zienkiewicz [8], Zielinski and Herrera [9], and Freitas and Ji [10] amongst others. Reviews on the subject may be found in Zielinski [11], Kita and Kamiya [12] and Jirousek and Wrobleski [5].

This paper is organized as follows. In section 2, the basic equations based on the Kirchhoff plate theory is explained in detail. Then, in section 3, the complete solutions and complete sets are shown. In section 4, the indirect Trefftz method is explained and in section 5, some numerical examples are shown to illustrate

the efficiency of the Trefftz method. Finally, in section 6, the conclusions are drawn, briefly.

2 Fundamental equations of classical plate theory

Consider a circular plate of thin uniform thickness (h) with isotropic material and radius a. The classical differential equation of motion for the transverse displacement w of a plate is given by [13]:

$$D\nabla^4 w + \rho h \frac{\partial^2 w}{\partial^2 t} = 0 \tag{1}$$

where $D = Eh^3/12(1-\nu^2)$ is known as the flexural rigidity of the plate and E is Young's modulus, h is the plate thickness, ν is Poisson's ratio, ρ is mass density of the plate material, t is time, and $\nabla^4 = \nabla^2 \cdot \nabla^2$, where ∇^2 is the Laplacian operator. When free vibrations are assumed, the motion is expressed as

$$w_i(r,\theta,t) = W^{(i)}(r,\theta)\cos(\omega_i t) \tag{2}$$

where ω_i is the natural frequency (expressed in radians/unit time) and $W^{(i)}(r,\theta)$ is its associated mode shape and a function only of the position coordinates. Substituting eqn. (2) into eqn. (1) yields

$$\left(\nabla^4 - \frac{\rho h \omega_i^2}{D}\right) \cdot W^{(i)}(r,\theta) = 0 \tag{3}$$

It is usually convenient to factor eqn. (3) into

$$\left(\nabla^2 + \omega_i\sqrt{\frac{\rho h}{D}}\right) \cdot \left(\nabla^2 - \omega_i\sqrt{\frac{\rho h}{D}}\right) \cdot W^{(i)} = 0 \tag{4}$$

Whence, by the theory of linear differential equations, the complete solution to eqn. (4) can be obtained by superimposing the solutions to the equations:

$$\nabla^2 W_1^{(i)} + k_i^2 W_1^{(i)} = 0 \tag{5}$$

$$\nabla^2 W_2^{(i)} - k_i^2 W_2^{(i)} = 0 \tag{6}$$

where $k_i^2 = \omega_i\sqrt{\frac{\rho h}{D}}$. Thus, the general solution to eqn. (4) in polar coordinates is:

$$W^{(i)} = W_1^{(i)} + W_2^{(i)} \tag{7}$$

Based on Hooke's law and Kirchhoff's assumptions, the bending and twisting moment–displacement relations are given by [13]:

$$M_r = -D \cdot \left[\frac{\partial^2 w}{\partial r^2} + \frac{\nu}{r}\frac{\partial w}{\partial r} + \frac{\nu}{r^2}\frac{\partial^2 w}{\partial \theta^2} \right] \tag{8}$$

$$M_\theta = -D \cdot \left[\nu \frac{\partial^2 w}{\partial r^2} + \frac{1}{r}\frac{\partial w}{\partial r} + \frac{1}{r^2}\frac{\partial^2 w}{\partial \theta^2} \right] \tag{9}$$

$$M_{r\theta} = -D \cdot (1-\nu)\frac{1}{r}\frac{\partial}{\partial \theta}\left(\frac{\partial w}{\partial r} - \frac{w}{r} \right) \tag{10}$$

Based on Kirchhoff plate theory, the shear forces–displacement relation can be obtained as:

$$Q_r = -D\frac{\partial}{\partial r}\left[\frac{\partial^2 w}{\partial r^2} + \frac{1}{r}\frac{\partial w}{\partial r} + \frac{1}{r^2}\frac{\partial^2 w}{\partial \theta^2} \right] \tag{11}$$

$$Q_\theta = -D\frac{1}{r}\frac{\partial}{\partial \theta}\left[\frac{\partial^2 w}{\partial r^2} + \frac{1}{r}\frac{\partial w}{\partial r} + \frac{1}{r^2}\frac{\partial^2 w}{\partial \theta^2} \right] \tag{12}$$

Based on Kirchhoff plate theory, equivalent change of slopes of the normal and tangential about the midsurface is given as follow:

$$\phi_r = -\frac{\partial w}{\partial r} \tag{13}$$

$$\phi_\theta = \frac{\partial w}{\partial \theta} \tag{14}$$

3 Complete solutions and complete sets

Trefftz methods can be considered as the boundary-type solution procedure employing the regular T-complete functions satisfying the governing equations. Therefore, the input data generation is much easier than the domain-type solution procedures such as the finite element and the finite difference methods. Moreover, the formulations are regular and thus, much simpler than the ordinary boundary element methods employing the singular fundamental solutions. The complete solutions and complete sets corresponding to the governing equations (5) and (6) are used as weighting and/or trial functions. In the case of polar co-ordinates, the T-complete solution of the homogeneous equation of the biharmonic eqn. (5) can be found using separation of variables [14]:

$$W_1^{(i)} = \sum_{n=0}^{\infty} \left[a_n J_n(k_i r) + b_n Y_n(k_i r)\right] \cdot \mathrm{Cos}(n\theta) + \left[c_n J_n(k_i r) + d_n Y_n(k_i r)\right] \cdot \mathrm{Sin}(n\theta) \tag{15}$$

The T-complete solution of the eqn. (6) can be found using separation of variables [14]:

$$W_2^{(i)} = \sum_{n=0}^{\infty} \left[a_n I_n(k_i r) + b_n K_n(k_i r)\right] \cdot \mathrm{Cos}(n\theta) + \left[c_n I_n(k_i r) + d_n K_n(k_i r)\right] \cdot \mathrm{Sin}(n\theta) \tag{16}$$

where r is the Euclidean distance from the origin to a domain point, and θ is the angle between the x-axis and the radial vector from the origin to the domain point. The special functions used in the expressions from eqn. (15) are Bessel functions of the first kind ($J_n(k_i r)$) and the second kind ($Y_n(k_i r)$). Also, the special functions used in the expressions from eqn. (16) are modified Bessel functions of the first kind ($I_n(k_i r)$) and the second kind ($K_n(k_i r)$). The coefficients of Bessel functions in equations (15) and (16) determine the mode shape and are solved for from the boundary conditions.

If the boundary conditions possess symmetry with respect to one or more diameters of the circle, then the terms involving sin (nθ) are not needed. For solid circular plates, the terms involving $Y_n(k_i r)$ and $K_n(k_i r)$ in equations (15) and (16) must be discarded in order to avoid singularity of deflections and stresses (i.e., avoid infinite values) at the plate centre, r = 0. Then, the T-complete sets of solutions for interior domain problem ($0 \le r \le a$) are as follows:

$$\mathbf{B}_w = \left[J_n(k_i r)\mathrm{Cos}(n\theta), J_n(k_i r)\mathrm{Sin}(n\theta), I_n(k_i r)\mathrm{Cos}(n\theta), I_n(k_i r)\mathrm{Sin}(n\theta) \right] \quad n = 0,1,2,...$$

4 Indirect Trefftz formulation

The indirect formulation, considered as the original formulation presented by Trefftz in 1926, the solution of the problem is approximated by the superposition of the functions satisfying the governing equation and then, the unknown parameters are determined so that the approximate solution satisfies the boundary condition by means of the collocation, the least square or the Galerkin method [12]. In this approach, the trial functions are expanded in terms of a sequence of linearly independent Trefftz functions and a discrete set of unknown coefficients a. However, the weighting functions may be chosen in different ways. When the Dirac delta function is used, the method leads to the Trefftz collocation method (TCM). If the Trefftz function is employed as the weight function, the method leads to the Trefftz Galerkin method (TGM) [15]. To illustrate the weighted residual procedure [16], we shall consider the

determination of a function (u), which may be a quantity within a region Ω bounded, by Γ, defined by the general equation:

$$L(u) = 0 \qquad \text{in } \Omega \tag{17}$$

subject to the boundary conditions:

$$\begin{array}{llll} w - \overline{w} = 0 & \phi_s - \overline{\phi}_s = 0 & \phi_n - \overline{\phi}_n = 0 & \text{on } \Gamma_c \\ w - \overline{w} = 0 & \phi_s - \overline{\phi}_s = 0 & M_n - \overline{M}_n = 0 & \text{on } \Gamma_s \\ Q_n - \overline{Q}_n = 0 & M_{ns} - \overline{M}_{ns} = 0 & M_n - \overline{M}_n = 0 & \text{on } \Gamma_f \end{array} \tag{18}$$

These conditions are obtained from natural boundary and Γ_c, Γ_s and Γ_f stand for clamped, simply supported and free boundary conditions for which the displacement is specified, and the quantities ($\overline{\bullet}$) stands for specified boundary values. The operator L may be either differential or integral operator and is also either linear or nonlinear in nature. If u^0 is some approximation to you then equations (17) and (18) will not be satisfied exactly. Let us assume that errors involved are:

$$\begin{array}{lll} L(u^0) = E_1 & & \\ w(u^0) - \overline{w} = E_2 \quad , & \phi_s(u^0) - \overline{\phi}_s = E_3 \quad , & \phi_n(u^0) - \overline{\phi}_n = E_4 \\ M_n(u^0) - \overline{M}_n = E_5 \quad , & M_{ns}(u^0) - \overline{M}_{ns} = E_6 \quad , & Q_n(u^0) - \overline{Q}_n = E_7 \end{array} \tag{19}$$

where E_1-E_7 are residual error functions. To determine the approximate solution of u^0 some weighted integral of errors, defined in eqn. (19), is set to zero, so that:

$$\begin{aligned} &\int_\Omega w_1^*\left(L(u^0)\right)\cdot d\Omega + \int_{\Gamma_w} w_2^*\left(w^0 - \overline{w}\right)\cdot d\Gamma + \int_{\Gamma_{\phi s}} w_3^*\left(\phi_s{}^0 - \overline{\phi}_s\right)\cdot d\Gamma + \int_{\Gamma_{\phi n}} w_4^*\left(\phi_n{}^0 - \overline{\phi}_n\right)\cdot d\Gamma \\ &+ \int_{\Gamma_{Mn}} w_5^*\left(M_n{}^0 - \overline{M}_n\right)\cdot d\Gamma + \int_{\Gamma_{Ms}} w_6^*\left(M_{ns}{}^0 - \overline{M}_{ns}\right)\cdot d\Gamma + \int_{\Gamma_{Mns}} w_7^*\left(Q_n{}^0 - \overline{Q}_n\right)\cdot d\Gamma = 0 \end{aligned} \tag{20}$$

where w_i^* (i=1-7) are a set of independent weighting functions and in this case, the operator L is defined as follow:

$$L(u) = \nabla^2 W_1^{(i)} + k_i^2 W_1^{(i)} \tag{21}$$

$$L(u) = \nabla^2 W_2^{(i)} - k_i^2 W_2^{(i)} \tag{22}$$

Now suppose that the approximate solution of the generalized displacements $W_1^{(i)}$ and $W_2^{(i)}$ can be expressed by a series as:

$$W_1^{(i)} = \sum N_{W_1^{(i)}} a_j \tag{23}$$

$$W_2^{(i)} = \sum N_{W_2^{(i)}} a_j \tag{24}$$

where a_j are undetermined coefficients, $N_{W_1^{(i)}}$ and $N_{W_2^{(i)}}$ are the complete sets of Trefftz functions. $N_{W_1^{(i)}}$ and $N_{W_2^{(i)}}$ are chosen such that they satisfy *a priori* the homogeneous equations in equations (5) and (6), i.e. for any function $N_{W_1^{(i)}}$ and $N_{W_2^{(i)}}$, we have:

$$\nabla^2 N_{W_1^{(i)}} + k_i^2 N_{W_1^{(i)}} = 0 \tag{25}$$

$$\nabla^2 N_{W_2^{(i)}} - k_i^2 N_{W_2^{(i)}} = 0 \tag{26}$$

Substituting equations (25) and (26) into equations (8)-(14) and transforming the polar co-ordinate system to the local co-ordinate system (n,s), the variables in eqn. (20) can be written as:

$$\begin{aligned} w^0 &= \sum N_{1i} a_i = \mathbf{N_1 a} \quad , \quad \phi_s{}^0 = \sum N_{2i} a_i = \mathbf{N}_2 \mathbf{a} \\ \phi_n{}^0 &= \sum N_{3i} a_i = \mathbf{N}_3 \mathbf{a} \quad , \quad M_n{}^0 = \sum N_{4i} a_i = \mathbf{N}_4 \mathbf{a} \\ M_{ns}{}^0 &= \sum N_{5i} a_i = \mathbf{N}_5 \mathbf{a} \quad , \quad Q_n{}^0 = \sum N_{6i} a_i = \mathbf{N}_6 \mathbf{a} \end{aligned} \tag{27}$$

where **a** is undetermined coefficients, $\mathbf{N_i}$ (i=1-6) is the complete sets of Trefftz functions. In the Galerkin method, the Trefftz functions are also used as the weighting functions such that [17, 18]:

$$\begin{aligned} w_1^* &= N_1 \quad , \quad w_2^* = N_{6j} \quad , \quad w_3^* = -N_{5j} \\ w_4^* &= -N_{4j} \quad , \quad w_5^* = N_{3j} \quad , \quad w_6^* = N_{2j} \quad , \quad w_7^* = -N_{1j} \end{aligned} \tag{28}$$

where functions N_{ij} (i=1-6, j=1,2,3,..) can be obtained by introducing the T-complete functions into equations (8)-(14). Substituting equations (27) and (28) into eqn. (20), we obtain the jth equation of the system of linear equations in the following discrete form:

$$\begin{aligned} &\int_{\Gamma_w} N_{6j}\left(N_{1i} - \overline{w}\right) \cdot d\Gamma - \int_{\Gamma_{\phi s}} N_{5j}\left(N_{2i} - \overline{\phi}_s\right) \cdot d\Gamma - \int_{\Gamma_{\phi n}} N_{4j}\left(N_{3i} - \overline{\phi}_n\right) \cdot d\Gamma \\ &+ \int_{\Gamma_{Mn}} N_{3j}\left(N_{4i} - \overline{M}_n\right) \cdot d\Gamma + \int_{\Gamma_{Mns}} N_{2j}\left(N_{5i} - \overline{M}_{ns}\right) \cdot d\Gamma - \int_{\Gamma_{Qn}} N_{1j}\left(N_{6i} - \overline{Q}_n\right) \cdot d\Gamma = 0 \end{aligned} \tag{29}$$

The domain integral term in eqn. (29) can be transformed into a boundary integral by using Green's second identity. The matrix equation for the solution of the problem is

$$\mathbf{Ka} = \mathbf{f} \tag{30}$$

where

$$\begin{aligned}\mathbf{K} = &\int_{\Gamma_w} N_{6j}N_{1i}\cdot d\Gamma - \int_{\Gamma_{\phi s}} N_{5j}N_{2i}\cdot d\Gamma - \int_{\Gamma_{\phi n}} N_{4j}N_{3i}\cdot d\Gamma + \int_{\Gamma_{Mn}} N_{3j}N_{4i}\cdot d\Gamma \\ &+ \int_{\Gamma_{Mns}} N_{2j}N_{5i}\cdot d\Gamma \quad - \int_{\Gamma_{Qn}} N_{1j}N_{6i}\cdot d\Gamma\end{aligned} \tag{31}$$

and

$$\begin{aligned}\mathbf{f} = &\int_{\Gamma_w} N_{6j}\overline{w}\cdot d\Gamma - \int_{\Gamma_{\phi s}} N_{5j}\overline{\phi}_s\cdot d\Gamma - \int_{\Gamma_{\phi n}} N_{4j}\overline{\phi}_n\cdot d\Gamma + \int_{\Gamma_{Mn}} N_{3j}\overline{M}_n\cdot d\Gamma \\ &+ \int_{\Gamma_{Mns}} N_{2j}\overline{M}_{ns}\cdot d\Gamma - \int_{\Gamma_{Qn}} N_{1j}\overline{Q}_n\cdot d\Gamma\end{aligned} \tag{32}$$

The resulting matrix K is full. The unknown generalized parameters ***a*** can be determined from eqn. (30) using Gaussian elimination method with row pivots. Substituting the determined coefficients a back into series (27), we can obtain any quantity that we need either inside the domain or on the boundary.

5 Numerical examples

Two simple examples are presented to illustrate the use of the indirect Trefftz method and the accuracy of the numerical results. The solutions have been obtained by using the Trefftz Galerkin Method (TGM). The boundary variables include constant, linear and quadratic interpolations. For simplicity, ν=0.3 and D=1 have been used in the following examples.

5.1 Example 1: clamped circular plate all round

In the present example, a clamped circular plate is considered and frequency parameters are obtained. Owing to the presence of a smooth boundary, continuous elements have been adopted. Values of frequency parameter ($\lambda^2 = \omega a^2\sqrt{\frac{\rho h}{D}}$) found using indirect Trefftz method are tabulated in Table 1, where n and s refer to the number of radial and circumferential nodes, respectively. Inspection of table 1 shows that, the frequency parameters obtained using this method is in good agreement. Table 1 shows the convergence of the

Table 1: Frequency parameter ($\lambda^2 = \omega a^2 \sqrt{\frac{\rho h}{D}}$) for clamped circular plate (ν=0.3).

	λ^2 for value of n												
n / s	0	1	2	3	4	5	6	7	8	9	10	11	12
0	**10.2208 (10.215)**	**21.2613 (21.26)**	**34.8808 (34.88)**	**51.0367 (51.04)**	**69.6724 (69.6659)**	**90.7446 (90.7390)**	**114.2333 (114.2126)**	**140.0672 (140.0561)**	**168.2468 (168.2445)**	**198.7818 (198.7561)**	**231.5875 (231.5732)**	**266.7015 (266.6790)**	**304.0838 (304.0601)**
1	**39.7782 (39.771)**	**60.8400 (60.82)**	**84.5848 (84.58)**	**111.0283 (111.01)**	**140.1145 (140.1079)**	**171.8196 (171.8029)**	**206.0947 (206.0706)**	**242.8922 (242.8782)**	**282.2064 (282.1977)**	**324.0360 (324.0036)**	**368.2944 (368.2734)**	**415.0183**	**464.1439**
2	**89.1136 (89.104)**	**199.0638 (120.08)**	**153.8344 (153.81)**	**190.3296 (190.30)**	**229.5225 (229.5186)**	**271.4585 (271.4283)**	**316.0217 (316.0015)**	**363.2454 (363.2097)**	**413.0649**	**465.4374**	**520.3873**	**577.9216**	**637.9160**
3	**158.2061 (158.183)**	**120.0996 (199.06)**	**242.7364 (242.71)**	**289.2040 (289.17)**	**338.4128 (338.4113)**	**390.4180 (390.3896)**	**445.1256**	**502.5218**	**562.5909**	**625.3000**	**690.6384**	**758.5617**	**829.0944**
4	**247.0241 (247.005)**	**297.7695 (297.77)**	**351.3375 (351.38)**	**407.7572 (407.72)**	**466.9488**	**528.9080**	**593.6532**	**661.1583**	**731.3238**	**804.2328**	**879.7749**	**957.9644**	**1038.8373**
5	**355.5864 (355.568)**	**416.2416 (416.20)**	**479.6976 (479.65)**	**546.0166 (545.97)**	**615.1392**	**687.0689**	**761.8152**	**839.3188**	**919.5449**	**1002.4822**	**1088.2081**	**1176.5586**	**1267.6448**
6	**483.9120 (483.872)**	**554.4141 (554.37)**	**627.7530 (627.75)**	**704.0001 (703.95)**	**783.0482**	**864.8892**	**949.5642**	**1037.033**	**1127.2806**	**1220.3144**	**1316.0932**	**1414.5121**	**1515.7006**
7	**631.9190 (631.914)**	**712.3027 (712.30)**	**795.5784 (795.52)**	**881.6742 (881.67)**	**970.6340**	**1062.4340**	**1157.0202**	**1254.5055**	**1354.6816**	**1457.7124**	**1563.4906**	**1671.9921**	**1783.2039**
8	**799.7018 (799.702)**	**890.0078 (889.95)**	**983.1360 (983.07)**	**1079.1225 (1079.0)**	**1177.9996**	**1279.7075**	**1384.2120**	**1491.5816**	**1601.7604**	**1714.7052**	**1830.4706**	**1949.0459**	**2070.2500**
9	**987.2792 (987.216)**	**1087.3506 (1087.4)**	**1190.3880 (1190.4)**	**1296.2880 (1296.2)**	**1405.0502**	**1516.6351**	**1631.1097**	**1748.4105**	**1868.4870**	**1991.3906**	**2117.1041**	**2245.6225**	**2376.9525**

(…) are taken from [19].

WIT Transactions on Modelling and Simulation, Vol 49, © 2009 WIT Press
www.witpress.com, ISSN 1743-355X (on-line)

WIT Transactions on Modelling and Simulation, Vol 49, © 2009 WIT Press
www.witpress.com, ISSN 1743-355X (on-line)

Table 2: Frequency parameter ($\lambda^2 = \omega a^2\sqrt{\frac{\rho h}{D}}$) for simply supported circular plate (ν=0.3).

	λ^2 for value of n												
n / s	0	1	2	3	4	5	6	7	8	9	10	11	12
0	**4.9372 (4.977)**	**13.9054 (13.94)**	**25.6137 (25.65)**	**39.9676 (39.95)**	**56.8516 (56.84)**	**76.2129 (76.20)**	**98.0100 (97.99)**	**122.1909 (122.17)**	**148.7424 (148.72)**	**177.6355 (177.61)**	**208.8314 (208.81)**	**242.3314**	**278.1223**
1	**29.7243 (29.76)**	**48.4833 (48.51)**	**70.1238 (70.14)**	**94.5561 (94.54)**	**121.7050 (121.70)**	**151.5361 (151.51)**	**183.9549 (183.94)**	**218.9512 (218.95)**	**256.5122 (256.49)**	**296.5628 (296.54)**	**339.1122**	**384.0816**	**431.5175**
2	**74.1665 (74.20)**	**102.7790 (102.80)**	**134.3049 (134.33)**	**168.6881 (168.67)**	**205.8651 (205.85)**	**245.7996 (245.77)**	**288.4222 (288.41)**	**333.7563 (333.72)**	**381.6943 (381.66)**	**432.2241**	**485.3649**	**541.0741**	**599.3193**
3	**138.3211 (138.34)**	**176.8102 (176.84)**	**218.2119 (218.24)**	**262.5048 (262.48)**	**309.6192 (309.60)**	**359.5574 (359.53)**	**412.2524 (412.22)**	**467.6838 (467.64)**	**525.7849**	**586.6084**	**650.0460**	**716.1511**	**784.8402**
4	**222.2186 (222.21)**	**270.5696 (270.56)**	**321.8436 (321.84)**	**376.0496 (376.01)**	**433.0561 (433.04)**	**492.9288 (492.91)**	**555.6391 (555.59)**	**621.0562**	**689.2725**	**760.1600**	**833.8233**	**910.1082**	**989.0396**
5	**325.8747 (325.84)**	**384.0816 (384.06)**	**445.2522 (445.21)**	**509.2694 (509.26)**	**576.2400**	**646.0238**	**718.6152**	**794.0560**	**872.2571**	**953.2038**	**1036.9044**	**1123.3222**	**1212.4324**
6	**449.2280 (449.22)**	**517.3350 (517.3)**	**588.3535**	**662.2902**	**739.1329**	**818.8182**	**901.3204**	**986.7137**	**1074.9217**	**1165.8810**	**1259.5401**	**1356.0069**	**1717.5222**
7	**592.3382**	**670.2921**	**751.1984**	**835.0366**	**921.7296**	**1011.3036**	**1103.7677**	**1199.0291**	**1297.1522**	**1398.0868**	**1501.7950**	**1608.3308**	**1455.2699**
8	**755.2053**	**843.0312**	**933.7913**	**1027.4589**	**1124.0597**	**1223.5304**	**1325.9065**	**1431.1089**	**1539.1498**	**1649.9844**	**1763.6640**	**1880.1763**	**1999.4312**
9	**937.8293**	**1035.4880**	**1136.1618**	**1239.6736**	**1346.1561**	**1455.4988**	**1567.7640**	**1682.8865**	**1800.8140**	**1921.5948**	**2045.2101**	**2171.6532**	**2300.8330**

(…) are taken from [19].

natural frequencies with the number of out-of-plane shape functions. The values are compared with the ones published by Leissa [19]. For the fundamental frequency, this method gives acceptable results with a maximum discrepancy of 0.03% clamped boundary conditions.

5.2 Example 2: simply supported circular plate all round

A simply supported circular plate with uniform thicknesses is taken as an example. The corresponding discretisation and the number of elements can be similarly adopted as example 1. Values of frequency parameter found using indirect Trefftz method are tabulated in table 2. For the fundamental frequency, this method gives acceptable results with a maximum discrepancy of 0.01% simply supported boundary conditions. It can be seen that, by comparison with the Leissa's results [19], the present method is able to give satisfactory results.

6 Conclusions

The purpose of the present paper is free vibration analysis of thin circular plates by indirect Trefftz method. In thin plate vibration problems, we will deal with the governing equation with the homogeneous boundary conditions. The Trefftz methods can be classified into the indirect and direct formulations. Most of the researchers have been studying the indirect formulations. In this article, indirect formulation has been applied to thin plate vibration problems. The main conclusions of this paper can be summarized as follows:

1. The indirect Trefftz formulation is very similar to the direct boundary element formulation.
2. The computational accuracy of the indirect Trefftz method is strongly dependent on the condition numbers of the coefficient matrices.
3. Although the examples are relatively simple, we may say that numerical solutions prove that the present method is not only effective but also provides accurate numerical results.

References

[1] Trefftz, E., Ein gegenstuck zum ritzschen verfharen, In Proc. 2nd Int. Cong. Appl. Mech., pp. 131-137, 1926.
[2] Weeeën, F. V., Application of the boundary integral equation method to Reissner's plate model, Int. J. Numer. Meth. Engng., 18, pp. 1-10, 1982.
[3] Weeeën, F. V., Application of the direct boundary element method to Reissner's plate model, in Boundary Element Method in Engineering, C. A. Brebbia (ed.), Springer, Berlin, pp. 487-499, 1982.
[4] Lei, X. Y. & Hung, M. K., Mixed method of BIEM & FEM to solve free vibration of Reissner's plate, in Boundary Elements, Q. H. Du (ed.), Pergamon Press, Oxford, 1986.
[5] Jirousek, J. & Wroblewski, A., T-elements: State of the art and future trends. Archives of Comp. Meth. in Engng, 3(4), pp. 323-434, 1996.

[6] Cheung, YK., Jin, WG. & Zienkiewicz, OC., Direct solution procedure for solution of harmonic problems using complete, non-singular, Trefftz functions. Com. Appl. Num. Meth., 5, pp. 159-169, 1989.
[7] Jin, W.G., Cheung, YK. & Zienkiewicz, OC., Trefftz method for Kirchhoff plate bending problems. Int. J. Num. Meth. Eng., 36, pp. 765-781, 1993.
[8] Zielinski, AP. & Zienkiewicz, OC., Generalized finite element analysis with t-complete boundary solution functions. Int. J. Num. Meth. Eng., 21, pp. 509-528, 1985.
[9] Zielinski, AP. & Herrera, I., Trefftz method: fitting boundary conditions. Int. J. Num. Meth. Eng., 24, pp. 871-891, 1987.
[10] Freitas, J. & Ji, Z., Hybrid-Trefftz finite element formulation for simulation of singular stress fields. Int. J. Num. Meth. Eng., 39, pp. 281-308, 1996.
[11] Zielinski, AP., On trial functions applied in the generalized Trefftz method. Advances in Engineering Software, 24, pp. 147-155, 1995.
[12] Kita, E. & Kamiya, N., Trefftz method: an overview. Advances in Engineering Software, 24, pp. 3-12, 1995.
[13] Reismann, H., Elastic Plates: theory and Application, Wiley, New York, 1988.
[14] Finlayson, B.A., the Method of weighted Residuals and variational Principles, Academic Press, New York, 1972.
[15] Reddy, J.N., Energy Principles and Variational Methods in Applied Mechanics, McGraw-Hill, 2001.
[16] Banerjee, P.K., The boundary element Methods in Engineering, 2nd ed, McGraw-Hill, 1981.
[17] Hochard, Ch. & Proslier, L., A simplified analysis of plate structures using Trefftz-functions, Int. J. Numer. Meth. Engng, 34, pp. 179-195, 1992.
[18] Portela, A. & Charafi, A., Trefftz boundary element-multi region formulation, Int. J. Numer. Meth. Engng., 45, pp. 821-840, 1999.
[19] Leissa, A.W., Vibration of Plates, NASA SP.160, Washington, 1969.

Section 7
Fluid flow

This page intentionally left blank

Meshless, BE, FE and FD methods analysis of the flow and concentration in a water reservoir

K. Sakamoto[1], M. Kanoh[2] & T. Kuroki[3]
[1]*Environment Division, Matsue Doken Co., Ltd., Japan*
[2]*Department of Civil Engineering, Kyushu Sangyo University, Japan*
[3]*Baikoen, Japan*

Abstract

In an earlier study, three methods, the meshless, the boundary element (BEM), and the weighted finite difference (WFDM) were developed to obtain numerically stable and convergent results for the concentration distribution and flow around a DO-supplying machine in a water reservoir. The poor-oxygen layer, which is short of or lacks dissolved oxygen (DO), sometimes causes pollution in the water in a reservoir. An attempt was made to ameliorate the concentration of oxygen in the lower layer of the reservoir by using a machine that supplies DO. Field studies in a few water reservoirs led to reports of a phenomenon in which the distance reached by the DO-rich water was more than 300 metres in spite of the very low velocity of the water flow. To numerically represent the phenomenon described above, we would like to investigate the numerical solutions of the meshless method, the BEM, the finite element method (FEM), and the finite difference method (FDM) and compare them with the observed results. With reference to the velocity vectors of the water flow calculated by the FDM, the BEM, and the FEM and observed in our model simulation described above, the effect and accuracy of the alternative meshless method were estimated.

Keywords: meshless method, boundary element method, finite element method, finite difference method, and flow and concentration in water reservoirs.

1 Introduction

By using a machine that supplies DO (dissolved oxygen), we successfully ameliorated the concentration of oxygen in the lower layer of water areas, such

WIT Transactions on Modelling and Simulation, Vol 49, © 2009 WIT Press
www.witpress.com, ISSN 1743-355X (on-line)
doi:10.2495/BE090291

as a water reservoir or the sea (Sakamoto et al. [1]). Our DO-supplying machine dissolved the high concentration of oxygen (about 100 mg per litre: [mg/L]) in the water of the tank of the machine at a depth of about 50 metres. The DO-rich water flowed out to the lower layer of the water area in a horizontal direction. The observed velocity of the water flow was considerably small (almost 0.1 m/sec [metre per second]); however, the distance reached by the DO-rich water was observed to be more than 300 metres in the B reservoir. To obtain evidence to explain the phenomena, the model simulation of a water reservoir was investigated and newly reconstructed in our laboratory so that the observed results of the model simulation could represent the phenomena described above; in this way, we obtained some observed velocity vectors and the distributions of the DO concentration in the model. The analogy between the differences of the water temperature and the DO concentration was adopted and expected to reproduce the horizontal direction of the water flow and the convective diffusion of the DO of the water reservoir into our model simulation. The meshless method, the BEM, the FEM, the FDM, and the WFDM were newly investigated and applied to numerically simulate the phenomena. They were then compared with the observed data obtained in the model simulation.

2 Governing equations

Three equations, i.e., continuous, Navier-Stokes (N-S), and convective -diffusion equations, govern the flow and diffusion in a water reservoir. In the vertical (x_1, x_2) plane, as illustrated in fig. 1, these equations are shown as follows:

$$u_{1,1} + u_{2,2} = 0 \tag{1}$$

$$\dot{u}_1 + u_1 \cdot u_{1,1} + u_2 \cdot u_{1,2} - \nu(u_{1,11} + u_{1,22}) = -P_{,1}/\rho \tag{2_1}$$

$$\dot{u}_2 + u_1 \cdot u_{2,1} + u_2 \cdot u_{2,2} - \nu(u_{2,11} + u_{2,22}) = -P_{,2}/\rho + g \tag{2_2}$$

$$\dot{C} + u_1 \cdot C_{,1} + u_2' \cdot C_{,2} - D_1 \cdot C_{,11} - D_2 \cdot C_{,22} = 0 \tag{3}$$

$$\rho = \rho_0 + C \rfloor 10^{-6}(1 - \rho_{DO}/\rho_0) \tag{4}$$

where u_1 and u_2 describe the velocities of the x_1 and x_2 directions, respectively, P is the pressure, g is the gravity acceleration, ν is the kinematic viscosity, C is the concentration of dissolved oxygen (DO), and D_1 and D_2 are the diffusion coefficients of the x_1 and x_2 directions, respectively. Here, $C_{,1}$ and $C_{,2}$ describe the derivatives of C differentiated with respect to x_1 and x_2, respectively, $C_{,11}$ and $C_{,22}$ are the derivatives of C differentiated twice with respect to x_1 and x_2, respectively. The density ρ is connected to the DO concentration C, as written in Equation (4), where ρ_0 and ρ_{DO} describe the densities of the pure water and the dissolved oxygen, respectively. The velocity u_2', which is shown in the above Equation (3), is defined as written in Equation (5):

$$u_2' = u_2 + (1 - \rho_{DO}/\rho_0)\rho g t = u_2 + \alpha g t \qquad (5_1)$$

$$_{t+\Delta t}u_2' = {}_t u_2 + \alpha g \Delta t \quad \text{in the finite difference expression} \qquad (5_2)$$

where $_{t+\Delta t}u_2'$ and $_t u_2$ are the velocities at time (t+Δt) and time (t) in the vertical direction, respectively. The second term ($\alpha g \Delta t$) of the right-hand side of Equation (5) means that the DO concentration increases the velocity of the vertical direction, and α describes the density of the liquid that dissolves DO. Here, the velocity increase is caused by the liquid density ρ, the gravity acceleration g, and the time increment Δt. We expect that the velocity increase in the convective diffusion can be a device or evidence to explain the phenomenon in which the distance reached by the DO-rich water was more than 300 metres in spite of the very low velocity of the water flow.

3 Application of the meshless method

We applied the meshless method to a flow analysis in the steady state and a concentration analysis in the unsteady state in a water reservoir, as shown in fig. 1. The penalty method was used so that the pressure terms would be eliminated in the N-S equations and the difficulty of the pressure boundary conditions would be avoided in the meshless method (Sakamoto et al. [1]).

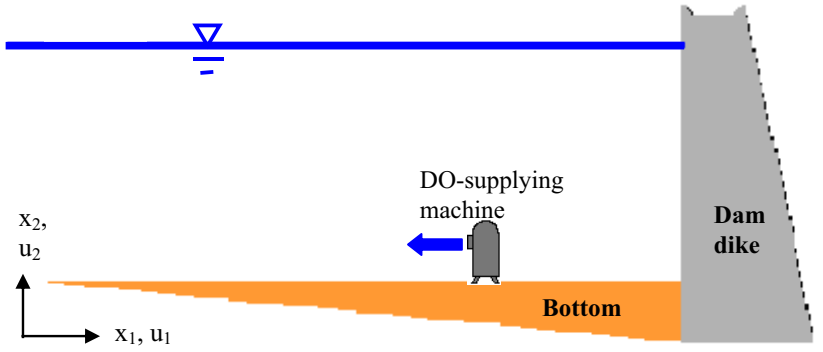

Figure 1: Analytical domain and concept of a DO-supplying machine in a water reservoir.

3.1 Meshless method for flow and concentration analyses

3.1.1 Simultaneous equations for the meshless method of flow analysis

Using $\underline{u}_1$ and $\underline{u}_2$ at time (t-Δt) and adopting the penalty method, the following expression is obtained (Kanoh et al. [2]):

$$\underline{u}_1 \cdot u_{1,1} + \underline{u}_2 \cdot u_{1,2} - \lambda(u_{1,11} + u_{2,12}) - \nu(u_{1,22} + u_{2,12} + 2u_{1,11}) = 0 \qquad (6_1)$$

$$\underline{u}_1 \cdot u_{2,1} + \underline{u}_2 \cdot u_{2,2} - \lambda(u_{1,12} + u_{2,22}) - \nu(u_{2,11} + u_{1,12} + 2u_{2,22}) = 0 \qquad (6_2)$$

where $u_{2,12}$ is the derivative of $u_{2,1}$ differentiated with respect to x_2. The unknown values u_1 and u_2 are expressed as Equation (7) using the global expansion function Xj (= $(r^2+c^2)^{-1/2}$) of the mesh-free RBF collocation method (Divo et al. [3]),

$$\underline{u}_1 \cdot u_{2,1} + \underline{u}_2 \cdot u_{2,2} - \lambda(u_{1,12} + u_{2,22}) - \nu(u_{2,11} + u_{1,12} + 2u_{2,22}) = 0 \qquad (7_1), (7_2)$$

where r equals $\{(x-x_j)+(y-y_j)\}^{1/2}$ and c is the constant. Solving the simultaneous Equation (8), the unknowns (α_j and β_j) can be obtained.

$$\left\{\left(\underline{u}_1 \frac{\partial X_j}{\partial x_1} + \underline{u}_2 \frac{\partial X_j}{\partial x_2}\right) - (\nu+\lambda)\frac{\partial^2 X_j}{\partial {x_1}^2} - \nu\left(\frac{\partial^2 X_j}{\partial {x_1}^2} + \frac{\partial^2 X_j}{\partial {x_2}^2}\right)\right\}\alpha_j - (\nu+\lambda)\frac{\partial^2 X_j}{\partial x_1 \partial x_2}\beta_j = 0 \quad \ldots.(8_1)$$

$$-(\nu+\lambda)\frac{\partial^2 X_j}{\partial x_1 \partial x_2}\alpha_j + \left\{\left(\underline{u}_1 \frac{\partial X_j}{\partial x_1} + \underline{u}_2 \frac{\partial X_j}{\partial x_2}\right) - (\nu+\lambda)\frac{\partial^2 X_j}{\partial {x_2}^2} - \nu\left(\frac{\partial^2 X_j}{\partial {x_1}^2} + \frac{\partial^2 X_j}{\partial {x_2}^2}\right)\right\}\beta_j = 0 \quad \ldots.(8_2)$$

Substituting the obtained values of α_j and β_j into Equation (7), the values of u_1 and u_2 in the steady state can be calculated using the meshless method.

3.1.2 Meshless method formulation for concentration analysis

Here, we deal with the concentration analysis in the unsteady state in the area surrounding the DO-supplying machine. First, the concentration in the steady state is expressed as Equation (9) with Equation (10) (Kanoh et al. [2]).

$$C = \gamma_j Xj = \beta_j/(r^2+c^2)^{1/2} \qquad (9)$$

$$\left\{\left(\underline{u}_1 \frac{\partial X_j}{\partial x_1} + \underline{u}_2 \frac{\partial X_j}{\partial x_2}\right) - \left(D_1 \frac{\partial^2 X_j}{\partial {x_1}^2} + D_2 \frac{\partial^2 X_j}{\partial {x_2}^2}\right)\right\}\gamma_j = 0 \qquad (10)$$

Secondly, the transient convective-diffusion equation is rewritten as follows:

$$C_{,t} + L(C) = 0 \qquad (11)$$

where $C_{,t}$ is the time derivative of C and L(C) has the terms of convection and diffusion in the steady state. Thirdly, applying the finite difference scheme, Equation (11) yields

$$(C^{t+\Delta t} - C^t)/\Delta t + \{L^{t+\Delta t}(C) + L^t(C)\}/2 = 0 \qquad (12)$$

$$C^{t+\Delta t} + L^{t+\Delta t}(C)\cdot\Delta t/2 = C^t - L^t(C)\cdot\Delta t/2 \qquad (13)$$

where $C^{t+\Delta t}$ and C^t are the concentrations at time (t+Δt) and time (t), respectively, and $L^{t+\Delta t}$ and L^t are the terms of convection and diffusion at time (t+Δt) and time(t), respectively. Finally, using Equations (9), (10), and (13), the meshless method can analyse the DO concentration in the unsteady state.

3.2 Boundary conditions and boundary discretisation

Both the boundary conditions and the boundary discretisation for the flow and concentration analyses have been previously proposed for the meshless method, the BEM, the FEM, the FDM, and the WFDM (Sakamoto et al. [1], Kanoh et al. [2]).

4 Reconstructed model simulation

We reconstructed a simulation model in our laboratory and obtained some observed velocity vectors and the distributions of the DO concentration in the model. In reference to the observed results, we tried to obtain some evidence to explain the phenomena that the distance reached by the DO-rich water was more than 300 metres in a reservoir in spite of the small velocity of the water flowing out. For this purpose, it was necessary to reproduce, in our model simulation, the density flow and convective diffusion of the DO concentration in the lower layer of a water reservoir at a depth of about 50 metres.

4.1 Objective of the reconstruction and simulation technique

There were two objectives in our reconstructed model and simulation technique. First, an outlet was set on the lower part of the left side wall of the model so that we could reproduce the horizontal direction of water flow of the lower layer of the water reservoir. Secondly, the density difference between 10 mg/L and 100 mg/L in the DO concentration was changed to the density difference of the water temperature, since it was very difficult to make up the high concentration of DO of 100 mg/L in our model simulation at a depth of about 0.8 metres. Referring to Table 1, the density difference between 10 mg/L and 100 mg/L in DO was equal to the difference of the water temperature between 15 degrees centigrade (15.00°C) and 14.55 degrees centigrade (14.55°C). We iced the water that flowed out of the tank of the model and could easily control the difference of the water temperature between 15.00°C and 14.55°C. The analogy between the

Table 1: Density difference between 100 mg/L and 30 mg/L in DO and that of the water temperature among 15.00, 14.87, and 14.55 (°C).

Place / Value	B water reservoir (waterdepth:50m)	Our model simulation (water depth:0.8m)
Maximum DO value (mg/L)	100	30
Water head (Kg/cm^2)	5.0	0.08
Value of ρ (using Equation (4): at 15°C)	0.999127+0.0001	0.999127+0.00003
Water temperature that corresponds to the above value of ρ (°C)	14.55 (=15.0-0.45)	14.87 (=15.0-0.13)

differences of the water temperature and the DO concentration was adopted and expected to reproduce the horizontal direction of water flow and the convective diffusion of the DO of the water reservoir into our model simulation.

Here, 5 Kg/cm^2 (kilogram per square centimetre) corresponds to 0.5 MPa (megapascal) in the international system of units (SI).

5 Results and discussion

As described above, we reconstructed a new simulation model in our laboratory and were able to observe some velocity vectors and obtain the distributions of the DO concentration in the model. In reference to the observed results, we tried to obtain some evidence to explain the phenomena that the distance reached by the DO-rich water was more than 300 metres in a reservoir in spite of the small velocity of the water flowing out. The numerical results of the meshless method, the BEM, the FEM, and the WFDM are also discussed in this section in order to obtain some evidence to explain the phenomena.

5.1 Observed values in a model around a DO-supplying machine

5.1.1 Flow velocity in a model

Fig. 2 is an illustration of the velocity vectors caused by a DO-supplying machine in a reservoir model visualised using aluminium flakes, a strobe light, and a digital VTR. In the area neighbouring the outflow point, the velocity vectors in the horizontal direction were distinguished, and the values of the velocities were larger than those in other areas. In other areas, which were toward the centre or more than 0.9 metres from the outflow point, the velocity values became less than 1cm/sec.

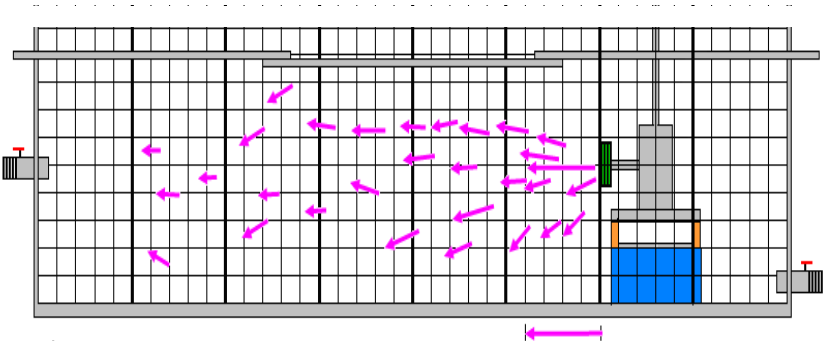

Figure 2: Observed velocity vectors around a DO-supplying machine (DO: 30mg/L).

5.1.2 Concentration distribution of DO in a model

Fig. 3 is an illustration of the concentration distribution caused by a DO-supplying machine in a reservoir model visualised using a pigment (methylene

blue) and a VTR. The speed of diffusion of the DO-rich water (DO: 100mg/L) was obviously quicker than that in DO-poor water (DO: 10mg/L; the figure was omitted in this paper), and the observed direction of the diffusion was mainly down or horizontal.

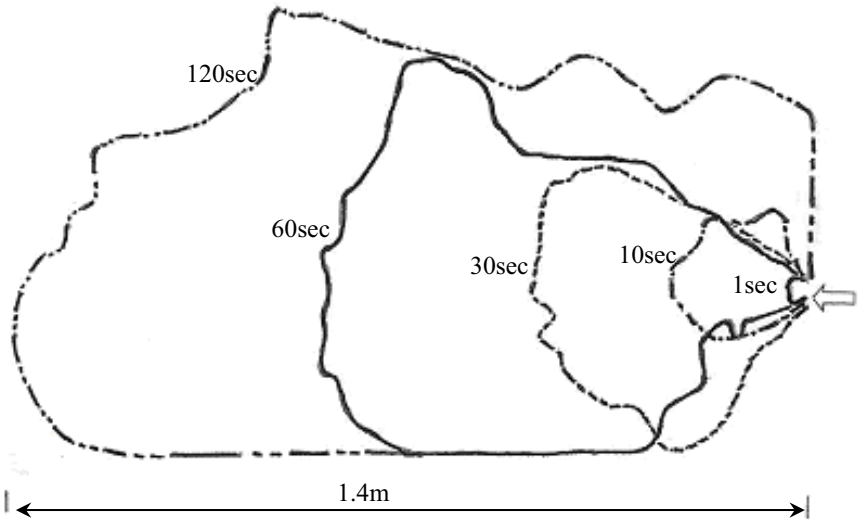

Figure 3: Observed areas of diffusion of pigment (DO: 100mg/L).

5.2 Flow analysis in the model of a water reservoir

5.2.1 Meshless method calculation of the flow in the model

Fig. 4 is an illustration of the velocity vectors in the model of a water reservoir calculated by the meshless method, in which the number of the points in the meshless method is 3,201 and the three values of λ, C, and ν are 1,000.0, 1.0, and 0.001, respectively. The stability and convergence of the flow analysis around the machine to supply DO using the meshless method seemed satisfactory.

5.2.2 FEM, BEM, and FDM calculation of the flow in the reservoir model

Fig. 5 is an illustration of the velocity vectors in the reservoir model calculated by the FEM, in which the number of elements in the FEM is 3,072 and the two values of λ and ν are 1,000.0 and 0.001, respectively. The penalty method was introduced, as in the meshless method. The stability and convergence of the flow analysis using the FEM seemed satisfactory. The stability and convergence of the flow analysis using both the BEM and the FDM also seemed satisfactory (the figures to illustrate those velocity vectors have been omitted). These three methods could yield qualitatively similar solutions to the true results of several flow problems that were observed in simulation models constructed in our laboratory.

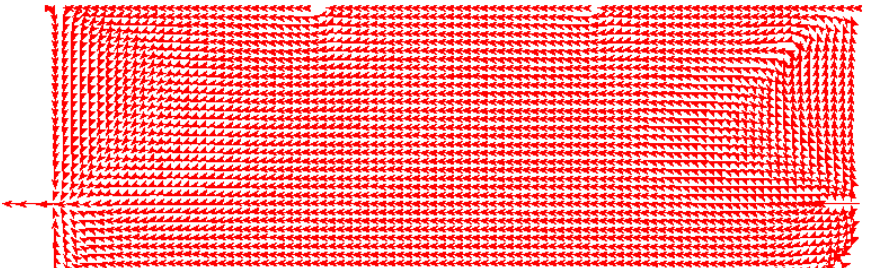

Figure 4: Velocity vectors using the meshless method (number of the points: 3,201).

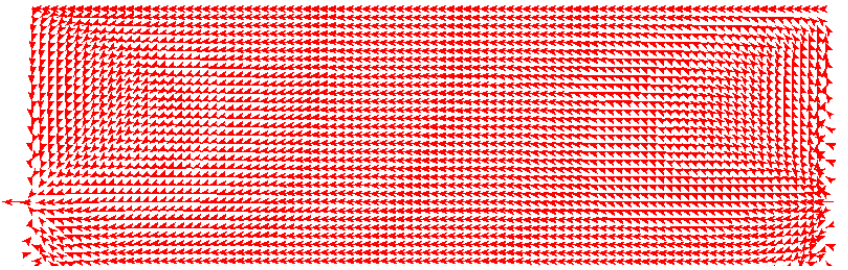

Figure 5: Velocity vectors using the FEM (number of the points: 3,201).

5.3 DO concentration analysis in the model of a water reservoir

5.3.1 Time required by the four numerical methods for the DO analysis

Table 2 shows the time required by the four numerical methods for analysing the DO concentration in the model. When the number of the divisions of the analytical domain was 3,201, the FDM, the BEM, and the meshless method needed almost 7, 10, and 6 times the time required for the FEM, respectively. For the purposes of saving time, the FEM was the best; the meshless method was second best; the FDM was the third best; and the BEM was the poorest performer. On the other hand, for the purpose of saving the time and labour required for preparing the input data, the meshless method was the best, the FDM was second best, the FEM was the third best, and the BEM was the worst.

5.3.2 FEM calculation of the concentration distribution

Figs. 6(a) and (b) are illustrations of the concentration distribution calculated using the FE method, in which the number of divisions in the FEM is 3,201 and the two values of λ and ν are 1,000.0 and 0.001, respectively. Comparing fig. 6(a) (not adopting the term: $\alpha g \Delta t$) with fig. 6(b) (adopting the term: $\alpha g \Delta t$), it was noted that the term ($\alpha g \Delta t$) of the velocity increase brought the areas of the DO distribution down in the FEM analysis.

Table 2: The time required by the four methods for analysing the unsteady convective diffusion of DO for 60 seconds in a model of a water reservoir.

Relative computational time / Numerical method	Number of divisions: 3,201	Time increment: Δt (sec)
FEM	1.00	0.1
FDM	7.00	1.0
BEM	10.1	1.0
Meshless method	6.03	20

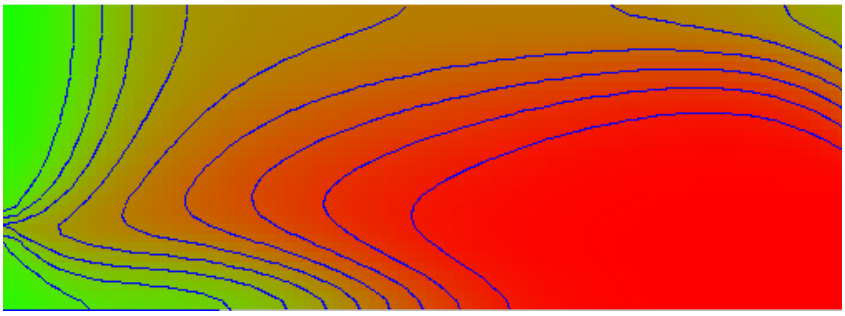

(a)

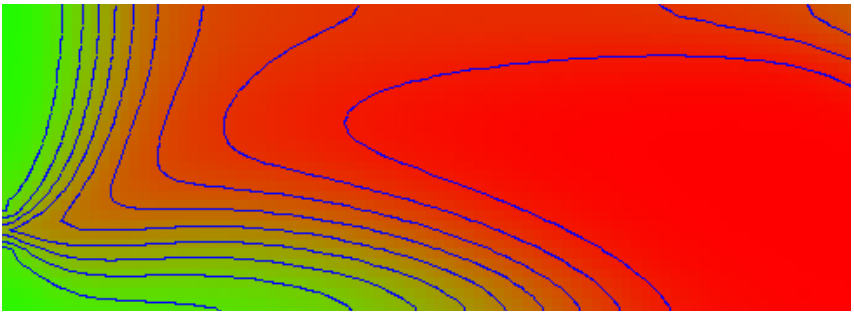

(b)

Figure 6: (a) DO-concentration distribution calculated using the FEM without the term ($\alpha g \Delta t$) [t=420sec]. (b) DO-concentration distribution calculated using the FEM with the term ($\alpha g \Delta t$) [t=420sec].

5.3.3 Meshless calculation of the concentration distribution

Fig. 7 is an illustration of the concentration distribution calculated using the meshless method, in which the term of the velocity increase ($\alpha g \Delta t$) is adopted,

the number of divisions in the meshless method is 3,201, and the value of ν is 0.001 (the figures to illustrate the concentration distribution calculated without the term ($\alpha g \Delta t$) have been omitted). Referring to figs. 6 and 7, the solutions of the meshless method showed the same tendency as those of the FEM in this problem. We considered that the convergence and accuracy of the FE, the FD, the BE, and the meshless methods for this problem were satisfactory (the figures to illustrate the concentration distribution calculated using the FD and the BE methods have been omitted).

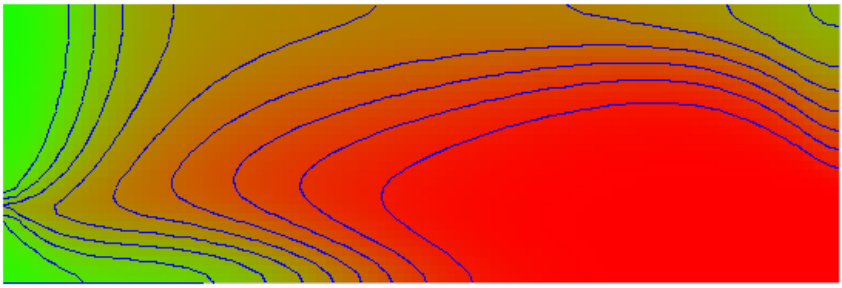

Figure 7: DO-concentration distribution using the meshless method with the term ($\alpha g \Delta t$) [t=420sec].

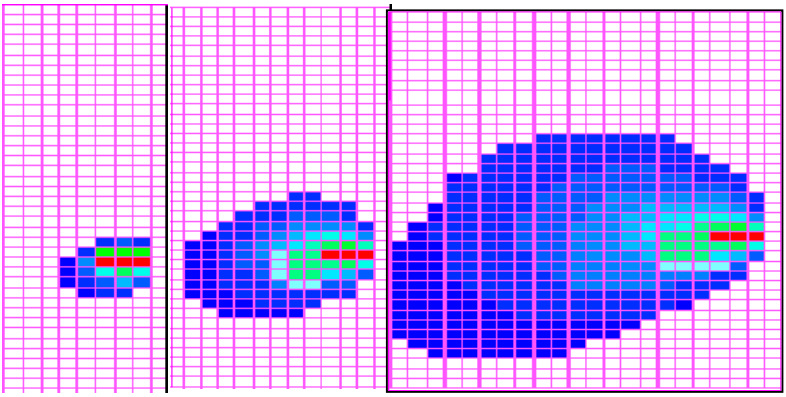

t = 1sec t = 10sec t = 60sec

Figure 8: DO-concentration distribution using the WFDM with the term ($\alpha g \Delta t$).

5.3.4 WFDM calculation of the concentration distribution

Fig. 8 is an illustration of the concentration distribution calculated using the WFDM, in which the term of the velocity increase ($\alpha g \Delta t$) is adopted, the number

of divisions in the WFDM is 25,600, and the value of ν is 0.001 (the figures to illustrate the concentration distribution calculated without the term ($\alpha g \Delta t$) have been omitted). We considered that the convergence and accuracy of the WFDM for this problem were satisfactory. It seemed that the term ($\alpha g \Delta t$) of the velocity increase could make the areas of the diffusion wider in the vertical and flowing-out directions and the speed of the convective diffusion higher than in the analyses of the WFDM when this velocity increase was not applied.

6 Conclusion

In summary, (1) the meshless method, the BEM, the FEM, the FDM, and the WFDM were newly investigated and applied to the analysis of the flow and convective diffusion in a water reservoir; (2) the stability and convergence of the five kinds of analysis using these methods described above seemed satisfactory; (3) in this paper, it was proposed that the DO concentration increased the velocity of the vertical direction, where the velocity increase was caused by the water density ρ, the gravity acceleration g, and the time increment Δt; (4) the velocity increase could make the areas of the diffusion wider in the vertical and outflow directions and make the speed of the convective diffusion be higher than in the analyses of these methods when this velocity increase was not applied; (5) the analogy between the differences of the water temperature and the DO concentration was adopted and expected to reproduce the horizontal direction of the water flow and the convective diffusion of the DO of the water reservoir into our model simulation; (6) it seemed that the wide areas of diffusion and quick speed of convective diffusion could explain the phenomena in which the distance reached by the DO-rich water was more than 300 metres in spite of the very low velocity of the water flow.

References

[1] Sakamoto, K., Kanoh, M., &. Kuroki T., Meshless and BE analysis of flow and concentration around a DO-supplying machine, *Proc. of the 30th World Conf. on Boundary Elements and Other Mesh Reduction Methods*, ed. C.A. Brebbia, WIT PRESS, Maribor, Slovenia, pp. 23-32, 2008.

[2] Kanoh, M., Nakamura, N., Kuroki T., & Sakamoto, K., Meshless analysis of flow and concentration in a water reservoir, *Proc. of the 29th World Conf. on Boundary Elements and Other Mesh Reduction Methods*, ed. C.A. Brebbia, WIT PRESS, Southampton, UK, pp. 169-178, 2007.

[3] Divo E., Kassab A., and Zahab El., Parallel domain decomposition meshless modeling of dilute convection-diffusion of species, *Proc. of 27th World Conf. on Boundary Elements and Other Mesh Reduction Methods*, ed. C.A. Brebbia, WIT PRESS, Florida, USA, pp.79-89, 2005.

This page intentionally left blank

Natural convection around a 3D hotstrip simulated by BEM

J. Ravnik & L. Škerget
University of Maribor, Faculty of Mechanical Engineering, Slovenia

Abstract

A 3D viscous flow solver was developed using a single domain and subdomain boundary element method. The solver was accelerated using wavelet compression and the fast multipole method.

In this paper we present results of a natural convection simulation around a hotstrip. The hotstrip is located in a cavity filled with air, its height is one half of the cavities height. The flow generated by the hotstrip source is analysed in terms of flow structures and heat transfer. The position of the hotstrip is varied, its influence of the flow and heat transfer is also analysed. The problem was simulated for air ($Pr = 0.71$) and for Rayleigh number values up to $Ra = 3.15 \cdot 10^5$. The results were compared with PIV measurements done by Corvaro and Paroncini.

The results show, that the hotstrip generates two large cylindrical vortical structures, one on each side as well as two small vortices on top of the hotstrip. The size of the vortices is related to the position of the hotstrip within the cavity. Heat transfer analyses show that the heat flux is largest on the sides of the hotstrip, while through the top heat losses are small.
Keywords: boundary element method, adaptive cross approximation, wavelet transform, hotstrip.

1 Introduction

Usage of the Boundary Element Method for simulation of fluid flow and heat transfer problems is, due to the nonlinearity and non-homogeneity of the governing equations, very challenging. Recently, we developed a 3D BEM based numerical method capable of simulation laminar viscous flow and heat transfer using a combination of single-domain BEM, subdomain BEM, wavelet transform and fast multipole method (Ravnik et al. [2–5]). The method solves the velocity vorticity

WIT Transactions on Modelling and Simulation, Vol 49,
www.witpress.com, ISSN 1743-355X (on-line)
doi:10.2495/BE090301

formulation of Navier-Stokes equations and was validated using benchmark problems such as 3D channel flow, lid driven cavity flow and natural convection in a cavity.

The governing equations of the velocity vorticity formulation of Navier-Stokes equations are the kinematics equation, the vorticity transport equation and the energy transport equation. The unknown fields are the velocity field, the vorticity field and the temperature field. The boundary conditions for the velocity and temperature fields are prescribed by the user and can be of Dirichlet or Neumann type. The developed algorithm calculates boundary values of vorticity using fast multipole accelerated single domain BEM on the kinematics equation. These values serve as Dirichlet type boundary conditions for the vorticity transport equation. The transport equations are solved by sub-domain BEM. The equations are solved repeatedly in a under-relaxed nonlinear loop until convergence is achieved.

In this paper, we present results of a simulation of natural convection. Study of natural convection phenomena is important because it is used in many engineering applications, such as cooling of electronic circuits and conditioning of air. Furthermore, natural convection does not depend on any electronic or mechanical equipment and is thus very cheap. For these reasons, natural convection a subject of constant investigation by both numerical and experimental techniques (Oztop and Bilgen [6], Aydin and Yang [7]).

The source of natural convection, simulated in this paper, is a hotstrip located in a cavity filled with air. Its height is one half of the cavities height. The flow generated by the hotstrip source is analysed in terms of flow structures and heat transfer. Influence of the position of the hotstrip on flow and heat transfer is also analysed. The problem was simulated for air ($Pr = 0.71$) and for Rayleigh number values up to $Ra = 3.15 \cdot 10^5$. The results were compared with PIV measurements done by Corvaro and Paroncini [1, 8].

2 Problem description

In this work we will consider air as the working fluid, for which density ρ_0, viscosity ν_0 and diffusivity α_0 will be considered constant. The Prandtl number will be set to $Pr = \nu_0/\alpha_0 = 0.71$. We chose the characteristic length scale to be the width of the enclosure H. The Rayleigh Ra number, which is the only parameter in the non-dimensional governing equations, is defined as:

$$Ra = Pr\frac{g_0\beta_T H^3 \Delta T}{\nu_0^2}, \tag{1}$$

where T is temperature, ΔT is the temperature difference between the hot and cold walls, $g_0 = 9.81 m/s^2$, and β_T is the thermal volume expansion coefficient. The gravity force works in the negative z direction. The cavity, hotstrip and the boundary conditions are shown in Figure 1.

Corvaro and Paroncini [1] preformed a 2D PIV experiment on a hotstrip problem. The width and height of their enclosure were $H = 0.05$ m. The depth of the

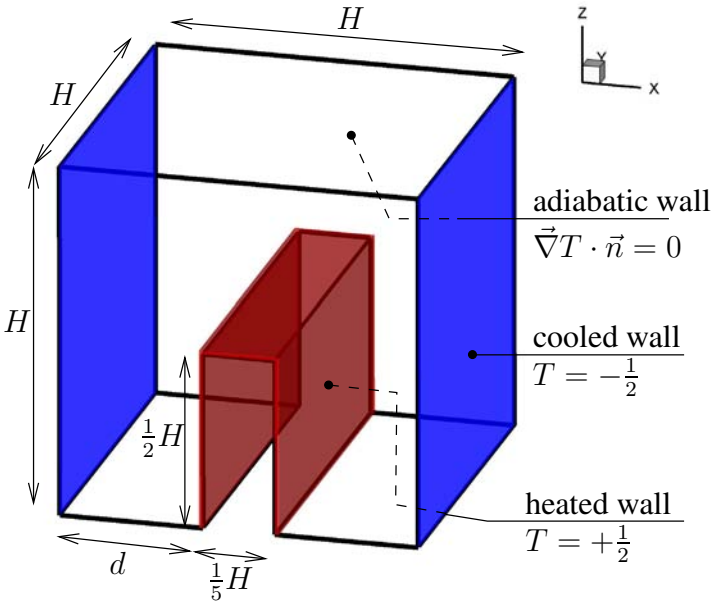

Figure 1: Geometry of the hotstrip problem and boundary conditions. Two distances of the hotstrip from the left ($x = 0$) wall were considered; $d = 0.4H$ (central position) and $d = 0.5H$ and $d = 0.6H$. The width of the hotstrip is $0.2H$ in all cases. The hotstrip is heated to $T = +0.5$, while the walls as $x = 0$ and $x = H$ are cooled to $T = -0.5$. All other walls are adiabatic, i.e. there is no temperature flux through them.

enclosure was 0.42 m, with which they achieved a 2D flow field. They measured the flow field in the central plane of the enclosure for Rayleigh number values between $Ra = 6.39 \times 10^4$ and $Ra = 3.16 \times 10^5$. We chose the minimum and maximum Ra of their experiments to compare their measurements to our simulations.

3 Simulation results

Since the experiment was done with a 2D technique measuring the flow field in the central plane of the cavity, we decided to examine the difference between the 2D and 3D cases. Thus simulations in 2D were preformed too. The 3D code was used to make 2D simulations by setting the appropriate boundary conditions and making the mesh only one element deep.

The mesh used in the 3D simulation had $20 \times 16 \times 6$ quadratic 27-node elements with 16133 nodes, which resulted in a nonlinear system of equations with 273539 degrees of freedom. The $2D$ mesh had $30 \times 30 \times 1$ quadratic 27-node elements with 10173 nodes, which resulted in a nonlinear system of equations with 93732

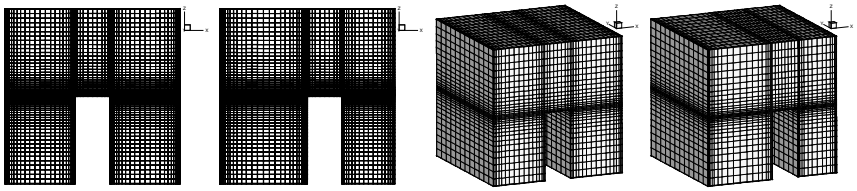

Figure 2: Presentation of the 2D $30 \times 30 \times 1$ element meshes (left) and 3D $20 \times 16 \times 6$ element meshes (right) for two positions of the hotstrip.

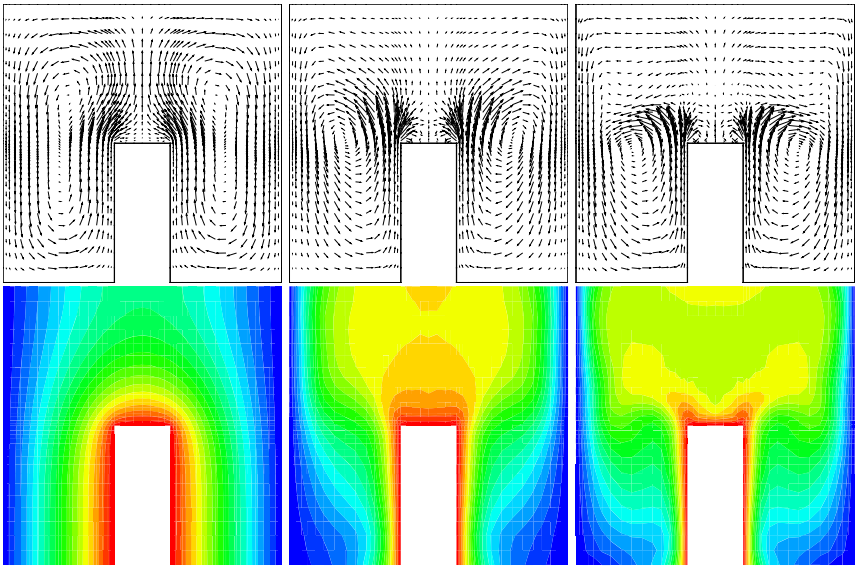

Figure 3: 3D simulation of natural convection around a hotstrip located in the central position ($d = 0.4H$). Velocity vectors (top row) and temperature contours (bottom row) are shown on a central plane at $y = 0.5H$. $Ra = 10^3$ (left), $Ra = 6.39 \cdot 10^4$ (middle), $Ra = 3.16 \cdot 10^5$ (right).

degrees of freedom. The meshes are shown in Figure 2.

3.1 Hotstrip located in the centre of the cavity

Figure 3 shows the velocity vectors and temperature contours of the 3D simulation, where the hotstrip was located in the centre of the cavity ($d = 0.4H$), in the $y = 0.5H$ plane for $Ra = 10^3$, $Ra = 6.39 \cdot 10^4$ and $Ra = 3.16 \cdot 10^5$. The hotstrip heats the surrounding air inducing two main vortices - one on each side of the hotstrip. At the top of the hotstrip, two smaller vortices are located. They keep the hot air close to the top of the hotstrip, making heat transfer from the top of the hotstrip small compared to the heat transfer from the sides of the hotstrip. Hot air from

Table 1: Heat transfer presented in terms of the Nu number value for hotstrip in the central position $d = 0.4H$. 2D and 3D results are presented for a range of Rayleigh number values.

Ra	$x = H$	$x = 0$	$x = 0.4H$	$z = 0.5H$	$x = 0.6H$
			2D		
10^3	-1.8980	-1.8980	1.5000	0.7766	1.5000
10^4	-2.1506	-2.1506	1.8592	0.5665	1.8592
6.39×10^4	-3.8125	-3.8125	3.5326	0.5575	3.5326
10^5	-4.3368	-4.3368	4.0399	0.5958	4.0399
3.16×10^5	-5.7959	-5.7959	5.4640	0.6675	5.4640
			3D		
10^3	-1.8958	-1.8958	1.5029	0.7782	1.5029
10^4	-2.1276	-2.1276	1.8377	0.5729	1.8377
6.39×10^4	-3.6164	-3.6164	3.3752	0.4846	3.3752
10^5	-4.1205	-4.1205	3.8558	0.5320	3.8558
3.16×10^5	-5.6071	-5.6071	5.2333	0.7473	5.2333

the sides of the hotstrip is transported upwards by convection making the thermal boundary layer thin and thus resulting in high heat transfer. At $Ra = 10^3$ the centre of the main vortices is above the hotstrip. As the Rayleigh number increases, the centre of the main vortices moves downward. At $Ra = 3.16 \cdot 10^5$ it is located by the side of the vertical hotstrip walls.

Table 1 presents Nusselt number values, as a non-dimensional measure of heat transfer, for all walls within the cavity as a function of the Rayleigh number. Heat losses through the cold walls located in planes $x = H$ and $x = 0$ are represented with negative values. Heat flux emitted by the side walls of the hotstrip located in planes $x = 0.4H$ and $x = 0.6H$ is shown along with the heat flux through the top hotstrip wall located as $z = 0.5H$. When the hotstrip is located in the centre of the cavity the resulting temperature and flow fields for the Rayleigh number values considered is steady and symmetrical across the $x = 0.5H$ plane. Thus heat transfer through both cold walls of the cavity takes equal values, as well as heat flux coming through both side wall of the hotstrip. The appearance of the small vortices at the top of the hotstrip makes heat flux through the top of the hotstrip small. The ratio between heat flux through the side and through the top of the hotstrip increases with increasing Rayleigh number and reaches a value of approximately 10 for the highest Rayleigh number considered.

3.2 Hotstrip located off-centre

Next we examine the flow field and heat transfer in the case where the hotstrip is positioned in an off-central position at $d = 0.5H$ (see Figure 1 for sketch). Off-central position of the heat source brings non-symmetry into the problem. Velocity vectors and temperature contours for this case are shown in Figure 4. Due to the non-symmetry the main vortices now have different sizes.

The left vortex is larger, while the right vortex is squeezed in the narrow region between the hotstrip and the cold wall. In contrast to the symmetrical $d = 0.4H$ case, we observe that the centres of the main vortices are not located by the side of the hotstrip at high Rayleigh numbers, but they remain above the hotstrip. Small vortices above the top of the hotstrip may be found in this case as well. They limit the heat flux from the top of the hotstrip.

Table 2 presents heat fluxes through the cold and hot wall in the cavity. Due to non-symmetry of the problem, the heat fluxes are also non-symmetrical. Since the hotstrip is located closer to the right ($x = H$) wall the temperature gradients are larger at this wall. Thus more heat is dissipated through the right ($x = H$) wall than through the left ($x = 0$) wall. This fact is true for the low Rayleigh number values $Ra \leq 10^4$. At $Ra \approx \times 10^5$ the heat losses through both cold walls are approximately equal. The difference in heat losses through the left and right cold

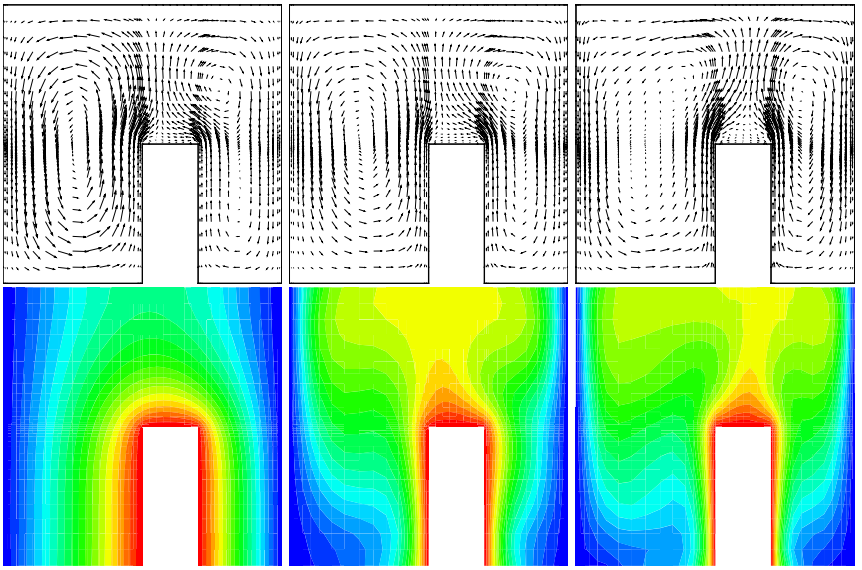

Figure 4: 3D simulation of natural convection around a hotstrip located in the off-central position ($d = 0.5H$). Velocity vectors (top row) and temperature contours (bottom row) are shown on a central plane at $y = 0.5H$. $Ra = 10^3$ (left), $Ra = 6.39 \cdot 10^4$ (middle), $Ra = 3.16 \cdot 10^5$ (right).

Table 2: Heat transfer presented in terms of the Nu number value for hotstrip in the off-central position $d = 0.5H$. 2D and 3D results are presented for a range of Rayleigh number values.

Ra	$x = H$	$x = 0$	$x = 0.5H$	$z = 0.5H$	$x = 0.7H$
			2D		
10^3	-2.4724	-1.5276	1.2793	0.8053	1.8948
10^4	-2.6334	-2.0065	1.8784	0.6682	2.0746
6.39×10^4	-3.6594	-3.8080	3.4966	0.6607	3.3074
10^5	-4.1692	-4.3359	3.9408	0.6606	3.9069
3.16×10^5	-5.6877	-5.8030	5.2297	0.6980	5.5734
			3D		
10^3	-2.4685	-1.5239	1.2840	0.8004	1.9020
10^4	-2.6214	-1.9422	1.8311	0.6515	2.0757
6.39×10^4	-3.6356	-3.6338	3.4109	0.6285	3.2355
10^5	-4.1423	-4.1362	3.8613	0.6176	3.8065
3.16×10^5	-5.7560	-5.6026	5.1694	0.7171	5.4808

walls is more prominent at low Rayleigh number values and at high Ra. The reason for this phenomena can be explained by looking at the flow field in Figure 4. At high Ra values, the right main vortex moves over the top of the hotstrip, while at low Ra it remains in the narrow space between the hotstrip and the wall. When the main vortex is between the side of the hotstrip and the cold wall, it results in high temperature gradients along the walls and thus causes high heat flux. This does not happen in the case of high Ra value.

3.3 Small vortices on top of the hotstrip

A unique feature of the considered problem is the existence of the small vortices on top of the hotstrip. These vortices keep the hot air above the hotstrip limiting the heat transfer. A detail of flow streamlines above the hotstrip is shown in Figure 5. Since the flow fields are steady and symmetrical when the hotstrip is located in the centre of the cavity we observe the existence of two symmetrical vortices on top of the hotstrip. The size of the vortices is very small at $Ra = 10^3$ and grows with increasing Rayleigh number. This symmetry is lost in the case, when the hotstrip is located off-centre. We observe that for lower Rayleigh values the right vortex, i.e. the vortex on the side which is closest to the cold wall, is larger than the left vortex.

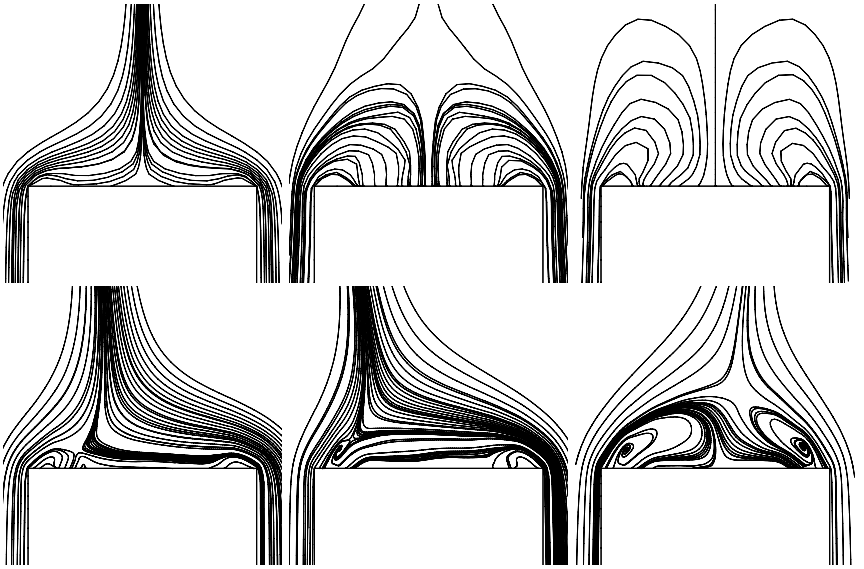

Figure 5: 3D simulation of natural convection around a hotstrip. Streamlines around the top of the hotstrip are shown for $d = 0.4H$ (top row) and $d = 0.5H$ (bottom row). $Ra = 10^3$ (left), $Ra = 6.39 \cdot 10^4$ (middle), $Ra = 3.16 \cdot 10^5$ (right).

At the highest Rayleigh number, the vortices seem approximately equally large, but from their shape, it is evident that the symmetry is lost. Due to inherent physical instability of air being heated from below, steady solution of this problem may not be sufficient. If the Rayleigh number would be higher, the problem should be simulated unsteadily. The existence of small vortices was confirmed by experiment by Corvaro and Paroncini [1].

3.4 Comparison between 2D and 3D simulation

Three dimensional structure of the flow field is shown in Figure 6. We present isosurfaces of the y component of the velocity field. The y component is directed normal to the main vortical motion, i.e. it is the direction that the 2D case considers to be irrelevant. We observe that the v_y is indeed small compared to the velocities in other two directions in the low Ra case. But when the Rayleigh number is increased, the flow in the y direction is not to be neglected. Comparing the heat transfer between the 2D and 3D cases, given in Tables 1 and 2, this conclusion is confirmed. We see, that the Nusselt number obtained with the 2D simulation are close to the 3D values for low Rayleigh number values. As the Rayleigh number increases, the difference between the 2D and 3D Nusselt number prediction becomes larger.

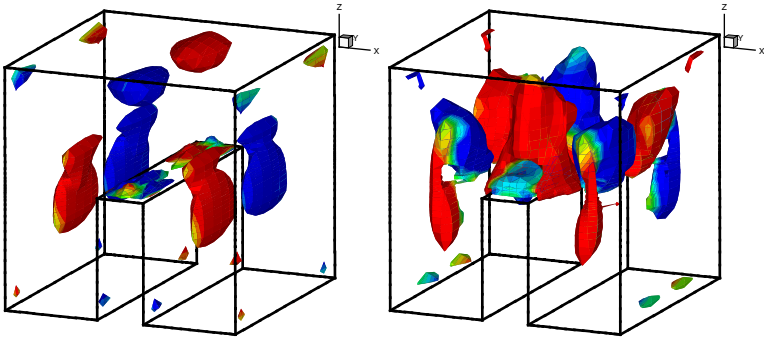

Figure 6: 3D simulation of natural convection around a hotstrip located in the central position ($d = 0.4H$). Isosurfaces of y velocity component are shown. $|\vec{v}_y|/|\vec{v}| = 0.1$, $Ra = 10^3$ (left), $|\vec{v}_y|/|\vec{v}| = 0.5$, $Ra = 3.16 \cdot 10^5$ (right). Color indicates v_y direction – blue is negative, red is positive.

4 Conclusions

A boundary element based code was use to simulate laminar viscous fluid flow and heat transfer around a hotstrip in a cavity. The code is based on a combination of single domain BEM and sub-domain BEM and was accelerated using the fast multipole method.

Two cases were simulated. Firstly, the hotstrip was placed in a centre of a square cavity filled with air. Rayleigh number values, which were based on the temperature difference between the hotstrip and the cold walls, up to $Ra = 3.16 \cdot 10^5$ were considered. Flow in this case is symmetrical and steady. Two large vortices appear in the cavity accompanied by two small vortical structures on top of the hotstrip. By examining the difference between 2D and 3D simulation, we observed that as the Rayleigh number increases 3D effects soon become important.

In the second case, the hotstrip was located off-centre. This destroyed the symmetry of the solution. The main structures remained - the two large vortices, one on each side of the hotstrip, and the two small vortices on top of the hotstrip. But their size and position are no longer symmetrical and vary greatly with Rayleigh number.

Heat transfer was studied in terms of estimating wall heat fluxes. If the hotstrip is located symmetrically, then the heat fluxes on opposite walls are equal. Off-central position of the hotstrip causes non-symmetrical distribution of fluxes. Most of the heat flux is emitted from the sides of the hotstrip, only a small amount is emitted from the top. This is caused by the existence of small vortices on top of the hotstrip, which keep warm air in place.

The findings of this analysis are in accordance with the experimental results of Corvaro and Paroncini [1].The BEM based flow solved thus proved capable of simulating the flow and predicting the heat transfer.

References

[1] Corvaro, F. & Paroncini, M., An experimental study of natural convection in a differentially heated cavity through a 2D-PIV system. *International Journal of Heat and Mass Transfer*, **52**, pp. 355–365, 2009.
[2] Ravnik, J., Škerget, L. & Žunič, Z., Combined single domain and subdomain BEM for 3D laminar viscous flow. *Eng Anal Bound Elem*, **33**, pp. 420–424, 2009.
[3] Ravnik, J., Škerget, L. & Žunič, Z., Fast single domain–subdomain BEM algorithm for 3D incompressible fluid flow and heat transfer. *Int J Numer Meth Engng*, **77**, pp. 1627–1645, 2009.
[4] Ravnik, J., Škerget, L. & Žunič, Z., Comparison between wavelet and fast multipole data sparse approximations for Poisson and kinematics boundary – domain integral equations. *Comput Meth Appl Mech Engrg*, **198**, pp. 1473–1485, 2009.
[5] Ravnik, J., Škerget, L. & Žunič, Z., Velocity-vorticity formulation for 3D natural convection in an inclined enclosure by BEM. *Int J Heat Mass Transfer*, **51**, pp. 4517–4527, 2008.
[6] Oztop, H. & Bilgen, E., Natural convection in differentially heated and partially divided square cavity with internal heat generation. *Int J Heat Fluid Flow*, **48**, pp. 1470–1479, 2005.
[7] Aydin, O. & Yang, W., Natural convection in enclosures with localized heating from below and symmetrical cooling from sides. *Int J Num Meth Heat Fluid Flow*, **10**, pp. 519–529, 2000.
[8] Corvaro, F. & Paroncini, M., A numerical and experimental analysis on the natural convective heat transfer of a small heating strip located on the floor of a square cavity. *Applied Thermal Engineering*, **28**, pp. 25–35, 2008.

Boundary integral method for Stokes flow with linear slip flow conditions in curved surfaces

C. Nieto, M. Giraldo & H. Power
Instituto de Energía y Termodinámica,
Universidad Pontificia Bolivariana, Colombia
School of Mechanical, Materials and Manufacturing Engineering,
The University of Nottingham, UK

Abstract

The no slip boundary condition is traditionally used to predict velocity fields in macro scale flows. When the scale of the problem is about the size of the mean free path of particles, it is necessary to consider that the flow slips over the solid surfaces and the boundary condition must be changed to improve the description of the flow behaviour with continuous governing fluid flow equations. Navier's slip boundary condition states that the relative velocity of the fluid respect to the wall is directly proportionally to the local tangential shear stress. The proportionally constant is called the slip length, which represent the hypothetical distance at the wall needed to satisfy the condition of no-slip flow. Some works have misused boundary conditions derived from Navier's work to model slip flow behaviour for example by employing expressions, for diagonal and curved surfaces, that were derived for flat infinite surfaces aligned with coordinate axes. In this work, the creeping flow of a Newtonian fluid under linear slip conditions is simulated for the cases of a Slit and a Couette mixer by means of the Boundary Element Method (BEM). In the evaluation of such flows, different magnitudes of slip length from 0 (no slip) to 1.0 are analysed in an effort to understand the effect of the slip boundary condition on the physical behaviour of the simulation system. Analytic solutions for both geometries under slip flow are used to estimate $L2$ norm error, which is below 0.25% for Couette flow and 1.25% for Slit flow, validating the approximation applied.
Keywords: slip flow, linear slip boundary conditions, boundary integral methods, Couette mixer.

WIT Transactions on Modelling and Simulation, Vol 49,
www.witpress.com, ISSN 1743-355X (on-line)
doi:10.2495/BE090311

1 Introduction

Microsystems Technology (MST) devices are widely used in life sciences and chemistry applications, and its potential uses extend to medical sample testing [1] and drug delivery systems [2]; gas and liquid heat exchangers [3, 4] and chemical mixers [5] for enhancement of heat and mass transfer rates; and fluid control and measurement [6] devices. Micro heat exchangers and mixers are currently used for steam gas reforming to produce alternative fuels [7], nuclear resources exploiting [8], micro integrated circuits cooling [9], micro fuel cells [10], among others.

When geometry devices are scaled down, the surface-to-volume ratio increases dramatically so that the surface related phenomena become increasingly dominant, e.g. micro heat exchangers and micro mixers present higher heat and mass transfer rates than macro systems of equal capacity [11]. Therefore, some new features emerges when mechanical structures are sufficiently small, and it becomes important to understand the various types of interactions that arises between the fluid flow constituents and the solid surfaces that contain it.

Different phenomena associated with surface-fluid interactions can be expected when the continuum assumption is close to being broken. For gases, four important effects appear: rarefaction, compressibility, viscous heating and thermal creep. In liquids, phenomena like wetting, adsorption and electrokinetics may be present [12]. However, in both liquids and gases, a phenomenon known as the slip flow regime emerges as a consequence of an insufficient number of molecules in the sampling region [13], affecting the momentum transport at solid-fluid interfaces compared with no slip type flows (i.e. macro scale flows).

So far, micro fluid flow behaviour has been studied under continuum [14] as well molecular approaches [15, 16], with the aim of characterize and optimize the operation of MST systems. In order for a fluid to be modelled as a continuum, all of its properties (i.e. kinematic, transport and thermodynamics properties) must be continuous; for that to be possible, enough molecules must be included compared to the length scale of the flow. In the case of gases, this premise is satisfied when the length scale based on transport properties is greater than 1 μm (10^{-6} m); for liquids the length scale is based on transport properties and must be larger than 10 nm (10^{-8} m) [17]. Appropriate velocity slip and temperature conditions at the wall surface must be used to employ continuum models to describe flow behaviour in microflow devices. Navier's slip boundary condition states that the relative tangential fluid velocity, u_t^f, with relation to wall velocity, U_t^w, is directly proportionally to the local shear rate projection in the tangential direction, $\dot{\gamma}_t$, as presented in equation (1). The proportionally constant is called slip length L_s, and represent the hypothetical distance at the wall needed to satisfy the no-slip flow condition [17].

$$u_t^f - U_t^w = L_s \dot{\gamma}_t \tag{1}$$

The main difficulty present when applying the previous boundary condition is related to evaluation of tangential shear rate at solid-fluid interface. Linear boundary slip conditions have been applied to predict microflow behaviour in plane

geometries with continuum governing equations. Attempts to apply this type of boundary conditions for curved surfaces have conducted to inappropriate micro-flow results due to mistreatment of mathematical models (see [18] for a compilation of those works). Boundary Integral Methods (BIM) relate boundary values for velocity and traction into the integral equations, rather than values throughout the domain like in other partial differential equation numerical solution schemes. Evaluation of slip fluid flow behaviour with BIM can be done by expressing tangential shear rate present in the slip boundary condition (1) in terms of surface tractions at boundaries. This allows a more efficient and easy to use numerical evaluation scheme to analyse micro fluid flow under slip flow regime.

Luo and Pozrikidis [19] study the motion of spherical particles in infinite fluid and near a plane wall subjected to slip boundary conditions. The boundary integral formulation presented in this work takes advantage of the axial symmetry of the boundaries with respect to the axis that is normal to the wall and passes through the particle center, reducing the solution to a system of one-dimensional integral equations. The previous system of equations is valid for sphere and the zero-thickness disk, since the axisymmetry is lost as these particles tumble under the influence of a shear flow. Results for torque and drag over sphere show reduction associated to slip condition at those scales demonstrated the validity of numerical values when compared with analytic results.

The objective of this paper is to present an implementation of a direct BIM to solve Stokes equations under slip boundary conditions for curved geometries. The tangential shear rate at solid-fluid interfaces is evaluated in terms of the surface traction; producing accurate results for fluid flow behaviour in plane and curved geometries not subjected to symmetry conditions. This will allow the evaluation of more complex geometries such as present in micro-scale devices, like T type mixers, micro-finned heat exchangers, control valves, among others. Analytic solutions for Couette and Slit flow are used to test the numerical results obtained when taking into consideration different types of boundary conditions: the first has only Robin boundary conditions while the second is a mixed boundary condition problem (Robin, Dirichlet and Neumann).

This paper is divided as follows. Governing equations for Stokes flow are presented in Section 2. The next section shows integral representation for governing equations presenting slip boundary conditions which are defined in terms of surface traction at the collocation points. Then the numerical scheme used to solve the set of equations and boundary conditions is presented. Numerical results for Couette and Slit flow are compared with analytic results through evaluation of $L2$ norm error. Finally, conclusions regarding physical and mathematical considerations are given.

2 Governing equations

Fluid flow in micro scale devices usually happens at very low Reynolds number due to the magnitudes of velocities and characteristic lengths are small enough compared to fluid density and viscosity. In these cases, fluid flow can be mod-

elled by application of the Stokes system of equations (2), which states a balance between the pressure force in the fluid and the viscous-shear force at all points in the fluid.

$$\frac{\partial u_i}{\partial x_i} = 0 \qquad \frac{\partial \sigma_{ij}}{\partial x_j} = 0 \tag{2}$$

where

$$\sigma_{ij} = -p\delta_{ij} + \mu\left(\frac{\partial u_i}{\partial x_j} + \frac{\partial u_j}{\partial x_i}\right) \tag{3}$$

In equations (2)–(3), $\vec{u}$ is the velocity, p the pressure, δ_{ij} the Kronecker delta, and μ is the viscosity of the fluid.

Boundary conditions are defined depending to the problem that is being solved. In the case of Couette flow (or the flow between concentric cylinders), the external cylinder is stationary while the internal one rotates at a constant angular dimensionless velocity of value 1. For Slit flow (or fully developed flow between parallel plates), the superior and inferior surfaces are stationary, while at the entrance and exit the perpendicular velocities are made zero and the tractions are given only by a pressure difference between them. For the cases shown dimensionless pressure, Δp equal to 1 is considered. Slip behaviour defined in equation (1) is considered by expressing local tangential shear rate in terms of vector surface traction defined in (4). Additionally, variation in momentum transport at solid-fluid interface is analysed by evaluation of slip length L_s between zero (no slip condition) and 1.0.

3 Boundary integral formulation for slip flow regime

The Stokes velocity field has the following direct integral representation formulae for an arbitrary point x in a closed domain Ω_i filled with a Newtonian fluid [20]:

$$c_i\, u_i(x) - \int_S K_{ij}(x,y)u_j(y)dS_y + \int_S u_i^j(x,y)f_j(y)dS_y = 0 \tag{4}$$

where f is the vector surface tractions ($f_j(y) = \vec{\sigma}_{ij}(\vec{u},p)n_j$), and c is a constant dependent on the position of the source point. For internal points $c = 1$ and for point at a smooth boundary $c = 1/2$. The Stokeslet and the corresponding surface traction or Stresslet for two dimensions are given by:

$$u_i^j(x,y) = -\frac{1}{4\pi}\left[\ln\left(\frac{1}{r}\right)\delta_{ij} + \frac{(x_i - y_i)\,(x_j - y_j)}{r^2}\right] \tag{5}$$

$$K_{ij}(x,y) = -\frac{1}{\pi}\frac{(x_i - y_i)(x_j - y_j)(x_k - y_k)n_k(y)}{r^4} \tag{6}$$

being r the Euclidean distance between point x and y, $r = |x - y|$.

The tangential projection of the surface traction can be expressed as follows:

$$f_i s_i = \sigma_{ij} n_j s_i = \left[-p n_i s_i + \mu \left(\frac{\partial u_i}{\partial x_j} + \frac{\partial u_j}{\partial x_i} \right) n_j s_i \right]$$
$$= \mu \left(\frac{\partial u_i}{\partial x_j} + \frac{\partial u_j}{\partial x_i} \right) n_j s_i \tag{7}$$

Thus, the slip boundary condition in tangential direction can be expressed in terms of the tangential projection of the surface traction in the following form:

$$u_t^f - U_t^w = L_s f_i s_i = L_s \dot{\gamma}_t \tag{8}$$

due to the local shear rate projection in the tangential direction, $\dot{\gamma}_t$ is defined as:

$$\dot{\gamma}_t = \left(\frac{\partial u_i}{\partial x_j} + \frac{\partial u_j}{\partial x_i} \right) n_j s_i \tag{9}$$

where s_i is the tangential vector to the boundary surface. The tangential and normal components of fluid velocity can be expressed as:

$$u_t^f = u_i s_i \quad u_n^f = u_i n_i \tag{10}$$

Given the dependency of fluid velocity with nodal values of surface traction at the boundaries, a new system of equations will be defined to simultaneously consider this effect. After discritization using the BIM, equations (4), (8), and (10) can be written in matrix form as:

$$[H][\vec{u}] = [G][\vec{f}] \tag{11}$$

$$[S][\vec{u}] - L_s[S][\vec{f}] = [\vec{U_t^w}] \tag{12}$$

$$[N][\vec{u}] = [\vec{U_n^w}] \tag{13}$$

$[H]$ and $[G]$ being the usual matrices in BEM, $[\vec{u}]$ and $[\vec{f}]$ are, respectively, the velocity and surface traction vectors from the boundary problem, and $[S]$ and $[N]$ are matrices for each element built from the tangential and normal vectors in the following arrangements.

$$[S] = \begin{bmatrix} s_1^1 & s_2^1 & 0 & 0 & 0 & 0 & \cdots \\ 0 & 0 & s_1^2 & s_2^2 & 0 & 0 & \cdots \\ 0 & 0 & 0 & 0 & s_1^3 & s_2^3 & \cdots \\ \vdots & \vdots & \vdots & \vdots & \vdots & \vdots & \ddots \end{bmatrix} \tag{14}$$

$$[N] = \begin{bmatrix} n_1^1 & n_2^1 & 0 & 0 & 0 & 0 & \cdots \\ 0 & 0 & n_1^2 & n_2^2 & 0 & 0 & \cdots \\ 0 & 0 & 0 & 0 & n_1^3 & n_2^3 & \cdots \\ \vdots & \vdots & \vdots & \vdots & \vdots & \vdots & \ddots \end{bmatrix} \tag{15}$$

The super index in the previous array represents the node number. The new system of equations is then defined in next form:

$$[A][\vec{X}] = [\vec{b}] \tag{16}$$

where new matrices and vectors are defined as (dropping all [ ]):

$$[A] = \begin{bmatrix} H & -G \\ S & -L_s S \\ N & 0 \end{bmatrix} \tag{17}$$

$$[\vec{b}] = \begin{bmatrix} 0 \\ \vec{U}_t \\ \vec{U}_n \end{bmatrix} \tag{18}$$

$$\vec{X} = \begin{bmatrix} \vec{u} \\ \vec{f} \end{bmatrix} \tag{19}$$

The solution of this complete system of equations conduces to the evaluation of velocities and tractions at the boundaries taking into account the effect of slip conditions over flow behaviour and was solved by simple Gauss elimination method.

4 Integral equation discretization

Geometry discretization for numerical integration will be made with quadratic elements with the aim to improve evaluation of velocity and surface tractions at boundaries and to produce a more reliable micro scale flow behaviour. The interpolation scheme for a function $X(\varepsilon)$ is given by:

$$X(\varepsilon) = \psi_1(\varepsilon)X^{(1)} + \psi_2(\varepsilon)X^{(2)} + \psi_3(\varepsilon)X^{(3)} \tag{20}$$

where $X^{(1)}, X^{(2)}, X^{(3)}$ are the values of $X(\xi)$ on the three nodes of the element and the interpolation functions $\vec{\psi}$ are as follows:

$$\psi_1 = \tfrac{1}{2}\varepsilon(\varepsilon - 1); \quad \psi_2 = (1-\varepsilon)(1+\varepsilon); \quad \psi_3 = \tfrac{1}{2}\varepsilon(\varepsilon + 1) \tag{21}$$

Standard Guassian Quadrature is used to evaluate the final set of integrals resulting from applying the interpolation function (20). Telles' Transformation [21] and Rigid Body Motion [22] are used to avoid singularity present when integrating over the same element where the source point is located.

5 Numerical results

In this section the test performed for the direct boundary integral formulation implemented to predict slip behaviour for Couette and Slit flow is presented, taking into account different momentum transport at the solid-fluid interface by variations of the slip length condition.

5.1 Couette flow

An analytic solution for the tangential fluid velocity in Couette flow under linear slip boundary conditions is given by ([18]):

$$u_t = \frac{\omega}{A-B}\left(Ar - \frac{1}{r}\right) \tag{22}$$

where

$$A = 1 - \frac{2\dfrac{L_s}{r_e}}{r_e^2}; \quad B = 1 - \frac{2\dfrac{L_s}{r_i}}{r_i^2} \tag{23}$$

and being ω, r_e and r_i, the angular velocity for internal cylinder, external and internal radius, respectively. Tangential velocity u_t is given for any radius r. The slip length L_s variates between zero (no slip condition) and 1.0 to account for momentum transport variation at both the internal and external cylinders. When L_s is dropped to zero in equation (22), it reduces to Couette flow for no slip conditions as is presented in [23]. A regular mesh was used to solve the linear system of equations: 48 quadratic elements on both boundary surfaces and 300 uniformly distributed internal points. It is important to point out that these internal nodes are not required for the solution of the problem, but only for flow visualization and numerical error evaluation.

Results for both no slip and slip Couette flow are presented in Table 1. Momentum transport modification at the boundaries is evidenced by the reduction in fluid velocities near the internal cylinder (70% for the higher slip length evaluated respect to the no slip condition) as shown in Figure 1(A). For the outer cylinder, the slip regimen induce a velocity over this boundary, which tends to reduce as the slip length is increased, showing the continuity in transport momentum through the fluid flow.

Errors below 0.25% indicate the good performance of direct boundary integral formulation implemented in the system of equations (10). It is also observed that there is a considerable reduction in error as the slip length is increased in spite of discontinuity in the velocity at the wall and the fluid imposed by the variation in this value. This could be explained by reduction in momentum transferred by the surfaces to the fluid which implies an overall reduction in flow velocity.

Table 1: Assessment of Couette flow under slip conditions.

L_s	0	0.1	0.25	0.5	1.0
$L2\ norm\ (\%)$	0.248	0.252	0.175	0.127	0.063

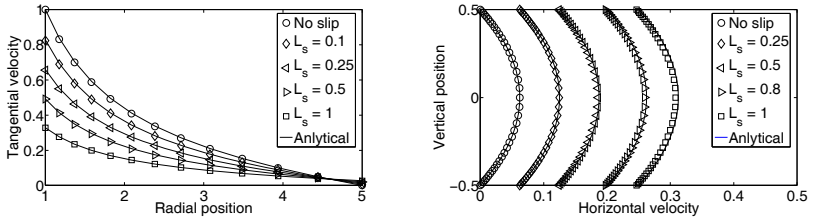

(A) (B)

Figure 1: Velocity profiles for slip (A) Couette and (B) slit flow.

5.2 Slit flow

The analytic solution for velocity profile under slip flow over the horizontal surfaces is available in [24]:

$$u_1 = \frac{h^2}{2\mu}\frac{\Delta P}{L}\left[1 - \left(\frac{x_2}{h}\right)^2\right] + \frac{h}{\mu}\frac{\Delta P}{L}L_s \tag{24}$$

where L is the channel length, h its height and ΔP the imposed pressure difference. The second term in the right side of equation (24) accounts the slip effect in the velocity profile. It reduces to no slip when L_s is dropped to zero as presented in [23]. The tested mesh consisted of 160 quadratic elements on the outer surface refined at a the corners and 600 internal collocation points.

The results for this case shown an error below to 1.2%, showing a good description of fluid flow for this geometry as can seen in Figure 1(B). An increase in fluid flow velocities is observed with respect to the no slip conditions indicating the effect of slip flow over momentum transport at boundaries. A detailed observation of results in Figure 1(B) and Table 2 shows that deviation from analytic results increase as flow goes from no slip to slip behaviour. Despite the mesh refinement applied at the corners, numerical evaluation of normal and tangential vectors at this positions affects the interior flow description. Furthermore, since the channel has a height equal to the maximum slip length evaluated, an increase over this limit can conduce to unrealistic results according to the definition of slip length in boundary condition (1).

Table 2: Assessment of Slit flow under slip conditions.

L_s	0	0.1	0.25	0.5	1.0
$L2\ norm\ (\%)$	0.009	0.252	0.557	0.931	1.182

6 Conclusions

A direct boundary integral method was used to evaluate slip flow behaviour for two traditional fluid flow problems. Results for both problems presented accurate results when compared with analytic results. As expected, a reduction in momentum transportation occurs at the fluid-solid interfaces due to slip regimen, leading to a change in the flow behaviour. A modified system of equations was used to evaluate slip flow in terms of surface traction and the usual matrices in BEM. Despite the system of equations increased from N to $2N$, the computational effort is kept at low levels, which permits its application to the solution of more complex flow systems.

Acknowledgements

C. Nieto is supported in his PhD program by the Universidad Pontificia Bolivariana and COLCIENCIAS under the Convocatoria Banco de Proyectos Tesis Doctorales.

References

[1] Gad-el Hak, M., *MEMS: Applications*. CRC Press: Virginia, pp. 11–20, 2006.
[2] C. Kleinstreuer, J.L. & Koo, J., Microfluidics of nano-drug delivery. *International Journal of Heat and Mass Transfer*, **51(1)**, pp. 5590–5597, 2008.
[3] L. Shui, J.E. & van den Berg, A., Multiphase flow in micro- and nanochannels. *Sensors and Actuators B: Chemical*, **121(1)**, pp. 263–276, 2007.
[4] M. Giraldo, Y.D. & Williams, R., Boundary integral study of nanoparticle flow behaviour in the proximity of a solid wall. *Journal of Physics D: Applied Physics*, **41(8)**, pp. 1–10, 2008.
[5] D. Bothe, C.S. & Warnecke, H.J., Fluid mixing in a t-shaped micro-mixer. *Chemical Engineering Science*, **61(9)**, pp. 2950–2958, 2006.
[6] J. Alvarado, J.M. & Soriano, G., Development and characterization of a capacitance-based microscale flowmeter. *Flow Measurement and Instrumentation*, **20(2)**, pp. 81–84, 2009.
[7] A.Y. Tonkovich, Y.W.D.Q.T.L.P., S. Perrya & Rogersa, W.A., Microchannel process technology for compact methane steam reforming. *Chemical Engineering Science*, **59(22–23)**, pp. 4808–4817, 2004.
[8] X. Li, R.L.P. & Dewson, S.J., Heat exchangers for the next generation of nuclear reactors. *Proc. of International Congress on Advances in Nuclear Power Plants*, eds. R.R.M.K. F. L. Bowman, S. Anghaie & A. Rao, ICAPP: Reno, pp. 201–209, 2006.
[9] H. Lee, J.S.J.B.M.K., Y. Jeong & Chun, K., Package embedded heat exchangernext term for stacked multi-previous termchipnext term module. *Sensors and Actuators A: Physical*, **114(2–3)**, pp. 204–211, 2004.
[10] S. Won Cha, R.O. & Prinz, F.B., The influence of size scale on the performance of fuel cells. *Solid State Ionics*, **175(1–4)**, pp. 789–795, 2004.

[11] Hu, G. & Li, D., Multiscale phenomena in microfluidics and nanofluidics. *Chemical Engineering Science*, **62(13)**, pp. 3443–3454, 2007.
[12] G. Karniadakis, A.B. & Aluru, N., *Microflows and Nanoflows: Fundamentals and Simulation*. Springer: New York, p. 487, 2005.
[13] Thompson, P.A. & Troian, S.M., A general boundary condition for liquid flow at solid surfaces. *Nature*, **389(1)**, pp. 360–362, 1997.
[14] Gad-el Hak, M., Gas and liquid transport at the microscale. *Heat Transfer Engineering*, **27(4)**, pp. 1–17, 2006.
[15] Bird, G., *Molecular gas dynamics and direct simulation of gas flows*. Oxford University Press: Oxford, p. 484, 1994.
[16] Sadus, R.J., *Molecular simulation of fluids: Theory, applications and object-orientation*. Elsevier: Amsterdam, p. 562, 1999.
[17] Nguyen, N.T. & Wereley, S.T., *Fundamentals and Applications of Microfluidics*. Artech House: Norwood, p. 487, 2006.
[18] R. W. Barber, X.J.G., Y. Sun & Emerson, D.R., Isothermal slip flow over curved surfaces. *Vacuum*, **76(1)**, pp. 73–81, 2004.
[19] Luo, H. & Pozrikidis, C., Effect of surface slip on stokes flow past a spherical particle in infinite fluid and near a plane wall. *Journal of Engineering Mathematics*, **62(1)**, pp. 1–21, 2008.
[20] Power, H. & Wrobel, L., *Boundary Integral Methods in Fluid Mechanics*. Computational Mechanics publications: Southhampton, pp. 147–194, 1995.
[21] Telles, J., A self-adaptative coordinate transformation for efficient numerical evaluation of general boundary element integrals. *International Journal for Numerical Methods in Engineering*, **24(1)**, pp. 959–973, 1987.
[22] Brebbia, C. & Dominguez, J., *Boundary Elements: An Introductory Course*. Computationanl Mechanics Publications: Southampton, p. 400, 1992.
[23] Currie, I., *Fundamental Mechanics of Fluids*. Macerl Dekker: New York, pp. 259–262, 2003.
[24] Matthews, M.T. & Hill, J.M., Newtonian flow with nonlinear navier boundary condition. *Acta Mechanica*, **191(1)**, pp. 195–217, 2007.

Development of a Boundary Element Method-based numerical wave tank technique for the prediction of nonlinear wave kinematics and dynamics around offshore structures

H. G. Sung
Maritime and Ocean Engineering Research Institute, KORDI, Korea

Abstract

This paper presents recent accomplishments of the development of the Boundary Element Method (BEM) for nonlinear waves around offshore structures and resulting wave forces. In order to investigate the capability of the present method, the nonlinear diffraction problem of a truncated circular cylinder is simulated. It is found that the present method is fairly accurate for wave forces and run-ups when compared with experimental results and also with other numerical results.
Keywords: BEM, nonlinear waves, offshore structures, nonlinear diffraction.

1 Introduction

Nowadays, activities for marine gas and oil exploration move continuously into deeper ocean year by year. In order to design offshore structures for ultra deep sea, wave forces on offshore structures must be predicted with high accuracy. A number of theoretical, numerical and experimental studies have been developed for this purpose, but it seems that there still remains uncertainty to some extent.

In order to deal with nonlinear waves and resulting wave forces for high waves, it is necessary to apply a nonlinear method rather than the conventional linear theory. It is debatable whether nonlinear solutions based on the perturbation method are applicable for steep waves. It is also obvious that experimental studies in offshore basins are expensive for the preliminary design stage. Therefore, it is commonly accepted that numerical methods are appropriate for evaluating nonlinear wave forces on a body in large waves. Thus

WIT Transactions on Modelling and Simulation, Vol 49, © 2009 WIT Press
www.witpress.com, ISSN 1743-355X (on-line)
doi:10.2495/BE090321

the present study is focused upon the numerical method. Hence the present paper is aimed to investigate the capability of the present numerical method, namely, the so-called a BEM-based numerical wave tank technique (Boo and Kim [1], Kim [10]), for the prediction of nonlinear wave forces and run-ups on offshore structures.

The numerical methods widely used in practice are based upon the usual assumption of an ideal fluid, and higher-order boundary elements as a field solver. This is partially justified because most successes in simulating nonlinear free surface waves have been relying upon boundary elements. It is also known as the numerical wave tank technique, which is conceived as a promising tool for predicting the nonlinear hydrodynamic behavior of offshore structures (Kim [10]).

Since the pioneering work of Longuet-Higgins and Cokelet [13] on spatially periodic nonlinear waves in two dimensions, many studies have been made on this kind of problems. To name a few, Dommermuth et al. [3] successfully calculated plunger-type waves within the framework of potential theory. Xü [22] investigated the kinematics of three-dimensional plunging breakers by using bi-quadratic boundary elements as an extension of Longuet-Higgins and Cokelet [13]. Nonlinear diffraction forces are reported in the literature such as Ferrant [4, 5], Boo and Kim [1], etc. Grilli and his colleagues have been trying to develop an efficient BEM for nonlinear wave evolution as shown in Grilli et al. [8], Guyenne and Grilli [9], and Grilli et al. [7], etc.

It is worthwhile to mention the paper written by Kristiansen et al. [12] in connection with the present paper. They tried to verify the conventional design tool of BEM in predicting diffracted wave elevation around a vertical circular cylinder. Applicability and shortcomings of the method were suggested.

The present paper is organized as follows. First, we present the mathematical formulation of the model with numerical formulation. Finally, we apply the method to the problem of nonlinear waves around the truncated circular cylinder. We compare the numerical results with those of experiments and other computation.

2 Mathematical formulation

We assume the fluid is incompressible and non-viscous, and also the flow is irrotational. So, we can define the velocity potential, as the scalar function, $\Phi(\vec{x},t)$, of spatial variables, $\vec{x} \equiv (x,y,z)$, and time variable, t. The velocity potential is related to the fluid velocity vector, $\vec{u} = (u,v,w)$ by $\vec{u} = \nabla\Phi$, where ∇ means the gradient operator. Thus, mass conservation becomes Laplace's equation for the potential in the fluid domain, $\Omega(t)$,

$$\nabla^2\Phi(\vec{x},t) = 0 \tag{1}$$

The boundary of the fluid domain is composed of the free surface, body boundary, and far field boundaries. Appropriate boundary conditions (*i.e.*, Dirichlet or Neumann) are stated in the below.

The kinematic and dynamic free surface conditions are expressed in an Eulerian representation as,

$$\frac{\partial \zeta}{\partial t} = -\nabla_H \Phi \cdot \nabla_H \zeta + \frac{\partial \Phi}{\partial z} \tag{2}$$

$$\frac{\partial \Phi}{\partial t} = -gz - \frac{1}{2}\left|\nabla \Phi\right|^2 - \frac{p_a}{\rho} \tag{3a}$$

where ζ denotes the vertical position of the free surface as a function of the horizontal position and time, say, $\zeta = \zeta(x, y, t)$. The operator ∇_H means the horizontal component of the gradient operator. The constant g is the gravitational acceleration and ρ the fluid density. p_a is the atmospheric or applied pressure on the free surface. Due to the local movement of the collocation points, boundary condition (3a) must be modified as follows.

$$\frac{d}{dt}\Phi(\vec{x},t) = \frac{\partial}{\partial t}\Phi(\vec{x},t) + \frac{\partial \zeta}{\partial t}\frac{\partial \Phi}{\partial z} = -gz - \frac{1}{2}\left|\nabla \Phi\right|^2 - \frac{p_a}{\rho} + \left[-\nabla_H \Phi \cdot \nabla_H \zeta + \frac{\partial \Phi}{\partial z}\right]\frac{\partial \Phi}{\partial z} \tag{3b}$$

The body boundary condition states that the normal velocity of the fluid particle on the body boundary is equal to the normal component of the velocity of the body,

$$\nabla \Phi \cdot \vec{n} = \vec{V} \cdot \vec{n} \tag{4}$$

where $\vec{n} = (n_x, n_y, n_z)$ is the outwards unit normal vector, and $\vec{V}$ is the body velocity, which is either given by the specified motion of the disturbance or obtained from the body equations of motion. This condition can also be used for wave-making boundary in the vertical upstream side. On the bottom boundary and other stationary parts of solid boundary, no-flow boundary condition is prescribed.

3 Solution methodology

3.1 Boundary element method

The bi-quadratic BEM of Sung [18] and Sung et al. [19] is utilized in numerical solution of the governing equation, Eq. (1), with time-dependent nonlinear free surface boundary conditions Eqs. (2) and (3). In this paper, we briefly restate the principal features of the method and its implementation.

In the first place, the Green's second identity transforms Laplace equation into the well-known boundary integral equation,

$$\alpha(\vec{x})\Phi(\vec{x}) = \int_\Gamma \left[\Phi(\vec{\xi})\frac{\partial G}{\partial n}(\vec{\xi},\vec{x}) - \frac{\partial \Phi}{\partial n}(\vec{\xi})G(\vec{\xi},\vec{x})\right] d\Gamma_\xi \tag{5}$$

where $\alpha(\vec{x})$ is the normalized interior solid angle at point $\vec{x}$, $G(\vec{\xi},\vec{x}) = 1/4\pi r$ is the free-space Green's function, where $r = |\vec{r}| = |\vec{\xi} - \vec{x}|$ is the distance from the source point $\vec{\xi}$ to the field point $\vec{x}$. An analytic expression for the solid angle can be obtained by considering a trivial solution of the Laplace equation, to say a constant function, as $\alpha(\vec{x}) = \int_\Gamma \partial G(\vec{\xi},\vec{x})/\partial n_\xi d\Gamma_\xi$. This expression is substituted into the boundary integral equation to obtain an improved form of the integral equation as follows.

$$\int_{\Gamma}\left\{\left[\Phi(\vec{\xi})-\Phi(\vec{x})\right]\frac{\partial G}{\partial n}(\vec{\xi},\vec{x})-\frac{\partial \Phi}{\partial n}(\vec{\xi})G(\vec{\xi},\vec{x})\right\}d\Gamma_{\xi}=0 \tag{6}$$

It can be seen that the singularity of the first term is reduced by order of one, which means from the numerical point of view, all the integrations become regular through this improvement.

From the accuracy point of view, the higher the order of elements becomes, the more accurate the obtained solution will be. Practice, however, compels us to take a compromising order of approximation. As a result, "bi-quadratic elements" using 3×3 nodes are taken as shown in Figure 1 in which a typical bi-quadratic elements and the parameter space are sketched.

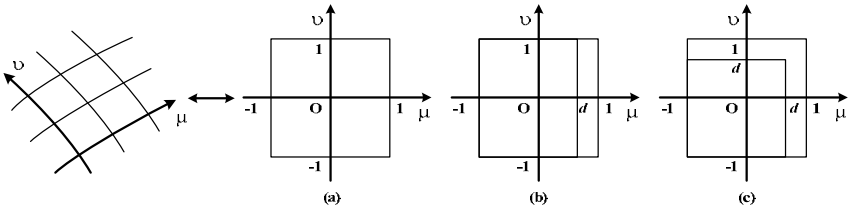

Figure 1: Bi-quadratic element and its parameter space: (a) continuous case, (b) single-edge case, (c) double-edge case

For appropriate treatment of the intersection line between two different boundaries, discontinuous elements are utilized around corners and edges as Brebbia [2] indicated, while conventional continuous elements are used elsewhere. The single-edge discontinuous elements are pertinent around edges or intersection lines and the double-edge discontinuous elements are suitable around corners. Throughout the computations, freedom nodes are taken at $d=2/3$ for both kinds of discontinuous elements.

Using the isoparametric bi-quadratic elements, geometry and variables on each element can be expressed in terms of basis functions

$$\left[\vec{x},\varphi,q\right]=\sum_{\mathrm{m}=0}^{8}N_{\mathrm{m}}(\mu,\upsilon)\left[\vec{x}_m^{j},\varphi_m^{j},q_m^{j}\right]\text{on } E_{\mathrm{j}} \text{ with, } q=\varphi_n \tag{7}$$

where $\vec{x}$ is the position vector of the boundary surface, the subscripts in variables designate the local node numbers, the ordering of which is depicted in Figure 2. Superscripts denote the number of the element on which variables are defined. Function N_m is the product Lagrangian basis function, and E_{j} is the j^{th} element. By using this expression, the boundary integral equations are discretized.

To obtain the algebraic equations for the velocity potentials and their normal derivatives at each nodal point, the collocation method is applied. In this paper, collocation points correspond to nodal points. The discretized and collocated boundary integral equations form the following linear system of equations.

$$\alpha(\vec{x}_i)\varphi(\vec{x}_i)=\sum_{j=1}^{N_e}\sum_{\mathrm{k}=0}^{8}\left[\varphi_{\mathrm{k}}^{\mathrm{j}}D_{\mathrm{k}}^{\mathrm{j}}(\vec{x}_i)-q_{\mathrm{k}}^{\mathrm{j}}S_{\mathrm{k}}^{\mathrm{j}}(\vec{x}_i)\right], \tag{8}$$

where $D_k^j(\vec{x}_i)$ and $S_k^j(\vec{x}_i)$ are the influence coefficients due to the doublet and source distribution.

The numerical integration for influence coefficients due to source and doublet distribution is as follows: (1) regular integrals are calculated by a bi-directional Gauss-Legendre quadrature method; (2) singular integrals, in which the distance vanishes at the collocation point are completely desingularized by means of the rectangular polar coordinates mapping on each subdivision of parameter space and then Gauss-Legendre numerical integration is applied.

3.2 Numerical radiation condition

It is well known that the treatment of the radiation condition affects the entire solution and that it is closely related with the method of generating nonlinear waves in a numerical wave tank. Several kinds of numerical radiation condition are proposed for three-dimensional nonlinear diffraction problem. They may be categorized into two groups: wave damping zone technique (Boo and Kim [1], Kim et al. [11], Ferrant [4]) and decomposition method (Ferrant [5]).

In this paper, the following new radiation condition is proposed by combining these two methods as follows.

$$\begin{aligned}\frac{d\varphi(\vec{\mathrm{x}},\mathrm{t})}{d\mathrm{t}} &= \left[1-\gamma(\mathrm{x},\mathrm{y})\right]\left\{-\frac{1}{2}\,|\nabla\varphi|^2-\mathrm{g}z+\left[\frac{\partial\varphi}{\partial z}-\nabla_H\varphi\cdot\nabla_H\zeta\right]\frac{\partial\varphi}{\partial z}\right\}\\ &\quad+\gamma(\mathrm{x},\mathrm{y})\left\{\frac{d\varphi_{RF}(\vec{\mathrm{x}},\mathrm{t})}{dt}-\beta\left[\varphi(\vec{\mathrm{x}},\mathrm{t})-\varphi_{RF}(\vec{\mathrm{x}},\mathrm{t})\right]\right\},\qquad \vec{\mathrm{x}}\in \mathrm{S_f},\end{aligned} \tag{9}$$

$$\begin{aligned}\frac{d\zeta(\mathrm{x},\mathrm{y},\mathrm{t})}{d\mathrm{t}} &= \left[1-\gamma(\mathrm{x},\mathrm{y})\right]\left\{\frac{\partial\varphi}{\partial \mathrm{z}}-\nabla_H\varphi\cdot\nabla_H\zeta\right\}\\ &\quad+\gamma(\mathrm{x},\mathrm{y})\left\{\frac{d\zeta_{RF}(\mathrm{x},\mathrm{y},\mathrm{t})}{d\mathrm{t}}-\beta\left[\zeta(\mathrm{x},\mathrm{y},\mathrm{t})-\zeta_{RF}(\mathrm{x},\mathrm{y},\mathrm{t})\right]\right\},\boldsymbol{x}\in \mathrm{S_f}\end{aligned} \tag{10}$$

where $\gamma(\mathrm{x},\mathrm{y})$ is named the Homotopy parameter and β is a time constant to retrieve the incident waves. These equations must be understood as time-dependent boundary conditions for a given grid point $\boldsymbol{x}=(x,y,z)$. The subscript RF denotes a quantity of the Rienecker and Fenton wave (Rienecker and Fenton [16]).

The RF waves are given by

$$\varphi_{RF}(\mathrm{x},\mathrm{z},\mathrm{t}) = (\mathrm{B}_0+c)\mathrm{x}+\sum_{j=1}^{\mathrm{N}}\mathrm{B}_j\frac{\cosh\left[j\mathrm{k}(\mathrm{z}+\mathrm{h})\right]}{\cosh(\,j\mathrm{kh})}\sin\left[j\mathrm{k}(\mathrm{x}-\mathrm{ct})\right] \tag{11}$$

$$\zeta_{RF}(\mathrm{x},\mathrm{t}) = \frac{\mathrm{a}_0}{2}+\sum_{j=1}^{\mathrm{N}}\mathrm{a}_j\cos\left[j\mathrm{k}(\mathrm{x}-\mathrm{ct})\right] \tag{12}$$

where c and k are the phase speed and the wave number, respectively. The coefficients B_j, $\mathrm{a}_j\,(j=0,1,\cdots,\mathrm{N})$ are determined so that the nonlinear free surface conditions and compatibility conditions are satisfied usually when the wave height and the wave period are specified. The error can be controlled by the truncation order N only, which is 40 in the present computation.

Specifically, $\gamma(\mathrm{x},\mathrm{y})$ is determined by the horizontal distance R_{xy} from the center of the cylinder in this paper as follows.

$$\gamma(\mathrm{x},\mathrm{y}) = \begin{cases} 0 & \text{if} \mathrm{R}_{xy} \le \mathrm{R}_D \\ \sin^2\left[(\mathrm{R}_{xy} - \mathrm{R}_D)/2(\mathrm{R}_T - \mathrm{R}_D)\right] & \text{if} \mathrm{R}_D \le \mathrm{R}_{xy} \le \mathrm{R}_T \\ 1 & \text{if} \mathrm{R}_{xy} \ge \mathrm{R}_T \end{cases} \tag{13}$$

The three zones above are named as the D (Diffraction) zone, the T (Transient) zone, and the RF (Rienecker and Fenton wave) zone. At the RF zone, equations (9) and (10) assert that the solution converges to the RF wave after several wave periods. The value of the RF wave potential is specified on radiation boundaries at all times. Around the body, however, the potential and the wave elevation are gradually set to zero at $\mathrm{t} = 0$ in order to avoid impulsive responses. The present method is compared with the work of Ferrant [4]. This scheme is able to describe nonlinear diffraction waves near the body accurately, and the incident waves are well recovered away from the body.

3.3 Evaluation of the wave forces and moments

In order to evaluate the wave forces and moments, we calculate as follows.

$$\left(\vec{\mathrm{F}}, \vec{\mathrm{M}}\right) = \int_{\mathrm{S}_b} \mathrm{p}(\vec{\mathrm{x}},\mathrm{t})\left(\vec{\mathrm{n}}, \vec{\mathrm{r}} \times \vec{\mathrm{n}}\right) d\mathrm{S} = -\rho \int_{\mathrm{S}_b} \left[\varphi_t + \frac{1}{2}|\nabla\varphi|^2 + \mathrm{gz}\right]\left(\vec{\mathrm{n}}, \vec{\mathrm{r}} \times \vec{\mathrm{n}}\right) d\mathrm{S} \tag{14}$$

Using Leinitz' rule, we can transform the surface integral of the time derivative of the velocity potential into sum of the time derivative of the surface integral of the velocity potential and the line integral term that is defined along the intersection line of the free surface and the body boundary.

A more orthodox method of solution is the use of the concept of acceleration potential. The time derivative of the velocity potential, $\partial\Phi/\partial t$, is of great concern in time simulation of fully nonlinear free surface waves around the offshore structures, particularly for the wave forces prediction. It can be estimated by using the backward time difference formula, which however leads to inaccurate results and unstable solutions. According to our understanding, we can also utilize the concept of the acceleration potential, $\Psi(\vec{x},t) = \partial\Phi/\partial t + \nabla\Phi\cdot\nabla\Phi/2$ which postulates the continuity of the normal acceleration. This idea was originally suggested in series of Tanizawa's works [21]. In this paper the procedure given by Tanizawa is borrowed and some implemental issues are explained. Thus we start from the boundary condition for the acceleration potential as follows.

$$\frac{\partial}{\partial n}\left(\frac{\partial\Phi}{\partial t}\right) = \vec{A}\cdot\vec{n} - \left[(\nabla\Phi\cdot\nabla)\nabla\Phi\right]\cdot\vec{n} \tag{15}$$

where $\vec{A}$ means the acceleration vector on the body boundary, which is zero in this case. The expression for the second term is stated for two-dimensions in Tanizawa [21]. For the three dimensional case, the equation of the particle acceleration in Fochesato et al. [6] can be utilized for the present purpose. Interested readers can refer to the paper by [6].

3.4 Miscellaneous aspects

In this study, the linear system of algebraic BEM equations is solved using the iterative solver GMRES (Generalized Minimal RESidual) originally devised by Saad and Schultz [17] which is known as a *NlogN* method, where N is the degree of freedom. For the time integration of the time-dependent system, the fourth-order Runge-Kutta (RK4) method with minimum truncation error (Ralston and Rabinowitz [15]) is adopted by considering accuracy and stability.

3.5 Perturbation-based solution method

In order to investigate systematically the overall capability and performance of the fully nonlinear method, the present study utilizes the perturbation-based solution scheme. Traditionally in it, the whole solution is expressed as follows.

$$\Phi = \varepsilon\Phi^{(1)} + \varepsilon^2\Phi^{(2)} + H.O.T. \tag{16}$$

$$\zeta = \varepsilon\zeta^{(1)} + \varepsilon^2\zeta^{(2)} + H.O.T. \tag{17}$$

where $\varepsilon = kA_I$ is known as smallness parameter, when k is the wavenumber and A_I the amplitude of incident waves. The superscript means the order of the solution. $H.O.T.$ means higher-order terms. As well-known, the free surface boundary conditions for the first-order of solution can be written as follows.

$$\frac{\partial\zeta^{(1)}}{\partial t} = \frac{\partial\Phi^{(1)}}{\partial z} \; at \; z = 0 \tag{18a}$$

$$\frac{\partial\Phi^{(1)}}{\partial t} = -g\zeta^{(1)} \; at \; z = 0 \tag{19a}$$

The second-order ones are of the following form.

$$\frac{\partial\zeta^{(2)}}{\partial t} = \frac{\partial\Phi^{(2)}}{\partial z} + \zeta^{(1)}\frac{\partial^2\Phi^{(1)}}{\partial z^2} - \nabla_H\Phi^{(1)}\cdot\nabla_H\zeta^{(1)} \; at \; z = 0 \tag{18b}$$

$$\frac{\partial\Phi^{(2)}}{\partial t} = -g\zeta^{(2)} - \zeta^{(1)}\frac{\partial^2\Phi^{(1)}}{\partial z\partial t} - \frac{1}{2}\left|\nabla\Phi^{(1)}\right|^2 \; at \; z = 0 \tag{19b}$$

Here the atmospheric pressure has been set to zero for brevity.

The incident wave potentials for each order are known as:

$$\Phi_I^{(1)} = \frac{g}{k\omega}\frac{\cosh k(z+h)}{\cosh kh}\sin(kx - \omega t) \tag{20}$$

$$\Phi_I^{(2)} = \frac{3g}{8k^2}\frac{\cosh 2k(z+h)}{\sinh^4 kh}\sin(2kx - 2\omega t) \tag{21}$$

The solution can be obtained by decomposition of the solution into the sum of incident and scattered parts. In the present study, the first- and second-order solutions can be compared with the fully nonlinear results.

4 Numerical results

While the present study is under development, this paper contains the first-order computation only. The second-order and fully nonlinear simulations are postponed to near future. Figure 2 shows the grid systems for the first-order and

second-order solutions. An appropriate grid should resolve the evolution of incident and scattered wave for each order of solution, and so each grid has its own dimension.

An example of free surface shape is shown in Figure 3. The scattered part and total waves surface are separately displayed.

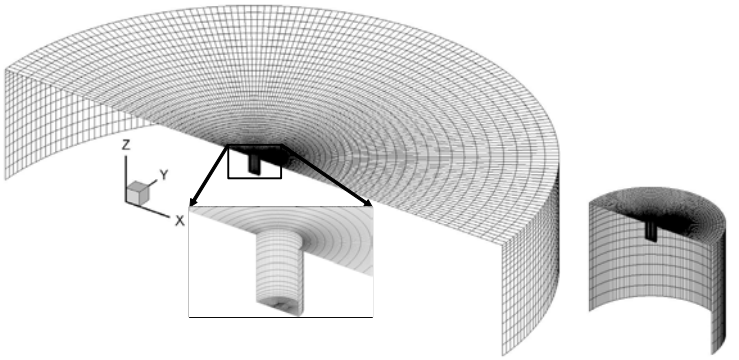

Figure 2: Grid systems for the first-order (left) and second-order (right) solutions.

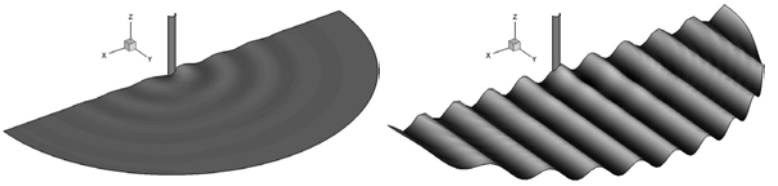

Figure 3: Free surface shape at $t = 14T$ of the first-order solution for the case of $kR = 0.657$ (left-scattered part, right-total=incident+scattered).

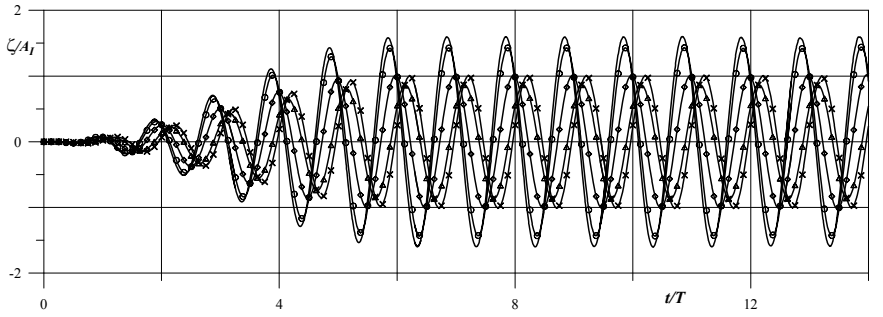

Figure 4: Time series of wave runups for the case of $kR = 0.657$ (line: $\theta = 0$, line with circle: $\theta = \pi/4$, line with diamond: $\theta = \pi/2$, line with triangle: $\theta = 3\pi/4$, line with cross: $\theta = \pi$; the angle is so defined that $\theta = \pi$ corresponds to the lee side of the cylinder).

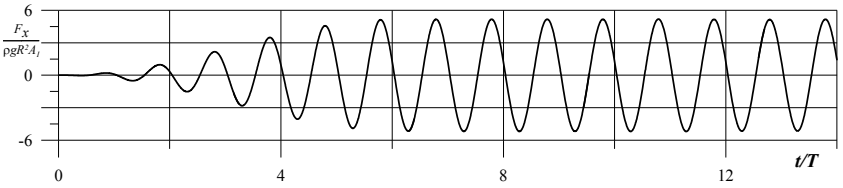

Figure 5: Time series of horizontal wave force for the case of $kR = 0.657$.

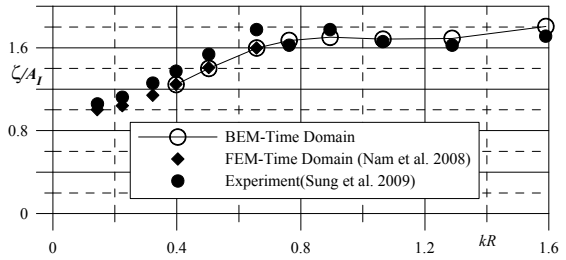

Figure 6: Comparison of wave runup at upstream point of the cylinder ($r = R$, $\theta = 0$) with numerical computation by FEM (Nam et al. [14]) and experiment (for the wave steepness, $H/\lambda = 1/30$, Sung et al. [20]).

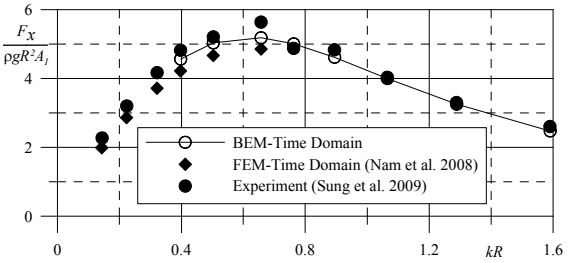

Figure 7: Comparison of horizontal wave force with numerical computation by FEM (Nam et al. [14]) and experiment (Sung et al. [20]).

Time series of wave elevations along the cylinder surface for the case of $kR = 0.657$ are shown in Figure 4. Corresponding time series of horizontal wave force behaves as in Figure 5.

For qualitative comparison, a series of experiments has been carried out, and a detailed description of the experimental study can be referred to Sung et al. [20]. Comparison of present first-order computation with experiments is shown in Figure 6 and Figure 7. The experimental results were obtained for the case of intermediate wave steepness, $H/\lambda = 1/30$, which can be regarded as 'linear case'. It can be concluded that the present method is fairly accurate for wave forces and run-ups on the whole when compared with experimental results and also with other numerical results.

The second-order and fully nonlinear computation is postponed, and lastly the need to incorporate nonlinearity into the numerical solution is demonstrated. Figure 8 shows nonlinearity of the wave runup, wave forces, and moment, where time series behaves very differently from a pure sinusoidal pattern. Higher-order components seem to be strongly inherent in this case of $kR = 0.657$ and $H/\lambda = 1/10$, which will be analyzed more thoroughly with fully nonlinear computation.

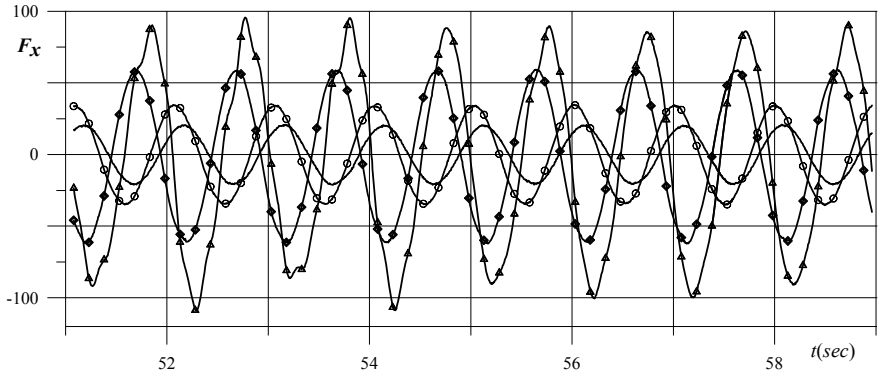

Figure 8: Experimental results of nonlinearity of the wave runup, wave forces and moment for the case of $kR = 0.762$ (line: $H/\lambda = 1/50$, line with circle: $H/\lambda = 1/30$, line with diamond: $H/\lambda = 1/16$, line with triangle: $H/\lambda = 1/10$).

5 Summary and concluding remarks

This paper presented recent accomplishments of the development of the Boundary Element Method (BEM) for nonlinear waves around offshore structures and resulting wave forces. Basic characteristics of the present method of solution were briefly stated with a state-of-the-art review on computational methods of prediction for nonlinear wave forces on offshore structures by using BEM. The perturbation-based first- and second-order solution methods were stated for comparison with the fully nonlinear scheme. In order to investigate the capability of the present method, diffraction problem of a truncated circular cylinder is simulated. The present paper includes the numerical results with first-order solution only, while second-order and fully nonlinear methods are being developed and complete solutions are expected to come up soon. It is found out that the present method is fairly accurate for wave forces and run-ups on the whole when compared with experimental results and also with other numerical results. It is also demonstrated that highly nonlinear features manifest clearly for incident waves with high steepness, *i.e.* $H/\lambda = 1/16$ or $H/\lambda = 1/10$. These phenomena will be dealt with more thoroughly by fully nonlinear simulation in near future.

Acknowledgements

The author acknowledges support from a grant from the Ministry of Knowledge and Economics of Korea through the principal R&D program: "Core Methodologies for Design of LNG FSRU's Structure and Mooring System."

References

[1] Boo, S.Y. and Kim, C.H. "Fully nonlinear diffraction due to a vertical circular cylinder in a 3-D HOBEM numerical wave tank", Proceedings of the Sixth International Offshore and Polar Engineering Conference, 1996, 3, 23-30.
[2] Brebbia, C.A. *Topics in boundary element research. Vol. 1: Basic principles and applications*, 1984 (Springer-Verlag, Berlin).
[3] Dommermuth, D.G., Yue, D.K.P., Lin, W.M., Rapp, R.J., Chan, E.S. and Melville, W.K. "Deep-water plunging breakers: A comparison between potential theory and experiments", Journal of Fluid Mechanics, 1988, 184, 267-288.
[4] Ferrant, P. "Time domain computation of nonlinear diffraction loads upon three dimensional floating bodies", Proceedings of the Fifth International Offshore and Polar Engineering Conference, 1995, 3, 280-288.
[5] Ferrant, P. "Runup on a cylinder due to waves and current: Potential flow solution with fully nonlinear boundary conditions", Proc., 8th Int. Offshore and Polar Engineering Conf., Vol. 3, 1998, 332~339.
[6] Fochesato, C, Grilli, ST, and Guyenne, P. "Note on nonorthogonality of local curvilinear coordinates in a 3-D Boundary Element Method," *Intl. J. Num. Methods Fluids*, Vol. 48, 2005, 305–324.
[7] Grilli, S.T., Dias, F., Guyenne, P., Fochesato, C. and F. Enet (2008), "Progress In Fully Nonlinear Potential Flow Modeling of 3D Extreme Ocean Waves." Chapter in *Advances in Numerical Simulation of Nonlinear Water Waves* (Series in Advances in Coastal and Oc. Engng.). World Scientific Pub., 2009, 55 pps. (n Press)
[8] Grilli, S.T., P. Guyenne and F. Dias (2001), "A fully non-linear model for three-dimensional overturning waves over an arbitrary bottom," *Intl. J. Num. Methods Fluids*, 35, pp. 829-867.
[9] Guyenne, P. and Grilli, S.T. (2006), "Numerical study of three-dimensional overturning waves in shallow water," *J. Fluid Mech.*, 547, pp. 361-388.
[10] Kim, C.H. "Recent progress in numerical wave tank research", Proceedings of the Fourth International Offshore and Polar Engineering Conference, 1995, 3, 1-9.
[11] Kim, M.H., Celebi, M.S. and Park, J.C. "Nonlinear wave-body interactions by numerical wave tank simulations", Proceedings of the third international conference on hydrodynamics, 1998, 1, 139-144.
[12] Kristiansen, T., Baarholm, R. and Stansberg, C. T. "Validation of Second-order Analysis in Predicting Diffracted Wave Elevation around a Vertical Circular Cylinder", Proc., 14th ISOPE Conference, 2004, 342~349.

[13] Longuet-Higgins, M.S. and Cokelet, E.D. "The deformation of steep surface waves on water, I. A numerical method of computations", Proc. Roy. Soc. London, 1976, Ser. A, 350, 1-26.
[14] Nam, B.W., Sung, H.G., Kim, Y.S., and Hong, S.Y. "Linear and high-order computations for wave field around truncated cylinder in waves using finite element method", Journal of Ships & Ocean Engineering, Vol 46, pp. 43-52.
[15] Ralston, A. and Rabinowitz, P. *A first course in numerical analysis*, 2nd ed., 1978 (McGraw-Hill Book Company).
[16] Rienecker, M.M. and Fenton J.D. "A Fourier approximation method for steady water waves", Journal of Fluid Mechanics, 1981, Vol. 104, pp. 119~137
[17] Saad, Y. and Schultz, M.H. "GMRES: A generalized minimal residual algorithm for solving nonsymmetric linear systems", SIAM J. Sci. Stat. Comput., 1986, 7, 856-869.
[18] Sung, H.G. A numerical analysis of nonlinear diffraction problem in three dimensions by using higher-order boundary element method, 1999, Ph.D. Thesis (Seoul National University).
[19] Sung, H.G., Hong, S.Y. and Choi, H.S. "Evaluation of non-linear wave forces on a fixed body by the higher-order boundary element method", Journal of Mechanical Engineering Science (Proceedings of the Institution of Mechanical Engineers Part C), 2000, 214, 825-839.
[20] Sung, H.G., Nam, B.W., Hong, S.Y., Kim, Y.S., Kim, J.H. Kim, and Choi, S.K. "Experimental study of wave forces on a truncated circular cylinder in extreme seas", 2009, In preparation.
[21] Tanizawa K. Nonlinear simulation of floating bodies in waves, Proceedings of the Sixth International Offshore and Polar Engineering Conference 1996; 3: 414-420.
[22] Xü, H. Numerical study of fully nonlinear water waves in three dimensions, 1992, Ph.D. Dissertation (MIT).

Section 8
Electrical engineering and electromagnetics

This page intentionally left blank

Motion of nanoscale contaminant particles in air bearings under electrostatic charges: a case study

B. W. Yeigh[1], R. H. Polwort[2] & G. S. Gipson[3]
[1]*Office of the President,*
State University of New York Institute of Technology, USA
[2]*Plant Engineering, The Charles Machine Works, Inc., USA*
[3]*Department of Civil & Environmental Engineering,*
Oklahoma State University, USA

Abstract

This case study examines the possible effect that electrostatic forces may have on debris particle motion through the interface between two sliding surfaces in an air bearing. It uses as an example the read/write head and disk surface of a typical modern hard disk drive. The Reynolds equation for compressible fluids at high bearing numbers is solved using a factored implicit scheme. A first-order molecular slip correction is also applied. Debris particle motion equations are derived with corrections for gravity, drag, and the Saffman lift effect from previous studies and combined with an equation for electrostatic forces proposed in this study. Aluminum debris particles ranging from 150 to 300nm are introduced and tracked by solving motion equations using Runge-Kutta methods. Electrostatic forces acting on a debris particle were found to affect trajectories at levels of charge far lower than anticipated. Charges at levels as low as 1.5 electrons influenced particle motion significantly.

Keywords: molecular slip, Reynolds equation for compressible fluids, nano particles, factored implicit scheme, Runge-Kutta, surface mechanics, electrostatic forces, particle contamination.

1 Introduction

Air has a number of advantages as a lubricant: abundant supply, cleanliness, and lack of environmental and health issues associated with its use compared to a

WIT Transactions on Modelling and Simulation, Vol 49, © 2009 WIT Press
www.witpress.com, ISSN 1743-355X (on-line)
doi:10.2495/BE090331

petroleum-based product. However, because of its low viscosity, the speed of an air-lubricated bearing must be several times higher than an oil-lubricated bearing to support the same load. Even though the high speeds required by the air bearing preclude its use in some heavy load applications, there are just as many applications where air bearings are suited or even more ideal than oil-lubricated bearings. They include: machine tool spindles, turbo-machinery, instrument bearings such as gyroscopes, dental drills, textile processing devices, and magnetic media data recording devices (disk drives).

Loose particle(s) inside disk drives (e.g., air bearings) can be detrimental. With air bearing clearance in the sub 30nm level, the particle size does not have to be large to cause serious damages to the disk. Failed disk drives show buildup of debris on the head, possibly from loose particles and lubricant. Whether the loose particles come from fine particles accumulated on the leading edge tapers [10] or from contaminant whiskers that broke off from the trailing edge [8], these particles can lead to third-body abrasions of disk surface. Several questions arise. First, inside the air bearing, where do trapped particles go? Do they adhere to the slider/disk or wash out of the bearing? What operating conditions force loose particles to move towards the slider? When do they move toward the disk surface?

2 Numerical solution for the compressible Reynolds equation

Relying on the pressure generated by the relative motion of sliding surfaces, geometry, and fluid viscosity, hydrodynamic bearings push the contact surfaces apart. Through the converging gap, the fluid enters through the higher of the two opening known as the leading edge and exits the lower trailing edge by the relative motion of the surfaces. The Reynolds equation calculates the pressure generated between the two surfaces. In the continuum form, the differential equation is obtained from the Navier–Stokes and continuity equations. Derivations are easily found [2, 7, 16].

In the derivation, surfaces are assumed smooth and contain negligible traction. The Newtonian fluid between the surfaces obeys laminar flow rules. Constant fluid viscosity and isothermal conditions also apply. The inertial forces within the fluid are neglected. At the boundaries, nonslip conditions apply [1]. At steady state operations the time derivative goes to zero and is achieved when the pressure wave having half of the sliding velocity travels across the length of the bearing [15].

The extreme values of the clearance (i.e., $\sim 10^{-8}$m) require a correction to the conventional flow theory, which assumes the flow velocity at the boundary to equal the boundary velocity. This "no-slip" or continuum theory applied to compressible fluid at ultra-low clearances, the continuum Reynolds equation fails to deliver reasonable solutions. For Knudsen number $Kn << 1$, slip flow accurately models compressible gas lubrication conditions. Transitional flow occurs for Kn between 0.1 and 10; for even larger Kn, free molecular flow conditions exist in the bearings. The correction is made through the flow factor,

Q. Applying the above assumptions and conditions, Navier-Stokes and continuity equations with appropriate correction factors yield [12]:

$$\nabla \cdot \left(Qh^3 P \nabla P\right) = 6\mu V \cdot \nabla Ph + 12\mu \frac{\partial Ph}{\partial t} \tag{1}$$

where h, P, μ, V, t, and Q represent the characteristic length of the flow, bearing pressure, viscosity, velocity, time, and flow factor, respectively. With Q=1, the equation reduces to a continuum model. For this study, we use the first order slip model Q=1+(6aKn_0)/(PH), where a=(2-α)/α is the accommodation factor.

Although the finite element method (FEM) has been used in the solution of the Reynolds equation [14], the finite difference method appears to be the method of choice for many researchers [3, 4, 6, 9]. Singular perturbation techniques for asymptotic solution [5] had also been tried but had not gained popular support. In addition to the above numerical techniques, a widely known alternating direction implicit method is chosen to solve the Reynolds equation with first-order slip in this study. A factored implicit scheme (FIS) outlined in White and Nigam [15] is used with corrections made to the first del operator.

$$\nabla \cdot \left(hP \nabla P\right) + 6\lambda_a P_a \nabla \cdot \left(h^2 \nabla P\right) = 6\mu V \cdot \nabla Ph + 12\mu \frac{\partial Ph}{\partial t} \tag{2}$$

where h, P, λ_a, P_a, μ, and t represent the gas bearing spacing, gas bearing pressure, mean free path of the gas at ambient pressure, ambient pressure, lubricant viscosity, and time, respectively.

The bearing number, Λ, is a nondimensional quantity measuring the ratio of Couette flow to Poiseulle flow. Continuum solutions are invalid for high Λ. This question has been addressed through molecular gas film lubrication [6]. In traditional finite difference schemes with uniform meshes nonphysical oscillations propagate throughout the fluid, rendering the numerical solution useless. The question is addressed through variable meshing [15].

3 Lift effects on particle motion

A slider of length, l, and pitch, θ, rides above a disk spinning at $\hat{\Omega}$ (or slides with a linear velocity $\hat{U}$) is presented in fig. 1. The slider and disk are separated by h. The minimum clearance (h_m), slider length, and pitch angle are taken in the neighborhood of 3 μm, 2 mm, and 150 μrad, respectively. A spherical of diameter (100 to 350 nm), d, enters the air bearing.

The motion of a particle inside an air bearing can be described fully by its position vector $\vec{x}_p(x_p, y_p, z_p)$ and velocity vector $\vec{v}_p(u_p, v_p, w_p)$. Time derivatives result in six coupled differential equations that are solved simultaneously at each time step.

Zhang and Bogy [17, 18] considered the effects of lift on the motion of particles in the recessed region of a slider. This study examined four important forces inside the air bearing—drag, Saffman, Magnus, and gravity forces. Their

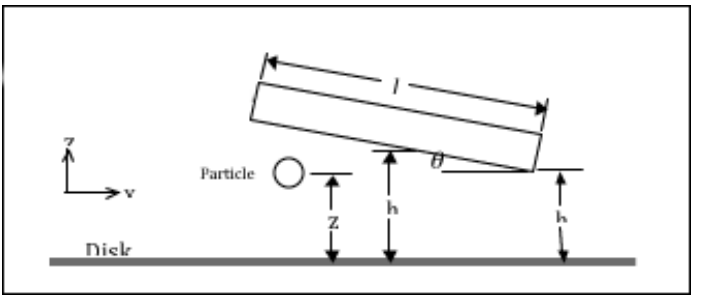

Figure 1: Simplified slider-disk assembly.

investigation revealed a relationship between the lift forces and particle size, relative velocity, and particle density.

Liu and his colleagues [11] used the Boltzmann equation to study the kinetic theory of sphere drag in transition flows. In addition to particle drag, the particle can be "lifted" in the direction perpendicular to the fluid flow, known as the Saffman lift force. If particle velocity is greater than fluid velocity, the force will point upward toward the slider, and vice versa [13]. This result is valid for very small Reynolds numbers. As the sphere flows through air, the gravitational pull (or push) is of order d^3. Compared to the drag components in the *x*-*y* plane, which is of order d^2, only the *z*-component is significant.

The fourth lift force considered by Zhang and Bogy is the Magnus force stemming from a spin of the sphere in a fluid. Mangus force, however, is an order of magnitude smaller than Saffman force and is not considered in the present study.

4 Effects of electrostatic charges on particle motion

It is difficult to measure exactly how much electrostatic charge is present in a contaminant particle. Consequently, the Bohr radius is used to estimate the maximum charge on an aluminum sphere. Given the diametrical range of 100-350nm, a 100nm aluminum sphere may hold roughly 844 million hydrogen atoms or equivalents. A 350nm sphere can hold in excess of 36 billion hydrogen atoms or equivalents. Assuming that each hydrogen atom is ionized, 100-350nm aluminum sphere can be charged on the order of 1.3516 x 10^{-10} Coulombs (C) and 5.7950 x 10^{-9} C, respectively. Coulomb's Law gives the electrostatic force:

$$f_E = \frac{1}{4\pi\varepsilon_0}\frac{Q_p Q^*}{r^2} = 8.9918\times10^6\frac{Q_p Q^*}{r^2} \tag{3}$$

where Q_p and Q^* measure electrostatic charges on the particle and slider (or disk). The distance between Q_p and Q^* is the value, *r*.

Drag, Saffman, gravity, and electrostatic forces combine to influence particle motion. Saffman, gravity, and electrostatic forces all act in the direction perpendicular to the fluid flow.

$$\dot{F}_p = f_{L(drag,Saffman,gravity,Magnus)} + f_E \tag{4}$$

Dimensional coordinates and bearing parameters are made dimensionless. Horizontal components are normalized with respect to slider length, and vertical components are divided by minimum height. The product of rotational speed $\hat{\Omega}$ and circumference yields the linear sliding velocity $\hat{U}$. Velocity components are normalized by $\hat{U}$, and time is multiplied by $\hat{\Omega}$ to produce T:

$$X = \frac{x}{l} \qquad U = \frac{u}{\hat{U}} \qquad T = \hat{\Omega}t \tag{5}$$

Applying the chain rule conveniently transforms other dimensional variables into dimensionless variables. For example,

$$\frac{dX_p}{dT} = \frac{dx_p}{dt}\frac{dt}{dT}\frac{dX_p}{dx_p} = \frac{\hat{U}}{\hat{\Omega}l}U_p, \qquad \frac{dY_p}{dT} = \frac{\hat{U}}{\hat{\Omega}l}V_p, \qquad \frac{dZ_p}{dT} = \frac{\hat{U}}{\hat{\Omega}l}W_p \tag{6}$$

Similarly, the acceleration components in the three orthogonal coordinates are also given by the chain rule. The *Z*-component acceleration has contributions from drag, Saffman, gravity, and electrostatic forces [12]:

$$\begin{aligned}\frac{dW_p}{dT} = {} & \frac{3}{4}\frac{\hat{U}}{\hat{\Omega}h_m}\frac{\rho_g}{\rho_p}\frac{C_D}{D}\overline{U}\left(W_g - W_p\right) + \frac{9.69}{\pi}\frac{\hat{U}\tilde{U}}{\hat{\Omega}h_m D}\frac{\rho_g}{\rho_p}\sqrt{\frac{v_g h_m \kappa}{\hat{U}^2 h_m}} \\ & + \frac{\hat{U}}{\hat{\Omega}h_m}\left(\frac{\rho_g}{\rho_p} - 1\right)\frac{h_m}{\hat{U}^2}g + \frac{1.717308\times 10^{10}}{\rho_p r^2 {h_m}^3 D^3}\frac{Q_p Q^*}{\hat{\Omega}\hat{U}}\end{aligned} \tag{7}$$

where C_D, ρ_g, κ, v_g, $\overline{U} = \frac{\left|\overline{v}_g - \overline{v}_p\right|}{\hat{U}}$, $D = \frac{d}{h_m}$, and $\tilde{U} = \frac{\Delta U}{\hat{U}}$ represent drag coefficient, gas density, velocity gradient, gas velocity, quotient of the velocity norm and sliding velocity, and dimensionless particle diameter, and dimensionless velocity, respectively.

A system of six coupled differential equations at each time step, ΔT, are solved using the classical Runge-Kutta method. Once solutions at time step *n+1* are found, the time derivatives in eqn. 6 are rewritten as simple slopes:

$$\frac{dX_p}{dT} \cong \frac{X_{p(n+1)} - X_{p(n)}}{\Delta T}, \frac{dY_p}{dT} \cong \frac{Y_{p(n+1)} - Y_{p(n)}}{\Delta T}, \frac{dZ_p}{dT} \cong \frac{Z_{p(n+1)} - Z_{p(n)}}{\Delta T} \tag{8}$$

The slope equations above accurately approach the true value of the derivatives using a very small time step, ΔT. Once positions at time step *(n+1)* are solved, all parameters in the acceleration equations are updated then iterated. The

iterations stop once the particle has either passed out of the air bearing or has impacted on the surfaces.

5 Numerical results

The air bearing used in this study has a typical cavity depth of 3μm and a 50nm flying height. Disk speed in the *x*-direction, $\hat{U}$, was set at 20 m/s. The particles chosen were assumed to consist of aluminum spheres with a density, ρ_p, of 4000 kg/m^3. Diameters of the particles used began at 150nm, which was incremented by 50nm for each new simulation, to a maximum particle diameter of 300nm. The following parameters were used for each simulation: initial position, $X_p = 0$, Y_p= *constant,* and $Z_p = 0.5$; initial velocity in *Y*-direction, $V_p = 0$; initial velocity in *Z*-direction, $W_p = 0$.

Initial particle velocity, U_p remains between 0.25 and 1.0 at the entrance to the bearing. Initial particle speeds slower than 0.25 or faster than 1.0 (1.0 is equal to the speed of the disk) are unlikely to occur in real world environments; therefore, although transport solutions are attainable for these numbers, they are trivial.

The results of the initial runs for trace number 1 (no electrostatic input) in figs. 2–5 agree with findings by Zhang and Bogy in their previous work because the Saffman lift force increases according to the square of the particle radius. Thus, particles below 100nm are negligibly affected. Electrostatic force was added in successive runs until the particle first impacted with either the slider or the disk. One equivalent H+ ion contains the same amount of charge as one electron, or 1.602 x 10^{-19}C. The measurement of charge in equivalent H+ ions is merely a convenient method to change the electrostatic charge of the particle within the confines of a numeric program. The use of equivalent H+ ions also puts an upper bound on the amount of maximum charge the particle can acquire. Through the use of the Bohr's radius of 5.29167x10^{-11}m, the volume of a hydrogen atom, can be calculated. The volume of a particle sphere is divided by

Table 1: Results from particle motion study.

Diameter (nm)	Trace No.	H+ Ions	Charge (x10^{18} C)
150	2	11.4	1.82
150	3	19.0	3.04
150	4	35.6	5.70
200	2	9.6	1.54
200	3	16.9	2.70
200	4	33.7	5.41
250	2	1.5	2.35
250	3	4.4	7.04
250	4	13.2	2.11
300	2	2.3	3.65
300	3	20.7	3.32
300	4	28.5	4.56

the volume of an H+ ion to determine the maximum number of ions possible in a given diameter.

Fig. 2 is a plot of the motion study results for a particle diameter of 150nm. The first impact occurred at an equivalent H+ ion number of 11.4. This is only a fraction of the maximum possible number of H+ ions of 2.85 x 10^9. Trace (3) impacted at H+ ions equal to 19.0 and trace (4) impacted at H+ ions equal to 35.6. Note the electrostatic force in trace number 4 exceeded the small Saffman force and impacted the disk.

The results for a particle diameter of 200nm are represented in fig. 3. Initial particle speed for all runs of d = 200nm was 1.0. The first impact occurred at an equivalent H+ ion count of 9.6. Successive impacts were noted at H+ counts of 16.8 and 33.7.

Fig. 4 shows results from the study of a particle with a diameter of 250nm for initial speed of 1.0. The effect of the Saffman force dominating drag and gravity is shown through the sharp upward swing of trace (1). The number of equivalent H+ ions to first impact on trace (2) is only 1.5. This is a significant decrease. Trace (4) impact occurred at 13.2 equivalent H+ ions.

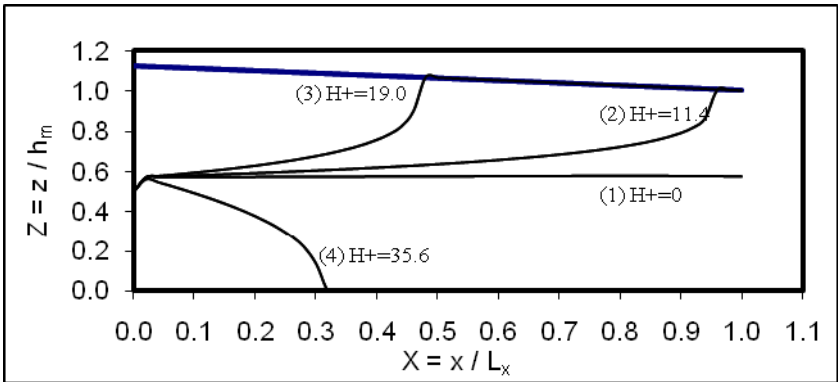

Figure 2: Particle diameter 150nm.

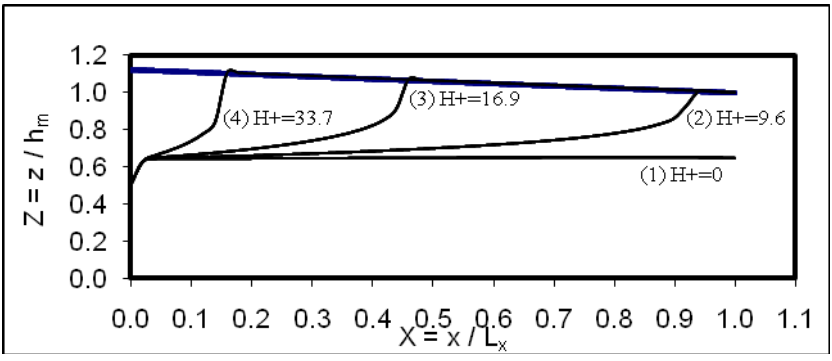

Figure 3: Particle diameter 200nm.

The last particle size studied has a diameter of 300nm. The results are plotted as fig. 5. At this particle size and larger, gravity and drag forces are insignificant. At this particle size the trajectory is very sensitive to the initial speed. However, the first impact occurred at an equivalent H+ ion count of 2.3, which is slightly higher than the first impact of the particle of fig. 4. This may be due to discrepancies in the model resulting from the differing initial speed, but is more likely to be caused by the particle's increasing mass. Successive impacts occurred at H+ counts of 20.7 and 28.5. These counts too are higher than the d = 250nm particle, but note that the Saffman force has been exceeded with impact occurring on the disk.

6 Conclusions

If electrostatic charges are present in the air bearing, they can be a significant factor in the path taken by a particle. All particle trajectories through the air bearing were affected at lower charges than anticipated, which makes the

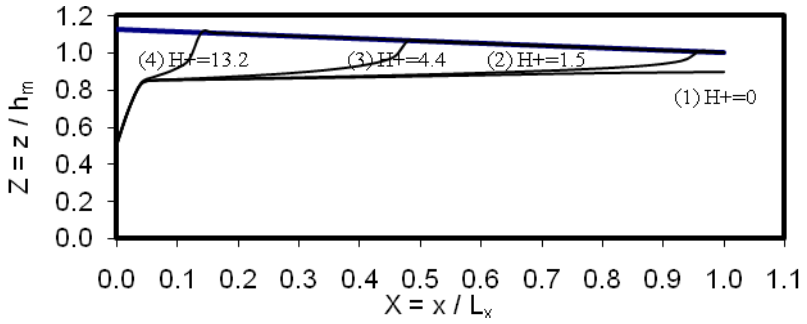

Figure 4: Particle diameter 250nm.

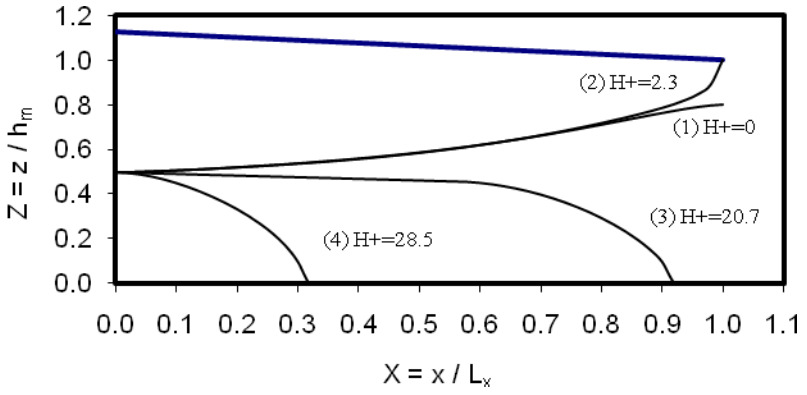

Figure 5: Particle diameter 300nm.

findings of this study very significant. Only a minute charge is needed to induce a trajectory change. This small magnitude (~1.5 H+ ions, or 2.35x 10^{-19}C) might be sufficient to ionize particles that exert an electrostatic force. Electrostatic charges are very likely present at these small magnitudes. High-speed debris flows are well known to produce electrostatic charges.

If electrostatic forces are generated within the bearing, then there are surely instances when even fewer charges than simulated can be present. Such an amount will affect a trajectory change. The initial particle height in all trial runs was set at a conservative $Z_p = 0.5$. Trial runs conducted at initial height closer to the disk or slider have resulted in trajectory changes at some very low magnitudes.

It is proposed that electrostatic forces could explain why debris tends to accumulate in the cavity area. If such debris enters the cavity area on the slider, a charged particle would tend to remain.

Understanding particle path changes at very low electrical charges could be significant. In the presence of electrostatic charges in modern air bearings, contaminant control methods in the hard disk drive environment will need to be devised. What effects do oscillating charges have on particle motion? To illustrate, after writing the particle transport program, the first initial runs produced a few particle paths that oscillated between the disk and plate surfaces like a sine wave. Realizing such an event is a low probability it was discovered the routine that examined the distance r in the electrostatic force was reversed to select the longest dimension. This reversed the direction of the electrostatic force and produced *repulsion*. If the slider could push the particles, impact damage on the disk surface and debris accumulation on the slider could be possible.

Dedication and acknowledgement

This paper is dedicated to Dr. G. Steven Gipson who passed away on April 22, 2009 after a long courageous battle with pancreatic cancer. Over the past three decades he made significant contributions in engineering mechanics at all scales, especially in boundary element methods. The authors acknowledge Seagate Technology for initial funding for this work.

References

[1] Bhushan, B., (ed.), *Tribology and Mechanics of Magnetic Storage Devices*, New York, Springer-Verlag, 1990.

[2] Cameron, A., *Basic Lubrication Theory*, 3rd ed., Wiley: New York, Wiley, 1981.

[3] Castelli, V. & Pirvics, J., Review of Numerical Methods in Gas Bearing Film Analysis. *Journal of Lubrication Technology*, pp. 778-792, 1968.

[4] Coleman, R, The Numerical Solution of Linear Elliptic Equations. *Journal of Lubrication Technology*, pp. 773-776, 1968.

[5] DiPrima, R.C., Asymptotic Method for an Infinitely Long Slider Squeeze-Film Bearing. *Journal of Lubrication Technology*, pp. 173-183, 1968.
[6] Fukui, S. & Kaneko, R., Analysis of Ultra-Thin Gas Film Lubrication Based on Linearized Boltzmann Equation: First Report—Derivation of a Generalized Lubrication Equation Including Thermal Creep Flow. *Journal of Tribology*, 110, pp. 253-262, 1988.
[7] Gross, W., Matsch L., Castelli, V., Eshel, A., Vohr, J. & Wildmann, M., *Fluid Film Lubrication*, Wiley: New York, 1980.
[8] Hiller B. & Singh, G., Interaction of Contamination Particles With the Particulate Slider/Disk Interface. *Advanced Information Storage Systems*, 173(2), 1991.
[9] Hu, Y. & Bogy, D., Dynamic Stability and Spacing Modulation of Sub-25nm Fly Height Sliders. *Journal of Tribology*, 119, pp. 646-652, 1997.
[10] Koka, R. & Kumaran, A., Visualization and Analysis of Particulate Buildup on the Leading Edge Taper Sliders. *Advanced Information Storage Systems*, 161(2), 1991.
[11] Liu, V., Pang, S. & Jew, H., Sphere Drag in Flows of Almost-Free Molecules. *Physics of Fluids*, 8(5), pp. 788-796, 1965.
[12] Polwort, R., Motion of Nanoscale Contaminant Particles in Air Bearings, Master's thesis, Oklahoma State University, 1999.
[13] Saffman, P., The Life on a Small Sphere in a Slow Shear Flow. *Journal of Fluid Mechanics*, 22(2), pp. 385-400, 1965.
[14] Tokuyama, M. & Shinichi, H., Dynamic Flying Characteristics of Magnetic Head Slider With Dust. *Journal of Tribology*, 116, pp. 95-100, 1994.
[15] White, J. & Nigam, A., A Factored Implicit Scheme for the Numerical Solution of the Reynolds Equation at Very Low Spacing. *Transactions of the ASME*, 102, pp. 80-85, 1980.
[16] Williams, J., *Engineering Tribology*, Oxford: New York, 1994.
[17] Zhang, S. & Bogy, D., Effects of Lift on the Motion of Particles in the Recessed Regions of a Slider. *Physics of Fluids*, 9, pp. 1265-1272, 1997.
[18] Zhang, S. & Bogy, D., Slider Designs for Controlling Contamination. *Journal of Tribology*, 119, pp. 537-540, 1997.

Boundary element modeling of horizontal grounding electrodes using the set of generalized telegrapher's equations

D. Poljak[1], K. El Khamlici Drissi[2] & R. Goic[1]
[1]*University of Split, Croatia*
[2]*Blaise Pascal University, France*

Abstract

The analysis of a horizontal grounding electrode has been carried out using the set of generalized telegrapher's equations. The integro-differential relationships arising from the full wave model are numerically handled via the Galerkin–Bubnov scheme of the Indirect Boundary Element Method (GB-IBEM). Some illustrative numerical results for the current and voltage induced along the horizontal electrode are given in the paper.

Keywords: boundary elements, grounding systems, antenna theory, generalized telegrapher's equations.

1 Introduction

Studies of grounding systems, because they are an important component in lightning protection systems (LPS), are of great interest in electromagnetic compatibility (EMC) and high voltage (HV) applications. One of the applications of particular interest nowadays is LPS for wind turbines. As they are environmentally attractive (no pollution) and wind is free to use these wind turbines have been widely used. On the other hand, they are extremely vulnerable to lightning strikes due to their special shape and isolated locations mainly in high altitude areas. Analysis of grounding systems can be undertaken by the aid of the transmission line model (TLM) [1–3] or the full wave model, also referred to as the antenna model (AM) [4–6]. The latter is considered to be the rigorous one. The key-parameter in the full wave model is the equivalent current distribution along the grounding electrode. The full wave model of the

WIT Transactions on Modelling and Simulation, Vol 49, © 2009 WIT Press
www.witpress.com, ISSN 1743-355X (on-line)
doi:10.2495/BE090341

electrode presented in this work is based on the set of Telegrapher's equations. In particular, the effect of a lossy ground is taken into account via the corresponding reflection coefficient thus avoiding the rigorous approach based on the analytically demanding and numerically time consuming Sommerfeld integrals. The integro-differetial expressions arising from the proposed full wave model are numerically treated by means of the Galerkin-Bubnov scheme of the Boundary Element Method (GB-IBEM) [7]. Solving the set of generalized telegrapher's equations first the current distribution and subsequently the scattered voltage along the electrode are obtained.

2 Equivalent antenna model of the grounding electrode

The geometry of interest, shown in Fig 1, is the horizontal grounding electrode of length L and radius a, buried in a lossy medium at depth d and excited by an equivalent current source.

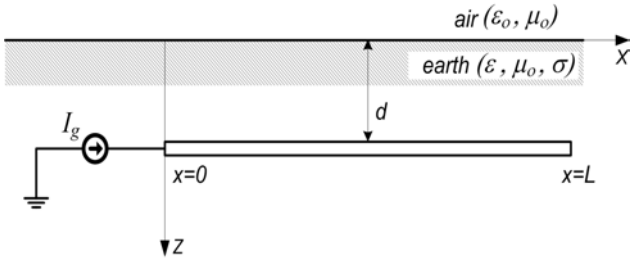

Figure 1: Horizontal grounding wire energized by a current generator I_g.

The wire dimensions are assumed to satisfy the thin wire approximation (TWA) conditions [7, 8].

2.1 The generalized telegrapher's equations for a horizontal grounding electrode

The governing equations for the current and voltage induced along the grounding electrode can be derived by enforcing the continuity conditions for the tangential components of the electric field along the wire surface.

The total field composed from the excitation field $\vec{E}^{exc}$ and scattered field $\vec{E}^{sct}$ is equal to the product of the current along the electrode $I(x)$ and surface internal impedance $Z_s(x)$ per unit length of the electrode:

$$\vec{e}_x \cdot \left(\vec{E}^{exc} + \vec{E}^{sct} \right) = Z_s(x) I(x) \quad \text{on the wire surface} \tag{1}$$

The surface internal impedance $Z_s(x)$ is given by [9, 10]:

$$Z_s(x) = \frac{Z_{cw}}{2\pi a} \frac{I_0(\gamma_{wa})}{I_1(\gamma_{wa})} \tag{2}$$

where $I_0(\gamma_w)$ and $I_1(\gamma_w)$ are modified Bessel functions of the zero and first order respectively, while Z_{cw} and γ_w are given by [9, 10]:

$$Z_{cw} = \sqrt{\frac{j\omega\mu_w}{\sigma_w + j\omega\varepsilon_w}} \tag{3}$$

$$\gamma_w = \sqrt{j\omega\mu(\sigma_w + j\omega\varepsilon_w)} \tag{4}$$

For the case of very good conductors (conductivity of order of 10^6 S/m), the surface impedance $Z_s(x)$ can be neglected. The scattered electric field can be expressed in terms of the vector potential $\vec{A}$ and the scalar potential φ, and according to the thin wire approximation [7, 8] only the axial component of the magnetic potential differs from zero and it can be written:

$$E_x^{sct} = -j\omega A_x - \frac{\partial\varphi}{\partial x} \tag{5}$$

The vector and scalar potential are, respectively, given by particular integrals:

$$A_x = \frac{\mu}{4\pi}\int_0^L I(x')g(x,x')dx' \tag{6}$$

$$\varphi(x) = \frac{1}{4\pi\varepsilon_{eff}}\int_0^L q(x')g(x,x')dx' \tag{7}$$

The complex permittivity of the lossy ground ε_{eff} is given by:

$$\varepsilon_{eff} = \varepsilon_r\varepsilon_0 - j\frac{\sigma}{\omega} \tag{8}$$

with ε_{rg} and σ being the corresponding permittivity and conductivity, respectively, of the ground, while $q(x)$ denotes the charge distribution along the line, $I(x')$ is the induced current along the line, and $g(x,x')$ is the corresponding Green's function of the form:

$$g(x,x') = g_0(x,x') - \Gamma_{ref}\,g_i(x,x') \tag{9}$$

where $g_0(x,x')$ denotes the lossy medium Green function:

$$g_0(x,x') = \frac{e^{-\gamma R_1}}{R_1} \tag{10}$$

and $g_i(x,x')$ is, according to the image theory, given by:

$$g_i(x,x') = \frac{e^{-\gamma R_2}}{R_2} \tag{11}$$

while the propagation constant of the lower medium is defined as:

$$\gamma = \sqrt{j\omega\mu\sigma - \omega^2\mu\varepsilon} \tag{12}$$

and R_1 and R_2 are given by:

$$R_1 = \sqrt{(x-x')^2 + a^2}, \quad R_2 = \sqrt{(x-x')^2 + 4d^2} \tag{13}$$

The influence of a ground-air interface is taken into account via the following reflection coefficient (RC) [6]:

$$\Gamma_{ref} = \frac{\frac{1}{\underline{n}}\cos\theta - \sqrt{\frac{1}{\underline{n}} - \sin^2\theta}}{\frac{1}{\underline{n}}\cos\theta + \sqrt{\frac{1}{\underline{n}} - \sin^2\theta}}; \quad \theta = arctg\frac{|x-x'|}{2d}; \quad \underline{n} = \frac{\varepsilon_{eff}}{\varepsilon_0} \tag{14}$$

The main advantage of RC approach versus rigorous Sommerfeld integral approach is a simplicity of the formulation and appreciably less computational cost. Generally, RC approach produces results roughly within 10% of these obtained via rigorous Sommerfeld integral approach [7]. The linear charge density and the current distribution along the electrode are related through the continuity equation:

$$q = -\frac{1}{j\omega}\frac{dI}{dx} \tag{15}$$

Substituting continuity equation (15) into (7) gives:

$$\varphi(x) = -\frac{1}{j4\pi\omega\varepsilon_{eff}}\int_0^L \frac{\partial I(x')}{\partial x'} g(x,x')dx' \tag{16}$$

while substituting equations (6) and (16) into (5) leads to the following integral relation for the scattered electric field:

$$E_x^{sct} = -j\omega\frac{\mu}{4\pi}\int_0^L I(x')\,g(x,x')\,dx' + \frac{1}{j4\pi\omega\varepsilon_{eff}}\frac{\partial}{\partial x}\int_0^L \frac{\partial I(x')}{\partial x'}\,g(x,x')\,dx' \tag{17}$$

Finally, for the case of grounding electrodes the excitation function does not exist in the form of the tangential field, i.e. [4]:

$$E_x^{exc} = 0 \tag{18}$$

Combining equations (1), (17) and (18) results in the following homogeneous integral equation of the Pocklington type for the unknown current distribution induced along the horizontal grounding electrode:

$$j\omega\frac{\mu}{4\pi}\int_0^L I(x')g(x,x')\,dx' - \frac{1}{j4\pi\omega\varepsilon_{eff}}\frac{\partial}{\partial x}\int_0^L \frac{\partial I(x')}{\partial x'}g(x,x')\,dx' + Z_s(x)I(x) = 0 \tag{19}$$

The knowledge of the current distribution induced along the electrode provides the assessment of the scattered voltage. To derive the telegrapher's type equations for the current and voltage induced along the electrode, the scattered voltage concept has to be included in the formulation. The scattered voltage along the horizontal electrode is defined by a line integral of a scattered vertical field component from the remote soil to the wire surface:

$$V^{sct}(x) = -\int_{\infty}^{d} E_z^{sct}(x,z)dz \tag{20}$$

The vertical field component can be expressed in terms of the scalar potential gradient, i.e.:

$$E_z^{sct} = -\frac{\partial \varphi}{\partial z} \tag{21}$$

and the scattered voltage along the wire can be written as follows:

$$V^{sct}(x) = \int_{-\infty}^{d} \frac{\partial \varphi}{\partial z} dz = \frac{d}{dz} \int_{-\infty}^{d} \varphi(x,z)dz \tag{22}$$

Integration from the infinite soil to the conductor surface and assuming the scalar potential in the remote soil to be zero [11] and according to equation (16) leads to the scattered voltage along the electrode:

$$V^{sct}(x) = -\frac{1}{j4\pi\omega\varepsilon_{eff}} \int_0^L \frac{\partial I(x')}{\partial x'} g(x,x')dx' \tag{23}$$

Combining equations (19) and (23) results in the set of the generalized telegrapher's equations for the horizontal grounding electrode:

$$\int_0^L \frac{\partial I(x')}{\partial x'} g(x,x')dx' + Y'V^{sct}(x) = 0 \tag{24}$$

$$\frac{dV^{sct}(x)}{dx} + j\omega L' \int_0^L I(x')g(x,x')dx' + Z_s(x)I(x) = 0 \tag{25}$$

where the corresponding equivalent inductance, admittance, capacitance and conductance per unit length of the wire are given by:

$$L' = \frac{\mu}{4\pi} \tag{26}$$

$$Y' = j4\pi\omega\varepsilon_{eff} = G' + j\omega C', \qquad C' = 4\pi\varepsilon, \qquad G' = 4\pi\sigma \tag{27}$$

2.2 The current source excitation

The grounding electrode is energized by the injection of an equivalent ideal current source with one terminal connected to the grounding electrode and the other one grounded at infinity, as shown in Fig 1. This current source is included into the integro-differential equation formulation through the following boundary conditions:

$$I(0) = I_g, \quad I(L) = 0 \tag{28}$$

where I_g denotes the impressed unit current generator.

3 Boundary element procedures

The unknown current $I^e(x)$ along the wire segment can expressed, as follows:

$$I^e(x') = \{f\}^T \{I\} \tag{29}$$

Collecting the contributions from each element the integro-differential equation (19) is transferred into the following matrix equation:

$$\sum_{j=1}^{M} [Z]_{ji} \{I\}_i = 0, \qquad \text{and} \quad j = 1, 2, ..., M \tag{30}$$

where M is the total number of segments and $[Z]_{ji}$ is the mutual impedance matrix representing the interaction of the i-th source with the j-th observation segment, respectively:

$$[Z]_{ji} = -\frac{1}{4 j\pi\omega\varepsilon_{eff}} \left(\int_{\Delta l_j} \{D\}_j \int_{\Delta l_i} \{D'\}_i^T g(x,x')dx'dx + \right.$$
$$\left. + k^2 \int_{\Delta l_j} \{f\}_j \int_{\Delta l_i} \{f\}_i^T g(x,x')dx'dx \right) + \int_{\Delta l_j} Z_L(x) \{f\}_j \{f\}_i^T dx \tag{31}$$

Matrices $\{f\}$ and $\{f'\}$ contain the shape functions while $\{D\}$ and $\{D'\}$ contain their derivatives, and Δl_i, Δl_j are the widths of i-th and j-th boundary elements. A linear approximation over a boundary element is used in this work:

$$f_i = \frac{x_{i+1} - x'}{\Delta x} \qquad f_{i+1} = \frac{x' - x_i}{\Delta x} \tag{32}$$

as this choice was proved to be optimal one in modeling various wire structures.

The excitation function in the form of the current source I_g is taken into account as a forced boundary condition at the first node of the solution vector, i.e.:

$$I_1 = I_g \quad \text{and} \quad I_g = 1e^{j0} \tag{33}$$

Once the current distribution is obtained the scattered voltage defined by equation (23) can be readily evaluated using the boundary element formalism.

As the differentiation of the current distribution variation along the segment is simply given by:

$$\frac{\partial I(x')}{\partial x'} = \frac{I_{i+1} - I_i}{\Delta x} \tag{34}$$

the scattered voltage can be computed from the following formula:

$$V^{sct}(x) = -\frac{1}{j4\pi\omega\varepsilon_{eff}} \sum_{i=1}^{M} \frac{I_{i+1} - I_i}{\Delta x} \int_{x_i}^{x_{i+1}} g(x,x')dx' \tag{35}$$

4 Numerical results

Figure 2 shows the frequency response at the center of the electrode characterized by the following parameters: L=20m, d=1m, a=5mm and I_g=1A. The ground conductivity is σ=0.01 S/m while the permittivity is ε_r=10. The results computed via the BEM and the Modified Transmission Line Model (MTLM) are compared to the results obtained via NEC using Sommerfeld integral approach to account for the presence of the ground-air interface. The agreement between the results obtained via the different approaches is found to be relatively satisfactory for the given set of parameters.

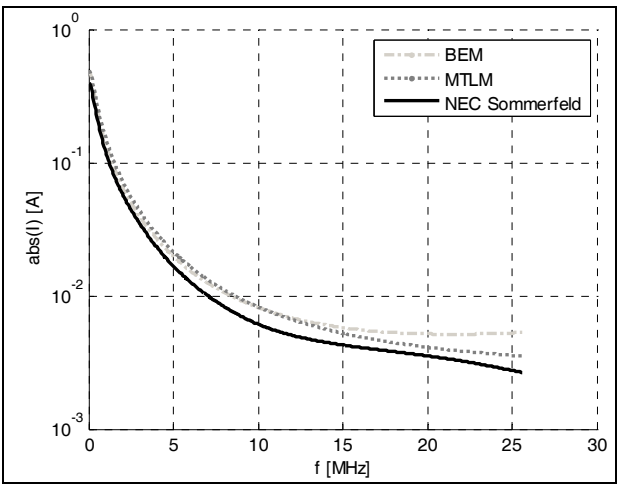

Figure 2: Current induced at the center of the grounding wire versus frequency (L=20m, d=1m, a=5mm, σ=0.01 S/m, ε_r=10).

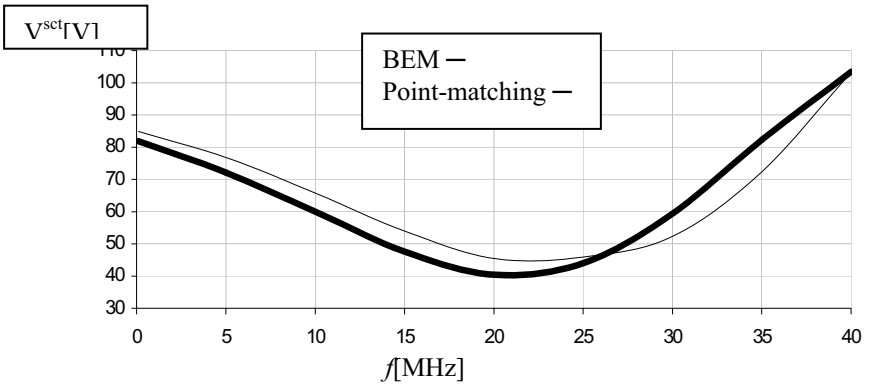

Figure 3: Voltage spectrum at the input of the grounding electrode (L=10m, d=1m, a=5mm, σ=0.01 S/m, ε_r=10).

Figure 3 shows the voltage spectrum at the driving point for a horizontal grounding electrode characterized by the following parameters: L=10m, d=1m, a=5mm and I_g=1A. The ground conductivity is σ=0.01S/m, while the permittivity is ε_r=10.

The agreement between the results obtained via BEM is in a plausible agreement with the results obtained via point matching technique.

5 Concluding remarks

The paper deals with modeling of grounding systems based on the generalized telegrapher's equations and related boundary element procedures. The integral relationships arising from the full wave model are numerically treated by using the Galerkin–Bubnov scheme of the Indirect Boundary Element Method (GB-IBEM). The results obtained for the current distribution and scattered voltage induced along the horizontal grounding electrode agree satisfactorily with the results obtained via other methods.

Future work will involve the treatment of complex grounding systems including interconnected conductors.

References

[1] Y. Liu, M. Zitnik, R. Thottappillil, "An Improved Transmission Line Model of Grounding System", IEEE Trans. EMC, Vol.43, No.3, pp. 348-355, 2001.

[2] G. Ala, M. L. Di Silvestre, "A Simulation Model for Electromagnetic Transients in Lightning Protection Systems", IEEE Trans. EMC, Vol.44, No.4, pp.539-534, 2003.

[3] M.I. Lorentzou, N.D. Hatziargyriou, C.Papadias, "Time Domain Analyisis of Grounding Electrodes Impulse Response", IEEE Trans. Power Delivery, No 2., pp. 517-524, Apr. 2003.

[4] L. Grcev , F. Dawalibi, "An Electromagnetic Model for Transients in Grounding Systems", IEEE Trans. Power Delivery, No 4., pp. 1773-1781, Oct. 1990.

[5] L. D. Grcev, F.E. Menter, "Transient Electro-magnetic Fields Near Large Earthing Systems", IEEE Trans. Magnetics, Vol. 32, pp. 1525-1528, May 1996.

[6] D. Poljak, V. Roje, "The Integral equation method for ground wire impedance", Constanda, C., Saranen, J., Seikkala, S. (Ed), Integral methods in science and engineering, Vol. I, Longman, UK., 139-143, 1997.

[7] D. Poljak, "Electromagnetic Modelling of Wire Antenna Structures", WIT Press, Southampton-Boston, 2002.

[8] R.G. Olsen, M.C. Willis, "A Comparison of Exact and Quasi-static Methods for Evaluating Grounding Systems at High Frequencies", IEEE Trans. Power Delivery, Vol. 11, No 2, pp. 1071-1081, April 1996.

[9] F. Tesche, M. Ianoz, F. Carlsson, *EMC Analysis Methods and Computational Models*, John Wiley and Sons, New York 1997.

[10] D. Poljak, F. Rachidi, S. Tkachenko, Generalized Form of Telegrapher's Equations for the Electromagnetic Field Coupling to Finite Length Lines above a Lossy Ground, *IEEE Trans. EMC,* Vol. 49, No 3., pp. 689-697, Aug. 2007.
[11] D. Poljak, Generalized Form of Telegrapher's Equations for the Electromagnetic Field Coupling to Buried Wires of Finite Length, *IEEE Trans. EMC,* 2009.
[12] J. Wallart, K. E. K. Drissi, F. Paladian, "Study of propagation constant for a single buried wire in a lossy ground," in *Proc. EMC '98 Symposium*, vol. 2, Roma, 1998, pp. 557–562.

This page intentionally left blank

Provisional study on the 3-D Cauchy condition surface method for fusion plasma shape identification

M. Itagaki[1], T. Maeda[1], A. Wakasa[1] & K. Watanabe[2]
[1]*Graduate School of Engineering, Hokkaido University, Japan*
[2]*National Institute for Fusion Science, Japan*

Abstract

The 2-dimensional (2-D) Cauchy condition surface (CCS) method to identify the plasma boundary shape has been expanded to deal with 3-D nuclear fusion plasma. This 3-D CCS method solves a set of boundary integral equations in terms of 3-D vector potential with the aid of measured magnetic sensor signals and coil current data. Results obtained in a trial calculation for axisymmetric plasma indicate that this new 3-D method can also determine the plasma boundary shape accurately in the same way as the 2-D CCS method. The authors' research group has a plan to improve this 3-D CCS method to analyse fusion plasma that has a helical geometry.

Keywords: nuclear fusion, plasma boundary, Cauchy condition surface method, magnetic sensor, vector potential, vacuum field, boundary integral equation.

1 Introduction

To know the boundary shape of plasma in a nuclear fusion device is important for the control of its operation and for diagnostic purposes. As the plasma temperature in such a device is higher than a hundred million deg. K (Kelvin), it is almost impossible to place any sensor inside the plasma. Usually, the plasma boundary shape is indirectly estimated with the aid of on-line computing from signals of magnetic sensors located outside the plasma. For this purpose, the Cauchy condition surface (CCS) method [1] has already been established for a tokamak-type fusion device, e.g., the JT-60 of the Japan Atomic Energy Agency (JAEA). Here, the Cauchy condition surface (CCS) is defined as a surface where

WIT Transactions on Modelling and Simulation, Vol 49, © 2009 WIT Press
www.witpress.com, ISSN 1743-355X (on-line)
doi:10.2495/BE090351

both the Dirichlet and the Neumann conditions are unknown. The geometry of tokamak plasma is axisymmetric so that the analysis using the CCS method can be made in a 2-dimensional (2-D), r-z system. On the other hand, 3-D analyses are required for non-axisymmtric plasma, e.g., in a helical type device such as the LHD (Large Helical Device) of the National Institute for Fusion Science (NIFS), Japan. The CCS method, however, has not yet been expanded for application to a 3-D space analysis.

The aim of the present work is to investigate whether the CCS method can also be applied to a 3-D system that has a much larger number of unknowns than a 2-D system. Modifying a 3-D boundary element code to solve the Poisson equation, a prototype of 3-D CCS method code has been developed. The present paper deals with tokamak-type axisymmetric plasma, which can be also analyzed using the 2-D CCS method, to demonstrate the fundamental performance as a 3-D code. The authors intend to tackle an actual 3-D geometry such as the helical one in a later paper.

2 Three-dimensional CCS method

In the 3-D version of the CCS method proposed here, the CCS (Γ_C) is assumed to have a torus shape and to be located in the actual plasma region in 3-D space, as illustrated in fig. 1. In the present work the Dirichlet condition and the Neumann condition along the CCS are the vector potential and its derivative, respectively, while they were the magnetic flux and its derivative in the conventional 2-D CCS method [1, 2].

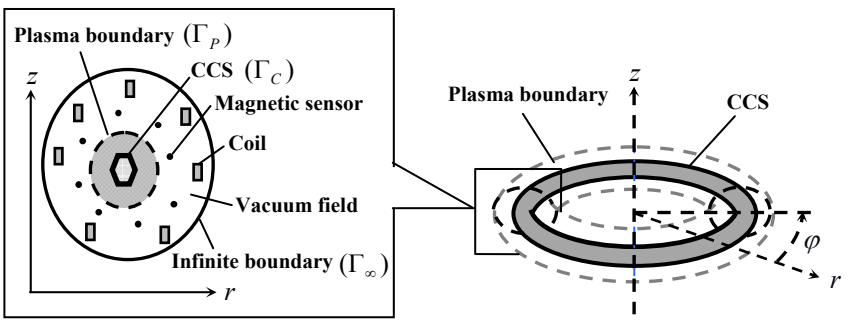

Figure 1: Extention of CCS method to a 3-D system.

The torus shape CCS is divided into a certain number of boundary elements, each of which has 9 nodal points. The first step of the analysis is to obtain the values of the Dirichlet and Neumann conditions at each nodal point in such a way that they will be consistent with the magnetic sensor signals. For this purpose, one solves the set of boundary integral equations for a vacuum field in the same way adopted in the 2-D CCS method calculation.

2.1 Vector Laplacian

The magnetic field $\mathbf{B}$ is given by $\mathbf{B} = \nabla \times \mathbf{A}$ in terms of the vector potential $\boldsymbol{A}$. The relationship between $\boldsymbol{A}$ and the current density $\boldsymbol{j}$ is described by the Poisson equation

$$\nabla^2 \boldsymbol{A} = -\mu_0 \boldsymbol{j} . \tag{1}$$

In a 3-D Cartesian coordinate system, the two quantities in eqn (1) are expressed as $\boldsymbol{A} = (A_x, A_y, A_z)$ and $\boldsymbol{j} = (j_x, j_y, j_z)$. The vector Laplacian in this system has the simple relationship

$$(\nabla^2 \boldsymbol{A})_k = \nabla^2 A_k \quad (k = x, y, z) . \tag{2}$$

That is, the vector Laplacian can be given by a set of the scalar Laplacian of each Cartesian scalar component. In a cylindrical or spherical coordinate system, on the other hand, the expression of the vector Laplacian is not so straightforward. Because of this, the authors adopt the 3-D Cartesian coordinate system for the analysis to obtain the 3-D distribution of vector potential. However, it is easy to transform the result, once calculated in the Cartesian coordinate system, into the other coordinate systems.

2.2 Hypothetical assumption of vacuum field

One here assumes mathematically that there is no plasma current, i.e., vacuum everywhere outside the CCS. The effect of the actual plasma current is transformed into the hypothetical CCS. It is interesting to point out that at any point outside the plasma boundary the vector potential calculated under this assumption is exactly the same as the vector potential caused by the existence of the plasma current. The proof for this is given in the Appendix.

2.3 Boundary integral equations

Assuming that the current density term in eqn (1) is the coil current only, the corresponding boundary integral equations for a vacuum field are given by eqns (3) and (4), using the sensor signals and the coil current data.

(i) For points i on the CCS (Γ_C):

$$\int_{\Gamma_C} \left(\phi_i^* \frac{\partial A_k}{\partial n} - A_k \frac{\partial \phi_i^*}{\partial n} \right) d\Gamma = \frac{1}{2} A_{k,i} . \quad (k = x, y, z) . \tag{3}$$

(ii) For the magnetic sensor locations i:

$$\int_{\Gamma_C} \left\{ \left(\mathcal{L} \phi_i^* \right) \frac{\partial A_k}{\partial n} - A_k \left(\mathcal{L} \frac{\partial \phi_i^*}{\partial n} \right) \right\} d\Gamma = (\mathcal{L} A_{k,i}) - \mathcal{L} W_{k,i} . \quad (k = x, y, z) . \tag{4}$$

The fundamental solution ϕ_i^* in eqns (3) and (4) satisfies the 3-D scalar Laplace equation with the Dirac delta function

$$\nabla^2 \phi_i^* = \delta_i . \tag{5}$$

The quantity $W_{k,i}$ in eqn (4) is the contribution of external coil currents to the vector potential at the point i, which can be calculated following

$$(W_{x,i}, W_{y,i}, W_{z,i}) = \mathbf{W}_i = \frac{\mu_0}{4\pi} \sum_{L \in Coils} \int_{\Omega} \frac{\mathbf{j}_L(\mathbf{r}_L)}{|\mathbf{r}_i - \mathbf{r}_L|} d\Omega_L \tag{6}$$

with $\mathbf{j}_L(\mathbf{r}_L)$ being the electric current density of the L-th coil. Equation (6) can be simplified for an axisymmetric tokamak device. That is, the coil contribution can be represented as a scalar quantity

$$W_i = \mu_0 \sum_{L \in Coils} I_L \, \psi^*(r, z; a, b) \tag{7}$$

using the L-th coil current I_L and the fundamental solution of the Grad-Shafranov equation for the axisymmetric geometry [1, 2]

$$\psi^*(r, z; a, b) = \frac{\sqrt{ar}}{\pi k} \left[\left(1 - \frac{k^2}{2} \right) K(k) - E(k) \right] \tag{8}$$

with

$$k^2 = \frac{4ar}{(r+a)^2 + (z-b)^2}. \tag{9}$$

The functions $K(k)$ and $E(k)$ are the complete elliptic integrals of the first and second kinds, respectively.

The detailed form of the operator $\mathcal{L}$ in eqn (4) depends on the type of magnetic sensor. In the tokamak-type device, for example, $\mathcal{L}$ is unity for magnetic flux sensors, while for magnetic field sensors it is given by

$$\mathcal{L} = \sin\theta \frac{1}{r} + \sin\theta \cos\varphi \frac{\partial}{\partial x} + \sin\theta \sin\varphi \frac{\partial}{\partial y} - \cos\theta \frac{\partial}{\partial z}, \tag{10}$$

where r denotes the major radius, φ the toroidal angle and θ the sensor angle respectively, at the sensor position.

Equations (3) and (4) are discretized, coupled and can be expressed in a matrix form. Once all the values of the Dirichlet conditions (A_k) and the Neumann conditions ($\partial A_k / \partial n$) on Γ_C have been given by solving the matrix equation in a least square sense, the distribution of vector potential can be calculated using the boundary integral equation

$$A_{k,i} = \int_{\Gamma_C} \left(\phi_i^* \frac{\partial A_k}{\partial n} - A_k \frac{\partial \phi_i^*}{\partial n} \right) d\Gamma. \quad (k = x, y, z) \tag{11}$$

for arbitrary points 'i'.

2.4 Plasma boundary determination

In a nuclear fusion device, the magnetic field lines lie on nested toroidal magnetic surfaces. A plasma current line also lies on such a magnetic surface. To determine the plasma boundary, it is convenient to introduce a so-called magnetic surface function, ψ, which satisfies [3]

$$\mathbf{B} \cdot \nabla \psi = 0 . \tag{12}$$

One can define the plasma boundary as the outermost closed surface that is formed with the contour of ψ. For example, in tokamak-type axisymmetric plasma, the poloidal magnetic flux function ψ is defined as [1]

$$\psi = rA_{\varphi} , \tag{13}$$

where r denotes the major radius and A_{φ} the toroidal component of the vector potential.

3 Numerical examples

The ultimate goal of the authors' research is to identify the shape of non-axisymmetric plasma. Unfortunately a detailed model for such a complicated system has not yet been completed. As a second best, the case of axisymmetric plasma is dealt with to demonstrate the validity of the present 3-D CCS formulation. The following inverse analysis result is compared with the reference solution given by a direct analysis using the reliable equilibrium code SELENE [4] in JAEA.

One here assumes that 240 magnetic flux sensors and 960 magnetic field sensors are arranged outside the torus shape plasma. The Cauchy condition surface, which also has a torus shape, is placed within a domain that can be supposed to be inside the actual plasma. The ellipse in the centre of fig. 2 is the cross-section of the CCS on the r-z plane. Here the ellipse was set to have a major radius of 0.13m and a minor radius of 0.09m. This 3-D tube-shape CCS was divided into 16 discontinuous quadratic boundary elements, each of which has 9 nodal points.

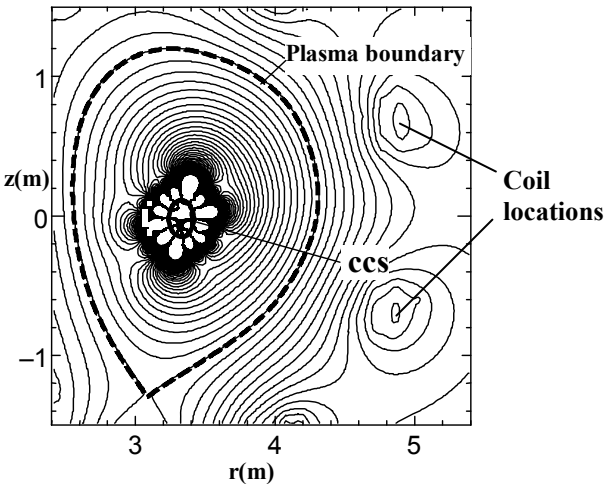

Figure 2: Contours of magnetic flux and the outermost magnetic surface.

Introducing the external coil current contributions $W_{k,i}$ and the magnetic sensor signals $\mathcal{L}A_{k,i}$, one can calculate A_k following eqns (3), (4) and (11). The magnetic flux function $\psi = rA_\varphi$ can then be obtained for arbitrary points 'i'. Thus, the outermost magnetic flux surface can be found by drawing contours of ψ. The solid lines in fig.2 are the obtained contours of magnetic flux. Note here that the contours drawn inside the plasma boundary have no physical meaning. Among the contours, however, the outermost closed curve represents the outermost magnetic surface, i.e. the plasma boundary. This reconstructed plasma boundary agrees well with the reference boundary profile (the dotted closed line in fig. 2) that had been assumed beforehand for the SELENE direct analysis. Coil locations outside the plasma are also found in fig. 2.

4 Conclusion and further remarks

A prototype of 3-dimensional CCS method code has been developed, in which the formulation is based on the 3-D distribution of vector potential. Before tackling complicated 3-D geometries, a preliminary 3-D test calculation was made for axisymmetric plasma. The results obtained here indicate that the new 3-D method can also determine the plasma boundary shape accurately in the same way as the 2-D CCS method.

The authors' future plan is to analyse the actual non-axisymmetric 3-D plasma in the LHD, which has a helical geometry. To realise this, the following problems should be solved:

(i) The x-, y- and z-components in eqn (4) should be solved simultaneously for an actual magnetic field sensor. For a flux loop signal, eqn (4) might be further integrated along the flux loop.

(ii) As it is difficult to derive mathematically the 3-D magnetic surface function ψ that satisfies $\mathbf{B}\cdot\nabla\psi = 0$ in a helical system, one needs to seek a practical way of drawing the magnetic field line that is tangential to the field vector.

(iii) Further, the rotational symmetry (not axisymmetry), which is peculiar to LHD, should be incorporated into the boundary integral formulation in order to reduce the number of unknowns.

Acknowledgements

The authors wish to express their gratitude to Dr. K. Kurihara of JAEA for his helpful guidance on the CCS method. Further, he kindly provided them with the reference JT-60 plasma data used in the numerical demonstration in section 3. This research was supported by the Ministry of Education, Culture, Sports, Science and Technology, Grant-in-Aid for Scientific Research (C), 20560762, 2008. This work was also performed with the support and under the auspices of the NIFS Collaboration Research Program (NIFS08KLHH308).

Appendix: validity of the vacuum field assumption for the plasma region

The proof shown below is written in terms of vector potential. Kurihara originally gave the proof in terms of magnetic flux in his work [5].

Now consider the domain Ω_{C-P} that is sandwiched between the plasma boundary (Γ_P) and the CCS (Γ_C), as illustrated in fig. 3.

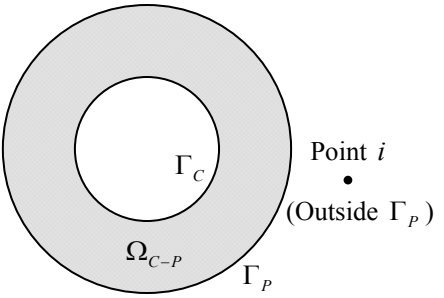

Figure 3: The domain Ω_{C-P} between Γ_P and Γ_C.

(i) Vector potential caused by the existence of plasma current:

The boundary integral equation in this case is written in the form

$$c_i \tilde{A}_{k,i} = \int_{\Gamma_C} \left(\phi_i^* \frac{\partial A_k}{\partial n} - A_k \frac{\partial \phi_i^*}{\partial n} \right) \mathrm{d}\Gamma + \int_{\Omega_{C-P}} (\mu_0 j_k) \phi_i^* \, \mathrm{d}\Omega + W_{k,i} \,. \tag{A1}$$

By adding

$$\int_{\Gamma_P} \left(\phi_i^* \frac{\partial A_k}{\partial n} - A_k \frac{\partial \phi_i^*}{\partial n} \right) \mathrm{d}\Gamma - \int_{\Gamma_P} \left(\phi_i^* \frac{\partial A_k}{\partial n} - A_k \frac{\partial \phi_i^*}{\partial n} \right) \mathrm{d}\Gamma = 0 \tag{A2}$$

to the RHS of eqn (A1), one obtains

$$c_i \tilde{A}_{k,i} = \int_{\Gamma_P} \left(\phi_i^* \frac{\partial A_k}{\partial n} - A_k \frac{\partial \phi_i^*}{\partial n} \right) \mathrm{d}\Gamma + W_{k,i} + c_i^{\#} \tilde{A}_{k,i}^{\#} \,, \tag{A3}$$

where the quantity $c_i^{\#} \tilde{A}_{k,i}^{\#}$ is given by

$$c_i^{\#} \tilde{A}_{k,i}^{\#} = \int_{\Gamma_C - \Gamma_P} \left(\phi_i^* \frac{\partial A_k}{\partial n} - A_k \frac{\partial \phi_i^*}{\partial n} \right) \mathrm{d}\Gamma + \int_{\Omega_{C-P}} (\mu_0 j_k) \phi_i^* \, \mathrm{d}\Omega \,. \tag{A4}$$

It should be noted that $c_i^{\#} = 0$ for any point outside Ω_{C-P}. Equation (A1) can then be transformed into

$$c_i \tilde{A}_{k,i} = \int_{\Gamma_P} \left(\phi_i^* \frac{\partial A_k}{\partial n} - A_k \frac{\partial \phi_i^*}{\partial n} \right) \mathrm{d}\Gamma + W_{k,i} \tag{A5}$$

that has no term related to the plasma current.

(ii) Vector potential when assuming a vacuum field for the plasma region:

The CCS method is based on the boundary integral equation for a vacuum field

$$c_i A_{k,i} = \int_{\Gamma_C} \left(\phi_i^* \frac{\partial A_k}{\partial n} - A_k \frac{\partial \phi_i^*}{\partial n} \right) \mathrm{d}\Gamma + W_{k,i}\,, \tag{A6}$$

which has no inhomogeneous term related to the plasma current. By adding

$$\int_{\Gamma_P} \left(\phi_i^* \frac{\partial A_k}{\partial n} - A_k \frac{\partial \phi_i^*}{\partial n} \right) \mathrm{d}\Gamma - \int_{\Gamma_P} \left(\phi_i^* \frac{\partial A_k}{\partial n} - A_k \frac{\partial \phi_i^*}{\partial n} \right) \mathrm{d}\Gamma = 0 \tag{A7}$$

to the RHS of eqn (A6), one obtains

$$c_i A_{k,i} = \int_{\Gamma_P} \left(\phi_i^* \frac{\partial A_k}{\partial n} - A_k \frac{\partial \phi_i^*}{\partial n} \right) \mathrm{d}\Gamma + W_{k,i} + c_i^{\#} A_{k,i}^{\#} \tag{A8}$$

with

$$c_i^{\#} A_{k,i}^{\#} = \int_{\Gamma_{C-P}} \left(\phi_i^* \frac{\partial A_k}{\partial n} - A_k \frac{\partial \phi_i^*}{\partial n} \right) \mathrm{d}\Gamma\,. \tag{A9}$$

The value of $c_i^{\#}$ in eqn (A9) must be zero for any point outside Ω_{C-P}. Thus one obtains

$$c_i A_{k,i} = \int_{\Gamma_P} \left(\phi_i^* \frac{\partial A_k}{\partial n} - A_k \frac{\partial \phi_i^*}{\partial n} \right) \mathrm{d}\Gamma + W_{k,i}\,. \tag{A10}$$

(iii) Conclusion

As the RHS of eqn (A10) is exactly the same as the RHS of eqn (A5), it is concluded that eqn (A6) is identical to eqn (A1), i.e., $A_{k,i} = \tilde{A}_{k,i}$. That is, the vector potential calculated under the assumption of a vacuum field even for the plasma region is exactly the same as the vector potential caused by the existence of plasma current.

References

[1] Kurihara, K., *Fusion Eng. Des.*, 51-52, pp. 1049-1057, 2000.
[2] Itagaki, M., Yamaguchi, S., Fukunaga, T., *Nucl. Fusion*, 45, pp. 153-162, 2005.
[3] Wesson, J, "*Tokamaks* (*Second edition*)", The Oxford Engineering Series 48, Clarendon Press, Oxford, 1997.
[4] Takeda, T., Tsunematsu, T., *JAERI-M 8042*, Japan Atomic Energy Research Institute, 1978.
[5] Kurihara, K., *Nucl. Fusion*, 33, pp. 399-412, 1993.

Author Index

This page intentionally left blank

WITPRESS ...for scientists by scientists

Boundary Collocation Techniques and their Application in Engineering

J.A. Kołodziej *and* ***A.P. Zieliński*****,** *University of Technology, Poland*

Methods of mathematical modelling applied in contemporary computational mechanics can be either purely numerical or analytical-numerical procedures. Purely analytical solutions lose their popularity because of strong limitations connected with simple regions and the mostly linear equations to which they can be applied. Obviously, the fundamental monographs (for example, insert those on elastic solids, fluid mechanics or heat exchange) are always popular and often quoted, but rather as sources of comparative benchmarks confirming correctness and accuracy of computer solutions.

This volume can be divided into two parts. In the first part is a general presentation of the boundary collocation approach and its numerous variants. In the second part the method is applied to many different engineering problems, showing its properties, accuracy and convergence. Both evident advantages and also limitations of the approach are clearly presented. The observations are based mainly on investigations carried out in the last two decades by the authors and their co-operators. The monograph includes figures and tables that present results of numerical examples. A considerable number (above 1000) of papers and monographs concerning the discussed approach are quoted. They are listed separately in each chapter, which makes the literature survey easier to use.

ISBN: 978-1-84564-394-2 2009 apx 300pp
apx £99.00/US$198.00/€129.00
eISBN: 978-1-84564-395-9

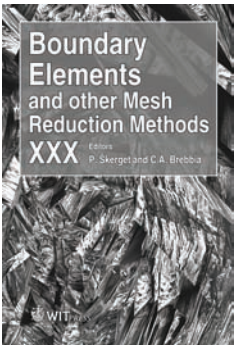

Boundary Elements and Other Mesh Reduction Methods XXX

Edited by: ***L. ŠKERGET****, University of Maribor, Slovenia and* ***C.A. BREBBIA****, Wessex Institute of Technology, UK*

The major motivation behind the Boundary Element Method (BEM) was to reduce the dependency of analysis on the definition of meshes. This has allowed the method to expand naturally into new techniques such as Dual Reciprocity while all other Mesh Reduction Methods (MRM). MRM and BEM continue to be very active areas of research with many of the resulting techniques being successfully applied to solve increasingly complex problems.

This book contains papers presented at the much-acclaimed Thirtieth International Conference on Boundary Elements and other Mesh Reduction Methods. The proceedings contain papers on practically all major developments in Boundary Elements, including the most recent MRM techniques, grouped under the following topics: Fluid Flow; Heat Transfer; Electrical Engineering and Electromagnetics; Damange Mechanics and Fracture; Mesh Reduction Techniques; Advanced Compatational Techniques.

The book should be of interest to engineers and scientists within the areas of numerical analysis, boundary elements and meshless methods.

WIT Transactions on Modelling and Simulation, Vol 47
ISBN: 978-1-84564-121-4 2008 288pp
£95.00/US$190.00/€123.50
eISBN: 978-1-84564-329-4